

Advances in Civil Engineering

# Mechanical and Hydraulic Properties of Rock Joints

Lead Guest Editor: Zhi Cheng Tang

Guest Editors: Richeng Liu, Yingchun Li, Man Huang, Xiaobo Zhang, and Suguang Xiao



---



# **Mechanical and Hydraulic Properties of Rock Joints**

Advances in Civil Engineering

---

## **Mechanical and Hydraulic Properties of Rock Joints**

Lead Guest Editor: Zhi Cheng Tang

Guest Editors: Richeng Liu, Yingchun Li, Man  
Huang, Xiaobo Zhang, and Suguang Xiao



---

Copyright © 2021 Hindawi Limited. All rights reserved.

This is a special issue published in "Advances in Civil Engineering." All articles are open access articles distributed under the Creative Commons Attribution License, which permits unrestricted use, distribution, and reproduction in any medium, provided the original work is properly cited.






# Chief Editor

Cumaraswamy Vipulanandan, USA
















## Associate Editors

Chiara Bedon , Italy  
Constantin Chalioris , Greece  
Ghassan Chehab , Lebanon  
Ottavia Corbi, Italy  
Mohamed ElGawady , USA  
Husnain Haider , Saudi Arabia  
Jian Ji , China  
Jiang Jin , China  
Shazim A. Memon , Kazakhstan  
Hossein Moayedi , Vietnam  
Sanjay Nimbalkar, Australia  
Giuseppe Oliveto , Italy  
Alessandro Palmeri , United Kingdom  
Arnaud Perrot , France  
Hugo Rodrigues , Portugal  
Victor Yepes , Spain  
Xianbo Zhao , Australia

## Academic Editors

José A.F.O. Correia, Portugal  
Glenda Abate, Italy  
Khalid Abdel-Rahman , Germany  
Ali Mardani Aghabaglou, Turkey  
José Aguiar , Portugal  
Afaq Ahmad , Pakistan  
Muhammad Riaz Ahmad , Hong Kong  
Hashim M.N. Al-Madani , Bahrain  
Luigi Aldieri , Italy  
Angelo Aloisio , Italy  
Maria Cruz Alonso, Spain  
Filipe Amarante dos Santos , Portugal  
Serji N. Amirkhania, USA  
Eleftherios K. Anastasiou , Greece  
Panagiotis Ch. Anastasopoulos , USA  
Mohamed Moafak Arbili , Iraq  
Farhad Aslani , Australia  
Siva Avudaiappan , Chile  
Ozgur BASKAN , Turkey  
Adewumi Babafemi, Nigeria  
Morteza Bagherpour, Turkey  
Qingsheng Bai , Germany  
Nicola Baldo , Italy  
Daniele Baraldi , Italy

Eva Barreira , Portugal  
Emilio Bastidas-Arteaga , France  
Rita Bento, Portugal  
Rafael Bergillos , Spain  
Han-bing Bian , China  
Xia Bian , China  
Huseyin Bilgin , Albania  
Giovanni Biondi , Italy  
Hugo C. Biscaia , Portugal  
Rahul Biswas , India  
Edén Bojórquez , Mexico  
Giosuè Boscato , Italy  
Melina Bosco , Italy  
Jorge Branco , Portugal  
Bruno Briseghella , China  
Brian M. Broderick, Ireland  
Emanuele Brunesi , Italy  
Quoc-Bao Bui , Vietnam  
Tan-Trung Bui , France  
Nicola Buratti, Italy  
Gaochuang Cai, France  
Gladis Camarini , Brazil  
Alberto Campisano , Italy  
Qi Cao, China  
Qixin Cao, China  
Iacopo Carnacina , Italy  
Alessio Cascardi, Italy  
Paolo Castaldo , Italy  
Nicola Cavalagli , Italy  
Liborio Cavaleri , Italy  
Anush Chandrappa , United Kingdom  
Wen-Shao Chang , United Kingdom  
Muhammad Tariq Amin Chaudhary, Kuwait  
Po-Han Chen , Taiwan  
Qian Chen , China  
Wei Tong Chen , Taiwan  
Qixiu Cheng, Hong Kong  
Zhanbo Cheng, United Kingdom  
Nicholas Chileshe, Australia  
Prinya Chindaprasirt , Thailand  
Corrado Chisari , United Kingdom  
Se Jin Choi , Republic of Korea  
Heap-Yih Chong , Australia  
S.H. Chu , USA  
Ting-Xiang Chu , China

Zhaofei Chu , China  
Wonseok Chung , Republic of Korea  
Donato Ciampa , Italy  
Gian Paolo Cimellaro, Italy  
Francesco Colangelo, Italy  
Romulus Costache , Romania  
Liviu-Adrian Cotfas , Romania  
Antonio Maria D'Altri, Italy  
Bruno Dal Lago , Italy  
Amos Darko , Hong Kong  
Arka Jyoti Das , India  
Dario De Domenico , Italy  
Gianmarco De Felice , Italy  
Stefano De Miranda , Italy  
Maria T. De Risi , Italy  
Tayfun Dede, Turkey  
Sadik O. Degertekin , Turkey  
Camelia Delcea , Romania  
Cristoforo Demartino, China  
Giuseppe Di Filippo , Italy  
Luigi Di Sarno, Italy  
Fabio Di Trapani , Italy  
Aboelkasim Diab , Egypt  
Thi My Dung Do, Vietnam  
Giulio Dondi , Italy  
Jiangfeng Dong , China  
Chao Dou , China  
Mario D'Aniello , Italy  
Jingtao Du , China  
Ahmed Elghazouli, United Kingdom  
Francesco Fabbrocino , Italy  
Flora Faleschini , Italy  
Dingqiang Fan, Hong Kong  
Xueping Fan, China  
Qian Fang , China  
Salar Farahmand-Tabar , Iran  
Ilenia Farina, Italy  
Roberto Fedele, Italy  
Guang-Liang Feng , China  
Luigi Fenu , Italy  
Tiago Ferreira , Portugal  
Marco Filippo Ferrotto, Italy  
Antonio Formisano , Italy  
Guoyang Fu, Australia  
Stefano Galassi , Italy

Junfeng Gao , China  
Meng Gao , China  
Giovanni Garcea , Italy  
Enrique García-Macías, Spain  
Emilio García-Taengua , United Kingdom  
DongDong Ge , USA  
Khaled Ghaedi, Malaysia  
Khaled Ghaedi , Malaysia  
Gian Felice Giaccu, Italy  
Agathoklis Giaralis , United Kingdom  
Ravindran Gobinath, India  
Rodrigo Gonçalves, Portugal  
Peilin Gong , China  
Belén González-Fonteboa , Spain  
Salvatore Grasso , Italy  
Fan Gu, USA  
Erhan Güneyisi , Turkey  
Esra Mete Güneyisi, Turkey  
Pingye Guo , China  
Ankit Gupta , India  
Federico Gusella , Italy  
Kemal Hacıfendioglu, Turkey  
Jianyong Han , China  
Song Han , China  
Asad Hanif , Macau  
Hadi Hasanzadehshooiili , Canada  
Mostafa Fahmi Hassanein, Egypt  
Amir Ahmad Hedayat , Iran  
Khandaker Hossain , Canada  
Zahid Hossain , USA  
Chao Hou, China  
Biao Hu, China  
Jiang Hu , China  
Xiaodong Hu, China  
Lei Huang , China  
Cun Hui , China  
Bon-Gang Hwang, Singapore  
Jijo James , India  
Abbas Fadhil Jasim , Iraq  
Ahad Javanmardi , China  
Krishnan Prabhakan Jaya, India  
Dong-Sheng Jeng , Australia  
Han-Yong Jeon, Republic of Korea  
Pengjiao Jia, China  
Shaohua Jiang , China

MOUSTAFA KASSEM , Malaysia  
Mosbeh Kaloop , Egypt  
Shankar Karuppannan , Ethiopia  
John Kechagias , Greece  
Mohammad Khajehzadeh , Iran  
Afzal Husain Khan , Saudi Arabia  
Mehran Khan , Hong Kong  
Manoj Khandelwal, Australia  
Jin Kook Kim , Republic of Korea  
Woosuk Kim , Republic of Korea  
Vaclav Koci , Czech Republic  
Loke Kok Foong, Vietnam  
Hailing Kong , China  
Leonidas Alexandros Kouris , Greece  
Kyriakos Kourousis , Ireland  
Moacir Kripka , Brazil  
Anupam Kumar, The Netherlands  
Emma La Malfa Ribolla, Czech Republic  
Ali Lakirouhani , Iran  
Angus C. C. Lam, China  
Thanh Quang Khai Lam , Vietnam  
Luciano Lamberti, Italy  
Andreas Lampropoulos , United Kingdom  
Raffaele Landolfo, Italy  
Massimo Latour , Italy  
Bang Yeon Lee , Republic of Korea  
Eul-Bum Lee , Republic of Korea  
Zhen Lei , Canada  
Leonardo Leonetti , Italy  
Chun-Qing Li , Australia  
Dongsheng Li , China  
Gen Li, China  
Jiale Li , China  
Minghui Li, China  
Qingchao Li , China  
Shuang Yang Li , China  
Sunwei Li , Hong Kong  
Yajun Li , China  
Shun Liang , China  
Francesco Liguori , Italy  
Jae-Han Lim , Republic of Korea  
Jia-Rui Lin , China  
Kun Lin , China  
Shibin Lin, China

Tzu-Kang Lin , Taiwan  
Yu-Cheng Lin , Taiwan  
Hexu Liu, USA  
Jian Lin Liu , China  
Xiaoli Liu , China  
Xuemei Liu , Australia  
Zaobao Liu , China  
Zhuang-Zhuang Liu, China  
Diego Lopez-Garcia , Chile  
Cristiano Loss , Canada  
Lyan-Ywan Lu , Taiwan  
Jin Luo , USA  
Yanbin Luo , China  
Jianjun Ma , China  
Junwei Ma , China  
Tian-Shou Ma, China  
Zhongguo John Ma , USA  
Maria Macchiaroli, Italy  
Domenico Magisano, Italy  
Reza Mahinroosta, Australia  
Yann Malecot , France  
Prabhat Kumar Mandal , India  
John Mander, USA  
Iman Mansouri, Iran  
André Dias Martins, Portugal  
Domagoj Matesan , Croatia  
Jose Matos, Portugal  
Vasant Matsagar , India  
Claudio Mazzotti , Italy  
Ahmed Mebarki , France  
Gang Mei , China  
Kasim Mermerdas, Turkey  
Giovanni Minafò , Italy  
Masoomah Mirrashid , Iran  
Abbas Mohajerani , Australia  
Fadzli Mohamed Nazri , Malaysia  
Fabrizio Mollaioli , Italy  
Rosario Montuori , Italy  
H. Naderpour , Iran  
Hassan Nasir , Pakistan  
Hossein Nassiraei , Iran  
Satheeskumar Navaratnam , Australia  
Ignacio J. Navarro , Spain  
Ashish Kumar Nayak , India  
Behzad Nematollahi , Australia

Chayut Ngamkhanong , Thailand  
Trung Ngo, Australia  
Tengfei Nian, China  
Mehdi Nikoo , Canada  
Youjun Ning , China  
Olugbenga Timo Oladinrin , United Kingdom  
Oladimeji Benedict Olalusi, South Africa  
Timothy O. Olawumi , Hong Kong  
Alejandro Orfila , Spain  
Maurizio Orlando , Italy  
Siti Aminah Osman, Malaysia  
Walid Oueslati , Tunisia  
SUVASH PAUL , Bangladesh  
John-Paris Pantouvakis , Greece  
Fabrizio Paolacci , Italy  
Giuseppina Pappalardo , Italy  
Fulvio Parisi , Italy  
Dimitrios G. Pavlou , Norway  
Daniele Pellegrini , Italy  
Gatheeshgar Perampalam , United Kingdom  
Daniele Perrone , Italy  
Giuseppe Piccardo , Italy  
Vagelis Plevris , Qatar  
Andrea Pranno , Italy  
Adolfo Preciado , Mexico  
Chongchong Qi , China  
Yu Qian, USA  
Ying Qin , China  
Giuseppe Quaranta , Italy  
Krishanu ROY , New Zealand  
Vlastimir Radonjanin, Serbia  
Carlo Rainieri , Italy  
Rahul V. Ralegaonkar, India  
Raizal Saifulnaz Muhammad Rashid, Malaysia  
Alessandro Rasulo , Italy  
Chonghong Ren , China  
Qing-Xin Ren, China  
Dimitris Rizos , USA  
Geoffrey W. Rodgers , New Zealand  
Pier Paolo Rossi, Italy  
Nicola Ruggieri , Italy  
JUNLONG SHANG, Singapore

Nikhil Saboo, India  
Anna Saetta, Italy  
Juan Sagaseta , United Kingdom  
Timo Saksala, Finland  
Mostafa Salari, Canada  
Ginevra Salerno , Italy  
Evangelos J. Sapountzakis , Greece  
Vassilis Sarhosis , United Kingdom  
Navaratnarajah Sathiparan , Sri Lanka  
Fabrizio Scozzese , Italy  
Halil Sezen , USA  
Payam Shafigh , Malaysia  
M. Shahria Alam, Canada  
Yi Shan, China  
Hussein Sharaf, Iraq  
Mostafa Sharifzadeh, Australia  
Sanjay Kumar Shukla, Australia  
Amir Si Larbi , France  
Okan Sirin , Qatar  
Piotr Smarzewski , Poland  
Francesca Sollecito , Italy  
Rui Song , China  
Tian-Yi Song, Australia  
Flavio Stochino , Italy  
Mayank Sukhija , USA  
Piti Sukontasukkul , Thailand  
Jianping Sun, Singapore  
Xiao Sun , China  
T. Tafsirojjaman , Australia  
Fujiao Tang , China  
Patrick W.C. Tang , Australia  
Zhi Cheng Tang , China  
Weerachart Tangchirapat , Thailand  
Xiixin Tao, China  
Piergiorgio Tataranni , Italy  
Elisabete Teixeira , Portugal  
Jorge Iván Tobón , Colombia  
Jing-Zhong Tong, China  
Francesco Trentadue , Italy  
Antonello Troncone, Italy  
Majbah Uddin , USA  
Tariq Umar , United Kingdom  
Muahmmad Usman, United Kingdom  
Muhammad Usman , Pakistan  
Mucteba Uysal , Turkey




Ilaria Venanzi , Italy  
Castorina S. Vieira , Portugal  
Valeria Vignali , Italy  
Claudia Vitone , Italy  
Liwei WEN , China  
Chunfeng Wan , China  
Hua-Ping Wan, China  
Roman Wan-Wendner , Austria  
Chaohui Wang , China  
Hao Wang , USA  
Shiming Wang , China  
Wayne Yu Wang , United Kingdom  
Wen-Da Wang, China  
Xing Wang , China  
Xiuling Wang , China  
Zhenjun Wang , China  
Xin-Jiang Wei , China  
Tao Wen , China  
Weiping Wen , China  
Lei Weng , China  
Chao Wu , United Kingdom  
Jiangyu Wu, China  
Wangjie Wu , China  
Wenbing Wu , China  
Zhixing Xiao, China  
Gang Xu, China  
Jian Xu , China  
Panpan , China  
Rongchao Xu , China  
HE YONGLIANG, China  
Michael Yam, Hong Kong  
Hailu Yang , China  
Xu-Xu Yang , China  
Hui Yao , China  
Xinyu Ye , China  
Zhoujing Ye, China  
Gürol Yildirim , Turkey  
Dawei Yin , China  
Doo-Yeol Yoo , Republic of Korea  
Zhanping You , USA  
Afshar A. Yousefi , Iran  
Xinbao Yu , USA  
Dongdong Yuan , China  
Geun Y. Yun , Republic of Korea

Hyun-Do Yun , Republic of Korea  
Cemal YİĞİT , Turkey  
Paolo Zampieri, Italy  
Giulio Zani , Italy  
Mariano Angelo Zanini , Italy  
Zhixiong Zeng , Hong Kong  
Mustafa Zeybek, Turkey  
Henglong Zhang , China  
Jiupeng Zhang, China  
Tingting Zhang , China  
Zengping Zhang, China  
Zetian Zhang , China  
Zhigang Zhang , China  
Zhipeng Zhao , Japan  
Jun Zhao , China  
Annan Zhou , Australia  
Jia-wen Zhou , China  
Hai-Tao Zhu , China  
Peng Zhu , China  
QuanJie Zhu , China  
Wenjun Zhu , China  
Marco Zucca, Italy  
Haoran Zuo, Australia  
Junqing Zuo , China  
Robert Černý , Czech Republic  
Süleyman İpek , Turkey






# Contents

## **Effect of Morphology Parameter Determination on Contact Behavior of Rock Joints under Compressive Loading**

Feng Tian Tang and Zhi Cheng Tang 

Research Article (8 pages), Article ID 6669422, Volume 2021 (2021)

## **Numerical Simulation of the Nonlinear Flow Properties in Self-Affine Aperture-Based Fractures**

Xin Zhou , Jianlong Sheng , Ruili Lu , Zuyang Ye , and Wang Luo 

Research Article (11 pages), Article ID 6687878, Volume 2021 (2021)

## **Stability Assessment of High and Steep Cutting Rock Slopes with the SSPC Method**

Hongliang Tao, Guangli Xu, Jingwen Meng, Ronghe Ma, and Jiaying Dong 



Research Article (10 pages), Article ID 8889526, Volume 2021 (2021)

## **A Typical Basalt Platform Landslide: Mechanism and Stability Prediction of Xiashan Landslide**

Yongliang Huang, Zhiwei Sun, Chunyan Bao , Man Huang , Anyuan Li, and Minghao Liu 

Research Article (14 pages), Article ID 6697040, Volume 2021 (2021)

## **A Fractal Model for Predicting the Relative Permeability of Rough-Walled Fractures**

Zuyang Ye , Wang Luo, Shibing Huang , Yuting Chen, and Aiping Cheng



Research Article (10 pages), Article ID 6623275, Volume 2021 (2021)

## **A New Statistical Parameter for Determining Joint Roughness Coefficient (JRC) considering the Shear Direction and Contribution of Different Protrusions**

Jiu-yang Huan , Zhi-qiang Zhang , Ming-ming He , and Ning Li 

Research Article (15 pages), Article ID 6641201, Volume 2021 (2021)

## **Shear Characteristics and Strength Criterion of Frozen Joints under Different Opening Degrees**

Shiwei Shen , Lin Gan, Chang Liu , and Shulin Dai





Research Article (13 pages), Article ID 6636968, Volume 2021 (2021)

## **Comparative Study on Mineral-Scale Microcrack Propagation of Shale under Different Loading Methods**

Jianyong Zhang , Zhendong Cui , Weige Han, Kai Si , and Yan Zhao


Research Article (18 pages), Article ID 6621347, Volume 2021 (2021)

## **Dynamic Mechanical Characteristics of Fractured Rock Reinforced by Different Grouts**

Siming Kao , Guangming Zhao , Xiangrui Meng, Yingming Li , Zenghui Liu, Ruofei Zhang, Jun Zhou, and Shunjie Huang 


Research Article (14 pages), Article ID 8897537, Volume 2021 (2021)

## **The Friction Angle of the Leiyang Marble Surface after Exposure to High Temperature**

Meng Hong Peng and Man Huang 

Research Article (10 pages), Article ID 8852686, Volume 2021 (2021)

### **Correlations between Geometric Properties and Permeability of 2D Fracture Networks**

Xiaolin Wang , Liyuan Yu , and Hanqing Yang 





Research Article (7 pages), Article ID 6645238, Volume 2021 (2021)

### **Study on Permeability of Deep-Buried Sandstone under Triaxial Cyclic Loads**

Mingqiang Sheng , Awei Mabi, and Xigen Lu 

Research Article (9 pages), Article ID 6635245, Volume 2021 (2021)

### **Change Detection and Feature Extraction of Debris-Flow Initiation by Rock-Slope Failure Using Point Cloud Processing**

Xiaoying He , Zeqing Yu , John M. Kemeny, Ann Youberg , and Yunkun Wang 

Research Article (11 pages), Article ID 6659996, Volume 2021 (2021)

### **Research on Bearing Theory of Squeezed Branch Pile**

Hong-wei Ma , Yi-ying Wu , Yu Tong, and Xiao-qiang Jiang

Research Article (12 pages), Article ID 6637261, Volume 2020 (2020)

### **Study on Identification of Construction Method for Ultra-Large-Span Tunnel**

Xu Chongbang  and Qin Youlin 


Research Article (11 pages), Article ID 6625940, Volume 2020 (2020)

### **A Method and Equipment for Continuously Testing the Permeability Coefficient of Rock and Soil Layers**

Wei Chen , Datian Cui, Meng Xu, and Rongchao Xu 





Research Article (6 pages), Article ID 6639892, Volume 2020 (2020)

### **Structural Mechanical Characteristics and Instability Law of Roof Key Block Breaking in Gob-Side Roadway**

Xinfeng Wang , Mingyuan Lu, Yuhao Gao, Wenbo Luo, and Wengang Liu

Research Article (12 pages), Article ID 6682303, Volume 2020 (2020)

### **Experimental Study on the Temperature Field of Cold Region Tunnel under Various Groundwater Seepage Velocities**

Shiding Cao , Taishan Lu , Bo Zheng , and Guozhu Zhang 


Research Article (14 pages), Article ID 6695099, Volume 2020 (2020)

### **Analysis of Rock $\beta$ -Dynamic Parameters and the Stability of Earthquake Dangerous Rocks Based on PFC**

Yun Tian , Lin-feng Wang , Biao Zeng , and Hong-hua Jin 

Research Article (17 pages), Article ID 6659254, Volume 2020 (2020)

### **Application of Digital Image Correlation Technique for the Damage Characteristic of Rock-like Specimens under Uniaxial Compression**

Jing Chai, Yongliang Liu , YiBo OuYang, Dingding Zhang, and Wengang Du

Research Article (11 pages), Article ID 8857495, Volume 2020 (2020)

# Contents

---

## **Estimation of the Occurrence Time of Thaumassite Sulfate Attack on Tunnel Lining Concrete**

Chongbang Xu, Xiaojing Gao , Xuefeng Li, and Kaishun Zhang




Research Article (11 pages), Article ID 6656304, Volume 2020 (2020)

## **Experimental Study on Mechanical Properties of Deep Buried Granite under Different Confining Pressures**

Jun Zhao  and Tan Zhang


Research Article (10 pages), Article ID 6640497, Volume 2020 (2020)

## **Effects of Different Conditions of Water Cooling at High Temperature on the Tensile Strength and Split Surface Roughness Characteristics of Hot Dry Rock**

Hanbo Cui , Jupeng Tang , and Xintong Jiang 


Research Article (23 pages), Article ID 8868140, Volume 2020 (2020)

## **Response Analysis of Deep Foundation Excavation and Dewatering on Surface Settlements**

Xian Li, Tingguo Zhou, Yixian Wang , Junling Han, Yanqiao Wang, Fang Tong, Delong Li, and Jinmei Wen


Research Article (10 pages), Article ID 8855839, Volume 2020 (2020)

## **Stability Analysis of Jointed Rock Slope by Strength Reduction Technique considering Ubiquitous Joint Model**

Ruili Lu, Wei Wei , Kaiwei Shang, and Xiangyang Jing

Research Article (13 pages), Article ID 8862243, Volume 2020 (2020)

## **Constitutive Model of Swelling Gypsum Rock**

Chongbang Xu, Xiaojing Gao , Kaishun Zhang, Zhiguo Liu, and Fan Zhao

Research Article (9 pages), Article ID 8878005, Volume 2020 (2020)

## Research Article

# Effect of Morphology Parameter Determination on Contact Behavior of Rock Joints under Compressive Loading

Feng Tian Tang and Zhi Cheng Tang 

Faculty of Engineering, China University of Geosciences, Wuhan 430074, Hubei, China

Correspondence should be addressed to Zhi Cheng Tang; zctang@cug.edu.cn

Received 28 November 2020; Accepted 10 July 2021; Published 24 July 2021

Academic Editor: Hassan Nasir

Copyright © 2021 Feng Tian Tang and Zhi Cheng Tang. This is an open access article distributed under the Creative Commons Attribution License, which permits unrestricted use, distribution, and reproduction in any medium, provided the original work is properly cited.

The closure behavior of rock joints is of critical importance to the study of hydromechanical behaviors and geophysical properties of jointed rock masses. Theoretical contact models, used to predict the relations of normal stress versus closure deformation, rely on morphology parameters of rock joint as the input parameters. The relevance of the contact models depends on the inherent assumptions and the accuracy with which the input parameters are determined. In the present study, morphology parameters of three rock joints are determined by the spectral moment approach and peak identification method, respectively. The differences are found to vary significantly depending on the selected method. The phenomenon would be related to the definition of an asperity peak on joint profile. The spectral method only considers the so-called asperity peaks, while the deterministic approach further accounts for the asperity shoulders. Finally, the morphology parameters determined by the two methods are treated as the input parameters of a validated theoretical model. The comparisons between the theoretical curves and the experimental results indicate that parameters determined by the deterministic method would be more reliable.

## 1. Introduction

Rock joints affect the mechanical properties of rocks, so do the morphology parameters of joints [1, 2]. Topography of a solid surface has small-scale geometric features with random shapes and sizes, usually called “asperities.” Distribution of asperities over the surface forms a random geometric structure which is in general known as “roughness,” playing an important role in the mechanical behaviors of two contact rough surfaces, e.g., shear strength, closure deformation, or contact stiffness of rock joint. Various parameters have been proposed to describe rock joint topography based on different characterizing approaches. For rock joint, the application of available morphology parameters can fall broadly into three categories: (1) describing the geometrical features, such as Tse and Cruden [3], International Society for Rock Mechanics [4], Xie et al. [5], Belem et al. [6], Zhang et al. [7], and Li and Zhang [8]; (2) establishing the peak shear strength criteria, such as Barton and Choubey [9], Tatone and Grasselli [10], and Rasouli and Harrison [11];

and (3) serving as input parameters for theoretical contact models, such as Greenwood and Williamson [12], Brown and Scholz [13], Misra [14], Lanaro and Stephansson [15], and Xia et al. [16]. Here, we pay special attention to the last one, mainly including average peak radius of curvature ( $\beta$ ), peak density ( $\eta$ ), and standard deviation of peak height ( $\sigma_s$ ). As such, the relevance of the theoretical models is dependent on their inherent assumptions and the accuracy with which the input parameters are determined.

Commonly, two methods are used to determine the mentioned morphology parameters. According to Nayak [17], a random and isotropic surface with a Gaussian height distribution can be adequately characterized by zeroth ( $M_0$ ), second ( $M_2$ ), and fourth ( $M_4$ ) moments of the power spectral density function. To better capture the topography of a natural solid surface with anisotropic roughness nature, average values of spectral moments obtained from a finite number of cross sections in a surface were used [18]. Essentially, the spectral moment approach is in a statistical sense [19], rather than a method based on the real asperities

randomly distributed on the rough surface. The other method to determine the morphology parameters is based on individually identified asperity peaks as local maxima [20], and the above three parameters can then be calculated directly from these identified peaks, called as peak identification method (deterministic method). The deterministic method can avoid the averaging treatment inherent to the previously described spectral moment approach and is based on the actual 3D surface topography. Both the methods, suffering from varied sources of uncertainty, can serve as input parameters to theoretical models to describe the contact behaviors of a rock joint [21]. However, there is no analysis available in the literature to comprehensively compare the differences of the two methods for “real” rock joint (not numerically generated surfaces). Accordingly, the main objective of the present study is to provide a comprehensive understanding towards the quantification of morphology parameters of rock joints by the spectral moment approach and the deterministic method.

## 2. Methodology

*2.1. Morphology of Rock Joint.* The topography of a rock joint is usually composed of small-scale unevenness and large-scale waviness [4], which have different influences on the joint closure behaviors [16, 21]. Three rock joints with nominal length of 300 mm are selected for the analysis of peak spatial features, as shown in Figure 1. Rock joint J-I is composed of only unevenness component and J-II is composed of both unevenness and waviness components, while J-III is mainly composed of waviness component [22]. To sufficiently characterize the morphology, sample interval of 1.0 mm is used in  $x$  and  $y$  directions (generally, sample interval is within the range from 0.3 to 1.0 mm). Average heights (m) of the three rock joints are 1.65, 3.58, and 8.70 mm, respectively. Gaussian distribution function, equation (1), is used to analyze the distribution of asperity height, and all the fitting results are listed in Table 1 [23]. The high correlation indicates that the morphologies of the three rock joints exhibit Gaussian distribution. Hence, the spectral moment approach can be used to evaluate the morphology parameters.

$$f(z) = \frac{1}{\sqrt{2\pi}\sigma} \exp\left[-\frac{1}{2}\left(\frac{z-\mu}{\sigma}\right)^2\right], \quad (1)$$

where  $f(\bullet)$  is the symbol of Gaussian function,  $z$  is the surface height,  $\sigma$  is the standard deviation of height, and  $\mu$  is the expectation of height.

*2.2. Spectral Moment Approach.* For a given rough profile with a Gaussian height distribution, the asperity height denoted by  $Z(x)$ , the spectral moments,  $M_0$ ,  $M_2$ , and  $M_4$ , can be determined by the following [17]:

$$\begin{aligned} M_0 &= \text{AVG}\left[\left(Z^2\right)\right], \\ M_2 &= \text{AVG}\left[\left(\frac{dz}{dx}\right)^2\right], \\ M_4 &= \text{AVG}\left[\left(\frac{d^2z}{dx^2}\right)^2\right], \end{aligned} \quad (2)$$

where AVG represents the arithmetic average.

Once  $M_0$ ,  $M_2$ , and  $M_4$  are known, the morphology parameters,  $\beta$ ,  $\eta$ , and  $\sigma_s$ , can then be calculated by [17]

$$\begin{aligned} \beta &= 0.375\sqrt{\frac{\pi}{m_4}}, \\ \eta &= \frac{1}{6\pi\sqrt{3}}\left(\frac{m_4}{m_2}\right), \\ \sigma_s &= \left(1 - \frac{0.8968}{\alpha}\right)^{0.5} \sqrt{m_0}, \end{aligned} \quad (3)$$

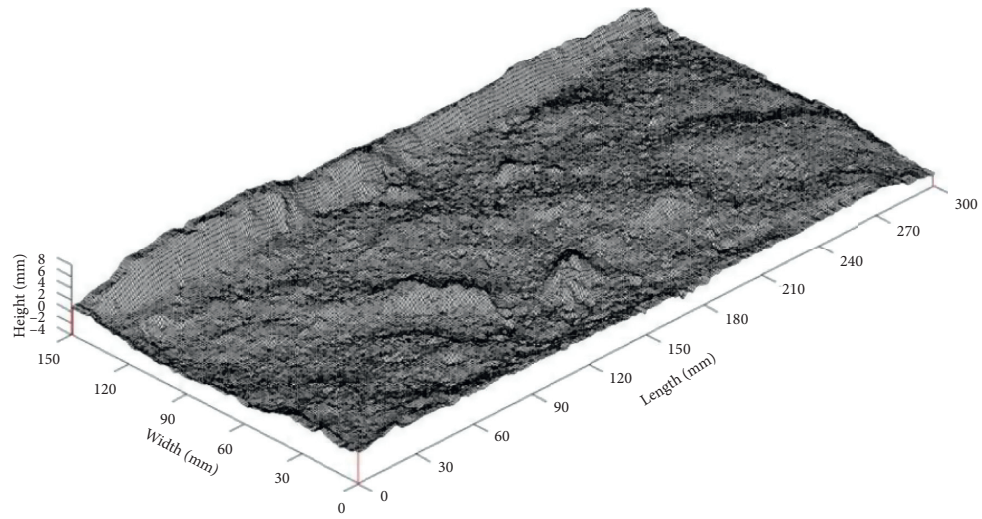
where  $\alpha = (m_0 m_4)/m_2^2$ , which is called the bandwidth parameter.

According to McCool [18], the value of the three parameters may vary significantly when calculated for an arbitrary single 2D trace. To overcome the limitations, 9 sectional profiles with equal spacing of 15 mm parallel to the analysis direction ( $x$  direction in the present study) are extracted (Figure 2). The spectral moments for each profile are calculated, and the averaged value is used to determine the corresponding morphology parameters.

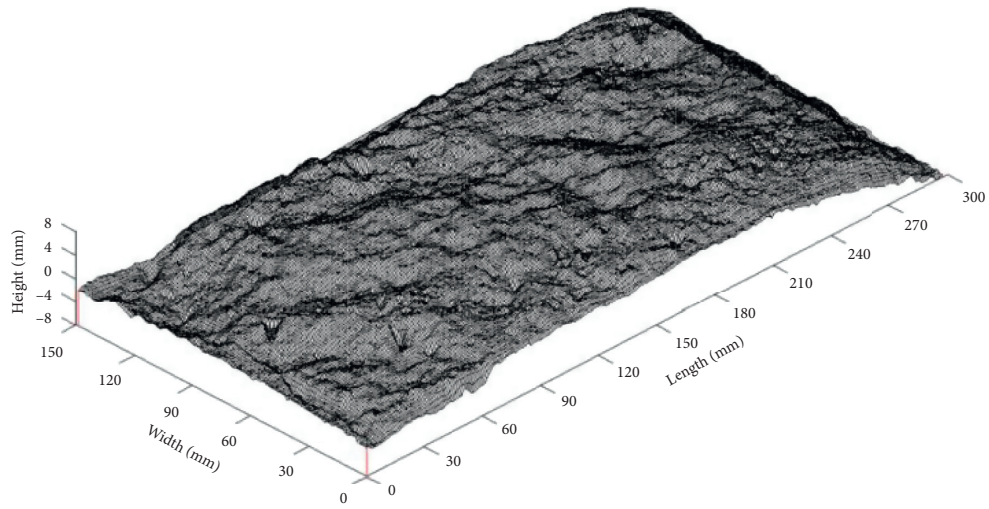
*2.3. Deterministic Method.* As schematically shown in Figure 3, a peak on a profile is defined as a point with height higher than its  $N$  adjacent points ( $N = 3, 5, 7, \dots$ ). An N-PP criterion identifies a point as a peak if its height exceeds that of its  $(N - 1)$  nearest neighbor points, resulting in  $0.5(N - 1)$  points on each side of the peak. Compared to 5PP and 7PP criteria, 3PP criterion would be more reliable to identify the peaks on a rock joint profile, which was also widely used [21, 22, 24–27]. The peak density and standard deviation of peak height can be directly calculated as all the peaks are identified. The radius of curvature for each peak is accurately and uniquely determined by its circumcircle. Then, the arithmetic average value of all the asperity peak radii is treated as the overall curvature of the profile.

## 3. Analysis of Morphology Parameters

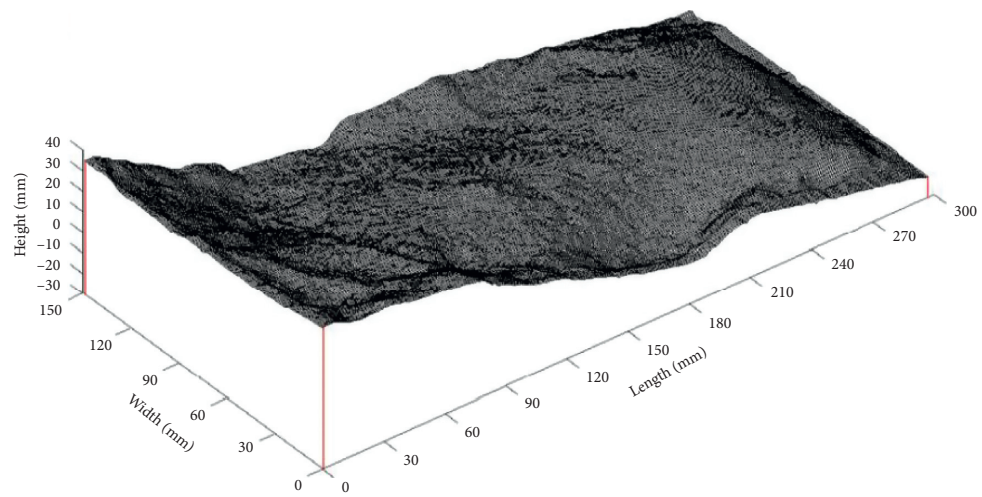
*3.1. Average Peak Radius of Curvature.* Figure 4 shows the variations of the average peak radii of curvature for the three rock joints. We can clearly observe that with the increase of roughness (denoted by the average asperity height, similarly



(a)



(b)



(c)

FIGURE 1: Morphology of the three rock joints. (a) J-I. (b) J-II. (c) J-III.

TABLE 1: Parameters for Gaussian distribution obtained by equation (1).

Sample	Fitting parameters		Correlation coefficient
	$\mu$	$\sigma$	
J-I	0.33	2.21	0.994
J-II	1.12	1.86	0.928
J-III	0.27	1.57	0.909

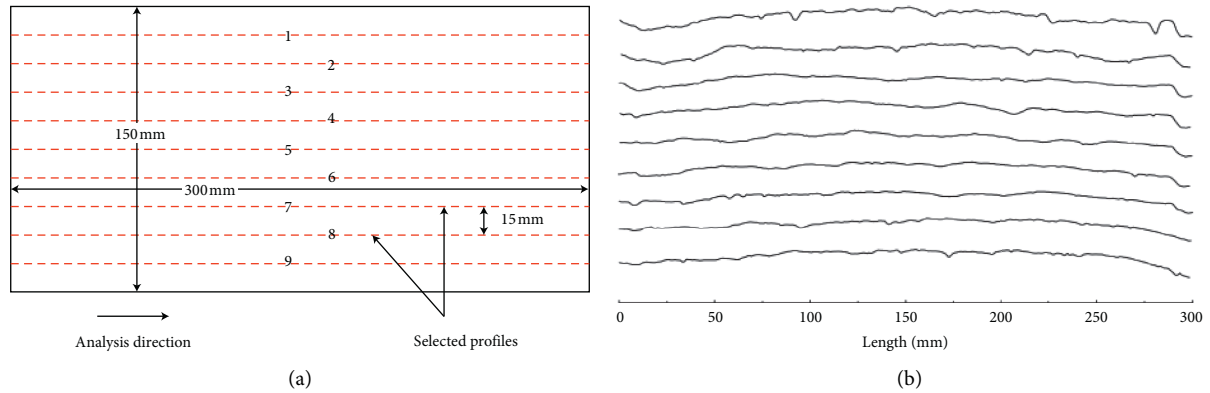


FIGURE 2: Method to select joint profiles. (a) Position of joint profiles for morphology analysis. (b) Selected joint profiles (J-II is taken as an example).

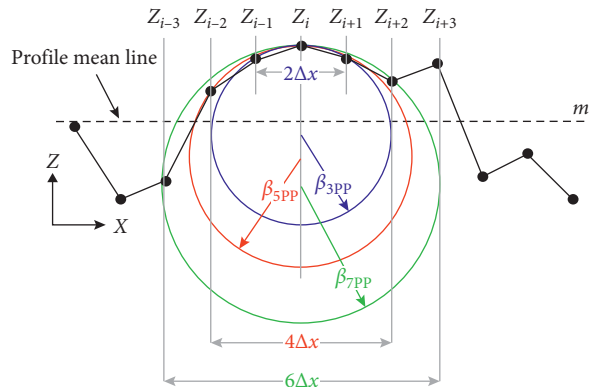


FIGURE 3: Schematic plot for 3PP, 5PP, and 7PP criteria on rock joint profile.

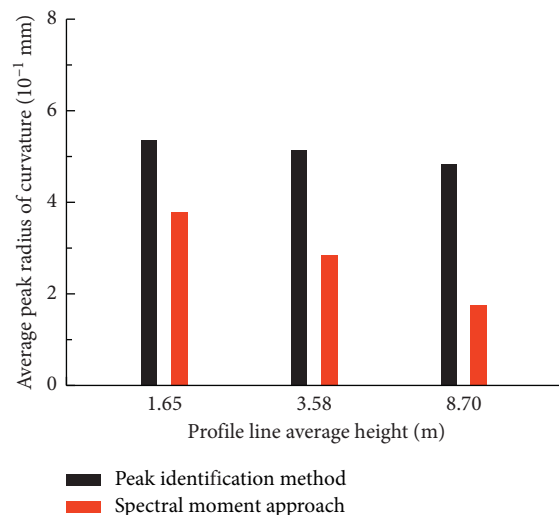


FIGURE 4: Average peak radius of curvature for the three joint profiles.



hereinafter), the radii determined by the peak identification method exhibit small volatility, while the ones determined by the spectral moment approach are significantly lower and exhibit an obvious downward trend throughout the whole roughness range. As the average asperity heights increase from 1.65 to 8.70 mm, the average peak radii of curvature determined by the spectral moment approach decrease from 0.386 to 0.182 mm, with a reduction of about 52.8%, while the ones determined by the peak identification method decrease from 0.55 to 0.44 mm, only with a reduction of about 18.5%. With consideration of the nature of the two methods, it can be inferred that the spectral moment approach would underestimate the average peak radius of curvature and there is a more pronounced trend as surface roughness increases.

**3.2. Peak Density.** Figure 5 shows the variations of peak density for the three rock joints. In the present study, the peak density means the linear density that is calculated by the peak number divided by the profile nominal length. The peak density determined by the peak identification method decreases with the increase of roughness. However, there is an onward trend throughout the whole roughness range for the one determined by the spectral moment approach. As the average asperity heights increase, the peak density determined by the spectral moment approach increases from 0.39 to 0.46, with an increase of about 17.9%, while the one determined by the peak identification method decreases from 0.28 to 0.15, with a reduction of about 46.4%. The peak density is also reported to decrease with the increase of roughness, as is the case for the peak identification method which is in line with many theoretical and experimental observations for rough surfaces [28, 29]. As such, it can be inferred that the results for the peak identification method have a much more trustworthy physical background than the ones for the spectral moment approach. Essentially, the deterministic method imposes a stricter definition of an asperity peak and results in a lower peak density, while the spectral moment approach does not necessarily trace the real asperity peaks, but possibly the shoulder of an asperity [19], thus resulting in a higher peak density.

**3.3. Standard Deviation of Peak Height.** Figure 6 shows the variations of the standard deviation of peak heights for the three rock joints with varied roughness. The peak identification method always results in a higher standard deviation throughout the roughness range. The absolute difference and the ratio,  $\sigma_{s\_SMA}/\sigma_{s\_PIM}$ , increase as the roughness increases, where  $\sigma_{s\_SMA}$  and  $\sigma_{s\_PIM}$  are the values determined by the spectral moment approach and peak identification method, respectively. For the spectral moment approach, the standard deviation of peak height increases almost linearly with the increase of roughness ( $R^2 = 0.89$ ), while the other shows an exponential relation ( $R^2 = 0.96$ ). The peak identification method accounts for the strictly determined asperity peaks on a profile (Figure 3), whereas the spectral moment approach may rely on peak shoulders, rather than the real peaks, resulting in a lower standard deviation of asperity peak heights.

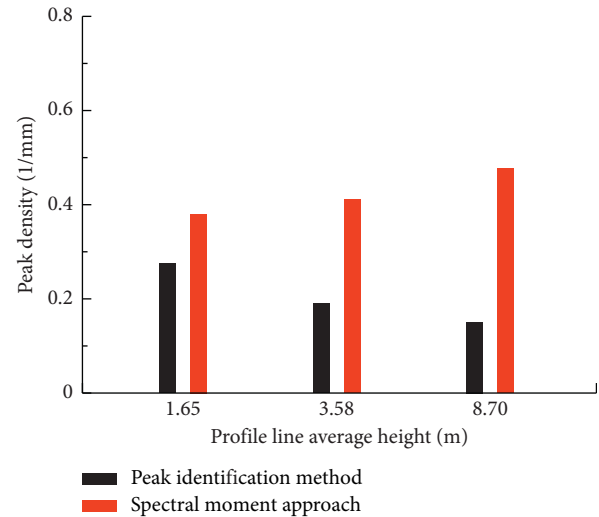


FIGURE 5: Peak density for the three joint profiles.

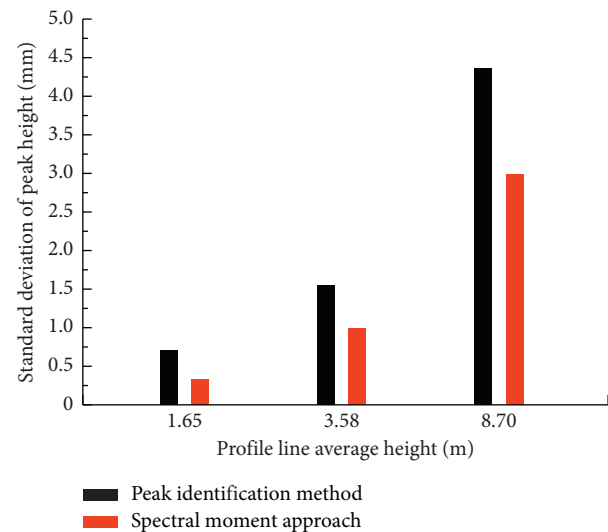


FIGURE 6: Standard deviation of peak height for the three joint profiles.

## 4. Theoretical Application

In this section, the effectiveness of determining the morphology parameters is illustrated by comparing predictions by an available theoretical closure model with experimental results.

**4.1. Theoretical Model.** Recently, a theoretical closure model with the inclusion of asperity interaction was developed by the first author and his co-workers [27], which can partly capture the closure behaviors between a “waviness” surface and an “unevenness” surface based on static equilibrium and deformation compatibility. As shown in Figure 7, the waviness is simplified by a periodic function and has identical amplitude. When an external load  $P$  is applied to a waviness surface, the pressure distribution of contact area for waviness ( $r$ ) can be determined by equation (4). Then, the

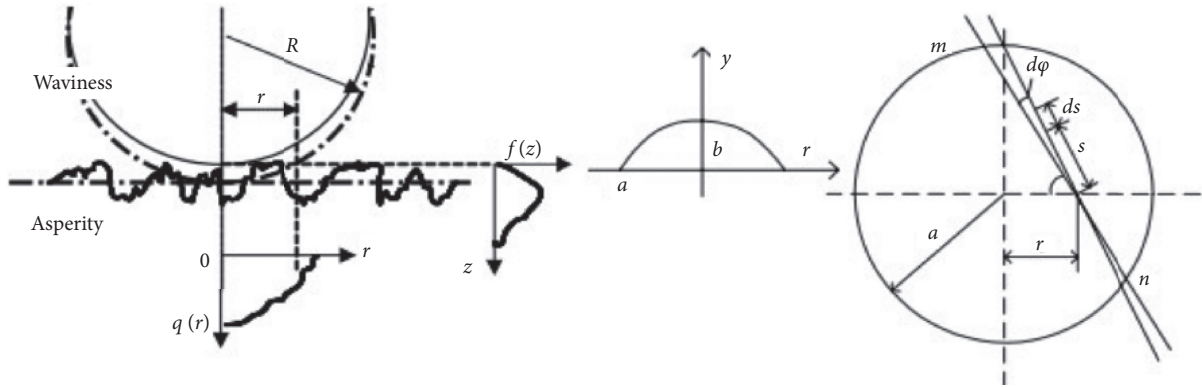


FIGURE 7: Contact between a “waviness” and an “unevenness.”

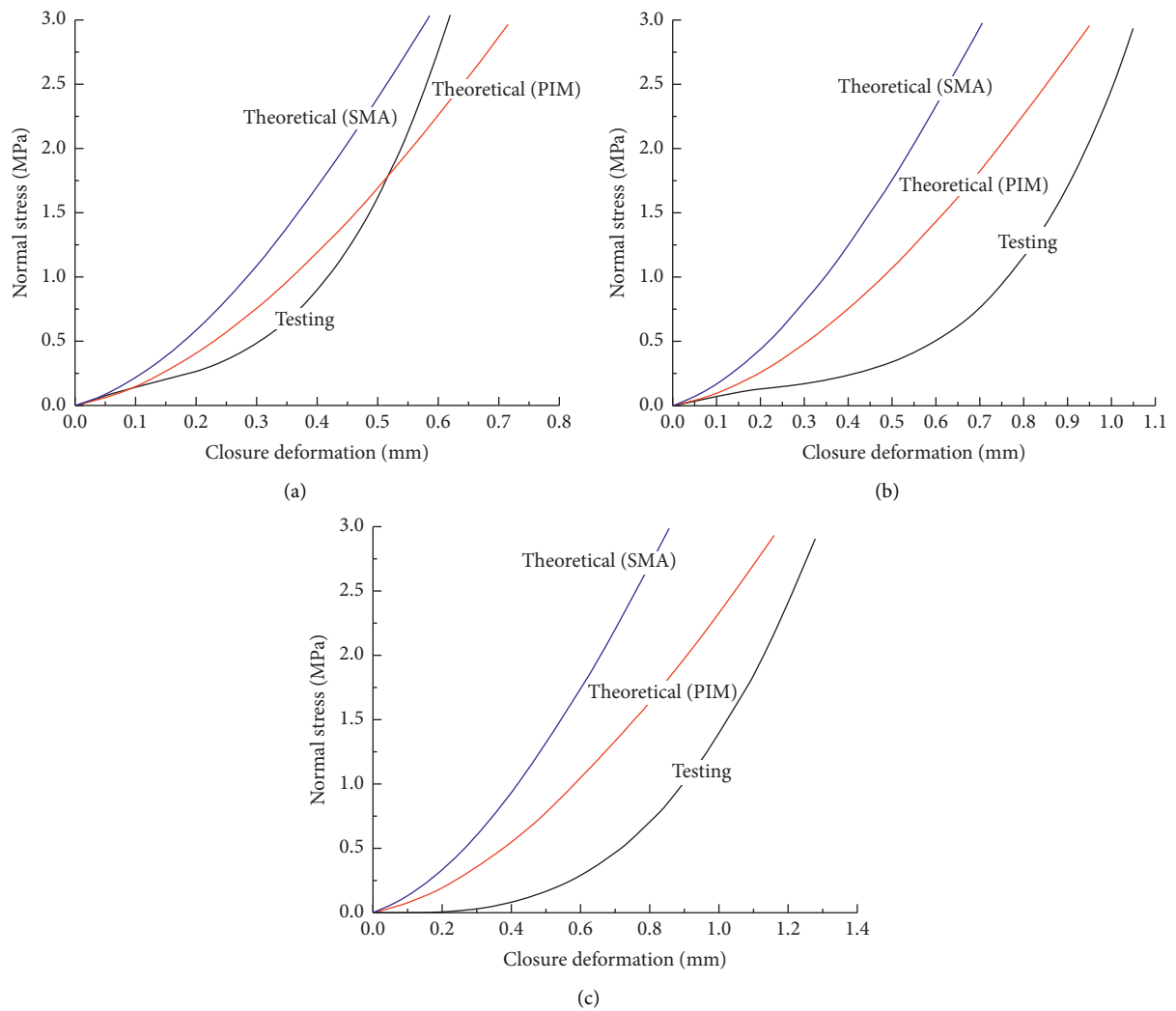


FIGURE 8: Comparison between experimental results and calculated curve. (a) J-I. (b) J-II. (c) J-III.

waviness deformation ( $w$ ) and the asperity deformation ( $u$ ) can be determined by equations (5) and (6), respectively.

$$q_w(r) = \frac{p}{\pi c} \left( \frac{1}{r^2 + 4b^2} - \frac{1}{a^2 + 4b^2} \right), \quad (4)$$

$$w(r) = \frac{2P}{\pi^2 E' bc} \int_0^{\pi/2} \left[ a \tan\left(\frac{1}{2b} \sqrt{a^2 - r^2 \sin^2 \varphi}\right) - \frac{2b}{a^2 + 4b^2} \sqrt{a^2 - r^2 \sin^2 \varphi} \right] d\varphi, \quad (5)$$

$$u(r) = \frac{a^2 - r^2}{2R} + w(a) - w(r), \quad (6)$$

where  $r$  is the distance from the contact center;  $R$  is the curvature radius of waviness;  $a$ ,  $b$  are the radii of circular contact area and a special curve, respectively;  $\varphi$  is the angle shown in Figure 7; and  $c = \ln(a^2 + 4b^2/4b^2) - a^2/a^2 + 4b^2$ .

The effect of deformed asperity interaction on the overall closure deformation of a rock joint is considered by a simplified approach as a uniform displacement on the surface caused by a mean pressure,  $p_{\text{nom}}$ , which can be directly estimated by the Greenwood and Williamson model [8] by the first iteration. As the pressure distribution of asperity contact is relevant to the asperity deformation ( $u$ ), the asperity pressure ( $q_a$ ) at the contact area can be given by the following equation:

$$q_a(r) = \frac{4}{3} \eta E' \sqrt{B} \int_0^{u(r)} \left[ u(r) + p_{\text{nom}} \frac{\sqrt{A}}{E' - z} \right]^{3/2} f(z) dz, \quad (7)$$

where  $E' = E/2(1 - \nu^2)$  in which  $E$  is Young's modulus and  $\nu$  is Poisson's ratio;  $A$  is the nominal contact area.

The steps to solve the model are as follows: (1) assign non-zero initial values for  $a$ ,  $b$  and calculate the waviness deformation,  $w(r)$  and  $w(a)$ , by equation (5); (2) calculate the asperity deformation,  $u(r)$ , by equation (6); (3) calculate the contact force by using equation (7) on the basis of the asperity deformation determined by equation (6); and (4) repeat the above procedures until the following equilibrium conditions are satisfied:  $q_a(0) = q_w(0)$  and  $q_a(a/2) = q_w(a/2)$ .

**4.2. Comparisons.** Tang et al. [22] and Tang [23] performed a series of closure tests on artificial rock joints with Young's modulus  $E = 6.1$  GPa and Poisson's ratio  $\nu = 0.16$ . The morphologies of the three rock joints are shown in Figure 1. Figure 8 illustrates the comparison between experimental and theoretical results for the three joints. Generally, the theoretical curves solved by the model with morphology parameters determined by the peak identification method are closer to the experimental data than the case of the spectral moment approach. Thus, it seems to be more reliable to use the peak identification method to analyze the contact behaviors of rock joint as it includes all available information of the surface rather than relying on a statistical

sense. However, it should be noted that the contact spots are three-dimensional for any real contact between rough rock joints, leading to the discrepancy between the testing curve and theoretical curve.

## 5. Conclusions

Due to the fact that the relevance of theoretical contact models is dependent on the peak identification assumptions and the determination accuracy, the present study provides a comparison for determining the input parameters of these theoretical models by using two methods. The peak identification method follows a stricter definition of an asperity peak on a surface and can avoid the statistical averaging, while the spectral moment approach is based on 2D traces that may probably trace peak shoulders rather than the peaks. As such, a larger peak density and a lower standard deviation of peak height can be observed for the spectral moment approach. In addition, the spectral moment approach underestimates the average peak radius of curvature for the three rock joint profiles, which would be more pronounced as the roughness increases. The effectiveness of determining morphology parameters is verified by comparing the curves determined by a theoretical model with the experimental results. It would be more reliable to use the morphology parameters obtained by the deterministic method to predict the contact behaviors of rock joint.

## Data Availability

The data used to support the findings of this study are included within the article.

## Conflicts of Interest

The authors declare that there are no conflicts of interest regarding the publication of this paper.

## Acknowledgments

The authors gratefully acknowledge the support from the National Natural Science Foundation of China under project no. 41672302 and the Fundamental Research Funds for the Central Universities, China University of Geosciences (Wuhan), under project no. CUGGC09.

## References

- [1] Y. Liu, F. Dai, L. Dong, N. Xu, and P. Feng, "Experimental investigation on the fatigue mechanical properties of intermittently jointed rock models under cyclic uniaxial compression with different loading parameters," *Rock Mechanics and Rock Engineering*, vol. 51, no. 1, pp. 47–68, 2018.
- [2] Y. Liu, F. Dai, P. Fan, N. Xu, and L. Dong, "Experimental investigation of the influence of joint geometric configurations on the mechanical properties of intermittent jointed rock models under cyclic uniaxial compression," *Rock Mechanics and Rock Engineering*, vol. 50, no. 6, pp. 1453–1471, 2017.
- [3] R. Tse and D. M. Cruden, "Estimating joint roughness coefficients," *International Journal of Rock Mechanics and Mining Science & Geomechanics Abstracts*, vol. 16, no. 5, pp. 303–307, 1979.
- [4] International Society for Rock Mechanics, "Suggested methods for the quantitative description of discontinuities in rock masses," *International Journal of Rock Mechanics and Mining Science & Geomechanics Abstracts*, vol. 15, no. 6, pp. 319–368, 1978.
- [5] H. Xie, J.-A. Wang, and M. A. Kwaśniewski, "Multifractal characterization of rock fracture surfaces," *International Journal of Rock Mechanics and Mining Sciences*, vol. 36, no. 1, pp. 19–27, 1999.
- [6] T. Belem, M. Souley, and F. Homand, "Modeling surface roughness degradation of rock joint wall during monotonic and cyclic shearing," *Acta Geotechnica*, vol. 2, no. 4, pp. 227–248, 2007.
- [7] G. Zhang, M. Karakus, H. Tang, Y. Ge, and L. Zhang, "A new method estimating the 2D joint roughness coefficient for discontinuity surfaces in rock masses," *International Journal of Rock Mechanics and Mining Sciences*, vol. 72, pp. 191–198, 2014.
- [8] Y. Li and Y. Zhang, "Quantitative estimation of joint roughness coefficient using statistical parameters," *International Journal of Rock Mechanics and Mining Sciences*, vol. 77, pp. 27–35, 2015.
- [9] N. Barton and V. Choubey, "The shear strength of rock joints in theory and practice," *Rock Mechanics and Rock Engineering*, vol. 10, no. 1, pp. 1–54, 1977.
- [10] B. S. Tatone and G. Grasselli, "A method to evaluate the three-dimensional roughness of fracture surfaces in brittle geomaterials," *Review of Scientific Instruments*, vol. 80, no. 12, Article ID 125110, 2009.
- [11] V. Rasouli and J. P. Harrison, "Assessment of rock fracture surface roughness using Riemannian statistics of linear profiles," *International Journal of Rock Mechanics and Mining Sciences*, vol. 47, no. 6, pp. 940–948, 2010.
- [12] J. A. Greenwood and J. B. P. Williamson, "Contact of nominally flat surfaces," *Proceedings of the Royal Society of London—Series A: Mathematical and Physical Sciences*, vol. 295, no. 1442, pp. 300–319, 1966.
- [13] S. R. Brown and C. H. Scholz, "Closure of random elastic surfaces in contact," *Journal of Geophysical Research: Solid Earth*, vol. 90, no. B7, pp. 5531–5545, 1985.
- [14] A. Misra, "Micromechanical model for anisotropic rock joints," *Journal of Geophysical Research: Solid Earth*, vol. 104, no. B10, pp. 23175–23187, 1999.
- [15] F. Lanaro and O. Stephansson, "A unified model for characterisation and mechanical behaviour of rock fractures," *Thermo-Hydro-Mechanical Coupling in Fractured Rock*, vol. 160, no. 5, pp. 989–998, 2003.
- [16] C. C. Xia, Z. Q. Yue, L. G. Tham, C. F. Lee, and Z. Q. Sun, "Quantifying topography and closure deformation of rock joints," *International Journal of Rock Mechanics and Mining Sciences*, vol. 40, no. 2, pp. 197–220, 2003.
- [17] P. R. Nayak, "Random process model of rough surfaces," *Journal of Lubrication Technology*, vol. 93, no. 3, pp. 398–407, 1971.
- [18] J. I. Mc Cool, "Relating profile instrument measurements to the functional performance of rough surfaces," *Journal of Tribology*, vol. 109, no. 2, pp. 264–270, 1987.
- [19] B. Bhushan and P. L. Ko, "Introduction to tribology," *Applied Mechanics Reviews*, vol. 56, no. 1, pp. B6–B7, 2003.
- [20] J. A. Greenwood, "A unified theory of surface roughness," *Proceedings of the Royal Society of London. A. Mathematical and Physical Sciences*, vol. 393, no. 1804, pp. 133–157, 1984.
- [21] Z. C. Tang, Y. Y. Jiao, and L. N. Y. Wong, "Theoretical model with multi-asperity interaction for the closure behavior of rock joint," *International Journal of Rock Mechanics and Mining Sciences*, vol. 97, pp. 15–23, 2017.
- [22] Z.-C. Tang, Q.-S. Liu, C.-C. Xia, Y.-L. Song, J.-H. Huang, and C.-B. Wang, "Mechanical model for predicting closure behavior of rock joints under normal stress," *Rock Mechanics and Rock Engineering*, vol. 47, no. 6, pp. 2287–2298, 2014.
- [23] Z.-C. Tang, *Mechanical behaviors of rock joint under different contact state and columnar jointed rock mass*, Ph.D thesis, Tongji University, Shanghai, China, 2013.
- [24] G. Swan, "Determination of stiffness and other joint properties from roughness measurements," *Rock Mechanics and Rock Engineering*, vol. 16, no. 1, pp. 19–38, 1983.
- [25] G. Swan and S. Zongqi, "Prediction of shear behaviour of joints using profiles," *Rock Mechanics and Rock Engineering*, vol. 18, no. 3, pp. 183–212, 1985.
- [26] Z. C. Tang and Y. Y. Jiao, "A self-consistent model with asperity interaction for the mechanical behavior of rock joints under compressive loading," *International Journal of Rock Mechanics and Mining Sciences*, vol. 100, pp. 23–27, 2017.
- [27] C. Y. Poon and B. Bhushan, "Surface roughness analysis of glass-ceramic substrates and finished magnetic disks, and Ni-P coated Al-Mg and glass substrates," *Wear*, vol. 190, no. 1, pp. 89–109, 1995.
- [28] Z. C. Tang, C. C. Xia, Y. Y. Jiao, and L. N. Y. Wong, "Closure model with asperity interaction in normal contact for rock joint," *International Journal of Rock Mechanics and Mining Sciences*, vol. 83, pp. 170–173, 2016.
- [29] G. Zavarise, M. Borri-Brunetto, and M. Paggi, "On the reliability of microscopical contact models," *Wear*, vol. 257, no. 3, pp. 229–245, 2004.

## Research Article

# Numerical Simulation of the Nonlinear Flow Properties in Self-Affine Aperture-Based Fractures

Xin Zhou <sup>1,2</sup>, Jianlong Sheng <sup>1,2</sup>, Ruili Lu <sup>3</sup>, Zuyang Ye <sup>1,2</sup> and Wang Luo <sup>1,2</sup>

<sup>1</sup>School of Resources and Environmental Engineering, Wuhan University of Science and Technology, Wuhan 430081, China

<sup>2</sup>Hubei Key Laboratory for Efficient Utilization and Agglomeration of Metallurgical Mineral Resources, Wuhan University of Science and Technology, Wuhan 430081, China

<sup>3</sup>Changjiang Institute of Technology, Wuhan 430212, China

Correspondence should be addressed to Zuyang Ye; [yezuyang@wust.edu.cn](mailto:yezuyang@wust.edu.cn)

Received 3 November 2020; Accepted 29 May 2021; Published 7 June 2021

Academic Editor: Yingchun Li

Copyright © 2021 Xin Zhou et al. This is an open access article distributed under the Creative Commons Attribution License, which permits unrestricted use, distribution, and reproduction in any medium, provided the original work is properly cited.

In order to study the effect of fracture geometry on the nonlinear flow properties in aperture-based fractures, a fractal model based on the self-affinity is proposed to characterize the three-dimensional geometry of rough-walled fractures. By solving the N–S (Navier–Stokes) equation directly, the relationships between the Forchheimer-flow characteristics, fractal dimension, and standard deviation of the aperture have been obtained. The Forchheimer equation is validated to describe the nonlinear relationship between flow rate and pressure gradient. For lower flow rate, the influence of the fractal dimension almost can be ignored, but the linear coefficient increases and the hydraulic aperture decreases with increasing standard deviation of the aperture, respectively. For larger flow rate, the nonlinear coefficient increases with the growth of the standard deviation of the aperture and fractal dimension. Thus, an empirical relationship between the nonlinear coefficient, fractal dimension, and standard deviation of aperture is proposed. In addition, the critical Reynolds number decreases with the increase of the standard deviation of the aperture and the fractal dimension, and the numerical results are generally consistent with the experimental data.

## 1. Introduction

Fractures are prevalent among the natural rock masses under geological action. Compared with the intact rock, the permeability of fractures is much larger, and fractures become the dominant channels for fluid flow [1, 2]. Fracture-dominated flow plays an important role in many practical situations such as seepage control for fractured media [3, 4], hazardous waste isolation [5], slope engineering [6, 7], underground tunneling [8, 9], and many geological disasters.

Many efforts have been taken to investigate the hydraulic properties of fractures. Snow [10] has conceptualized the rough-walled fracture as the smooth parallel plate model, and the famous cubic law was derived. However, the surface roughness and aperture distribution of natural fractures are random and irregular [11, 12]. Consequently, there is no absolute smooth fracture in natural rock masses and it is difficult to satisfy the establishment conditions of cubic law,

which may lead to a large deviation in the prediction of fracture permeability. Based on the laboratory tests and numerical analysis, many researchers [13–21] found that the relationship between flow rate and pressure gradient in rough-walled fractures is nonlinear deviating from the cubic law.

To investigate the relationship between the nonlinear flow properties and the roughness of the fracture surface, Zhang and Tian [22] carried out numerical simulation of a single fracture with different roughness and tortuosity, and the results showed a certain deviation from the modified cubic law resulted by the flow tortuosity. Chen et al. [16] studied the relationship between the hydraulic aperture and Forchheimer equation's nonlinear coefficient by conducting flow tests under different confining pressures on twelve groups of granite cracks with different roughness. Yin et al. [19] analyzed the effects of the shearing process under a series of normal loads on nonlinear flow behavior in 3D

rough-walled fractures with different roughness by the shear-flow test. The abovementioned investigations on the impact of roughness on the nonlinear flow properties all use the JRC (Joint Roughness Coefficient) to represent the fracture surface roughness. However, the value of the JRC is obtained based on observation experiences; thus, the roughness of fracture surfaces cannot be accurately and quantitatively represented.

Some other influence factors of rough fractures on the nonlinear flow properties were also considered. For example, Xia et al. [23] found that different contact conditions and the root-mean square height of fractures had an evident impact on apparent transmissivity based on laboratory observations. Tsang [24] explored the impact of tortuous of flow path on flow behavior through experiments and found that the smaller the aperture distribution, the greater the influence of tortuosity. Xiong et al. [17] designed a saturated seepage test of fracture under low flow rate and evaluated the role of roughness and aperture in affecting the nonlinear flow properties. It is not difficult to find that there are many factors affecting the nonlinear flow properties of rough fractures. However, the effect of the standard deviation of the fracture aperture on the nonlinear flow properties is rarely discussed.

The main objective of this study is to study the nonlinear flow behavior in self-affine aperture-based rock fractures based on the fractal theory and Navier–Stokes equations. Based on the fractal theory, the rough-walled fracture is reconstructed by fractional Brownian motion, and the surface roughness and aperture distribution can be characterized by fractal dimension. For rough-walled fractures with different surface roughness and the standard deviation of the aperture, the nonlinear relationship between flow rate and pressure gradient can be well described by the Forchheimer equation. The mathematical relationship between the nonlinear coefficient, fractal dimensions, and the standard deviation of the aperture is also quantified.

## 2. Geometrical Model of Rough Fractures

Previous studies [18, 25–27] have shown that the fracture roughness can be described by self-affinity, which can be simulated using fractional Brownian motion (fBm). The height of rough fracture surfaces is described by a continuous and single random function  $Z(x)$ . The stationary increment  $[Z(x) - Z(x + \Delta)]$  over the distance  $\Delta$  follows a Gaussian distribution with mean zero and variance  $\delta^2$ . The self-affinity relating to fBm obeys the following expressions:

$$\begin{aligned} \langle Z(x) - Z(x + \lambda\Delta) \rangle &= 0, \\ \delta_{\lambda\Delta}^2 &= \lambda^{2H} \delta_{\Delta}^2 \Rightarrow \delta_{\lambda\Delta} = \lambda^H \delta_{\Delta}, \\ \delta_{\lambda\Delta}^2 &= \langle [Z(x) - Z(x + \lambda\Delta)]^2 \rangle, \\ \delta_{\Delta}^2 &= \langle [Z(x) - Z(x + \Delta)]^2 \rangle, \end{aligned} \quad (1)$$

where  $\langle \cdot \rangle$  is the mathematical expectation,  $x$  donates the coordinate component, and  $H$  represents the Hurst exponent varying from 0 to 1 and associated with the fractal dimension  $D$  by  $D = 3 - H$ .  $\lambda$  is a constant,  $\delta_{\lambda\Delta}^2$  and  $\delta_{\Delta}^2$  are the

variance corresponding to the height variation of fracture surface with the distance of  $\lambda\Delta$  and  $\Delta$ , respectively, and  $\delta$  is the standard deviation of the aperture.

To construct the geometrical model of rough-walled fractures, in present study, the successive random addition method (SRAM) [28–30] is used to generate the fracture surfaces. The generated square area is shown in Figure 1, and the specific steps are as follows:

- (1) In the given single square region, the initial random values of the four corners, which are labeled as number 1, satisfy the Gaussian distribution  $N(0, \delta_0^2)$
- (2) The center point of the square and midpoints of each side are marked by number 2, and their height are the average value of the four corners initial height and the average value of two points of each side, respectively; at the same time, the random values from  $N(0, \delta_1^2)$  should be added into all points, in which

$$\delta_1^2 = \frac{\delta_0^2}{2^{2H}} (1 - 2^{2H-2}). \quad (2)$$

- (3) Step (2) is repeated for each newly generated square, and the random values from  $N(0, \delta_n^2)$  should be added to all heights as well until  $2^n \times 2^n$  squares are created at iteration

$$\delta_n^2 = \frac{\delta_{n-1}^2}{2^{2H}} = \frac{\delta_0^2}{(2^{2H})^n} (1 - 2^{2H-2}). \quad (3)$$

- (4) No new square is inserted again, but we keep adding random values from  $N(0, \delta_j^2)$  to all points, in which

$$\delta_j^2 = \frac{\delta_{j-1}^2}{2^{2H}} = \frac{\delta_0^2}{(2^{2H})^j} (1 - 2^{2H-2}), \quad (4)$$

where  $j = n + 1, n + 2, \dots, NM$ ;  $NM$  is large enough, so  $\delta_{NM}/\delta_0$  is negligible

The upper and lower surfaces of rough fracture are generated using the SRAM. The height of low surface is  $Z_1(x, y)$ , and the height of the upper surface can be calculated by the following formula:

$$Z_2(x, y) = Z_1(x + \Delta x, y + \Delta y) + u, \quad (5)$$

where  $u$  is the mean aperture between the upper and lower surfaces. The distribution function of the fracture aperture can be expressed as

$$b(x, y) = \begin{cases} Z_2(x, y) - Z_1(x, y), & \text{if } Z_2(x, y) > Z_1(x, y), \\ 0, & \text{else.} \end{cases} \quad (6)$$

To demonstrate the reliability of the algorithm used to characterize the fracture surface geometry, Figure 2 shows the fracture aperture distribution diagram of four groups with different roughness. The side length of square  $L = 40$  mm,  $\delta = 0.15$  mm, and fractal dimensions are 2.1, 2.2, 2.3, and 2.4,

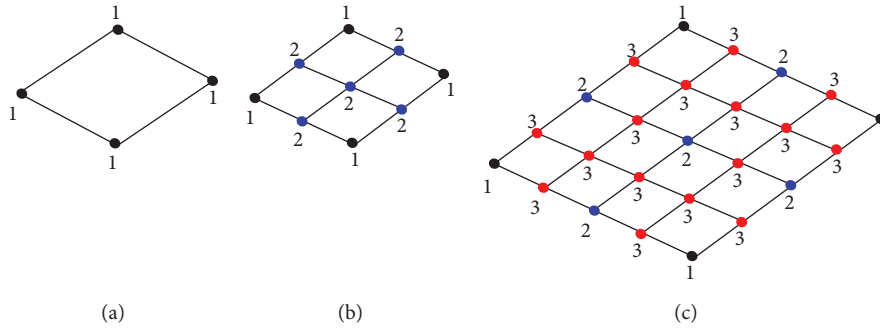


FIGURE 1: Illustration of the two-dimensional SRAM.

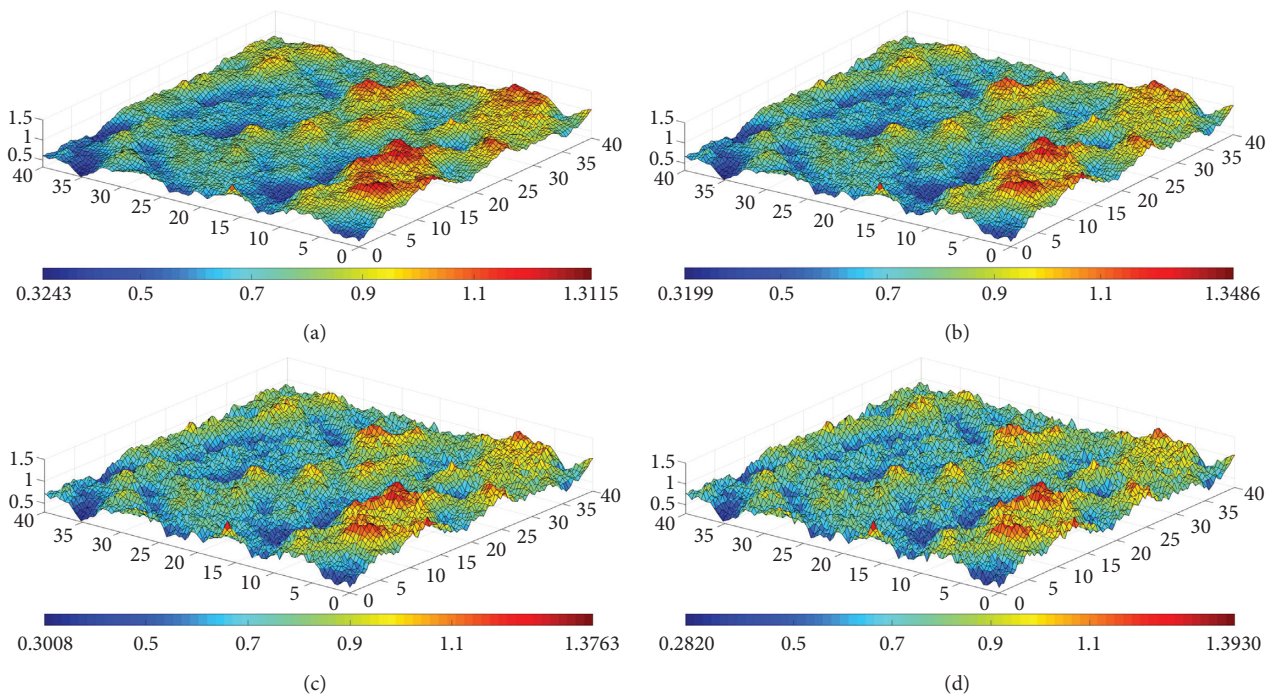


FIGURE 2: Comparison of the morphology of fracture models for  $\delta = 0.15$  mm (red represents large aperture; blue represents small aperture; unit: mm). (a)  $D = 2.1$ . (b)  $D = 2.2$ . (c)  $D = 2.3$ . (d)  $D = 2.4$ .

respectively. It can be seen that, with the increase of  $D$ , the maximum values of the aperture increase and the minimum values of the aperture decrease; the aperture distribution is more scattered, the variation of adjacent apertures is more fluctuated, and the degree of roughness is greater.

### 3. Theory of Flow Properties in Fractures

3.1. *Cubic Law.* Based on the smooth parallel plate model, the flow behaviour in a single fracture should obey the cubic law [10]:

$$Q = -\frac{wb^3}{12\mu}\nabla p, \quad (7)$$

where  $Q$  is the volumetric flow rate per unit time,  $b_h$  is the hydraulic aperture of the fracture,  $w$  is the fracture width,  $\mu$  is the dynamic viscosity, and  $\nabla p = (p_{in} - p_{out})/l$  is the pressure gradient between the inlet and outlet.

3.2. *Forchheimer Equation.* For larger flow rate, the flow behaviour of rough fractures is nonlinear due to the larger inertial effect. Thus, instead of equation (7), the Forchheimer equation [14, 15, 17, 19] is commonly applied to describe the nonlinear flow properties:

$$-\nabla P = AQ + BQ^2, \quad (8)$$

$$A = \frac{\mu}{kA_h} = \frac{12\mu}{wb_h^3}, \quad (9)$$

$$B = \frac{\beta\rho}{w^2b_h^2},$$

where  $A$  and  $B$  are the linear coefficient and nonlinear coefficient, respectively;  $k$  is the fracture permeability;  $\beta$  is the non-Darcy flow inertial coefficient which depends on the geometric characteristics of fracture surfaces [16, 31]; and  $\rho$  is the fluid density. When the flow rate is small, the inertia force is much less than the viscosity force; in other words, the quadratic term ( $BQ^2$ ) is much less than the linear term ( $AQ$ ), and equation (8) can be reduced to the cubic law.

**3.3. Distinguishing the Flow Regime.** In order to quantify the nonlinear flow behaviour of fractures, the Reynolds number  $Re$  is calculated as follows:

$$Re = \frac{\rho vb_h}{\mu} = \frac{\rho Q}{\mu w}, \quad (10)$$

where  $v$  is the average velocity of the fracture inlet. The Reynolds number  $Re$  represents the ratio of inertial force to viscous force in fracture flow, and the inertial effect is stronger with larger  $Re$ ; thus, it is easier to enter the nonlinear flow regime.

Simultaneously, the non-Darcy effect factor  $E$  is defined according to the Forchheimer equation:

$$E = \frac{BQ^2}{AQ + BQ^2}. \quad (11)$$

The physical meaning of  $E$  is the proportion of pressure gradient caused by nonlinear flow in the total pressure gradient, and it is a dimensionless coefficient ranging from 0 to 1 representing the degree of nonlinear flow. The greater the  $E$  is, the stronger the nonlinear effect is. At present,  $E = 0.1$  [15, 23, 32], and combined with equations (10) and (11), the critical Reynolds number  $Re_c$  for the transition from linear to nonlinear flow of fracture flow yields

$$Re_c = \frac{A\rho}{9B\mu w}. \quad (12)$$

The smaller the  $Re_c$  is, the more significant the inertia effect is and the easier it is to be the nonlinear flow state.

## 4. Numerical Simulation

**4.1. Governing Equation.** For the incompressible Newtonian fluid with a constant viscosity coefficient flowing in the rough fractures, the fluid motion is governed by the N-S equation and the continuity equation:

$$\rho(\mathbf{u} \cdot \nabla \mathbf{u}) - \mu \nabla^2 \mathbf{u} = -\nabla P, \quad (13)$$

$$\nabla \cdot \mathbf{u} = 0, \quad (14)$$

where  $\mathbf{u}$  and  $\nabla$  are the velocity vector and Hamiltonian operator, respectively. In this study, the fluid density is 997.1

(kg/m<sup>3</sup>), and the dynamic viscosity is  $0.894 \times 10^{-3}$  (Pa s) for water at 25°C. Since the flow rate is small and generally does not exceed the boundary of laminar flow, the laminar interface in finite element software COMSOL Multiphysics is selected for the solution [33].

**4.2. Numerical Procedure.** As shown in Figure 3, at first, three-dimensional rough fracture surfaces are generated based on the SRAM, and then, the solid fracture model is constructed by the Boolean operation. Next, the solid model is meshing to determine the microstructure of the computing model. Finally, the software COMSOL is employed to obtain a series of data of flow rate and pressure gradient which is fitted by the Forchheimer equation.

Considering the solution accuracy, calculation cost, and errors caused by different element sizes, the tetrahedral element size is set as 0.25 mm, and the number of grid elements ranges from 400 thousands to 600 thousands. The size of the fracture model is 40 mm × 40 mm, and the mean aperture  $u$  is 0.8 mm; the geometric parameters including the standard deviation of the aperture and fractal dimension are shown in Table 1. The left side of the fracture model is specified as inflow boundary, the range of  $Q$  is  $3.586 \times 10^{-8} \sim 3.228 \times 10^{-6}$  m<sup>3</sup>/s, the corresponding  $Re$  ranges from 1 to 90 according to equation (10). The right side of the fracture model is defined as outflow boundary and the pressure is set as zero, and the rest of the boundaries are impervious.

## 5. Results and Discussion

### 5.1. Relationship between Flow Rate and Pressure Gradient.

The relationships between flow rate and pressure gradient of five groups are shown in Figure 4. The fitting linear coefficient  $A$  and nonlinear coefficient  $B$  of the Forchheimer equation are presented in Table 1, and the coefficients of determination  $R^2$  are both greater than 0.99, which indicates the nonlinear relationship between the flow rate and pressure gradient in self-affine aperture-based fractures can be well described by the Forchheimer equation.

In Figure 4, with the increment of flowrate, the deviation between Forchheimer curves and cubic law increases drastically. This deviation is also strengthened with the increment of  $D$  and  $\delta$ , which indicates that flow resistance will be greater for the rougher surface. Zeng and Grigg [32] suggested that the Forchheimer-flow properties were mainly caused by inertial force; in other words, the inertial term  $\rho(\mathbf{u} \cdot \nabla \mathbf{u})$  in equation (13) was the main factor for the nonlinear behavior.

In order to analyze the primary factor of nonlinear flow behavior, Figure 5 compared the five velocity sections along the  $x$  direction when  $D = 2.5$  and  $Q = 5.3796 \times 10^{-7}$  m<sup>3</sup>/s of two fracture models with different  $\delta$  (0.09 mm and 0.21 mm). It can be seen that the velocity distribution is more scattered in the fracture with more heterogeneous aperture distribution, and the local velocity becomes relatively larger. As a result, the inertia effect of flow is enhanced, and the local energy dissipation is increased, which leads to the fluid entering nonlinear state.



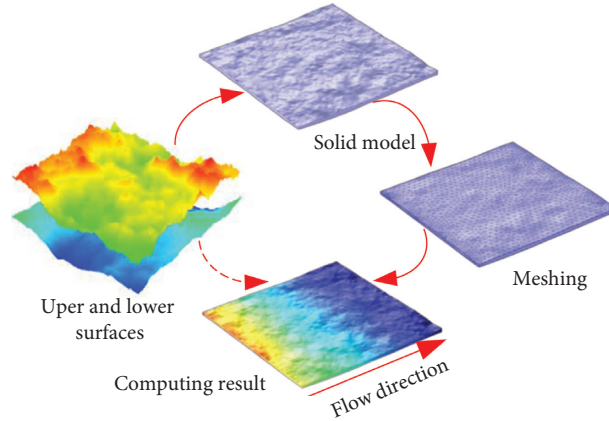


FIGURE 3: Modelling process of nonlinear flow through 3D rough fracture.

TABLE 1: The values for linear coefficient  $A$  and nonlinear coefficient  $B$ .

Standard deviation of aperture (mm)	$D=2.1$		$D=2.2$		$D=2.3$		$D=2.4$		$D=2.5$	
	$A$	$B$	$A$	$B$	$A$	$B$	$A$	$B$	$A$	$B$
$\delta = 0.09$	5.5111	1.1802	5.4536	1.2779	5.5118	1.3642	5.4648	1.4179	5.5147	1.5342
$\delta = 0.12$	5.6875	1.2289	5.6428	1.3294	5.6168	1.4194	5.6985	1.5478	5.6647	1.6495
$\delta = 0.15$	5.9625	1.2942	5.9763	1.4131	5.9316	1.5536	5.8904	1.6491	5.8862	1.8116
$\delta = 0.18$	6.2710	1.3749	6.1622	1.5075	6.2558	1.6758	6.0919	1.7666	6.1335	2.0007
$\delta = 0.21$	6.5353	1.4817	6.4933	1.5996	6.4495	1.7724	6.4531	1.9774	6.4546	2.2197

Notes:  $A$  ( $10^8 \text{ kg}\cdot\text{s}^{-1}\cdot\text{m}^{-5}$ );  $B$  ( $10^{14} \text{ kg}\cdot\text{m}^{-8}$ ).

**5.2. Analysis of Permeability of Rough Fractures.** Based on equation (9), the linear coefficient  $A$  is negatively correlated with the permeability of rough fractures. As shown in Table 1,  $A$  increases with the  $\delta$  increase, indicating that the permeability will be lower when the distribution of the aperture is more discrete and irrelevant for a larger  $\delta$ . The same phenomenon can also be found in Figure 6, the hydraulic aperture  $b_h$  decreases apparently with the  $\delta$  increases, and it is always less than the mean aperture 0.8 mm; therefore, the permeability of rough fractures is less than that of smooth fractures. Moreover, with the increment of  $\delta$ , the flow paths become more tortuous and the permeability becomes smaller.

However,  $D$  has no obvious effect on  $A$  except for a slight fluctuation as shown in Table 1. In other words, when the flow is small, the fractal dimension has little effect on the flow capacity of rough cracks. The section diagrams of streamline distribution are presented in Figure 7, for  $\delta = 0.21$  mm and  $Q = 2.152 \times 10^{-6} \text{ m}^3/\text{s}$  with  $D$  being 2.1, 2.3, and 2.5,  $y = 20$  mm, and  $x$  ranging from 25 mm to 40 mm. For same  $\delta$ , the streamline distribution is similar while the roughness of the fracture surfaces is greater for larger  $D$ , and there are some blank areas at the rough bulge. This is because the fluid flow in the fracture tends to the region with lower resistance and will bypass the high resistance area to form a dominant channel. Therefore, the effective flow space is substantially equal and the flow capacity does not change significantly. When the flow rate continues to increase, eddy flow will appear in these blank areas, resulting in accelerated energy consumption and the permeability of fractures being reduced [34].

**5.3. Analysis of Forchheimer-Flow Characteristics.** The  $B$  and  $\beta$  represent the degree of evolution of Forchheimer-flow properties, and the nonlinear flow is stronger with a greater value of  $B$  and  $\beta$ . In Table 1, the values of  $B$  increase with larger  $\delta$  and  $D$ , which indicates that the degree of flow nonlinearity is more drastic with the rougher surfaces and more heterogeneous aperture distribution.

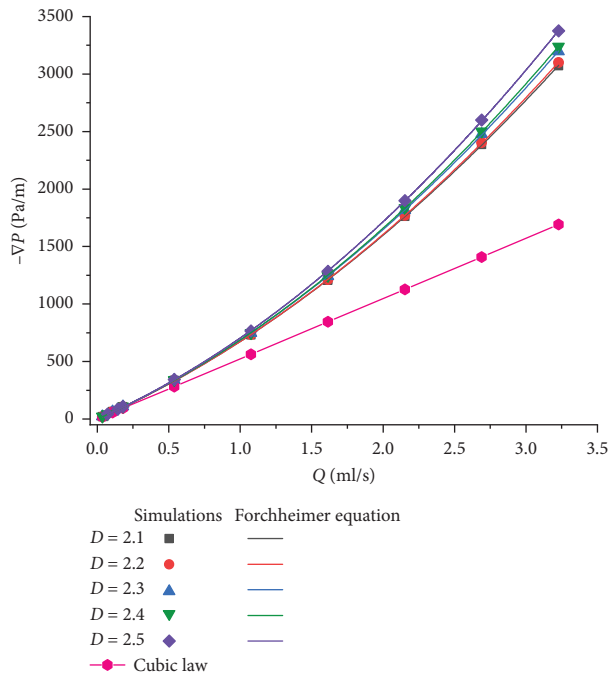
According to equation (9),  $B$  is proportional to  $\beta$  but inversely proportional to the square of  $b_h$ , so it is difficult for  $B$  to fully reflect the impact of fracture morphology on flow properties of rough fractures. Instead, Figure 8 shows the relationship between  $\delta$ ,  $D$ , and  $\beta$ . It is observed that  $\beta$  increases linearly with  $\delta$  and  $D$ . Therefore, the two-parameter expression is proposed:

$$\beta = \eta \delta D + m \delta + n D, \quad (15)$$

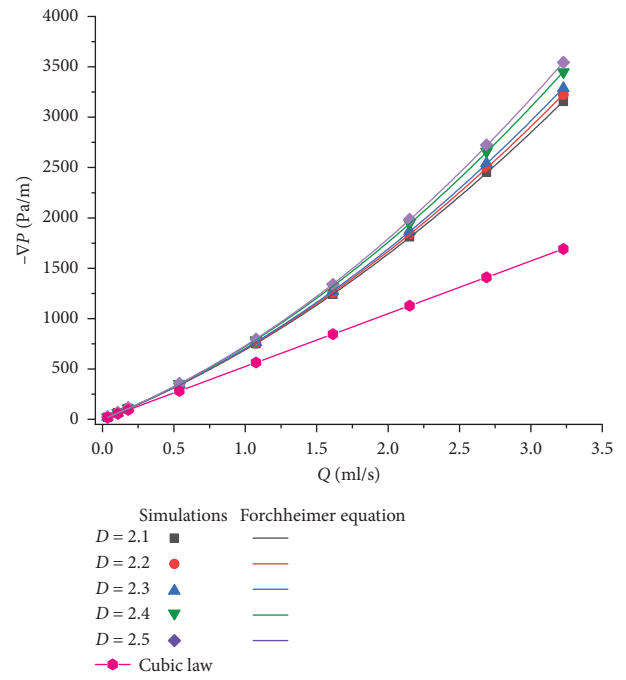
where  $\eta$ ,  $m$ , and  $n$  are empirical parameters. On the basis of nonlinear Levenberg–Marquardt algorithm, the fitting parameters  $\eta$ ,  $m$ , and  $n$  are 517.5,  $-967$ , and 49.39, respectively, and the coefficient of determination  $R^2$  is 0.9879, indicating that this expression could well explain the effect of morphology parameters on Forchheimer-flow properties. Combining with equation (12), the empirical model of nonlinear coefficient  $B$  is obtained:

$$B = \frac{\rho}{w^2 b_h^2} (517.5 \delta D - 967 \delta + 49.39 D). \quad (16)$$

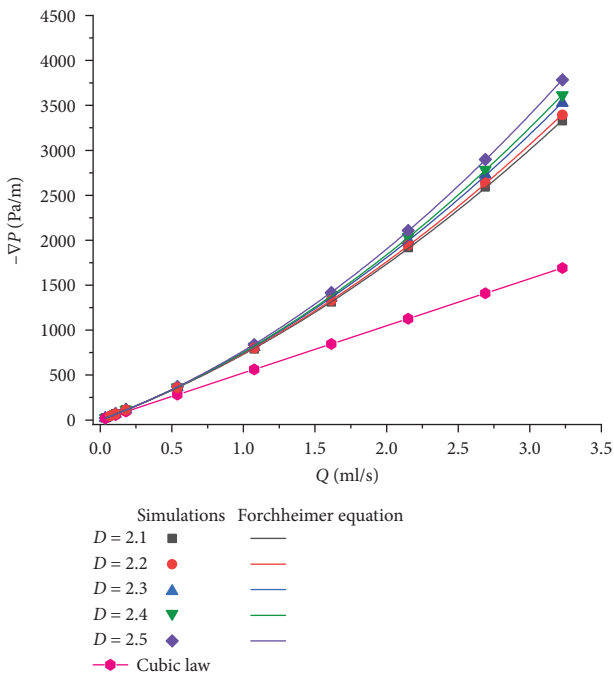
It should be noted that when the value of  $b_h$  decreases with the increment of  $\delta$ , the growth of  $B$  is more significant.



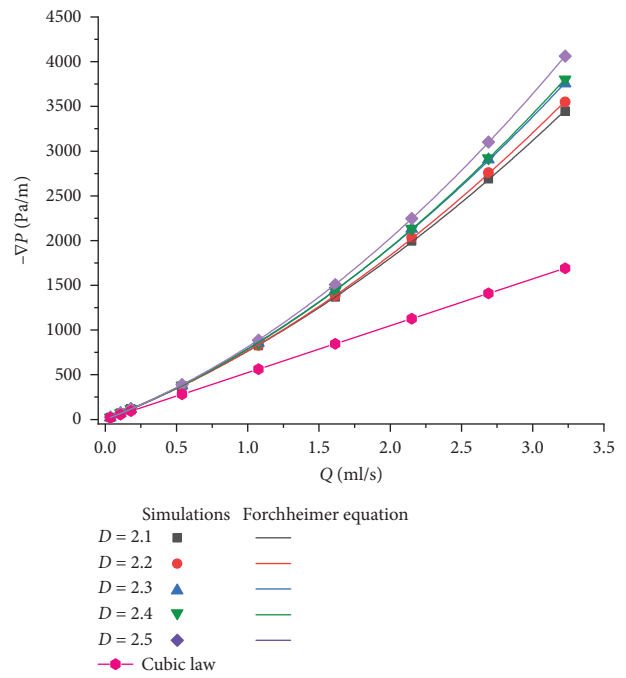
(a)



(b)



(c)



(d)

FIGURE 4: Continued.

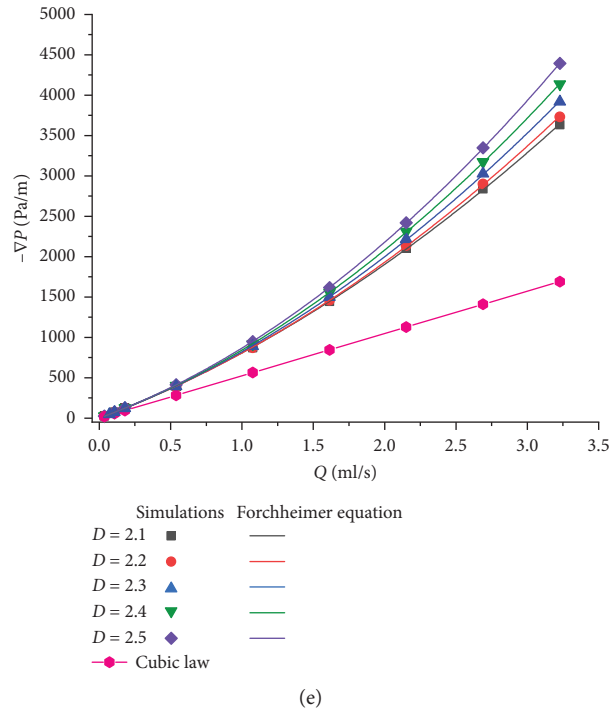


FIGURE 4: Relationship between flowrate and pressure gradient. (a)  $\delta = 0.09$  mm. (b)  $\delta = 0.12$  mm. (c)  $\delta = 0.15$  mm. (d)  $\delta = 0.18$  mm. (e)  $\delta = 0.21$  mm.

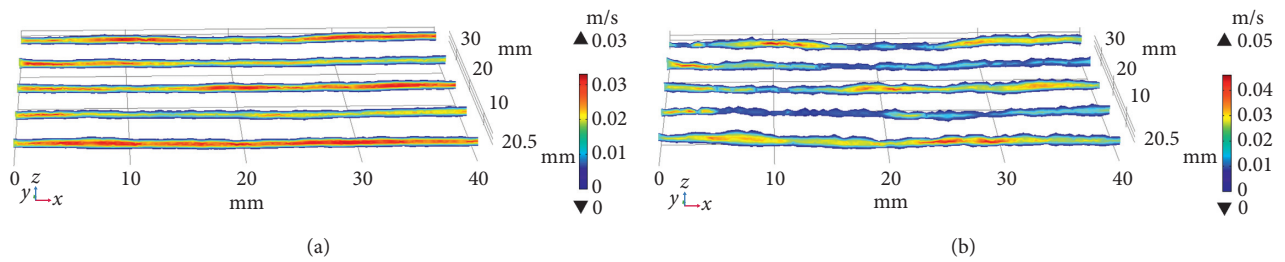


FIGURE 5: Velocity distribution for  $D = 2.5$ ,  $Q = 5.3796 \times 10^{-7} \cdot \text{m}^3/\text{s}$ . (a)  $\delta = 0.09$  mm. (b)  $\delta = 0.21$  mm.

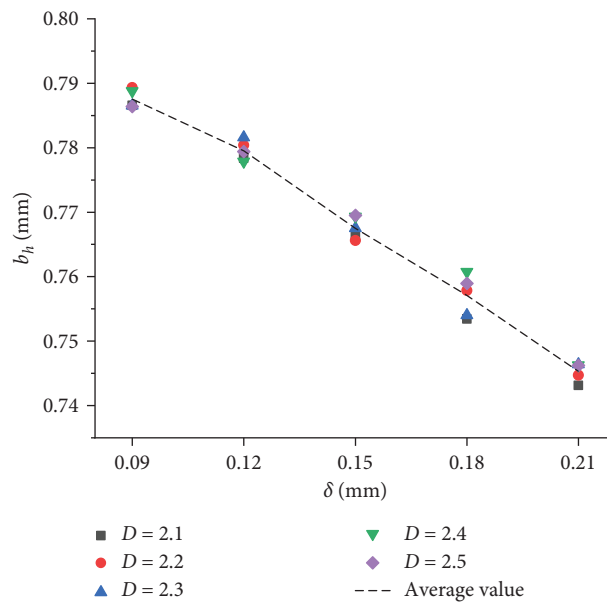


FIGURE 6: Relationship between the hydraulic aperture and geometric characteristics.

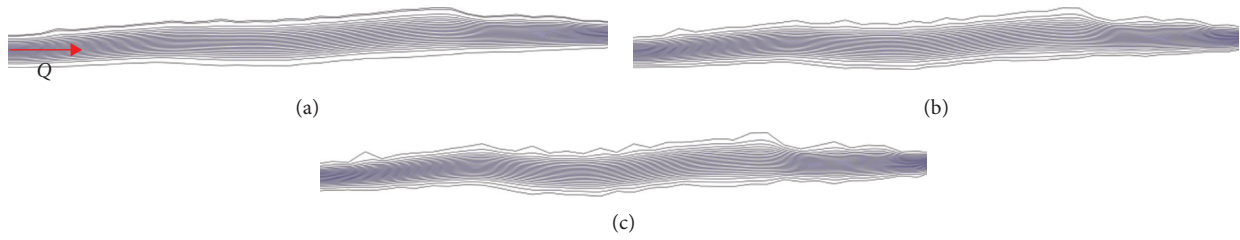


FIGURE 7: Diagram of streamline distribution for  $\delta = 0.21$  mm,  $Q = 2.152 \times 10^{-6} \cdot \text{m}^3/\text{s}$  ( $y = 20$  mm, flow direction  $x = 25 \sim 40$  mm). (a)  $D = 2.1$ . (b)  $D = 2.3$ . (c)  $D = 2.5$ .

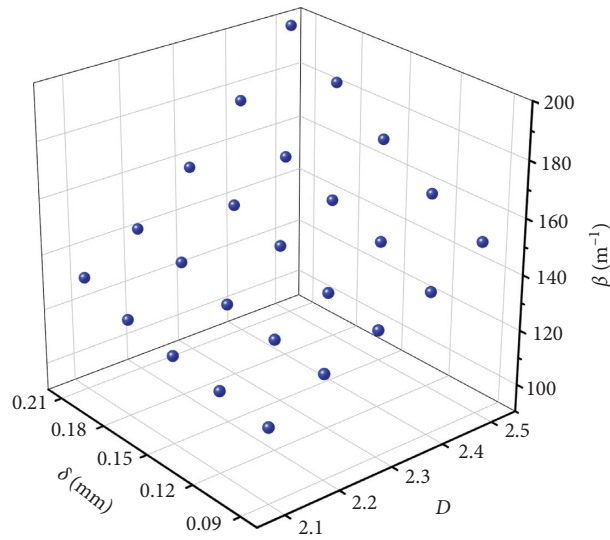


FIGURE 8: The relationship between the non-Darcy inertia coefficient and geometric characteristics.

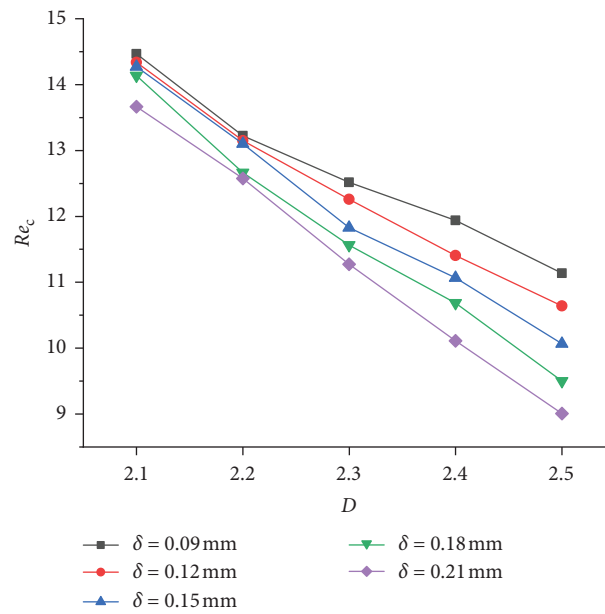


FIGURE 9: Relationship between the critical Reynolds number and geometric characteristics.

TABLE 2: Literature summaries about critical Reynolds number of flow in rock fractures.

Authors	Materials	Aperture ( $\mu\text{m}$ )	$Re_c$	Study method
Konzuk and Kueper	Tensile fractures of limestone	Mean = 381	2.8~14.3	Laboratory test
Javadi et al.	Tensile fractures of granite	—	0.001~25	Laboratory test
Zhang and Nemcik	Tensile fractures of sandstone	6.14~18.95	3.5~24.8	Laboratory test
Zimmerman et al.	3D fractures	Mean = 149	1~10.20	Numerical simulation
Chen et al.	Sedimentary and intrusive rocks	—	25~66	Field test
Qian et al.	Artificial parallel plate model	1000~2500	245~759	Laboratory test
This paper	3D rough fractures	Mean = 800	9.01~14.47	Numerical simulation

Therefore, the effect of  $\delta$  on the nonlinear flow behavior of the rough fractures is greater than that of  $D$ .

**5.4. Critical Reynolds Number.**  $Re_c$  can be used to evaluate the flow regime of fractures, representing the Reynolds number of the fluid flow going from the linear state to nonlinear state. When  $Re < Re_c$ , the flow behavior satisfied the cubic law on account of the inertia effect being very small and the viscous effect having a dominant role of fluid flow in fractures; when  $Re > Re_c$ , the flow behavior was controlled by the inertia effect, appearing Forchheimer-flow properties. As shown in Figure 9, for the same condition,  $Re_c$  has a decreasing trend with the increment of  $\delta$  and  $D$ , indicating that the fluid flow can more easily develop into nonlinear Forchheimer-flow resulting from the rougher surfaces and more heterogeneous aperture distribution.

Previous studies [13, 14, 35–38] on  $Re_c$  of flow in rock fractures are listed in the Table 2. In this study, for rough fractures of  $u = 0.8$  mm,  $\delta$  being 0.09~0.21 mm and  $D$  ranging from 2.1 to 2.5, the calculated values of  $Re_c$  are between 9.01 and 14.47, which are almost consistent with the previous researches.

## 6. Conclusions

In order to estimate the relationships between the nonlinear flow properties and self-affine fracture geometry, a systematic procedure with respect to the nonlinear flow analysis for the three-dimensional rough-walled fractures model is proposed based on the fractal characteristics, in which the roughness of fracture surfaces is characterized by the fractal dimension and the fractal model is generated by the SRAM. The numerical simulation of nonlinear flow analysis in self-affine aperture-based fractures is presented based on the fractal theory and N-S equation, in which the spatial variation of fracture geometry including roughness and aperture distribution is characterized by the fractal dimension and N-S equation is solved by the software COMSOL. The main conclusions are as follows:

- (1) The larger the fractal dimension, the greater the fracture surface roughness and the lower the correlation of the local aperture. The larger the standard deviation of the aperture, the greater the fluctuation of fracture surface and the more heterogeneous the aperture distribution.
- (2) The nonlinear relationship between flow rate and pressure gradient in self-affine aperture-based

fractures can be well described by the Forchheimer equation. The flow rate, standard deviation of the aperture, and fractal dimension can improve the deviation of pressure gradient from the cubic law.

- (3) With the increase of the standard deviation of the aperture, the linear coefficient of the Forchheimer equation is larger, and the hydraulic aperture becomes smaller. When the flow rate is small, fractal dimension has little effect on the permeability of fracture.
- (4) The nonlinear coefficient of the Forchheimer equation increases with the increment of the standard deviation of the aperture and fractal dimension, and the empirical expression between the nonlinear coefficient, the standard deviation of aperture, and the fractal dimension is proposed. The standard deviation of the aperture has greater impact on the nonlinear flow behavior than the fractal dimension. The critical Reynolds number decreases with the increase of standard deviation of the aperture and fractal dimension, and its measured range is 9.01~14.47, which is almost consistent with the previous results.

## Data Availability

The data used in the present study can be made available upon request from the authors.

## Conflicts of Interest

The authors declare that they have no conflicts of interest.

## Acknowledgments

The financial supports from the National Natural Science Foundation of China (Nos. 42077243 and 51709207), Natural Science Foundation of Hubei Province (No. 2018CFB631), and Visiting Researcher Fund Program of State Key Laboratory of Water Resources and Hydropower Engineering Science (2019SGG04) are gratefully acknowledged.

## References

- [1] C. Yao, Y. Shao, J. Yang, F. Huang, C. He, Q. Jiang et al., "Effects of non-darcy flow on heat-flow coupling process in complex fractured rock masses," *Journal of Natural Gas Science and Engineering*, vol. 83, Article ID 103536, 2020.

- [2] C. Yao, Y. Shao, and J. Yang, "Effects of fracture density, roughness, and percolation of fracture network on heat-flow coupling in hot rock masses with embedded three-dimensional fracture network," *Geothermics*, vol. 87, Article ID 101846, 2020.
- [3] Z. Ye, H. Qin, Y. Chen, and Q. Fan, "An equivalent pipe network model for free surface flow in porous media," *Applied Mathematical Modelling*, vol. 87, pp. 389–403, 2020.
- [4] Z. Ye, Q. Fan, S. Huang, and A. Cheng, "A one-dimensional line element model for transient free surface flow in porous media," *Applied Mathematics and Computation*, vol. 392, Article ID 125747, 2021.
- [5] I. Faoro, D. Elsworth, and T. Candela, "Evolution of the transport properties of fractures subject to thermally and mechanically activated mineral alteration and redistribution," *Geofluids*, vol. 16, no. 3, pp. 396–407, 2016.
- [6] S. Huang, Z. Lu, Z. Ye, and Z. Xin, "An elastoplastic model of frost deformation for the porous rock under freeze-thaw," *Engineering Geology*, vol. 278, Article ID 105820, 2020.
- [7] S. Huang, Y. Ye, X. Cui, A. Cheng, and G. Liu, "Theoretical and experimental study of the frost heaving characteristics of the saturated sandstone under low temperature," *Cold Regions Science and Technology*, vol. 174, Article ID 103016, 2020.
- [8] Z. C. Tang and Q. Z. Zhang, "Elliptical Hertz-based general closure model for rock joints," *Rock Mechanics and Rock Engineering*, vol. 54, no. 1, pp. 477–486, 2021.
- [9] Z. C. Tang, Q. Z. Zhang, and J. Peng, "Effect of thermal treatment on the basic friction angle of rock joint," *Rock Mechanics and Rock Engineering*, vol. 53, no. 4, pp. 1973–1990, 2020.
- [10] D. T. Snow, "A parallel plate model of fractured permeable media," M.Sc. thesis, University of California, Berkeley, CA, USA, 1965.
- [11] Z. Tang and Y. Jiao, "Choosing appropriate appraisal to describe peak spatial features of rock joint profiles," *International Journal of Geomechanics*, vol. 20, no. 4, Article ID 04020021, 2020.
- [12] Zhi Cheng Tang, "Experimental investigation on temperature-dependent shear behavior of granite discontinuity," *Rock Mechanics and Rock Engineering*, vol. 53, no. 9, pp. 4043–4060, 2020.
- [13] R. W. Zimmerman, A. Al-yaarubi, C. C. Pain et al., "Nonlinear regimes of fluid flow in rock fractures," *International Journal of Rock Mechanics & Mining Sciences*, vol. 41, no. 3, pp. 163–169, 2004.
- [14] Z. Y. Zhang and J. Nemcik, "Fluid flow regimes and nonlinear flow characteristics in deformable rock fractures," *Journal of Hydrology*, vol. 477, no. 16, pp. 139–151, 2013.
- [15] J. Q. Zhou, S. H. Hu, S. Fang et al., "Nonlinear flow behavior at low Reynolds numbers through rough-walled fractures subjected to normal compressive loading," *International Journal of Rock Mechanics & Mining Sciences*, vol. 80, pp. 202–218, 2015.
- [16] Y. F. Chen, J. Q. Zhou, S. H. Hu, R. Hu, and C. B. Zhou, "Evaluation of Forchheimer equation coefficients for non-Darcy flow in deformable rough-walled fractures," *Journal of Hydrology*, vol. 529, pp. 993–1006, 2015.
- [17] F. Xiong, Q. H. Jiang, Z. Y. Ye et al., "Nonlinear flow behavior through rough-walled rock fractures: The effect of contact area," *Computers & Geotechnics*, vol. 102, no. OCT, pp. 179–195, 2018.
- [18] M. Wang, Y. F. Chen, G. W. Ma, J. Q. Zhou, and C. B. Zhou, "Influence of surface roughness on nonlinear flow behaviors in 3D self-affine rough fractures: lattice Boltzmann simulations," *Advances in Water Resources*, vol. 96, pp. 373–388, 2016.
- [19] Q. Yin, G. W. Ma, H. W. Jing et al., "Hydraulic properties of 3D rough-walled fractures during shearing: An experimental study," *Journal of Hydrology*, vol. 555, pp. 169–184, 2017.
- [20] X. Zhang, H. Chen, C. Yao et al., "Seepage Characteristics of Triaxial Compression-Induced Fractured Rocks under Varying Confining Pressures," *International Journal of Geomechanics*, vol. 20, no. 9, Article ID 04020160, 2020.
- [21] F. Huang, C. Yao, J. Yang et al., "Connectivity evaluation of fracture networks considering the correlation between trace length and aperture," *Applied Mathematical Modelling*, vol. 88, pp. 870–887, 2020.
- [22] G. Zhang, Y. Tian, and L. Ying-Jun, "Numerical study on the mechanism of fluid flow through single rough fractures with different JRC," *Science China Physics, Mechanics & Astronomy*, vol. 49, no. 01, pp. 30–39, 2019.
- [23] C. C. Xia, X. Qian, P. Lin et al., "Experimental investigation of nonlinear flow characteristics of real rock joints under different contact conditions," *Journal of Hydraulic Engineering*, vol. 143, no. 3, Article ID 04016090, 2016.
- [24] Y. W. Tsang, "The effect of tortuosity on fluid flow through a single fracture," *Water Resources Research*, vol. 20, no. 9, pp. 1209–1215, 1984.
- [25] S. R. Brown, "Fluid flow through rock joints: the effect of surface roughness," *Journal of Geophysical Research: Solid Earth*, vol. 92, no. B2, pp. 1337–1347, 1987.
- [26] T. Liang, X. Liu, S. Wang, E. Wang, and Q. Li, "Study on the fractal characteristics of fracture network evolution induced by mining," *Advances in civil engineering*, vol. 2018, Article ID 9589364, 13 pages, 2018.
- [27] R. C. Liu, M. He, N. Huang et al., "Three-dimensional double-rough-walled modeling of fluid flow through self-affine shear fractures," *Journal of Rock Mechanics and Geotechnical Engineering*, vol. 12, no. 1, pp. 41–49, 2020.
- [28] H. H. Liu, G. S. Bodvarsson, S. Lu et al., "A corrected and generalized successive random additions algorithm for simulating fractional levy motions," *Mathematical Geology*, vol. 36, no. 3, pp. 361–378, 2004.
- [29] Z. Y. Ye, H. H. Liu, Q. H. Jiang et al., "Two-phase flow properties of a horizontal fracture: The effect of aperture distribution," *Advances in Water Resources*, vol. 76, pp. 43–54, 2015.
- [30] N. Huang, R. C. Liu, and Y. J. Jiang, "Numerical study of the geometrical and hydraulic characteristics of 3D self-affine rough fractures during shear," *Journal of Natural Gas Science and Engineering*, vol. 45, pp. 127–142, 2017.
- [31] G. Rong, J. Tan, H. B. Zhan et al., "Quantitative evaluation of fracture geometry influence on nonlinear flow in a single rock fracture," *Journal of Hydrology*, vol. 589, Article ID 125162, 2020.
- [32] Z. Zeng and R. Grigg, "A criterion for non-darcy flow in porous media," *Transport in Porous Media*, vol. 63, no. 1, pp. 57–59, 2006.
- [33] L. C. Zou, L. R. Jing, and V. Cvetkovic, "Shear-enhanced nonlinear flow in rough-walled rock fractures," *International Journal of Rock Mechanics & Mining Sciences*, vol. 97, pp. 33–45, 2017.
- [34] Z. L. Wang, L. F. Shen, Z. M. Xu et al., "Influence of roughness of rock fracture on seepage characteristics," *Chinese Journal of Geotechnical Engineering*, vol. 38, no. 7, pp. 1262–1268, 2016.
- [35] J. S. Konzuk and B. H. Kueper, "Evaluation of cubic law based models describing single-phase flow through a rough-walled fracture," *Water Resources Research*, vol. 40, no. 2, Article ID W02402, 2004.

- [36] M. Javadi, M. Sharifzadeh, K. Shahriar et al., "Critical Reynolds number for nonlinear flow through rough-walled fractures: the role of shear processes," *Water Resources Research*, vol. 50, no. 2, pp. 1789–1804, 2014.
- [37] Y. F. Chen, S. H. Hu, R. Hu et al., "Estimating hydraulic conductivity of fractured rocks from high-pressure packer tests with an Izbash's law-based empirical model," *Water Resources Research*, vol. 51, no. 4, pp. 2096–2118, 2015.
- [38] J. Qian, H. Zhan, S. Luo et al., "Experimental evidence of scale-dependent hydraulic conductivity for fully developed turbulent flow in a single fracture," *Journal of Hydrology*, vol. 339, no. 3-4, pp. 206–215, 2007.

## Research Article

# Stability Assessment of High and Steep Cutting Rock Slopes with the SSPC Method

Hongliang Tao,<sup>1</sup> Guangli Xu,<sup>1</sup> Jingwen Meng,<sup>2</sup> Ronghe Ma,<sup>3</sup> and Jiaying Dong<sup>3</sup> 

<sup>1</sup>Faculty of Engineering, China University of Geosciences, Wuhan, Hubei 430074, China

<sup>2</sup>Wuhan City Colledge, Wuhan, Hubei 430083, China

<sup>3</sup>Faculty of Electric Power Engineering, Kunming University of Science and Technology, Kunming, Yunnan 650500, China

Correspondence should be addressed to Jiaying Dong; [dong1986@kust.edu.cn](mailto:dong1986@kust.edu.cn)

Received 7 August 2020; Revised 27 January 2021; Accepted 7 April 2021; Published 20 April 2021

Academic Editor: Luis Neves

Copyright © 2021 Hongliang Tao et al. This is an open access article distributed under the Creative Commons Attribution License, which permits unrestricted use, distribution, and reproduction in any medium, provided the original work is properly cited.

The stability of high rock slopes has become a key engineering geological problem in the construction of important projects in mountainous areas. The original slope stability probability classification (SSPC) system, presented by Hack, has made obvious progress and been widely used in rock slope stability analysis. However, the selection and determination of some evaluation indexes in the original SSPC method are usually subjective, such as intact rock strength and weathering degree. In this study, the SSPC method based on geological data obtained in the prospecting tunnels was presented and applied. According to the field survey and exploration of the prospecting tunnels, the weathering degree of the slope rock mass was evaluated. The empirical equation for the maximum stable height of the slope was applied to the slope stability evaluation in the presented SSPC method. Then, the slope stability probability of numerous cutting slopes in the sandstone unit was evaluated using the presented system. Results of the Geostudio software based on the limited equilibrium analysis of the investigated slopes were compared with the results obtained by the SSPC method. The results indicate that the SSPC method is a useful tool for the stability prediction of high and steep rock slopes.

## 1. Introduction

The geomorphology in southwest China changes rapidly over short distances; in this region, large-scale projects such as hydropower stations were constructed, with complex geological conditions [1–3]. In recent years, the heights of cutting rock slopes can be as high as 300–500 m. For instance, the maximum cutting slope height at the Dagangshan project located in the Dadu River is 530 m, and the maximum cutting slope height at the Xiaowan project located in the Lancang River is 700 m [4]. Cutting slopes are prone to fail due to the disturbance on original geometry and strength [5], and assessing the stability of these rock slopes is an important and difficult task, due to ensure slope safety in period of construction and running.

Slope stability is affected by numerous factors, such as geological conditions, rock mass mechanical parameters, joint parameters, slope geometry, groundwater condition,

and excavation methods. At present, rock mass quality assessment, kinematical, analytical, and numerical analyses are the common methods in rock slope stability assessments [6]. However, the estimation of the parameters needed for the abovementioned methods is always challenging due to the heterogeneity of jointed slope masses [7, 8]. Since 1970, many rock mass classification systems that consider many affecting factors, such as the slope geometry, presence of water or water pressures, weathering effects, and excavation methods, have been proposed or modified and applied in the quantitative stability prediction of rock engineering [9–13]. The existing rock mass classification systems are becoming increasingly popular and are used in research on slopes worldwide as an accurate and useful tool for the rock slope stability assessment. In fact, shortcomings exist in most of the mentioned classification systems; for instance, failure modes of the slopes are always not taken into account, and only single-point data are used, but the slopes always have



large-scale and complex geological conditions. In addition, slope rock mass and exposure rock mass are always not distinctly differentiated in the existing approach [14]. To overcome the limitations previously, Hack (1998) [15] presented a new rock slope stability assessment approach (SSPC, slope stability probability classification), which has been used worldwide, especially in the research of road slopes in Spain [16], New Zealand, India [17], and Turkey [5, 6, 14] with good results. As a matter of fact, the method is generally suitable for slopes with a height of less than or equal to 45 m. Moreover, discontinuity property survey, weathering degree, and intact rock strength estimation involve high subjectivity and arbitrariness [14, 17, 18]. For these reasons, the SSPC method is rarely used in the high and steep cutting rock slopes [19].

In this study, key points of the SSPC method are introduced. Then, discontinuity surveys were carried out and data were collected and analyzed at four different prospecting tunnels, and discontinuity properties were obtained and input for the SSPC assessment system; stability of six proposed cutting slopes of the supported project is evaluated using the SSPC method.

## 2. Project Background

**2.1. Study Area.** The supported hydropower project is located upstream of the Dadu River, Sichuan Province, China, which flows through a valley with V shape. The reservoir has a normal pool level (NPL) of 2600 m, and the river's natural water level was approximately 2597 m. The basic seismic intensity of this area is VII degrees, indicating a relatively stable area. Slopes in this area were mainly in the metamorphic sandstone unit with upper Triassic and Jurassic bonobo groups. Rock fall phenomena and rock failure (sliding, toppling, and wedge failure seen in Figure 1) commonly occurred at natural slope in this region. In this paper, stability of six proposed cutting rock slopes seen in Figure 2 are studied, including tunnel-face slope (no. 1), intake slope (no. 2), the abutment slope (no. 3), slope of the toe board (no. 4), back-slope of the powerhouse (no. 5), and slope of the powerhouse in the left bank (no. 6) of the Dadu River. In Figure 2, four prospecting tunnels (PD09, PD01, PD07, and PD20) were arranged to find out the geological conditions of the abovementioned slopes. Specifically, discontinuity and rock mass properties, weathering degree, and other related parameters can be obtained by surveys and tests in the prospecting tunnels.

**2.2. Discontinuity Properties.** The discontinuity properties of the sandstone unit along the study area were determined by means of sample windows, scan lines performed at 5 locations, and other data that were collected by discontinuity statistics exposed in the 4 prospecting tunnels (PD09, PD01, PD07, and PD20, seen in Figure 2) distributed in the dam site. Accordingly, parameters of discontinuity such as the spacing, persistence, roughness, infill condition, and weathering degree were obtained with the suggestions of the International Society for Rock Mechanics (ISRM 2007) [20].

A total of 1276 discontinuities were collected and described, and the main joint sets are shown in Table 1, and a contour plot with Dips software [21] is presented in Figure 3.

Discontinuities develop in the studied slopes, collected in the corresponding prospecting tunnels, and natural exposures were divided into statistical and geological dominant joints based on the field survey and statistical analysis, as shown in Table 2.

Roughness and waviness parameters are of great importance for the stability of discontinuity-controlled failures. An increasing roughness profile of a discontinuity results in a substantial rise in the discontinuity shear strength. The sandstone unit in the study area commonly presents straight and rough discontinuity surfaces. In addition, the roughness of the same discontinuities can be classified as slightly curved ( $i = 2-4^\circ$ ) in large-scale roughness profiles and undulating (amplitude roughness  $>2-3$  mm) in small-scale roughness profiles with respect to the SSPC system. Commonly, no infill material in the discontinuities can be observed in sandstone, whereas surface staining can be observed. In addition, no karst phenomenon can be observed.

## 3. The SSPC System and Its Application

The original SSPC system was presented by Hack (1998) [15] for probabilistic stability assessments of rock slopes, and a related detailed description can be found in some literature [14, 16]. In this paper, only key points and the steps of stability assessment are introduced.

**3.1. Key Points of the SSPC.** The SSPC method encompasses a three-step evaluation of the slope stability probability, accordingly identifying three different rock masses (ERM, exposure rock mass; RRM, reference rock mass; SRM, slope rock mass) during evaluation [16].

- (a) ERM: exposed rock mass, which is directly observed on the exposure site of a natural or an old engineering slope
- (b) RRM: reference rock mass, which is the theoretical and imaginary fresh rock mass, undistributed due to the excavation
- (c) SRM: slope rock mass, which is the existing or proposed new slope to be cut (see Figure 4)
- (d) Two types of slope failure modes (orientation independent and orientation dependent) and the corresponding stability probability estimation methods are considered, with clear and simple needed-data collecting procedure

Figure 5 is the schematic diagram of the SSPC method; in the SSPC system, the slope stability probability can be evaluated on the basis of parameters obtained from the investigated exposure rock mass, such as the intact rock strength (IRS), discontinuity spacing (SPA), and condition of the discontinuities (CD). Obviously, the parameters obtained on the outcrop are significantly affected by weathering or excavation disturbances. The parameters of the ERM with different weathering and excavation

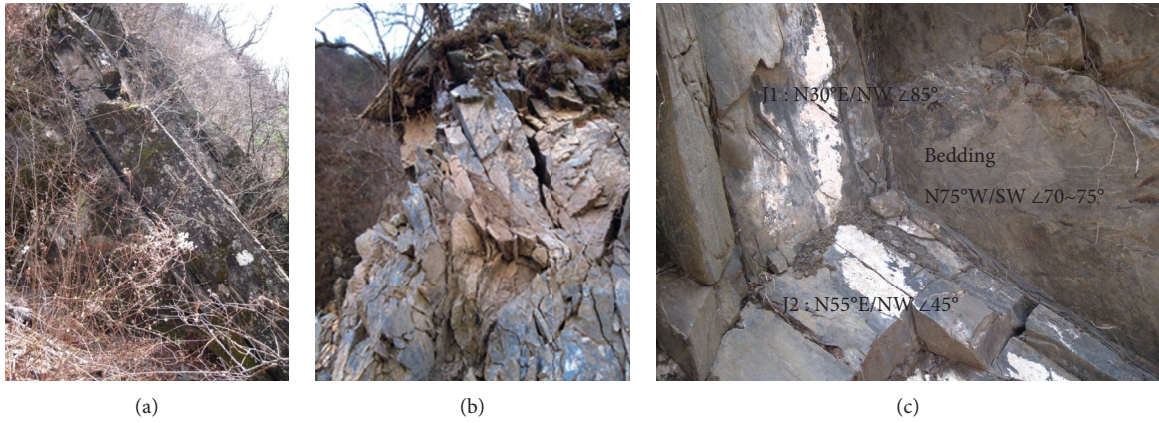


FIGURE 1: Failure of the natural slopes investigated: (a) sliding, (b) toppling, and (c) wedge failure.

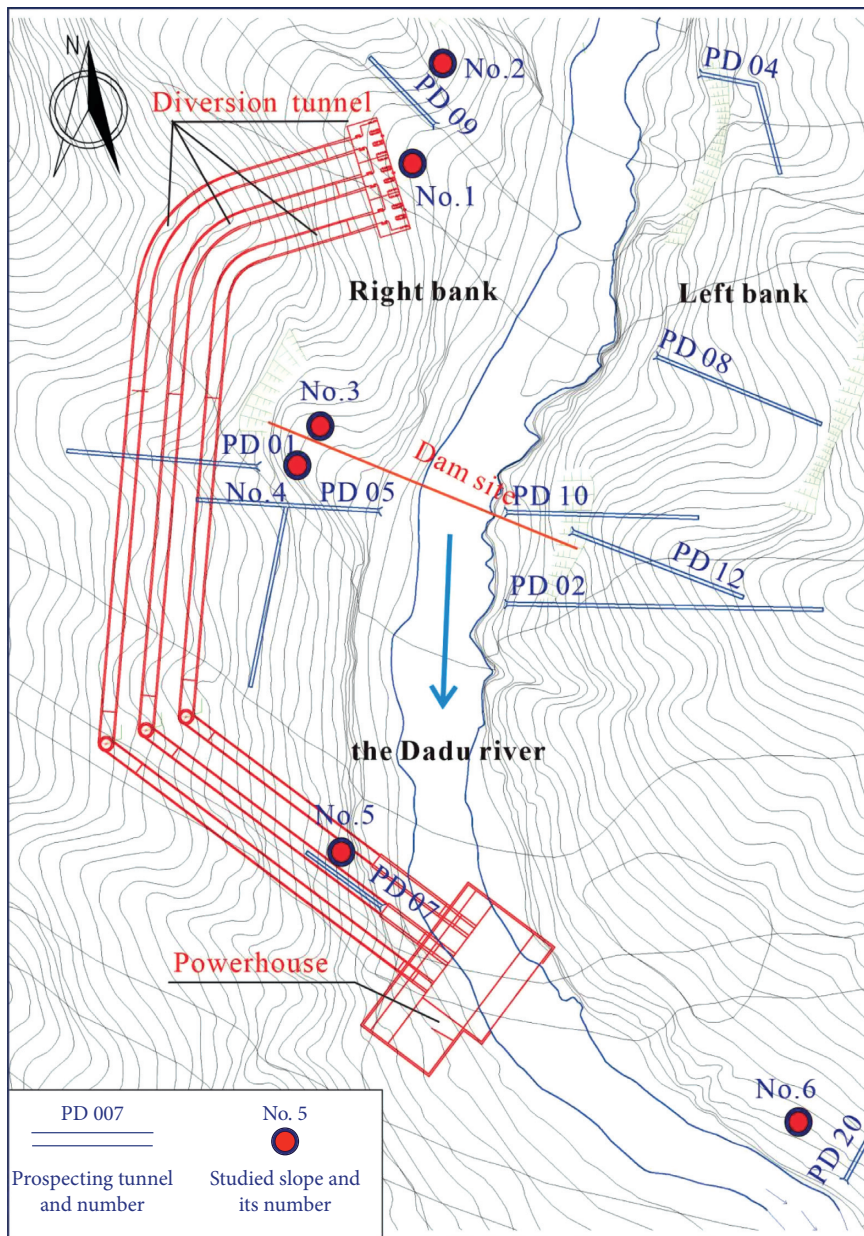


FIGURE 2: Distribution of the prospecting tunnels in the dam site.

TABLE 1: Characteristics of the surveyed discontinuity sets in the study area.

Discontinuity	Dip direction (°)	Dip (°)	Trace length (m)	Spacing (m)
1	318	66	<2	0.1–0.3
2	201	62	—	0.3–1
3	104	34	3–5	0.2–0.6
4	28	49	3–5	0.1–0.3

disturbance degrees in the same geotechnical unit can be converted to the RRM parameters [16]. The SRM stability is determined from the RRM with the adjustment of the parameters of SRM.

The shear strength parameters of the rock mass including internal friction angle  $\phi_{\text{mass}}$  and cohesion  $C_{\text{mass}}$  are used to assess the slope stability together with the height of the investigated slope ( $H_{\text{slope}}$ ) [22]. In case the dip of slope  $\text{dip}_{\text{slope}}$  is bigger than the internal friction angle  $\phi_{\text{mass}}$ , the maximum height of a stable slope ( $H_{\text{max}}$ ) can be determined by some empirical equations. The orientation-independent stability probability can be assessed using the parameters of  $H_{\text{max}}$ ,  $H_{\text{slope}}$ ,  $\phi_{\text{mass}}$ , and  $\text{dip}_{\text{slope}}$ . In addition, the probability of orientation-dependent stability can also be assessed according to the judgment graphs of the SSPC methods.

### 3.2. Calculation of the Shear Strength Parameters of the RRM.

Rock mass shear strength calculation is an important step in SSPC system; when calculation is carried out, parameters such as the intact rock strength (IRS), discontinuity spacing (SPA), roughness, infill, and karst are considered together. The IRS obtained in the laboratory or by the in situ test is divided by the weathering degree factor (WE) for calculating the reference rock intact rock strength (RIRS, see equation (1)). IRS is originally estimated using hammer blows and figure pressure; in this study, laboratory tests were performed, and the results show that intact rock strength of the fresh sandstone ranges from 136 MPa to 274 MPa, with an average value of 206 MPa. In addition, the slightly weathered sandstone has an average value of 148 MPa [23].

$$\text{RIRS} = \frac{\text{IRS}}{\text{WE}}. \quad (1)$$

The RSPA (discontinuity spacing of RRM) is determined considering three discontinuity sets that reveal minimum spacing values under the condition of more than three discontinuity sets revealed in the investigated rock mass. Consequently, factors 1, 2, and 3 are obtained using the graph presented in Figure 6. Then, SPA is calculated by equation (2), and the RSPA is calculated by equation (3), considering the factors of the weathering degree (WE) and method of excavation (ME). Referring to [15, 16], values of the WE and ME can be determined. In this paper, the weathering degree is divided according to the total joint number in a 5 m section of the prospecting tunnel, which is shown in Table 3.

$$\text{SPA} = (\text{Factor 1}) \times (\text{Factor 2}) \times (\text{Factor 3}), \quad (2)$$

$$\text{RSPA} = \frac{\text{SPA}}{(\text{WE} \times \text{ME})}. \quad (3)$$

TC, as the condition factor of a discontinuity, is calculated by equation (3). Here, Rl is a the large-scale roughness, Rs is the small-scale roughness, and Im and Ka are the factors of infill and karst, respectively. Considering weathering degree correction, TC of the reference rock mass named RTC is defined by equation (5).

$$\text{TC} = \text{Rl} \times \text{Rs} \times \text{Im} \times \text{Ka}, \quad (4)$$

$$\text{RTC} = \frac{\text{TC}}{(1.452 - 1.22 \times e^{-\text{WE}})^{0.5}}. \quad (5)$$

In the SSPC system, the weighted discontinuity condition CD is calculated by equation (5). Here, DS represents the discontinuity spacing. Similarly, the reference discontinuity condition (RCD) is calculated considering the weathering degree factor in Equation (7).

$$\text{CD} = \frac{(TC_1/DS_1) + (TC_2/DS_2) + (TC_3/DS_3)}{(1/DS_1) + (1/DS_2) + (1/DS_3)}, \quad (6)$$

$$\text{RCD} = \frac{\text{CD}}{\text{WE}}. \quad (7)$$

The friction angle ( $\phi_{\text{RM}}$ ) and cohesion ( $C_{\text{RM}}$ ) of a rock mass are calculated by equations (8) and (9). Here, RIRS is the intact rock strength, RSPA is the spacing, and RCD is the condition of discontinuities of the reference rock mass.

$$\phi_{\text{RM}} = (\text{RIRS} \times 0.2417) \times (\text{RSPA} \times 52.12) \times (\text{RCD} \times 5.779), \quad (8)$$

$$C_{\text{RM}} = (\text{RIRS} \times 94.27) \times (\text{RSPA} \times 28629) \times (\text{RCD} \times 3593). \quad (9)$$

### 3.3. Orientation-Dependent Stability Assessment of the SRM.

As mentioned above, in the SSPC system, both orientation-dependent and orientation-independent conditions are considered in the slope rock mass stability evaluation. As the term suggests, failures controlled by discontinuities such as planar sliding and toppling usually occur in the orientation-dependent stability analysis, while failures occur irrespective of a certain sliding surface in orientation-independent stability analysis. However, the probability of wedge failures cannot be evaluated in the SSPC system.

For the former type of stability assessment, factors such as the discontinuity condition (STC) and the apparent angle of the discontinuity dip in the direction of the slope dip (AP) are considered for evaluating the stability probability. The AP is obtained based on equation (10), where  $\alpha_s$  represents the direction,  $\alpha_j$  represents the dip direction of the discontinuity, and  $\beta_j$  represents the discontinuity dip.

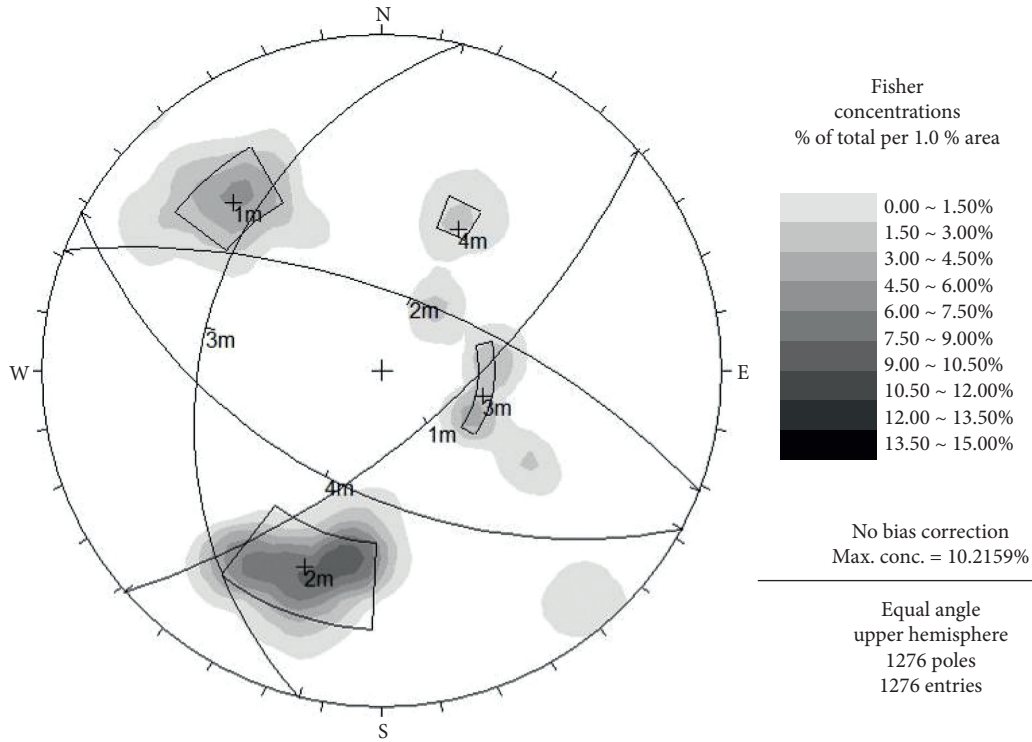


FIGURE 3: Contour plot of the field-surveyed discontinuity in the study area.

TABLE 2: Characteristics of the main discontinuity sets in the surveyed slopes.

Slope	Joint	Statistical dominant discontinuity			Geological dominant discontinuity			Note
		Dip direction (°)	Dip (°)	Spacing (m)	Dip direction (°)	Dip (°)	Spacing (m)	
1	B <sub>1</sub>	217	70	0.2–0.5	190	70	0.2–0.5	PD09
	J <sub>1</sub>	113	32	0.1–0.3	75	45	0.1–0.3	
	J <sub>2</sub>	138	83	0.1–0.3	305	55	0.1–0.3	
2	B <sub>1</sub>	217	70	0.2–0.5	215	75	0.3–0.6	
	J <sub>1</sub>	113	32	0.1–0.3	130	15	0.2–0.4	
	J <sub>2</sub>	138	83	0.1–0.3	130	80	0.2–0.4	
3	B <sub>1</sub>	194	66	0.1–0.5	190	60	0.1–0.5	PD01
	J <sub>1</sub>	122	54	0.2–0.6	120	55	0.2–0.6	
	J <sub>2</sub>	318	69	0.2–0.6	335	60	0.2–0.6	
4	B <sub>1</sub>	194	66	0.1–0.5	185	65	0.2–0.6	
	J <sub>1</sub>	122	54	0.2–0.6	125	60	0.3–0.7	
	J <sub>2</sub>	318	69	0.2–0.6	330	65	0.3–0.7	
5	B <sub>1</sub>	205	68	0.1–0.4	205	70	0.1–0.4	PD07
	J <sub>1</sub>	78	38	0.1–0.4	70	25	0.1–0.3	
	J <sub>2</sub>	327	64	0.2–0.4	315	60	0.3–0.4	
6	B <sub>1</sub>	195	75	0.2–0.5	200	50	0.1–0.4	PD20
	J <sub>1</sub>	325	45	0.1–0.3	140	85	0.2–0.4	
	J <sub>2</sub>	300	85	0.2–0.6	35	45	0.3–0.7	

Meanwhile, the discontinuity condition of the slope (STC) is determined by equation (11).

$$AP = \arctan [\cos(\alpha_s - \alpha_j) \tan \beta_j], \quad (10)$$

$$STC = RTC \times (1.452 - 1.220 \times e^{-SWE})^{0.5}. \quad (11)$$

For sliding failure, a relationship graph (see Figure 7(a)) between the STC and AP is employed to assess the occurrence probability of the slope. Furthermore, a relationship graph of the STC, AP, and  $\text{dip}_{\text{slope}}$  (see Figure 7(b)) is employed to evaluate the occurrence probability of the slope for toppling failure. In this paper, the probability results and the necessary parameters for

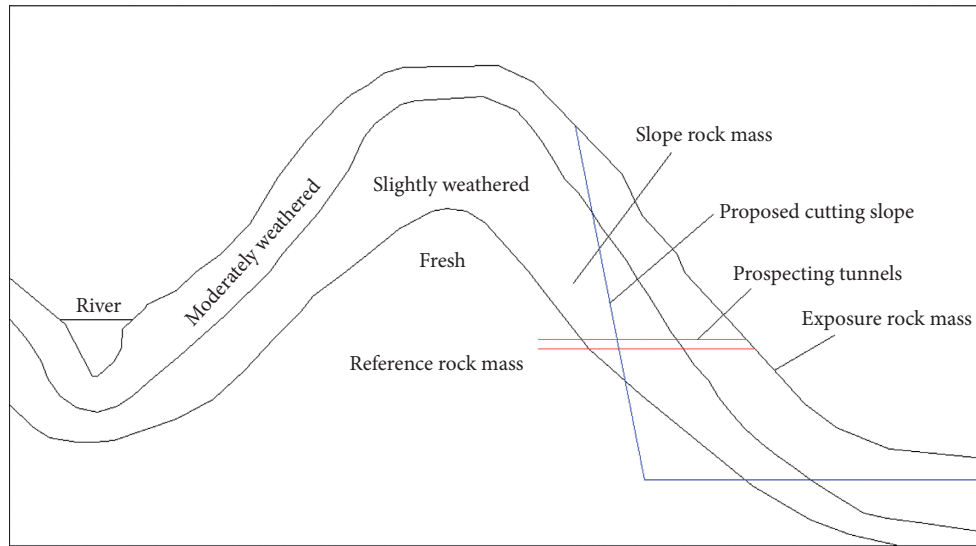


FIGURE 4: Sketch of exposures in rock masses of various degrees of weathering and different types of excavation indicating the concept of the reference rock mass.

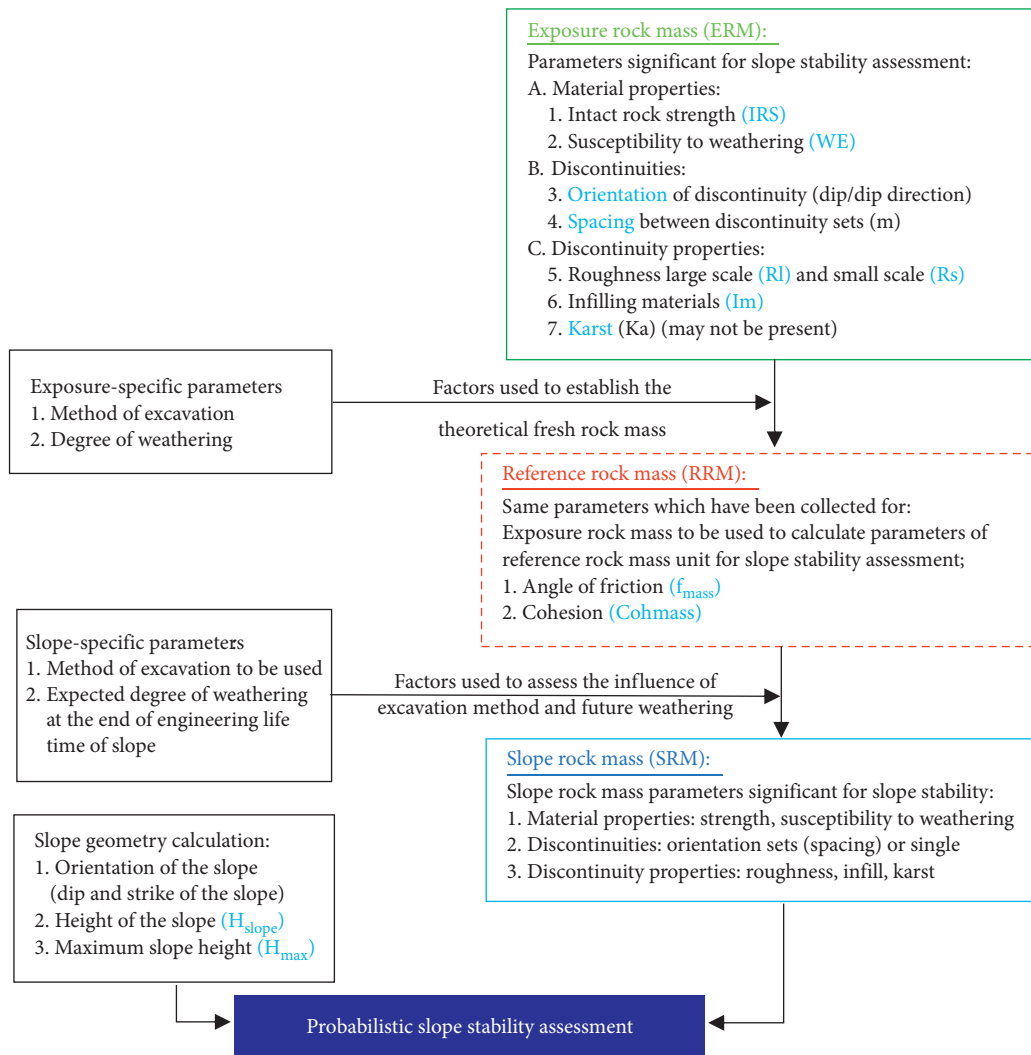


FIGURE 5: Flowchart of the SSPC method (modified after Canal A and Akin M, 2016).

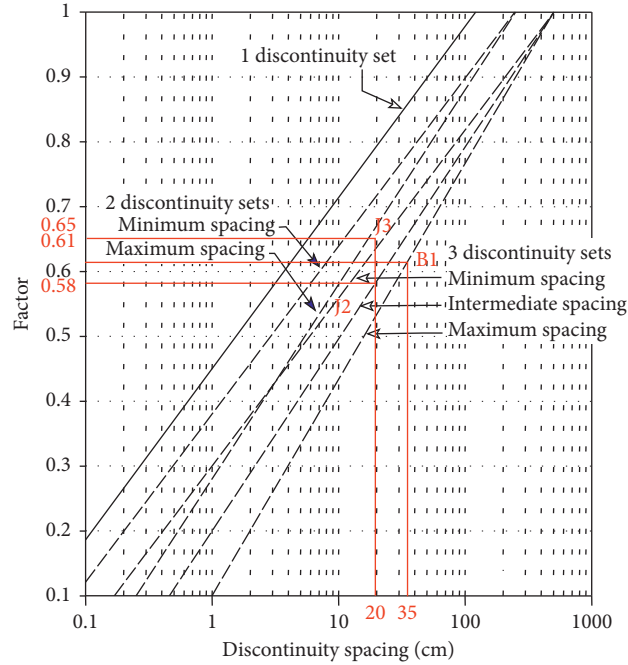


FIGURE 6: Factor determination graph in accordance with the discontinuity spacing [16].

TABLE 3: Weathering degree and its classification.

Degree	Joint number in a 5 m section	Value of WE
Complete	50–60	0.35
High	40–50	0.62
Moderate-high	30–40	0.77
Moderate-slight	20–30	0.92
Slight	10–20	0.95
Fresh	0–10	1.00

probability calculations in the study area are summarized in Table 4.

**3.4. Orientation-Independent Stability Assessment of the SRM.** Parameters needed in the calculation of stability of slope rock mass such as SIRS, SSPA, and SCD are determined as equation (12), in which the RRM values are corrected by the the weathering degree (SWE) and method of excavation (SME) for existing natural/excavated slopes.

Accordingly, the friction angle and cohesion of the slope mass are defined by equation (13). Obviously, an orientation-independent stability problem cannot occur under the condition of the  $\text{dip}_{\text{slope}} \leq \phi_{\text{SRM}}$  of the investigated slopes. However, the stability condition is evaluated on the basis of the maximum slope height ( $H_{\text{max}}$ ) [14, 16]. The orientation-independent slope stability probability can be easily determined by the chart seen in Figure 8. However, the assessment method of the maximum slope height ( $H_{\text{max}}$ ) was modified by Li et al. [19] if the height of slope is larger than 45 m. In this study, we assessed the  $H_{\text{max}}$  using the modified formulation  $H_{\text{max-Huang}}$ . The necessary parameters and probability calculations in the study area are summarized in

Table 5. A final assessment of the slopes (see Table 5) was performed by choosing the largest failure probability determined via the two analyses.

$$\begin{cases} \text{SIRS} = \text{RIRS} \times \text{SWE}, \\ \text{SSPA} = \text{RSPA} \times \text{SWE} \times \text{SME}, \\ \text{SCD} = \text{RCD} \times \text{SWE}, \end{cases} \quad (12)$$

$$\begin{cases} \phi_{\text{SRM}} = (\text{SIRS} \times 0.2417) \times (\text{SSPA} \times 52.12) \times (\text{SCD} \times 5.779), \\ C_{\text{SRM}} = (\text{SIRS} \times 94.27) \times (\text{SSPA} \times 28629) \times (\text{SCD} \times 3593), \end{cases} \quad (13)$$

$$\begin{cases} H_{\text{max-SSPC}} = \frac{[1.6 \times 10^4 \times C_{\text{SRM}} \times \sin(\text{dip}_{\text{slope}}) \times \cos(\phi_{\text{SRM}})]}{1 - \cos(\text{dip}_{\text{slope}} - \phi_{\text{SRM}})}, \\ H_{\text{max-Huang}} = (0.00651 + 0.00037m_i^{1.5}) \times \left(\frac{\sigma_{ci}}{\gamma}\right) e^{\text{GSI}(-0.0003m_i + 0.0483)}. \end{cases} \quad (14)$$

## 4. Discussion

Results seen in Tables 4 and 5 show that the calculated slopes were defined as stable. In addition, we also calculated the slope stability by the Geostudio software according to the step of the building model, parameters inputting, and calculating. Figure 9 is the typical simulation model of slope 2; compared with the outcome through the Geostudio software (Table 6), the results prove the validity and convenience of the SSPC methods introduced above. In addition, it is important selecting the suitable discontinuities for assessment of the stability probability in the SSPC method. In this study,

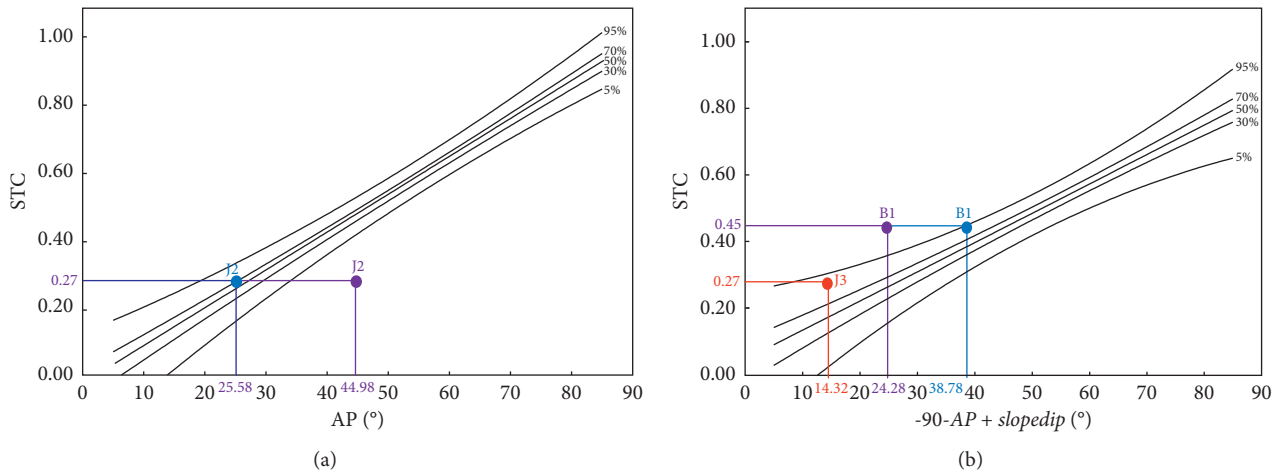


FIGURE 7: Flowchart of the SSPC methods determined by sliding and toppling (slope 1). (a) Sliding. (b) Toppling.

TABLE 4: Orientation-dependent stability probabilities of discontinuities at the typical investigated slopes.

Slope	Discontinuity	STC	AP	Sliding probability	Toppling probability	Slope stability probability
1	B <sub>1</sub>	0.45	-65.78	100%	95%	70%
	J <sub>2</sub>	0.27	25.58	70%	100%	
	J <sub>3</sub>	0.27	73.80	100%	100%	
2	B <sub>1</sub>	0.45	58.23	100%	100%	95%
	J <sub>1</sub>	0.27	21.88	95%	100%	
3	J <sub>2</sub>	0.27	82.28	100%	100%	95%
	B <sub>1</sub>	0.61	-42.41	100%	>95%	
4	J <sub>1</sub>	0.65	45.65	>95%	100%	95%
	J <sub>2</sub>	0.42	-54.08	100%	95%	
	B <sub>1</sub>	0.61	-42.41	100%	>95%	
5	J <sub>1</sub>	0.65	37.73	>95%	100%	>95%
	J <sub>2</sub>	0.65	-24.76	100%	>95%	
	B <sub>1</sub>	0.76	-60.26	100%	>95%	
6	J <sub>1</sub>	0.65	9.85	>95%	100%	>70%
	J <sub>2</sub>	0.65	81.33	100%	100%	
	B <sub>1</sub>	0.76	67.37	>70%	100%	

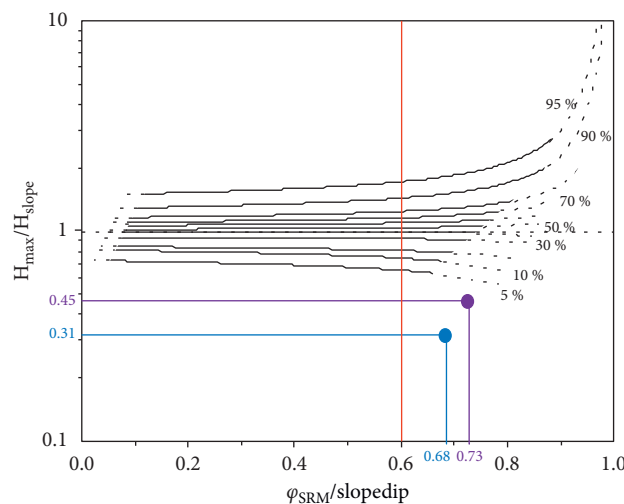


FIGURE 8: Flowchart of the SSPC methods determined by orientation-independent failure (slope 1).

TABLE 5: Summary of the orientation-independent stability probability at the investigated slopes.

Slope	$H_{\text{slope}}$ (m)	$\text{dip}_{\text{slope}}$ ( $^{\circ}$ )	$C_{\text{SRM}}$ (MPa)	$\phi_{\text{SRM}}$ ( $^{\circ}$ )	$H_{\text{max}}$ (m)	$H_{\text{max}}/H_{\text{slope}}$	$\phi_{\text{SRM}}/\text{dip}_{\text{slope}}$	Slope stability probability
1	105	63	0.584	37.84	1322.56	12.60	0.60	>95%
2	105	63	1.525	53.71	5044.85	48.05	0.85	>95%
3	180	73	1.030	39.27	2010.88	11.17	0.54	>95%
4	180	73	1.385	45.02	3045.16	16.92	0.62	>95%
5	90	73	0.648	30.89	1322.56	14.70	0.42	>95%
6	65	73	0.882	41.43	1849.98	28.46	0.57	>95%

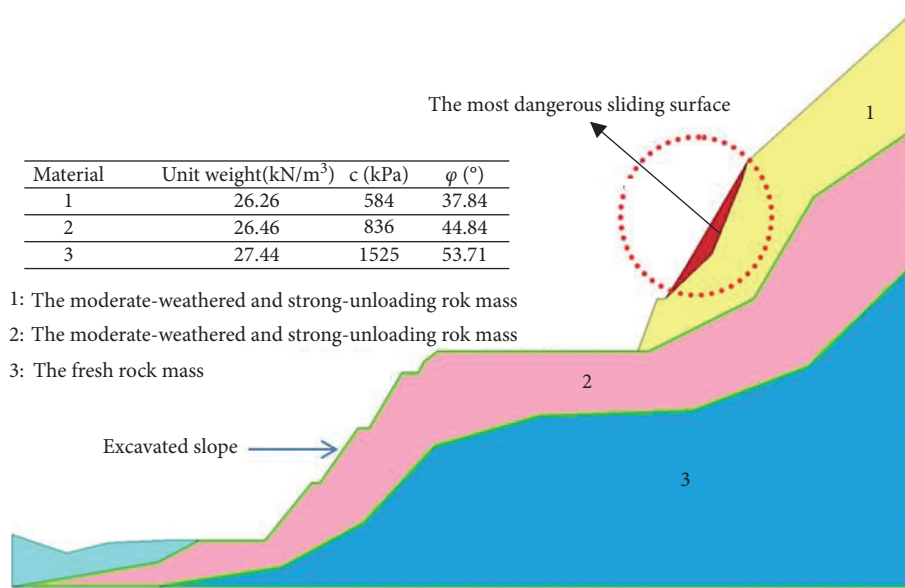


FIGURE 9: Typical simulation model of slope 2 using the Geostudio software.

TABLE 6: Summary of the stability assessment result using the Geostudio software and the SSPC method.

Slope	Safety factor values under different conditions			Stability assessment result by Geostudio	Stability probability by the SSPC method
	Normal	Rainstorm	Earthquake		
1	1.325	1.198	1.206	Stable	70%
2	1.188	1.301	1.377	Stable	95%
3	1.476	1.266	1.376	Stable	95%
4	1.408	1.285	1.293	Stable	95%
5	1.480	1.279	1.290	Stable	>95%
6	1.282	1.405	1.135	Stable	>70%

statistical dominant discontinuities obtained in the prospecting tunnels and natural outcrops were selected, but not the geological dominant discontinuities only obtained and determined by the natural outcrops.

### 5. Conclusions

In this study, the SSPC method based on geological data obtained in the prospecting tunnels was presented, and the slope stability probability of very high (50–300 m) and steep (60°–75°) cutting slopes in the sandstone unit was investigated using the proposed system. The following conclusions can be drawn.

Firstly, three sets of joints were presented in each studied slope. To overcome bias, laboratory data of the uniaxial compressive strength and rock mass strength parameters can be used for SSPC directly.

Secondly, statistically dominant discontinuities obtained in the prospecting tunnels and natural outcrops were suitable for the SSPC method, but not the geological dominant discontinuities only obtained and determined by the natural outcrops.

Finally, the formula of the critical slope height is optimized and applied to the stability evaluation, and the SSPC method based on geological data obtained in the prospecting tunnels can be accurately applied to the stability evaluation of high and steep rock slopes.



## Data Availability

The data used to support the findings of this study are included within the article.

## Conflicts of Interest

The authors declare that they have no conflicts of interest.

## Acknowledgments

This study was sponsored by the Program of the Yunnan Natural Science Foundation (no. 2015FD008) and Talent Development Program of Kunming University of Science and Technology (no. KKSJ201504022). The authors thank Zhenluo Shen for his contribution to the resolution improvement of the figures in this article.

## References

- [1] R. Huang, "Main characteristics of high rock slopes in southwestern China and their dynamic evolution," *Advances in Earth Science*, vol. 20, no. 3, pp. 292–297, 2005.
- [2] S. W. Song, X. M. Feng, B. Y. Xiang et al., "Research on key technologies for high and steep rock slopes of hydropower engineering in Southwest China," *Chinese Journal of Rock Mechanics and Engineering*, vol. 30, no. 1, pp. 1–22, 2011.
- [3] J. X. Dong, G. L. Xu, and S. S. Zhang, *A New Proposed Rockfall Hazard Rating System for Surrounding Slope in Large Hydropower Project*, pp. 1327–1340, EJGE, New York, NY, USA, 2014.
- [4] X. Y. Jing, Y. Wu, Y. Zeng et al., "Application of two dimensional limit equilibrium method in high slope engineering," *Design of Hydroelectric Power Station*, vol. 36, no. 4, pp. 1–3, 2020.
- [5] T. Ersoz and T. Topal, "Assessment of rock slope stability with the effects of weathering and excavation by comparing deterministic methods and slope stability probability classification (SSPC)," *Environmental Earth Sciences*, vol. 77, no. 547, pp. 1–18, 2018.
- [6] A. Canal and M. Akin, "Assessment of rock slope stability by probabilistic-based Slope Stability Probability Classification method along highway cut slopes in Adilcevaz-Bitlis (Turkey)," *Journal of Mountain Science*, vol. 13, no. 11, pp. 1893–1909, 2016.
- [7] Z. C. Tang, Q. Z. Zhang, and J. Peng, "Effect of thermal treatment on the basic friction angle of rock joint," *Rock Mechanics and Rock Engineering*, vol. 53, no. 4, pp. 1973–1990, 2020.
- [8] Z. Tang and Y. Jiao, "Choosing appropriate appraisal to describe peak spatial features of rock joint profiles," *International Journal of Geomechanics*, vol. 20, no. 4, Article ID 04020021, 2020.
- [9] Z. T. Bieniawski, "Engineering classification of jointed rock masses," *Journal of the South African Institution of Civil Engineering*, vol. 15, no. 12, pp. 343–353, 1973.
- [10] Z. Chen, "Recent developments in slope stability analysis," in *Proceedings of the 8th International Congress ISRM*, pp. 1041–1048, Tokyo, Japan, May 1995.
- [11] A. Singh, "Frhi — a system to evaluate and mitigate rockfall hazard in stable rock excavations," *J Div Civ Eng Inst Eng (India)*, vol. 85, pp. 62–75, 2004.
- [12] Y. C. Shi, Z. W. Wang, G. R. Wan, Z. Y. Wang, Q. Y. Chen, and S. C. Tang, "Study of mountain highway slope mass rating," *Chinese Journal of Rock Mechanics and Engineering*, vol. 24, no. 6, pp. 939–944, 2005.
- [13] L. Pantelidis, "Rock slope stability assessment through rock mass classification systems," *International Journal of Rock Mechanics and Mining Sciences*, vol. 46, no. 2, pp. 315–325, 2009.
- [14] X. Z. Li and Q. Xu, "Application of the SSPC method in the stability assessment of highway rock slopes in the Yunnan province of China," *Bulletin of Engineering Geology and the Environment*, vol. 75, no. 2, pp. 551–562, 2016.
- [15] H. R. G. K. Hack, *Slope Stability Probability Classification, SSPCp. 258*, 2nd edition, ITC, Enschede, The Netherlands, 1998.
- [16] R. Hack, D. Price, and N. Rengers, "A new approach to rock slope stability—a probability classification (SSPC)," *Bulletin of Engineering Geology and the Environment*, vol. 62, no. 2, pp. 167–184, 2003.
- [17] P. Lindsay, J. Anderson, F. Bourke, R. N. Campbell, and L. Clarke, "Predicting slope stability in open pit gold and coal mines," in *Proceedings of the New Zealand Minerals and Mining Conference Proceedings*, pp. 29–31, Wellington, New Zealand, October 2000.
- [18] L. Xiu-zhen, T. Rong-zhi, and G. Yan, "Modification of slope stability probability classification and its application to rock slopes in hydropower engineering regions," *Geologia Croatica*, vol. 72, pp. 71–80, 2019.
- [19] X. Z. Li, J. M. Kong, and S. W. Li, "Stability probability classification method for rock slope in hydropower engineering region," *Chinese Journal of Rock Mechanics and Engineering*, vol. 30, no. 2, pp. 4025–4032, 2011.
- [20] ISRM (International Society for Rock Mechanics), "The complete ISRM suggested methods for rock characterization, testing and monitoring: 1974-2007: suggested methods prepared by the commission on testing methods," *International Society for Rock Mechanics*, vol. 15, 2007.
- [21] Rocscience Inc. (1998) Dips v.5.0—graphical and statistical analysis of orientation data. Available online at: <http://www.rocscience.com>.
- [22] I. Das, S. Sahoo, C. van Westen, A. Stein, and R. Hack, "Landslide susceptibility assessment using logistic regression and its comparison with a rock mass classification system, along a road section in the northern Himalayas (India)," *Geomorphology*, vol. 114, no. 4, pp. 627–637, 2010.
- [23] R.-H. Ma, *HSSPC Method and its Application in High and Steep Rock Slope in Hydropower Engineering*, Kunming University of Science and Technology, Kunming, China, 2020.

## Research Article

# A Typical Basalt Platform Landslide: Mechanism and Stability Prediction of Xiashan Landslide

Yongliang Huang,<sup>1,2</sup> Zhiwei Sun,<sup>1</sup> Chunyan Bao ,<sup>1,3</sup> Man Huang ,<sup>1,3</sup> Anyuan Li,<sup>1,3</sup> and Minghao Liu <sup>4</sup>

<sup>1</sup>College of Civil Engineering, Shaoxing University, Shaoxing, Zhejiang 312000, China

<sup>2</sup>Zhejiang Nonferrous Metals Geological Exploration Bureau, Shaoxing, Zhejiang 312000, China

<sup>3</sup>Key Laboratory of Rock Mechanics and Geohazards of Zhejiang Province, Shaoxing University, Shaoxing, Zhejiang 312000, China

<sup>4</sup>State Key Laboratory of Frozen Soil Engineering, Cold and Arid Regions Environmental and Engineering Research Institute, Chinese Academy of Sciences, Lanzhou, Gansu 730000, China

Correspondence should be addressed to Chunyan Bao; baochunyan1985@126.com

Received 6 November 2020; Revised 29 December 2020; Accepted 24 March 2021; Published 5 April 2021

Academic Editor: Guoyang Fu

Copyright © 2021 Yongliang Huang et al. This is an open access article distributed under the Creative Commons Attribution License, which permits unrestricted use, distribution, and reproduction in any medium, provided the original work is properly cited.

The Xiashan landslide, which is classified as a typical basalt platform landslide, is the most massive landslide in Zhejiang Province, China. Once sliding occurs, it will pose a severe threat to the life and property of downstream residents and the nearby section of Hangzhou-Taizhou Expressway. On the basis of the geological conditions, present situation, and latest monitoring data of the landslide, this study finds that rainfall is the main influencing factor, and the creep mode is the main prediction mode of its subsequent deformation. The rainfall statistics of the landslide area in the past 30 years show that the rainfall and rainfall frequency in the landslide area display an increasing trend. The probability of heavy rain with rainfall intensity of 100–250 mm/day in the landslide area is very high. On this basis, combined with the numerical analysis method, a finite element model of the slope considering rainfall and groundwater conditions is constructed to analyze the causes and failure mechanism of this landslide comprehensively. Results indicate that the maximum tensile stress at the top of the trailing edge under the natural state is 5.10 MPa, which is very close to the saturated tensile strength of rock mass. Thus, tensile cracks are easily generated and developed, thereby causing the failure mode to be the hydraulic driving type. Also, with the increase in rainfall intensity, the slope plastic strain increases and the slope plastic zone develops and extends until it is completely penetrated. When the rainfall intensity is more than 200 mm/day, the slope safety factor is close to unity, and the slope approaches a failure condition. Therefore, the landslide should be controlled through water treatment and integrated with engineering measures.

## 1. Introduction

The mechanical and hydraulic characteristics of rock joints have an important influence on the strength and stability of engineering rock mass [1, 2]. Slope instability often occurs with the rapid development of infrastructure projects such as buildings, highways, railways, and bridges. Stability analysis is necessary for slope treatment. Whether subsequent processing will be carried out is decided in accordance with the results of stability analysis [3–5].

The traditional slope stability analysis method is qualitative analysis, which involves collecting meteorological, geological,

hydrological, and deformation information of landslides through on-site surveys, geological prospecting, and landslide monitoring. Afterward, combined with engineering experience, the causes, influencing factors, and failure mechanisms of landslides are analyzed. With the rapid development of mechanics and computer technology in modern times, numerical simulation research methods have emerged, which can make full use of computers' superior computing performance and have the characteristics of accuracy and speed. Therefore, numerical simulation has become the mainstream trend of slope stability analysis today. To use the numerical analysis method, a numerical model needs to be established based on

the relevant parameters obtained from the preliminary slope investigation and experiment. According to the stress-strain relationship, the numerical model can accurately calculate the real state of the slope under various conditions. The calculated results of slope displacement, stress, and strain can be expressed in the form of diagrams.

In recent years, many scholars have carried out a series of research on slope stability analysis. Cai [6], Wang [7], and Chen [8] collected information on the geological structure, material properties, and macroscopic deformation of a landslide by means of exploration, drilling, and Global Navigation Satellite System. They used the limit equilibrium method and finite element strength subtraction to research slope stability and found that water storage and rainstorm are closely related to landslide deformation. Zhou [9] et al. analyzed landslides in various ways, including field surveys, laboratory tests, and numerical simulations. They also believed that the intensity and duration of rainfall would affect the water pressure and shear strength of slopes. Rainfall significantly reduces the slope shear strength and increases the pore water pressure and soil weight. As a result, the slope stability is reduced. By studying the relationship between the internal stress state of the landslide caused by rainfall with time, Iverson [10], Calvillo [11], and Zhou [12] established a new slope mathematical model that can consider seepage. On the basis of the model, they analyzed the influence of rainfall infiltration on the saturated state, pore water pressure, displacement rate, and safety factor of landslide under different conditions. Their research shows that water level fluctuation, permeability, and shear strength are the key factors that affect seepage field and slope stability. Iverson [13] used a newly developed model to simulate the Oso landslide in the state of Washington, USA. The model results show that liquefaction depended strongly on initial sediment porosity. Conte [14] used the material point method (MPM) to simulate the run-out process of the Maierato landslide in Southern Italy. They think that the high pore water pressure caused by the large distortions of the moving soil mass leads to the serious reduction of the shear strength of the soil.

The Xiashan landslide, which occurred in Xiashan Administrative Village, Huishan Town, Xinchang County, Zhejiang Province, China, took place in an old landslide hidden danger area that includes three villages, namely, Xiashan, Lishan, and Tangli villages. To this day, this area is still the most massive landslide in Zhejiang Province, with a landslide volume of 8.25 million  $\text{m}^3$ , and is listed as a key monitoring geological hazard spot in the province. The Xiashan landslide has the typical characteristics of a basalt platform landslide [15, 16], and it exhibits intermittent activity because of many slides in the past.

At present, the landslide is unlikely to slide as a whole under normal conditions. However, heavy rain or long-term continuous rainfall may lead to local sliding and easily form barrier lakes at the foot of the slope [17]. The Shimen Reservoir, which is located on the west side of the landslide and has a storage capacity of approximately 4.5 million  $\text{m}^3$ , will be affected. A risk of dam break exists and poses a severe threat to the life and property of the downstream residents and the nearby section of Hangzhou-Taizhou Expressway.

This study analyzes the different aspects of the landslide. First, the geological conditions, landslide status, cause analysis, and failure mechanism of the Xiashan landslide are investigated on the basis of the investigation results and relevant data obtained in 2019. Second, the recent half-year displacement and groundwater level monitoring data of the landslide are sorted. In addition, the historical rainfall data of Xinchang County in the past 30 years are collected, and the future rainfall situation is predicted. Third, a landslide numerical model considering rainfall and groundwater conditions is constructed using the finite element software Midas GTS NX. Lastly, stability analysis is performed in accordance with the calculation results, and prevention and treatment suggestions are proposed.

## 2. Present Situation of the Xiashan Landslide

The Xiashan landslide is located in a low mountainous and hilly area and has a maximum relative height difference of 386.5 m. The considerable vertical height leads to an increased vertical geomorphic contrast, and the average natural slope of the terrain typically ranges within  $25^\circ$ – $40^\circ$ . Given the early human farming activities, local areas form a multistep terrain in the longitudinal direction. The step height difference is mostly within the range of 8–20 m, whereas a small part ranges within 30–35 m. Both sides of the Shimen Reservoir on the west side of the landslide are violently cut down by the river. A V-shaped valley landform is formed, and the undercut depth is generally larger than 100 m (Figure 1).

According to the drilling results, the rock and soil layers in the landslide area are divided into the following 15 layers from top to bottom (Figure 2): (1) silty clay layer containing crushed stones, (2) gravel layer containing cohesive soil, (3) basalt, (4) pebble subclay layer, (5) basalt, (6) sandy clay, (7) clay rock, (8) layer containing peat soil, (9) clay rock containing gravel, (10) layer containing peat soil, (11) basalt, (12) gravelly clay rock, (13) basalt, (14) silty clay layer containing gravel sand, and (15) tuff intercalated with tuffaceous sandstone.

The fracture developments of the Quaternary gravel layer, sedimentary rock containing sand (gravel) layer, and basalt layer in the landslide area lead to good permeability. The main sources of groundwater recharge are atmospheric precipitation and interlayer overflow recharge channels. The irrigation water recharge through channels and valley water recharge is the second source of replenishment. The hydraulic connection among aquifers is excellent. Groundwater is discharged from the surface in the form of spring water (scattered flow, gushing water, and seepage water) at the scarps, contact surface between aquifers and waterproof layer, front edge of the landslide, low-lying terrains, and landslide cracks.

Basalt joints and fissures developed due to the influence of the geological structure cut the rock mass under the effect of subsequent weathering. The joints and fissures along the slope direction greatly influence the stability of the landslide. The crust of the landslide area is raised and lowered repeatedly by the neotectonic movement. As a result, the rock

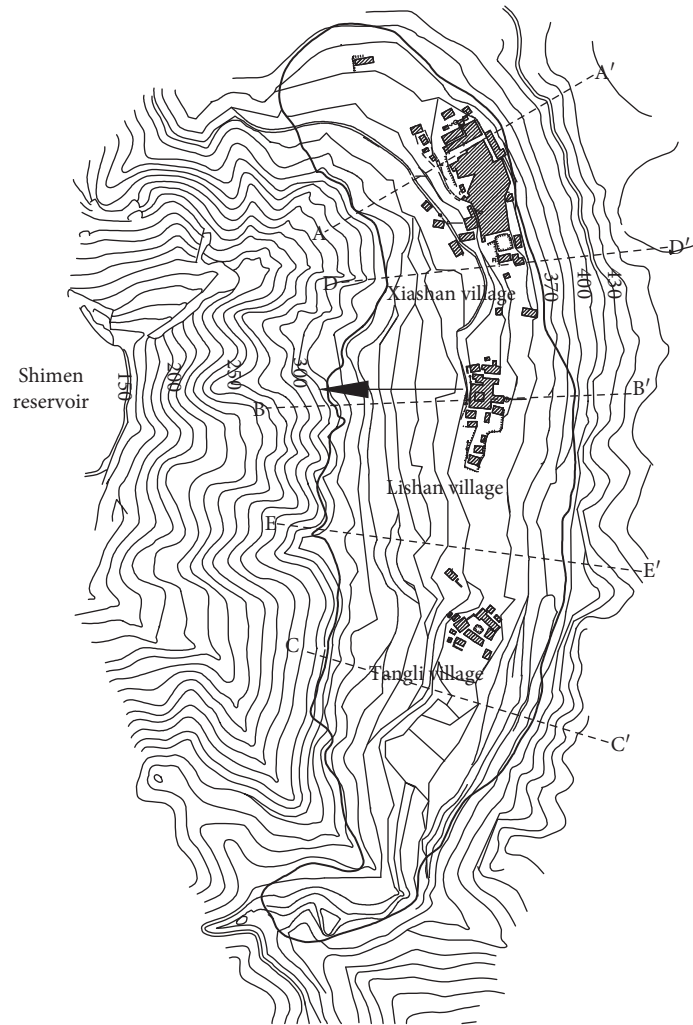
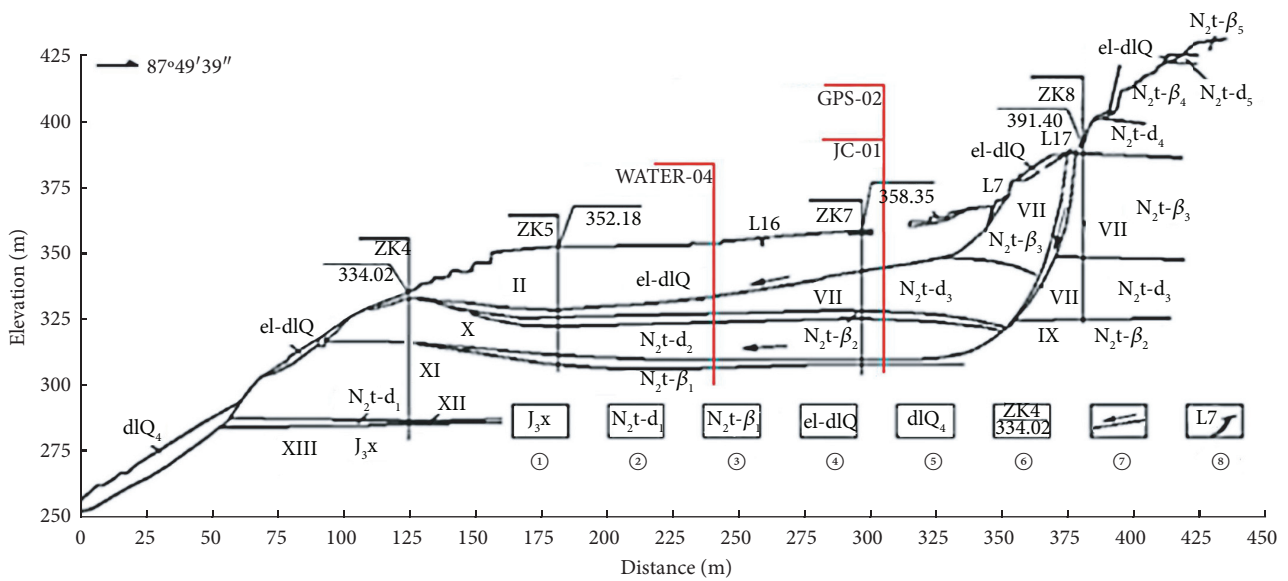


FIGURE 1: Planar graph of Xiashan landslide.



- |   |                                  |
|---|----------------------------------|
| ① Xishantou village group                           | ⑤ Talus accumulation             |
| ② Soft rock strata of the tonglingzhu village group | ⑥ Borehole and orifice elevation |
| ③ Basalt strata of the tonglingzhu village group    | ⑦ Sliding surface                |
| ④ Residual slope sediments                          | ⑧ Landslide cracks               |

FIGURE 2: Engineering geological map of typical section.

formations in the area often exhibit topographic inversion and many different lithological types. In addition, the alternating occurrence of eruptive and sedimentary layers always occurs, which is unfavorable to the stability of the landslide.

The cracks in the landslide area are vertically and horizontally developed into a grid shape. These cracks can be divided into tension and shear cracks depending on the causes. The width of the cracks is 0.3–3.0 m; such cracks mostly form steps, depressions, and ditches. Two sliding surfaces mainly control the Xiashan landslide. The shallow sliding surface is located at the contact point between gravel and silty clay, whereas the deep sliding surface is located at the contact point between the layer containing peat soil and the moderately or strongly weathered basalt. The trailing edge of the two sliding surfaces has a large inclination angle with cracks at the top, allowing the surface water to easily seep down. The middle part of the edge is relatively flat.

The residents of the original Xiashan, Lishan, and Tangli villages have been relocated, and the original landslide area is now completely restored into dry land. Most of the houses in the area have been demolished. The engineering activities in the site mainly include human farming activities on the surface of the slope, which can promote the infiltration of surface water on the landslide to a certain extent. The overall level of human engineering activities is average.

### 3. Causes and Failure Mechanism

**3.1. Cause Analysis.** Historical records and statistics and monitoring data of the seismic stations [18] indicate that 34 perceptible earthquakes occurred from the year of Yongyuan of the Han Dynasty (89 AD) to 1990. The common earthquakes had a magnitude of less than 4.75 with a weak intensity and low frequency, and no disaster occurred. The peak acceleration of the earthquake in Xinchang County was less than 0.05 g, and the corresponding basic earthquake intensity was lower than VI degrees, which belongs to the stable crustal area [19].

Three large-scale landslide activities have occurred since 1958. Rainfall is the dominant factor, and human intervention is the secondary factor. In terms of causes, the main factors include three aspects. First, rainwater rapidly converges from the former to the latter due to the large difference in the height between the middle and trailing edges of the slope. The terrain in the middle of the slope is relatively flat, and the surface water gathered in this area will accumulate and infiltrate. Both have adverse effects on slope stability. Second, the Quaternary gravel layer, sedimentary rock containing sand (gravel) rock layer, and basalt fissures have good permeability. The infiltration of rainwater loosens and softens the rock and soil, thereby resulting in a rapid decline in their cohesion forces and making the area prone to plastic deformation. Lastly, the rise in the water level at the trailing edge of the slope produces a tremendous hydrostatic pressure under the influence of rainfall. The water level difference will convert the hydrostatic pressure into an equivalent hydrodynamic pressure, which is conducive to the sliding of the sliding surface. As previously mentioned,

the human engineering activities in the landslide area are the secondary factor. Soil loosening caused by human plowing greatly helps the surface water infiltrate the landslide and promotes the development of the landslide from the other side.

**3.2. Failure Mechanism Analysis.** The failure mode of the Xiashan landslide belongs to the consequent layer sliding failure [20, 21]. In accordance with the mechanical mechanism of deformation and failure, the consequent layer sliding failure of the general rock slope can be divided into two modes: sliding tensile cracking type and hydraulic driving type.

Historical exploration data of the Xiashan landslide indicate that the cracks in the landslide are relatively developed, and the landslide mass is cut into a grid shape. Cracks appeared in every part of the landslide a few days after the landslide slipped on July 30, 1989. These cracks have a relatively short development time, and their width, length, and depth are relatively small. Moreover, these cracks have a weak effect on the stability of the landslide. The landslide is mainly controlled by the shallow weak surface in the slope. Given that the weak surface is located at the contact point of different rock layers, the cohesive force of the nearby rock and soil is small. Therefore, the shear strength of the weak surface is greatly affected by the internal friction angle. The inclination angle of the shallow weak surface is greater than its equivalent internal friction angle, and the sliding force of the sliding body is greater than its shear strength. In addition, the toe of the slope is a free surface, thus causing the slope to be likely to form tensile cracks at the trailing edge due to creep, which will lead to instability and failure. In such a case, the failure mode of the Xiashan landslide belongs to the sliding tensile cracking type (Figure 3).

During large-scale survey and mapping in 2003, 24 representative cracks were investigated, including tension cracks, bulging cracks, shear cracks, and other cracks with typical stress characteristics. The Xiashan landslide is characterized by the appearance of new cracks or the widening of previous cracks in the landslide body. The development degree of the tensile cracks on the trailing edge of the landslide body gradually increases over time. The width, length, and depth of the cracks significantly increase; the depth of the crack is more than 50 m and connects with the deep weak surface in the slope. Given that the inclination angle of the deep weak surface is less than its equivalent internal friction angle, the landslide can maintain a relatively stable state in its natural state even if the toe of the slope is in the air. The deformation and failure of a rock slope are not only related to the inclination shape, thickness, and mechanical properties of the weak surface, but are also affected by the groundwater and water content of the rock and soil in the slope. The vertical joints and fissures of basalt in the eruptive layer of the Pliocene Sheng County group are developed and easily lead to the downward infiltration of surface water. During rainfall, especially heavy ones, the surface runoff at the trailing edge of the slope flows into the cracks. A large amount of precipitation seeps into the sliding

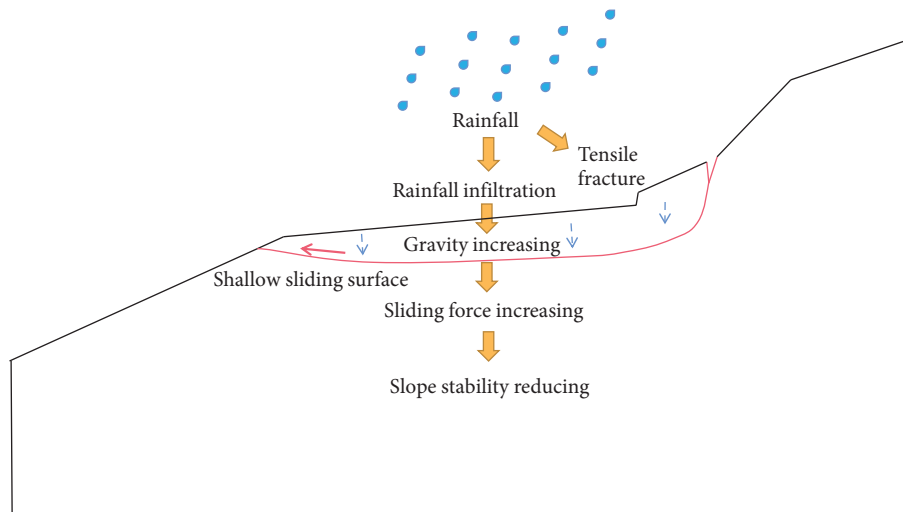


FIGURE 3: Schematic of sliding tensile cracking type.

mass and moves the aquifer into the saturation state. As a result, rock and soil particles will float, the spacing between the rock and soil particles will increase, and the shear strengths of the rock and soil will be reduced. After the water saturation level of each aquifer increases, the phreatic aquifer becomes a phreatic-confined or confined aquifer. Consequently, the bulk density of the rock and soil rapidly increases, the water buoyancy force rises, and the antisliding ability abruptly decreases. In addition, the slope of the sliding bed formed by the cracks at the trailing edge of the landslide is exceptionally steep. With the increase in rainfall intensity, the height of the water head in the cracks at the trailing edge of the landslide increases. The hydrostatic pressure caused by the rise in groundwater level, the hydrodynamic pressure formed by groundwater flow (i.e., uplift pressure), and the seepage pressure of the sliding zone (i.e., drag force) will also increase. When the rainfall intensity reaches a certain critical value, the sum of the driving forces (sliding force) generated by gravity and hydrostatic, hydrodynamic, and seepage pressures becomes greater than the weakened shear strength (antisliding force). As a result, the landslide slips and loses stability. At this time, the failure mode of the Xiashan landslide changes from the sliding tensile cracking type to the hydraulic driving type (Figure 4).

**3.3. Deformation Prediction.** An analysis of the landslide causes and failure mechanism shows that creep deformation is the main subsequent deformation mode of the Xiashan landslide. The organic soil and low-strength clay rock in the Tonglingzhu Village sedimentary section of the Pliocene Sheng County group are the control sliding surfaces of the landslide. The stability and deformation of the landslide are closely related to the groundwater content in the landslide body. In general, directly replenishing the groundwater in the deep slide through low-intensity, short-term rainfall is difficult. However, when the rainfall intensity is high or long-term rainfall occurs, the sliding surface softens and the saturation of the sliding body increases with the continuous infiltration of surface water, thereby resulting in sliding deformation.

Considering the sizeable transverse width of the landslide and the fluctuation change of the buried depth of the sliding surface, the possibility of continuous and integrated sliding in later period is minimal. When the emergency balance is unbalanced, the sliding mass in the entire landslide area is mainly segmented and discrete. The inclination angle of the gliding section of the leading edge is gentle, and the overall slip amount is small.

## 4. Monitoring Results and Rainfall Statistics

**4.1. Analysis of Monitoring Results.** Twenty years have passed since the major sliding of the Xiashan landslides occurred in 2001 due to continuous rainfall. To obtain an accurate understanding of the current situation of the landslide, this study collates and summarizes the monitoring data of deep displacement, surface displacement, rainfall, and groundwater level of the relevant monitoring points near the B-B section of the Xiashan landslide for half a year.

The accumulated displacement at 30.5 m below the JC-01 deep displacement monitoring point for the Xiashan landslide in the first half of 2020 is shown in Figure 5. The cumulative displacement data fluctuate between  $-0.2$  and  $0.2$  mm with time. Considering the error factors, such as the accuracy of the monitoring instruments and difficulty of field monitoring, no deep displacement is observed at 30.5 m below the monitoring point. The buried depth of the WATER-04 groundwater level monitoring point is relatively stable in the first half of 2020. The average depth of the water level is 34.26 m. As shown in Figure 6, April 2020 experienced 6 days of rain, with a total rainfall of 150 mm and a maximum daily rainfall of 45 mm. The cumulative displacement data range of the GPS-02 surface displacement monitoring points in April 2020 is 1.94–3.56 mm. The total surface slip in April is 1.6 mm, and the displacement rate is 0.05 mm/day. The overall trend is increasing with time.

Observing Figure 6, we find that the surface displacement curve has five rapid-rise periods. The rainfall intensity is less than 50 mm/day; thus, the acceleration of the ground

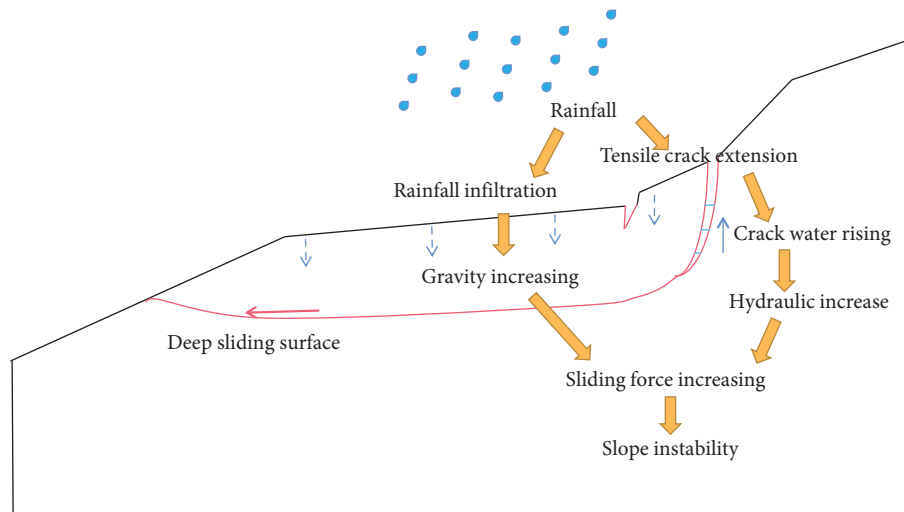


FIGURE 4: Schematic of hydraulic driving type.

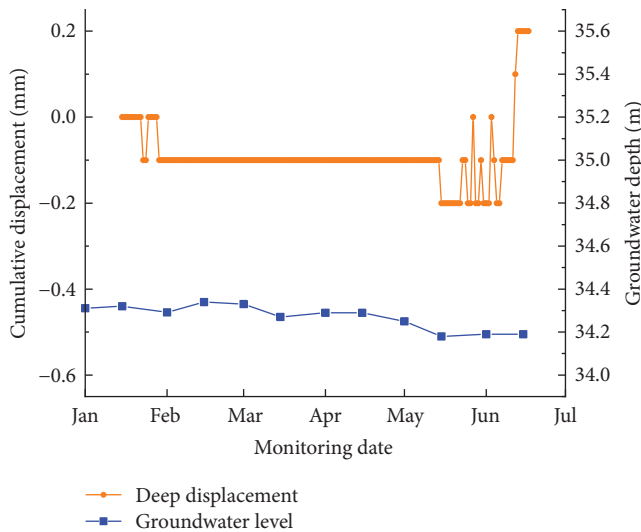


FIGURE 5: Deep displacement and groundwater level from January to June 2020.

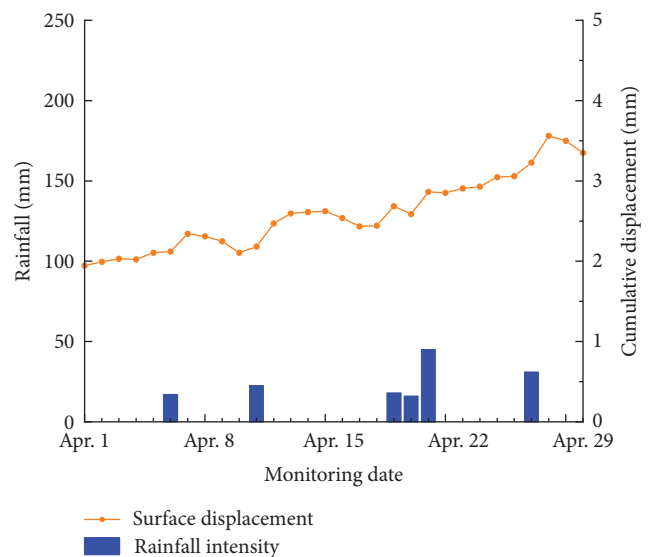


FIGURE 6: Surface displacement and rainfall in April 2020.

surface displacement caused by rainfall intensity is similar. Notably, these five rise periods all took place on the day or the next day of rain, thereby showing that slope deformation and rainfall have a very close relationship. The infiltration of rainwater can make the surface slope loose and softened, thus causing the slope cohesion to decrease rapidly, which in turn accelerates the surface displacement of the landslide. After a short increase in speed, with the end of rainfall, the water in the surface and shallow soil is discharged in the form of spring water (or water gushing or seepage) at the front edge of the landslide, low-lying terrain, and landslide cracks. The slope returns to its normal state. The surface displacement rate of the landslide decreases until it reaches a relatively slow value. A small amount of rainfall has little influence on landslide deformation. At a low rainfall intensity, the depth of rainwater infiltration is limited, with almost no impact on groundwater. Considering that no other water supply is available in the landslide area, the

change of groundwater level curve is small or even slightly decreased, thereby leading to no deep displacement of landslides, and the curve in Figure 6 fluctuates around 0.

On the basis of the above analysis, the Xiashan landslide is relatively stable due to the small rainfall and the low rainfall intensity in the first half of 2020. However, it has a slipping trend and is in a creep state. During summer or when the area is affected by typhoons, the greater rainfall intensity will further infiltrate into the groundwater. The deep displacement of the landslide caused by it may lead to speed sliding of the landslide.

**4.2. Historical Statistics and Prediction of Rainfall.** The rainfall in Zhejiang Province has been dominated by erosive rainfall for the past 30 years. The risk of soil erosion caused by rainfall is likely to increase significantly [22, 23]. Typhoons are one of the main factors that contribute to the surge in rainfall. The rainstorm brought by the typhoon is

highly sensitive to low-consolidation and unsaturated soil. Under the action of rapid infiltration, disasters, such as landslides and debris flows, can easily occur.

Xinchang County is relatively affected by typhoons. Statistics reveal that heavy rain (daily rainfall >100 mm) in Xinchang County lasts for 12 days, with the obvious effects of a typhoon observed in six days. Table 1 shows that the average daily rainfall in six days is 139.53 mm, and the process rainfall can reach 200–500 mm. Typhoon Lekima (1909) in 2019 exerted the most significant effect on Xinchang County. The rainfall reached 32 mm within three hours, and the daily rainfall reached 221 mm.

Research on extreme precipitation events in Xinchang County indicates that the frequency and intensity of such events display an increasing trend under the background of global warming (Figures 7 and 8). On the basis of the 221 mm rainfall from 11:00 a.m. on August 9, 2019, to 11:00 a.m. on August 10, 2019, and a rainfall tendency rate of 1.03 mm/year, the maximum daily rainfall is expected to reach 251.9 mm/day in 30 years. The existing waterproof and drainage facilities cannot adapt to the problem of the annually increasing rainfall.

## 5. Analysis of Numerical Result

**5.1. Numerical Model and Related Parameters.** The curved surface flow function in Midas GTS NX can be used to transform the boundary conditions of the water head and flow in the rainfall analysis. This function is applicable to the mandatory definition that the surface flow is equal to the rainfall intensity. When the ability of the soil surface to absorb rainfall is greater than the rainfall intensity, the soil layer can absorb the rainfall. Otherwise, only part of the rainfall is absorbed by the surface in accordance with the absorption capacity of the soil layer; the rest of the rainfall will flow along the surface of the ground.

The typical section, which is consistent with the main sliding direction of the Xiashan landslide, is selected as an example and analyzed using the finite element strength reduction method. This method does not need to assume the shape and position of the sliding surface, and the unstable sliding surface and corresponding stability safety factor of the slope can be automatically obtained by the program [23–27]. The Mohr-Coulomb model is used to simulate the soil behaviour. In order to emphasize the shear effect of the soil, the dilatancy is not considered. The physical and mechanical parameters of the landslide, groundwater parameters, and rainfall parameters used in the model are determined in accordance with survey results and relevant landslide data (Table 2). The calculation layering, grid division, and boundary constraints of the rock and soil are shown in Figure 9. In order to facilitate the calculation, the soil layers based on Figure 2 are combined and simplified in the modeling process. Six working condition models are set to examine the influence of groundwater and rainfall on slope stability.

Condition 1: gravity + normal groundwater level

Condition 2: gravity + normal groundwater level + rainfall intensity 50 mm/day for 1 day

Condition 3: gravity + normal groundwater level + rainfall intensity 100 mm/day for 1 day

Condition 4: gravity + normal groundwater level + rainfall intensity 150 mm/day for 1 day

Condition 5: gravity + normal groundwater level + rainfall intensity 200 mm/day for 1 day

Condition 6: gravity + normal groundwater level + rainfall intensity 250 mm/day for 1 day

**5.2. Simulation Results and Analysis.** Figure 10 shows the *X*-direction stress (tensile stress) diagram obtained from the static analysis in the natural state (working condition 1). In the figure, the stress at the top of the trailing edge is the maximum (5.10 MPa). The stratum is the third eruption layer with basalt lithology, with a saturated tensile strength of 5.33 MPa. The tensile stress at the top of the trailing edge is close to its saturated tensile strength in the natural state. In case of heavy rainfall, the tensile stress will further increase beyond its saturated tensile strength. Tensile cracks will then appear at the top of the trailing edge, and these cracks will gradually increase with time and affect the stability of the landslide. This observation is consistent with the conclusion regarding the previously analyzed landslide failure mechanism.

Figures 11–16 depict the equivalent plastic strain diagrams of the slopes under the six working conditions. The major strain inside the sliding body is concentrated on the contact zone of shallow sliding and deep creeping. The slope is mainly controlled by two sliding surfaces. Under the action of rainfall and groundwater, the rock and soil around the two sliding surfaces are prone to plastic deformation. This deformation is relatively apparent in the middle and trailing edges of the landslide. The maximum and average thicknesses of the sliding body are approximately 60.0 and 34.25 m, respectively. The rainfall intensity significantly affects the plastic zone of the slope. With the increase in rainfall intensity, the plastic zone of the slope develops and extends until it is completely penetrated, and the rock and soil masses in this zone are prone to violent sliding.

Table 3 and Figure 17 suggest that the slope safety factor is inversely proportional to the rainfall intensity and therefore decreases with the increase in the latter. The monitoring data in the first half of 2020 show that the daily rainfall is less than 50 mm, which corresponds to the numerical model of working conditions 1 and 2. A comparison between Figures 11 and 12 shows that the plastic strain is relatively large on the slope surface and decreases with the increase in depth. As the rainfall intensity increases from 0 mm/day to 50 mm/day, the plastic strain of the slope increases. At the same time, the plastic strain zone of the slope also expands and gradually penetrates near the shallow sliding surface. However, it is still concentrated in the upper part of the entire landslide area because the rainfall is relatively light, and the rainwater can only infiltrate the shallow soil. The increase in shallow soil saturation leads to the decrease in shear strength and slope safety factor. Then, the slope deformation rate increases. At this time, the slope is mainly controlled by the shallow sliding surface. This finding is the same as the conclusion obtained by



TABLE 1: Statistics of the typhoons that affect the rainfall in Xinchang County from 1990 to 2019.

Typhoon number	Name of typhoon	Start and end dates	Daily rainfall (mm)
9015	Abe	1990/8/31–1990/9/1	110.3
9219	Ted	1992/9/23–1992/9/24	125.8
0716	Krosa	2007/10/7–2007/10/8	134.7
1323	Fitow	2013/10/7–2013/10/8	134.9
1909	Lekima	2019/8/10–2019/8/11	221
1918	Mitag	2019/10/2–2019/10/3	101.5

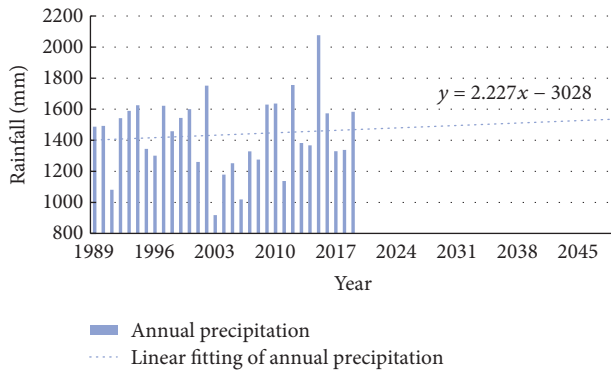


FIGURE 7: Annual precipitation and forecast in Xinchang County.

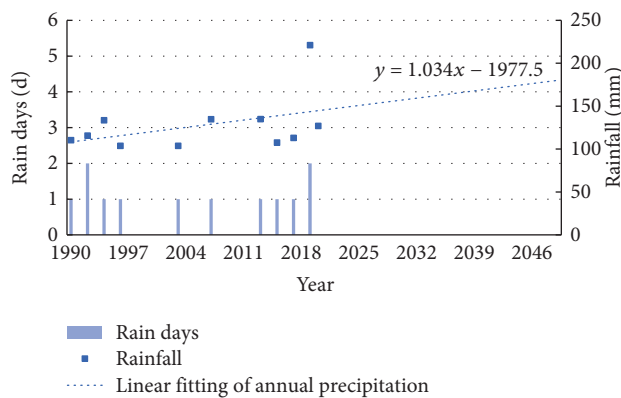


FIGURE 8: Rainfall situation and heavy rain forecast in Xinchang County over the years.

analyzing the monitoring data. When the rainfall intensity increases from 50 mm/day to 100 mm/day, the rainwater infiltration rate increases. The increase rate of deep soil saturation elevates, and the overall shear strength of the slope significantly decreases. In addition, the decline rate of the slope safety factor is at maximum. The critical sliding surface of the slope transits from the shallow layer to the deep layer. When the rainfall intensity increases from 100 mm/day to 250 mm/day, the rainwater penetration rate and infiltration speed reach the maximum. Shallow and deep soils tend to be saturated, and the shear strength is close to the minimum value. The decreasing trend of the slope safety factor is relatively gentle, and the slope is mainly controlled by the deep sliding surface.

The slope safety factor ranges from 1.042 to 1.151. When the rainfall intensity is less than 200 mm/day, the slope safety factor is less than 1.15, and the slope is in a relatively stable

stage. Otherwise, the slope safety factor is close to unity ( $SF = 1$ ), and the slope approaches a failure condition. Therefore, the landslide is generally in a stable state. In the case of rainfall, the slope is between unstable and relatively stable states. In conclusion, the slope is in the state of intermittent pushing creep. The source of the intermittent thrust is closely related to the increase in soil saturation caused by rainfall.

## 6. Prevention and Treatment Suggestion

The principle that should be followed in slope treatment is to detect problems as early as possible, prioritize prevention, identify the situation and treat it comprehensively, strive to find a radical solution, and avoid the possibility of future issues. Moreover, the solution should focus on water treatment. The prevention and treatment suggestions (Figure 18) are enumerated below:

- (1) The landslide should be continuously monitored, and more targeted monitoring items should be added, such as crack monitoring, stress monitoring, and microseismic monitoring. Establishing a network automatic real-time monitoring system facilitates the rapid extraction of various data in the database analysis, and an early warning model of dynamic disaster needs to be constructed. In accordance with the reliability measurement standard of stability evaluation, alarm valves can be set to provide accurate alarms when the area is unattended.
- (2) Large cross section intercepting ditches can be excavated on the stable stratum outside the slope top to effectively prevent external surface water from entering the landslide area. Moreover, the number of drainage ditches on the landslide surface can be increased and the cross-sectional area of drainage ditches can be enlarged to accelerate the discharge of surface water. The layout density of underground drainage facilities, such as seepage ditches, blind ditches, drainage holes, and water collection wells, should be increased. The maintenance and repair of the waterproof and drainage reinforcement facilities should be conducted on a regular basis.
- (3) Waterproof materials with strong adhesion features should be utilized to repair cracks on the slope surface. Also, restoring vegetation on the wasteland and setting up grid protection on the steep air face can enhance the slope stability.

TABLE 2: Relevant parameters of the rock and soil.

Structural layer	Elastic modulus $E$ (MPa)	Poisson's ratio $\nu$	Volumetric weight $\gamma$ (kN/m <sup>3</sup> )	Cohesion intercept $c$ (kPa)	Angle of internal friction $\phi$ (°)
Sliding mass	15	0.33	19.7	10.3	12.4
Strata III-IX	4000	0.23	21	300	50
Stratum X	5000	0.21	22	400	50

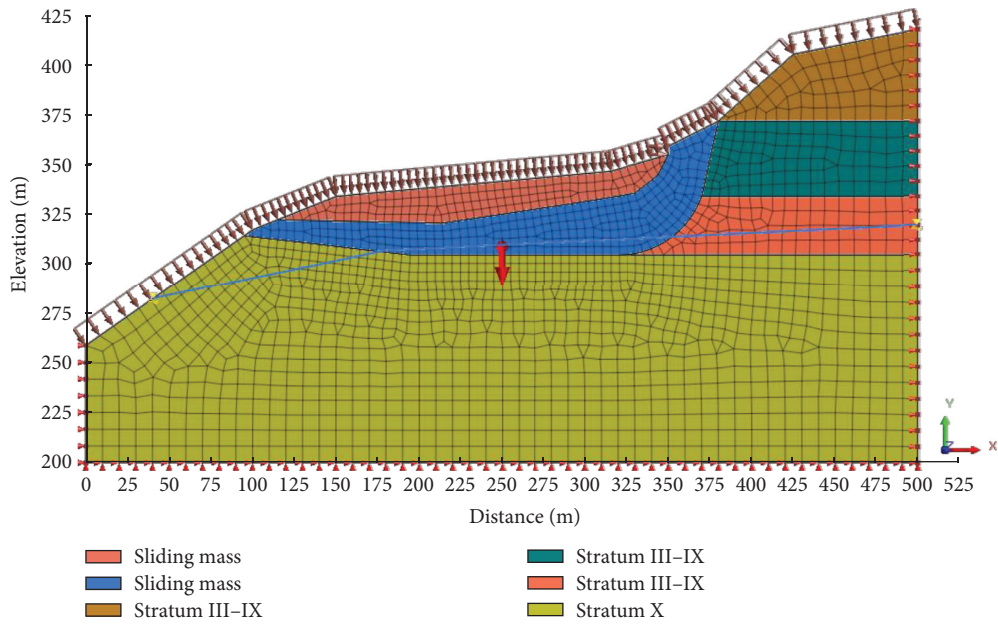


FIGURE 9: Landslide calculation model.

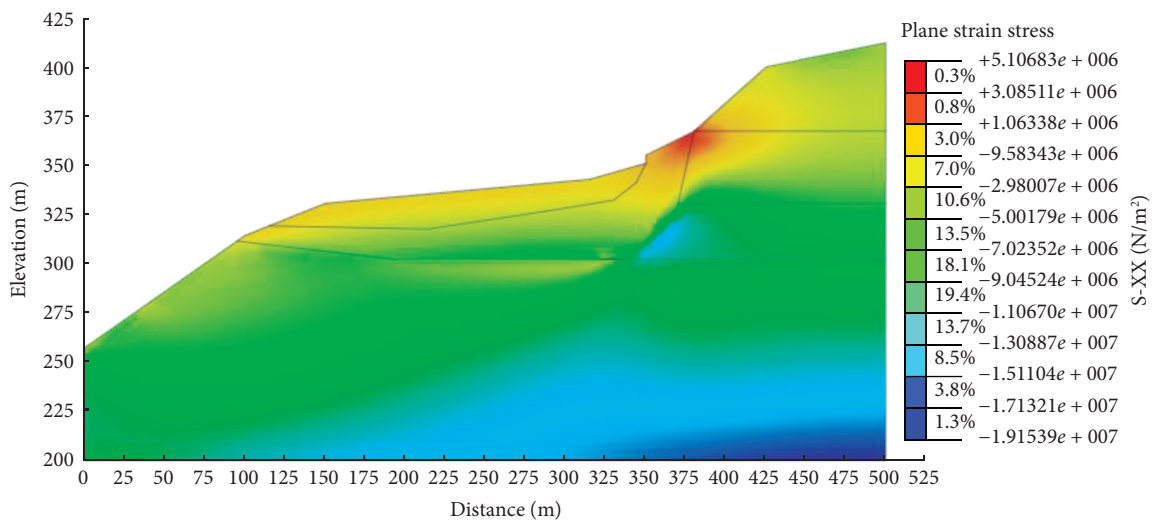


FIGURE 10: X-direction stress diagram of working condition 1.

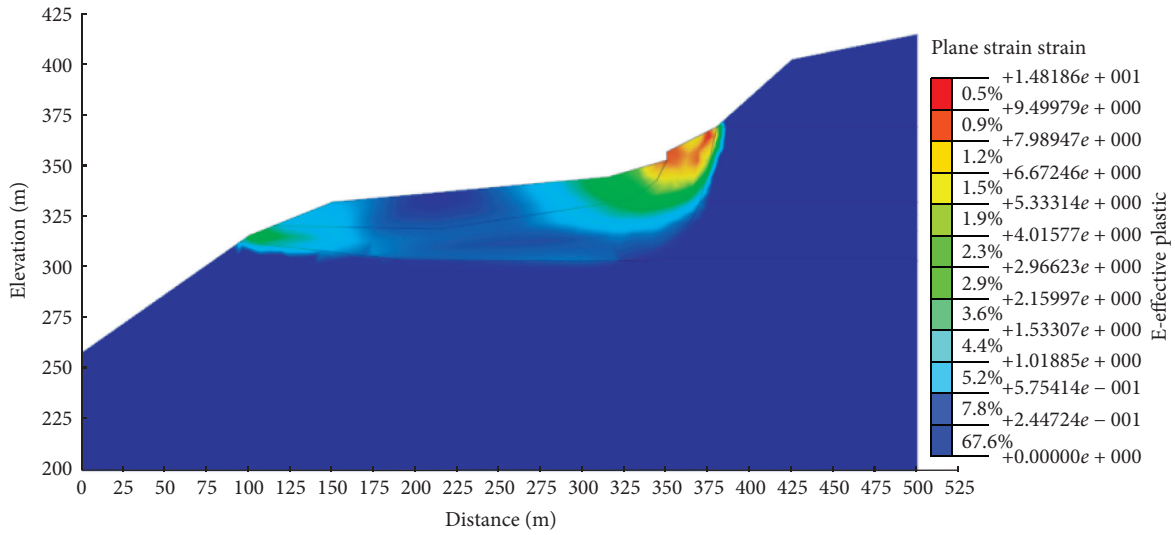


FIGURE 11: Plastic strain diagram of working condition 1.

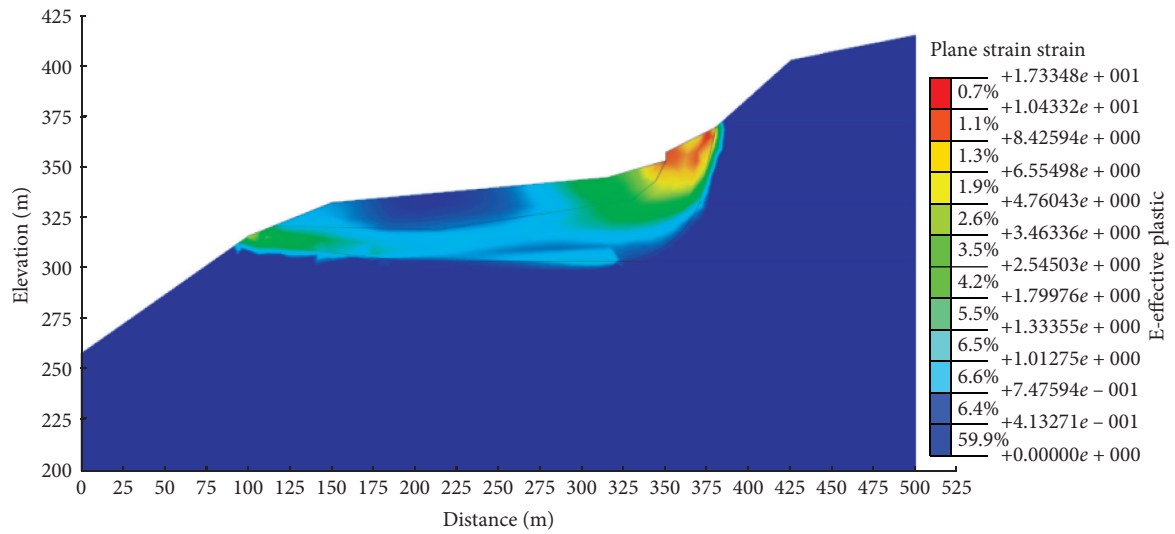


FIGURE 12: Plastic strain diagram of working condition 2.

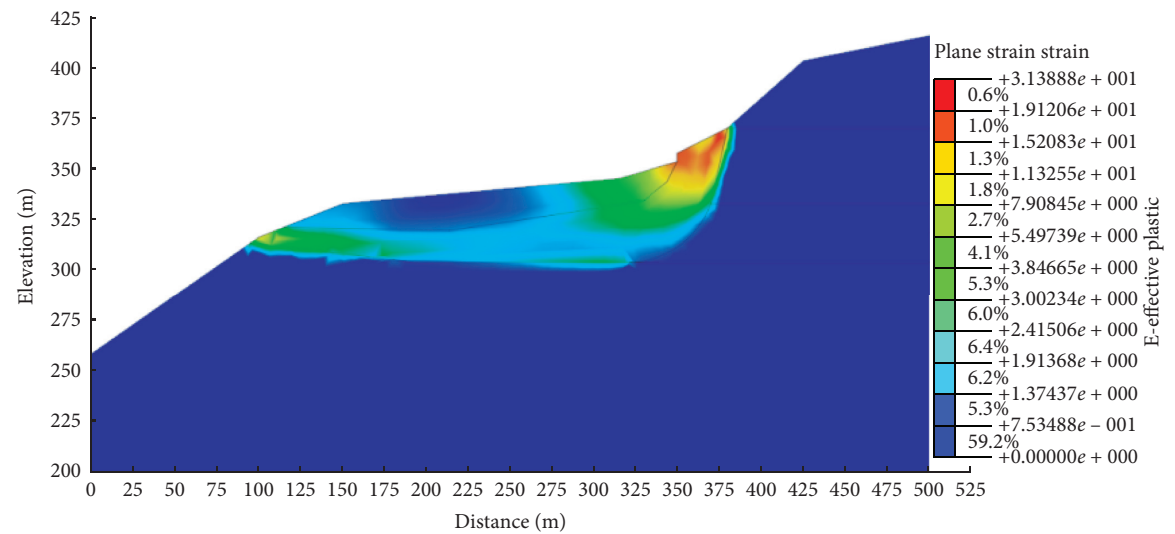


FIGURE 13: Plastic strain diagram of working condition 3.

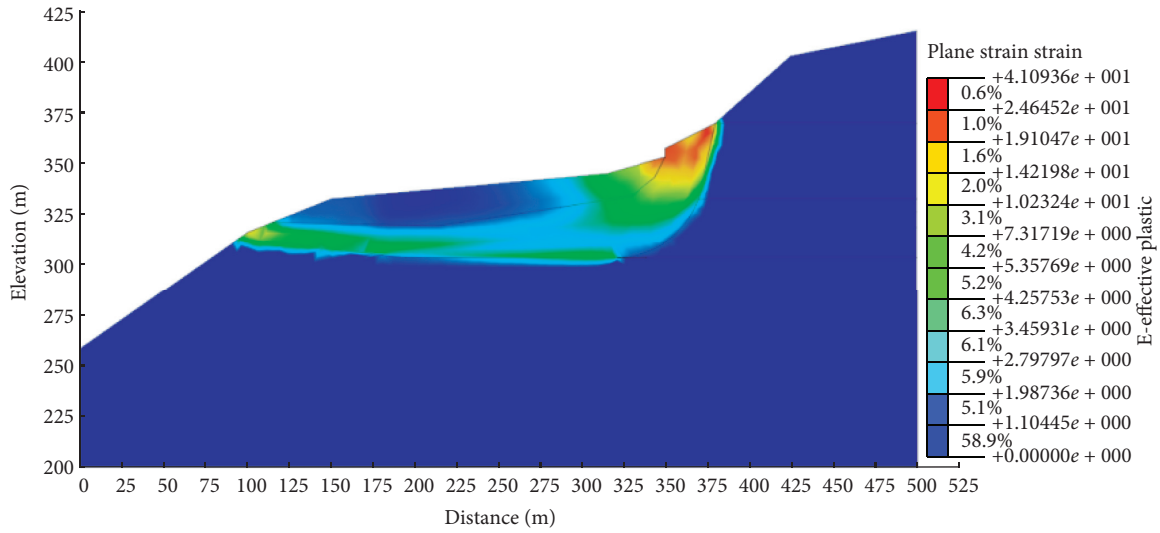


FIGURE 14: Plastic strain diagram of working condition 4.

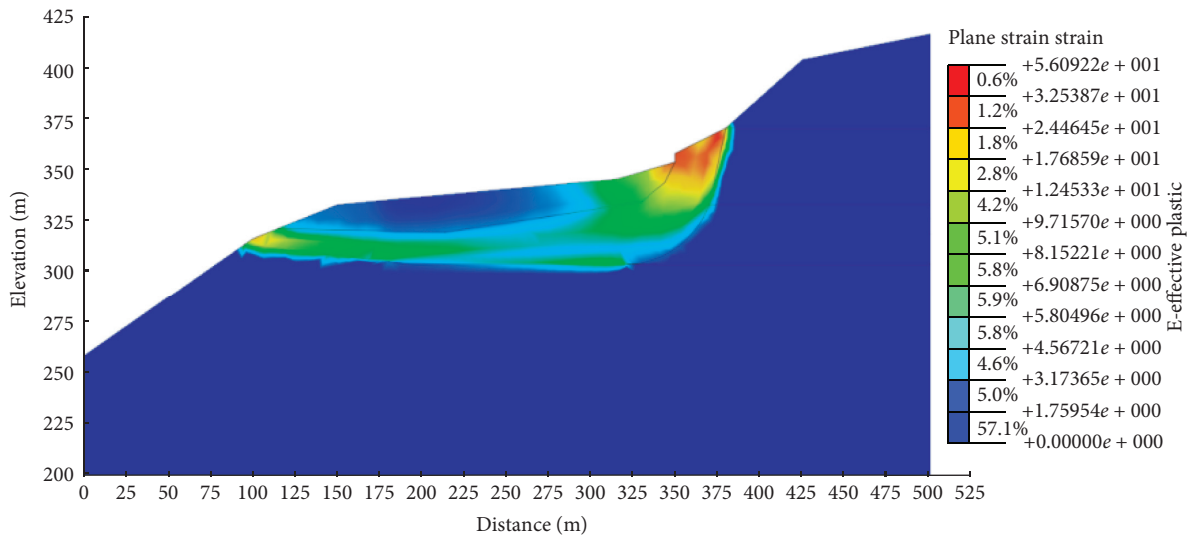


FIGURE 15: Plastic strain diagram of working condition 5.

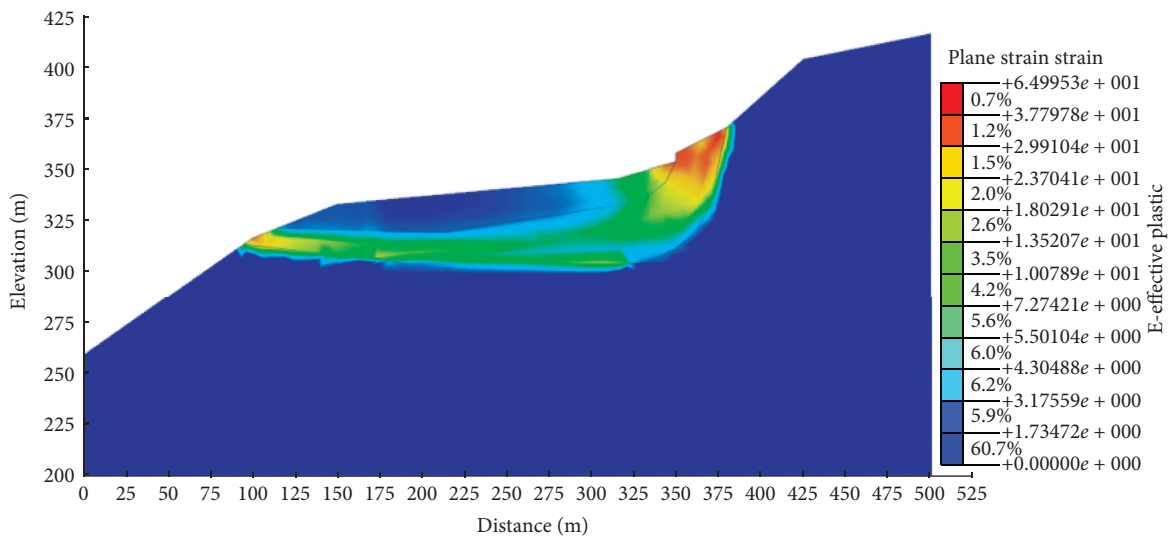


FIGURE 16: Plastic strain diagram of working condition 6.

TABLE 3: Slope safety coefficient in the six working conditions.

	Model 1	Model 2	Model 3	Model 4	Model 5	Model 6
Stability coefficient	1.151	1.125	1.087	1.062	1.049	1.042

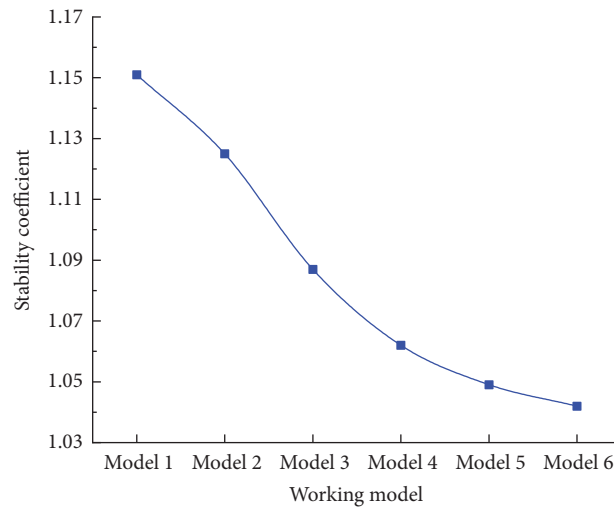


FIGURE 17: Variation diagram of the landslide stability coefficient with different rainfall intensities.

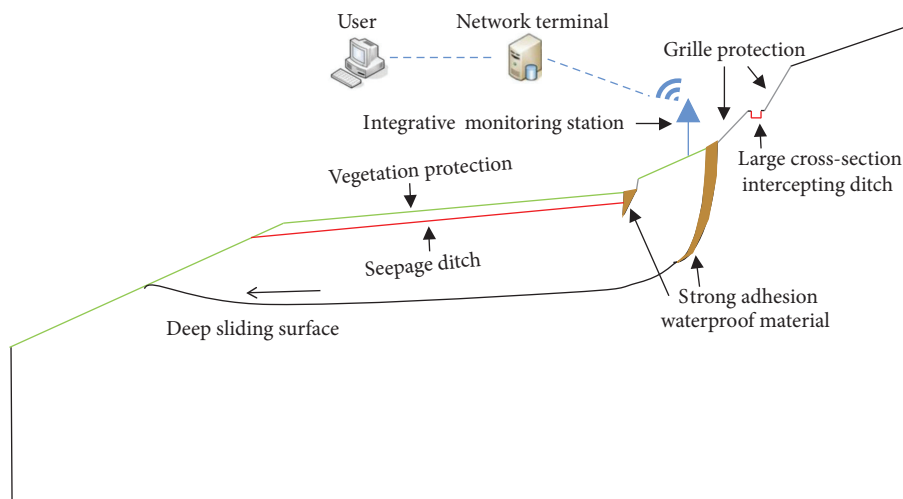


FIGURE 18: Schematic of prevention and treatment measures.

- (4) In the future, slope cutting and load reduction measures can be applied to reduce the height of the unstable part of the slope if engineering measures for reinforcement need to be taken after relevant research and demonstration [28–30].

## 7. Discussion

The accurate judgment of landslide stability plays an essential guiding role in slope engineering. This paper uses the qualitative and numerical analysis methods to study the failure mechanism and influencing factors of the Xiashan landslide. By analyzing the monitoring data, we conclude that rainfall has a strong influence on the slope deformation,

and the landslide is in a creep state. The numerical simulation results also prove this conclusion.

In a previous study of the Xiashan landslide, Yu [31] established a Xiashan landslide model with different groundwater levels for stability analysis. Zhu [32] evaluated the stability of the Xiashan landslide on the basis of survey results. Their studies indicated that rainfall is the main factor that causes the Xiashan landslide to slip. After more than 10 years, the latest survey results, monitoring data, and rainfall conditions of the Xiashan landslide have changed. This article selects SRM in Midas GTS NX software for simulation. Its correctness is dependent on the mechanical parameters of the rock and soil measured in the previous test, but it can quickly and accurately simulate the working

conditions that simultaneously consider rainfall and groundwater. Compared with the results of other studies, the development of cracks changes the failure mechanism of the Xiashan landslide. We conclude that the Xiashan landslide has transformed from the sliding tensile cracking type to the hydraulic driving type. We quantify the impact of rainfall intensity on the landslide stability and find that the critical rainfall intensity of the Xiashan landslide from the relatively stable stage to the unstable stage is 200 mm/day.

Although this paper has obtained many useful conclusions on the study of the Xiashan landslide, many deficiencies still need to be improved gradually. The monitoring data used for analysis in this paper are only the monitoring data from the first half of 2020 with a small amount of rainfall. The conclusions drawn from monitoring data with shorter time periods appear to be inadequate. Therefore, long-term monitoring data collection and analysis need to be continued. Also, the rainfall intensity in the numerical simulation study is the quantified data, so the difference between the effect of short-term heavy rainfall and long-term continuous rainfall on the landslide needs to be further studied. In addition, the specific mechanisms between rainfall and groundwater and between groundwater and rock must be studied in detail.

## 8. Conclusions

In this study, the geological conditions, present situation, rainfall, monitoring data, and numerical simulation results of the Xiashan landslide are analyzed. The current Xiashan landslide belongs to the failure mode caused by hydraulic drive. The deformation mode of the landslide is creeping deformation. The joints and fissures of rock mass are developed, and the eruption and sedimentary layers always appear alternately, which is unfavorable to the stability of the landslide. The latest monitoring results and numerical simulation prove that rainfall is the main factor that affects the slope stability.

The calculation results show that the stability coefficient is less than 1.05 when the rainfall intensity is more than 200 mm/day. This finding indicates that the slope is in an unstable state and is prone to sliding rapidly. Considering the influence of typhoons, the probability of heavy rain in the landslide area is extremely high, and a large rainstorm (daily rainfall >250 mm) may occur. Therefore, long-term monitoring and various drainage measures should be applied to implement comprehensive treatment.

## Data Availability

The data used to support the findings of this study are included within the article.

## Conflicts of Interest

The authors declare that they have no conflicts of interest regarding the publication of this paper.

## Acknowledgments

The authors acknowledge the financial support of the funding of the State Key Laboratory of Frozen Soil Engineering (Grant nos. SKLFSE201815 and SKLFSE201712) and the support of the Key Laboratory of Rock Mechanics and Geohazards of Zhejiang Province (Grant no. PCMGH-2016-Z-04).

## References

- [1] M. Huang, C. Hong, S. Du, and Z. Luo, "Experimental technology for the shear strength of the series-scale rock joint model," *Rock Mechanics and Rock Engineering*, vol. 53, no. 12, pp. 5677–5695, 2020.
- [2] M. Huang, D. Liu, C. Hong et al., "Representative sample sampling method for size effect experiment of jointed rock mass," *Geofluids*, Article ID 8870387, 2020.
- [3] Z. C. Tang, "Experimental investigation on temperature-dependent shear behaviors of granite discontinuity," *Rock Mechanics and Rock Engineering*, vol. 53, no. 9, pp. 4043–4060, 2020.
- [4] Z. C. Tang and Y. Zhang, "Temperature-dependent peak shear-strength criterion for granite fractures," *Engineering Geology*, vol. 269, Article ID 105552, 2020.
- [5] Z. C. Tang, Q. Z. Zhang, J. Peng, and Y. Y. Jiao, "Experimental study on the water-weakening shear behaviors of sandstone joints collected from the middle region of Yunnan province, P.R. China," *Engineering Geology*, vol. 258, Article ID 105161, 2019.
- [6] F. Cai and K. Ugai, "Numerical analysis of rainfall effects on slope stability," *International Journal of Geomechanics*, vol. 4, no. 2, pp. 69–78, 2004.
- [7] S. Wang, W. Xu, J. Liu, and G. Garcea, "Stability and failure mechanism analyses of the Zhenggang landslide in southwestern China," *Advances in Civil Engineering*, vol. 2018, Article ID 6128401, 2018.
- [8] M. L. Chen, P. F. Lv, W. Z. Nie et al., "The role of water and lithology on the deformation and failure of an aenclinal rock slope in a hydropower reservoir," *Advances in Civil Engineering*, vol. 2020, Article ID 8852227, 2020.
- [9] J.-w. Zhou, H.-b. Li, G.-d. Lu, Y. Zhou, J.-y. Zhang, and G. Fan, "Initiation mechanism and quantitative mass movement analysis of the 2019 Shuicheng catastrophic landslide," *Quarterly Journal of Engineering Geology and Hydrogeology*, vol. 54, no. 2, Article ID qjgh2020, 2020.
- [10] R. M. Iverson, "Landslide triggering by rain infiltration," *Water Resources Research*, vol. 36, no. 7, pp. 1897–1910, 2000.
- [11] M. Calvello, L. Cascini, and G. Sorbino, "A numerical procedure for predicting rainfall-induced movements of active landslides along pre-existing slip surfaces," *International Journal for Numerical and Analytical Methods in Geomechanics*, vol. 32, no. 4, pp. 327–351, 2008.
- [12] Y. Zhou, S.-c. Qi, L. Wang, M.-l. Chen, C. Xie, and J.-w. Zhou, "Instability analysis of a quaternary deposition slope after two sudden events of river water fluctuations," *European Journal of Environmental and Civil Engineering*, vol. 3, pp. 1–19, 2020.
- [13] R. M. Iverson, D. L. George, K. Allstadt et al., "Landslide mobility and hazards: implications of the 2014 Oso disaster," *Earth and Planetary Science Letters*, vol. 412, pp. 197–208, 2015.
- [14] E. Conte, L. Pugliese, and A. Troncone, "Post-failure analysis of the Maierato landslide using the material point method," *Engineering Geology*, vol. 277, Article ID 105788, 2020.
- [15] E. L. Harp, M. E. Reid, J. P. McKenna, and J. A. Michael, "Mapping of hazard from rainfall-triggered landslides in

- developing countries: examples from Honduras and Micronesia,” *Engineering Geology*, vol. 104, no. 3-4, pp. 295–311, 2009.
- [16] Y. N. Lu, X. H. Wu, and X. P. Li, “Stability analysis and countermeasures on landslide of mountain expressway,” *Construction Technology*, vol. 43, no. 5, pp. 92–96, 2014, in Chinese.
- [17] Y. Miyabuchi, F. Maeno, and S. Nakada, “The October 16, 2013 rainfall-induced landslides and associated lahars at Izu Oshima Volcano, Japan,” *Journal of Volcanology and Geothermal Research*, vol. 302, pp. 242–256, 2015.
- [18] Xinchang County Annals Compilation Committee, *Xinchang County, Xinchang County Annals*, Shanghai Bookstore, Shanghai, China, 1994, in Chinese.
- [19] Standardization Administration of China, *GB 18306-2015 Seismic Ground Motion Parameters Zonation Map of China*, China Standards Press, Beijing, China, 2015, in Chinese.
- [20] C. H. Liu, J. Xu, C. L. Cao, C. X. Chen, and X. T. Feng, “Analysis of bedding-slip failure mechanism of rock slope due to hydraulic drive,” *Chinese Journal of Rock Mechanics and Engineering*, vol. 24, no. 19, pp. 3529–3533, 2005.
- [21] Q. J. Hu, R. D. Shi, L. N. Zheng, Q. J. Cai, L. Q. Du, and L. P. He, “Progressive failure mechanism of a large bedding slope with a strain-softening interface,” *Bulletin of Engineering Geology and the Environment*, vol. 77, no. 1, pp. 69–85, 2017.
- [22] S. L. He, X. J. Guo, F. Y. Li, N. Li, and X. W. He, “Spatio-temporal variation of rainfall and rainfall erosivity in southern China in recent 60 years,” *Resources & Environment in the Yangtze Basin*, vol. 26, no. 9, pp. 1406–1416, 2017, in Chinese.
- [23] K. Emanuel, “Increasing destructiveness of tropical cyclones over the past 30 years,” *Nature*, vol. 436, no. 7051, pp. 686–688, 2005.
- [24] D. V. Griffiths and P. A. Lane, “Slope stability analysis by finite elements,” *Géotechnique*, vol. 49, no. 3, pp. 387–403, 1999.
- [25] T. Matsui and K.-C. San, “Finite element slope stability analysis by shear strength reduction technique,” *Soils and Foundations*, vol. 32, no. 1, pp. 59–70, 1992.
- [26] Y. C. Ma, P. D. Su, and Y. G. Li, “Three-dimensional non-homogeneous slope failure analysis by the strength reduction method and the local strength reduction method,” *Arabian Journal of Geosciences*, vol. 13, no. 1, p. 21, 2020.
- [27] W. Gao, X. Chen, X. Wang, and C. J. Hu, “Novel strength reduction numerical method to analyse the stability of a fractured rock slope from mesoscale failure,” *Engineering with Computers*, pp. 1–17, 2020.
- [28] L. Abramson, T. Lee, G. Boyce, and S. Sharma, *Slope Stability and Stabilization Methods*, John Wiley & Sons, New York, NY, USA, 2nd edition, 2002.
- [29] T. Ito and T. Matsui, “Methods to estimate lateral force acting on stabilizing piles,” *Soils and Foundations*, vol. 15, no. 4, pp. 43–59, 1975.
- [30] E. Conte, A. Troncone, and M. Vena, “Behaviour of flexible piles subjected to inclined loads,” *Computers and Geotechnics*, vol. 69, pp. 199–209, 2015.
- [31] B. T. Yu, H. Y. Sun, Y. Q. Shang, and H. Q. Li, “Characteristics and stability analysis of Xiashan landslide in Zhejiang province,” *Chinese Journal of Rock Mechanics and Engineering*, vol. 25, no. S1, pp. 2875–2881, 2006.
- [32] L. R. Zhu, G. S. Mao, K. D. Li, Z. G. Cheng, and E. K. Mao, “The geological characteristics and stability analysis of the Xiashan village landslide in Xinchang county, Zhejiang province,” *The Chinese Journal of Geological Hazard and Control*, vol. 19, no. 4, pp. 18–22, 2008, in Chinese.

## Research Article

# A Fractal Model for Predicting the Relative Permeability of Rough-Walled Fractures

Zuyang Ye <sup>1,2</sup>, Wang Luo,<sup>1,2</sup> Shibing Huang <sup>1,2</sup>, Yuting Chen,<sup>3</sup> and Aiping Cheng<sup>1,2</sup>

<sup>1</sup>School of Resource and Environmental Engineering, Wuhan University of Science and Technology, Wuhan 430081, China

<sup>2</sup>Hubei Key Laboratory for Efficient Utilization and Agglomeration of Metallurgic Mineral Resources, Wuhan University of Science and Technology, Wuhan 430081, China

<sup>3</sup>Changjiang Survey, Planning, Design and Research Co., Ltd., Wuhan 430010, China

Correspondence should be addressed to Shibing Huang; [huangshibing@wust.edu.cn](mailto:huangshibing@wust.edu.cn)

Received 24 October 2020; Revised 23 November 2020; Accepted 5 March 2021; Published 19 March 2021

Academic Editor: Jian Ji

Copyright © 2021 Zuyang Ye et al. This is an open access article distributed under the Creative Commons Attribution License, which permits unrestricted use, distribution, and reproduction in any medium, provided the original work is properly cited.

The relative permeability and saturation relationships through fractures are fundamental for modeling multiphase flow in underground geological fractured formations. In contrast to the traditional straight capillary model from porous media, the realistic flow paths in rough-walled fractures are tortuous. In this study, a fractal relationship between relative permeability and saturation of rough-walled fractures is proposed associated with the fractal characteristics of tortuous parallel capillary plates, which can be generalized to several existing models. Based on the consideration that the aperture distribution of rough-walled fracture can be represented by Gaussian and lognormal distributions, aperture-based expressions between relative permeability and saturation are explicitly derived. The developed relationships are validated by the experimental observations on Gaussian distributed fractures and numerical results on lognormal distributed fractures, respectively.

## 1. Introduction

Multiphase flow through fractured media is an important process for a number of practical applications, such as seepage control for rock slope [1, 2], petroleum reservoirs [3], nuclear waste disposal [4], and geologic storage of carbon dioxide [5]. In order to understand the influence of multiphase flow behavior in fractured media on implementation with these applications, numerical simulations have been applied in fractured media using a continuum method [6, 7] or a discrete fracture network model [8, 9]. In contrast to the macroscale continuum model, the flow behavior in the fractured rock is mainly governed by the presence of fracture, which can highly improve the permeability of rock masses [10–12]. For the fracture-dominated flow, the relative permeability of a single fracture is one of the key parameters to describe the multiphase flow behavior that controls the accuracy of modeling results during numerical simulations.

In the last decades, multiphase flow behavior in single fractures has been widely investigated through experiments [13–23], numerical simulations [24–28], and theoretical analysis [21, 28–30] by a number of researchers. Several models have been proposed to represent the relative permeability relationships in rough-walled fractures. Romm [13] firstly developed simple linear relationships between relative permeability and saturation for two different phases (water and kerosene) called the *X* model, but later poor performance was generally observed through other two-phase flow experiments [14–16, 20, 21] and numerical analysis [24, 27, 28] as a result of phase interference. Consequently, Fourar and Lenormand [29] proposed a viscous coupling model by considering significant interference between phases associated with viscosity. However, there is no consensus on the characteristic behavior of relative permeability in rough-walled fractures.

Some well-known models such as the Burdine model [31], Corey model [32], and Brooks and Corey model [33]



induced from porous media were also borrowed in fitting the relative permeability properties of fractures, according to the conceptualization of rough-walled fractures as two-dimensional porous media. In these conceptual models from porous media, the hypothesis that the flow paths are straight is in contradiction with the actual tortuous flow paths. The tortuosity factor is generally quantified by a power function of function with exponent parameter  $m$  and  $m=2$  is widely used in Brooks and Corey model [33] while the fitted value  $m$  of 1.0 is obtained during Liu et al.'s curve fitting [34]. The physical meaning of the tortuosity factor is still not clear for rough-walled fractures.

When the flow paths are controlled by capillarity during quasistatic displacement, the relative permeability of fracture is substantially influenced by aperture distribution. Some studies [23, 24, 27, 28] have been made to understand the relationships between relative permeability and aperture distribution for rough-walled fractures including numerical approaches for multiphase flow in single fractures, the sensitivity of spatial distribution between apertures on relative permeability predictions, and the determination of empirical parameters related to the residual saturation. However, explicit mathematical relationships between relative permeability and fracture-aperture distribution are still lacking.

A systematic study of relative permeability models with respect to flow tortuosity and its dependence on fracture-aperture distribution is a challenging task. Therefore, the primary objectives of this study are (1) to propose a generalized model for relative permeability in rough-walled fractures with consideration of the tortuosity fractal dimension, (2) to develop the relationships between relative permeability and aperture distribution of fractures, and (3) to assess the validity of the proposed model through experimental data and numerical results from the literature.

## 2. The Existing Relative Permeability Models

The relative permeability ( $k_r$ ) versus saturation ( $S_w$ ) relationship through rough-walled fractures has been extensively investigated due to their importance in engineering applications. On the observation of two-phase flow between water and kerosene through artificial parallel-plate fractures, Romm [13] presented the  $k_r$ - $S_w$  relationship firstly as a simple linear function:

$$k_r = S_w. \quad (1)$$

This linear relationship is also applied to the oil phase, so that the sum of relative permeabilities for water and oil phases was equal to one known as X-curve. It is indicated that each phase kept flowing in its self-governed capillary paths without impediment from the other phase.

According to experimental results from the distilled water-nitrogen gas flow through a transparent replica of a natural rock fracture [14], air-water flow in horizontal artificial fractures [15, 18], kerosene-water flow in a parallel glass plate fracture [16], nitrogen-water flow in smooth- and rough-walled glass fractures [21], and gas-water flow in an

induced fracture from a cylindrical basalt core [20], strong phase interference at the intermediate saturation was found and the relative permeability did not linearly depend on the saturation. Thus, several simple models were established or directly borrowed from porous media to describe the nonlinear behavior of relative permeability.

Based on the porous media approach, the rock fractures are conceptualized as two-dimensional connected porous media. Burdine [31] proposed one of the first theoretical models for  $k_r$ - $S_w$  relationship as

$$k_r = \frac{\int_0^{S_w} (dS_{we}/P_c^2)}{\int_0^1 (dS_{we}/P_c^2)}, \quad (2)$$

$$S_{we} = \frac{S_w - S_{wr}}{1 - S_{wr}}, \quad (3)$$

where  $S_{we}$  and  $S_{wr}$  are the effective saturation and residual saturation of the wetting fluid, respectively, and  $P_c$  is the capillary pressure. Nevertheless, all the capillary tubes in the Burdine model are assumed to be straight along the hydraulic gradient direction. In fact, the flow paths for porous media are quite tortuous. To take into consideration the tortuosity of the capillary tube, an additional tortuosity factor obtained from measured relative permeability data could be approximated as a power function of effective saturation. Then, a new version of the modified Burdine model is given as

$$k_r = S_{we}^2 \frac{\int_0^{S_w} (dS_{we}/P_c^2)}{\int_0^1 (dS_{we}/P_c^2)}. \quad (4)$$

The formulation of the Burdine model includes three parameters  $S_w$ ,  $S_{wr}$ , and  $P_c$ . The relative permeability function is not explicitly expressed within the Burdine model. Once  $P_c$  as a function of saturation is known, the  $k_r$ - $S_w$  relationship can be derived from equation (4).

Based on the laboratory experiments for a number of soil samples, Corey [32] and Brooks and Corey [33] proposed an empirical relationship between water saturation and capillary pressure in a general form as

$$S_{we} = \left( \frac{P_b}{P_c} \right)^\lambda, \quad (5)$$

where  $P_b$  is the air entry pressure and  $\lambda$  is the pore size distribution index. In Corey [32] relation,  $\lambda$  is equal to two.

Inserting equation (5) into equation (4) yields

$$k_r = S_{we}^{((2+3\lambda)/\lambda)}. \quad (6)$$

When  $\lambda=2$ , equation (6) is equivalent to the Corey model:

$$k_r = S_{we}^4. \quad (7)$$

Brooks and Corey [33] have discussed that media with a wide range of pore size distribution should have small values of  $\lambda$ . However, media with a uniform pore size could have  $\lambda$

values close to infinity such as the fractured media; equation (6) can be simplified as

$$k_r = S_{we}^3. \quad (8)$$

After the observation on several flow structures (bubbles, unstable bubbles, film flow, etc.) for water-air flows in an artificial fracture [15], Fourar and Lenormand [29] developed a viscous coupling model accounting for the coupling between the two fluids flowing simultaneously, whose interface is assumed to be a plane. Based on the pipe-flow model, the wetting phase is in contact with the capillary wall and the nonwetting phase flows in between. The  $k_r$ - $S_w$  function of the water phase is expressed as

$$k_r = \frac{S_w^2}{2} (3 - S_w). \quad (9)$$

As indicated by Huo and Benson [22] who presented a detailed comparison between the experimental data and existing models of the  $k_r$ - $S_w$  relationship, the  $X$ -curve could only describe the data from Romm [13]. The Corey model and Brooks and Corey model presented similar results and gave good representations for Chen and Horne's [21] test on randomly rough-walled fractures. The viscous coupling model provided good agreement with the data from Fourar et al. [15] experiment in horizontal artificial fractures and Chen and Horne's [21] on smooth- and homogeneously rough-walled fractures. Some other experimental data [14, 20] have a considerable deviation from any of the existing models.

While substantial progress has been made to investigate the relative permeability in rock fractures, there is no general model to predict the  $k_r$ - $S_w$  relationship of a rock fracture. We will develop a reasonable model in this paper and also demonstrate the relationship between the relative permeability and aperture distribution in rough fractures.

### 3. Fractal Model of Relative Permeability in Rough-Walled Fractures

A schematic of parallel capillary plates within a single rough-walled fracture is shown in Figure 1. For simplicity, the water-air two-phase flow through rough-walled fracture is focused on in this study. However, the mechanism and results can be extended to other multiphase flow systems. The flow rate  $q$  in a parallel capillary plate within a single fracture is given by cubic law:

$$q = \frac{b^3}{12\mu} \frac{\Delta P}{L_t} \Delta w, \quad (10)$$

where  $\Delta P$  is the pressure drop across the parallel capillary plate of length  $L_t$  (along the flow direction) and aperture  $b$ ,  $\mu$  is the viscosity of water, and  $\Delta w$  is the width of the capillary plate.

Based on the Young-Laplace equation, the parallel capillary plate with aperture  $b$  is related to the magnitude of capillary pressure  $P_c$  as

$$b = \frac{2T_s \cos \alpha}{P_c}, \quad (11)$$

where  $T_s$  is surface tension and  $\alpha$  is contact angle.

For a given capillary pressure  $P_c$ , a parallel capillary plate with an aperture equal to or less than  $(2T_s \cos \alpha / P_c)$  is generally filled by water and the rest by air. Integrating equation (10) from minimum aperture  $b_{\min}$  to the aperture  $b$ , the total flow rate  $Q$  of the entire fracture is given by

$$Q(P_c) = \int_{b_{\min}}^b q dN, \quad (12)$$

where  $dN$  is the number of capillary plates corresponding to aperture  $b$  with capillary pressure  $P_c$ .

When the aperture distribution of fracture is defined as a probability density function  $f(b)$ , inserting equation (10) into equation (12) leads to

$$Q(P_c) = \int_{S_{wr}}^{S_w} \frac{V \Delta P}{12\mu} \frac{b^2}{L_t^2} dS_w, \quad (13)$$

$$dS_w = \frac{b \Delta w L_t}{V} dN = \frac{b \Delta w L_t}{V} f(b) db, \quad (14)$$

where  $V$  is the total void volume within a single fracture and the residual saturation  $S_{wr}$  corresponds to the minimum aperture  $b_{\min}$ . As water flow is restricted to fracture aperture below the critical aperture  $b_{\min}$ , the water phase cannot flow in a continuous way and the volume fraction of the immobile water is defined as the residual saturation  $S_{wr}$ .

In the traditional approaches for developing a closed-form relative permeability model in porous media, the circle capillary plates are both assumed to be straight. In reality, the flow paths are generally tortuous based on the experimental observations. The essential assumption of the traditional approaches is that the tortuosity factor is quantified by a power function and the exponent value cannot be determined rigorously in theory, which highly depends on experience from the experimental measurements.

As a result of the geometrical complication of the aperture distribution, the length of the disorder and irregular parallel capillary plate is similar to the measures of coastline, rough surface, mountains, lakes, and islands, which follow the fractal geometry rather than the Euclidean geometry [35]. According to the self-similarity of a fractal capillary plate, the length of a fractal capillary plate can be expressed as

$$L_t \propto \varepsilon^{1-D_T}, \quad (15)$$

where  $\varepsilon$  is the length scale of measurement.

For the flow through heterogeneous porous media, the tortuous length of the capillary tube is generally calculated by a fractal scaling relationship  $L_t = \varepsilon^{1-D_T} L_0^{D_T}$  [36–39]. Similarly, we argue that the aperture  $b$  of parallel capillaries is analogous to the length scale  $\varepsilon$ . Hence, the length of a capillary plate with aperture  $b$  can be rewritten as

$$L_t = b^{1-D_T} L_0^{D_T}, \quad (16)$$

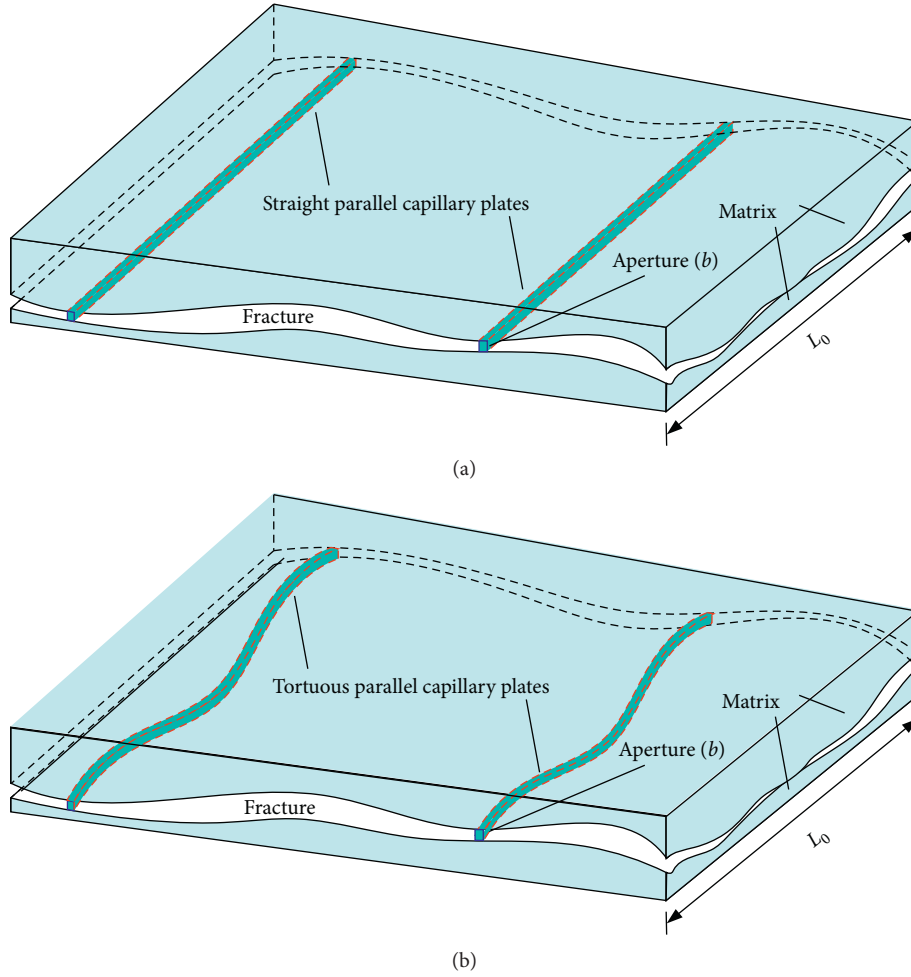


FIGURE 1: Schematic of capillary plate flow model with different apertures. (a) The straight parallel capillary model. (b) The tortuous parallel capillary model.

where  $D_T$  is the fractal dimension of the tortuous parallel capillary plate,  $L_0$  is the straight distance between inflow and outflow boundaries. For the fractal dimension of tortuous parallel capillary  $D_T=1$ ,  $L_t$  represents a straight flow path the same as the Burdine model.

Inserting equations (3) and (16) into (13) yields

$$Q(P_c) = \int_0^{S_{we}} \frac{V \Delta P}{12\mu} \frac{b^{2D_T}}{L_0^{2D_T}} dS_{we}. \quad (17)$$

For a given water-air flow system through a fixed fracture,  $\Delta P$ ,  $V$ , and  $L_0$  are assumed to be constants. By the concept of relative permeability proposed, the relative permeability  $k_r$  is given as

$$k_r = \frac{Q(P_c)}{Q_{sa}} = \frac{\int_0^{S_{we}} b^{2D_T} dS_{we}}{\int_0^1 b^{2D_T} dS_{we}}, \quad (18)$$

where  $Q_{sa}$  is the total flow rate under the saturated condition for the water phase.

Applying the Young-Laplace equation and substituting for  $b$  in equation (18) gives

$$k_r = \frac{\int_0^{S_{we}} (dS_{we}/P_c^{2D_T})}{\int_0^1 (dS_{we}/P_c^{2D_T})}. \quad (19)$$

When the tortuosity fractal dimension approaches one with respect to a straight parallel capillary plate, equation (19) can be reduced to the Burdine model equation (2).

Combining equations (5) and (19) gives

$$k_r = S_{we}^{(2D_T/\lambda)+1}. \quad (20)$$

For  $D_T/\lambda=0$  when  $\lambda \rightarrow \infty$  in which the unsaturated flow behavior in the rough-walled fracture is approximated to that in porous media with uniform pore size, equation (20) is reduced to the X-curve equation (1). For  $D_T/\lambda=1$ , equation (20) is reduced to the Brooks and Corey model equation (8). For  $D_T/\lambda=1.5$ , equation (20) is reduced to the Corey model equation (7). Thus, with one more parameter

$D_T$ , equation (20) can capture a relatively large range of the  $k_r$ - $S_w$  relationships as plotted in Figure 2.

#### 4. The Fractal Relative Permeability for Aperture-Based Fractures

Based on the Young-Laplace equation (11), equation (19) can also be presented in the form of aperture  $b$ :

$$k_r = \frac{\int_{b_{\min}}^b b^{2D_T+1} f(b) db}{\int_{b_{\min}}^{\infty} b^{2D_T+1} f(b) db} \quad (21)$$

For the tortuosity fractal dimension  $D_T=1$ , the numerator and denominator of equation (20) indicate the equivalent hydraulic apertures  $b_h$  and  $b_{\text{sat}}$  for unsaturated and saturated fracture, respectively; equation (21) is reduced to Li et al.'s model  $k_r = (b_h^3/b_{\text{sat}}^3)$  [30]. Once the probability density function  $f(b)$  of aperture distribution is known, the relative permeability can directly be determined from equation (21).

Measurements of aperture distribution from natural and artificial fractures have been performed through numerous measuring techniques including void casting [40], 3D laser/stereotopometric scanning [41–43], and computed tomography [22, 44, 45]. The measured aperture distributions are supported to be either Gaussian or lognormal. For the sake of completeness, Gaussian and lognormal distribution are both employed to evaluate the relationship between the relative permeability and aperture distribution.

**4.1. Normal Distribution-Based Fractures.** The Gaussian aperture distribution can be given by the following expression:

$$f(b) = \frac{1}{\sqrt{2\pi}\delta} e^{-((b-u)^2/2\delta^2)}, \quad \text{for } b \geq 0, \quad (22)$$

where  $u$  and  $\delta$  are the mean value and standard deviation of the aperture, respectively.

Before presenting the relative permeability relationship with respect to the aperture distribution, it is useful to define a derived integration function:

$$G(x, y) = \int_u^y b^x \frac{1}{\sqrt{2\pi}\delta} e^{-((b-u)^2/2\delta^2)} db. \quad (23)$$

By defining  $t = (|b-u|/\sqrt{2}\delta) > 0$ , the following equation can be obtained:

$$G(x, y) = \frac{|y-u|}{y-u} \frac{1}{\sqrt{\pi}} \int_0^{t_y} (u \pm \sqrt{2}\delta t)^x e^{-t^2} dt, \quad (24)$$

$$t_y = \frac{|y-u|}{\sqrt{2}\delta}. \quad (25)$$

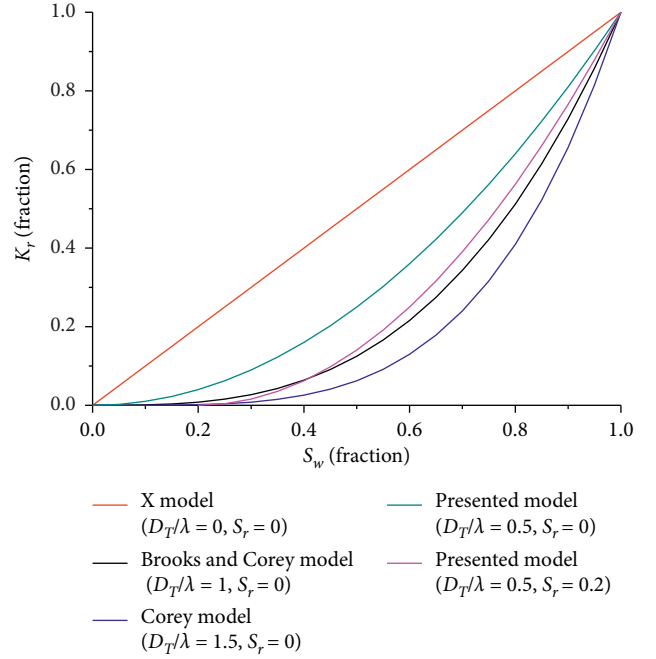


FIGURE 2: Relationships between relative permeability and saturation calculated from equation (20).

According to Newton's generalized binomial theorem [46], equation (24) can be rewritten as

$$\begin{aligned} G(x, y) &= \frac{|y-u|}{y-u} \frac{1}{\sqrt{\pi}} \int_0^{t_y} \sum_{k=0}^{\infty} C_y^k u^{x-k} (\pm \sqrt{2}\delta t)^k e^{-t^2} dt \\ &= \frac{|y-u|}{y-u} \frac{1}{\sqrt{\pi}} \sum_{k=0}^{\infty} C_y^k u^{x-k} (\pm \sqrt{2}\delta)^k \int_0^{t_y} t^k e^{-t^2} dt \\ &= \frac{|y-u|}{y-u} \frac{1}{2\sqrt{\pi}} \sum_{k=0}^{\infty} C_y^k u^{x-k} (\pm \sqrt{2}\delta)^k \\ &\quad \cdot \int_0^{t_y} (t^2)^{((k+1)/2)-1} e^{-t^2} dt^2 \\ &= \frac{|y-u|}{y-u} \frac{1}{2\sqrt{\pi}} \sum_{k=0}^{\infty} C_y^k u^{x-k} (\pm \sqrt{2}\delta)^k \gamma\left(\frac{k+1}{2}, t_y^2\right), \end{aligned} \quad (26)$$

where  $\gamma$  refers to Gamma function:

$$\begin{aligned} \gamma(x, y) &= \int_0^y t^{x-1} e^{-t} dt, \\ C_y^k &= \frac{y(y-1)L(y-k+1)}{k!}. \end{aligned} \quad (27)$$

A combination of equations (21) and (22) yields and, using equation (26), the relative permeability expression is obtained as

$$\begin{aligned}
 k_r &= \frac{\int_{b_{\min}}^b b^{2D_T+1} (1/\sqrt{2\pi} \delta) e^{-((b-u)^2/2\delta^2)} db}{\int_{b_{\min}}^{\infty} b^{2D_T+1} (1/\sqrt{2\pi} \delta) e^{-((b-u)^2/2\delta^2)} db}, \\
 &= \frac{\int_u^b b^{2D_T+1} (1/\sqrt{2\pi} \delta) e^{-((b-u)^2/2\delta^2)} db - \int_u^{b_{\min}} b^{2D_T+1} (1/\sqrt{2\pi} \delta) e^{-((b-u)^2/2\delta^2)} db}{\int_u^{\infty} b^{2D_T+1} (1/\sqrt{2\pi} \delta) e^{-((b-u)^2/2\delta^2)} db - \int_u^{b_{\min}} b^{2D_T+1} (1/\sqrt{2\pi} \delta) e^{-((b-u)^2/2\delta^2)} db} \\
 &= \frac{G(2D_T + 1, b) - G(2D_T + 1, b_{\min})}{G(2D_T + 1, \infty) - G(2D_T + 1, b_{\min})}.
 \end{aligned} \tag{28}$$

For  $D_T$  is assigned to be zero in mathematics, the water saturation can be calculated as

$$S_w = \frac{\int_{b_{\min}}^b b f(b) db}{\int_{b_{\min}}^{\infty} b f(b) db} = \frac{G(1, b) - G(1, b_{\min})}{G(1, \infty) - G(1, b_{\min})}. \tag{29}$$

Relative permeability and saturation equations (28) and (29) based on Gaussian aperture distribution are functions of the parameters  $D_T$  and  $b_{\min}$ . Figure 3 illustrates the  $k_r$ - $S_w$  relationships for Gaussian aperture-based fractures with different tortuosity fractal dimensions and minimum apertures. For a Gaussian aperture-based fracture with low  $D_T$  close to 2 when  $b_{\min}$  is kept at zero, the variation of the relative permeability  $k_r$  versus  $S_w$  is more pronounced and the relative permeability drops off rather rapidly with increasing  $D_T$ . This is because, for a higher  $D_T$ , a continuous flow path turns to be more tortuous and its component flow rate gets smaller according to the cubic law equation (10).

While the tortuosity fractal dimension  $D_T$  remains unchanged, with the growth of  $b_{\min}$  corresponding to the larger residual saturation, the slope of the  $k_r$ - $S_w$  curves is markedly elevated and the relative permeability decreases considerably. This may be a result of the fact that the number of capillary flow paths is fewer when much more void space is invalid to generate immobile capillary.

**4.2. Evaluation of the New Relationship Based on Lognormal Distribution.** The lognormal aperture distribution can be given by the following expression:

$$f(b) = \frac{1}{\sqrt{2\pi}\delta} e^{-((\ln b - u)^2/2\delta^2)}, \quad \text{for } b \geq 0. \tag{30}$$

Note that  $u$  and  $\delta$  are the mean value and standard deviation of the logarithm of aperture, respectively.

Similarly, the relative permeability based on the lognormal aperture distribution can be expressed as

$$k_r = \frac{\int_{b_{\min}}^b b^{2D_T+1} e^{-((\ln b - u)^2/2\delta^2)} d \ln b}{\int_{b_{\min}}^{\infty} b^{2D_T+1} e^{-((\ln b - u)^2/2\delta^2)} d \ln b}. \tag{31}$$

If defining  $t = ((\ln b - u)/\sqrt{2} \delta)$ , the relative permeability and saturation can be derived as

$$\begin{aligned}
 k_r &= \frac{\int_{t_{\min}}^t \left( e^{\sqrt{2} \delta t + u} \right)^{2D_T+1} e^{-t^2} dt}{\int_{t_{\min}}^{\infty} \left( e^{\sqrt{2} \delta t + u} \right)^{2D_T+1} e^{-t^2} dt} \\
 &= \frac{\int_{t_{\min}}^t e^{-[t - (\sqrt{2} (2D_T+1)\delta/2)]^2} dt}{\int_{t_{\min}}^{\infty} e^{-[t - (\sqrt{2} (2D_T+1)\delta/2)]^2} dt} = \frac{\text{erf}(\xi) - \text{erf}(\xi_{\min})}{1 - \text{erf}(\xi_{\min})},
 \end{aligned} \tag{32}$$

$$S_w = \frac{\text{erf}(t - \sqrt{2} \delta/2) - \text{erf}(t_{\min} - \sqrt{2} \delta/2)}{1 - \text{erf}(t_{\min} - \sqrt{2} \delta/2)}, \tag{33}$$

$$\begin{aligned}
 t_{\min} &= \frac{\ln b_{\min} - u}{\sqrt{2}\delta}; \\
 \xi &= t - \frac{\sqrt{2}(2D_T+1)\delta}{2}; \\
 \xi_{\min} &= t_{\min} - \frac{\sqrt{2}(2D_T+1)\delta}{2}.
 \end{aligned} \tag{34}$$

Relative permeability and saturation based on lognormal aperture distribution equations (32) and (33) are also a function of the parameters  $D_T$  and  $b_{\min}$ . A relatively large range of the  $k_r$ - $S_w$  relationships for lognormal aperture-based fractures with different tortuosity fractal dimensions and minimum apertures is depicted in Figure 4, indicating considerable sensitivity to the tortuosity fractal dimension and minimum aperture. Similar to the relative permeability curves shown in Figure 3, the relative permeability decreases with the increment of  $D_T$  for a specified  $b_{\min}$ , while it reduces considerably with the increment of  $b_{\min}$  for a specified  $D_T$ .

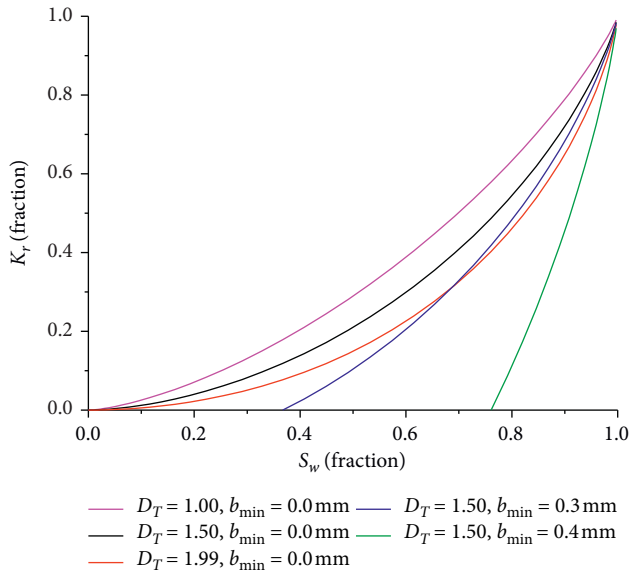


FIGURE 3: Predicted relationships between relative permeability and saturation with different tortuosity fractal dimensions and minimum apertures. The parameters used in equations (28) and (29) are  $u = 0.3$  mm and  $\delta = 0.1$  mm.

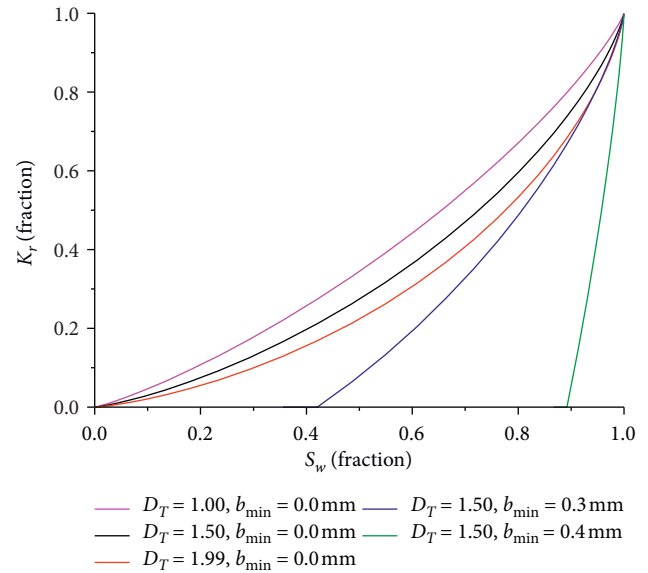


FIGURE 4: Predicted relationships between relative permeability and saturation with different tortuosity fractal dimensions and minimum apertures. The parameters used in equations (32) and (33) are  $u = 0.3$  mm and  $\delta = 0.2$  mm.

## 5. Model Validation and Prediction

**5.1. Experimental Validation against Laboratory Observations.** In order to demonstrate the validity of the proposed  $k_r$ - $S_w$  relationships in the form of equations (28) and (29), the comprehensive experimental measurements for the nitrogen-water flow of rough-walled fractures reported by Chen and Horne [21] are applied to be compared with our predictions. The  $k_r$ - $S_w$  data of two analog fractures (homogeneously and randomly rough-walled fractures) with Gaussian aperture distributions are both presented. The statistical parameters for homogeneously and randomly rough-walled fractures are  $u = 0.145$  mm and  $\delta = 0.03$  mm, and  $u = 0.24$  mm and  $\delta = 0.05$  mm, respectively.

Figure 5 shows good agreement between the proposed model and the data from Chen and Horne [21]. Based on the least square method, the fitted parameters are  $D_T = 1.75$  and  $b_{\min} = 0.136$  mm for homogeneously rough-walled fracture and  $D_T = 1.9$  and  $b_{\min} = 0.24$  mm for randomly rough-walled fracture. The values for the correlation coefficient ( $R^2$ ) of curve fitting are above 0.95. The predictions by other models including X-model, Brooks and Corey model, and Corey model are also plotted in Figure 4. The Brooks and Corey model gives better results than the X-model and Corey model. However, the residual saturation predicted using the Brooks and Corey model is specified as zero and diverges from the actual residual saturation ( $S_{wr} = 0.25$  and  $0.39$  for homogeneously and randomly rough-walled fractures, resp.) based on the experimental measurements.

Significantly, it is realized that the tortuosity fractal dimension  $D_T$  of the homogeneously rough-walled fracture is less than that of randomly rough-walled fracture. This can

be understood from the characteristics of the Gaussian aperture distribution, in which the aperture variation of the former does not have correlated spatial correlation whereas that of the latter does. Therefore, the flow paths formed in the homogeneously rough-walled fracture are less tortuous corresponding to lower  $D_T$ .

**5.2. Comparison with Numerical Solutions.** At the present time, there are a few systematic studies on experimental data based on lognormal distributed fracture with which theoretical prediction for fracture relative permeability can be compared. However, Pruess and Tsang [24] have developed a numerical model based on percolation theory to numerically study the two-phase flow properties in fractures with lognormal aperture distributions and the relative permeability data for two typical fractures with the same lognormal aperture distribution ( $u = 0.0818$  mm and  $\delta = 0.0043$  mm), and different anisotropy of spatial correlation are both calculated by simulating each phase flows separately in their filled void space. Based on a general simulator "MULKOM," the fracture aperture is discretized with  $20 \times 20$  grid blocks and a pressure difference is assigned to the inflow and outflow boundaries while the residual boundaries are impermeable.

Figure 6 shows matches between the simulated relative permeability-saturation relations and curves predicted using the proposed model, X model, Corey model, and Brooks and Corey model. For a given saturation, the X model generally overestimates the relative permeability and the Corey model generally underestimates the relative permeability, being in disagreement with the numerical results. The proposed model and Brooks and Corey model are overall closer to the measurements than the X model and Corey model predictions.

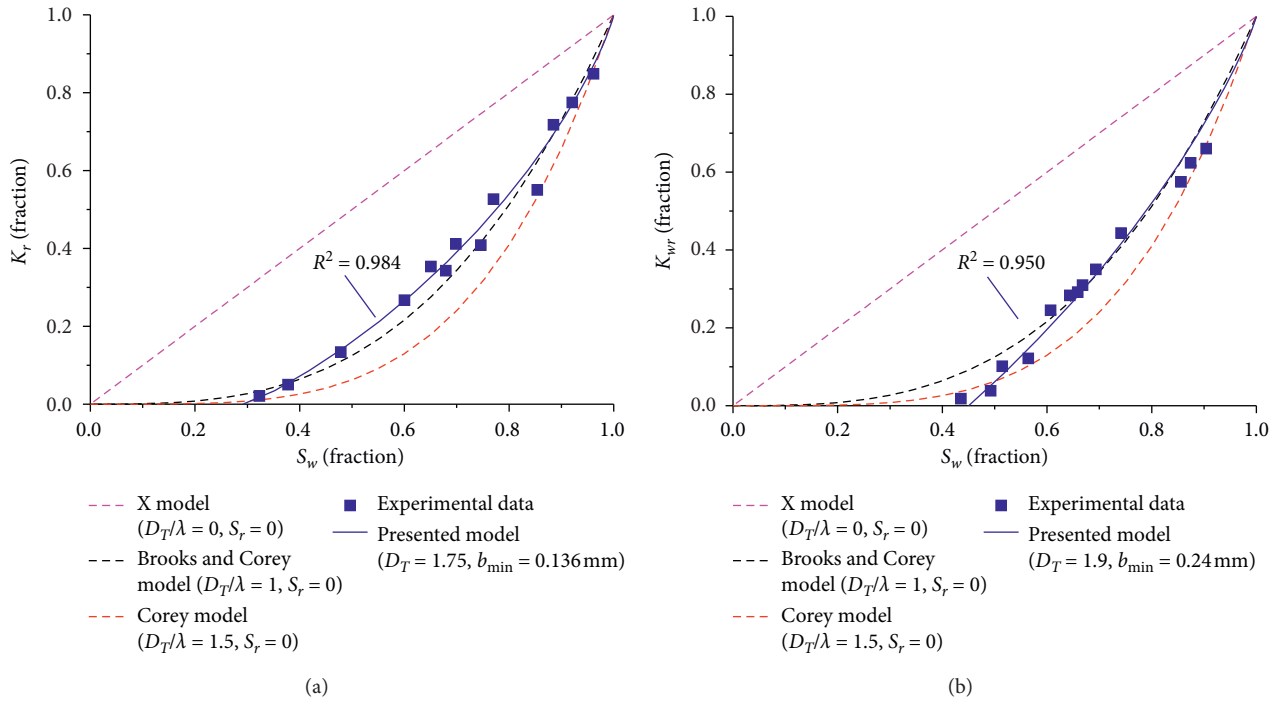


FIGURE 5: Comparisons of relative permeabilities between the present model and measured data: (a) homogeneously rough with  $u = 0.145 \text{ mm}$  and  $\delta = 0.03 \text{ mm}$  and (b) randomly rough with  $u = 0.24 \text{ mm}$  and  $\delta = 0.05 \text{ mm}$ .

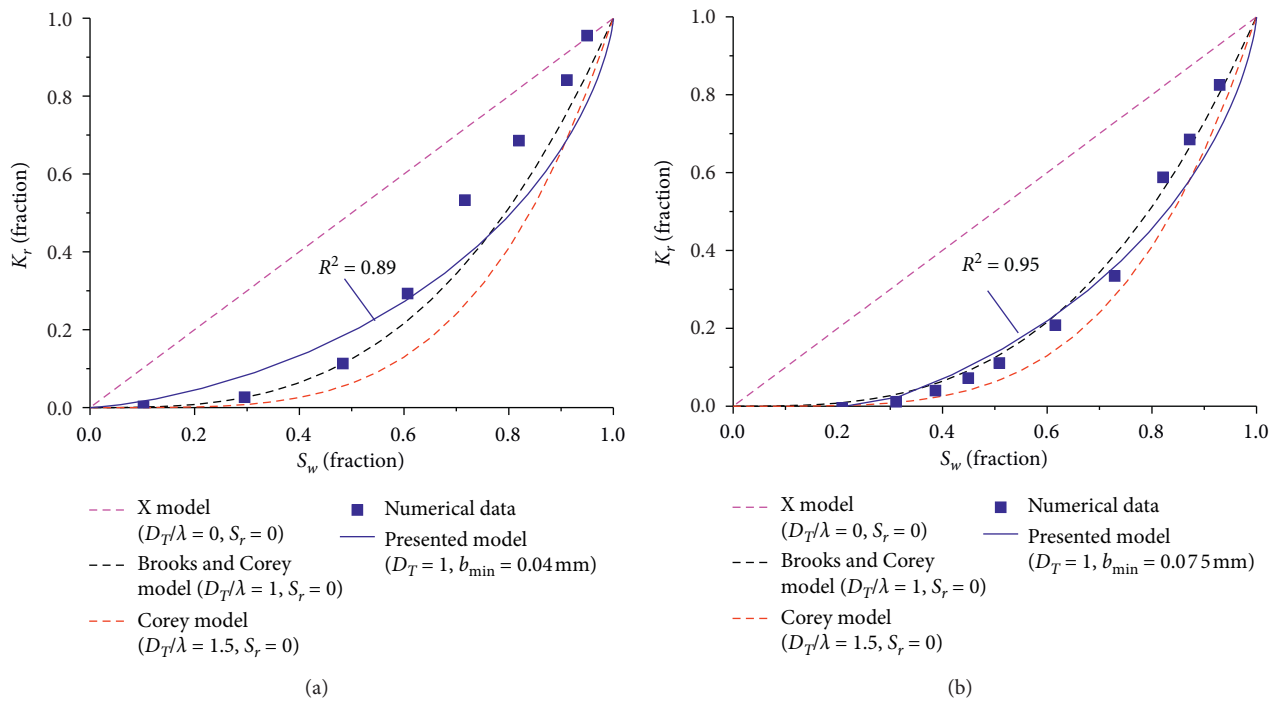


FIGURE 6: Comparisons of relative permeabilities between the present model and measured data for two fractures of the same lognormal aperture distribution with the mean value and standard deviation of  $0.0818 \text{ mm}$  and  $0.0043 \text{ mm}$ , respectively: (a) isotropic spatial correlation and (b) anisotropic spatial correlation.

As indicated in Figure 6, some discrepancies between the analytical predictions and numerical results are apparent; for example, relative permeabilities are somewhat too low for large saturations, while, at low saturations, relative permeabilities are somewhat too high. Agreement is rather good at intermediate saturations. Note that the resultant  $D_T$  values are identical with one, indicating that the flow paths in these two different spatial correlated fractures are close to straight without the influence of anisotropy of aperture distribution. This may be due to the insufficient statistical quantity of aperture elements as mentioned by Pruess and Tsang [24]; each fracture realization includes only 400 aperture elements and lacks the chance to generate tortuous flow paths in large probability.

## 6. Conclusions

The relative permeability in rough-walled fractures is a fundamental parameter in the multiphase flow through fractured media. A fractal model for estimating the relationship between relative permeability and saturation of rough-walled fractures is derived analytically based on the cubic law and the tortuous capillary model. The proposed model has considered the fractal characteristics of tortuous parallel capillary plates and can generalize the primary existing relationship in the literature. Based on the aperture-distributed dependence of relative permeability properties, the relative permeability expressions in the form of aperture with respect to Gaussian and log-normal distribution are both developed explicitly. The predictions of relative permeabilities from the proposed model are shown to be consistent with experimental observations for Gaussian distributed fractures and numerical data for lognormal distributed fracture. The fractal relative permeability model for rough-walled fracture is the terms of the tortuosity fractal dimension, determination of the tortuosity fractal dimension associated with aperture distribution is an interesting and challenging topic, and this work is in processing.

## Data Availability

The data used in the present study may be available upon request from the authors.

## Conflicts of Interest

The authors declare that they have no conflicts of interest regarding the publication of this paper.

## Acknowledgments

The financial support from the National Natural Science Foundation of China (nos. 42077243 and 51709207), Natural Science Foundation of Hubei Province (no. 2018CFB631), and Visiting Researcher Fund Program of State Key Laboratory of Water Resources and Hydropower Engineering Science (2019SGG04) are gratefully acknowledged.

## References

- [1] Z. Ye, "Numerical analysis of unsaturated seepage flow in two-dimensional fracture networks," *International Journal of Geomechanics*, vol. 17, no. 5, Article ID 04016118, 2017.
- [2] C. Yao, Y. Shao, J. Yang et al., "Effects of non-Darcy flow on heat-flow coupling process in complex fractured rock masses," *Journal of Natural Gas Science and Engineering*, vol. 83, Article ID 103536, 2020.
- [3] Y. Li, Y.-F. Chen, G.-J. Zhang, Y. Liu, and C.-B. Zhou, "A numerical procedure for modeling the seepage field of water-sealed underground oil and gas storage caverns," *Tunnelling and Underground Space Technology*, vol. 66, pp. 56–63, 2017.
- [4] H. H. Liu, C. Doughty, and G. S. Bodvarsson, "An active fracture model for unsaturated flow and transport in fractured rocks," *Water Resources Research*, vol. 34, no. 10, pp. 2633–2646, 1998.
- [5] C. Chang, Q. Zhou, M. Oostrom, T. J. Kneafsey, and H. Mehta, "Pore-scale supercritical CO<sub>2</sub> dissolution and mass transfer under drainage conditions," *Advances in Water Resources*, vol. 100, pp. 14–25, 2017.
- [6] Z. Ye, Q. Fan, S. Huang, and A. Cheng, "A one-dimensional line element model for transient free surface flow in porous media," *Applied Mathematics and Computation*, vol. 392, Article ID 125747, 2021.
- [7] Z. Ye, H. Qin, Y. Chen, and Q. Fan, "An equivalent pipe network model for free surface flow in porous media," *Applied Mathematical Modelling*, vol. 87, pp. 389–403, 2020.
- [8] Z. Ye, Q. Jiang, C. Yao et al., "The parabolic variational inequalities for variably saturated water flow in heterogeneous fracture networks," *Geofluids*, vol. 2018, Article ID 9062569, 16 pages, 2018.
- [9] F. Xiong, Q. Jiang, C. Xu, X. Zhang, and Q. Zhang, "Influences of connectivity and conductivity on nonlinear flow behaviours through three-dimension discrete fracture networks," *Computers and Geotechnics*, vol. 107, pp. 128–141, 2019.
- [10] C. Yao, Y. Shao, J. Yang et al., "Effects of fracture density, roughness, and percolation of fracture network on heat-flow coupling in hot rock masses with embedded three-dimensional fracture network," *Geothermics*, vol. 87, Article ID 101846, 2020.
- [11] X. Zhang, H. Chen, and C. Yao, "Seepage characteristics of triaxial compression-induced fractured rocks under varying confining pressures," *International Journal of Geomechanics*, vol. 20, no. 9, Article ID 04020160, 2020.
- [12] F. Huang, C. Yao, J. Yang, C. He, Y. Shao, and C. Zhou, "Connectivity evaluation of fracture networks considering the correlation between trace length and aperture," *Applied Mathematical Modelling*, vol. 88, pp. 870–887, 2020.
- [13] E. Romm, *Fluid Flow in Fractured Rocks*, Nedra Publishing House, Moscow, Russia, 1966.
- [14] P. Persoff and K. Pruess, "Two-phase flow visualization and relative permeability measurement in natural rough-walled rock fractures," *Water Resources Research*, vol. 31, no. 5, pp. 1175–1186, 1995.
- [15] M. Fourar, S. Bories, R. Lenormand, and P. Persoff, "Two-phase flow in smooth and rough fractures: measurement and correlation by porous-medium and pipe flow models," *Water Resources Research*, vol. 29, no. 11, pp. 3699–3708, 1993.
- [16] D. Pieters and R. Graves, "Fracture relative permeability: linear or non-linear function of saturation," in *Proceedings of the 1994 International Petroleum Conference and Exhibition of Mexico*, Veracruz, Mexico, October 1994.



- [17] S. Reitsma and B. H. Kueper, "Laboratory measurement of capillary pressure-saturation relationships in a rock fracture," *Water Resources Research*, vol. 30, no. 4, pp. 865–878, 1994.
- [18] S. Huang, Z. Lu, Z. Ye, and Z. Xin, "An elastoplastic model of frost deformation for the porous rock under freeze-thaw," *Engineering Geology*, vol. 278, Article ID 105820, 2020.
- [19] S. B. Huang, Y. H. Ye, X. Z. Cui, A. P. Cheng, and G. F. Liu, "Theoretical and experimental study of the frost heaving characteristics of the saturated sandstone under low temperature," *Cold Regions Science and Technology*, vol. 174, Article ID 103016, 2020.
- [20] S. P. Bertels, D. A. DiCarlo, and M. J. Blunt, "Measurement of aperture distribution, capillary pressure, relative permeability, and in situ saturation in a rock fracture using computed tomography scanning," *Water Resources Research*, vol. 37, no. 3, pp. 649–662, 2001.
- [21] Y. Chen and R. Horne, "Two-phase flow in rough-walled fractures: experiments and a flow structure model," *Water Resources Research*, vol. 42, no. 3, 2006.
- [22] D. Huo and S. M. Benson, "Experimental investigation of stress-dependency of relative permeability in rock fractures," *Transport in Porous Media*, vol. 113, no. 3, pp. 567–590, 2016.
- [23] N. Watanabe, K. Sakurai, T. Ishibashi et al., "New  $\nu$ -type relative permeability curves for two-phase flows through subsurface fractures," *Water Resources Research*, vol. 51, no. 4, pp. 2807–2824, 2015.
- [24] K. Pruess and Y. W. Tsang, "On two-phase relative permeability and capillary pressure of rough-walled rock fractures," *Water Resources Research*, vol. 26, no. 9, pp. 1915–1926, 1990.
- [25] R. J. Glass, M. J. Nicholl, and L. Yarrington, "A modified invasion percolation model for low-capillary number immiscible displacements in horizontal rough-walled fractures: influence of local in-plane curvature," *Water Resources Research*, vol. 34, no. 12, pp. 3215–3234, 1998.
- [26] R. Hughes and M. Blunt, "Network modeling of multiphase flow in fractures," *Advances in Water Resources*, vol. 24, no. 3–4, pp. 409–421, 2001.
- [27] Z. Ye, H.-H. Liu, Q. Jiang, and C. Zhou, "Two-phase flow properties of a horizontal fracture: the effect of aperture distribution," *Advances in Water Resources*, vol. 76, pp. 43–54, 2015.
- [28] Z. Ye, H.-H. Liu, Q. Jiang, Y. Liu, and A. Cheng, "Two-phase flow properties in aperture-based fractures under normal deformation conditions: analytical approach and numerical simulation," *Journal of Hydrology*, vol. 545, pp. 72–87, 2017.
- [29] M. Fourar and R. Lenormand, "A viscous coupling model for relative permeabilities in fractures," in *Proceedings of the 1998 SPE Annual Technical Conference and Exhibition*, New Orleans, LA, USA, September 1998.
- [30] Y. Li, Y.-F. Chen, and C.-B. Zhou, "Hydraulic properties of partially saturated rock fractures subjected to mechanical loading," *Engineering Geology*, vol. 179, pp. 24–31, 2014.
- [31] N. T. Burdine, "Relative permeability calculations from pore size distribution data," *Journal of Petroleum Technology*, vol. 5, no. 3, pp. 71–78, 1953.
- [32] T. Corey, "The interrelation between gas and oil relative permeabilities," *Producers Monthly*, vol. 19, no. 1, pp. 38–41, 1954.
- [33] R. Brooks and A. Corey, "Hydraulic properties of porous media," *Hydrology Papers*, Colorado State University, Fort Collins, CO, USA, 1964.
- [34] H.-H. Liu, M.-Y. Wei, and J. Rutqvist, "Normal-stress dependence of fracture hydraulic properties including two-phase flow properties," *Hydrogeology Journal*, vol. 21, no. 2, pp. 371–382, 2013.
- [35] B. Mandelbrot, *The Fractal Geometry of Nature*, W.H. Freeman, New York, NY, USA, 1983.
- [36] B. Yu and P. Cheng, "A fractal permeability model for bi-dispersed porous media," *International Journal of Heat and Mass Transfer*, vol. 45, no. 14, pp. 2983–2993, 2002.
- [37] G. Lei, P. C. Dong, S. Y. Mo, S. H. Gai, and Z. S. Wu, "A novel fractal model for two-phase relative permeability in porous media," *Fractals*, vol. 23, no. 2, Article ID 1550017, 2015.
- [38] B. Xiao, X. Zhang, W. Wang et al., "A fractal model for water flow through unsaturated porous rocks," *Fractals*, vol. 26, no. 2, Article ID 1840015, 2018.
- [39] B. Xiao, "Kozeny-Carman constant for gas flow through fibrous porous media by fractal-Monte Carlo simulations," *Fractals*, vol. 27, 2019.
- [40] S. Gentier, D. Billaux, and L. van Vliet, "Laboratory testing of the voids of a fracture," *Rock Mechanics and Rock Engineering*, vol. 22, no. 2, pp. 149–157, 1989.
- [41] F. Xiong, Q. Jiang, Z. Ye, and X. Zhang, "Nonlinear flow behavior through rough-walled rock fractures: the effect of contact area," *Computers and Geotechnics*, vol. 102, pp. 179–195, 2018.
- [42] X. Zhang, Q. Jiang, N. Chen, W. Wei, and X. Feng, "Laboratory investigation on shear behavior of rock joints and a new peak shear strength criterion," *Rock Mechanics and Rock Engineering*, vol. 49, no. 9, pp. 3495–3512, 2016.
- [43] Z. C. Tang and Z. Q. Zhang, "Elliptical Hertz-based general closure model for rock joints," *Rock Mechanics and Rock Engineering*, vol. 54, pp. 477–486, 2020.
- [44] Z. C. Tang, Q. Z. Zhang, and J. Peng, "Effect of thermal treatment on the basic friction angle of rock joint," *Rock Mechanics and Rock Engineering*, vol. 53, no. 4, pp. 1973–1990, 2020.
- [45] Z. C. Tang, "Experimental investigation on temperature-dependent shear behaviors of granite discontinuity," *Rock Mechanics and Rock Engineering*, vol. 53, no. 9, pp. 4043–4060, 2020.
- [46] A. Okounkov, "Binomial formula for MacDonald polynomials and applications," *Mathematical Research Letters*, vol. 4, no. 4, pp. 533–553, 1997.

## Research Article

# A New Statistical Parameter for Determining Joint Roughness Coefficient (JRC) considering the Shear Direction and Contribution of Different Protrusions

Jiu-yang Huan <sup>1</sup>, Zhi-qiang Zhang <sup>1,2</sup>, Ming-ming He <sup>1</sup>, and Ning Li <sup>1,2,3</sup>

<sup>1</sup>Institute of Geotechnical Engineering, Xi'an University of Technology, Xi'an 710048, China

<sup>2</sup>State Key Laboratory of Eco-hydraulics in Northwest Arid Region, Xi'an University of Technology, Xi'an 710048, China

<sup>3</sup>Shaanxi Key Laboratory of Loess Mechanics and Engineering, Xi'an University of Technology, Xi'an 710048, China

Correspondence should be addressed to Zhi-qiang Zhang; zhangzq87@xaut.edu.cn

Received 7 November 2020; Revised 26 December 2020; Accepted 25 January 2021; Published 10 February 2021

Academic Editor: Zhi Cheng Tang

Copyright © 2021 Jiu-yang Huan et al. This is an open access article distributed under the Creative Commons Attribution License, which permits unrestricted use, distribution, and reproduction in any medium, provided the original work is properly cited.

The mechanical properties of joints are important factors affecting the safety and stability of rock mass. The joint roughness coefficient (JRC) is a parameter for describing the roughness morphology of the joint surface, and its accurate quantification is very important to predict the shear strength. In the current statistical parameter methods for the estimation of joint roughness, the size of different protrusions on the joint surface was completely ignored, which did not correspond to the real failure mechanism of rock joint during the shear process. In this study, a new statistical parameter WPA was proposed for the estimation of JRC considering the shear direction and the contributions of different protrusions. First, the 10 standard roughness joint profiles were digitized based on image processing technology, and the obtained coordinate data were proved to be reliable by the calculation results of existing parameters. Secondly, the WPA value of 10 standard roughness joint profiles was calculated at a 0.5 mm sampling interval in two directions. The functional relationship between WPA and JRC indicated that they should be established in the same shear direction to maintain a high correlation. The JRC values of 10 standard roughness joint profiles in direction 2 were obtained based on the functional relationship established between WPA and JRC in direction 1, and the roughness of these 10 joint profiles was confirmed to be influenced by direction. Next, the effect of sampling interval on WPA was investigated. As the sampling interval increases, the WPA values gradually decreased and the correlation between them and JRC gradually declined. In practical application, a smaller sampling interval was recommended for more accurate prediction. Finally, the geometric coordinate data of 21 joint profiles given in the literature and 4 natural joint surfaces were obtained by graphics processing technology and 3D scanning technology, respectively. The JRC values of them were separately estimated by WPA in different directions. The results showed that the new statistical parameter WPA proposed in this paper can well describe the joint roughness considering the shear direction and the contribution of different protrusions.

## 1. Introduction

In natural rock masses, there are complex joints and structural planes with different morphologies, directions, and scales. The engineering geology of the rock mass is obviously different from the complete rock due to the characteristics of multiple fractures. A lot of practical engineering experience showed that the fracture in the rock mass plays a leading role in the deformation and destruction of slope and tunnel engineering [1–4]. Therefore,

the safety and stability of rock mass largely depended on the mechanical properties of intricate joints. Shear strength is the main strength characteristic of joints, and it is influenced by a variety of factors. Joint roughness is an important factor affecting the shear properties of the joint surface, and its quantitative determination makes it possible to predict the shear strength of the joint surface. Therefore, it is a challenging research task to accurately and reasonably estimate the roughness of the joint surface [5–9].

Based on the direct shear test of 136 natural joint specimens, Barton [8] proposed the JRC-JCS model which was widely used in rock mass engineering and put forward the joint roughness coefficient (JRC) to quantitatively describe the irregular morphology of the joint surface at the first time. The JRC-JCS model is shown in

$$\tau = \sigma_n \tan \left[ \text{JRC} * \left( \frac{\text{JCS}}{\sigma_n} \right) + \varphi_r \right], \quad (1)$$

where  $\tau$  is the shear strength, which can be obtained from the shear stress curve,  $\sigma_n$  is the normal stress, JRC is the joint roughness coefficient, JCS is the compressive strength of the joint wall, which can be obtained from the uniaxial compression test or the point load test of the complete rock, and  $\varphi_b$  is basic friction angle which can be obtained from the tilt test of the joint surface. For equation (1), if we have obtained the exact values of other parameters, we can get the JRC value by inverse calculation. However, this method can only provide a posteriori description of the roughness of the joint surface. In contrast, we prefer that the JRC and shear strength of the joint surface be obtained in advance to evaluate its safety and stability. According to this idea, Barton and Choubey [9] proposed 10 standard roughness joint profiles, and the JRC of the target joint can be determined by visual comparison. The JRC values of the standard profile were obtained by back calculation from equation (1) with a range of 0 to 20, as shown in Table 1.

As this empirical comparison method gives the way to determine the JRC value for the first time, the International Society for Rock Mechanics [10] recommends these 10 profiles as a standard method for evaluating the joint roughness coefficient. Although the empirical comparison method was very convenient and fast, its prediction value fluctuated with the personal experience of field engineers [11, 12].

To avoid the above situation, the statistical parameter method was gradually developed to quantify the JRC of the joint surface, such as the straight edge method [13], the modified straight edge method [14], the fractal dimension ( $D$ ) [15, 16], root mean square roughness index (RMS) and mean square values roughness index (MSV) [17], root mean square of the first deviation of profiles ( $Z_2$ ) [17–22], structure function ( $SF$ ) [17–19, 21–23], standard deviation of the angle ( $SDi$ ) [19], the roughness profile index ( $Rp$ ) [19–23], maximum inclination ( $\theta_{\max}^*$ ) [20, 21], the modified  $Z_2$  ( $Z_2'$ ) [24], mean positive angle parameter ( $\theta_{p+}$ ) [25], and mean tangent angle ( $\beta_{100\%}$ ) [22]. These parameters can be calculated from geometric coordinates of joint profile, as shown in Figure 1 [26], where  $x_i$  and  $y_i$  are the abscissa and ordinate of the joint profile, respectively.  $L$  is the horizontal length of the joint profile.  $\Delta x$  is the distance between the abscissa of adjacent coordinate point and it is usually a constant value at the same sampling interval.

It is practical to use JRC to systematically characterize the morphology of rock joints, and JRC provides a unified standard for all joint morphology description methods. However, the accuracy of JRC is highly dependent on the reasonableness of the statistical parameters used. At present,

many researchers believed that the rough morphology of joint surface has anisotropy because the strength and failure characteristics of rough joints were completely different in different shear directions [27–30]. Therefore, the directionality of rough topography should be considered when describing joint roughness. Most of the above statistical parameters had been confirmed to have a good correlation with JRC [13–25]. However, only a few statistical parameters could reflect the influence of shear direction on joint roughness, such as  $\theta_{\max}^*$ ,  $Z_2'$ ,  $\theta_{p+}$ , and  $\beta_{100\%}$  [20–22, 24, 25].

In recent years, some scholars had found that the failure of different morphologies of joint surfaces was different in the shear process [7, 31–35]. The failure scale of the big protrusion on the joint surface was larger than that of the small one. This indicated that the overall failure of the joint surface was closely related to the size of the joint protrusion, and the overall roughness of the joint should consider the size of protrusion corresponding to local roughness. However, in the current statistical parameter methods for the estimation of joint roughness, only the geometric characteristics of the joint surface were considered. The overall roughness parameters of the joint profile were usually obtained by averaging all local roughness parameters. The size of joint protrusion was completely ignored, and this could not reflect the real failure mechanism of the joint in the shear process.











In order to predict the JRC of joint profile more reasonably, a new statistical parameter considered the contribution degree of different protrusions and shear direction was proposed in this paper. Based on the 10 standard roughness joint profiles proposed by Barton and Choubey [9], the directionality of JRC was well verified. What is more, the impact of the sampling interval of joint profile data on both the WPA value and their correlation with JRC was also investigated. Finally, the practicability of WPA in evaluating JRC of the joint profile was well verified based on the joint profile given in the literature and the natural joint surface.

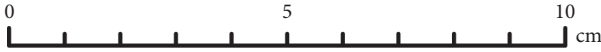
## 2. Derivation of New Statistical Parameters

In order to fill the gaps in existing studies, a new statistical parameter WPA (the weighted positive angle) was proposed in this paper to characterize the roughness of the joint profile. In the definition of WPA, the directionality of the shear process and the contribution of local roughness to the overall roughness were considered simultaneously.

As shown in Figure 2, the discrete form of the rough joint profile consists of a series of coordinate points ( $x_i, y_i$ ), and the horizontal coordinate spacing between adjacent coordinate points is the sampling interval  $\Delta x$ . The horizontal line corresponding to the lowest point of the joint profile (the ordinate is  $y_{\min}$ ) was defined as the lowest horizontal line, and the distance from the joint coordinate point to the lowest horizontal line was defined as the undulating height  $h$ . At the same sampling interval, the joint profile was divided into a few small joint segments, each of which could be considered as a microprotrusion. Finally, for a single microjoint segment, the area ( $A$ ) of the region enclosed by the joint profile and the lowest horizontal line was defined to

TABLE 1: 10 standard roughness joint profiles [9].

No.	Typical roughness profiles	JRC range
1		0~2 (0.4)
2		2~4 (2.8)
3		4~6 (5.8)
4		6~8 (6.7)
5		8~10 (9.5)
6		10~12 (10.8)
7		12~14 (12.8)
8		14~16 (14.5)
9		16~18 (16.7)
10		18~20 (18.7)

Scale  cm

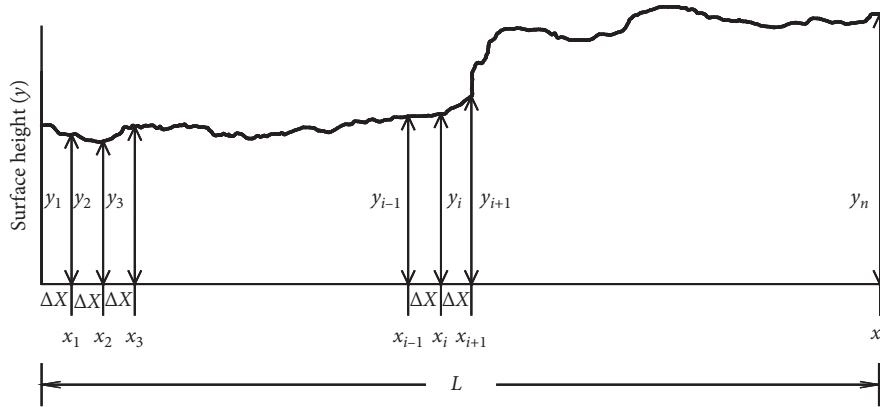


FIGURE 1: The diagram used to define geometric coordinates of a joint profile [26].

characterize the area (i.e., the size) of the microprotrusion. The area  $A_i$  of the  $i$ -th microprotrusion could be calculated by

$$A_i = \frac{\Delta x (h_{i+1} - h_i)}{2}. \quad (2)$$

In existing studies, the inclination angle of joint protrusion had been proved to have a great influence on the shear failure mechanism, and its physical significance was very clear [36, 37]. Therefore, the local inclination angle  $\theta$  was selected to describe the surface roughness of the microjoint segment, which could be calculated from the geometric coordinates of the local joint profile, as shown in

$$\theta = \tan^{-1} \left( \frac{y_{i+1} - y_i}{x_{i+1} - x_i} \right). \quad (3)$$

When  $\theta$  is positive, it indicates that the corresponding microjoint segment is oriented to the shear direction. On the contrary, when  $\theta$  is negative, it indicates that the

corresponding microjoint segment is in the direction of back shear. Based on the definition of microprotrusion, we assumed that the larger the microprotrusion size, the greater the contribution of surface roughness of microjoint segment to the overall roughness of joint profile. Therefore, the weight coefficient  $\gamma_i$  was defined to represent the contribution of  $i$ -th microjoint roughness and it could be calculated by

$$\gamma_i = \frac{A_i}{\sum_{i=1}^n A_i}. \quad (4)$$

In equation (4),  $n$  represents the number of all microjoint segments. The overall roughness  $R_i$  of  $i$ -th microjoint segment could be expressed by the product of surface roughness  $\theta_i$  and weight coefficient  $\gamma_i$ , as shown in

$$R_i = \theta_i^* \gamma_i. \quad (5)$$

From the available joint shear test results, we knew that contact and extrusion of the joint surface occurred only at

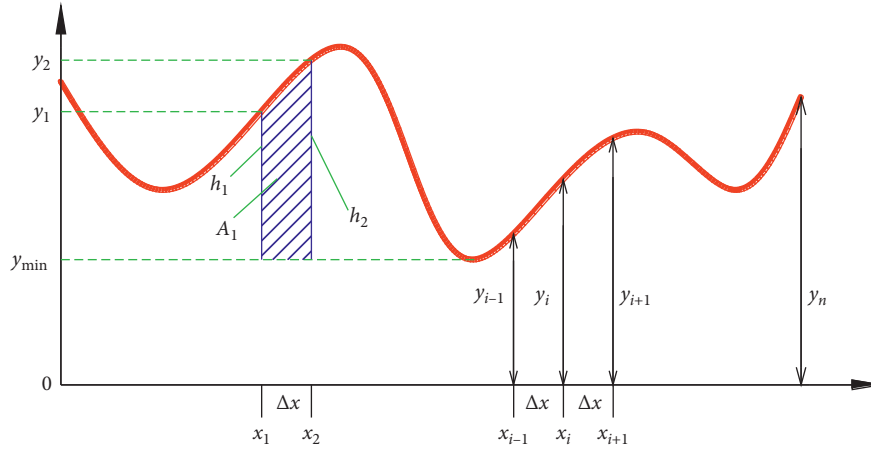


FIGURE 2: Schematic diagram of the area at microjoint segment.

the position facing the shear direction during the shear process. Therefore, referring to the treatment of Zhang et al. [24] and Belem et al. [25], when describing the roughness of joint profile along a certain shear direction, only the morphological data oriented to the shear direction were counted and involved in the roughness description. Considering the directionality of the shear process, the overall roughness  $R_i$  data of microjoint segment greater than 0 were recorded as  $R_{i+}$ . The newly proposed statistical parameter WPA (the weighted positive angle) for describing joint roughness in this paper could be obtained by summing all the values of  $R_{i+}$ , as shown in equation (6), where  $m$  represents the number of  $R_{i+}$ .

$$\text{WPA} = \sum_{i=1}^{i=m} R_i^+. \quad (6)$$

In the mathematical sense, the establishment of WPA is the process of calculating a weighted average of the local inclination angle  $\theta_i$  of the microjoint segment. In the physical sense, the dual effects of protrusion size and shear direction on the joint roughness are considered simultaneously in the definition of WPA, which can reflect the shear destruction mechanism of the joint surface to some extent. Therefore, the new statistical parameter WPA can not only reflect the shear direction of joints but also reflect the contribution of different protrusions to the overall roughness. This makes it possible to establish an important relationship between the roughness description and the shear mechanism of rock joints, which is rarely considered by the existing statistical parameters such as  $Z_2$  and  $R_p$ .

### 3. Preparation for Research

**3.1. Digitization of Barton's Joint Profiles.** In the currently available literature, the original version of the 10 standard roughness joint profiles originated from a journal paper published by Barton in 1977 [9]. Since the authors did not provide the raw data of the 10 joint profiles for the reader to review, later researchers could only obtain the geometric

coordinates of the 10 joint profiles in the image with the help of various indirect methods.

The initial data acquisition process for the 10 standard roughness joint profiles proposed by Barton was based on a profile comb (Figure 3). The sampling interval (SI) of the initial data is 0.5 mm because the spacing between the comb teeth is about 1 mm. The digitization of the 10 joint profiles using indirect methods is equivalent to the reacquisition of the original data, so the accuracy of our acquired data is limited by the accuracy of the original data. Therefore, the sampling interval for the digitizing process of the joint profile was set to 0.5 mm in this paper, and discrete data with larger sampling intervals could be obtained by an interpolation process.

In this paper, the image recognition method was chosen to complete the digitization of the joint profiles, and the image processing software was chosen to be GETDATA. We firstly used screenshot software to capture the image of each joint profile and saved it separately as a jpg image file. Before the data acquisition process, we also needed to remove useless pixels from the joint image and set the horizontal and vertical axes for it. The average horizontal length of 10 standard roughness joint profiles was about 99 mm, which was close to 100 mm. Among them, the 7th profile was the shortest (96 mm) and the 8th profile was the longest (101 mm) [8, 21]. According to the processing idea of Zheng and Qi [22], the horizontal length of the 10 joint profiles was assumed to be 100 mm, and the JRC values of them were assumed to be unchanged. After that, the geometric coordinates of the joint profile could be obtained through the automatic acquisition mode and point capture mode. The data point was at the center of the joint profile by default. This process was similar to Jang et al. [21], as shown in Figure 4, and the modified 10 standard roughness joint profiles are shown in Figure 5.

**3.2. Validation of Joint Profile Data.** In order to verify the accuracy of joint profile data obtained in Section 3.1, statistical parameters  $Z_2$  and  $R_p - 1$  that were widely used in

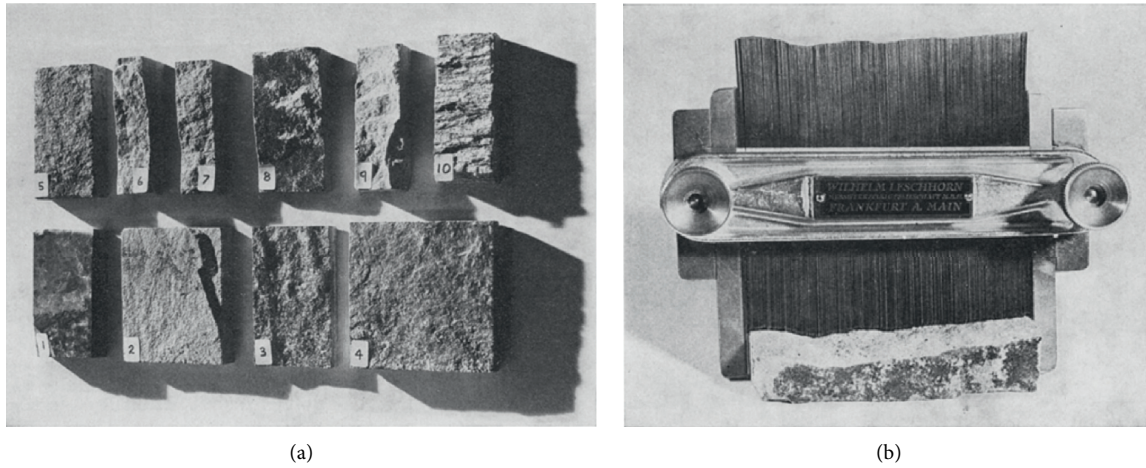


FIGURE 3: Procedure of using a profile comb to get a profile from the joint surface. (a) 10 typical joint surfaces. (b) Profile comb [8, 9].

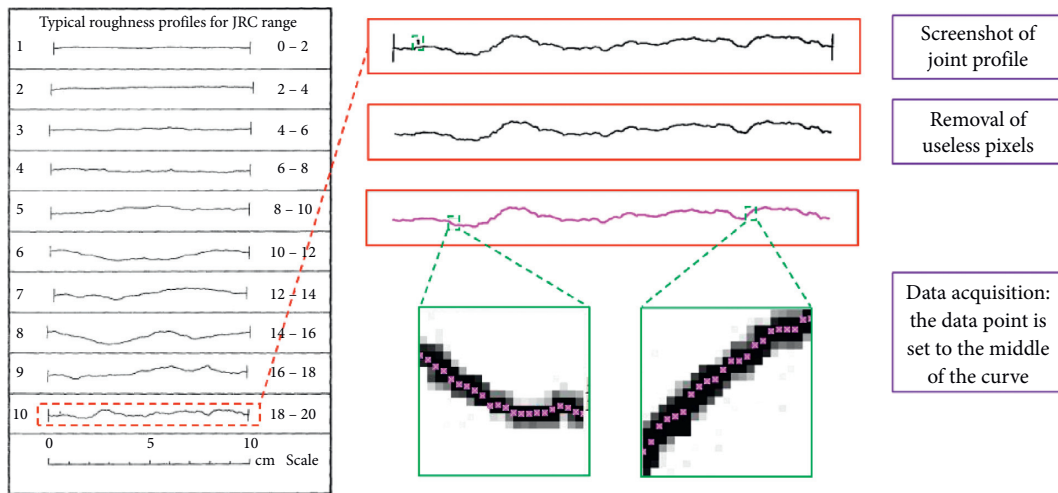


FIGURE 4: The diagram used to show the digitization of a joint profile.

actual engineering were recommended as representative for verification. Their definitions are as follows [17–23]:

$$Z_2 = \left[ \frac{1}{L} \int_{x=0}^{x=L} \left( \frac{dy}{dx} \right)^2 dx \right]^{1/2} = \left[ \frac{1}{(N-1)(Dx)^2} \sum_{i=1}^{N-1} (y_{i+1} - y_i)^2 \right]^{1/2}, \quad (7)$$

$$R_p - 1 = \frac{\sum_{i=1}^{N-1} [(x_{i+1} - x_i)^2 + (y_{i+1} - y_i)^2]^{1/2} - 1}{L},$$

where  $N$  is the number of discrete points in joint profile and it is 201 at 0.5 mm sampling interval. Under the condition of 0.5 mm sampling interval, the values of  $Z_2$  and  $R_p - 1$  of ten standard roughness joint profiles were calculated, and their fitting relationship with JRC was established by

$$JRC = a * \ln(P) + b, \quad (8)$$

where  $P$  represents the statistical parameters and  $a$  and  $b$  represent the regression coefficients. As shown in Figure 6, the values of  $Z_2$  and  $R_p - 1$  were showing a growth trend with the increase of the JRC value. The correlation coefficients squared of  $Z_2$  and  $R_p - 1$  with JRC calculated in our paper all exceeded 0.95, which was like the findings of other researchers [17–23]. This confirmed that the data acquisition

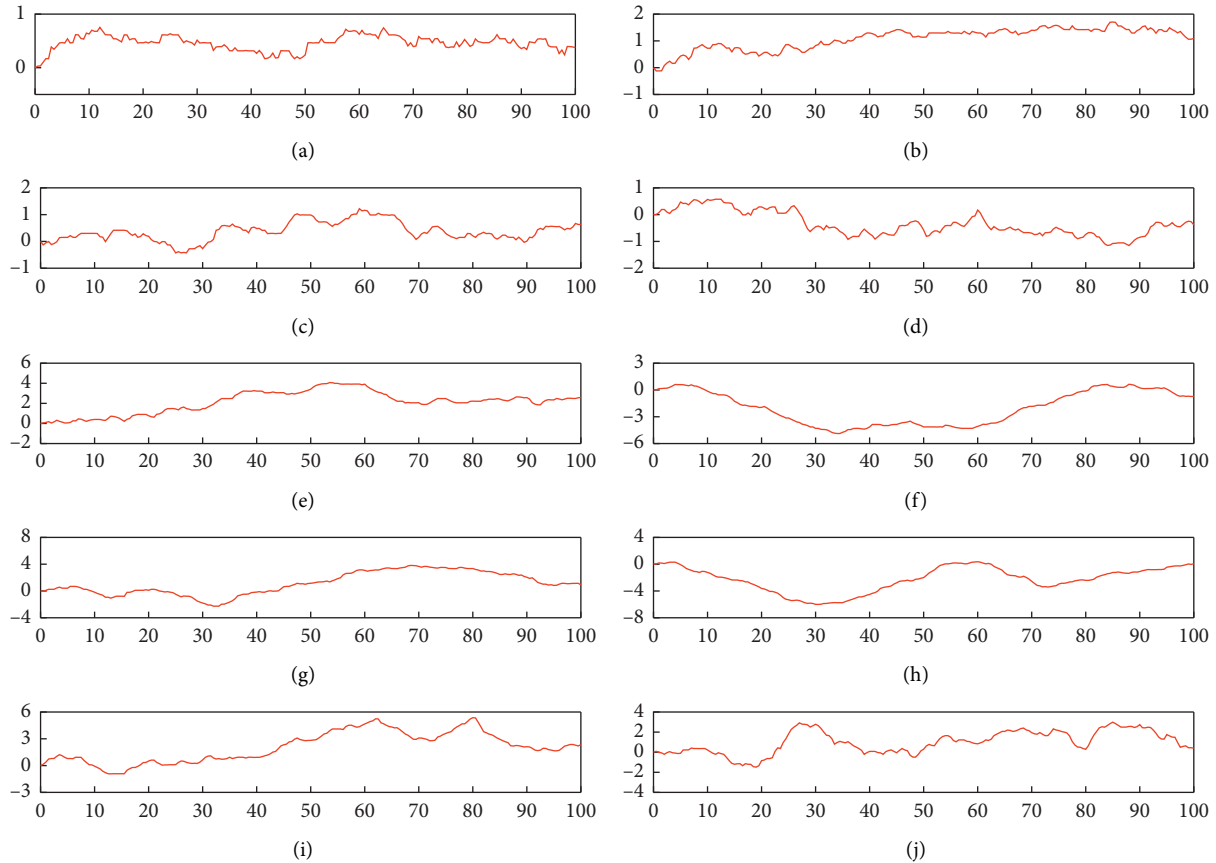


FIGURE 5: The modified 10 standard roughness profiles (unit: mm). (a) Profile 1. (b) Profile 2. (c) Profile 3. (d) Profile 4. (e) Profile 5. (f) Profile 6. (g) Profile 7. (h) Profile 8. (i) Profile 9. (j) Profile 10.

work of the Barton standard profiles in our paper was very accurate, and follow-up studies based on these acquired data were reliable.

#### 4. Validation of Correlation between WPA and JRC

Based on the coordinate data of 10 standard roughness joint profiles obtained before, the WPA of each joint profile under two shear directions was obtained according to the calculation process from equation (2) to equation (6). The calculation results of WPA are summarized in Table 2, and the corresponding sampling interval was set to 0.5 mm. For the convenience of subsequent description, shearing from left to right was noted as direction 1, and shearing from right to left was noted as direction 2.

At 0.5 mm sampling interval, each joint profile contains 200 microjoint segments; however, the number of microsegments involved in the calculation was not the same in direction 1 and direction 2. In direction 1, the WPA values of the joint profile increased consistently with the corresponding number. In direction 2, although the WPA values of the joint profile increased with the corresponding number as a whole, there were anomalies in the fifth and seventh joint profiles.

To validate the rationality of WPA when describing joint profile roughness, the functional relationships between WPA and JRC for different joint profiles in two shear directions were established in the same form as equation (3). As can be seen in Figure 7 and equations (9) and (10), the correlation between WPA and JRC of joint profile in direction 1 was better than that in direction 2, and the square of correlation coefficient ( $R^2$ ) is 0.9643 and 0.8883, respectively.

$$\begin{aligned} \text{JRC} &= 14.602 \ln(\text{WPA}) - 12.536, \\ R^2 &= 0.9643, \end{aligned} \quad (9)$$

direction 1,

$$\begin{aligned} \text{JRC} &= 13.502 \ln(\text{WPA}) - 10.308, \\ R^2 &= 0.8883, \end{aligned} \quad (10)$$

direction 2.

It is worth noting that this phenomenon is a good verification of the directionality of the joint roughness. When Barton proposed the 10 standard rough joint profiles, the default shear direction was from left to right [8]. So, the attached JRC values in Table 1 only represented the roughness of the joint profiles in direction 1 rather than

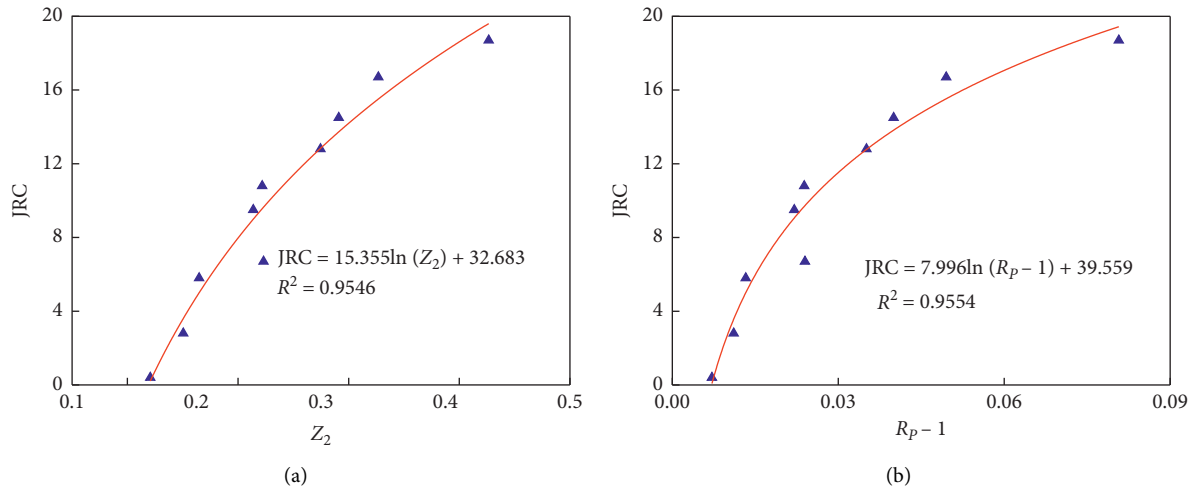


FIGURE 6: Fitting curves between statistical parameters and JRC. (a)  $Z_2$ . (b)  $R_p - 1$ .

TABLE 2: The WPA values of 10 joint profiles in different directions (SI = 0.5 mm).

Number of joint profiles	Direction 1		Direction 2	
	WPA	m	WPA	m
1	2.35	84	2.29	116
2	3.11	97	2.79	103
3	3.42	87	3.13	113
4	4.35	88	4.97	112
5	4.43	102	3.55	98
6	4.50	90	5.16	110
7	5.18	97	4.87	103
8	6.17	104	6.09	96
9	7.87	105	6.74	95
10	8.47	89	8.50	111

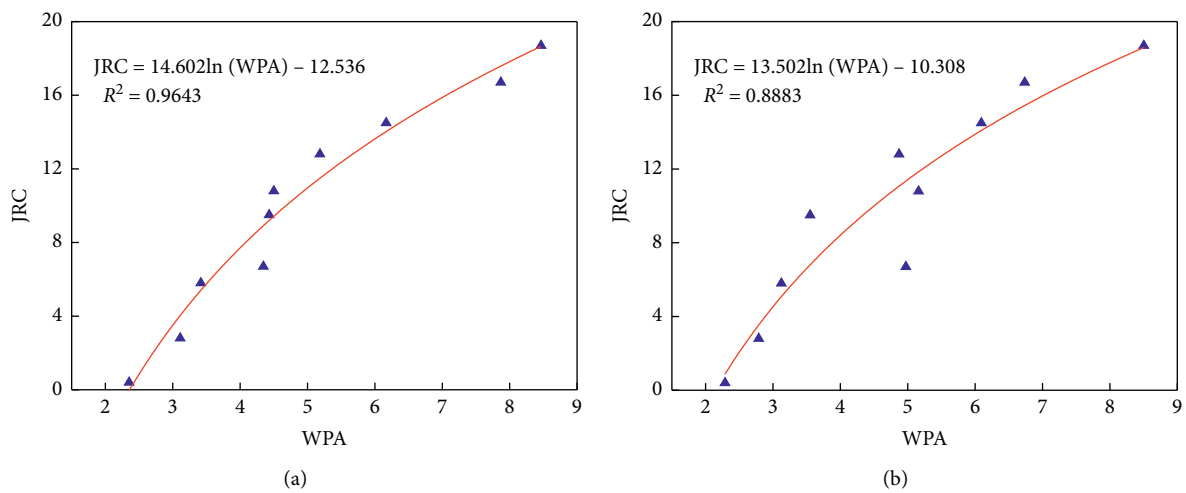


FIGURE 7: The functional relationships between WPA and JRC in two shear directions. (a) Direction 1. (b) Direction 2.

direction 2. As the data used in Figure 7(b) were based on different shear directions, so this showed that the joint roughness is directional. In summary, the functional

relationship between the statistical parameters and the JRC should be established in the same shear direction; otherwise, large errors will occur such as those shown in Figure 7(b).



Based on the above analysis, equation (9) was proposed to estimate the JRC of the joint profile at a sampling interval of 0.5 mm. Therefore, when we substitute the WPA values of 10 joint profiles in direction 2 into equation (9), the JRC values of 10 joint profiles in direction 2 can be obtained successfully. Table 3 shows the JRC values of 10 standard roughness joint profiles in two directions.

As can be seen from Table 3, the JRC values of 10 standard roughness joint profiles in two shear directions were verified to be different, which was consistent with the results obtained by Zheng and Qi [22]. Among them, the absolute difference of JRC in two directions of the fourth joint profile was the largest (4.18), and that of the tenth joint profile was the smallest (0.01). For the first joint profile, its JRC in direction 2 was negative, and this exceeded the limit where the minimum JRC value was 0. So, in order to keep the estimated JRC value of joint profiles in the normal range, the range of WPA should be larger than 2.35 965. In direction 2, the order of JRC sizes for the 10 standard roughness profiles had changed, as shown at the 4th, 5th, 6<sup>th</sup>, and 7th joint profiles.

## 5. Effect of Sampling Interval on WPA

In actual rock engineering, the accuracy of the joint surface data is greatly influenced by the sampling method and equipment, so the sampling interval varies widely. When the statistical parameter method is used to predict the roughness, the sampling interval conditions of joint profile data, statistical parameters, and corresponding function relationship must be consistent to ensure the correctness of this work [21, 22]. Therefore, in order to expand the application range of the new statistical parameters, the functional relationships between WPA and JRC were established under various sampling intervals. In Section 3.1, the geometric coordinate data of 10 standard roughness joint profiles were obtained at a 0.5 mm sampling interval. On this basis, the coordinate data of 10 joint profiles at sampling intervals of 1, 2, 4, and 10 mm could be easily obtained by interpolation.

In direction 1, the WPA values of 10 standard roughness joint profiles at 5 sampling intervals are shown in Table 4, and their variation with sampling interval is shown in Figure 8. It can be seen that the sampling interval had a great influence on the WPA values of joint profiles. With the increase of sampling interval from 0.5 mm to 10 mm, the WPA values of each joint profile decreased gradually, and the decreasing speed was first large and then small. In practical application, the sampling interval condition should be clarified to avoid confusion.

At sampling intervals of 1, 2, 4, and 10 mm, the relationship curve and functional relationship between WPA and JRC of 10 joint profiles are given in Figure 9. We can see that the JRC of the joint profile kept a positive correlation with WPA under all sampling interval schemes. For the convenience of description, the fitting formulas between WPA and JRC under different sampling intervals are summarized in Table 5. It can be seen that the  $R^2$  of the fitting formulas between WPA and JRC decreased from 0.9643 to 0.9311 with the increase of sampling interval from 0.5 mm to

10 mm. Overall, as the sampling interval increased, the correlation of the functional relationship between WPA and JRC decreased. This is because there must be an error between the obtained joint profile and the original joint profile, and this error increases as the sampling interval increases.

Figure 10 shows a comparison of the 10th joint profile obtained at 0.5 mm and 10 mm sampling intervals. The morphology of the joint profile obtained at the two sampling intervals was quite different. When the sampling interval changes from 0.5 mm to 10 mm, the sampling points of the joint profile decreased from 201 to 11 and many local rough features had been lost. Therefore, the WPA obtained from the joint profile data of the 10 mm sampling interval could not reflect the morphological characteristics of the original joint very well. This indicated that when we want to predict the roughness of the original joint profile, the sampling interval should be as small as possible; otherwise, the prediction accuracy will be reduced.

## 6. Validation of the WPA's Applicability

In order to show the advantage of WPA in predicting the JRC of the joint profile, we separately evaluated the roughness of the joint profile given in the literature and the natural joint surface.

### 6.1. JRC Estimation of the Joint Profiles Given in the Literature.

Firstly, we performed the corresponding digitization process in Section 3.1 on the joint profile given in the literature [18, 24, 38–41] at the sampling interval of 0.5 mm. Next, the WPA and corresponding JRC values of 21 joint profiles were calculated through equation (2) to equation (6) in two shear directions, as shown in Table 6.

The results showed that the JRC of these joint profiles was in 2 shear directions, where the difference of JRC of the 7th joint profile in two directions was as high as 25.4. Besides, the JRC of the 6th and 7th joint profiles in direction 1 had exceeded Barton's upper limit of 20. This indicated that the new statistical parameter WPA not only can well reflect the rough morphology but also can distinguish the differences of roughness in different shear directions. This cannot be achieved with the visual contrast method or the previous statistical parametric without considering directionality.

### 6.2. JRC Estimation of the Natural Joint Surface.

The 4 joint specimens used to evaluate roughness were collected from Taibai Mountain, Xi'an City, Shaanxi Province, China. As shown in Figure 11, the rock type is granite and the plane size is about 100 mm × 100 mm. The jointed surfaces of these specimens were produced by artificial load damage at the quarry and they were all not weathered.

The 3D point cloud data of 4 joint specimens were obtained by 3D scanner go! Scan 20, and then, they were imported into Geomagic Studio software. Firstly, the point cloud data were denoised, and then the coordinate system correction is completed. Finally, the joint surface data are separated, as shown in Figure 12.

TABLE 3: Comparison of JRC values in different directions for 10 standard roughness joint profiles.

Number of joint profiles	JRC values		Absolute difference
	Direction 1	Direction 1	
1	0.4	-0.44	0.84
2	2.8	2.45	0.35
3	5.8	4.13	1.67
4	6.7	10.88	4.18
5	9.5	5.96	3.54
6	10.8	11.42	0.62
7	12.8	10.58	2.22
8	14.5	13.84	0.66
9	16.7	15.33	1.37
10	18.7	18.71	0.01

TABLE 4: The WPA values of 10 joint profiles at 5 sampling intervals.

Number of joint profiles	Sampling intervals (mm)				
	0.5	1	2	4	10
1	2.35	1.64	1.15	0.75	0.58
2	3.11	2.45	1.39	1.21	0.73
3	3.42	2.87	2.57	1.95	1.42
4	4.35	3.88	2.69	2.05	1.48
5	4.43	4.03	3.75	3.10	2.37
6	4.50	4.26	4.10	3.74	2.63
7	5.18	4.44	3.96	3.50	2.16
8	6.17	5.86	5.72	5.54	5.08
9	7.87	7.58	6.99	6.19	5.54
10	8.47	7.92	6.44	5.49	4.87

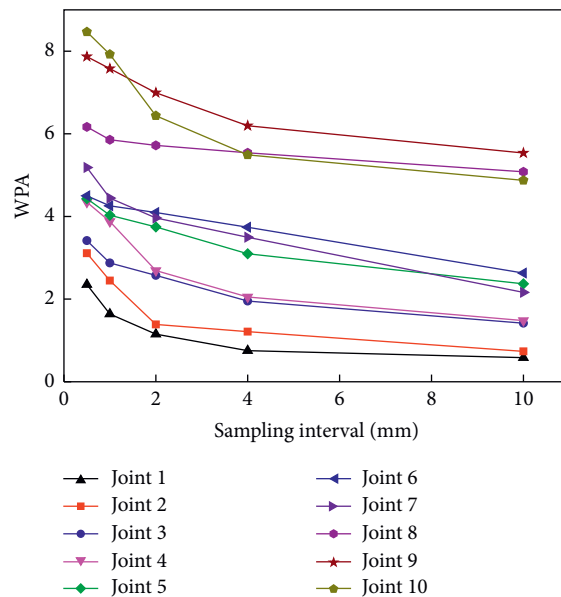


FIGURE 8: The effect of different sampling intervals on WPA values of 10 standard roughness joint profiles.

In this section, the roughness of the joint surface in different directions was represented by the roughness of the joint profile. The data of joint profile were obtained by Geomagic Studio software, and the acquisition method of joint profile data is shown in Figure 13. The interval of joint profiles on the joint surface was 15°, and the number of joint

profiles intercepted on each joint surface was 12. Since the roughness of each joint profile could be analyzed in two directions, the roughness of the joint surface could be described in 24 directions.

The 3D coordinate data of all joint profiles were processed by Surfer software, and the 2D coordinate data with a

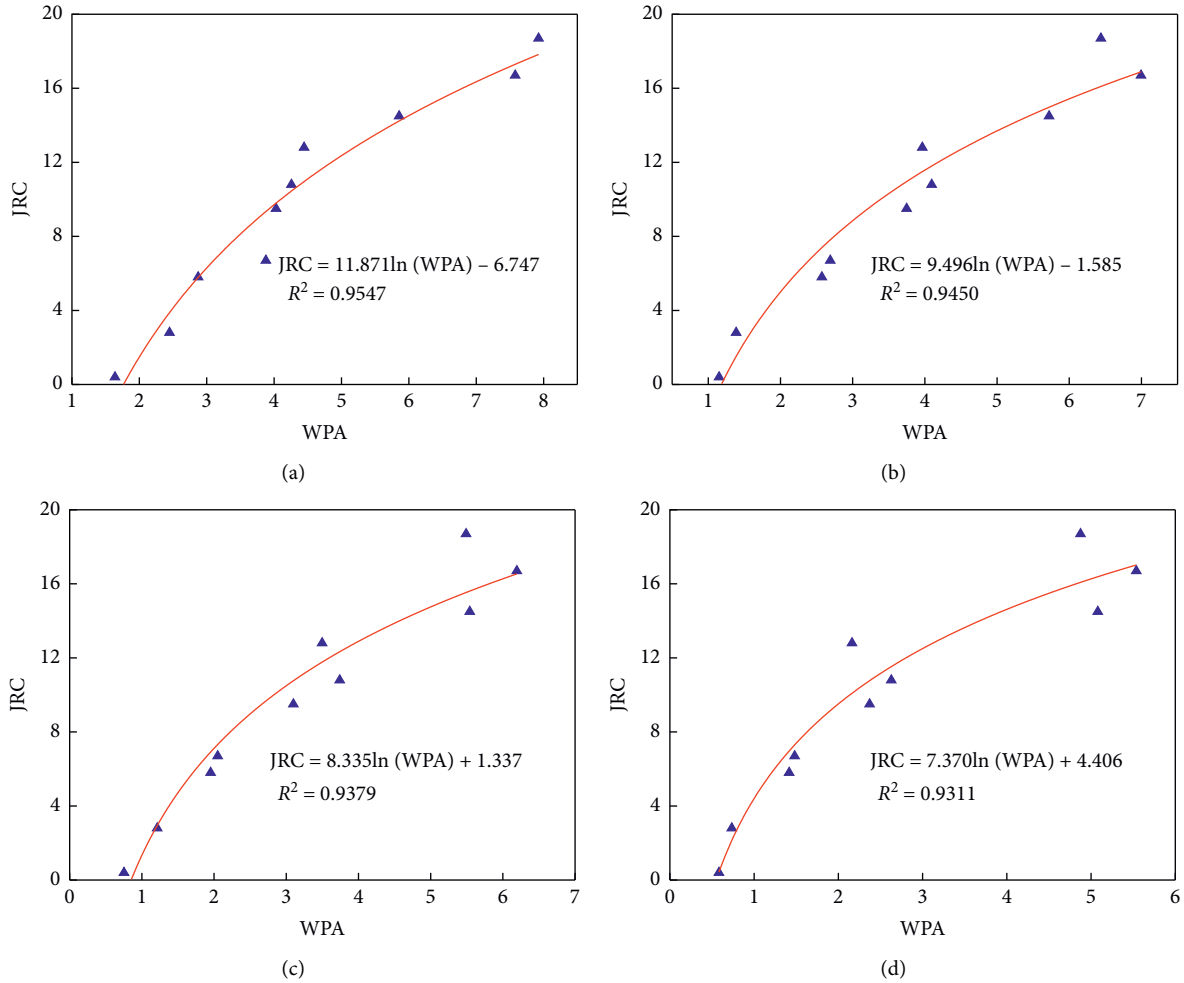


FIGURE 9: The functional relationships between WPA and JRC under different sampling intervals. (a) 1 mm. (b) 2 mm. (c) 4 mm. (d) 10 mm.

TABLE 5: The fitting formulas between WPA and JRC under different sampling intervals.

Sampling interval (mm)	Functional relationship	$R^2$
0.5	$JRC = 14.602 \ln(WPA) - 12.536$	0.9643
1	$JRC = 11.871 \ln(WPA) - 6.747$	0.9547
2	$JRC = 9.496 \ln(WPA) - 1.585$	0.9450
4	$JRC = 8.335 \ln(WPA) + 1.337$	0.9379
10	$JRC = 7.370 \ln(WPA) + 4.406$	0.9311

0.5 mm sampling interval were obtained. Then, the JRC values of these joint profiles in two directions were calculated using the new statistical parameter WPA, as shown in Figure 14.

It could be seen from Figure 14 that the JRC values of the four joint surfaces were different in 24 shear directions. Among them, the JRC of joint surface J-1 was the largest in 45° direction and the minimum in 300° direction. The JRC of

joint surface J-2 was the largest in the 210° direction and the minimum in the 150° direction. The JRC of joint surface J-3 was the largest in 255° direction and the minimum in 300° direction. The JRC of joint surface J-4 was the largest in the 15° direction and the minimum in the 240° direction. The above results showed that the new statistical parameter WPA proposed in this paper can well reflect the anisotropy of the joint surface roughness.

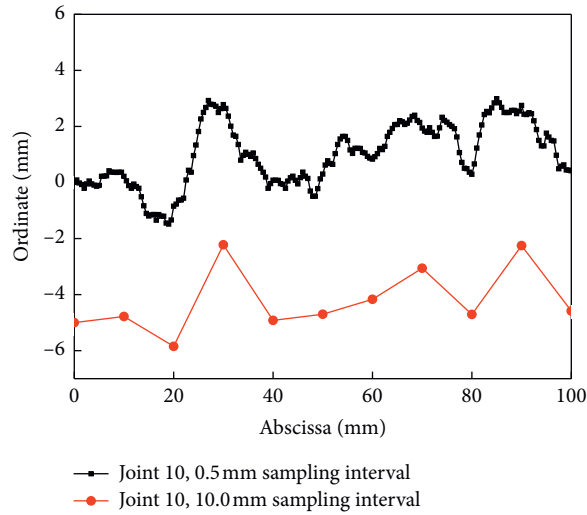


FIGURE 10: Comparison of the 10th joint profile obtained at 0.5 mm and 10 mm sampling intervals.

TABLE 6: The estimated JRC values of each joint profile using WPA.

Reference	No.	Length (mm)	JRC in literature	WPA		JRC	
				Direction 1	Direction 2	Direction 1	Direction 2
Yang [18]	1	50	13.18	5.10	5.37	11.24	12.00
	2	100	13.33	5.10	5.37	11.24	12.00
	3	200	13.46	5.10	5.37	11.24	12.00
Oding [38]	4	100	4–6	3.83	3.31	7.08	4.95
Ozvan et al. [39]	5	100	12	4.81	6.02	10.39	13.68
Zhang et al. [24]	6	50	19.2	14.97	5.40	26.98	12.08
	7	50	17.1	14.92	2.62	26.93	1.53
Yong et al. [40]	8	50	14.6	8.96	2.53	19.48	1.04
	9	100	14–16	4.88	5.01	10.61	11.00
	10	100	18–20	5.82	9.17	13.18	19.81
	11	100	14–16	6.73	3.26	15.30	4.72
	12	100	10–12	5.22	2.67	11.58	1.80
	13	100	6–8	3.21	2.59	4.49	1.36
	14	100	10–12	4.25	2.92	8.59	3.12
	15	100	4–6	3.14	2.99	4.17	3.46
Ye et al. [41]	16	100	2–4	2.76	2.45	2.29	0.55
	17	100	2–4	2.42	2.39	0.37	0.19
	18	170	7.704	3.21	2.87	4.49	2.88
	19	170	8.007	3.25	2.52	4.67	0.96
	20	170	7.955	3.18	2.41	4.37	0.31
	21	170	6.331	4.55	2.53	9.57	1.02

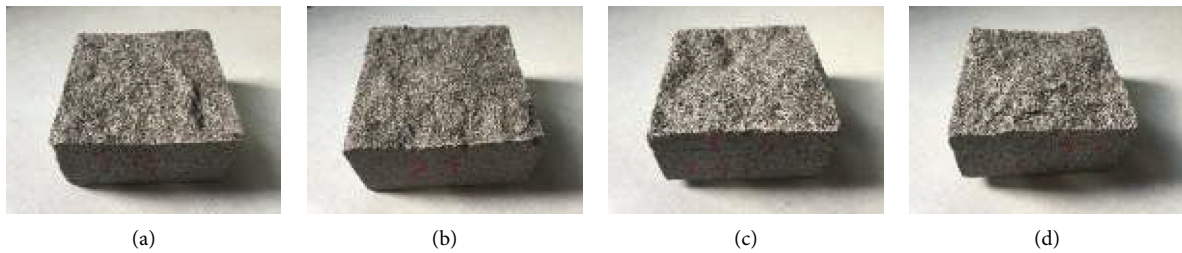


FIGURE 11: The 4 joint specimens used to evaluate roughness. (a) J-1. (b) J-2. (c) J-3. (d) J-4.

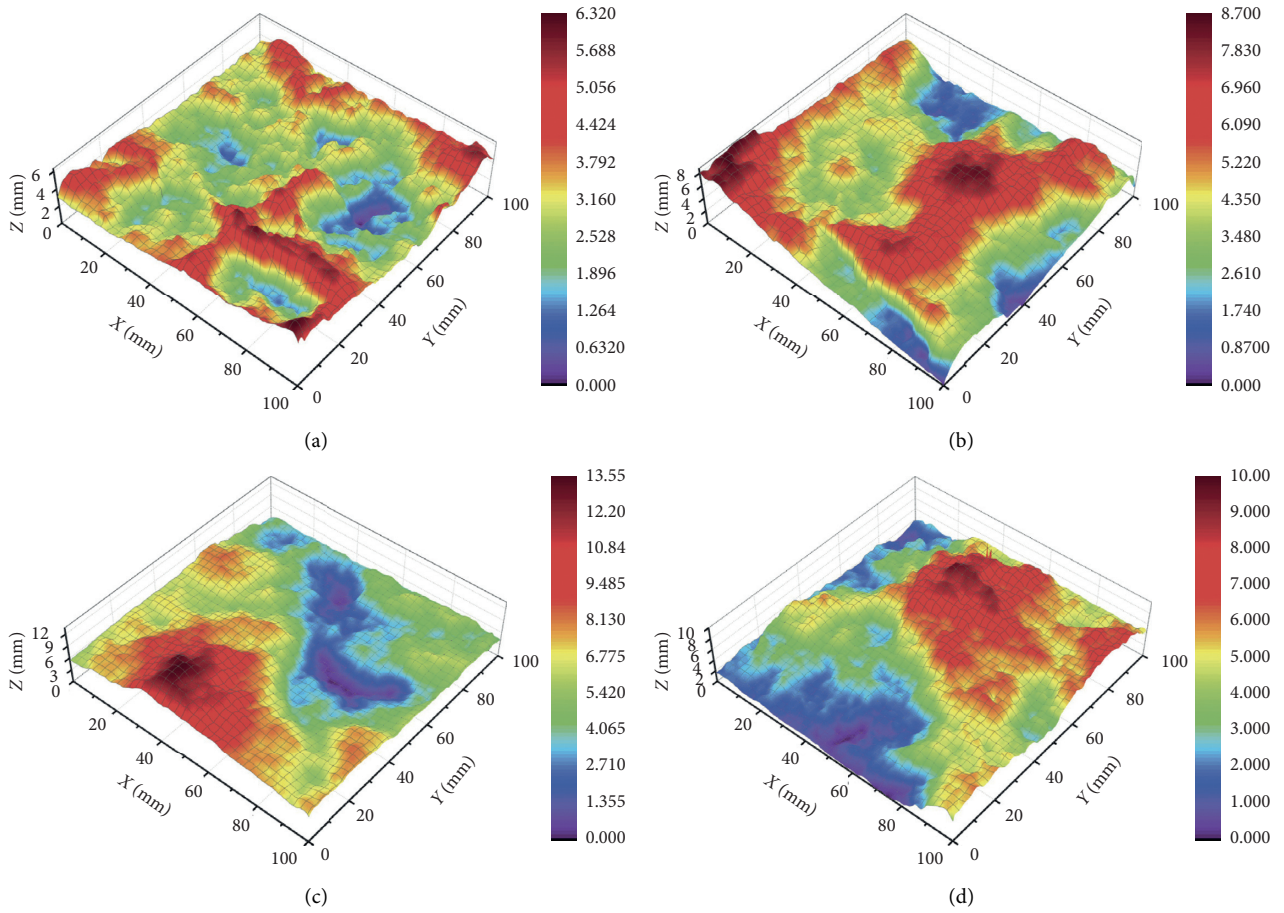


FIGURE 12: Schematic diagrams of 4 joint surface models. (a) Joint J-1. (b) Joint J-2. (c) Joint J-3. (d) Joint J-4.

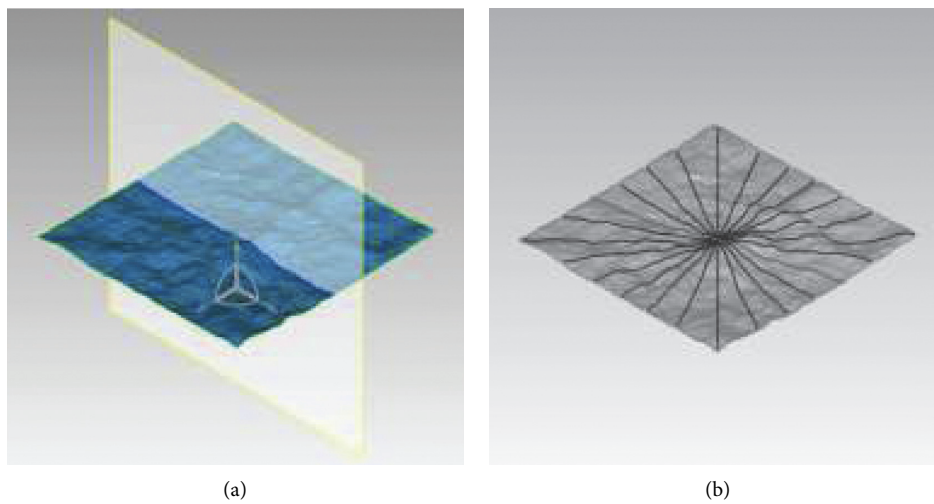


FIGURE 13: The acquisition method of joint profile data. (a) Interception of joint profiles through the system coordinate plane. (b) Location of 12 joint profiles on the joint surface.

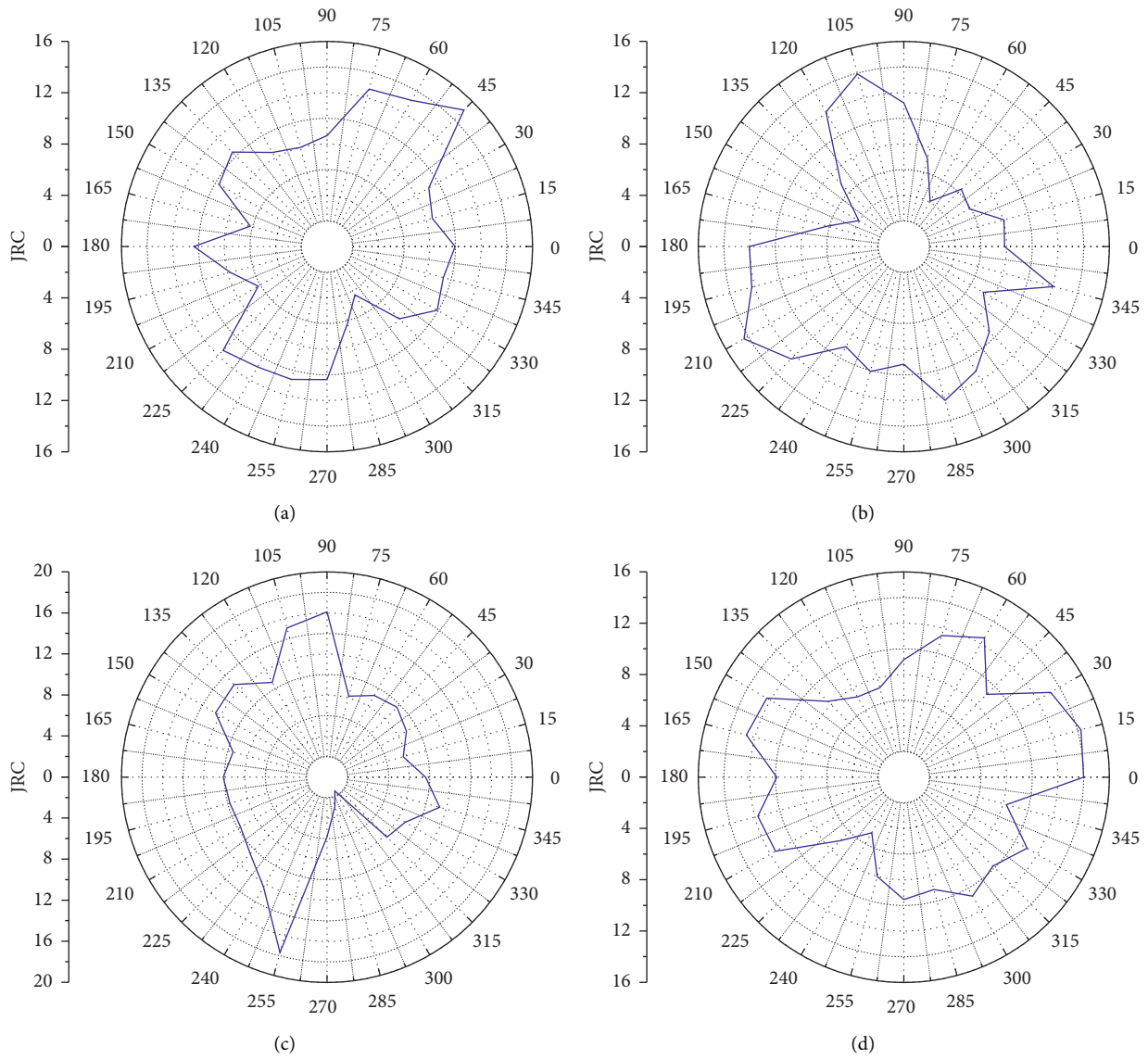


FIGURE 14: The JRC evaluation results of 4 joint surfaces in different directions. (a) Joint J-1. (b) Joint J-2. (c) Joint J-3. (d) Joint J-4.

### 7. Conclusion

In order to predict the shear strength of rock joints, a new statistical parameter WPA was proposed to estimate the joint roughness coefficient (JRC) of the joint profile in this paper. In the definition of WPA, the contribution degrees of different protrusions on joint profile and shear direction were well considered. First, we assumed that the larger the microprotrusion size, the greater the contribution of surface roughness of microjoint segment to the overall roughness of joint profile. Second, only the morphological data oriented to the shear direction were counted and involved in the roughness description. This provided a good response to the shear failure mechanism of the joint surface.

The 10 standard roughness joint profiles proposed by Barton were digitized using data processing software, and the currently widely used statistical parameters  $Z_2$  and  $R_p - 1$  were calculated based on the acquired coordinate data. The

results showed that the correlation between  $Z_2$  and  $R_p - 1$  and JRC was consistent with previous studies, which suggested that the digitization process of the joint profiles in this paper was reliable.

At 0.5 mm sampling intervals, the WPAs of the 10 standard roughness joint profiles in two shear directions were calculated, and their functional relationships with the JRC values were established separately. The results showed that the correlation between WPA and JRC calculated in direction 1 was higher than that in direction 2, and this well reflects the directivity of joint roughness. On this basis, the JRCs of the 10 standard roughness joint profiles in direction 2 were calculated and their size and order are different from those of direction 1.

The sampling interval of joint profile data had been confirmed to have a strong influence on both the WPA value and their correlation with JRC. As the sampling interval increased from 0.5 mm to 10 mm, the WPA values of each

joint profile gradually decreased, and the  $R^2$  of the functional relationship established between WPA and JRC decreased from 0.9643 to 0.9311. In practice, a small sampling interval is recommended; otherwise, the prediction accuracy will be reduced.

The JRCs of 21 joint profiles in the literature were obtained by the new statistical parameter WPA, and their values were significantly different in two directions. Besides, the point cloud data of four natural rock joint surfaces were obtained by 3D scanning technology. The roughness of each joint surface in 24 shear directions was described by JRC of the obtained 12 joint profiles, and it had been proved to be highly anisotropic. It could be confirmed that the new statistical parameter WPA proposed in this paper could well describe the joint roughness considering the shear direction and the contribution of different protrusions.

### Data Availability

The data used to support the findings of this study are included within the article.

### Conflicts of Interest

The authors declare that they have no conflicts of interest.

### Acknowledgments

This study was funded by the National Natural Science Foundation of China (11902249, 51179153, and 11872301), Natural Science Basic Research Program of Shaanxi (2020JM-453), and Scientific Research Program of Shaanxi Provincial Education Department (17JS091 and 2019JQ-395).

### References

- [1] D. D. Pollard and P. Segall, "Theoretical displacements and stresses near fractures in rock: with applications to faults, joints, veins, dikes, and solution surfaces," *Fracture Mechanics of Rock*, vol. 13, no. 8, pp. 277–349, 1987.
- [2] X. Yang, P. H. S. W. Kulatilake, H. Jing, and S. Yang, "Numerical simulation of a jointed rock block mechanical behavior adjacent to an underground excavation and comparison with physical model test results," *Tunnelling and Underground Space Technology*, vol. 50, pp. 129–142, 2015.
- [3] M. M. He, Z. Q. Zhang, J. Ren et al., "Deep convolutional neural network for fast determination of the rock strength parameters using drilling data," *International Journal of Rock Mechanics and Mining Sciences*, vol. 123, 2019.
- [4] M. He, Z. Zhang, J. Zheng, F. Chen, and N. Li, "A new perspective on the constant  $m$  of the hoek-brown failure criterion and a new model for determining the residual strength of rock," *Rock Mechanics and Rock Engineering*, vol. 53, no. 9, pp. 3953–3967, 2020.
- [5] Z. C. Tang, Q. Z. Zhang, and J. Peng, "Effect of thermal treatment on the basic friction angle of rock joint," *Rock Mechanics and Rock Engineering*, vol. 53, no. 4, pp. 1973–1990, 2020.
- [6] E. Hoek, "Strength of jointed rock masses," *Géotechnique*, vol. 33, no. 33, pp. 187–223, 1983.
- [7] F. D. Patton, "Multiple modes of shear failure in rock," in *Proceeding of the Congress of International Society of Rock Mechanics*, pp. 509–513, Lisbon, Portugal, September 1966.
- [8] N. Barton, "Review of a new shear-strength criterion for rock joints," *Engineering Geology*, vol. 7, no. 4, pp. 287–332, 1973.
- [9] N. Barton and V. Choubey, "The shear strength of rock joints in theory and practice," *Rock Mechanics*, vol. 10, no. 1-2, pp. 1–54, 1977.
- [10] N. R. Barton, "Suggested methods for the quantitative description of discontinuities in rock masses," *International Journal of Rock Mechanics & Mining Science & Geomechanics Abstracts*, vol. 15, no. 6, pp. 319–368, 1978.
- [11] A. J. Beer, D. Stead, and J. S. Coggan, "Technical note estimation of the joint roughness coefficient (JRC) by visual comparison," *Rock Mechanics and Rock Engineering*, vol. 35, no. 1, pp. 65–74, 2002.
- [12] S. M. Hsiung, A. Ghosh, M. P. Ahola, and A. H. Chowdhury, "Assessment of conventional methodologies for joint roughness coefficient determination," *International Journal of Rock Mechanics and Mining Sciences & Geomechanics Abstracts*, vol. 30, no. 7, pp. 825–829, 1993.
- [13] N. Barton and S. Bandis, "Effects of block size on the shear behavior of jointed rock," *The 23rd U.S Symposium on Rock Mechanics (USRMS) American Rock Mechanics Association*, pp. 739–760, 1982.
- [14] S. G. Du, Y. Chen, and L. B. Fan, "Mathematical expression of JRC modified straight edge," *Journal of Engineering Geology*, vol. 4, no. 2, 1996, in Chinese.
- [15] N. Turk, M. Greig, W. Dearman, and F. Amin, "Characterization of rock joint surfaces by fractal dimension," in *Proceedings of the U.S.Symposium on Rock Mechanics*, Tucson, Arizona, June 1987.
- [16] Y.-H. Lee, J. R. Carr, D. J. Barr, and C. J. Haas, "The fractal dimension as a measure of the roughness of rock discontinuity profiles," *International Journal of Rock Mechanics and Mining Sciences & Geomechanics Abstracts*, vol. 27, no. 6, pp. 453–464, 1990.
- [17] R. Tse and D. M. Cruden, "Estimating joint roughness coefficients," *International Journal of Rock Mechanics and Mining Sciences & Geomechanics Abstracts*, vol. 16, no. 5, pp. 303–307, 1979.
- [18] Z. Y. Yang, S. C. Lo, and C. C. Di, "Reassessing the joint roughness coefficient (JRC) estimation using Z 2," *Rock Mechanics and Rock Engineering*, vol. 34, no. 3, pp. 243–251, 2001.
- [19] X. Yu and B. Vayssade, "Joint profiles and their roughness parameters," *International Journal of Rock Mechanics and Mining Sciences & Geomechanics Abstracts*, vol. 28, no. 4, pp. 333–336, 1991.
- [20] B. S. A. Tatone and G. Grasselli, "A new 2D discontinuity roughness parameter and its correlation with JRC," *International Journal of Rock Mechanics and Mining Sciences*, vol. 47, no. 8, pp. 1391–1400, 2010.
- [21] H.-S. Jang, S.-S. Kang, and B.-A. Jang, "Determination of joint roughness coefficients using roughness parameters," *Rock Mechanics and Rock Engineering*, vol. 47, no. 6, pp. 2061–2073, 2014.
- [22] B. Zheng and S. Qi, "A new index to describe joint roughness coefficient (JRC) under cyclic shear," *Engineering Geology*, vol. 212, pp. 72–85, 2016.
- [23] N. H. Maerz, J. A. Franklin, and C. P. Bennett, "Joint roughness measurement using shadow profilometry," *International Journal of Rock Mechanics and Mining Sciences & Geomechanics Abstracts*, vol. 27, no. 5, pp. 329–343, 1990.

- [24] G. Zhang, M. Karakus, H. Tang, Y. Ge, and L. Zhang, "A new method estimating the 2D Joint Roughness Coefficient for discontinuity surfaces in rock masses," *International Journal of Rock Mechanics and Mining Sciences*, vol. 72, pp. 191–198, 2014.
- [25] T. Belem, F. Homand-Etienne, and M. Souley, "Quantitative parameters for rock joint surface roughness," *Rock Mechanics and Rock Engineering*, vol. 33, no. 4, pp. 217–242, 2000.
- [26] P. H. S. W. Kulatilake, G. Shou, T. H. Huang, and R. M. Morgan, "New peak shear strength criteria for anisotropic rock joints," *International Journal of Rock Mechanics and Mining Sciences & Geomechanics Abstracts*, vol. 32, no. 7, pp. 673–697, 1995.
- [27] F. Homand, T. Belem, and M. Souley, "Friction and degradation of rock joint surfaces under shear loads," *International Journal for Numerical and Analytical Methods in Geomechanics*, vol. 25, no. 10, pp. 973–999, 2001.
- [28] B. Liu, H. B. Li, and X. M. Zhu, "Experiment simulation study of strength degradation of rock joints under cyclic shear loading," *Chinese Journal of Rock Mechanics & Engineering*, vol. 30, no. 10, pp. 2033–2039, 2011, in Chinese.
- [29] B. Liu, H. B. Li, and Y. Q. Liu, "Experimental study of deformation behavior of rock joints under cyclic shear loading," *Rock and Soil Mechanics*, vol. 34, no. 9, pp. 2475–2481, 2013, in Chinese.
- [30] B. Li, Y. Jiang, T. Mizokami, K. Ikusada, and Y. Mitani, "Anisotropic shear behavior of closely jointed rock masses," *International Journal of Rock Mechanics and Mining Sciences*, vol. 71, pp. 258–271, 2014.
- [31] Z.-c. Tang, Q.-s. Liu, and J.-h. Huang, "New criterion for rock joints based on three-dimensional roughness parameters," *Journal of Central South University*, vol. 21, no. 12, pp. 4653–4659, 2014.
- [32] Z.-C. Tang, Q.-S. Liu, C.-C. Xia, Y.-L. Song, J.-H. Huang, and C.-B. Wang, "Mechanical model for predicting closure behavior of rock joints under normal stress," *Rock Mechanics and Rock Engineering*, vol. 47, no. 6, pp. 2287–2298, 2014.
- [33] J.-W. Park and J.-J. Song, "Numerical simulation of a direct shear test on a rock joint using a bonded-particle model," *International Journal of Rock Mechanics and Mining Sciences*, vol. 46, no. 8, pp. 1315–1328, 2009.
- [34] J.-W. Park and J.-J. Song, "Numerical method for the determination of contact areas of a rock joint under normal and shear loads," *International Journal of Rock Mechanics and Mining Sciences*, vol. 58, pp. 8–22, 2013.
- [35] R. Kumar and A. K. Verma, "Anisotropic shear behavior of rock joint replicas," *International Journal of Rock Mechanics and Mining Sciences*, vol. 90, pp. 62–73, 2016.
- [36] Y. C. Li, W. Wu, and B. Li, "An analytical model for two-order asperity degradation of rock joints under constant normal stiffness conditions," *Rock Mechanics and Rock Engineering*, vol. 1, pp. 1–15, 2018.
- [37] Y. C. Li, Z. Z. Liang, C. A. Tang, D. Q. Li, and C. Z. Wu, "Analytical modelling of the shear behaviour of rock joints with progressive degradation of two-order roughness," *International Journal for Numerical and Analytical Methods in Geomechanics*, vol. 43, no. 3, 2019.
- [38] N. E. Odling, "Natural fracture profiles, fractal dimension and joint roughness coefficients," *Rock Mechanics and Rock Engineering*, vol. 27, no. 3, pp. 135–153, 1994.
- [39] A. Özvan, İ. Dinçer, A. Acar, and B. Özvan, "The effects of discontinuity surface roughness on the shear strength of weathered granite joints," *Bulletin of Engineering Geology and the Environment*, vol. 73, no. 3, pp. 801–813, 2014.
- [40] R. Yong, J. Ye, Q. F. Liang, M. Huang, and S. G. Du, "Estimation of the joint roughness coefficient (JRC) of rock joints by vector similarity measures," *Bulletin of Engineering Geology & the Environment*, vol. 77, no. 2, pp. 1–15, 2017.
- [41] J. Ye, R. Yong, Q.-F. Liang, M. Huang, and S.-G. Du, "Neutrosophic functions of the joint roughness coefficient and the shear strength: a case study from the pyroclastic rock mass in shaoxing city, China," *Mathematical Problems in Engineering*, vol. 2016, pp. 1–9, 2016.



## Research Article

# Shear Characteristics and Strength Criterion of Frozen Joints under Different Opening Degrees

Shiwei Shen <sup>1</sup>, Lin Gan,<sup>1</sup> Chang Liu ,<sup>1,2</sup> and Shulin Dai<sup>1</sup>

<sup>1</sup>College of Construction Engineering, Jilin University, Changchun, Jilin 130026, China

<sup>2</sup>College of Art and Design, Jilin Jianzhu University, Changchun, Jilin 130118, China

Correspondence should be addressed to Chang Liu; [liuchang@jlju.edu.cn](mailto:liuchang@jlju.edu.cn)

Received 13 November 2020; Revised 8 December 2020; Accepted 28 December 2020; Published 30 January 2021

Academic Editor: Zhi Cheng Tang

Copyright © 2021 Shiwei Shen et al. This is an open access article distributed under the Creative Commons Attribution License, which permits unrestricted use, distribution, and reproduction in any medium, provided the original work is properly cited.

Samples of rock coupling joints were collected from the Jiangluling Tunnel of the G214 line in Qinghai province. Models with surface topographies similar to these joints were manually created. Freezing shear tests under different normal stress conditions were conducted to study the shear mechanical properties of these models. On this basis, the integral form of the peak shear strength criterion of frozen joints was proposed. Results show that the shear process of the ice layer can be divided into four stages, namely, initial deformation, continuously increasing shear stress, ice shearing, and residual shear. During the continuously increasing shear stress stage, the stress-strain curve is concave, and elastic deformation is not evident. Furthermore, the increase rate of shear stress generally rises as normal stress intensifies. In the ice shearing stage, shear stress does not decrease instantaneously, but plastic deformation is now detectable. When the opening degree is greater than the undulation difference of the joint surface under the action of all levels of normal stress, the shear stress in the ice sharply increases and drops due to local failure and reicing. Then, evident difference between the shear processes under freezing and normal temperature conditions was then obtained. On this basis, the failure forms of joint surfaces, theory of ice adhesion strength under different opening degrees and morphologies, and the shear failure forms of frozen joints under different conditions were considered. The integral form of the peak shear strength criterion of frozen joints was proposed. These results can lay a theoretical foundation for the stability analysis of rock mass engineering in permafrost areas.

## 1. Introduction

China is the third largest permafrost area globally, accounting for about 70% of the total land area. Rock mass engineering in permafrost areas is bound to encounter rock mass freezing. The structural plane of rock mass is the weakest part, and it plays a decisive role in the stability of rock mass engineering. The shear mechanical characteristics of joints are the main influencing factor in the stability of the rock slope and foundation engineering. Therefore, the same influencing factor is crucial in the stability of the rock slope and foundation engineering in permafrost areas. Shear strength controls the sliding failure of joints. Therefore, research on shear mechanical characteristics and strength criteria of frozen joints has important theoretical and practical significance for the stability of rock mass engineering in permafrost areas.

Over the past 40 years, scholars made important progress in this field. Barton [1] concluded that, under low normal stress condition (less than 40% of rock ultimate compressive strength), morphology is the main controlling factor of joint peak shear strength. On this basis, Grasselli [2] proposed that the peak shear strength of joints can be explained reasonably by using the 3D morphological parameters of joints. In addition, the contact state of joints is also an important factor affecting the peak shear strength of joints. In addition, various shear tests were performed on natural rock [3, 4] and cement mortar [5, 6]; these tests revealed the variation of shear displacement, shear strength criterion, and dilatancy angle of joint surfaces under different 3D morphologies and acceptance conditions.

In the research of shear mechanical characteristics of frozen rock and soil, Yulin et al. [7], Jing et al. [8], and

Anping et al. [9] took different properties of the soil as research objects and designed different test conditions to study the shear mechanical characteristics of frozen rock and soil under freezing and freeze-thaw cycles. Shunying et al. [10] took the sea ice of the Bohai Sea as the research object and conducted side-limited unilateral shear test under different loading speed, salinity, and temperature conditions; they analyzed the effects of these factors on the shear strength of the sea ice using experimental data and determined the functional relationships among brine volume, lateral stress, and shear strength. Qing et al. [11], Bo et al. [12], and Hongwei et al. [13] selected ice samples of different properties, analyzed the samples' internal structure, and conducted shear tests at different test temperatures and strain rates; they obtained the variation of shear strength with different strain rates and temperatures and the relationship between bubble content and shear strength.

In a study of the mechanical characteristics of rock joints under low temperature or freeze-thaw cycles, Tharp [14] analyzed the frost heave of cracks and reported the width-depth ratio of cracks; moreover, the shape of the crack tip had greater influence on the frost heave of cracks than the mechanical characteristics of rocks on both sides. Friederike [15] established the correlation between normal and shear strains of the concrete rough joint surface as well as ice body and concrete interface by shear test after freezing the artificial joint. Davies et al. [16] used centrifugal model test to test the temperature rise of the rock slope structural plane under freezing conditions and obtained the displacement field in the slope body; on this basis, they analyzed the stability of the slope. Davies et al. [17] conducted shear strength test on the rough interface between ice and concrete and established the relationship among normal strain, shear strain, and shear stress. Martin and Rivard [18] studied the strength deterioration of concrete under freeze-thaw cycles via shear test by taking joints of a dam body as the research object. In China, Quansheng et al. [19] analyzed the influence of the angle between the frozen front and the fissure surface on the fissure frost heave. Caichu et al. [20] reported three kinds of situations in the fissures, namely, in situ frost heaving of fractured water, fracture water discharge (no frost heaving), and frost heaving of crack ice growth caused by water and heat transfer. However, the mechanical characteristics of rock joints under freezing conditions have not yet been investigated locally and abroad.

Previous studies on the mechanics of frozen joints primarily consider the frost heave characteristics of joints, and most research objects are artificial joints or the shear strength of the interface between ice and concrete. However, the peak shear strength criterion of natural rock joints, especially frozen joints, still requires further research. In the current study, freezing shear tests of rock coupling joints (upper and lower joints fully coincide) in the Jiangluling Tunnel of the G214 line in Qinghai province are conducted to reveal the mechanical characteristics of freezing shear of joints under different normal stress conditions and the difference between the mechanical characteristics of freezing shear of joints and of conventional joints. On this basis, the integral form of the peak shear strength criterion of freezing

joints under different conditions is derived. The research results can provide theoretical basis for stability analysis of rock mass engineering in permafrost areas.

## 2. Specimen Preparation and Test Method

The shear tests of rock joints belong to destructive test. The failure of the original joint surface morphology is inevitable when applying shear stress. Thus, the original rock joints cannot be repeatedly used for another test. To ensure the consistency of the initial state of joint specimens in the same group, artificial specimens should be prepared on the basis of the original rock joints.

*2.1. Preparation of Artificial Joint Specimens.* On the basis of previous studies on the effect of structural plane size on shear strength, the difficulty of sampling and the direction of shearing are considered at the same time. Therefore, a rectangular structural surface with a size of  $200 \times 100 \times 100$  mm is selected. The original rock joint surface of the specimens is selected, and the upper and lower plates of each group of joints are numbered. After surface cleaning treatment, the lower plates of each group of joints are initially placed in a standard mold with the same size as the shear box (length  $\times$  width  $\times$  height =  $200$  mm  $\times$   $100$  mm  $\times$   $100$  mm). The inner parts of the mold are filled with cement mortar. In this manner, the joint surface is slightly higher than the mortar plane. After spraying vegetable oil on the surface of the specimen, the isolation film is set up. To bring them close together, the bubbles between the isolation film and the joint surface are removed.

In order to ensure the similarity between artificial joints and natural rock joints in terms of strength, the artificial joints are prepared using reverse control technology. The specific preparation process and parameters are as follows. The processed inner contour has the same shape as the original rock joint's outer contour. The outer contour has the same size as the shear box. The upper and lower parallel wooden modules are set on the original rock joint surface to form the area of artificial joints poured on the upper wall. In accordance with the design proportion, the raw materials of mortar are weighed and stirred evenly, and the mixture is poured into the mold. Ordinary Portland cement (42.5 R), standard sand, and water are selected. The mass ratio of water : cement : sand is 1 : 2 : 3. Silica powder (10% 920 U) and superplasticizer (2% FDN-F 2) are added at the same time. To ensure that the artificial material is closely connected with the joint surface, plate vibrator and vibrating rod are used to vibrate evenly, and the bottom isolation film is not folded. After pouring, the upper surface is smoothed, leveling it with the mold. After the specimen is maintained in water, the whole mold is turned over, and the isolation film is removed after removing the mold. The artificial joint surface of the upper plate, which is completely consistent with the lower plate of the original rock joint surface, is created [16, 17].

The man-made joint surface of the upper plate is then placed in the standard mold by repeating the above steps. At the same time, the man-made joint surface of the lower plate,

which is completely consistent with the previous surface, is prepared. The artificial joint specimens with the same composition and roughness are prepared by repeating the above steps.

**2.2. 3D Scanning of the Joint Surface.** TJXW-3D portable rock surface 3D topography instrument is used to scan 3D joints. The equipment photos are shown in Figure 1. The 3D morphology of each group of joints is shown in Figure 2.

The profiler uses an active triangulation method that combines stereo vision and binocular imaging methods. The measurement principle is through a digital grating projection device; a series of continuous grating stripes of different widths are projected on the surface of the object, which are affected by the surface shape to form deformed stripes, which are captured and recorded by the left and right cameras, and then calculated and compared by the left and right cameras. The results are matched to obtain the three-dimensional coordinates of the points on the measured surface, and then the surface topography parameter calculation formula is used to obtain the topography parameters of the object surface.

As shown in Figure 2, the maximum height difference (fluctuation difference) of the four groups of joints is about 10 mm, and the overall fluctuation difference is equal. However, the convexity and concavity of each group of joints are different. When subjected to horizontal shear, the convex part of the joint surface will prevent the production of horizontal displacement, which is the main part of its shear strength. In addition, when the joint surface is frozen with water, the part of the back shear direction is separated during the shear process, and the bond between the ice layer and the joint surface is also a component of shear strength.

**2.3. Specimen Freezing.** In this test, the rock coupling (complete occlusion of the upper and lower joints) joints of the Jiangluling Tunnel on the G214 line in Qinghai province are selected, and the joints are poured following the process described in the previous section. After 28 days of maintenance under standard conditions (temperature 20°C and relative humidity 90%), the joints are frozen.

According to relevant regulations, the freezing time of the rock freeze-thaw cycle test is not less than 4 hours. However, because of the large joint area, the ice layer will be completely frozen after 12 hours during the test. At the same time, according to the on-site temperature survey of the Jiangluling Tunnel, the lowest temperature in this place is about -35°C. To ensure that the test environment is close to the site, the freezing temperature is chosen to be set at -35°C. In accordance with the test design plan, the upper and lower joint surfaces are reserved for a certain amount of opening and placed in the finishing box. Except for the joint area, the remaining void parts are filled with the high-density EPS foam gasket. Water in the finishing box is placed in a low-temperature control box and then frozen at 12–35 h. The schematic of freezing is shown in Figure 3. The photos before and after freezing are shown in Figure 4. After freezing, the area where the joint surface is located (the white area on the

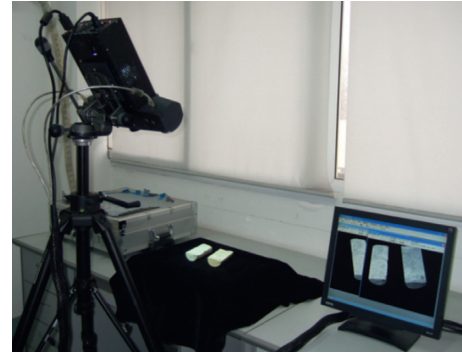


FIGURE 1: 3D scanner of the rock joint morphology.

right of Figure 3) is filled with ice. Its range is a rectangle surrounded by the maximum distance between the joint surface in the transverse and longitudinal directions.

**2.4. Method and Process of Direct Shear Test.** The shear test adopts the shear test machine of rock joints from the Key Laboratory of the Ministry of Geotechnical and Underground Engineering of Tongji University. The machine is composed of horizontal loading, vertical loading, and servo control systems. The photo of the test machine is shown in Figure 5.

In this study, the relative opening of the joint surface is the difference between the highest and lowest joint opening/joint surface height. The height difference of each joint surface is between 10 and 10.5 mm. Hence, the opening of frozen joints is designed to be 7, 10, and 13 mm (i.e., the relative opening is 0.7, 1.0, and 1.3, respectively) to highlight the effect of joint fluctuation on its shear properties. The same rock joint surface is used for testing to ensure the consistency of joint surface roughness and fluctuation in the same group of shear tests. Prior to the shear test, the joint is reserved for design opening and placed in a low-temperature control box to be frozen with water. To obtain the freezing shear characteristics of joints under different normal stresses and avoid the failure of ice under normal pressure, the shear tests of joints under normal stresses of 0.5, 1.0, 1.5, and 2.0 MPa are performed. The strength of the mortar prepared by the mixture ratio in the article can reach M7.5, and the maximum value of the normal stress applied in the test is only 2.0 MPa, which can completely ensure that the mortar has no damage during the experiment. Normal stress is applied to the design value in accordance with the load control mode, and the shear load is then applied in accordance with the deformation control mode.

During the test, a displacement sensor is installed at the four corners of the specimens, and the normal stress loading rate is set as 2 mm/min. The normal displacement and corresponding normal stress of the specimens during the loading process are read in real time. After adding the design load, the normal displacement sensor data are read every 5 min. The normal load is considered stable when the difference between two adjacent normal displacements is less than 0.01 mm. When the normal stress loading stabilizes, horizontal load is applied to the specimens, and shear tests

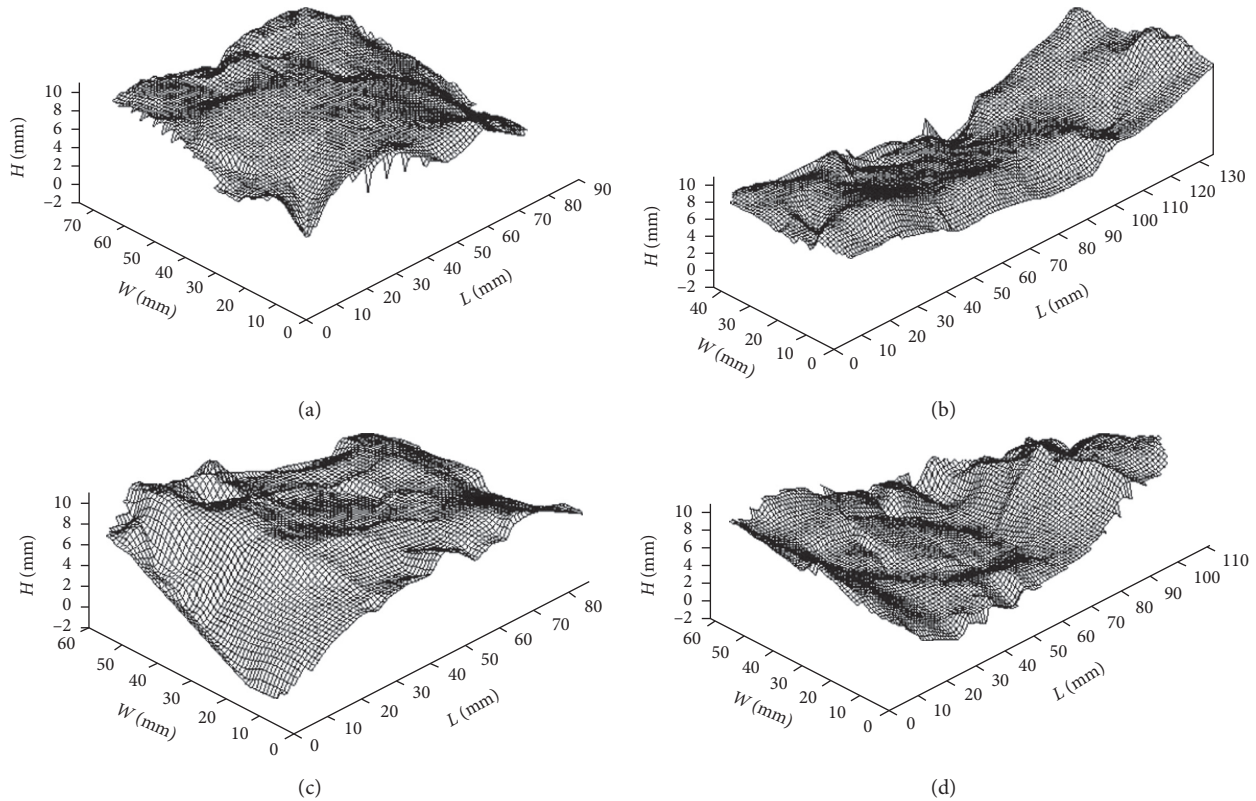


FIGURE 2: 3D topography of joint surfaces in each group. (a) Specimen 1. (b) Specimen 2. (c) Specimen 3. (d) Specimen 4.

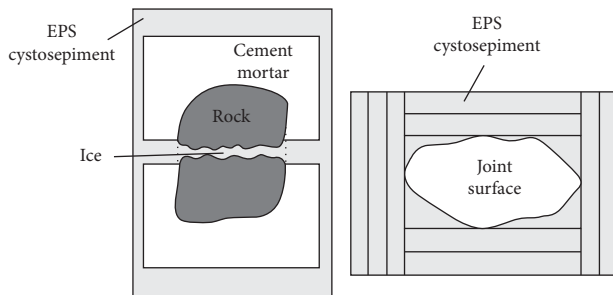


FIGURE 3: Schematic of freezing.

are conducted at a loading rate of 2 mm/min. Four horizontal displacement sensors are installed in the shear direction to read the shear displacement in the shear process in real time. The shear stress values of the specimens in the shear process under various test conditions are read by the shear stress sensors. Figure 6 shows the sensor installation photo.

### 3. Analysis of Test Results

To study the influence of different normal stresses on the shear characteristics of frozen joints, four groups of joints are subjected to 0.5, 1.0, 1.5, and 2.0 MPa normal stresses.

#### 3.1. Analysis of Freezing Shear Behavior of Joints with 7 mm Opening Degree.

The shear stress-shear displacement curves

of each group of specimens at 7 mm opening degree are shown in Figure 7.

As shown in Figure 7, the shear stress-shear displacement curve of frozen joints can be divided into the following four stages when the joint opening degree is 7 mm: (1) initial deformation stage: at this stage, the shear stress increases instantaneously (usually, 0.5–1.0 MPa). Also, no evident shear displacement occurs in the ice layer (usually, the shear displacement is less than 1 mm). However, as shown in Figures 7(c) and 7(d) schematics, a small abrupt change in shear stress occurs because water forms bubbles and voids in ice crystals during the freezing process, which are compacted under horizontal loads. At the same time, ice crystals around bubbles produce local rupture phenomenon, which leads to changes in shear stress. (2) Continuously increasing shear stress stage: continuous shear displacement occurs, and shear stress increases at this stage. The shear stress-shear displacement curve shows a concave form. Afterwards, ice shows a quasi-elastic property. With the increase in normal stress, the increase rate of shear stress increases gradually. (3) Ice shearing stage: when shear stress reaches the ultimate strength of ice, the shear stress-shear displacement curve begins to show a distinct convex form, and the ice begins plastic deformation. After the ultimate shear stress, the shear stress begins to decrease. (4) Residual shear stage: when the shear displacement reaches 15–20 mm, shear stress decreases with the increase in the shear displacement. However, the shear stress does not show the catastrophic property because the ice layer does not lose its strength completely.



FIGURE 4: Photographs of the specimen before and after freezing.

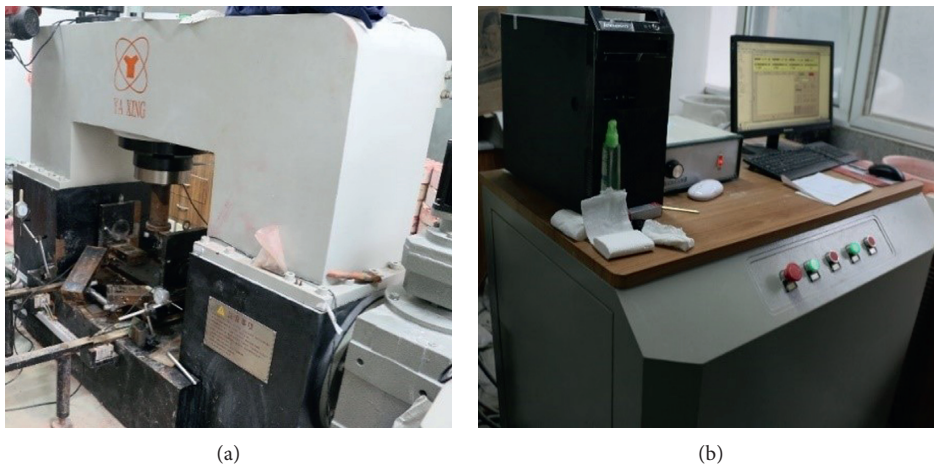


FIGURE 5: Shear test equipment. (a) Main engine. (b) Operator.



FIGURE 6: Displacement sensor installation photo.

Combined with the above phenomena, when the joint opening degree is less than the fluctuation of the rock joint surface (relative opening degree is less than 1), under normal stress, the ice will first produce 1–2 mm compressive deformation, which further reduces the relative opening degree. Therefore, the horizontal displacement of the ice layer is mainly caused by the slope-climbing effect along the rock joint surface. Producing brittle fracture is difficult. During ice layer shear-climbing, the protruding part of the original rock joint surface is closely occluded. Hence, the shear stress

resistance ability is strong. The shear failure of the ice layer occurs at this time, which is similar to creep failure. No evident shear fracture surface exists in the ice layer, but a flexible failure occurs when the bond strength between the ice layer and rock joints decreases gradually with the increase in shear displacement. After the shear test, the ice layer and the rock joint surface are not separated. However, the increase in shear displacement causes an evident dislocation phenomenon, and a certain bond strength between them is formed.

*3.2. Analysis of Freezing Shear Behavior of Joints with 10 mm Opening Degree.* The shear stress-shear displacement curves of each group of specimens at 10 mm opening degree are shown in Figure 8.

As shown in Figure 8, when the opening degree is 10 mm, the shear stress-shear displacement curve of frozen joints is generally similar to that of 7 mm opening degree. This curve can be divided into four stages: (1) initial deformation stage: the shear stress increases sharply in the initial stage of shear action because of the strength of the ice layer itself and the bonding effect between the ice layer and the rock joint interface. This phenomenon is shown by the instantaneous increase in the shear stress when the

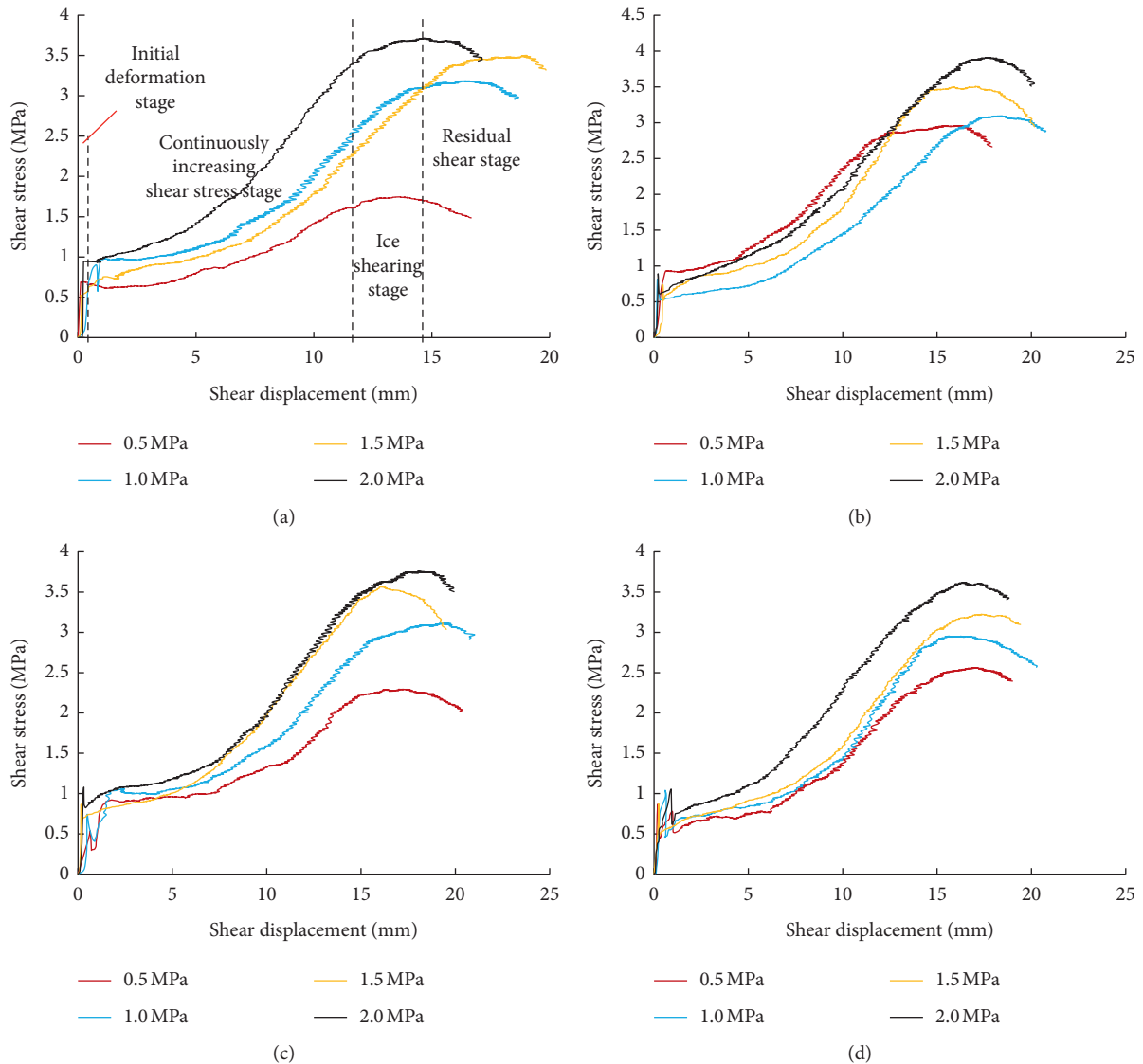


FIGURE 7: Shear stress-shear displacement curves of different normal stress joints with 7 mm opening degree. (a) Specimen 1#. (b) Specimen 2#. (c) Specimen 3#. (d) Specimen 4#.

horizontal displacement of the shear plane is less than 1 mm (about 0.5–1 MPa). (2) Continuously increasing shear stress stage: at this stage, the characteristics of the shear stress-shear displacement curve are similar to those of 7 mm openness. Generally, this curve shows concave characteristics. The rate of increase in shear stress rises as normal stress intensifies. However, the difference between the two is that the shear stress of the three specimens rapidly increases and drops at this stage. This difference is reflected under normal stress at all levels. The reason for this difference is the certain thickness of the ice layer at this time (when normal stress is applied, the ice will produce normal displacement, and its relative opening degree will decrease to 0.8–0.9). Therefore, during the shear process, no contact is made between rock joint planes, and the ice layer has certain brittle and destructive properties. When the ice layer is subjected to normal stress, the local failure occurs during shear, and the

shear stress increases and decreases sharply. At the same time, secondary compaction and cohesive force increase after ice breaking under normal stress. Moreover, the heat generated during the shear process makes the ice melt locally, and the ice melt rapidly contacts with the unmelted ice, resulting in reicing. Therefore, the increasing trend of shear stress is the same as that before the sharp increase in shear stress. (3) Ice shearing stage: when the shear displacement increases to about 15 mm, the ice begins to produce plastic deformation, and the shear stress-shear displacement curve is transformed into a distinct concave feature. However, due to the slow loading rate of shear stress (2 mm/min), brittle shear failure does not occur in the ice layer. (4) Residual shear stage: when the ice layer is sheared, the shear stress decreases gradually, but the shear stress does not show steep drop due to the cementation between the ice layer and the rock joints. However, from the residual shear stage curve

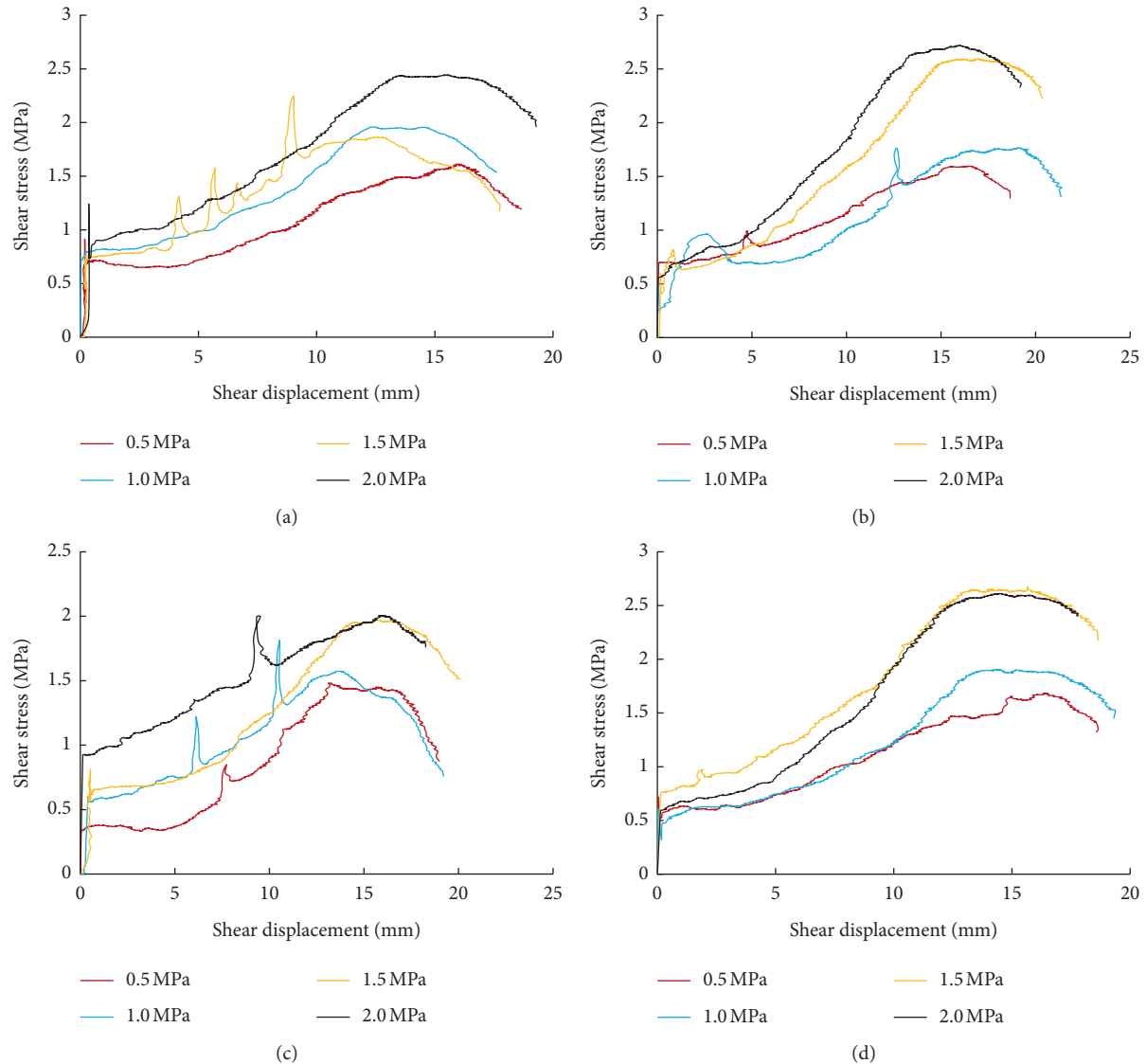


FIGURE 8: Shear stress-shear displacement curves of different normal stress joints with 10 mm opening degree. (a) Specimen 1#. (b) Specimen 2#. (c) Specimen 3#. (d) Specimen 4#.

analysis under different normal stress conditions, the shear stress reduction rate increases with the increase in normal stress.

In accordance with the shear test results under the condition of 10 mm opening degree (relative opening: 1.0), the ice initially produces a certain normal displacement under various normal stresses. Therefore, the relative opening degree of the ice is 0.8–0.9 in the shear process. Under this condition, except for areas with a large fluctuation of rock joint surfaces, joint surfaces do not collide with one another. At this time, the ice layer behaves between “pure shear-climbing.” In comparison with the condition with 7 mm opening degree, the climbing effect is evidently weakened, and the ability of resisting shear stress is reduced. Therefore, when the opening degree is 10 mm, the increasing speed of shear stress in the continuously increasing shear stress stage is less than that of the 7 mm opening degree, and

the peak shear stress is smaller than that of the 7 mm opening degree under similar conditions.

**3.3. Analysis of Freezing Shear Behavior of Joints with 13 mm Opening Degree.** The shear stress-shear displacement curves of each group of specimens under the condition of 13 mm opening degree are shown in Figure 9.

As shown in Figure 9, the shear stress-shear displacement relationship curve under the condition of an opening degree of 13 mm is evidently different from that under opening degrees 7 and 10 mm. The absolute value of normal displacement has no significant change (still 1–2 mm) compared with the opening degree conditions of 7 and 10 mm under various normal stresses. However, the relative opening degree is greater than 1. Therefore, during the shear process, the characteristics of each stage are as follows: (1)

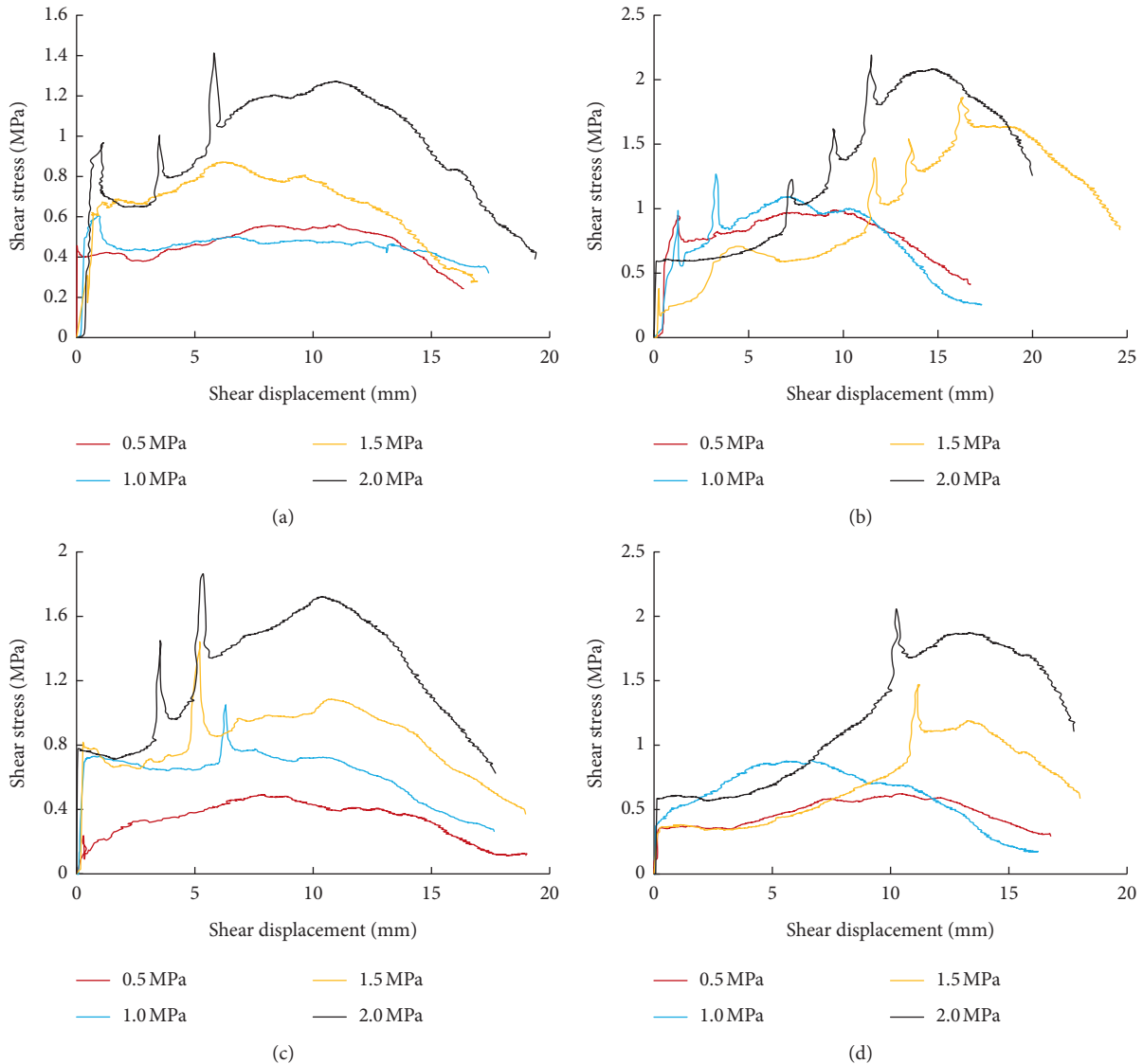


FIGURE 9: Shear stress-shear displacement curves of different normal stress joints with an opening degree of 13 mm. (a) Specimen 1#. (b) Specimen 2#. (c) Specimen 3#. (d) Specimen 4#.

initial deformation stage: the increase in shear stress in this stage is only 0.4–0.8 MPa. Thus, for the case of relative opening degree greater than 1, the compression effect of normal stress on the ice layer is not evident, and shear displacement can be produced under small shear stress. (2) Continuously increasing shear stress stage: the shear stress rapidly increases and drops at almost all levels of normal stress, and the increase is more evident than that under the condition of 10 mm. When the relative opening degree is greater than 1, bubbles and voids in the ice layer are not fully compacted, and local damage easily occurs at this stage, thereby resulting in a sudden increase in shear stress. At the same time, the ice melts locally by absorbing shear friction heat and soon contacts with the surrounding ice body, thereby prompting reicing and restoring the strength of the ice. As the ice thickness increases, bubbles and voids, as well as local damage, increase. In other words, the greater the normal stress, the more evident the characteristics. When

normal stress is large (i.e., 1.5 and 2.0 MPa), the shear stress increases sharply more than the maximum value of the subsequent increase. (3) Ice shear stage: the difference between this stage and the previous stage is significant, and the relative opening degree is greater than 1. When the normal stress is small (i.e., 0.5 and 1.0 MPa), the failure mode of the ice layer is similar to that of the case where the relative opening degree is less than 1. Plastic deformation occurs in the ice layer, and this phenomenon increases the ultimate shear stress slowly. When the normal stress is large (i.e., 1.5 and 2.0 MPa), the shear stress increases sharply at a small shear displacement (5–10 mm). It then returns to normal rapidly and continues to increase. Meanwhile, the shear stress increases sharply than the subsequent maximum shear stress. When the relative opening degree is greater than 1 and the bubbles and voids in the ice layer are not fully compacted, the local cracks penetrate during the shear process, thereby forming a failure surface that causes a



sudden increase in shear stress. The reicing caused by the contact of melted water formed by shear friction exothermic with the surrounding ice body restores its strength to a certain extent. However, in the subsequent shear process, the extreme shear stress of the recondensed ice layer is less than the previous steep increase stress due to the lower strength of the recondensed ice layer. (4) Residual shear stage: at this stage, the characteristics of the shear stress-shear displacement curve with relative opening degree greater than 1 are evidently different from those of other cases. The shear stress reduction rate increases evidently with the increase in normal stress, and the residual strength of the ice layer tends to be constant, which is similar to the residual strength of pure ice.

In accordance with the comprehensive analysis of the 13 mm open degree test, when the relative opening degree is greater than 1, bubbles and voids will be compressed under the normal stress at first, and slight damage will occur inside the ice crystal at the same time. These phenomena result in the reduction of ultimate shear strength under the normal stress at all levels due to the large thickness of the ice layer. During the shear process, the ice shows multiple local failure phenomena when the shear stress is applied and the normal stress is large (i.e., 1.5 and 2.0 MPa). These phenomena result in the sudden increase and decrease in the shear stress, accompanied by evident brittle failure phenomena. At the same time, the ultimate shear stress is due to the penetration of the ice fracture surface when the shear displacement is small. By contrast, when the opening degree is 13 mm, the thickness of the ice layer after normal stress is still greater than the maximum fluctuation difference of the joint surface. Therefore, during the shear process, the joint surfaces of the rock upper and lower plates do not contact. The ice layer is always in pure shear process, and no climbing and gnawing occur. At this time, the failure process cuts along the weakest surface. Previous studies have shown that the bond strength at the ice-rock interface is much less than the shear strength of the ice itself. Hence, the shear stress growth rate and peak shear stress value at the opening degree of 13 mm are significantly lower than those at the opening degrees of 7 and 10 mm.

#### 4. Peak Shear Strength Criterion of Frozen Joints

On the basis of the analysis in the preceding section, the shear behavior of frozen joints is evidently different from that of conventional joints. Therefore, the shear strength criterion of conventional coupled joints is inapplicable to frozen joints. When the joint surface is frozen and filled with water, its peak shear strength is affected by the shear strength of the ice itself and the bond strength between the ice and the joint surface. Following this theory, the criterion of peak shear strength of frozen joints is established.

The coordinate system of the rock joint surface topography is established. The length direction of the joint surface is the Y-axis, the width direction is the X-axis, and the height direction is the Z-axis, as shown in Figure 10.

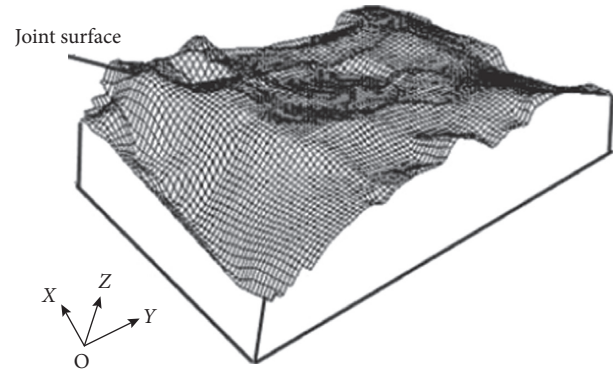


FIGURE 10: Schematic of the rock joint surface topography.

The joint surface is divided into several microelements. When it is sheared in the direction of the XOY plane, the microelements can be divided into two parts. If the angle between normal direction and shear direction is greater than 90 degrees, then the microelement body faces shear direction. It can also be regarded as an upward shear microelement body in the shear process. In the shear process on the joint surface, such microelements are characterized by the climbing effect. Wear or shear may occur in the process of ice shear displacement, which is the main aspect of resisting shear stress. If the angle between normal direction and shear direction in vitro is less than 90 degrees, then the microelement is separated during the shear process, and the strength of the microelement is the adhesion strength between the ice body and the joint surface. The shear schematic of the joint element is shown in Figure 11.

Following Mohr–Coulomb strength theory, in the shear process of the frozen joint surface, the shear stress of each element can be expressed as follows:

$$d\tau = c_i dl_i \cos \theta_i + \sigma_n \tan(\varphi_i + k), \quad (1)$$

where  $d\tau$  is the shear strength (MPa) of the element length;  $c_i$  is the cohesive force (MPa) of the ice or joint surface;  $dl_i$  is the infinitesimal length (m);  $\theta_i$  is the angle ( $^\circ$ ) between the microelement and the XOY plane;  $\sigma_n$  is the normal stress (MPa); and  $\varphi_i$  is the internal friction angle ( $^\circ$ ) of the ice or joint surface.  $k$  is a parameter related to roughness, which can be expressed by the following formula:

$$k = C \frac{1}{D \bullet JRC}, \quad (2)$$

where  $C$  is a constant coefficient related to opening degree;  $D$  is the opening degree (mm); and  $JRC$  is the roughness of the joint surface.

In this study,  $dl_i \cos \theta_i = dy$ , which is substituted into formula (1) to obtain the following formula:

$$d\tau = c_i dy + \sigma_n \tan(\varphi_i + k). \quad (3)$$

Therefore, the shear strength of the whole frozen joint surface can be expressed as the integral of the shear strength of each element to the projection area of the joint surface on the XOY plane, that is,

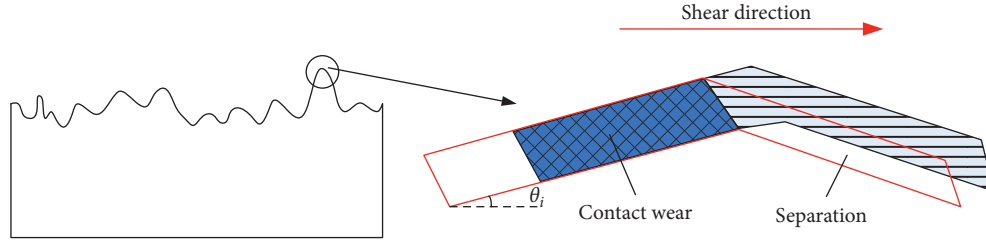


FIGURE 11: Shear schematic of the joint microelement.

$$\tau_p = \iint_{D_{xy}} d\tau = \iint_{D_{xy}} c_i dy dx + \sum_{D_{xy}} \sigma_n \tan(\varphi_i + k), \quad (4)$$

where  $D_{xy}$  is the projection area of the joint plane on the XOY plane.

The damaged specimens are taken out to observe the ice damage between frozen rock joints under various conditions. The results show that when the opening degree of the specimen is 13 or 10 mm under the low normal stress condition (normal stress is not greater than 1.0 MPa), the failure mode of the specimen is the separation failure between the rock joint surface and the ice layer (as shown in Figure 12(a)). At this time, because the opening of the specimens is larger than the fluctuation difference of the joint surface, or the specimens are subjected to a smaller normal stress when the two are approximately equal, the ice compaction is not evident. Hence, the climbing effect hardly occurs during the shear process, and the failure mode is the shear along the weakest surface. Previous studies [21] showed that the bond strength at the ice-rock interface is far less than the shear strength of the ice itself. Therefore, in this case, the failure of specimens overcomes the cohesion and friction between the ice layer and the joint surface, that is, the peak shear strength of specimens consists of the cohesion and friction between the ice layer and the joint surface. However, because the friction coefficient of ice is small, the friction force between ice and joint surface can be neglected compared with the bonding force. At this time, the bond strength between ice layer and joint surface plays a decisive role, that is, the shear strength of specimens is approximately equal to the bond strength between the ice layer and the joint surface. Following the theory of ice adhesion [22], the adhesion strength of ice can be measured by surface energy, and the relationship between ice adhesion and surface energy can be evaluated by the adhesion work ( $W_a$ ):

$$\tau_p = W_a = \gamma_s + \gamma_l - \gamma_{sl}, \quad (5)$$

where  $\gamma_s$  is the surface energy of the solid interface;  $\gamma_l$  is the surface energy of the liquid interface; and  $\gamma_{sl}$  is the interface energy between solid and liquid.

When the opening of specimens is 7 or 10 mm under high normal stress (normal stress is not less than 1.5 MPa), the failure mode of specimens is shear failure in ice. The failure of specimens at this time can be divided into two forms. When the opening of the specimen is 7 mm and the normal stress is greater than 1.5 MPa, the effect of ice compaction is evident, and its integrity is destroyed during

the compaction process. Therefore, during the shear process, shearing may occur in the ice (as shown in Figure 12(c)). When the opening of the specimens is 7 and 10 mm and the normal stress is not more than 1.0 MPa, the normal displacement of the ice layer is small, and the compaction effect is not evident. However, because the ice thickness is less than the fluctuation difference of the joint surface at this time, the biting effect is strong, and the ice layer and the joint surface do not separate under the climbing effect. The failure mode at this time is shear failure within the ice layer (as shown in Figure 12(b)). In this case, the failure of the specimens overcomes the cohesion in the ice layer and the occlusion force on the joint surface when climbing the slope. At this time, the climbing effect occurs on the shear-oriented joint surface, and shear failure occurs. The strength of this part of the area is determined by the shear strength. The projection area of all shear-oriented slope areas on the XOY plane is assumed to be  $D_{1xy}$ . Separation occurs on the joint surface in the direction of back shear, and the strength of this area is determined by the adhesion strength of ice. Assuming that the projection area of all slope areas along the back shear direction on the XOY plane is  $D_{2xy}$ , the adhesion strength of this part is equal to  $W_{1a}$ . The sketch of ice stress at this time is shown in Figure 11.

The cohesion of the rock joint surface is  $C_1$ ; the internal friction angle is  $\varphi_1$ ; the cohesion of ice is  $C_2$ ; and the internal friction angle is  $\varphi_2$ . The shear strength of the microelement facing the shear direction is controlled by the shear strength of the joint surface. Meanwhile, the adhesion strength of part microelements separated by shear is controlled by shear strength of ice. The shear strength of the frozen joint surface can be expressed as follows:

$$\begin{aligned} \tau_p &= \iint_{D_{xy}} d\tau = \iint_{D_{xy}} c_i dy dx + \sum_{D_{xy}} \sigma_n \tan(\varphi_i + k) \\ &= \iint_{D_{1xy}} f(c_i) dy dx + \sum_{D_{1xy}} \sigma_n \tan(f(\varphi_i) + k) \\ &\quad + \iint_{D_{2xy}} c_2 dy dx + \sum_{D_{2xy}} \sigma_n \tan(\varphi_2 + k), \end{aligned} \quad (6)$$

where  $f(C_i)$  is a function related to  $C_1$  and  $C_2$  and  $f(\varphi_i)$  is a function related to  $\varphi_2$  and  $\varphi_2$ .

The shear strength of the separated microelements can be expressed by the adhesion strength between the ice layer and the joint surface.

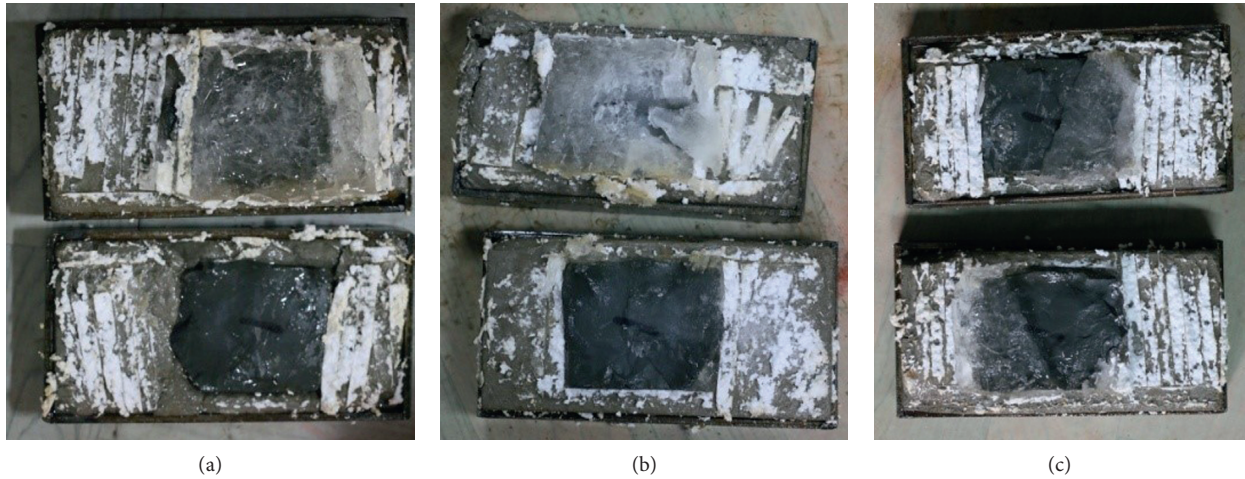


FIGURE 12: Photographs of shear failure patterns of frozen joints under different conditions. (a) Disengagement failure of the ice-rock interface. (b) Ice shear damage inside. (c) Shear failure in the ice layer.

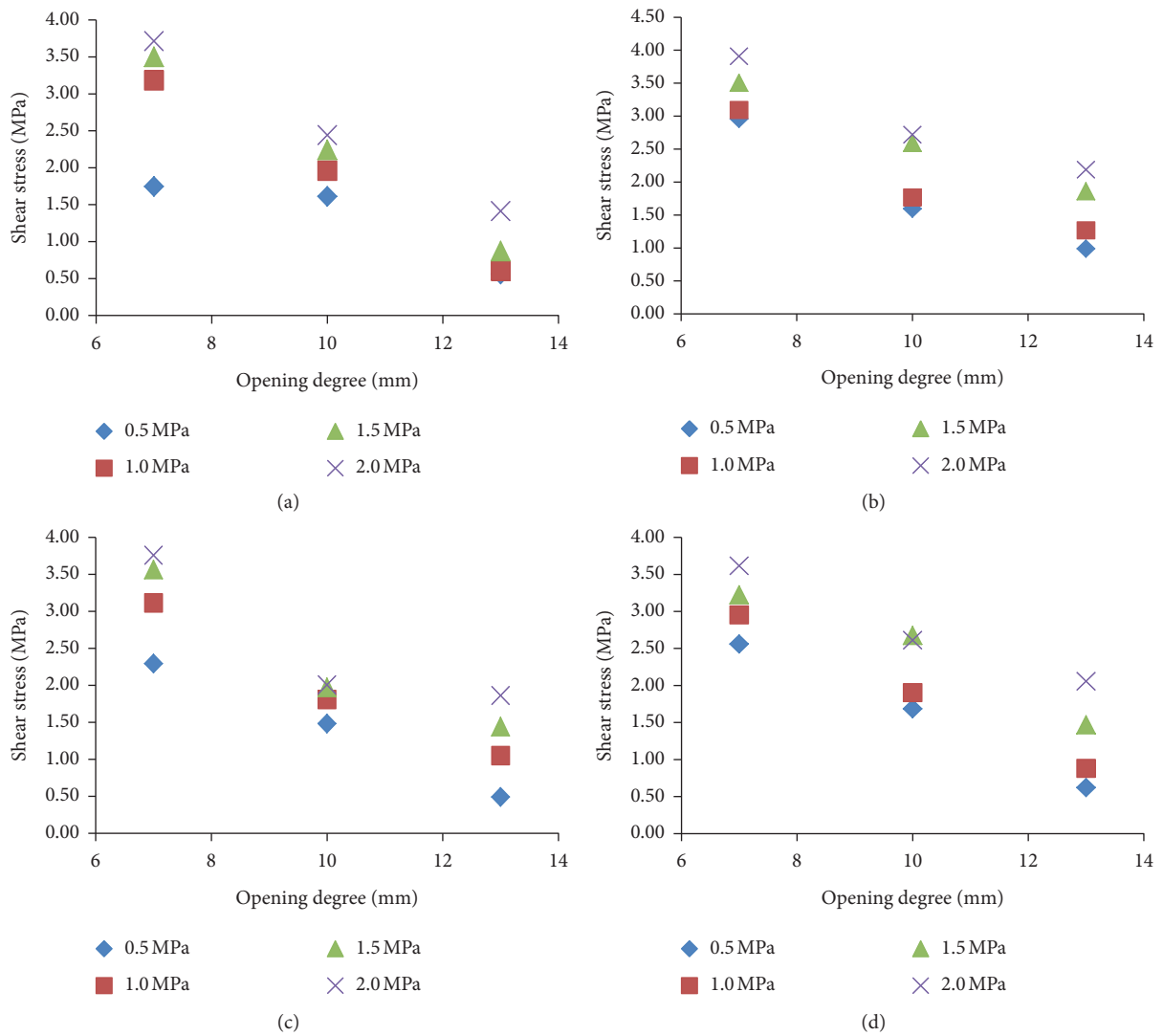


FIGURE 13: Evolution of peak shear strength of frozen joints under different conditions. (a) Specimen 1#. (b) Specimen 2#. (c) Specimen 3#. (d) Specimen 4#.

$$\iint_{D_{2xy}} c_2 dy dx + \sum_{D_{2xy}} \sigma_n \tan(\varphi_2 + k) = W_a. \quad (7)$$

Therefore,

$$\tau_p = \iint_{D_{1xy}} f(c_i) dy dx + \sum_{D_{1xy}} \sigma_n \tan(f(\varphi_i) + k) + W_a. \quad (8)$$

Evidently, the shear strength of frozen joint surfaces in formula (7) consists of the ice adhesion strength of the separated microelements and the climbing strength of the microelements facing the shear direction.  $f(C_i)$  and  $f(\varphi_i)$  are related to the shear strength of ice and rock joints, respectively. The climbing strength depends on the small values of the occlusion strength of the protruding part of the rock joint surface and the shear strength of the ice layer because the failure of specimens always cuts along the weakest part.

On this basis, when no slope-climbing effect occurs, the shear strength of the frozen joints is composed of the cohesive strength between the ice body and the joint surface. Furthermore, the peak shear strength of frozen joints is small. The peak shear strength increases when the joint surface opening is small, or the normal stress is large. Moreover, climbing effect and occlusion occur in the protruding part of the joint surface during the shear process. It can be seen from the figure that the greater normal stress corresponds to the greater peak shear strength of the joint under the conditions of each opening degree; at the same time, under the same normal stress, the greater opening degree corresponds to the smaller peak shear strength. This is consistent with the determinants of the strength of the frozen joint surface and the failure form under the conditions of different opening degrees mentioned above. Figure 13 shows the variation of peak shear strength of the joint surface under different conditions.

## 5. Conclusions

- (1) Under different normal pressures, the shear process of rock frozen joints can be divided into initial deformation, continuously increasing shear stress, ice shearing, and residual shear stages. The shear stress-shear displacement curve is concave in the continuously increasing shear stress stage, and the rate of increase in shear stress increases with the increase in normal stress. When the ice shear occurs, the shear stress does not decrease instantaneously. However, it decreases slowly after reaching the peak strength, thereby showing evident flexibility and destructive characteristics.
- (2) When the joint opening is close to or greater than its own fluctuation difference, under the action of larger normal stress, damage occurs inside the ice layer, and local failure is prone to occur during shear. The ice layer melts locally by absorbing shear friction heat

and soon contacts with the surrounding ice body, thereby resulting in reicing, which leads to rapid rise and fall in shear stress.

- (3) When the opening of the joint surface is large, the joint surface itself does not contact during shearing, and the failure is controlled by the adhesion strength between the ice layer and the joint surface. When the joint openness is small, the slope-climbing effect occurs in the shear process. At this time, the failure is controlled by overcoming the occlusion between joint surfaces and the adhesion strength of the ice layer. On the basis of the failure modes of frozen joints under different conditions, it can be divided into three types, namely, the breakage of the ice-rock interface, the shear failure of the ice layer, and the shear failure of the ice layer.
- (4) The coordinate system of the joint surface is established, and the microelement is divided. On the basis of the shear strength of the microelement facing shear direction and the adhesion strength of the microelement facing back shear direction during shear detachment, the integral form of the peak shear strength criterion of the joint surface under different opening degrees is derived, and the evolution law of the peak shear strength of frozen joints is obtained.

## Data Availability

The data used to support the findings of this study are available from the first author upon request.

## Conflicts of Interest

The authors declare that they have no conflicts of interest.

## Acknowledgments

This paper was supported by the National Natural Science Foundation of China (no. 41502270) and the National Key Laboratory of Frozen Soil Engineering of Chinese Academy of Sciences (no. SKLPSE201506).

## References

- [1] N. Barton, "The shear strength of rock and rock joints," *International Journal of Rock Mechanics and Mining Sciences & Geomechanics Abstracts*, vol. 13, no. 9, pp. 255–279, 1976.
- [2] G. Grasselli, *Shear strength of rock joints based on quantified surface description*, Ph.D Thesis, Swiss Federal Institute of Technology, Zürich, Switzerland, 2001.
- [3] Y. Liu, J. Liu, and C. Xia, "Research on strength behavior of rock mass containing discontinuous joints by direct shear test under different joint surface morphologies," *Rock and Soil Mechanics*, vol. 35, no. 5, pp. 1269–1274, 2014.
- [4] L. K. -Hui, C. Ping, Z. Ke et al., "Macro and meso characteristics evolution on shear behavior of rock joints," *Journal of Central South University*, vol. 22, no. 8, pp. 3 087–3 096, 2015.
- [5] J.-A. Wang, Y.-X. Wang, Q.-J. Cao et al., "Behavior of microcontacts in rock joints under direct shear creep loading," *International Journal of Rock Mechanics & Mining Sciences*, vol. 2, no. 7, pp. 217–229, 2015.

- [6] Z. Tang, Q. Liu, and X. Liu, "Shear behavior of rock joints and comparative study on shear strength criteria with three-dimensional morphology parameters," *Chinese Journal of Geotechnical Engineering*, vol. 36, no. 5, pp. 873–879, 2014.
- [7] L. Yu, X. Xu, M. Qiu et al., "Influence of freeze-thaw on shear strength properties of saturated silty clay," *Rock and Soil Mechanics*, vol. 31, no. 8, pp. 2448–2452, 2010.
- [8] J. Wang, H. Liu, C. Wu et al., "Influence of freeze-thaw cycles on dynamic characteristics of subgrade soils with different plasticity indices," *Chinese Journal of Geotechnical Engineering*, vol. 36, no. 4, pp. 633–639, 2014.
- [9] A. Zhao, A. Tang, J. Sun et al., "Test on shear strength of cement improved soil under freeze-thaw cycles," *Journal of Engineering of Heilongjiang University*, vol. 6, no. 1, pp. 28–31, 2015.
- [10] S. Ji, A. Wang, and H. Liu, "Analysis of influence factors on the confined compression strength of sea ice in the Bohai Sea," *Marine Science Bulletin*, vol. 33, no. 4, pp. 371–376, 2014.
- [11] Q. Jia, Z. Li, H. Han et al., "Experimental study on shear strength of freshwater ice in a reservoir," *Mathematics in Practice and Theory*, vol. 45, no. 5, pp. 132–137, 2015.
- [12] B. Liu, N. Liu, D. Li et al., "Strength test on frozen cracked red sandstone combined with ice," *Journal of China Coal*, vol. 41, no. 4, pp. 843–849, 2016.
- [13] H. Han, W. Huang, Q. Jia et al., "Study on the unconfined shear strength of large columnar-grained freshwater ice and its influential factors," *South-to-North Water Transfers and Water Science & Technology*, vol. 14, no. 6, pp. 39–45, 2016.
- [14] T. M. Tharp, "Conditions for crack propagation by frost wedging," *Geological Society of America Bulletin*, vol. 99, no. 1, p. 94, 1987.
- [15] K. Friederike, "Shear strength of ice-filled rock joints," *Annals of Glaciology*, vol. 31, pp. 463–467, 2000.
- [16] M. C. R. Davies, O. Hamza, and C. Harris, "The effect of rise in mean annual temperature on the stability of rock slopes containing ice-filled discontinuities," *Permafrost and Periglacial Processes*, vol. 12, no. 1, pp. 137–144, 2001.
- [17] M. C. R. Davies, O. Hamza, W. Bruce et al., "Laboratory measurement of the shear strength of ice-filled rock joints," *Annals of Glaciology*, vol. 31, 2000.
- [18] F.-A. Martin and P. Rivard, "Effects of freezing and thawing cycles on the shear resistance of concrete lift joints," *Canadian Journal of Civil Engineering*, vol. 39, pp. 1089–1099, 2012.
- [19] Q. Liu, Y. Kang, H. Xing et al., "Critical problems of freeze-thaw damage in fractured rock and their research status," *Rock and Soil Mechanics*, vol. 33, no. 4, pp. 971–978, 2012.
- [20] C. Xia, J. Huang, C. Han et al., "Methods of frost-heave ratio evaluation and classification of frost-heave susceptibility of tunnel surrounding rocks in cold regions," *Chinese Journal of Rock Mechanics and Engineering*, vol. 32, no. 9, pp. 1876–1885, 2013.
- [21] Z. Tang, C. Xia, and Y. Song, "New peak shear strength criteria for roughness joints," *Chinese Journal of Geotechnical Engineering*, vol. 35, no. 3, pp. 571–577, 2015.
- [22] Y. Ding, S. Tang, and H. Wu, "Study on influence of surface microstructure on ice adhesion strength," *Surface Technology*, vol. 44, no. 4, pp. 74–78, 2015.

## Research Article

# Comparative Study on Mineral-Scale Microcrack Propagation of Shale under Different Loading Methods

Jiayong Zhang <sup>1,2,3</sup>, Zhendong Cui <sup>1,2,3</sup>, Weige Han,<sup>4</sup> Kai Si <sup>5</sup> and Yan Zhao<sup>5</sup>

<sup>1</sup>Key Laboratory of Shale Gas and Geoengineering, Institute of Geology and Geophysics, Chinese Academy of Sciences, Beijing 100029, China

<sup>2</sup>Innovation Academy for Earth Science, CAS, Beijing 100029, China

<sup>3</sup>College of Earth and Planetary Sciences, University of Chinese Academy of Sciences, Beijing 100049, China

<sup>4</sup>School of Civil Engineering, Shijiazhuang Tiedao University, Shijiazhuang, Hebei 050043, China

<sup>5</sup>School of Mechanics and Civil Engineering, China University of Mining and Technology (Beijing), Beijing 100083, China

Correspondence should be addressed to Zhendong Cui; [cuizhendong@mail.iggcas.ac.cn](mailto:cuizhendong@mail.iggcas.ac.cn)

Received 26 November 2020; Revised 10 December 2020; Accepted 17 December 2020; Published 29 January 2021

Academic Editor: Zhi Cheng Tang

Copyright © 2021 Jiayong Zhang et al. This is an open access article distributed under the Creative Commons Attribution License, which permits unrestricted use, distribution, and reproduction in any medium, provided the original work is properly cited.

Producing a sufficient volume of multiscale crack networks is key to enhancing recovery of shale gas. The formation of crack network largely depends on initiation and propagation of microcracks. To reveal the influence of different loading methods on the propagation of mineral-scale microcracks, this study used the Voronoi tessellation technique to establish a cohesive zone model of shale mineral distribution and applied six different boundary conditions to represent different loading methods. Crack path characteristics, rupture characteristics, continuous crack propagation and turning, and en echelon intermittent crack propagation under different loading methods were compared and analyzed. The essence of different loading methods affecting the length and complexity of cracks was the spreading range of tensile microcracks. The mechanical properties of minerals led to dissimilarities in continuous crack propagation and turning. The formation and propagation of en echelon intermittent fractures of different scales were mainly impacted by the heterogeneity of minerals and mineral aggregates. The spreading direction and connection form of en echelon intermittent fractures were mainly affected by the loading method. Conclusions arising from mineral-scale simulations contribute to understanding the mechanism of microcrack propagation resulting from different loading methods, and these conclusions have a guiding significance to enhanced shale gas recovery.

## 1. Introduction

Shale gas exists in low-porosity and low-permeability shale formations. Producing a sufficient volume of multiscale crack networks is the key to enhancing the recovery of shale gas. At present, academia and industry are more concerned about the macrocrack network, and less research is focused on the propagation of microcracks. However, existing studies show that the formation of crack networks largely depends on the growth of microcracks. Minerals are the basic units of shale. Research on the physical nature of mineral-scale microcracks can reveal their propagation mechanism.

Scholars have carried out static experimental observations on the characteristics of mineral-scale microcracks after the failure of rock through the use of optical microscopes, scanning electron microscopes (SEM), computed tomography (CT), and other types of equipment. Fujii et al. [1] found that more than 90% of the tensile cracks in granite after tensile failure exist in the form of intergranular fractures, and the remaining 10% are transgranular fractures. Minerals that form microcracks at different angles to the tensile direction are unusual. Zhong et al. [2] summarized microcrack failure modes of shale in a triaxial compression experiment and categorized them into three types: tensile failure, shear failure, and slip failure. Daigle et al. [3]

compared the differences between microcracks in siliceous clay and calcareous clay. Cheng and Wong [4] compared the characteristics of tensile microcracks and shear microcracks produced by the uniaxial compression of marble and analyzed the influence of mineral grains on the types of microcracks. Lan et al. [5] carried out SEM observation of microcracks before and after a triaxial compression test of shale and found that the spatial distribution of microcracks conforms to the power-law distribution, with a defined self-affine and hierarchical structure. This study suggests that the mechanical responses of minerals have different effect on shale fracturing.

The above experiments were all static observation and analysis and did not evaluate the growth process of microcracks. SEM with an in situ loading apparatus makes it possible to observe continuous growth of microcracks. Zhao et al. [6] found in a uniaxial compression experiment of Fangshan marble that along with initiation, propagation, and connection of microcracks, the closure of microcracks also occur. Cui et al. [7, 8] observed the dynamic process of microcrack initiation and propagation and discovered microscopic en echelon intermittent fractures for the first time. They summarized the hierarchical distribution characteristics of en echelon intermittent fractures and hypothesized that the cause may be related to the heterogeneity of minerals. Zuo et al. [9] observed the continuous propagation process of main cracks and branch cracks in the microscopic region and performed finite element calculations on their fracture toughness. Dong et al. [10] found that cracks propagate in the form of microcrack connections at the microscopic scale. In other words, the microcracks near the crack tip are always in a state of competition. Microcracks connected to the crack tip become the main crack. After the main crack propagates, microcracks that are not connected to the crack tip are closed owing to stress release. Tang [11] studied the evolution of microdamage in marble under uniaxial compression and proposed a multiscale damage power-law model for cracks. Renard et al. [12] performed CT scans on the entire process of monzonite triaxial compression under 25 MPa confining pressure and used digital image correlation methods to quantitatively analyze the initiation, closure, aggregation, and penetration characteristics of microcracks at different loading stages. These observations of the continuous growth of microcracks found many interesting phenomena that are different from the growth of macroscopic cracks. Unfortunately, none of the observations involved the distribution of minerals in the microregion, so it is impossible to clarify the influence of minerals on the growth of microcracks and thus only hypothetical explanations can be given regarding the mechanism of different observed phenomena.

The in situ experimental observation of the continuous growth of microcracks based on mineral distribution is difficult. The strain and stress of the microregion also cannot be obtained easily. Scholars have developed many numerical models based on mineral distribution, such as the universal

distinct element code (UDEC) particle boundary model [13, 14], three-dimensional distinct element code (3DEC)-Voronoi model [15, 16], distinct element model (DEM) based on three-dimensional polygons [17], particle flow code (PFC)-grain-based model (GBM) [15, 18, 19], and the Irazu-GBM model [20]. Li et al. [21, 22] used the finite discrete element method based on grains to study factors, including boundary conditions and rock geometry, affecting the fracture growth process in granite under uniaxial compression. Lan et al. [23] carried out a uniaxial compression experiment of a mineral distribution model based on UDEC. The authors found that heterogeneity of grain size affected the distribution of tensile stress, and rocks with such grains are more likely to produce tensile microcracks than rocks with uniform grains. Li et al. [17] studied the influence of grain size on microcrack propagation based on the 3D polycrystalline discrete element method-Voronoi model. The authors reported that in specimens with larger grain sizes, the convenient path for crack propagation is along the loading direction, which results in a series of vertical tensile fractures. When the grain size was small, the microcracks were more scattered. Xu et al. [24] established a uniaxial compression experimental model based on the microstructure of coal. They found that microcracks at the mineral interfaces occur due to heterogeneous strain of minerals. The authors concluded that the generation of tensile microcracks dominated the failure behavior of the rock under uniaxial compression. Zhou et al. [25] established PFC-GBM to study the proportion of shear and tensile cracks during crack propagation. Saadat and Taheri [26] carried out uniaxial compression experiments based on the cohesive contact model of PFC to study the formation and propagation of microcracks in the shear zone.

The abovementioned mathematical simulations of microcrack propagation based on mineral distribution models were all set as uniaxial compression tests. The results suggest that tensile fractures dominated the uniaxial compression failure behavior of rock. However, hydraulic fracturing is not a simple uniaxial compression. In hydraulic fracturing, the fractures are first partially opened, and then the proppant enters to propagate the fractures. At the same time, the high pressure of the fracturing fluid pushes both sides of the fractures to move. In this process, the shale is in a complex stress state of tension, shear, and compression [27]. Observations of hydraulic fracturing cracks show that the characteristics of microcracks produced by tensile, shear, tension-shear, and compression-shear are different [28–30]. Other experimental studies focused on tensile and three-point bending loading, and the observed crack network and microcrack propagation were found to be quite different from uniaxial compression [9, 31]. Therefore, it has important significance to study the rupture characteristics of microcracks under different loading methods. On the macroscale, some scholars have compared the peak stress, macrocrack propagation, and fracture characteristics of rocks under different loading methods [32–34]. However, on the mineral scale, it is essential to determine what characteristics of the microcracks are produced under different loading methods such as tension, shear, tension-shear, and

compression-shear. It is also essential to determine the difference between microcrack growth and evolutionary form under different loading methods and what types of microcracks dominates the fracture of the rock. These important questions need to be addressed.

To reveal the influence of different loading methods on the propagation of mineral-scale microcracks, this study used the Voronoi tessellation technique to establish a cohesive zone model (CZM) based on mineral distribution. Considering the heterogeneity of minerals, various mechanical parameters were set for different minerals. Six loading methods were designed, that is, modeling tension, tension-shear, shear, and compression-shear stresses. We compared and analyzed the crack length, fractal dimension, rupture characteristics, continuous crack propagation and turning, and an echelon intermittent fracture propagation. The comparative analysis uncovered the mechanism of how different loading methods affect the growth of mineral-scale microcracks.

## 2. Cohesive Zone Model Based on Mineral Distribution

**2.1. Voronoi Tessellation Technique.** To establish a heterogeneous shale mineral model, we added a Voronoi tessellation technique into Abaqus using a Python script. This technique contains four steps as shown in Figure 1. First, a certain number of randomly distributed control points were generated in the model sketch (Figure 1(a)). Then, the adjacent control points were triangulated based on the Delaunay triangulation (Figure 1(b)). When the circumference of the constructed triangle included control points in addition to those at the vertices, the triangle was abandoned, and new triangles were formed until all control points formed vertices. Third, the circumcenters of adjacent triangles were connected (Figure 1(c)). Finally, the control points and triangles were removed and the Voronoi grains were generated (Figure 1(d)).

**2.2. Numerical Calculation Principle of the Cohesion Zone Model.** CZM was proposed by Dugdale [36] and Barenblatt [37]. This model helped in solving the research difficulties caused by the crack tip stress singularity and is widely used in the study of interface delamination of composite materials [38]. Strom and Parmigiani [39] used CZM to explain the penetration and deflection behavior of cracks when passing through the bedding surface based on the stress-energy method and verified the applicability of the model.

**2.2.1. Constitutive Equation of Cohesive Element.** The cohesive element is based on the linear elastic constitutive model of the traction-separation law. Before the cohesive element is damaged, the stress and strain satisfy the following linear elastic relationship:

$$\begin{Bmatrix} t_n \\ t_s \\ t_t \end{Bmatrix} = \begin{bmatrix} K_{nn} & K_{ns} & K_{nt} \\ K_{ns} & K_{ss} & K_{st} \\ K_{nt} & K_{st} & K_{tt} \end{bmatrix} \begin{Bmatrix} \varepsilon_n \\ \varepsilon_s \\ \varepsilon_t \end{Bmatrix}. \quad (1)$$

The symbol  $t$  represents stress,  $\varepsilon$  represents strain, the subscript  $n$  represents the normal direction, and the subscripts  $s$  and  $t$  are two tangential directions perpendicular to the normal direction. For uncoupled constitutive relations, only  $K_{nn}$ ,  $K_{ss}$ , and  $K_{tt}$  need to be defined.

**2.2.2. Fracture Propagation Criteria. Initial Damage Criterion.** The maximum principal stress control criterion was used in the simulation. That is, when the normal tensile stress or tangential stress reaches the corresponding strength, it will break:

$$\text{MAX} \left\{ \frac{\langle \sigma_n \rangle}{N_{\max}}, \frac{\sigma_s}{S_{\max}}, \frac{\sigma_t}{T_{\max}} \right\} = 1, \quad (2)$$

where  $\sigma_n$  is the normal stress;  $\sigma_s$  and  $\sigma_t$  are the shear stresses in two directions;  $N_{\max}$  is the tensile strength; and  $S_{\max}$  and  $T_{\max}$  are the shear strengths in the two directions;  $\sigma_n$  is expressed as

$$\begin{cases} \langle \sigma_n \rangle = 0, & \sigma_n < 0, \\ \langle \sigma_n \rangle = \sigma_n, & \sigma_n \geq 0. \end{cases} \quad (3)$$

The cohesive element will not produce initial damage in a purely compressed state.

**Damage Evolution Criterion.** In this study, the damage evolution criterion was based on effective displacement, and the damage variable  $D$  was defined as

$$D = \frac{\delta_m^f (\delta_m^{\max} - \delta_m^0)}{\delta_m^{\max} (\delta_m^f - \delta_m^0)}, \quad (4)$$

where  $\delta_m^f$  is the effective displacement at failure, taken as 0.01 in the model,  $\delta_m^0$  is the effective displacement at the initial evolution of damage,  $\delta_m^{\max}$ , and is the maximum effective displacement during the loading process.

**2.2.3. Principle of Acoustic Emission Simulation.** The Abaqus simulation results were extracted using a Python script, and the results were processed by MATLAB programming to simulate the acoustic emission (AE) during the loading process [40]. Through the AE location and characteristic parameters, the crack rupture condition was further described, which provided an effective means for in-depth analysis of the crack propagation process. The method to obtain the AE location can be described as follows. The node coordinates of the damaged element were extracted and the coordinates of the center point of the damaged element were calculated, which were then used as the point of the AE event location. The number of damaged elements was regarded as



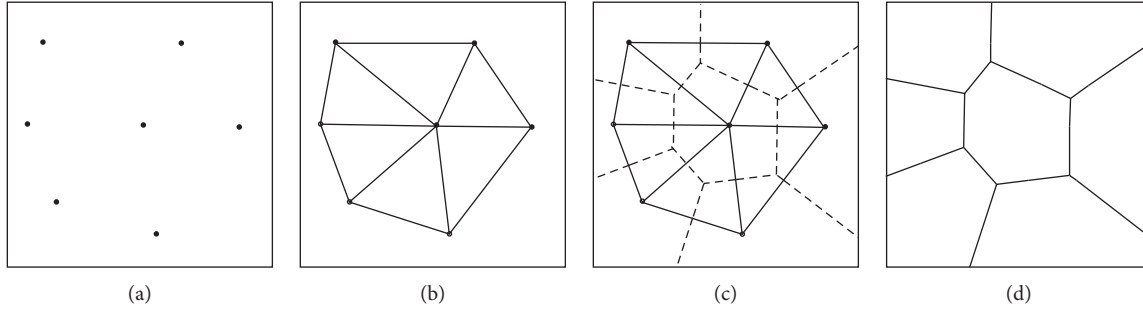


FIGURE 1: Four steps to generate random Voronoi polygons [35].

the number of AE events. Extracting the total energy dissipated per volume of the damaged element gave the AE energy.

The parameter MMIXDME, which can be used to determine the type of rupture, is defined as follows:

$$\text{MMIXDME} = \frac{G_s + G_t}{G_T}, \quad (5)$$

$$G_T = G_n + G_s + G_t,$$

where  $G_n$  is the Type I tensile fracture energy;  $G_s$  is the Type II slip fracture energy;  $G_t$  is the Type III tear fracture energy; and  $G_T$  is the sum of  $G_n$ ,  $G_s$ , and  $G_t$ .

The value range of MMIXDME is between 0 and 1. When MMIXDME is 0, it indicates a tensile fracture; when the value is 1, it indicates a shear fracture, and when the value is between the 0 and 1, there is a tensile-shear mixed fracture.

### 3. Mathematical Model

**3.1. Model Design.** A 2D geometric model (6 mm × 6 mm) was established in Abaqus, as shown in Figure 2(a). To create a heterogeneous mineral model of shale, this 2D geometric model was divided into 722 Voronoi units using the Voronoi tessellation technique. Each Voronoi unit represented a mineral grain, and the grain size was assigned according to the study of Ji et al. [41]. Quartz, feldspar, kaolinite, and illite were randomly assigned to Voronoi units for a content of 30%, 30%, 20%, and 20%, respectively, and are represented by gray scales from high to low in Figure 2(b). Finally, the generated Voronoi units were meshed with a 0.08-mm quadrilateral grid. Zero-thickness cohesive elements were globally inserted into grain boundaries and meshes. Each mineral set contains four-node plane strain elements (CPE4) and zero-thickness cohesive elements at the boundaries of the CPE4. The mineral boundary set was created with the remaining cohesive elements at dissimilar mineral boundaries. The parameters of the CPE4 for different minerals are listed in Table 1. The parameters of cohesive elements in minerals (at boundaries of CPE4) and cohesive elements at boundaries of dissimilar minerals are shown in Table 2. It should be noted that mechanical properties of mineral boundaries depend on bond strength, and there is currently no uniform method for characterizing the bond strength of solid clay. Many experimental studies found that compared

with clay minerals, mineral boundaries have a higher bulk density and stronger cementation [42–45]. Therefore, the mineral boundary strength parameters were set slightly larger than those of kaolinite but smaller than those of feldspar in this model.

The total number of elements in the model was 21,242, of which 6,830 were CPE4 and 14,412 were cohesive elements. We set the total loading time to 1 s, the minimum increment size to 1E-7 s, and the maximum increment size to 0.1 s.

**3.2. Loading Methods.** Six loading methods were designed as shown in Figure 3, which accounted for possible stress states of hydraulic fracturing, such as tension, shear, tension-shear, and compression-shear. The mechanical boundary conditions of the model are listed in Table 3.

## 4. Results

This study successfully compared the mineral-scale micro-crack path, AE, continuous crack propagation and turning, and an echelon intermittent crack propagation under different loading methods.

**4.1. Crack Path.** The longer and more complex the crack produced by fracturing, the more gas-containing holes are opened, and the greater the effect on the improvement of shale gas recovery. The crack length can be measured and the complexity of the crack path can be characterized by the fractal dimension. In this study, the box dimension method was used to calculate the fractal dimension of cracks under six different loading methods. Larger fractal dimensions indicated more complicated cracks.

The principle of the box dimension method is as follows. Cover the cracked area with square boxes with side length  $r$ . Some entire boxes are empty and the rest of the boxes cover a part of the crack.  $N(r)$  is the number of boxes covering the cracks; when  $r \rightarrow 0$ , the fractal dimension is as follows:

$$D = - \lim_{r \rightarrow 0} \frac{\log N(r)}{\log r}. \quad (6)$$

The geometric features of the fracture paths are shown in Figure 4. The crack length exhibited the same trend as the fractal dimension. The crack length of tension and tension-shear was longer, and the fractal dimension was larger. The

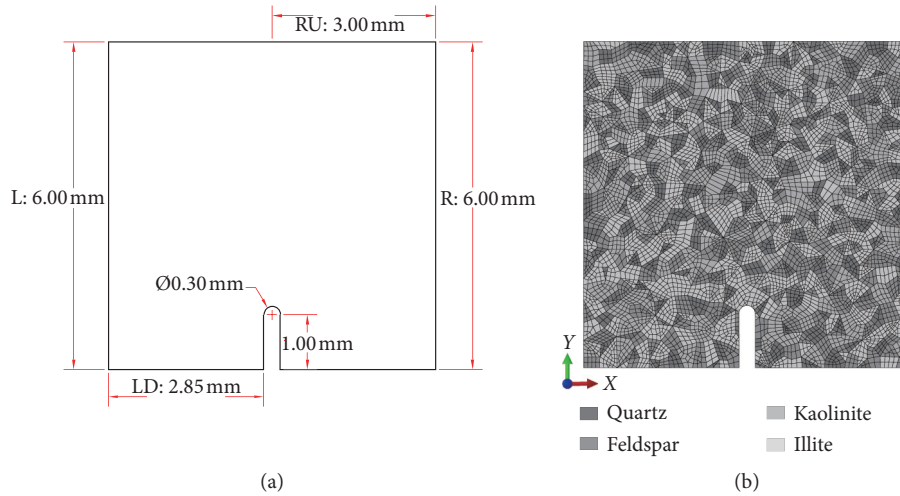


FIGURE 2: (a) 2D geometric model with its dimensions. The notch was 0.3 mm wide and 1.15 mm high. For the ease of reference, the left boundary of the model is marked as L, the lower left boundary is marked as LD, the right boundary is marked as R, and the upper right boundary is marked as RU. (b) Heterogeneous rock mineral model, quartz, feldspar, kaolinite, and illite are represented by gray scales from high to low.

TABLE 1: Mineral composition and parameters of CPE4 of different minerals.

Mineral	Percentage	Elastic modulus (GPa)	Poisson's ratio
Quartz	30	40	0.21
Feldspar	30	35	0.23
Kaolinite	20	22	0.25
Illite	20	18	0.24

TABLE 2: Parameters of cohesive elements in minerals (at boundaries of CPE4) and cohesive elements at boundaries of dissimilar minerals.

Cohesive element	$K_{nn}$ (MPa·m <sup>-1</sup> )	$K_{ss}$ (MPa·m <sup>-1</sup> )	$K_{tt}$ (MPa·m <sup>-1</sup> )	Tensile strength (MPa)	Shear strength (MPa)
In quartz	120	120	120	6	12
In feldspar	110	110	110	5	10
In kaolinite	90	90	90	2	4
In illite	80	80	80	1	2
At the boundaries of dissimilar minerals	100	100	100	3	6

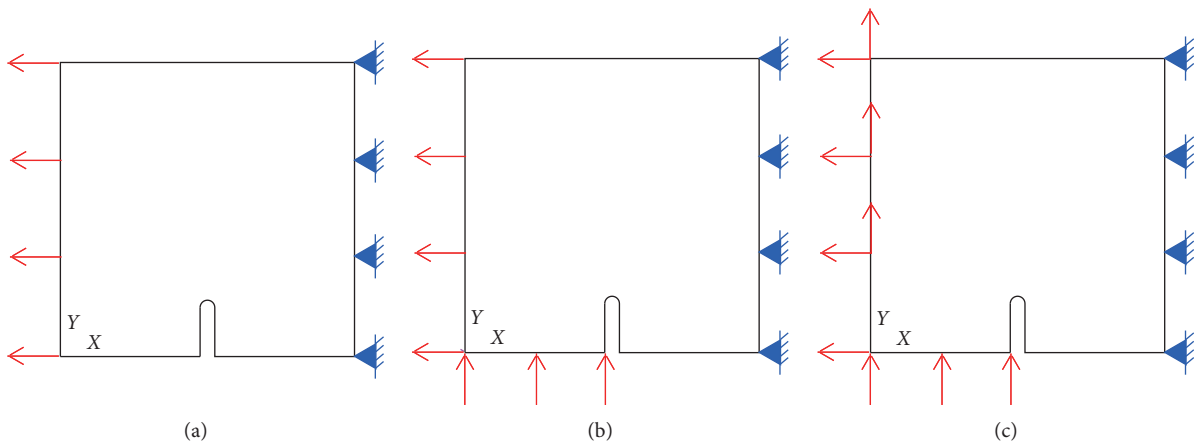


FIGURE 3: Continued.

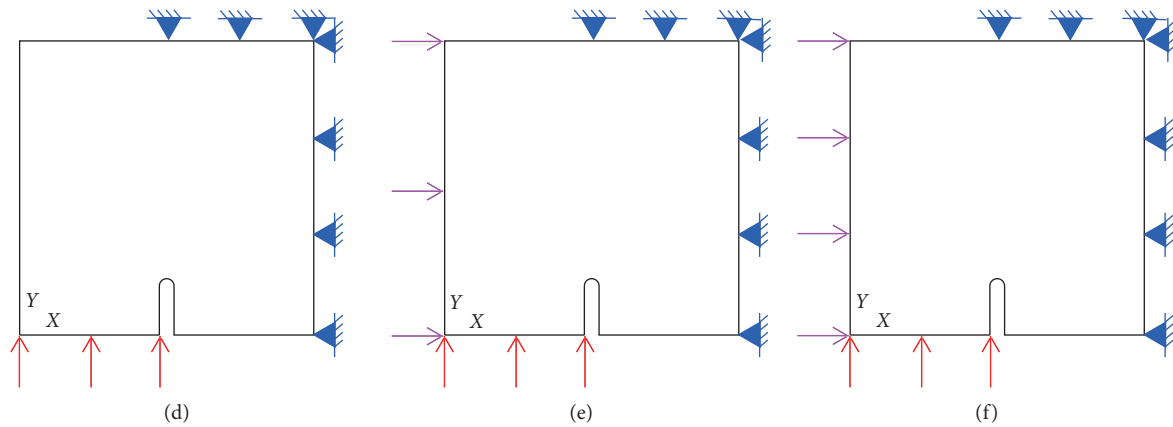


FIGURE 3: Six different loading methods. (a) Loading method I: a displacement load of  $X = -0.2$  mm is applied to the left boundary L and the right boundary R is fixed. (b) Loading method II: a displacement load of  $X = -0.2$  mm is applied to the left boundary L; a displacement load of  $Y = 0.2$  mm is applied to the lower left boundary LD, and the right boundary R is fixed. (c) Loading method III: the left boundary L is applied with  $X = 0.2$  mm,  $Y = 0.2$  mm displacement load, the left lower boundary LD is applied with  $Y = 0.2$  mm displacement load, and the right boundary R is fixed. (d) Loading method IV:  $Y = 0.2$  mm displacement load is applied to the lower left boundary LD, and the right boundary R and the upper right boundary RU are fixed. (e) Loading method V: a pressure load of  $X = 10$  MPa is applied to the left boundary L; a displacement load of  $Y = 0.2$  mm is applied to the lower left boundary LD, and the right boundary R and upper right boundary RU are fixed. (f) Loading method VI: the left boundary L is applied with a pressure load of  $X = 20$  MPa, the left lower boundary LD is applied with a displacement load of  $Y = 0.2$  mm, and the right boundary R and the upper right boundary RU are fixed.

TABLE 3: Mechanical boundary conditions.

	I	II	III	IV	V	VI
L	$X = -0.2$ mm	$X = -0.2$ mm	$(-0.2$ mm, $0.2$ mm)	—	$X = 10$ MPa	$X = 20$ MPa
LD	—	$Y = 0.2$ mm	$Y = 0.2$ mm	$Y = 0.2$ mm	$Y = 0.2$ mm	$Y = 0.2$ mm
R	$(0,0)$	$(0,0)$	$(0,0)$	$(0,0)$	$(0,0)$	$(0,0)$
RU	—	—	—	$(0,0)$	$(0,0)$	$(0,0)$

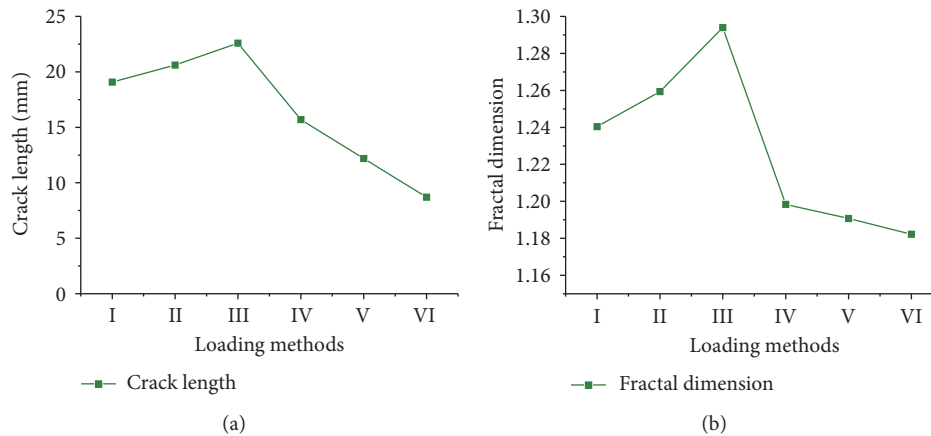


FIGURE 4: Geometric features of fracture paths under six different loading methods. (a) Crack length; (b) Fractal dimension.

crack length of shear and compression-shear was smaller, and the fractal dimension was lower. In loading methods I–III, the crack length and fractal dimension gradually increased, whereas in loading methods IV–VI, the crack length and fractal dimension gradually decreased.

**4.2. Acoustic Emission (AE).** The AE varied for crack paths under each of the six loading methods. The type of fracture,

AE counts, and AE energy were extracted, as shown in Figure 5.

In contrast to the parabolic change of crack length and fractal dimension, for loading methods I–VI, the AE counts, proportion of AE counts, and proportion of AE energy of tensile fractures decreased gradually. Meanwhile, AE counts and AE energy of shear fractures increased. The AE energy of the tensile fractures first increased and then decreased in general. In loading methods I–III, the total AE counts were

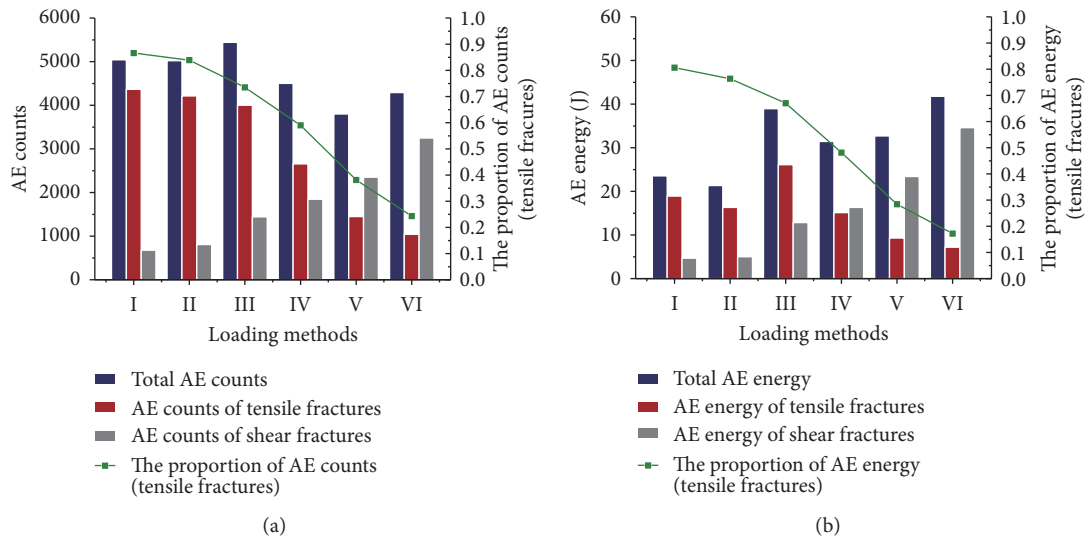


FIGURE 5: AE features under six different loading methods. (a) AE counts; (b) AE energy.

higher than those in loading methods IV–VI, but the total AE energy for I–II was lower.

**4.3. Continuous Crack Propagation and Turning.** In homogeneous materials, the crack propagation path is controlled only by force; therefore, the crack grows relatively flat and smooth. However, in heterogeneous materials such as shale, the fracture path is often complicated. These different minerals and their boundaries affect continuous propagation and turning of cracks. Figure 6 shows the final crack path (in red) under loading methods I–VI. The continuous growth and turning of cracks in different minerals and mineral boundaries are marked with arrows in different colors.

**4.3.1. Propagation and Turning of Cracks in Kaolinite and Illite.** Among the six loading methods, the cracks were relatively flat and smooth when they propagated in the larger grains of kaolinite and illite. The length of each segment of the crack through these regions was longer, and thus these regions accounted for a higher proportion of the total crack length. When the crack tip was blocked by quartz and feldspar, the crack turned and the turning angle was low.

When small grains of kaolinite and illite were surrounded by quartz and feldspar, many small-scale inflections were produced inside the kaolinite and illite. In loading methods I–III, these inflections were relatively small. In loading methods IV–VI, there were more inflections with larger amplitudes.

**4.3.2. Propagation and Turning of Cracks at Mineral Boundaries.** In loading methods I–III, only a small proportion of the cracks propagated along the mineral boundary. These segments usually propagated for a short distance along the mineral boundary and then turned into a kaolinite or illite grain. The positions of the cracks along the mineral boundary in loading methods IV–VI were similar.

In loading method IV, cracks had more inflections, whereas in loading method V, crack inflections were reduced. In loading method VI, the cracks were smooth with almost no inflection, forming a shear arc.

**4.3.3. Propagation and Turning of Cracks in Quartz and Feldspar.** The cracks rarely extended directly through quartz and feldspar. When it occurred at the end of the crack propagation process, the crack shape was relatively straight. However, when it occurred in the middle of the crack propagation process, there were more inflections.

**4.4. En Echelon Intermittent Fractures.** In addition to continuous propagation and turning, cracks were also generated, extended, and connected in a discontinuous manner, that is, en echelon intermittent cracks were created (Figure 7).

The propagation process of en echelon intermittent fractures is divided into five stages.

**Stage 1:** the small-scale en echelon intermittent fractures initiate and form the first large-scale en echelon intermittent fracture. In loading methods I, V, and VI, the en echelon intermittent fractures spread to the upper left direction. In loading methods II and III, the en echelon intermittent fractures spread to the upper right direction; whereas in loading methods IV, en echelon intermittent fractures were initiated both in the upper left and upper right directions.

**Stage 2:** In loading method I, the second and third large-scale en echelon intermittent fractures were almost formed simultaneously. The direction of the second en echelon intermittent fracture was to the upper left, and the direction of the third en echelon intermittent fracture was to the upper right. The second large-scale en echelon intermittent fracture in loading methods II–V was located in the middle of the sample,

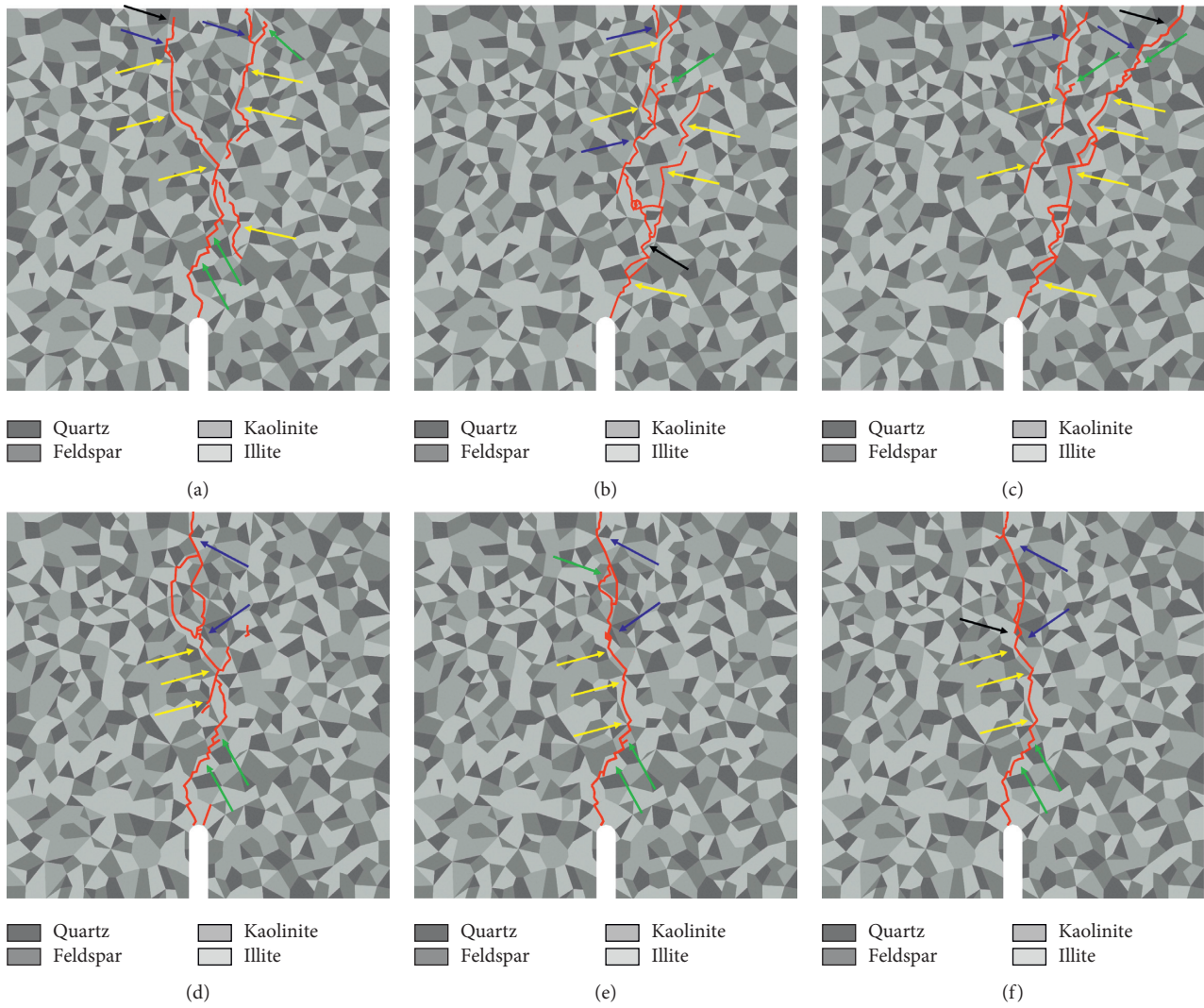


FIGURE 6: Continuous growth and deflection of cracks (in red) under six different loading methods. The yellow arrows refer to crack growth in large scales of kaolinite and illite, the green arrows refer to crack growth in smaller scales of kaolinite and illite surrounded by quartz and feldspar, the blue arrows show crack growth in the boundary between different minerals, and the black arrows refer to crack growth in quartz and feldspar.

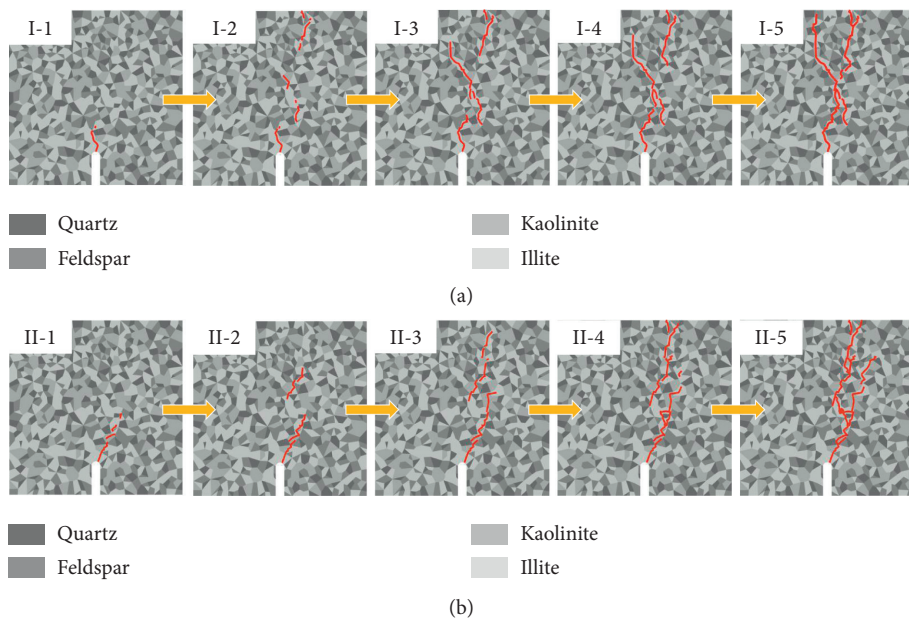


FIGURE 7: Continued.

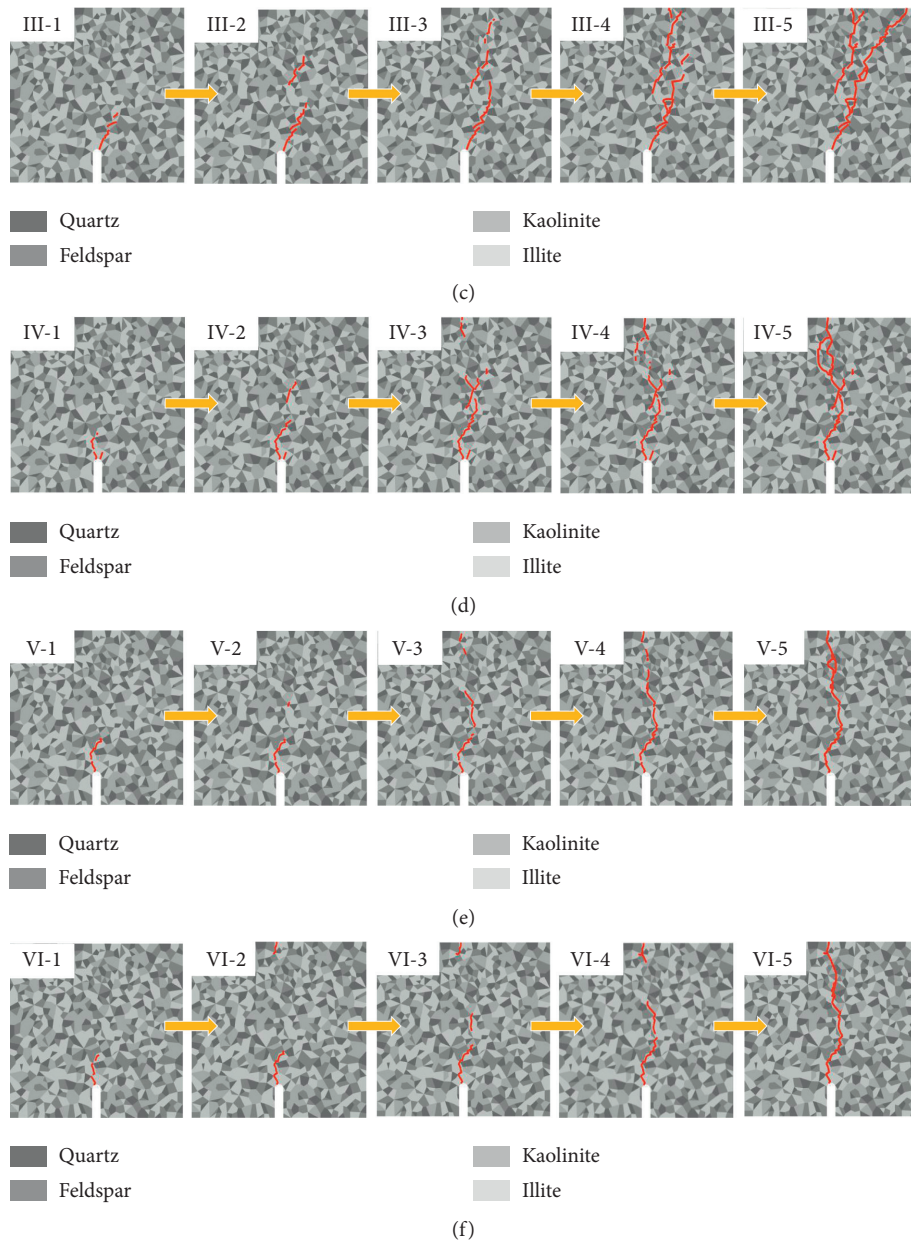


FIGURE 7: The initiation and evolution of en echelon intermittent fractures under six different loading methods. Every loading method is shown with five figures that demonstrate the growth of en echelon intermittent fractures over time.

whereas it was located at the top of the sample in loading method VI. The directions of the second large-scale en echelon intermittent fractures in loading methods II–V were all to the upper right. From loading method II to loading method V, the length of the second large-scale en echelon intermittent fractures gradually decreased.

Stage 3: the third large-scale en echelon intermittent fractures in loading methods II, IV, V, and VI were all formed on the top of the sample. During this stage, the first and second large-scale en echelon intermittent fractures moved toward each other but did not connect.

The three large-scale en echelon intermittent fractures in loading method I were also connected. In loading method III, the third en echelon intermittent fracture formed in the middle of the model and connected to the crack at the lower position.

Stage 4: in loading methods I, IV, V, and VI, the two large-scale en echelon intermittent fractures at the middle and lower positions connected at this stage. However, in loading methods II and III, the two en echelon intermittent fractures in the middle and upper positions connected.

Stage 5: In this stage, the remaining en echelon intermittent fractures connected and the rock was broken.

The connection type of the en echelon intermittent fractures of scales under different loading methods was quite different and is summarized as follows:

- (1) *Wing Crack Connections*. After the formation of en echelon intermittent fractures, adjacent en echelon intermittent fractures were connected by generating wing cracks at both ends, and these resembled an S-shape or a reverse S-shape. The wing crack connection was evident in the connection of two large-scale en echelon intermittent fractures and was also produced in the connection of small-scale en echelon intermittent fractures. Wing crack connections appeared in all six loading methods.
- (2) *Fragment Connection*. In loading methods II–VI, there were en echelon intermittent fractures that appeared to connect in the form of fragments. In loading method III, fragments were generated in the small-scale en echelon intermittent fracture connection. The fragments in loading methods II, IV, V, and VI were generated during the large-scale en echelon intermittent fracture connection. The fragment positioning for loading methods IV–VI was the same. With the increase in lateral pressure, the size of the fragments gradually decreased.
- (3) *X-Shaped Crack Connection*. For loading methods I and IV, the en echelon intermittent fractures appeared to create an X-shaped connection. The scale of X-shaped cracks in loading method I was larger than that in loading method IV.
- (4) *Not Connected or Not Connected at the Crack Tip*. The large-scale en echelon intermittent fracture in the lower part of loading method II propagated to the upper right direction, but the crack tips were not connected with other cracks. Instead, fragments were generated in the middle of the crack that connected with the other two penetrating cracks, and the en echelon intermittent fracture that extended to the upper right was abandoned by the main crack. In loading method III, the en echelon intermittent fracture in the lower position directly propagated to the upper right and did not connect with the cracks at the upper position. Consequently, the cracks at the upper position were abandoned by the main crack.

## 5. Discussion

In rock damage theory, microdamages converge to form microcracks, and then microcracks extend or connect with other microcracks to form macrocracks [46]. Based on this theory, the strain contour and AE location before the formation of macroscopic cracks in loading methods I and IV were derived as shown in Figure 8. The AE characteristics of microcracks before macrocrack formation were extracted by

programming in Python, and the AE location map was drawn using MATLAB software. In tensile loading (loading method I), the deformations of different minerals were nonuniform. Owing to the lower tensile strength, kaolinite, and illite have greater strain compared to quartz and feldspar. Because of the widespread distribution of such minerals, a large number of widely distributed microcracks were generated in the rock. Most of them were tensile microcracks, whereas very few were shear microcracks. The widely distributed tensile microcracks significantly increased the potential spread range of the cracks. The cracks could extend freely or could connect to the remaining microcracks. This led to the formation of longer length and more complicated cracks. In loading method IV (shear loading), strain first occurred at both ends of the maximum shear stress line. The strain in the rest of the rock did not reach failure displacement, even when the strain of the quartz and feldspar minerals around the notch did not reach the failure displacement. There were no widely distributed microcracks in the front of the crack propagation path; only the right-inclined and parallel tensile microcracks were generated on the right side. When the mineral at the crack tip could not be directly sheared, the crack connected with the nearest tensile microcrack. This considerably reduced the potential spread range of cracks.

Compared with loading method IV, the lateral pressure in loading methods V and VI was equivalent to directly increasing the horizontal tensile strength of the rock. However, the increment in shear strength was the normal stress multiplied by the friction coefficient that was less than 1; therefore, the increased amplitude of shear strength was much smaller than that of tensile strength. The minerals at the crack tip could be sheared directly, but the surrounding minerals had not reached its tensile strength. Lateral pressure inhibited the generation of tensile microcracks around the crack tip. As a result, the potential spread range of cracks was further reduced, and the length and complexity of the cracks were also reduced. However, the changing trend of the crack length and fractal dimension of loading methods I–III was opposite to the trend of the amount and proportion of tensile fractures. This can be explained with the following analysis. In loading method I, the direction of the maximum tensile force is horizontal. The tensile microcracks spread and tended to propagate in the vertical direction. In loading methods II and III (tensile-shear loading), the shear and tensile forces were superimposed, causing the maximum tensile force to rotate clockwise from the horizontal direction. The tensile microcracks tended to spread in the upper right direction; as a result, the main crack connected more with the tensile microcracks on the upper right of the rock. This led to an increase in the length and complexity of the cracks. This study showed that the length and complexity of the crack cannot be simply determined by measuring the number of tensile cracks, and the spread range of the tensile microcracks is the fundamental reason.

In geology, it is believed that tortuous cracks occur due to tension, and the smooth and straight cracks occur due to shear [2]. This study demonstrated that different loading

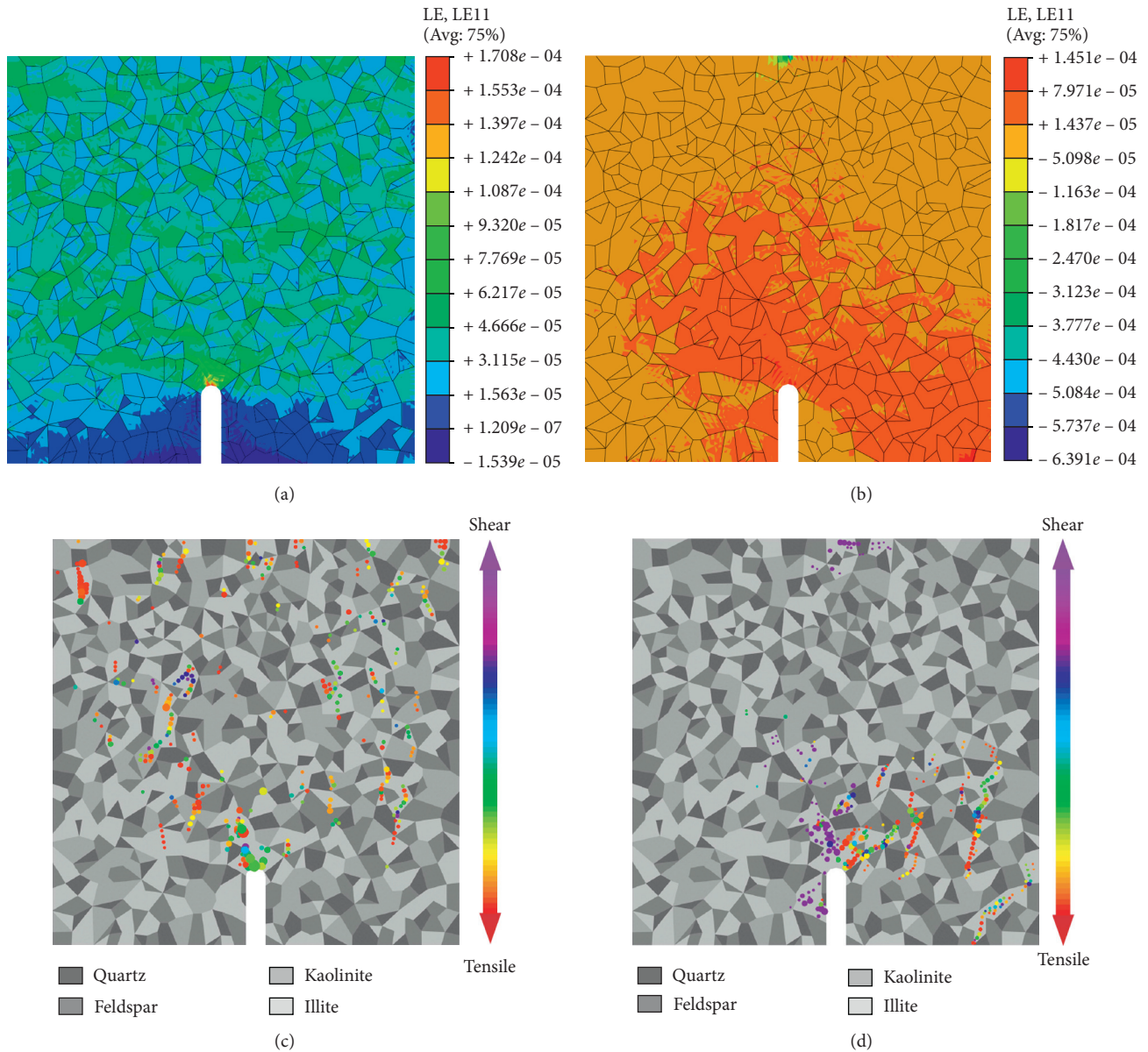


FIGURE 8: In loading method I (tensile loading) and loading method IV (shear loading), the strain and microfracture before the formation of macro-cracks. (a, b) Strain contour before macro-crack formation in loading methods I and IV, respectively. (c, d) In loading methods I and IV, the AE location of the microcracks distributed in the rock before the macrocrack formed. Red dots are the AE location of tensile fractures, purple dots are the AE location of shear fractures, and the colors between the two are the AE location of tensile-shear fractures. The size of the dot represents the level of AE energy. The AE energy of microfracture before the macrocrack formed is relatively small, so the AE energy magnification of this figure is larger than the others in this paper.

methods affecting the complexity of cracks were in the spread range of tensile microcracks. Tensile loading can not only cause bedding and fissures to fracture but can also produce tensile microcracks in widely distributed weak minerals such as kaolinite and illite. Therefore, the crack has a high degree of complexity and a large spread range. Shear loading only produces parallel tensile microcracks on one side of the shear line and can only rupture the cracks on one side. The crack propagates along the direction of the maximum shear force; therefore, the tensile microcrack on one side cannot be extended easily, and the possibility of the

main crack and the tensile microcrack connecting is reduced. As a result, the shear crack has a low degree of complexity and a small spread range.

The differences in the continuous propagation and turning of cracks in different minerals are mainly caused by different mechanical responses of the minerals. Figure 9 shows the superposition of the AE location and crack path. Owing to the low tensile and shear strengths of weak minerals such as kaolinite and illite, microcracks easily produced tensile or shear fractures, so there was no need to connect with the surrounding tensile microcracks.



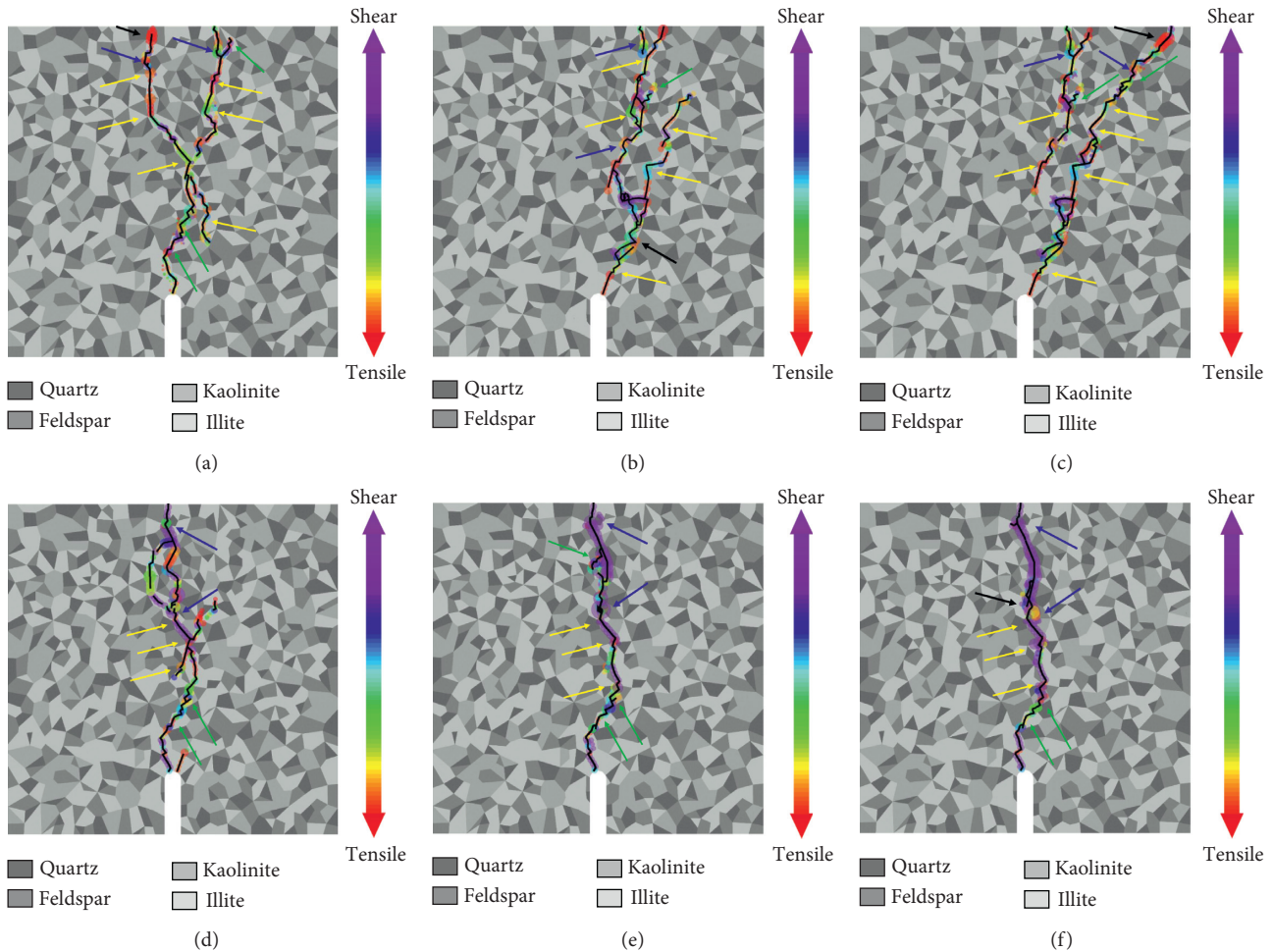


FIGURE 9: AE location on the fracture path under six different load methods. The yellow arrows refer to the crack growth in a wide region of kaolinite and illite, the green arrows refer to the crack growth in a small region of kaolinite and illite that was surrounded by quartz and feldspar, the blue arrows refer to the crack growth in the boundary of different minerals, and the black arrows refer to the crack growth in quartz and feldspar. Red dots are the AE location of tensile fractures, purple dots are the AE location of shear fractures, and the colors between the two are the AE location of tensile-shear fractures. The size of the dot represents the level of AE energy.

Therefore, in most cases, the crack propagation was relatively straight and the steering was relatively smooth. When weak minerals were surrounded by hard minerals such as quartz and feldspar, there were more external barriers to crack propagation, causing many types of mineral fractures. As a result, more crack inflections occurred. The tensile and shear strengths at the mineral boundary were higher than that of kaolinite and illite. Therefore, in loading methods I–III, the crack only extended at the mineral boundary for a short period of time and then went back into the weak mineral. The fracture types were all tensile fractures. Loading method IV mainly produced shear fractures at the mineral boundary. When the crack deviated from the maximum shear stress line (centerline), it connected to the tensile fracture occurred in the adjacent kaolinite and illite and then returned to the shear centerline. As the lateral pressure in loading methods V and VI increased, the tensile strength of kaolinite and illite increased, and it was not easy to generate tensile fracture. Therefore, the crack continued to extend

along the mineral boundary in the form of a shear arc. The tensile and shear strengths of quartz and feldspar were considerably high. The tensile strength was lower than the shear strength. Therefore, when cracks passed through the quartz and feldspar, they were all tensile fractures. In loading methods I and III, the situation when cracks passed through the quartz and feldspar was similar to that of breaking the last piece of strong supporting mineral, whereas in loading methods II and VI, the cracks broke the hard mineral after several inflections.

En echelon intermittent cracks were first proposed in macroscopic fractures. Cui and Han [31] observed discontinuous microcracks in experiments for the first time and explained their hierarchical structure. Figure 10 shows the AE location of small-scale en echelon intermittent crack initiation. The small-scale en echelon intermittent cracks were all blocked by strong minerals such as quartz and feldspar, and no cracks were generated in the strong minerals. The heterogeneous strain on strong and weak minerals

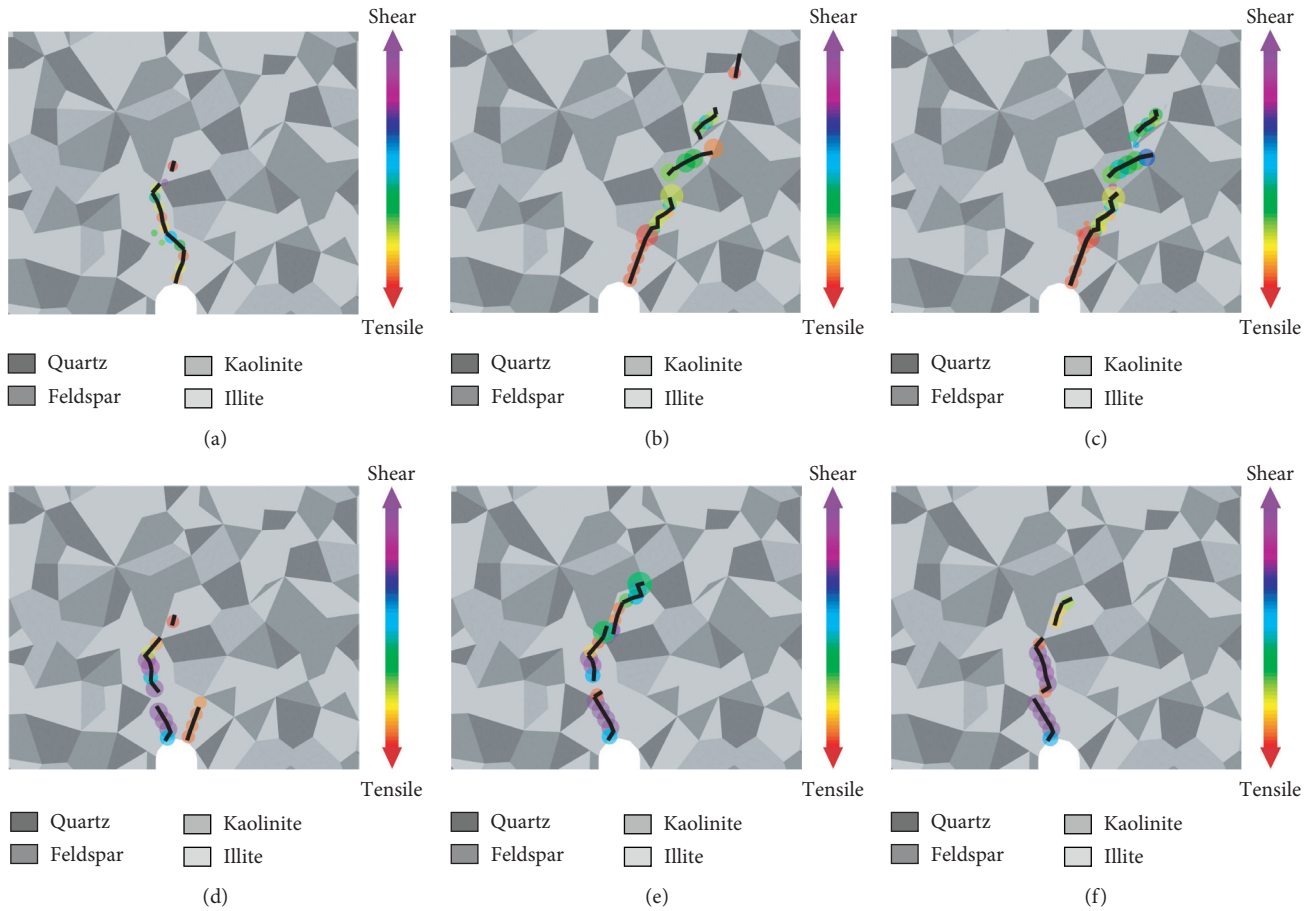


FIGURE 10: The initiation of small-scale en echelon intermittent fractures under six different load methods. Red dots are the AE location of tensile fractures, purple dots are the AE location of shear fractures, and the colors between the two are the AE location of tensile-shear fractures. The size of the dot represents the level of AE energy.

caused the weak minerals to reach failure displacement first, and thus, small-scale en echelon intermittent cracks were generated.

Based on this, the occurrence of large-scale en echelon intermittent cracks was also related to the barrier of strong mineral aggregates. The AE location of the second large-scale en echelon intermittent crack formation is shown in Figure 11, and there was no AE location in the strong mineral aggregates. The heterogeneous strain between the strong mineral aggregates and the weak minerals caused the weak minerals to be blocked by the strong mineral aggregates from reaching the failure displacement. Cui and Han [31] defined the position between the en echelon intermittent cracks as rock bridges. This study found that, regardless of the formation of large-scale or small-scale en echelon intermittent cracks, the rock bridges were composed of strong minerals or strong mineral aggregates.

Regardless of the scale of the en echelon intermittent crack, the spreading of cracks is related to the loading method. In loading methods I–III, en echelon intermittent cracks were mostly tensile fractures, and these were generated perpendicular to the direction of maximum tensile force. However, in loading methods IV–VI, en echelon intermittent cracks were mostly shear fractures, which were

generated in the direction close to the shear centerline, and the greater the lateral pressure, the more obvious this tendency. It is worth noting that during the formation of large-scale en echelon intermittent cracks in loading methods IV and V, the shear strain was concentrated at both ends of the centerline; therefore, the middle part of the rock did not reach displacement due to shear failure but reached displacement from tensile failure. As the lateral pressure increased, the length of the crack in the middle of the rock decreased. In loading method VI, no cracks occurred in the middle part of the rock, and shear fracture occurred in the upper part. Consistent with the previous analysis, lateral pressure suppressed the occurrence of tensile fracture.

Wing cracks were the most common connection types for en echelon intermittent cracks. When there were strong minerals or strong mineral aggregates in the en echelon intermittent cracks, the wing cracks bypassed the strong minerals or strong mineral aggregates to produce fragmented connections. The AE location of the fragment formation process for loading method IV is shown in Figure 12. As the shear force could not cut the strong mineral aggregates (shown in Figure 8), tensile microcracks were formed on the right side of the shear crack. The cracks connected to the tensile microcracks around the boundary of

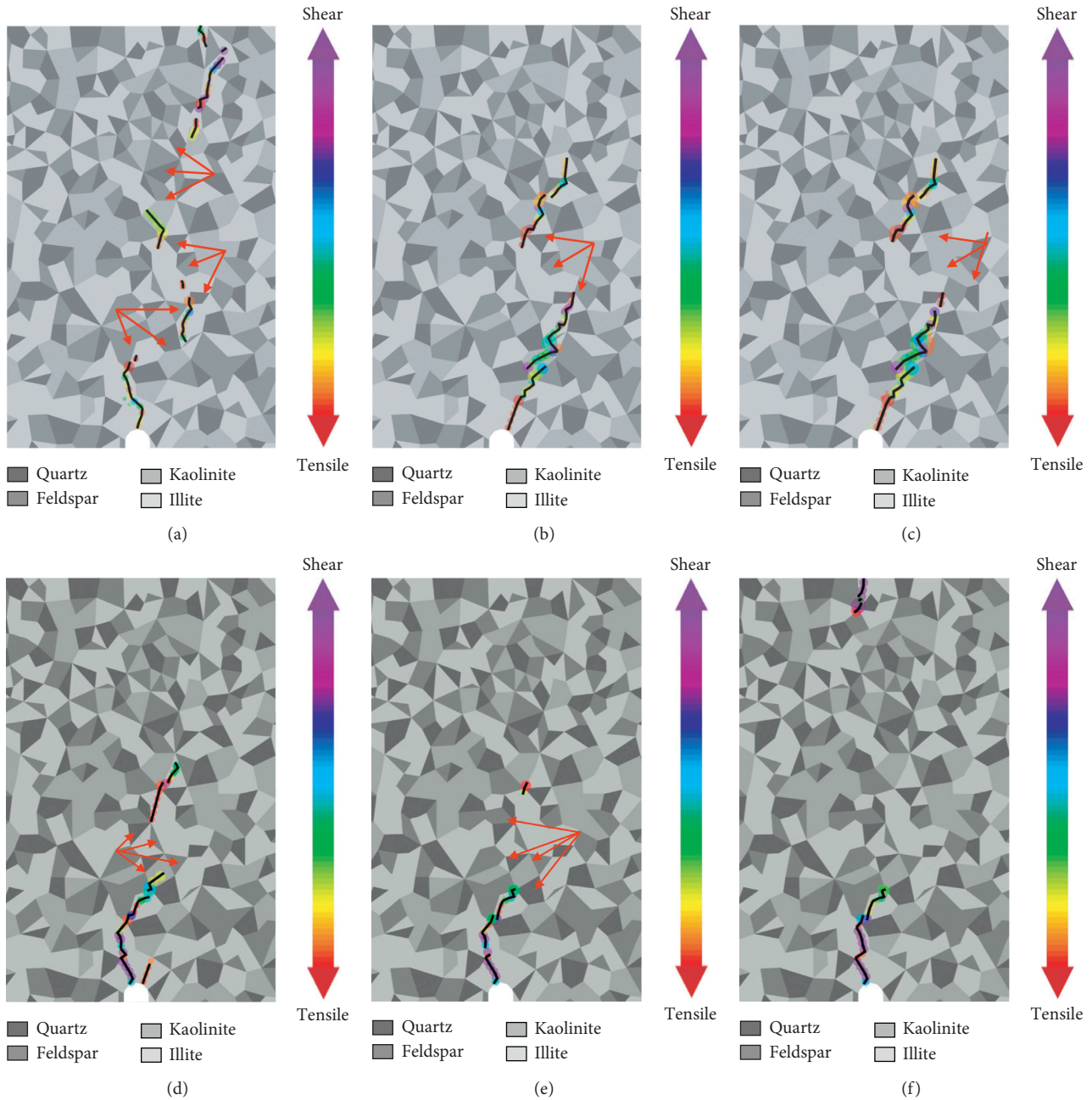


FIGURE 11: The AE location when the second large-scale en echelon intermittent fractures were formed under six different loading methods. The red arrows refer to the strong mineral aggregate. Red dots are the AE location of tensile fractures, purple dots are the AE location of shear fractures, and the colors between the two are the AE location of tensile-shear fractures. The size of the dot represents the level of AE energy.

the strong mineral aggregates and eventually formed fragments. In loading methods II and III, the tensile microcracks had a large distribution range, so there were many small fragments. The lateral pressure in loading methods V and VI restrained the generation range of tensile microcracks. As lateral pressure increased, the size of the fragments decreased.

The AE location of the X-shaped crack formation process for loading methods I and IV is shown in Figure 13. In loading method I, tensile microcracks were widely generated, and en echelon intermittent cracks with different directions were formed. When the en echelon intermittent

cracks extended to the center, they met in the middle to form an X-shaped crack. However, in loading method IV, the en echelon intermittent crack in the middle of the rock was blocked by strong minerals and could not continue to grow. Shear microcracks that extended to the upper left formed in the middle of the crack under shear loading. The crack in the lower part propagated and connected to it, forming an X-shaped crack. The spreading range of tensile microcracks is larger than that of shear microcracks. Therefore, the size of the X crack in loading method I is larger than that in loading method IV.

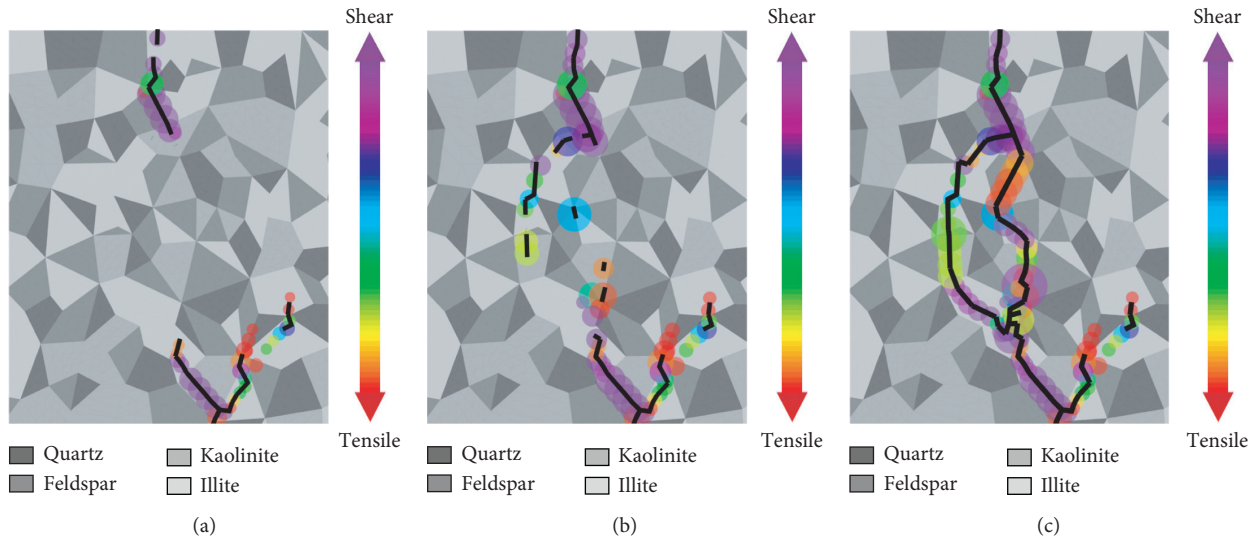


FIGURE 12: The formation process and AE location of fragment in loading method IV. Red dots are the AE location of tensile fractures, purple dots are the AE location of shear fractures, and the colors between the two are the AE location of tensile-shear fractures. The size of the dot represents the level of AE energy.

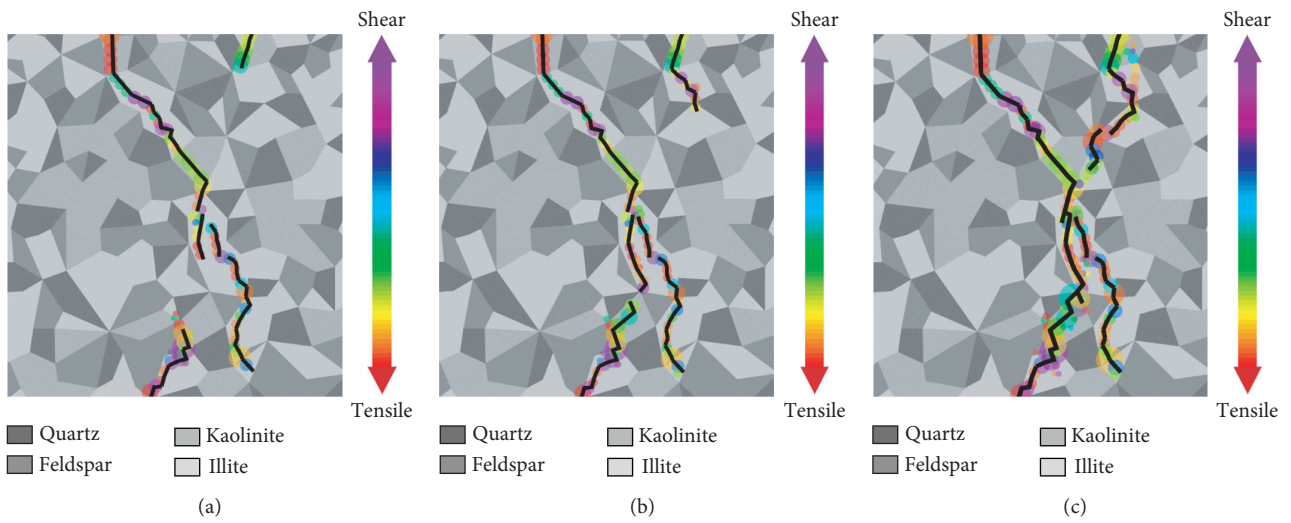


FIGURE 13: Continued.

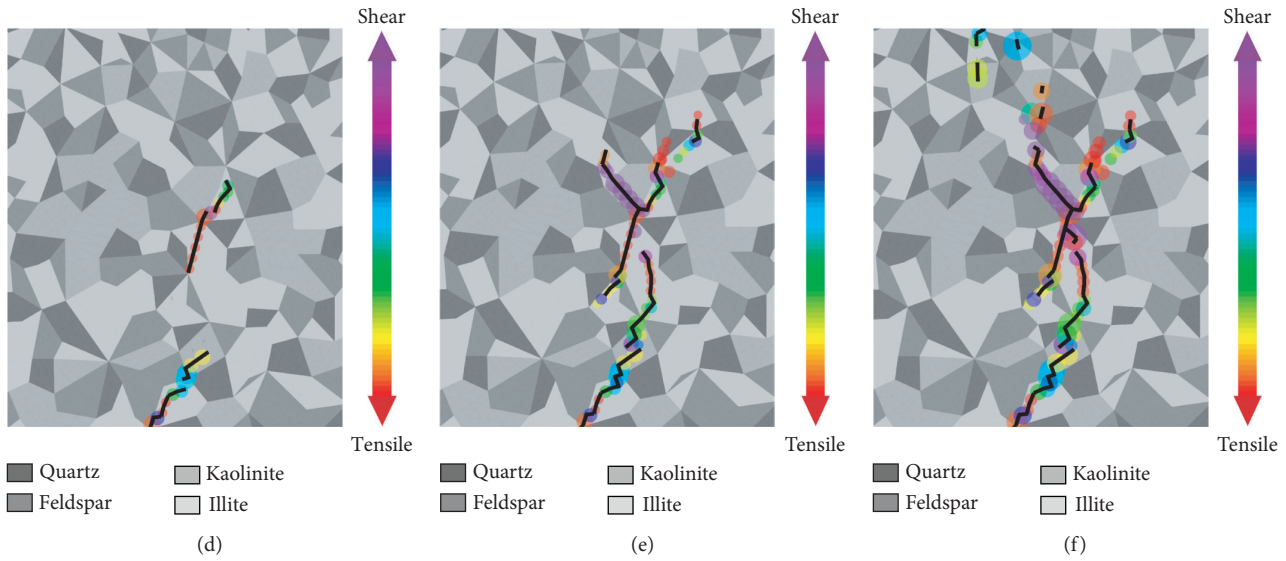


FIGURE 13: X fracture formation and AE location for loading methods I ((a), (b), (c)) and IV ((d), (e), (f)). Red dots are the AE location of tensile fractures, purple dots are the AE location of shear fractures, and the colors between the two are the AE location of tensile-shear fractures. The size of the dot represents the level of AE energy.

Following this research, in-depth studies can still be conducted in many aspects. In the future, we could set different degrees of mineral heterogeneity by ratio and size in each loading method to further confirm the role of heterogeneity and the loading method. For different loading methods, further study is needed on the similarities and differences in the en echelon intermittent crack connections when compared with connections between naturally occurring cracks, pores, and fissures. Previous studies used fractal theory to summarize the multiscale and hierarchical distribution of cracks [11], and it was found that the en echelon intermittent cracks also show the characteristics of multiscale and hierarchical distribution. The fractal study of en echelon intermittent cracks should consider the effects of loading methods, mineral heterogeneity, pores, natural fissures, and bedding. Besides, how to make the en echelon intermittent cracks more fully connected is also an important issue for the improvement of shale gas recovery. This study provides a significant reference for future research for the loading method to increase the complexity of fractures. The combination of fractal dimension and crack length per unit area demonstrated here is a promising way to evaluate the effect of fracturing in future studies.

## 6. Conclusions

In this study, the Voronoi tessellation technique was used to establish a shale CZM based on mineral distribution, and six different loading methods were applied. Based on the rock damage theory, combined with the crack path, strain contour, and AE, the initiation and propagation of microcracks under different loading methods were compared and analyzed. The following are the main conclusions drawn from this study.

- (1) The essence of different loading methods affecting crack length and complexity was the spread range of tensile microcracks. Tensile loading formed a large

number of widely distributed tensile microcracks in the rock, so the crack length was longer and the twists and turns were more complicated. In contrast, shear loading only produced parallel tensile microcracks on the right side of the maximum shear line, and the cracks tended to extend along the direction of the maximum shear force, resulting in a shorter crack length and low complexity.

- (2) The mechanical properties of various minerals and mineral boundaries are different; therefore, the mechanical responses to different loading methods are different. This leads to differences in continuous crack propagation and steering under different loading methods.
- (3) The formation and propagation of en echelon intermittent cracks of different scales were mainly affected by the heterogeneity of minerals and mineral aggregates. The differences in displacements at failure of different minerals led to the generation of small-scale en echelon intermittent cracks separated by strong minerals. Similarly, the differences in displacements at failure of different mineral aggregates led to the generation of large-scale en echelon intermittent cracks separated by strong mineral aggregates.
- (4) The spreading direction and connection form of en echelon intermittent cracks were mainly affected by the loading method. The en echelon intermittent cracks propagated perpendicular to the direction of maximum tensile stress during tensile and tensile-shear loading, with various connection methods. In shear and compression-shear loading, the en echelon intermittent cracks spread near the maximum shear stress line. As the lateral pressure increased, the cracks tended to concentrate more on the centerline, and the connection method became simpler.

## Data Availability

The data used to support this study will be made available from the corresponding author upon request.

## Conflicts of Interest

The authors declare no conflicts of interest.

## Acknowledgments

This work was supported by the National Key Research and Development Project (Grant No. 2019YFC1509705), the Second Tibetan Plateau Scientific Expedition and Research Program (STEP) (Grant No. 2019QZKK0904), and the National Natural Science Foundation of China (Grant No. 41972296).

## References

- [1] Y. Fujii, T. Takemura, M. Takahashi, and W. Lin, "Surface features of uniaxial tensile fractures and their relation to rock anisotropy in Inada granite," *International Journal of Rock Mechanics and Mining Sciences*, vol. 44, no. 1, pp. 98–107, 2007.
- [2] J. Zhong, S. Liu, Y. Ma et al., "Macro-fracture mode and micro-fracture mechanism of shale," *Petroleum Exploration and Development*, vol. 42, no. 2, pp. 269–276, 2015.
- [3] H. Daigle, N. W. Hayman, E. D. Kelly, K. L. Milliken, and H. Jiang, "Fracture capture of organic pores in shales," *Geophysical Research Letters*, vol. 44, no. 5, pp. 2167–2176, 2017.
- [4] Y. Cheng and L. N. Y. Wong, "Microscopic characterization of tensile and shear fracturing in progressive failure in marble," *Journal of Geophysical Research: Solid Earth*, vol. 123, no. 1, pp. 204–225, 2018.
- [5] H. X. Lan, J. H. Chen, and Y. M. Wu, "Spatial characterization of micro and nanoscale micro-cracks in gas shale before and after triaxial compression test," *Engineering Geology*, vol. 26, no. 1, pp. 24–35, 2018.
- [6] Y. Zhao, J. Huang, and R. Wang, "Real-time SEM observations of the microfracturing process in rock during a compression test," *International Journal of Rock Mechanics and Mining Sciences & Geomechanics Abstracts*, vol. 30, no. 6, pp. 643–652, 1993.
- [7] Z. D. Cui, D. A. Liu, X. Li et al., "In-situ observation on the micro-nano cracks of shale," *Chinese Journal of Underground Space and Engineering*, vol. 13, no. 1, pp. 117–123, 2017.
- [8] Z. D. Cui, X. Li, D. A. Liu et al., "In-situ observation of en echelon intermittent cracks of shale in micro-nano scale," *Engineering Geology*, vol. 26, no. 1, pp. 85–90, 2018.
- [9] J.-P. Zuo, Y.-L. Li, C. Liu et al., "Meso-fracture mechanism and its fracture toughness analysis of Longmaxi shale including different angles by means of M-SENB tests," *Engineering Fracture Mechanics*, vol. 215, pp. 178–192, 2019.
- [10] J. N. Dong, Y. Jin, M. Chen et al., "Study on shale fracture toughness and micro-characterization of mode I crack using DCB specimen and SEM method," *Chinese Journal of Underground Space and Engineering*, vol. 15, no. S1, pp. 205–210, 2019.
- [11] H.-D. Tang, "Multi-scale crack propagation and damage acceleration during uniaxial compression of marble," *International Journal of Rock Mechanics and Mining Sciences*, vol. 131, p. 104330, 2020.
- [12] F. Renard, J. McBeck, N. Kandula, B. Cordonnier, P. Meakin, and Y. Ben-Zion, "Volumetric and shear processes in crystalline rock approaching faulting," *Proceedings of the National Academy of Sciences*, vol. 116, no. 33, pp. 16234–16239, 2019.
- [13] T. Kazerani and J. Zhao, "Micromechanical parameters in bonded particle method for modelling of brittle material failure," *International Journal for Numerical and Analytical Methods in Geomechanics*, vol. 34, no. 18, pp. 1877–1895, 2010.
- [14] F. Q. Gao and D. Stead, "The application of a modified Voronoi logic to brittle fracture modelling at the laboratory and field scale," *International Journal of Rock Mechanics and Mining Sciences*, vol. 68, pp. 1–14, 2014.
- [15] X. Wang and M. Cai, "Modeling of brittle rock failure considering inter- and intra-grain contact failures," *Computers and Geotechnics*, vol. 101, pp. 224–244, 2018.
- [16] E. Ghazvinian, M. S. Diederichs, and R. Quey, "3D random Voronoi grain-based models for simulation of brittle rock damage and fabric-guided micro-fracturing," *Journal of Rock Mechanics and Geotechnical Engineering*, vol. 6, no. 6, pp. 506–521, 2014.
- [17] X. F. Li, H. B. Li, and J. Zhao, "3D polycrystalline discrete element method (3PDEM) for simulation of crack initiation and propagation in granular rock," *Computers and Geotechnics*, vol. 90, pp. 96–112, 2017.
- [18] R. P. Bewick, P. K. Kaiser, W. F. Bawden, and N. Bahrani, "DEM simulation of direct shear: 1. Rupture under constant normal stress boundary conditions," *Rock Mechanics and Rock Engineering*, vol. 47, no. 5, pp. 1647–1671, 2014.
- [19] R. P. Bewick, P. K. Kaiser, and W. F. Bawden, "DEM simulation of direct shear: 2. Grain boundary and mineral grain strength component influence on shear rupture," *Rock Mechanics and Rock Engineering*, vol. 47, no. 5, pp. 1673–1692, 2014.
- [20] A. Abdelaziz, Q. Zhao, and G. Grasselli, "Grain based modelling of rocks using the combined finite-discrete element method," *Computers and Geotechnics*, vol. 103, pp. 73–81, 2018.
- [21] X. F. Li, H. B. Li, and J. Zhao, "The role of transgranular capability in grain-based modelling of crystalline rocks," *Computers and Geotechnics*, vol. 110, pp. 161–183, 2019.
- [22] X. F. Li, H. B. Li, L. W. Liu, Y. Q. Liu, M. H. Ju, and J. Zhao, "Investigating the crack initiation and propagation mechanism in brittle rocks using grain-based finite-discrete element method," *International Journal of Rock Mechanics and Mining Sciences*, vol. 127, pp. 1–20, 2020.
- [23] H. Lan, C. D. Martin, and B. Hu, "Effect of heterogeneity of brittle rock on micromechanical extensile behavior during compression loading," *Journal of Geophysical Research*, vol. 115, no. B1, 2010.
- [24] H. Xu, G. Wang, C. Fan, X. Liu, and M. Wu, "Grain-scale reconstruction and simulation of coal mechanical deformation and failure behaviors using combined SEM digital rock data and DEM simulator," *Powder Technology*, vol. 360, pp. 1305–1320, 2020.
- [25] J. Zhou, H. Lan, L. Zhang, D. Yang, J. Song, and S. Wang, "Novel grain-based model for simulation of brittle failure of Alxa porphyritic granite," *Engineering Geology*, vol. 251, pp. 100–114, 2019.
- [26] M. Saadat and A. Taheri, "A cohesive grain based model to simulate shear behaviour of rock joints with asperity damage in polycrystalline rock," *Computers and Geotechnics*, vol. 117, p. 103254, 2020.

- [27] A. Ougier-Simonin, F. Renard, C. Boehm, and S. Vidal-Gilbert, "Microfracturing and microporosity in shales," *Earth-Science Reviews*, vol. 162, pp. 198–226, 2016.
- [28] W. Zeng, J. Zhang, W. Ding et al., "Fracture development in Paleozoic shale of Chongqing area (South China). Part one: fracture characteristics and comparative analysis of main controlling factors," *Journal of Asian Earth Sciences*, vol. 75, pp. 251–266, 2013.
- [29] X. Guo, Y. Li, R. Liu, and Q. Wang, "Characteristics and controlling factors of micropore structures of the Longmaxi shale in the Jiaoshiba area, Sichuan basin," *Natural Gas Industry B*, vol. 1, no. 2, pp. 165–171, 2014.
- [30] S. B. Tang, X. J. Liu, J. Luo, and Z. Dong, "Theoretical model for tensile and shear crack initiation at the crack tip in rock subjected to hydraulic pressure," *Chinese Journal of Rock Mechanics and Engineering*, vol. 36, no. 9, pp. 2124–2135, 2017.
- [31] Z. Cui and W. Han, "In situ Scanning electron microscope (SEM) observations of damage and crack growth of shale," *Microscopy and Microanalysis*, vol. 24, no. 2, pp. 107–115, 2018.
- [32] H. P. Xie, J. F. Liu, Y. Ju, J. Li, and L. Z. Xie, "Fractal property of spatial distribution of acoustic emissions during the failure process of bedded rock salt," *International Journal of Rock Mechanics and Mining Sciences*, vol. 48, no. 8, pp. 1344–1351, 2011.
- [33] J. M. Ramsey and F. M. Chester, "Hybrid fracture and the transition from extension fracture to shear fracture," *Nature*, vol. 428, no. 6978, pp. 63–66, 2004.
- [34] F. K. Xiao, G. Liu, T. Qin et al., "Acoustic emission (AE) characteristics of fine sandstone and coarse sandstone fracture process under tension-compression-shear stress," *Chinese Journal of Rock Mechanics and Rock Engineering*, vol. 35, no. S2, pp. 3458–3472, 2016.
- [35] Z. Wu, F. Yu, P. Zhang, and X. Liu, "Micro-mechanism study on rock breaking behavior under water jet impact using coupled SPH-FEM/DEM method with Voronoi grains," *Engineering Analysis with Boundary Elements*, vol. 108, pp. 472–483, 2019.
- [36] D. S. Dugdale, "Yielding of steel sheets containing slits," *Journal of the Mechanics and Physics of Solids*, vol. 8, no. 2, pp. 100–104, 1960.
- [37] G. I. Barenblatt, "The mathematical theory of equilibrium cracks in brittle fracture," *Advances in Applied Mechanics*, vol. 7, pp. 55–129, 1962.
- [38] M. Shen, H. Liu, and J. S. Yu, "Measurement of traction separation curve in cohesive zone of material fracture," *Experimental Mechanics*, vol. 33, no. 3, pp. 395–409, 2018.
- [39] J. L. Strom and J. P. Parmigiani, "Transition of crack path at bi-material interfaces," *Engineering Fracture Mechanics*, vol. 115, no. 1, pp. 13–21, 2014.
- [40] W. Han, Z. Cui, and J. Zhang, "Fracture path interaction of two adjacent perforations subjected to different injection rate increments," *Computers and Geotechnics*, vol. 122, 2020.
- [41] L. Ji, M. Lin, G. Cao, and W. Jiang, "A core-scale reconstructing method for shale," *Scientific Reports*, vol. 9, p. 4364, 2019.
- [42] F. J. Uim and Y. Abousleiman, "The nanogranular nature of shale," *Acta Geotechnica*, vol. 1, no. 2, pp. 77–88, 2006.
- [43] V. Kumar, M. E. Curtis, N. Gupta, C. H. Sondergeld, and C. S. Rai, "Estimation of elastic properties of organic matter in woodford shale through nanoindentation measurements," in *The Proceedings of the SPE Canadian Unconventional Resources Conference*, Society of Petroleum Engineers, Calgary, Alberta, Canada, October 2012.
- [44] A. Deirieh, J. A. Ortega, F.-J. Ulm, and Y. Abousleiman, "Nanochemomechanical assessment of shale: a coupled WDS-indentation analysis," *Acta Geotechnica*, vol. 7, no. 4, pp. 271–295, 2012.
- [45] S. Abedi, M. Slim, R. Hofmann, T. Bryndzia, and F.-J. Ulm, "Nanochemo-mechanical signature of organic-rich shales: a coupled indentation-EDX analysis," *Acta Geotechnica*, vol. 11, no. 3, pp. 559–572, 2016.
- [46] T.-F. Wong, R. H. C. Wong, K. T. Chau, and C. A. Tang, "Microcrack statistics, Weibull distribution and micro-mechanical modeling of compressive failure in rock," *Mechanics of Materials*, vol. 38, no. 7, pp. 664–681, 2006.

## Research Article

# Dynamic Mechanical Characteristics of Fractured Rock Reinforced by Different Grouts

Siming Kao , Guangming Zhao , Xiangrui Meng, Yingming Li , Zenghui Liu, Ruofei Zhang, Jun Zhou, and Shunjie Huang 

State Key Laboratory of Mining Response and Disaster Prevention and Control in Deep Coal Mines, Anhui University of Science and Technology, Huainan 232001, China

Correspondence should be addressed to Guangming Zhao; [guangmingzhao@163.com](mailto:guangmingzhao@163.com)

Received 28 September 2020; Revised 25 November 2020; Accepted 17 January 2021; Published 29 January 2021

Academic Editor: Zhi Cheng Tang

Copyright © 2021 Siming Kao et al. This is an open access article distributed under the Creative Commons Attribution License, which permits unrestricted use, distribution, and reproduction in any medium, provided the original work is properly cited.

In order to investigate the dynamic mechanical properties of the fractured rocks reinforced with different slurries, the prefabricated and grouted sandy mudstone specimens were tested on a Split Hopkinson Pressure Bar (SHPB), and their dynamic failure processes were shot via a high-speed camera. The test results showed that under dynamic loading, grouting reinforcement can relieve the rock failure at the fracture part. With the increase of the impact speed, the dynamic specific strength of the modified epoxy resin grouting increases from 0.85 to 1.01, and its specific strain rate increases from 1.09 to 1.04; the dynamic specific strength and specific strain rate of cement slurry grouting increase from 1.78 to 0.95 and from 0.60 to 0.98, respectively. As a whole, the specimen reaches or approaches the dynamic parameters of the intact rock specimen after grouting repair, the stability of the rock reinforced by modified epoxy resin grouting is superior to that of the rock reinforced by cement slurry grouting, and the latter can acquire high dynamic strength under low-speed impact. The improved damage-type Zhuwangtang (ZWT) model can be used to describe the dynamic mechanical behaviors of the fractured rocks reinforced by grouting very well.

## 1. Introduction

During the deep coal mining and tunneling process, the mining activity breaks the original mechanical equilibrium. According to the theory of loose circle of surrounding rocks [1], a crushed zone will appear within a certain range of the roadway, and many fractures exist in the surrounding rock mass. If the fractured zone is not properly disposed, the original fractured zone may further evolve into a crushed zone due to the impact load generated by blasting in the construction, vibrating effect of surrounding rocks tunneled by heading machine, and the impact formed by roof fracture of the coal seam, and thus the support difficulty will be further aggravated. The grouting construction method can improve the physical and mechanical properties of the reinforced surrounding rocks and block the original fractures, so as to improve the overall strength and stability of the surrounding rocks. Therefore, the grouting construction method has been extensively applied in engineering practice.

The grouting reinforcement of rock mass has been extensively investigated both in China and western countries. In the aspects of rock grouting reinforcement mechanism and repair of fractured rocks, it is deemed that after grouting reinforcement, the residual strength [2] and peak shear strength [3] of the rock mass will be improved, the non-deformability will be strengthened, and the grouting concretion stone can keep stable bearing capacity within a large range. Although the rock strength will be improved after it is reinforced by common grouting materials such as cement slurry, polyurethane, and epoxy resin [4–6], different slurries exert different reinforcing effects on rocks or rock-like materials, and they differ in slurry groutability, initial strength and cohesiveness to rocks, etc. Among the factors influencing the grouting reinforcement, the slurry diffusion laws during the construction and slurry stability after the construction are also very important, so investigating the slurry diffusion laws under all kinds of conditions [7–10] and quantitatively evaluating the slurry stability [11] under



different grouting parameters will be of great importance. As the geological environment for grouting is ever-changing, the individual demands for grouting materials in engineering are increasing year by year, and regarding slurry groutability, controllability, stability, and durability and economical efficiency, many scholars have developed new-type grouting materials, made modifications, and achieved abundant results [12–15]. The dynamic characteristics of grouting concretion stones with different grouting contents and moisture contents have been probed in recent years [16].

Most of the above research studies focus on the improvement of static mechanical properties of rock mass after grouting reinforcement, the grouting reinforcement effect, slurry diffusion laws, and slurry modification. These research studies are significant for revealing the rock grouting reinforcement mechanism and improving the grouting reinforcement effect. However, few studies have focus on the impact resistance of fractured rock mass after grouting reinforcement under different strain rates, the reinforcing effects of different slurries on fractured rock mass, and failure laws of fractured rock mass and those of fractured rock mass after grouting reinforcement under the dynamic impact load. After grouting, the fractured rock mass may bear blasting impact load, roof fracture impact, and dynamic disturbance of heading machine. The range of dynamic load strain rate is large and the impact strength is high, which will usually result in secondary failure of fractured rock mass after grouting reinforcement. Hence, it is urgent to explore into the impact resistance and failure laws of fractured rock mass after grouting reinforcement, and then studying the dynamic characteristics of fractured rock masses reinforced by different slurries under different strain rates will be of great realistic significance.

In this paper, the sandy mudstone specimens were preset fractures manually, and the fractures were filled with cement slurry and modified epoxy resin slurry. An impact test of fractured rock masses reinforced by different grouting materials was carried out under different strain rates on a Split Hopkinson Pressure Bar (SHPB), and their dynamic failure process was captured via a high-speed camera. The results contributed to understanding of the dynamic failure laws of fractured surrounding rocks, revealed the impact resistance of fractured rock masses reinforced with different slurries under different strain rates, and provided a reference for the grouting reinforcement engineering for fractured rock mass.

## 2. Test Materials and Test Method

**2.1. Test Materials.** The rock used in the test was common sandy mudstone in coal mining and tunnel engineering. The rock masses were collected from Luling Coal Mine of the Huaibei Mining Group with burial depth of  $-580.5$  m, density of  $2,560 \text{ kg} \times \text{m}^{-3}$ , and uniaxial compressive strength of  $22.5 \text{ MPa}$ .

**2.2. Test Method.** The rock cores of intact rock masses with good homogeneity were taken using a vertical core drilling

machine. The rock cores were cut with a rock cutter according to the length slightly greater than the design size. The specimens were processed according to rock mechanics test requirements, and the two end faces of each specimen were grinded with SHM-200 double-end-face grinding machine until its nonparallelism and nonperpendicularity were both not smaller than  $0.02 \text{ m}$ . The processed specimen is  $30 \text{ mm}$  in length and  $50 \text{ mm}$  in diameter. To mitigate the impact of fracture size on the specimens, a  $0.2 \text{ mm}$  fracture was cut from the cross section of each specimen with the cutter, and the cutting depth was one half of the specimen diameter. The specimens with cut fractures were grouped, where one group was kept in original shape; one group was filled with neat cement grout (water cement ratio:  $0.6$ ), and the cement was ordinary Portland cement with mark of P.O 42.5; another group was filled with high-permeability modified epoxy resin grouting material, which was double-component grouting material, where material A was the prepared epoxy resin and material B was curing agent, and their mixing ratio was  $2:1$ .

The specimen was intertwined for one circle using adhesive tape before grouting, and a grouting hole was reserved at the top. The mixed slurry was slowly injected into the fracture with an injector and gently vibrated with  $0.1 \text{ mm}$  steel wire to eliminate the gas sealed in the fracture. After the fracture was fully filled with the slurry, the hole mouth was kept upward for  $24 \text{ h}$ , the cement and epoxy resin were initially coagulated, and the external adhesive tape was taken down for the sake of curing. The cement grouting specimens were cured in a standard curing box while epoxy resin grouting specimens were cured at normal temperature. After  $28$  days of curing, the wave velocity of each specimen is measured, and the specimens with obvious abnormal wave velocity are excluded. The three types of specimens are shown in Figure 1.

**2.3. Test System and Test Principle.** Bars and punches used in the SHPB test system (Figure 2) are 40Cr alloy steels, density is  $7,800 \text{ kg} \times \text{m}^{-3}$ , yield strength is greater than  $800 \text{ MPa}$ , elastic wave velocity  $C_0$  is  $5,410 \text{ m} \times \text{s}^{-1}$ , bar diameter is  $50 \text{ mm}$ , and lengths of the incident bar and transmitting bar are  $2.00 \text{ m}$  and  $1.50 \text{ m}$ , respectively. Punches are cone-shaped punches recommended by the International Society for Rock Mechanics [17], and its maximum diameter is  $50 \text{ mm}$ . According to 1D elasticity theory of waves, average stress, average strain, and average strain rate of samples can be obtained [18], namely,

$$\sigma_s(t) = \frac{EA}{2A_s} [\varepsilon_I(t) + \varepsilon_R(t) + \varepsilon_T(t)], \quad (1)$$

$$\varepsilon_s(t) = \frac{C_0}{L_s} \int_0^t [\varepsilon_T(t) - \varepsilon_I(t) + \varepsilon_R(t)] dt, \quad (2)$$

$$\dot{\varepsilon}_s(t) = \frac{C_0}{L_s} [\varepsilon_T(t) - \varepsilon_I(t) + \varepsilon_R(t)], \quad (3)$$

where  $L_s$  is the sample length;  $E$  is the elasticity modulus of the incident (transmitting) bar;  $A$  and  $A_s$  are the cross-

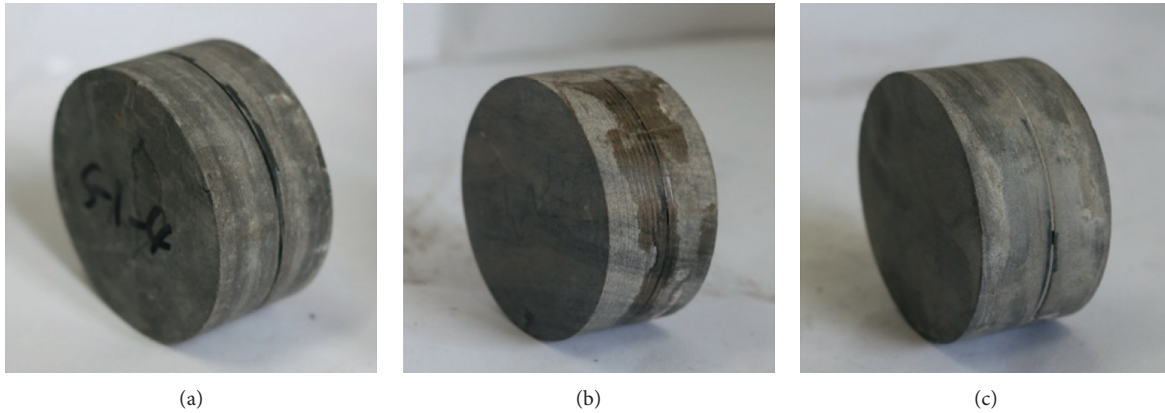


FIGURE 1: Specimens: (a) fracture specimen, (b) modified epoxy resin grouting, and (c) cement grouting.



FIGURE 2: SHPB test system.

sectional area of the incident (transmitting) bar and the sample;  $\varepsilon_I(t)$  is the incident wave strain signal;  $\varepsilon_R(t)$  is the reflected wave strain signal;  $\varepsilon_T(t)$  is the transmitted wave strain signal. To prevent the influence of stress unbalance on the test result, data are processed in this test through the “3-wave analysis” method.

**2.4. Testing Program.** The processed and cured specimens were grouped and numbered. To keep the acquired impact speeds of specimens in different groups under the same atmospheric pressure as consistent as possible, the test started from a low atmospheric pressure level. After the specimens in Group A, B, C, and D were tested under fixed atmospheric pressure, the test was continued by elevating the atmospheric pressure to the next pressure level. The concrete testing program is seen in Table 1.

### 3. Results and Discussion

**3.1. Dynamic Stress Equilibrium.** A reliable dynamic test should ensure that the dynamic stress equilibrium before the specimen is destroyed [19]. Therefore, it is necessary to check

the dynamic stress equilibrium to ensure the validity of the test. The dynamic stress at both ends of the specimen during the loading process can be obtained by the strain gauge on the bar. It can be seen from the curve that the stress at the transmission end of the specimen is less than that at the incident end within  $25 \mu\text{s}$  at the initial loading stage. During this period, the stress wave was reflected in the specimen for many times, and the dynamic stress at both ends of the specimen reached a state of equilibrium, while the stress equilibrium time was less than the failure time of the specimen, thus ensuring that the failure of the specimen occurred after the stress equilibrium. The typical dynamic stress at both ends of the specimen is shown in Figure 3.

**3.2. Influence of Grouting Reinforcement on Dynamic Stress-Strain Relationship of Fractured Rock Mass.** As an important index used to study material properties, the stress-strain relationship of a material is its own mechanical property, which can reflect its deformation and failure laws under the external loading action. The impact failure laws of fractured rock can be judged, and the rock grouting reinforcement effect can be verified through the dynamic stress-strain relationship.

TABLE 1: Test scheme.

Group	Specimen form	Grouting material	Number of specimens				
			0.2 MPa	0.4 MPa	0.6 MPa	0.8 MPa	1.0 MPa
A	Complete	None	3	3	3	3	3
B	Prefracture	None	3	3	3	3	3
C	Prefracture	Cement slurry	3	3	3	3	3
D	Prefracture	Modified epoxy resin	3	3	3	3	3

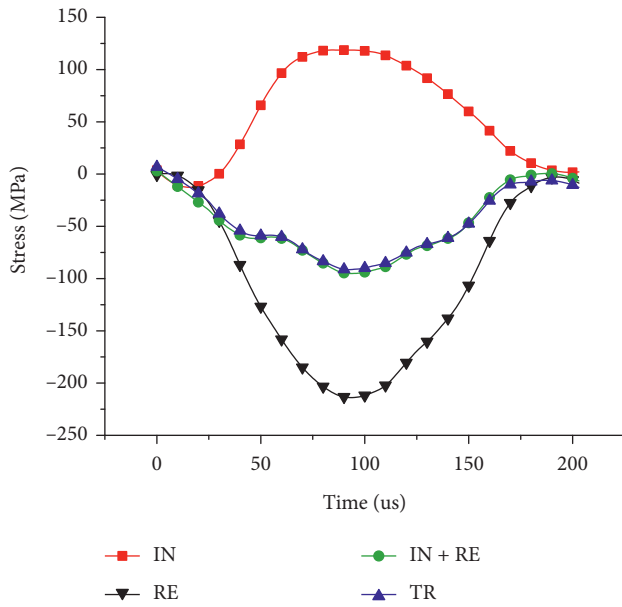


FIGURE 3: Typical dynamic stresses on both ends of specimen.

The delay time was calculated according to the specimen length, distance from strain gauge to bar end, and the wave propagation velocity in incident bar and transmission bar and specimen. The initial positions of wave forms were aligned through the translation waveform method, and the parameters of impact specimens such as stress and strain were calculated using the three-wave model. The stress-strain relationships of intact rock, fractured rock, fractured specimen filled with epoxy resin, and fractured specimen filled with cement slurry under gas pressure of 0.6 MPa are shown in Figure 4.

It could be observed from the stress-strain relation curves of all specimens under the same pressure that except for the stress-strain relation curve of the fractured specimen, the stress-strain relation curve shapes of other three specimens were basically similar and largely divided into four phases: elastic phase, below 60 MPa, was a straight-line part, at the time the stress and strain were under linear relation, and this linear relation might not be kept nearby 60 MPa–100 MPa, which should be the elastic limit of the specimen. Following elastic phase, there was a slightly flat part, namely, yield phase. After the yield phase, the stress-strain relation curve continued to rise until the limit of peak strength, namely, strengthening phase. Afterwards, each of the specimens would enter failure phase. Due to the existence of fracture, initial fracture occurred at the bottom of

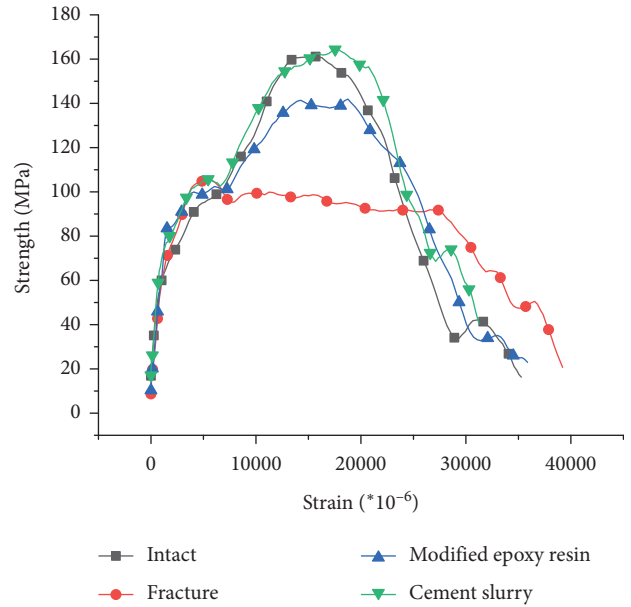


FIGURE 4: Stress-strain curve of four types of specimens (0.6 MPa).

the fracture of the fractured specimen after it entered the yield phase, and the stress firstly declined and then was kept unchanged, while the strain continued to increase without strengthening phase until secondary failure. Under low-speed impact with atmospheric pressure of 0.6 MPa, the peak strength of the fractured specimen filled with cement slurry was reached and even exceeded the peak strength of intact rock, but the peak strength of the fractured specimen filled with modified epoxy resin was somehow lower. The stress-strain curve of the fractured specimen filled with modified epoxy resin was flat at the peak point, indicating that the modified epoxy resin exerted a certain buffering effect on the fracture under low-speed impact. It could be intuitively seen from the stress-strain curves that the grouting reinforcement by filling the fracture could improve the mechanical properties of the rock and reach or approach the status of the original intact rock.

**3.3. Influence of Grouting Reinforcement on Dynamic Peak Strength of Fractured Rock Mass.** The dynamic compressive strength of rock is an important index reflecting its impact resistance. The effect of grouting reinforcement on the fractured rock can be judged through its strength. The average dynamic strength of specimens in each group was calculated, and the impact speed-peak strength relation curve was drawn as shown in Figure 5.

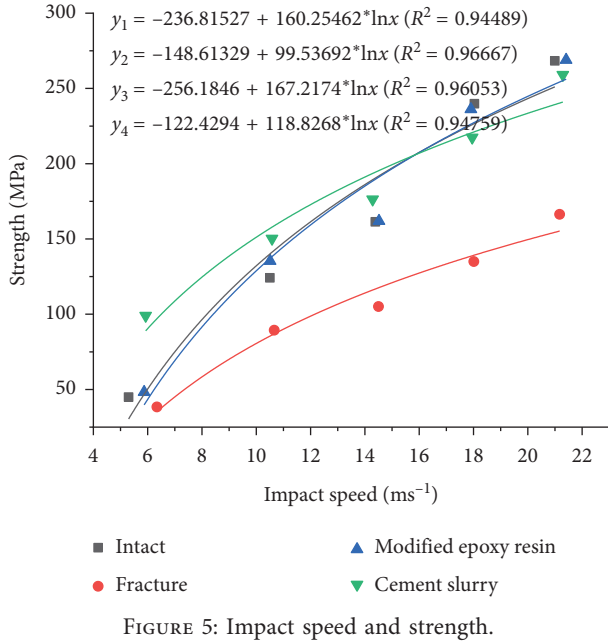


FIGURE 5: Impact speed and strength.

As shown in Figure 5, the peak strengths of the intact rock specimen, fractured rock specimen, and fractured specimen filled with slurry presented a natural logarithmic relationship with the impact speed of the punch. The strength of the fractured rock specimen was smaller than those of other three specimens under all impact speeds, and the strength gap was enlarged with the increase of impact speed. Taken the peak strength curve of the intact rock specimen as the reference, the peak strength curve of the specimen filled with epoxy resin was approximately overlapped with that of the intact specimen, indicating that the fracture filling with epoxy resin could effectively recover the strength of the fractured rock. Though being able to improve the strength of the fractured rock, fracture filling with cement slurry showed different properties from epoxy resin filling. Under low impact speed, the peak strength of the fractured rock filled with cement slurry was higher than that of the intact rock specimen. When the impact speed was elevated to above 16 m/s, the peak strength of the fractured rock filled with cement slurry was lower than that of the intact rock. The main reason was that microfractures would be formed at the filling interface after the cement slurry with high dry shrinkage rate was totally cured, and then the cement slurry filled specimen and fractured specimen shared approximate properties which could also be proved through the curve shape. Due to the existence of the microfractures, the microfractures had enough time to be closed under low-speed impact. As the strength of the filling cement was higher than that of sandy mudstone, its peak strength was higher than that of the intact sandy mudstone. The impact strain rate was high under high-speed impact, so the specimen that already underwent a failure before the microfractures were closed, the specimen strength bore greater influence from the fractures than from the strain rate, and thus the peak strength was slightly smaller than that of the intact specimen.

In the natural logarithm of impact speed taken as the  $x$ -coordinate and peak strength as the  $y$ -coordinate, the curve is drawn as seen in Figure 6.

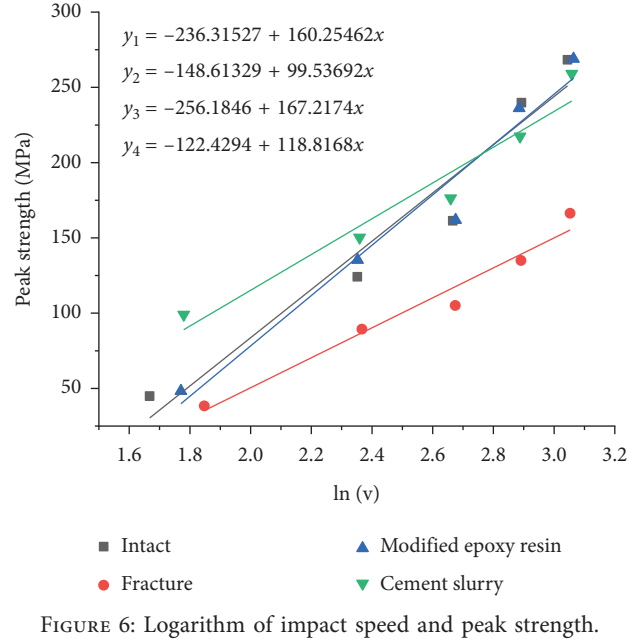


FIGURE 6: Logarithm of impact speed and peak strength.

The following was set:

$$k_1 = \frac{d\sigma}{d \ln(v)} \quad (4)$$

The slope of each fitting straight line could be solved as follows:

$$\begin{aligned} k_{\text{int}} &= 160.25462, \\ k_{\text{fra}} &= 99.53692, \\ k_{\text{epo}} &= 167.2174, \\ k_{\text{cem}} &= 118.8168. \end{aligned} \quad (5)$$

The straight slope (167.2174) of the specimen filled with epoxy resin was approximate to that (160.25462) of the intact specimen, and the two specimens had equivalent dynamic properties; the straight slope (118.8168) of the specimen filled with cement slurry was approximate to that (99.53692) of the fractured specimen, and their dynamic properties were approximate.

Taken the slope  $k$  value of the strength curve of the intact rock as the criterion, the factor reflecting the repair degree of other specimens was defined as follows:

$$\gamma_{ai} = \frac{k_i}{k} \times 100\%. \quad (6)$$

The repair factors of the specimens were calculated as seen in Table 2.

Through statistical Table 2, the fractured sandy mudstone filled with epoxy resin had equivalent properties to the original intact rock as a whole: the favorable reinforcement effect could be achieved, while the reinforcement effect of cement slurry was not as good as epoxy resin.

According to the fitted curve of test data, the peak strengths under different speeds were calculated. Taken the strength value of the intact specimen under each impact

TABLE 2: Statistical table of specimen repair factor  $\gamma_a$ .

Category	Intact	Fracture	Modified epoxy resin	Cement slurry
$k$	160.25462	99.53692	167.2174	118.8168
$\gamma_a$	100%	62.11%	104.34%	74.14%

speed as the criterion, the dynamic specific strength factor was defined as follows:

$$\eta_i = \frac{\sigma_i}{\sigma_{0i}} \quad (7)$$

The strength values of all specimens under different impact speeds were normalized (Table 3), and the dynamic specific strength factor-impact speed relation curve was drawn as shown in Figure 7.

By analyzing Table 3 and Figure 7, it can be obviously observed that the dynamic specific strength of the fractured specimen was approximately 0.6, that of the specimen filled with epoxy resin was 0.85 at low speed and 1 at both medium and high speed, and that of the specimen filled with cement slurry was 1.7 at low speed, declined to 1.00 or so at 16 m/s, and then was gradually reduced as the impact speed was further accelerated. The dynamic strength of the fractured specimen filled with cement slurry was superior to that of the specimen filled with epoxy resin under low-speed impact, but the situation was on the contrary under high-speed impact, and moreover, the properties of the specimen filled with epoxy resin were close to those of the intact specimen.

**3.4. Influence of Grouting Reinforcement on Strain Rate of Fractured Rock Mass.** Strain rate refers to the strain (deformation) change of a material relative to time, and it is a measure used to characterize the material deformation speed. The strain rate is related to both impact speed and material properties. Studies show that the dynamic impact strength is high at high strain rate. The strain rate-impact speed relations embodied in different specimens are displayed in Figure 8.

The middle flat parts were intercepted from the strain rate-time relation curves of the specimens as the samples, and the mean value of each specimen was taken as its strain rate. From the strain rate-impact speed relation curves, the strain rate of each specimen presented a linear relation with impact speed, namely, it was gradually increased with the impact speed, but the straight slope varied.

The following was set:

$$k'_i = \frac{d\dot{\epsilon}}{dv} \quad (8)$$

The slope of each fitting straight line was as follows:

$$\begin{aligned} k'_{\text{int}} &= 20.94325, \\ k'_{\text{fra}} &= 25.5988, \\ k'_{\text{epo}} &= 21.37621, \\ k'_{\text{cem}} &= 23.87668. \end{aligned} \quad (9)$$

The slope of the fractured specimen was the maximum, 25.59881, and its strain rate was most obviously influenced by

the impact speed. Because of the fracture, it could acquire greater strain under impact pressure, and thus its strain rate was higher than other specimens. The straight slope of the strain rate was 23.87668 for the cement slurry filled specimen, as microfractures would be formed after dry shrinkage of cement slurry. This type of specimen showed the characteristics of the fractured specimen, and its slope was also close to that of the fractured specimen, but its strain rate was lower, mainly because both strength and stiffness of the induration of cement slurry used to fill the specimen were larger than those of sandy mudstone. For the specimen filled with epoxy resin and the intact specimen, the straight slopes of strain rates were 21.37621 and 20.94325, respectively, which were quite close, along with equivalent properties. The straight slope of strain rate of the specimen filled with epoxy resin was slightly greater than that of the intact rock specimen, because the fracture filler was modified epoxy resin which was of a certain tenacity with hardness smaller than rock, and it could be easily deformed during the impact process.

Similarly, the slope  $k'$  value of the strain rate curve of the intact rock was taken as the criterion, and the factor used to reflect the repair degree of other specimens was defined as follows:

$$\gamma_{bi} = \frac{1}{(k'_i/k')} \times 100\%. \quad (10)$$

The damage repair factor of each specimen was calculated as seen in Table 4.

As seen in Table 4, in consideration of the overall strain rate, the repair degree of the fractured specimen filled with epoxy resin was approximate to the intact specimen, followed by the specimen filled with cement slurry. The main reason lied in that the epoxy resin filling material could be closely adhered to the specimen by virtue of high fluidity and high viscosity but low dry shrinkage rate. However, the cement slurry with poor fluidity was prone to bubbling, the shrinkage rate could be high after curing, and a weak plane could be easily generated on the surface of the filled fracture. This could be observed from Figures 9 and 10 after the specimen underwent crushing. The filling interface was separated from the specimen filled with cement slurry, indicating poor cohesive force of cement slurry. It could be seen from the separated grouting surface that the cured body of the slurry contained a small quantity of bubbles. For the specimen filled with epoxy resin, the cured slurry was still adhered to the specimen after the failure, while the failure degree at the nongrouting side was higher than that at the grouting side.

The strain rates under different impact speeds were calculated based on the fitted curves of their strain rate data. By taking the strain rate of the intact specimen as the criterion, the specific strain rate was defined as follows:

TABLE 3: Statistical table of specimen strength and dynamic specific strength.

Impact speed $\text{ms}^{-1}$	Strength (intact) (MPa)	Fracture		Modified epoxy resin		Cement slurry	
		Strength (MPa)	$\eta_1$	Strength (MPa)	$\eta_2$	Strength (MPa)	$\eta_3$
6	50.82	29.73	0.59	43.43	0.85	90.46	1.78
8	96.92	58.37	0.60	91.53	0.94	124.64	1.29
10	132.68	80.58	0.61	128.85	0.97	151.16	1.14
12	161.90	98.73	0.61	159.34	0.98	172.82	1.07
14	186.61	114.07	0.61	185.11	0.99	191.13	1.02
16	208.00	127.36	0.61	207.44	1.00	207.00	1.00
18	226.88	139.09	0.61	227.14	1.00	221.00	0.97
20	243.76	149.57	0.61	244.75	1.00	233.51	0.96
22	259.04	159.06	0.61	260.69	1.01	244.84	0.95

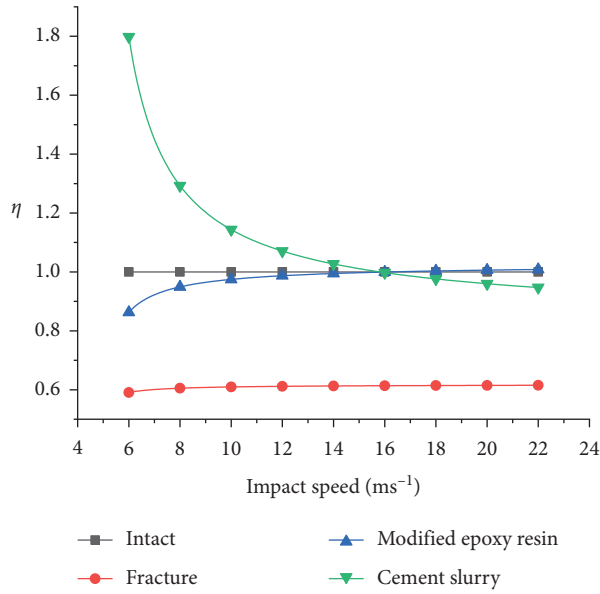


FIGURE 7: Impact speed-dynamic specific strength.

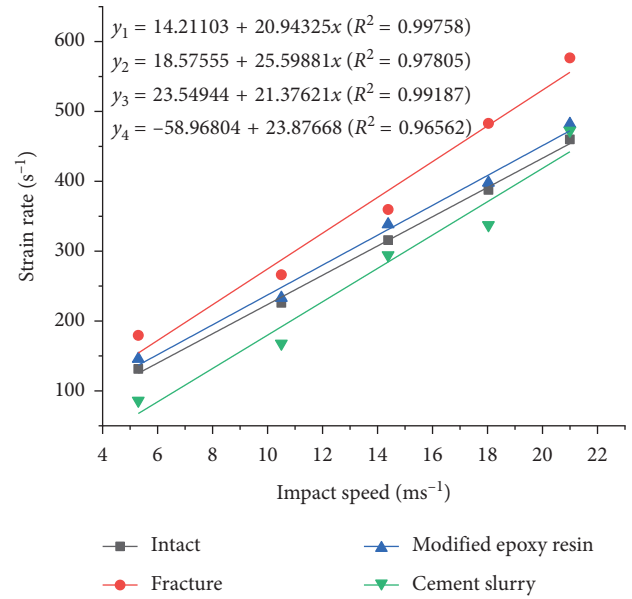


FIGURE 8: Impact speed-strain rate.

$$\zeta_i = \frac{\dot{\epsilon}_i}{\dot{\epsilon}_{0i}} \quad (11)$$

The strain rates of the specimens under different impact speeds were normalized, the statistical results are listed in Table 5, and the specific strain rate-impact speed relation curves were drawn (Figure 11).

As shown in Table 5 and Figure 11, the specific strain rate of the fractured specimen was approximately unchanged. And it kept an identical trend with the intact rock in the aspect of strain rate. Moreover, its strain rate was higher than that of the original rock. Relative to sandy mudstone, one between the two filling materials was hard and the other was soft with different change trends of their strain rates. With the impact speed increased, the specimen filled with epoxy resin showed a gradually declining specific strain rate, which was then approaching 1, and the specific strain rate of the specimen filled with cement slurry gradually rose and also approximated to 1. The specific strain rate of the specimen filled with cement slurry seemed to have stronger sensitivity to the impact speed, and the change was more evident, but the specific strain rate of the specimen filled with epoxy resin

was always approximate to 1, manifesting that the repaired rock was approximate to the intact rock in properties.

### 3.5. Influence of Grouting Reinforcement on Failure Mode of Fractured Rock Mass

**3.5.1. Specimen Failure Mode.** To understand the detailed failure laws of the specimen during the impact process, their impact failure processes were synchronously shot by using Phantom high-speed camera (NIKOR normal lens with NIKOR 50 mm focal length) produced by U.S. Vision Research, Inc., where the shooting frequency was 84,000 frames/second. The failure process of some specimens at an atmospheric pressure of 0.4 MPa is shown in Figures 12–14.

As shown in Figure 12, the specimen was compressed at the end of the incident bar in the beginning. A new through fracture was formed at the middle fracture tip as the stress wave amplitude was gradually enlarged. Due to the existence of the middle fracture, the original support was eliminated after the new through fracture was formed, and the specimen part close to the incident bar rapidly moved and rushed at

TABLE 4: Statistical table of specimen repair factor  $\gamma_b$ .

Category	Intact	Fracture	Modified epoxy resin	Cement slurry
$k$	20.94325	25.59881	21.37621	23.87668
$\gamma_b$	100%	81.81%	97.97%	87.71%

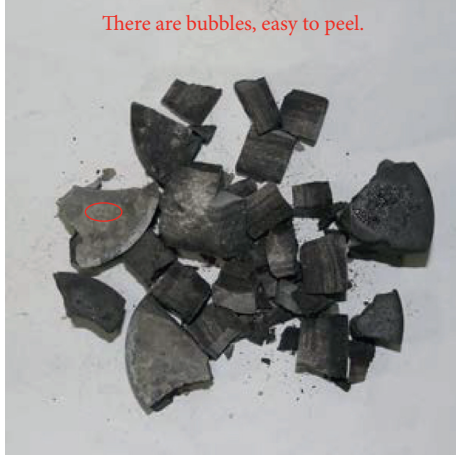


FIGURE 9: Cement slurry filling.



FIGURE 10: Modified epoxy resin filling.

the other side under the action of force at the end part. Influenced by the compressive stress on the end face of the new fracture and the pressure formed after the two end faces of the fracture contacted each other, fracturing occurred at the fracture end on the specimen part close to the end of the incident bar. After then, the whole specimen was under compaction state and jointly bore the subsequent impact load. Due to the new through fracture formed at the middle crack tip, the specimen on one side of the fracture first breaks into a large piece. Under the low-speed impact state, the large piece of specimen that broke along the fracture end could still be seen.

After grouting, both cured slurries could effectively fill the fracture and facilitate the recovery of the stress transfer path with a certain shrinkage space. Therefore, the initial

specimen failure was delayed, and the failure part usually started from the nongrouting half and then stretched to the fracture tip until the grouting part. Under low-speed impact, the cured modified epoxy resin filler was of higher tenacity than cured cement, so was its cohesive force. Therefore the grouting side was kept relatively intact in comparison with the cement slurry filled specimen. Under high-speed impact, the loaded strain rate was high, the loading time was short, and the gap at the specimen fracture experienced compression failure before adjustment, so the gaps among the three specimens were not apparent, and the pictures of their failure processes were not displayed any longer.

### 3.5.2. Mechanism Analysis of Specimen Failure Mode.

Assume that the stress-bearing conditions of one transient specimen after the stress equilibrium are shown in Figure 15(a). One part of the section where the fracture was located was intercepted as the study object, and uniform pressure  $\sigma_N$  acted upon the section of the specimen connection part. According to the equilibrium of force system, the following could be acquired:

$$\sigma_N \cdot \frac{\pi r^2}{2} - \sigma_d \cdot \pi r^2 = 0. \quad (12)$$

The following was then obtained:

$$\sigma_N = 2\sigma_d. \quad (13)$$

The upper part of the section ABCD is taken as the study object. Assume that shear force  $F_s$  and bending moment  $M$  exist on the section ABCD:

$$F_s = 2 \int_0^r \sigma_d \cdot \sqrt{r^2 - x^2} dx, \quad (14)$$

$$M = 2 \int_0^r \sigma_d \cdot \sqrt{r^2 - x^2} \cdot r dx. \quad (15)$$

The integral transformation of the above two equations was implemented, and  $x = r \sin \theta$  and  $dx = r \cos \theta d\theta$  were set.

The following was then obtained:

$$F_s = 2\sigma_d \int_0^{\pi/2} r^2 \cos^2 \theta d\theta = \frac{1}{2} \pi r^2 \sigma_d, \quad (16)$$

$$M = 2\sigma_d \int_0^{\pi/2} r^3 \sin \theta \cos^2 \theta d\theta = \frac{2}{3} r^3 \sigma_d. \quad (17)$$

As shear force and bending moment exist on the section ABCD, shear stress and positive tensile stress would certainly exist. Although the compressive stress  $\sigma_N$  of the undamaged part was larger than other parts, the shear behavior of rock had a great influence on the stability of rock structure [20–23]. The shear strength and tensile strength of rock material were far lower than compressive strength, so the primary causes for failure were shear stress and tensile stress. In consideration of stress concentration at the fracture tip, it could be judged that the section ABCD would be the first one to experience failure. The failure process of the

TABLE 5: Statistical table of specimen strain rate and specific strain rate.

Punch velocity (ms <sup>-1</sup> )	Strain rate of intact (s <sup>-1</sup> )	Fracture		Modified epoxy resin		Cement slurry	
		Strain rate (s <sup>-1</sup> )	$\zeta_1$	Strain rate (s <sup>-1</sup> )	$\zeta_2$	Strain rate (s <sup>-1</sup> )	$\zeta_3$
6	139.87	172.17	1.23	151.81	1.09	84.29	0.60
8	181.76	223.37	1.23	194.56	1.07	132.05	0.73
10	223.64	274.56	1.23	237.31	1.06	179.80	0.80
12	265.53	325.76	1.23	280.06	1.05	227.55	0.86
14	307.42	376.96	1.23	322.82	1.05	275.31	0.90
16	349.30	428.16	1.23	365.57	1.05	323.06	0.92
18	391.19	479.35	1.23	408.32	1.04	370.81	0.95
20	433.08	530.55	1.23	451.07	1.04	418.57	0.97
22	474.96	581.75	1.22	493.83	1.04	466.32	0.98

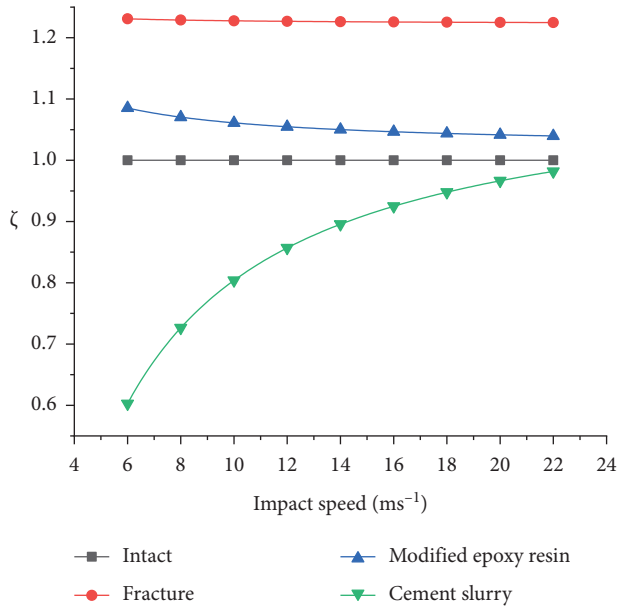


FIGURE 11: Impact speed-specific strain rate.

fractured specimen recorded by the high-speed camera rightly shows that the failure starts on this section.

After grouting reinforcement, the stress could be transferred at the fracture or microfractures which could be easily compacted, and they could transfer the stress after compaction. The following was obtained according to the principle of equilibrium:

$$\sigma_{N1} + \sigma_{N2} = 2\sigma_d. \quad (18)$$

Assume that the two end faces of each specimen are always parallel during the initial loading process, and satisfy Hooke's law before failure:

$$\sigma_{N1} = E_1 \cdot \varepsilon, \quad (19)$$

$$\sigma_{N2} = E_2 \cdot \varepsilon. \quad (20)$$

It is substituted into equation (18):

$$\frac{1}{\sigma_{N1}} = \frac{1}{2\sigma_d} + \frac{1}{2\sigma_d} \frac{E_2}{E_1}. \quad (21)$$

From equation (21),  $\sigma_{N1}$  is gradually reduced with the increase of  $E_2$ , suggesting that the fracture filling can effectively reduce the stress acting upon the intact rock.  $\sigma_{N1} = \sigma_d$  when  $E_2 = E_1$ ;  $\sigma_{N1} < \sigma_d$  when  $E_2 > E_1$ , indicating that if the elasticity modulus of the cured grouting material is greater than rock, the stress borne by the grouting side will be larger than that at the intact side.

**3.6. Establishment and Verification of Constitutive Relation of Grouting Reinforced Fractured Rock Mass.** For brittle materials such as rock and concrete, their dynamic mechanical properties under impact load may differ a lot from their static mechanical properties, which is generally related to the strain rate. With one nonlinear elastomer and two Maxwell bodies, the ZWT model [24] can show viscous-elastic characteristics within a wide range of strain rate, and it can be used to describe the constitutive behaviors of nonlinear viscoelasticity of typical high polymers very well [25]. In view of characteristics of rock materials, such as fractures and gaps, many scholars have used the improved ZWT model [26–30] to simulate the mechanical behaviors of brittle materials such as rock at different strain rates. Under impact load, the strain rate of rock materials can be stabilized at a high level, so the Maxwell body describing low strain rate in the ZWT model was deleted in this study. In consideration of the strain softening behaviors of rock materials under impact action, a damage body was used to replace the nonlinear elastomer in the ZWT model, and an improved damage-type ZWT model was established for the grouting reinforced fractured rock mass (Figure 16).

Assume that the microelement strength of the damage body follows Weibull statistical distribution, and then the probability density function was

$$\square p(\varepsilon) = \frac{m}{F_0} \left( \frac{\varepsilon}{F_0} \right)^{m-1} \exp \left[ - \left( \frac{\varepsilon}{F_0} \right)^m \right], \quad (22)$$

where  $\varepsilon$  is a variable characterizing the microelement strength, and here it means axial strain;  $m$  and  $F_0$  are Weibull distribution parameters.

Hereby is a definition of damage variable:

$$D = \frac{N_f}{N}, \quad (23)$$



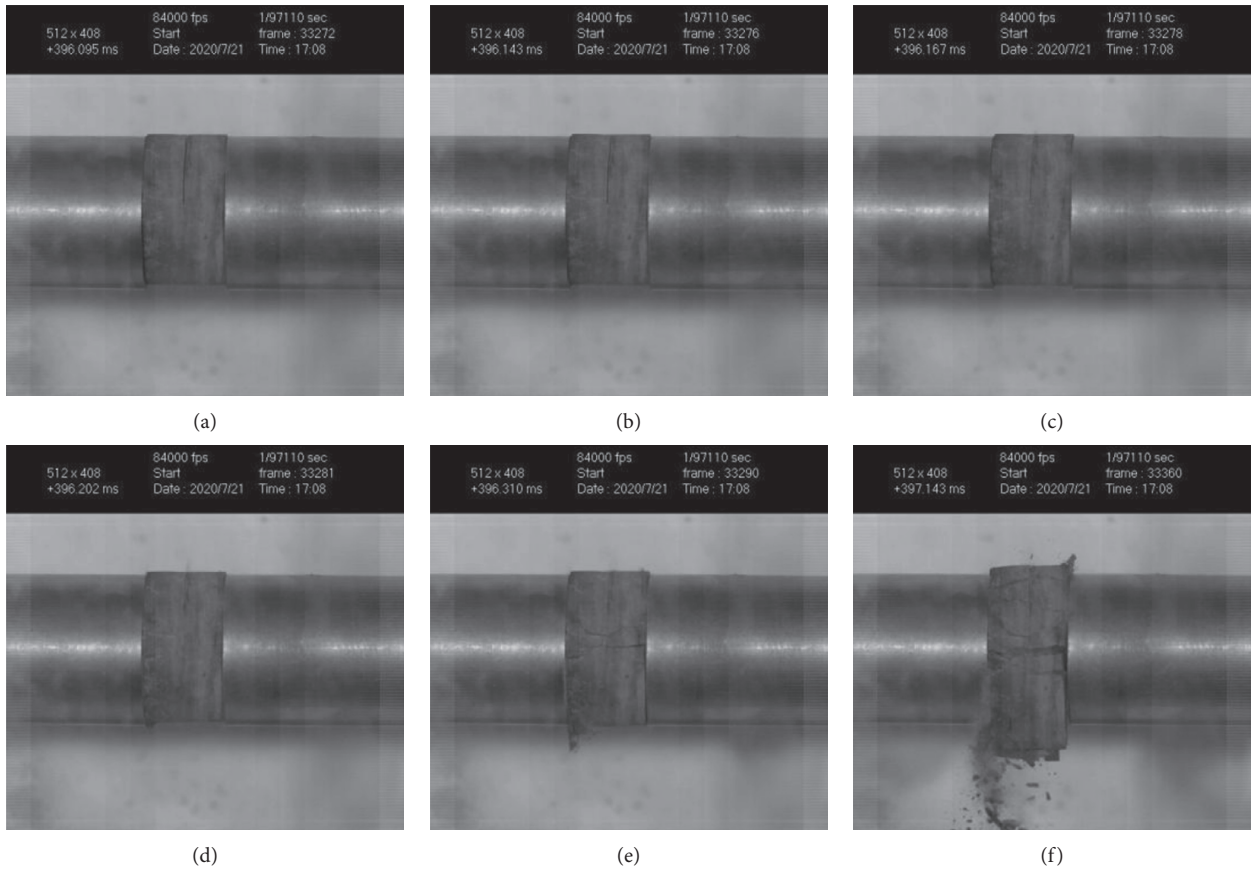


FIGURE 12: Failure of cracked specimen. (a) 0 us, (b) 48 us, (c) 72 us, (d) 107 us, (e) 215 us, and (f) 1048 us.

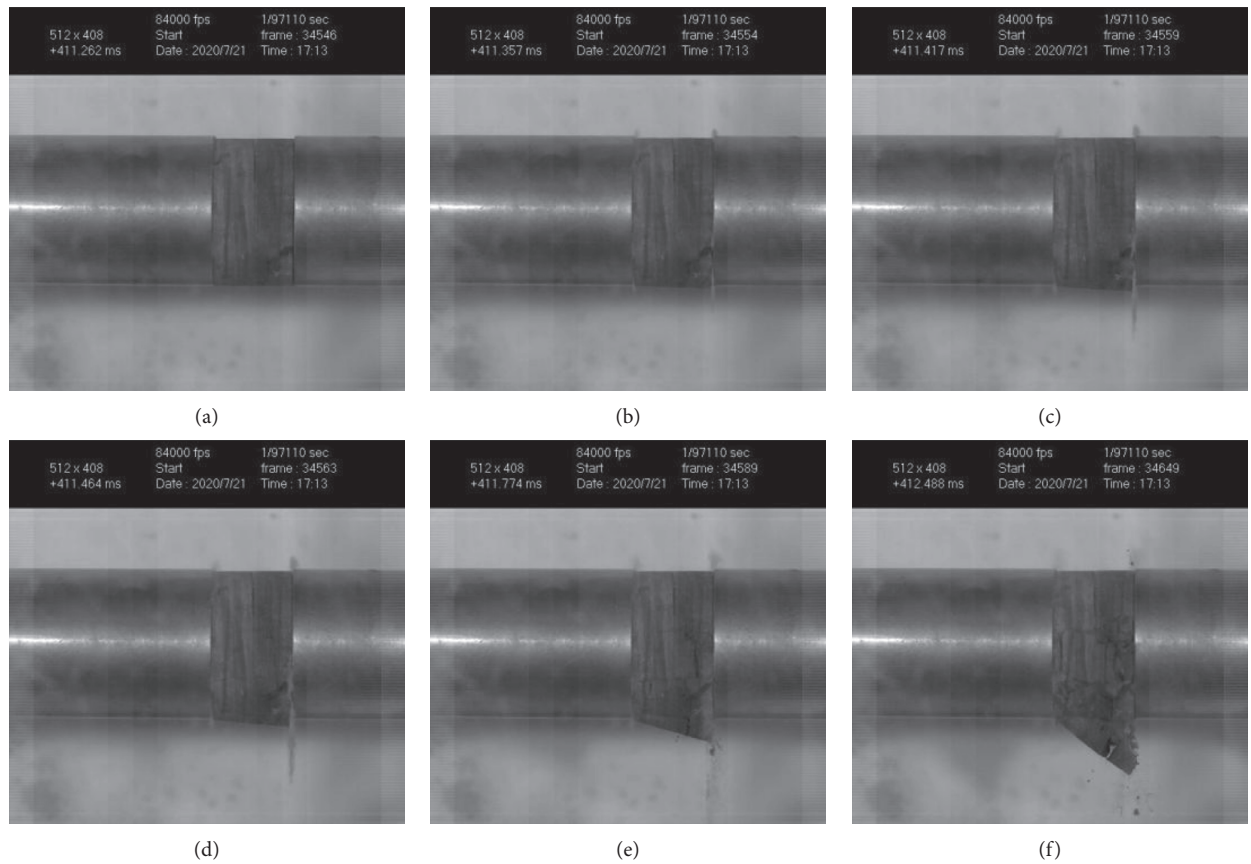


FIGURE 13: Failure of crack specimen filled with epoxy resin. (a) 0 us, (b) 95 us, (c) 155 us, (d) 202 us, (e) 512 us, and (f) 1226 us.

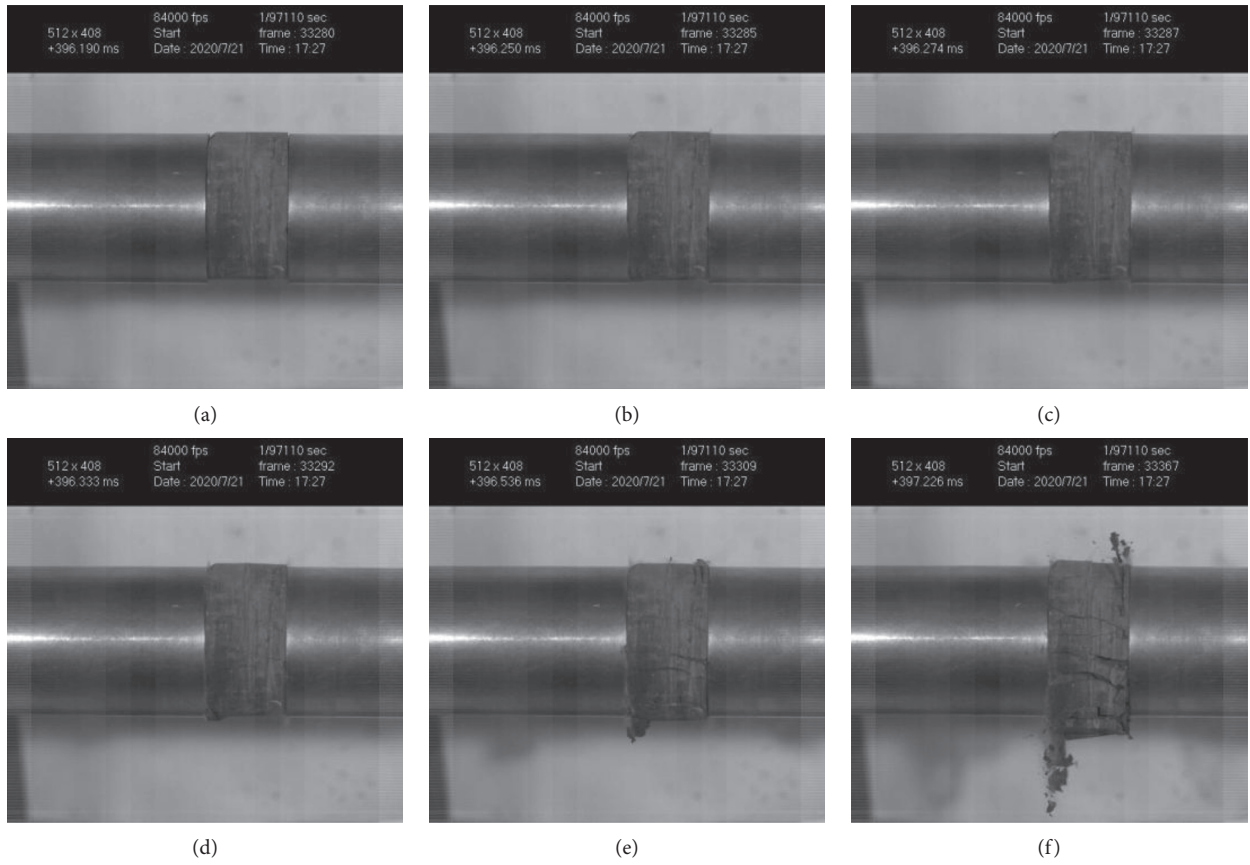


FIGURE 14: Failure of fracture specimen filled with cement (0.4 MPa). (a) 0 us, (b) 60 us, (c) 84 us, (d) 143 us, (e) 346 us, and (f) 1036 us.

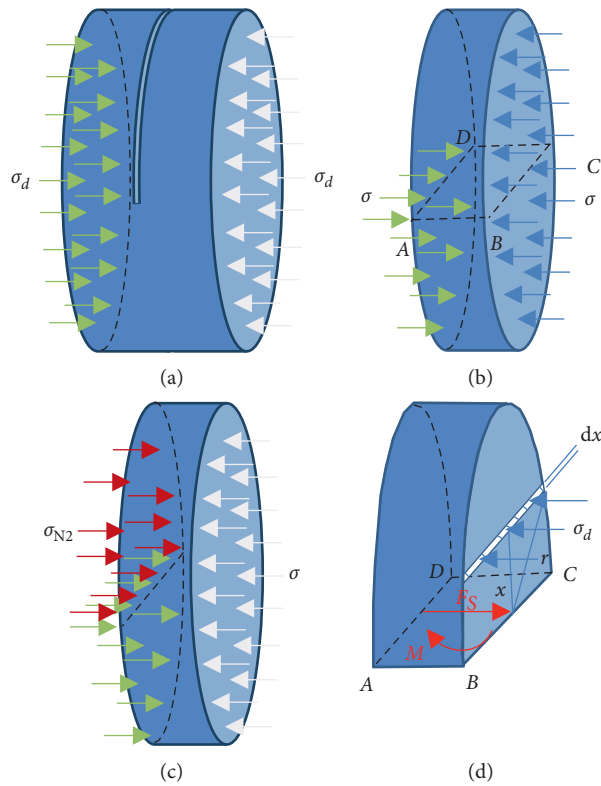


FIGURE 15: Force analysis.

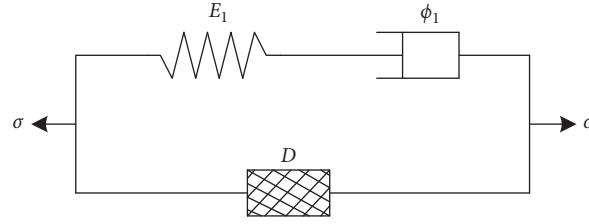


FIGURE 16: Improved damaged ZWT model.

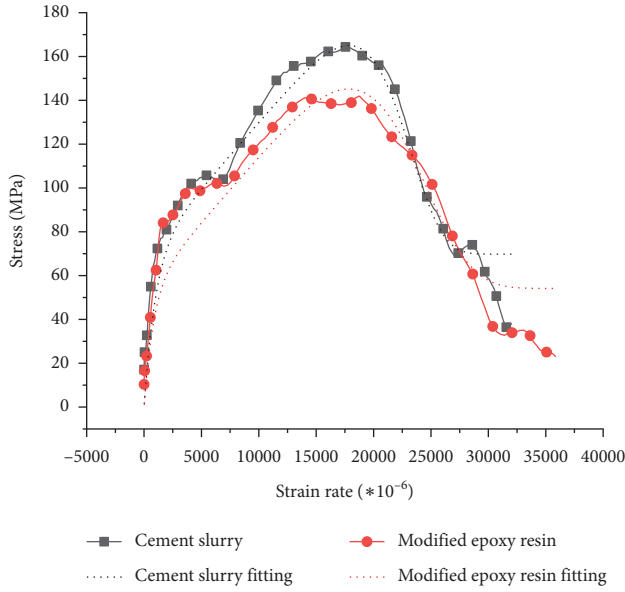


FIGURE 17: Fitting of stress-strain.

where  $N_f$  is the number of already damaged microelements and  $N$  is the total number of microelements.

The statistical damage model can be obtained through integral computation:

$$D = 1 - \exp \left[ - \left( \frac{\varepsilon}{F_0} \right)^m \right]. \quad (24)$$

According to the constitutive models of damage body (follow Weibull distribution) and Maxwell body and given the loading at constant strain rate can be realized in the SHPB test, it is never difficult to acquire the constitutive relation of the viscous-elastic damage model as follows:

$$\sigma(\varepsilon) = E_0 \varepsilon \cdot \exp \left[ - \left( \frac{\varepsilon}{F_0} \right)^m \right] + E_1 \varphi_1 \dot{\varepsilon} \cdot \left[ 1 - \exp \left( \frac{\varepsilon}{\varphi_1 \dot{\varepsilon}} \right) \right], \quad (25)$$

where  $E_0$  is the elastic model before the damage body is damaged;  $E_1$  is the spring stiffness of the Maxwell body;  $\dot{\varepsilon}$  is the test strain rate; and  $\varphi_1$  is the relaxation time.

For verifying the adaptability of the constitutive relation of the viscous-elastic damage model, this formula was used to fit the fractured rock reinforced by cement slurry grouting at a strain rate of  $294 \text{ s}^{-1}$  with the fractured rock reinforced by epoxy resin grouting at a strain rate of  $237 \text{ s}^{-1}$ , the fitted curves are shown in Figure 17, and fitting parameters are listed in Table 6. It could be seen that the constitutive

TABLE 6: Fitting parameters.

Grouting materials	$E_0/\text{MPa}$	$F_0$	$m$	$E_1/\text{MPa}$	$\varphi_1/\mu\text{s}$	$\dot{\varepsilon}$	$R^2$
Cement slurry	6.01	0.023	8.4	69.2	3.431	294	0.93067
Modified epoxy resin	6.01	0.024	6.1	62.9	3.631	237	0.88033

relation of the viscous-elastic damage model could be used to describe the mechanical behaviors of the grouting reinforced fractured rock mass under the action of impact load.

#### 4. Conclusion

A fracture (0.2 mm in width) was cut from the intact sandy mudstone specimen, and then a fractured specimen was manually fabricated. Epoxy resin slurry and cement slurry were grouted into the fracture to simulate the fracture filling through grouting and investigate the reinforcement mechanisms of different grouting materials for fractured specimens. The failure processes of the specimens were recorded using a high-speed camera. To sum up, the following conclusions were drawn:

- (1) The peak impact strength of each specimen has a natural logarithmic linear relation with the punch speed. With the increase of the impact speed, the dynamic specific strength of the modified epoxy resin grouting increases from 0.85 to 1.01 and decreases from 1.78 to 0.95 for the fractured specimen filled with cement slurry, manifesting that the fracture repair effect of modified epoxy resin is better than that of cement slurry. However, under low-speed impact, the strength of the fractured sandy mudstone filled with cement slurry is higher than that of the specimen filled with modified epoxy resin.
- (2) The strain rate of each specimen presented a linear relation with punch speed. With the increase of the impact speed, the specific strain rate of the modified epoxy resin grouting decreased from 1.09 to 1.04 and increased from 0.60 to 0.98 for the fractured specimen filled with cement slurry, meaning that the intactness of the specimen filled with modified epoxy resin was superior to that of the specimen filled with cement slurry. The specific strain rate of the latter showed stronger sensitivity to the impact speed with more obvious change, while that of the former was

always approximate to 1, indicating approximate properties of repaired rock to the intact rock.

- (3) The ZWT model was improved, and a viscous-elastic damage model with one damage body and one Maxwell body in series connection was adopted, as it could realize a good fitting effect on the stress-strain curves of grouting reinforced fractured rock masses under the impact load.

## Data Availability

All data, models, and code generated or used during the study appear in the submitted article.

## Conflicts of Interest

The authors declared that they have no conflicts of interest to this work.

## Acknowledgments

The authors would like to extend sincere gratitude to the National Key R&D Program (grant no. 2017YFC0603003), National Natural Science Foundation Program (grant nos. 51974009, 51774012, 51674008, and 51974007), Key Research and Development Projects in Anhui Province (201904a07020010), Funding for Scientific Research Activities of Academic and Technological Leaders in Anhui Province (2018d187), Funding Project for Outstanding and Top-Notch Talent Training in Colleges and Universities (grant no. gxbjZD2016051), Leading Talent Program of "Provincial Special Funding Program" in Anhui Province, and Innovation Team Construction Project of the Scientific Research Platform for Colleges and Universities in Anhui for funding our scientific research activity, and to the State Key Laboratory of Mining Response and Disaster Prevention and Control in Deep Coal Mines for providing SHPB equipment.


## References

- [1] F. Dong, H. Song, and Z. Guo, "Support theory of roadway surrounding rock loose circle," *Journal of China Coal Society*, vol. 19, no. 1, pp. 21–32, 1994.
- [2] N. Zhang and C. Hou, "Mechanical properties of broken rock after grouting reinforcement," *Rock and Soil Mechanics*, vol. 19, no. 3, pp. 50–53, 1998.
- [3] Q. Liu, G. Lei, and C. Lu, "Experimental study of grouting reinforcement influence on mechanical properties of rock fracture," *Chinese Journal of Rock Mechanics and Engineering*, vol. 36, no. S1, pp. 3140–3147, 2017.
- [4] Z. Wang, L. Li, and C. Wang, "Experimental study on failure of cracked rock-like material after grouting reinforcement," *Journal of Central South University*, vol. 49, no. 4, pp. 957–963, 2018.
- [5] H.-L. Le and S. R. Sun, "Effect of grouting materials and inclination angle of pre-existing flaw on uniaxial compressive strength and failure mode of rock-like specimens," *Rock and Soil Mechanics*, vol. 39, no. s1, pp. 211–219, 2018.
- [6] G. Li, C. Sun, Y. Sun et al., "Macroscopic and microcosmic consolidation law of loose coal grouting based on the "two media-three interfaces" model," *Journal of China Coal Society*, vol. 44, no. 2, pp. 427–434, 2019.
- [7] S. Li, R. Liu, Q. Zhang et al., "Research on C-S slurry diffusion mechanism with time-dependent behavior of viscosity," *Chinese Journal of Rock Mechanics and Engineering*, vol. 32, no. 12, pp. 2415–2421, 2013.
- [8] J. Wei, B. Yao, Y. Liu et al., "Grouting fluid diffusion law and variable mass seepage model for fractured coal," *Journal of China Coal Society*, vol. 45, no. 1, pp. 204–212, 2020.
- [9] S. Li, R. Liu, Q. Zhang, and X. Zhang, "Protection against water or mud inrush in tunnels by grouting: a review: a review," *Journal of Rock Mechanics and Geotechnical Engineering*, vol. 8, no. 5, pp. 753–766, 2016.
- [10] L. Wang and T. Li, "The calculation of grouting diffusion radius on based bingham fluid for chunnel that passes through fractured rock mass," *Applied Mechanics & Materials*, vol. 256–259, pp. 1280–1286, 2013.
- [11] C. Zhang, J. Yang, and G. Zhang, "Experiment and application research on stability performance of filling grouting slurry," *Chinese Journal of Rock Mechanics and Engineering*, vol. 37, no. s1, pp. 3604–3612, 2018.
- [12] Z. Shi, L. Fan, and Y. Song, "Study on properties of cement-based grouting material in high temperature," *Chinese Journal of Underground Space and Engineering*, vol. 14, no. 4, pp. 974–980, 2018.
- [13] W. Li, F. U. A. Shaikh, L. Wang et al., "Experimental study on shear property and rheological characteristic of superfine cement grouts with nano-SiO addition," *Construction and Building Materials*, vol. 228, Article ID 117046, 2019.
- [14] X. Guan, H. Zhang, and Z. Yang, "Research of high performance inorganic-organic composite grouting materials," *Journal of China Coal Society*, vol. 45, no. 3, pp. 902–910, 2020.
- [15] S. Fei, S. Li, R. Liu, Q. Zhang, Z. Li, and H. Liu, "Performance and engineering application of effective microfine cement-based grout (EMCG) for water-rich sand strata," *Chinese Journal of Rock Mechanics and Engineering*, vol. 38, no. 7, pp. 1420–1433, 2019.
- [16] J. Zhan and L. I. Tao, "SHPB tests and numerical simulation of dynamic behavior of grouting-reinforced fractured mudstone," *Rock and Soil Mechanics*, vol. 38, no. 7, pp. 2096–2102, 2017.
- [17] Y. X. Zhou, K. Xia, X. B. Li, H. B. Li, and F. Dai, "Suggested methods for determining the dynamic strength parameters and mode-I fracture toughness of rock materials," *International Journal of Rock Mechanics and Mining Sciences*, vol. 49, pp. 105–112, 2002.
- [18] J. M. Lifshitz and H. Leber, "Data processing in the split Hopkinson pressure bar tests," *International Journal of Impact Engineering*, vol. 15, no. 6, pp. 723–733, 1994.
- [19] X. Li, Z. Zhou, T.-S. Lok et al., "Innovative testing technique of rock subjected to coupled static and dynamic loads," *International Journal of Rock Mechanics and Mining Sciences*, vol. 45, no. 5, pp. 739–748, 2008.
- [20] Z. C. Hong, Q. Z. Zhang, and J. Peng, "Effect of thermal treatment on the basic friction angle of rock joint," *Rock Mechanics and Rock Engineering*, vol. 53, no. 4, pp. 1973–1990, 2020.
- [21] Z. C. Tang, Q. Z. Zhang, J. Peng, and Y. Y. Jiao, "Experimental study on the water-weakening shear behaviors of sandstone joints collected from the middle region of Yunnan province P. R. China," *Engineering Geology*, vol. 258, Article ID 105161, 2020.
- [22] Z. C. Tang, "Experimental investigation on temperature-dependent shear behaviors of granite discontinuity," *Rock*

- Mechanics and Rock Engineering*, vol. 53, no. 9, pp. 4043–4060, 2020.
- [23] Z. Tang and Y. Jiao, “Choosing appropriate appraisal to describe peak spatial features of rock joint profiles,” *International Journal of Geomechanics*, vol. 20, no. 4, Article ID 04020021, 2020.
- [24] Z. Tang, *Dynamic Mechanical Properties of Epoxy Resin Under High Strain Rate*, University of Science and Technology of China, Hefei, China, 1981, in Chinese.
- [25] K. Imai and H. Lehmann, “The oxygen affinity of haemoglobin Tak, a variant with an elongated beta chain,” *Biochimica et Biophysica Acta*, vol. 412, no. 2, pp. 288–294, 1975, in Chinese.
- [26] S. Hu and D. Wang, “Dynamic constitutive relation of concrete under impact,” *Explosion and Shockwave*, vol. 22, no. 3, pp. 242–246, 2002.
- [27] L. Xie, G. Zhao, and X. Meng, “Research on damage visco-elastic dynamic constitutive model of soft rock and concrete materials,” *Chinese Journal of Rock Mechanics and Engineering*, vol. 32, no. 4, pp. 857–864, 2013.
- [28] R. Shan, R. Cheng, and W. Gao, “Study on dynamic constitutive model of anthracite of Yunjialing coal mine,” *Chinese Journal of Rock Mechanics and Engineering*, vol. 25, no. 11, pp. 2258–2263, 2006.
- [29] L. Miao, *Experimental Studies of Dynamic Constitutive Properties of Jointed Rock Masses: Analysis of Stress Waves*, University of Science and Technology, Beijing, China, 2018, in Chinese.
- [30] J. Zhu, X. Li, and F. Gong, “Dynamic characteristics and damage model for rock under uniaxial cyclic impact compressive loads,” *Chinese Journal of Geotechnical Engineering*, vol. 35, no. 3, pp. 531–539, 2013.

## Research Article

# The Friction Angle of the Leiyang Marble Surface after Exposure to High Temperature

Meng Hong Peng<sup>1</sup> and Man Huang <sup>2</sup>

<sup>1</sup>Arts Academy of Shaoxing University, Shaoxing 312000, Zhejiang, China

<sup>2</sup>School of Civil Engineering, Shaoxing University, Shaoxing 312000, Zhejiang, China

Correspondence should be addressed to Man Huang; hmcadx@126.com

Received 2 August 2020; Revised 22 November 2020; Accepted 8 January 2021; Published 29 January 2021

Academic Editor: Bangbiao Wu

Copyright © 2021 Meng Hong Peng and Man Huang. This is an open access article distributed under the Creative Commons Attribution License, which permits unrestricted use, distribution, and reproduction in any medium, provided the original work is properly cited.

There is a lack of information about the temperature-dependent nature of the rock surface, which is one of the essential parameters to predict the surface friction. In the present study, we experimentally study the effect of temperature on the basic friction angle of the marble surface through the direct shear test under the low normal loading condition and tilting test (Stimpson/disk tilt test). The basic friction angle gradually decreases with the increase in temperature from 20°C to 600°C for the two kinds of the tilting test. The results indicate that the Stimpson test on samples with the length-to-diameter ratio of 2 can be more reliable to estimate the basic friction angle of the rock surface after exposure to high temperatures. The results illustrate that the sliding angle depends on the surface condition. With the increase in the repetitive measurements, the sliding angle decreases as the marble surface is cleaned, and the parameter increases as the marble surface is not cleaned.

## 1. Introduction

With the development of spiritual civilization in China, more attention has been paid to the protection of the culture. As for the stone cultural relics, the fire can cause major hidden disasters. The corresponding physical and mechanical properties can usually be altered by the fire-induced high temperature. The surface friction is one of the important properties, and it has not been comprehensively investigated in the past. Recently, the topic has motivated the research interest, including rock mechanics and historic preservation. In general, the surface friction can be reflected by the basic friction angle of the flat surface, which is an intrinsic property of a rock, determined by the mineral composition and texture of the material [1, 2], and used to estimate the shear strength of a rock joint [1, 3, 4]. According to Barton [1, 5], the basic friction angles of many rock types ranged from 21° to 38°, in which the sedimentary rock has a lower basic friction angle (ranging from 25° to 30°) than that of the igneous and metamorphic rocks (ranging from 30° to 35°). After that, many researchers have investigated the

property [6–14]. Recently, due to the demand for high temperature applications in underground engineering, many researchers have focused on understanding the temperature-dependent mechanical behavior of rocks. Although an ISRM-suggested method has been proposed by Alejano et al. [15], there is no experimental data available about the temperature-dependent nature of the basic friction angle [14]. Recent investigations indicated that the basic friction angle of the rock joint was greatly influenced by the testing method [2, 10, 11, 13, 16]. According to Ulusay and Karakul [2], the tilt test and direct shear test are the two commonly used methods to determine the basic friction angle of the rock joint in the laboratory. Experimental results showed that the value measured by the direct shear test is lower than that measured by the tilt test [10]. In essence, smooth surfaces are more suitable for determining the joint basic friction angle due to the parameter reflecting the adhesion of two contact surfaces [16]. From a practical point of view, such surfaces can hardly be available, and the measurement cannot be done. From a scientific point of view, as long as the surface finish is

consistent on all tested rock specimens, the results can be used to analyze [14].

To better understand the effect of wearing on the basic friction angle of rock joints, researchers performed successive repetitions (tests) on the same specimens, and the mean value of the first several repetitions was used as the basic friction angle [9, 10, 16], in which the number of repetitions usually ranged between three and five. Alejano et al. [11] further recommended that three repetitions were sufficient, but a fourth supplementary repetition should be performed when the maximum difference between one of the results and the median was larger than  $3^\circ$ . Other researchers [6, 10, 13, 17] found that, with the increase in repetitions, the tilt test would probably provide an underestimation of the basic friction angle, especially when the surface was cleaned before each test. However, contradictory phenomena were also observed by Jang et al. [13].

In the present study, both the direct shear test and tilt test were performed to measure the friction angle of marble surfaces after exposure to different temperatures (20, 200, 400, and  $600^\circ\text{C}$ , respectively). The characteristics of the sliding angles in relation to exposed temperatures were statistically analyzed. The effect of surface conditions (not cleaned or cleaned) was also investigated by tilt tests through repetitive measurements. The present study would be the first step to comprehensively understand the temperature-dependent shear behavior of the rock joint after thermal treatment, which is helpful in providing some insights to the variation of the joint basic friction angle with the increase in temperature and also be a pioneer to establish a peak shear strength criterion for the rock joint by considering the temperature effect that has been rarely studied in the literature.

## 2. Materials and Methods

The Leiyang marble is relatively homogeneous in texture and composition and is composed of dolomite and calcite with a small amount of white mica. The grain size is about 0.5 to 1 mm. The UCS is approximately 122.2 MPa (by using 3 specimens with length of 100 mm and diameter of 50 mm), and the tensile strength is about 4.11 MPa (by the Brazilian test using 6 specimens with diameter of 50 mm and height of 25 mm). Laboratory core drill and saw machines were used to prepare cylindrical specimens with length-to-diameter ratios ( $L/D$ ) of 0.5, 1, 2, and 4, respectively, as shown in Figure 1(a). The diameter of the samples was 50 mm. Samples with the length-to-diameter ratio of 1 were used to perform the direct shear test; samples with the length-to-diameter ratio of 0.5 were used to perform the disk tilt test; samples with the length-to-diameter ratio of 4 or 2 were used to perform the Simpson test.

In the present study, the post-high-temperature treatment is used to study the temperature-dependent surface friction nature of the three types of rocks, which means that the thermal treatment is first applied to the specimens alone by an electrical high-temperature furnace (Figure 1(b)). All the samples were firstly subjected to dry processing which was performed by putting the samples into a drying oven

and baking them at  $105^\circ\text{C}$  for 48 h to remove natural moisture content. According to the available experimental procedures, there is no well-recognized standard to heat the rock. According to the performance of the high-temperature furnace and also the work done by other researchers [18, 19], thermal treatment was performed on the dried samples in an electrical furnace with the following procedures:

- (i) Heat the dried samples at a rate of  $5^\circ\text{C}/\text{min}$  until to a predetermined temperature in the furnace chamber, which is 200, 400, and  $600^\circ\text{C}$  (referred as the #200 surface, #400 surface, and #600 surface, respectively). The scenarios of thermal treatments are shown in Figure 1(c).
- (ii) Maintain the samples at the predetermined temperature for 120 min.
- (iii) Turn off the furnace and allow it to naturally cool to the room temperature (about  $20^\circ\text{C}$ ).

A manually operated tilting apparatus combined with a free downloadable digital slope meter (Max Protractor), built into a Huawei cell phone, was used to measure the sliding angle ( $1.0^\circ$  accuracy), as shown in Figure 1(d). Before each test, the horizontality was confirmed by the electrolytic bubble. The tilting procedures followed the approaches stated by Alejano et al. [7]. The tilting rate was about  $0.5^\circ/\text{s}$  until the upper specimen began to slide. The tilting device was stopped when the upper block slides about 10% of the sample length. To examine the effect of wear on the friction angle of the rock surface, both cleaned and not cleaned after each measurement were considered. A soft brush was used to remove the abraded rock particles.

Direct shear tests were performed using the RMT-150 direct shear machine (Figure 1(e)). Hydraulic pressure sensors and displacement gauges were installed to accurately control and measure the shear force, vertical force, shear displacement, and vertical displacement. The shear rate was set as 0.5 mm/min. Five levels of normal stresses from 0.2 MPa to 1.0 MPa were applied (0.1, 0.4, 0.6, 0.8, and 1.0 MPa, respectively). The point on the stress–shear displacement curve, where the slope begins to stabilize, was selected as the shear strength of the rock surfaces.

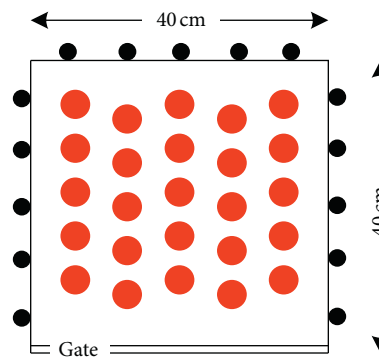
## 3. Basic Friction Angle

**3.1. Direct Shear Test.** The shear strength increases linearly with the increase of normal stress, as shown in Figure 2, with a very good linear correlation coefficient of 0.98 or more. The basic friction angle was considered as the slope angle of the regression line. For samples after exposure to temperatures from the room temperature onward, the determined basic friction angles are  $32.8^\circ$ ,  $32.0^\circ$ ,  $31.1^\circ$ , and  $29^\circ$ , respectively. It can be observed that the basic friction angle becomes smaller as the surface exposed to higher temperature.

**3.2. Tilt Test.** Both the measured initial sliding angles obtained by tilt tests with no repetitive measurements and the statistical results are listed in Table 1 (the average values were used to analyze in the following). For samples with the



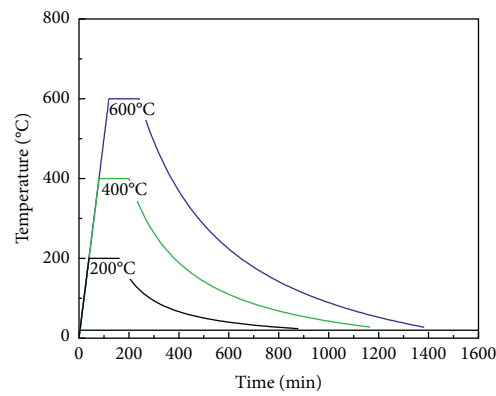
(a)



The way to place the specimens  
(top view)

- Silicon carbide bar
- Specimen

(b)



(c)

FIGURE 1: Continued.



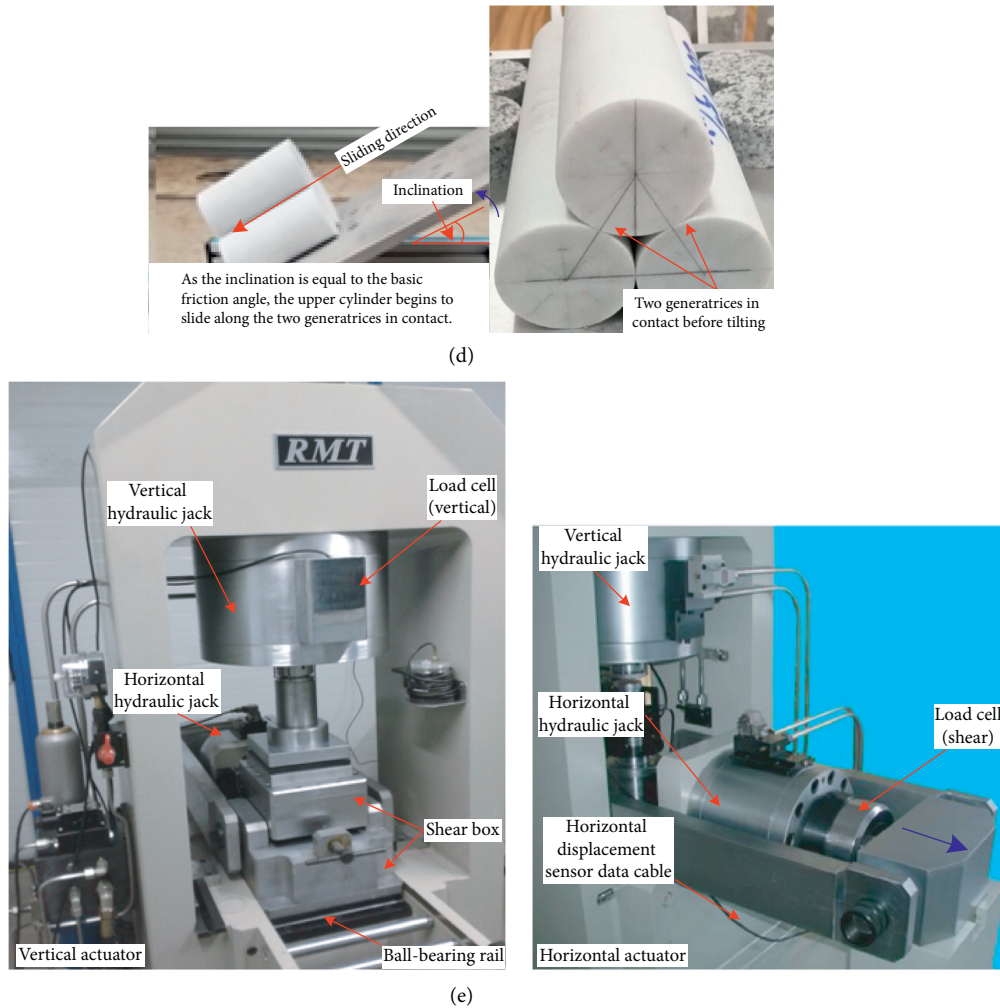


FIGURE 1: (a) Leiyang marble samples, (b) electrical furnace, (c) scenario of thermal treatment with a natural cooling rate, (d) assembly photo of the cylindrical specimen in the tilt test, and (e) RMT-301 servo-hydraulic test equipment.

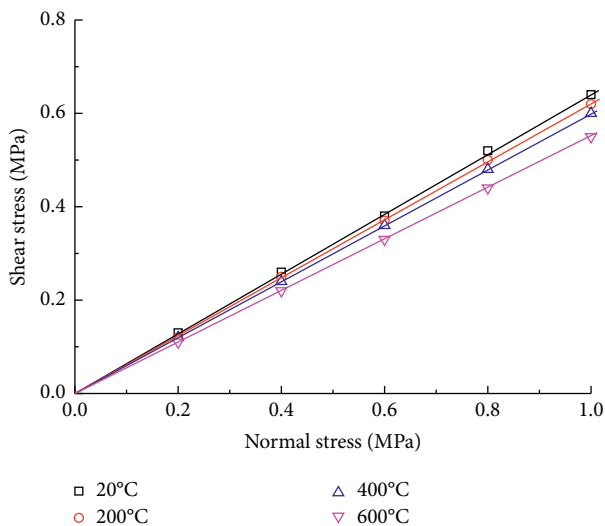


FIGURE 2: Shear strengths versus normal stresses measured by direct shear tests for surfaces after different temperatures (the solid line is the regression line).

length-to-diameter ratio of 4, the results showed the following: (1) the initial sliding angles of #20 and #200 surfaces were 33.9° and 33.4°, respectively, which are about 2° higher than that of the #400 surface (around 31.7°); (2) the initial sliding angle for the #600 surface declined to 26.9°; (3) the standard deviations generally increased with the increase of temperatures, indicating that the marble surfaces exhibit temperature-dependent properties and tend to be inhomogeneous after exposure to high temperatures. For samples with the length-to-diameter ratio of 2, the initial sliding angles decreased with the increase of exposed temperatures. The average initial sliding angle of the #20 surface was 4° higher than that of the #600 surface. The standard deviation of the #400 surface was the largest one. As for the disk tilt test ( $L/D=0.5$ ), the obtained initial sliding angles changed slightly with the increase of exposed temperatures, and the values, distributed in a narrow range of 21.8°–24.5°, were lower than that of Stimpson test results.

Generally, the average initial sliding angles decreased with the increase of exposure temperatures for each test type. Temperature has a greater influence on the Stimpson

TABLE 1: The initial sliding angles of marble surfaces after exposure to different temperatures.

No.	Experimental data under each temperature												Normalized by the average value at 20°C																									
	ST (L/D=2)						ST (L/D=4)						DT						ST (L/D=2)						ST (L/D=4)						DT							
	20	200	400	600	20	400	600	20	200	400	600	20	200	400	600	20	200	400	600	20	200	400	600	20	200	400	600	20	200	400	600	20	200	400	600	20	200	400
1	34	36	31	30	34	33	31	30	31	30	27	26	25	23	1.00	1.06	0.91	0.88	1.00	0.97	0.91	0.88	1.00	0.88	1.00	0.97	0.91	0.88	1.00	0.88	1.00	0.96	0.93	0.85				
2	34	32	30	29	35	34	35	33	33	33	27	26	25	24	1.00	0.94	0.88	0.85	1.03	1.00	1.03	0.97	1.00	0.85	1.03	1.00	1.03	0.97	1.00	0.96	0.93	0.89						
3	33	32	34	26	34	30	35	30	35	30	25	27	26	25	0.97	0.94	1.00	0.76	1.00	0.88	1.03	0.88	1.00	0.88	1.03	0.88	1.00	0.88	1.00	1.08	1.04	1.00						
4	35	34	35	25	34	32	36	28	36	28	26	25	23	23	1.03	1.00	1.03	0.74	1.00	0.94	1.06	0.82	1.00	0.94	1.06	0.82	1.00	0.96	0.88	0.88								
5	34	36	32	28	34	33	38	27	36	27	26	25	24	23	1.00	1.06	0.94	0.82	1.00	0.94	0.88	1.00	0.82	1.00	0.94	0.88	1.00	0.96	0.92	0.88								
6	34	37	34	28	34	32	30	29	28	29	28	26	21	21	1.00	1.09	1.00	0.82	1.00	0.94	0.88	1.00	0.82	1.00	0.94	0.88	1.00	0.93	0.75	0.75								
7	34	32	35	26	33	31	31	30	25	24	27	24	21	27	1.00	0.94	1.03	0.76	0.97	0.91	0.91	0.88	1.00	0.88	1.00	0.96	1.00	0.96	1.08	1.08								
8	33	30	32	27	34	32	29	30	25	28	22	22	20	20	0.97	0.88	0.94	0.79	1.00	0.94	0.85	0.88	1.00	0.94	0.85	0.88	1.00	1.12	0.88	0.80								
9	33	33	30	29	34	33	35	31	23	24	22	22	22	22	0.97	0.97	0.88	0.85	1.00	0.97	1.03	0.88	1.00	0.97	1.03	0.91	1.00	1.04	0.96	0.96								
10	33	34	31	30	34	34	36	31	24	25	23	24	25	23	1.00	1.00	0.91	0.88	1.00	1.00	1.06	0.91	0.88	1.00	1.06	0.91	1.00	1.04	0.96	0.79								
11	35	34	29	24	34	36	32	33	25	24	23	24	23	23	1.03	1.00	0.85	0.71	1.00	1.06	0.94	0.97	1.00	1.06	0.94	0.97	1.00	0.96	0.92	0.92								
12	34	36	34	25	34	32	31	26	25	26	25	26	21	23	1.00	1.06	1.00	0.74	1.00	0.94	0.91	0.76	1.00	0.94	0.91	0.76	1.00	1.04	0.84	0.92								
13	32	32	31	26	35	30	30	28	25	27	21	22	21	22	0.94	0.94	0.91	0.76	1.03	0.88	0.88	0.82	1.00	0.88	0.82	1.00	1.08	0.84	0.88									
14	34	32	29	25	35	31	32	26	26	27	24	21	21	21	1.00	0.94	0.85	0.74	1.03	0.91	0.94	0.76	1.00	0.94	0.76	1.00	1.04	0.92	0.81									
15	35	31	30	25	33	36	31	33	25	26	24	26	24	20	1.03	0.91	0.88	0.74	0.97	1.06	0.91	0.97	1.00	1.06	0.94	0.97	1.00	1.04	0.96	0.80								
16	34	31	31	24	34	35	29	31	25	26	25	26	25	20	1.00	0.91	0.91	0.71	1.00	1.03	0.85	0.91	1.00	1.03	0.85	0.91	1.00	1.04	1.00	0.80								
17	35	30	33	23	35	35	34	34	26	25	23	25	23	19	1.03	0.88	0.97	0.68	1.03	1.03	1.00	1.00	1.00	1.03	1.00	1.00	0.96	0.88	0.73									
18	35	35	32	28	35	33	32	29	26	26	26	26	21	19	1.03	1.03	0.94	0.82	1.03	0.97	0.94	0.85	1.00	0.97	0.94	0.85	1.00	1.00	0.81	0.73								
19	33	35	32	29	34	32	33	29	26	26	26	26	21	22	0.97	1.03	0.94	0.85	1.00	0.94	0.97	0.85	1.00	0.94	0.97	0.85	1.00	1.00	0.81	0.85								
20	35	32	32	26	34	32	33	28	25	25	25	23	23	23	1.03	0.94	0.94	0.76	1.00	0.94	0.97	0.82	1.00	0.94	0.97	0.82	1.00	1.00	0.92	0.92								
21	34	33	31	26	33	33	31	30	24	25	23	23	20	20	1.00	0.97	0.91	0.76	0.97	0.97	0.91	0.88	1.00	0.97	0.91	0.88	1.00	1.04	0.96	0.83								
22	34	34	30	27	34	31	31	31	23	23	23	23	20	24	1.00	1.00	0.88	0.79	1.00	0.91	0.91	0.91	1.00	0.91	0.91	0.91	1.00	1.00	0.87	1.04								
23	32	34	34	25	33	34	32	33	23	28	23	28	23	24	0.94	1.00	1.00	0.74	0.97	1.00	0.94	0.97	1.00	1.00	0.94	0.97	1.00	1.22	1.00	1.04								
24	34	32	31	26	33	37	30	30	23	21	21	21	21	23	1.00	0.94	0.91	0.76	0.97	1.09	0.88	0.88	1.00	0.88	1.00	0.91	0.91	1.00	1.00	1.00								
25	—	33	28	29	—	30	30	31	23	26	22	22	22	22	—	0.97	0.82	0.85	—	0.88	0.88	0.91	1.00	1.13	0.96	0.96												
26	—	32	30	25	—	32	29	31	22	25	22	21	21	21	—	0.94	0.88	0.74	—	0.94	0.85	0.91	1.00	1.14	1.00	0.95												
27	—	35	34	26	—	31	30	30	24	24	24	21	20	20	—	1.03	1.00	0.76	—	0.91	0.88	0.88	1.00	1.00	0.88	0.83												
28	—	36	32	28	—	33	31	30	24	22	25	20	20	20	—	1.06	0.94	0.82	—	0.97	0.91	0.88	1.00	0.92	1.04	0.83												
29	—	34	31	28	—	33	34	29	23	21	23	21	21	21	—	1.00	0.91	0.82	—	0.97	1.00	0.85	1.00	0.91	1.00	0.91												
30	—	35	32	27	—	32	30	30	23	26	22	22	23	23	—	1.03	0.94	0.79	—	0.94	0.88	0.88	1.00	1.13	0.96	1.00												
31	—	—	—	—	—	—	—	—	24	24	21	21	21	21	—	—	—	—	—	—	—	—	—	—	—	1.00	0.88	0.88										
32	—	—	—	—	—	—	—	—	23	25	24	21	21	21	—	—	—	—	—	—	—	—	—	—	—	1.00	1.09	1.04	0.91									
33	—	—	—	—	—	—	—	—	23	23	23	23	22	22	—	—	—	—	—	—	—	—	—	—	—	—	1.00	1.00	0.96									
34	—	—	—	—	—	—	—	—	23	24	22	22	22	22	—	—	—	—	—	—	—	—	—	—	—	—	1.00	1.04	0.96	0.96								
35	—	—	—	—	—	—	—	—	24	23	20	20	20	20	—	—	—	—	—	—	—	—	—	—	—	—	1.00	0.96	0.83	0.83								
36	—	—	—	—	—	—	—	—	23	23	21	20	20	20	—	—	—	—	—	—	—	—	—	—	—	—	1.00	1.00	0.91	0.87								
<b>Max</b>	35	37	35	33	35	37	38	34	28	28	28	27	27	27	1.03	1.09	1.03	0.97	1.03	1.09	1.12	1.00	1.00	1.00	1.00	1.00	0.96	0.96										
<b>Min</b>	32	30	28	23	32	30	29	26	22	21	20	19	19	19	0.94	0.88	0.82	0.68	0.94	0.88	0.85	0.76	1.00	0.95	0.91	0.86												
<b>Ave</b>	33.9	33.4	31.7	26.9	34	32.7	32	30	24.5	24.9	22.7	21.8	21.8	21.8	1.00	0.98	0.93	0.79	1.00	0.96	0.94	0.88	1.00	1.02	0.93	0.89												
<b>SD</b>	0.9	1.89	1.83	2.16	0.66	1.80	2.37	1.99	1.44	1.71	1.70	1.83	0.03	0.06	0.05	0.06	0.05	0.06	0.02	0.05	0.07	0.06	1.0	1.19	1.18	1.27												

Max: maximum; Min: minimum; Ave: average; SD: standard deviation.

test than that of the disk tilt test, partly manifested by dispersion of measurements and calculated standard deviation. The temperature-dependent nature of the initial sliding angle was much more obvious for samples with the length-to-diameter ratio of 4.

**3.3. Comparison.** As shown in Figure 3, the difference was small (within  $1.5^\circ$ ) for the results obtained by the direct shear test and Stimpson test as the exposed temperatures were no more than  $400^\circ\text{C}$ . For #600 surfaces ( $L/D = 4$ ), the initial sliding angle was about  $3.1^\circ$  lower than that of the direct shear test. From the room temperature onward, the average initial sliding angle of samples ( $L/D = 2$ ) was consistent with the basic friction angle (about  $0.6^\circ$ – $1.2^\circ$  higher). However, the results obtained by the disk tilt test were about  $7.1^\circ$ – $8.3^\circ$  lower than the basic friction angle. The Stimpson test on samples with the length-to-diameter ratio of 2 can be used to estimate the basic friction angle of the rock surface after exposure to high temperatures.

**3.4. Mechanisms.** In the literature, the following is considered to be the possible reasons for the variation of the joint basic friction angle after exposure to high temperatures [16]: (1) state change and loss of water; (2) change in physical and mechanical properties of minerals, especially the transition of crystals and the change of mineral composition; (3) microcracks induced by the unbalanced thermal stress and microroughness resulted from the dehydration process or changes/loss in mineral composition; (4) change in the thermodynamic property of the randomly distributed microasperities. As the temperature is relatively low, only physical changes occur. The chemical changes can usually be observed under the high temperature condition. In general, the competition among the abovementioned factors causes a change in the basic friction angle of rock surfaces.

To better understand the surface attribute of the Leiyang marble after different thermal treatments, Figure 4 presents the results of the SEM test for the rock (with a magnification ratio of 100). It is clear that the number of microcracks generally increase as the temperature increases from room temperature to  $600^\circ\text{C}$ . However, the microroughness seems to be smoother as the surface after exposure to higher temperature. Under the low normal stress condition, the microroughness on the marble surfaces would dominate the friction nature, and a decreasing trend with the increase in treatment temperature can be obtained.

#### 4. Repetitive Measurement for Sliding Angles

Figure 5(a) shows the tilt test results of marble surfaces under the room temperature condition when not cleaned. The sliding angles increased as the measurements continued within the first 50 repetitions. After that, the values were kept almost constant. At the 50th measurement, the sliding angles were about  $35^\circ$ ,  $36^\circ$ , and  $26^\circ$  for the surfaces with the length-

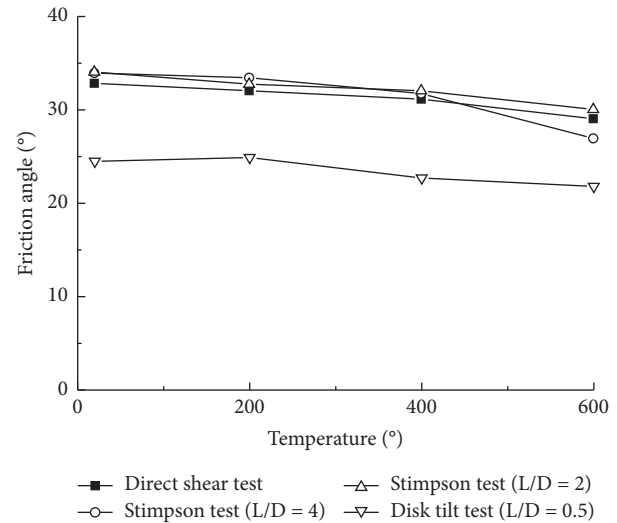


FIGURE 3: Variation and comparison of the friction angles obtained by tests.

to-diameter ratio of 4, 2, and 0.5, respectively. The first 20 repetitions caused the greatest influence on the friction behavior of the marble surface, in which the sliding angles were  $33^\circ$ – $43^\circ$  ( $L/D = 4$ ) and  $33^\circ$ – $38^\circ$  ( $L/D = 2$ ) for the Stimpson test, and distributed within a range of  $21^\circ$ – $34^\circ$  for the disk tilt test. After 50 repetitions, the average sliding angles obtained by the Stimpson test were always higher than those by the disk tilt test. Figure 5(b) shows the tilt test results of marble surfaces under the room temperature condition when cleaned. The sliding angles showed a wave-like decrease change as the measurements continued within the first 25 repetitions. After that, the sliding angle slightly fluctuated in some ranges. At the first 10 measurements, the sliding angles obtained by the Stimpson test were  $25^\circ$ – $41^\circ$ , obviously higher than those by the disk tilt test. After 30 repetitions, the difference between the results obtained by the Stimpson test on the sample with the length-to-diameter ratio of 2 and the disk tilt test was small.

The trend of sliding angle measurements for marble surfaces after exposure to high temperatures was similar to those under the room temperature condition, only excepting the results of the #200 surface obtained by the disk tilt test. In the first 50 repetitions, the sliding angles distributed in a range when not cleaned: (1) for #200 surfaces (Figure 6(a)),  $25^\circ$ – $43^\circ$  ( $L/D = 4$ ) and  $31^\circ$ – $40^\circ$  ( $L/D = 2$ ) for the Stimpson test and  $22^\circ$ – $33^\circ$  for the disk tilt test; (2) for #400 surfaces (Figure 7(a)),  $34^\circ$ – $43^\circ$  ( $L/D = 4$ ) and  $28^\circ$ – $38^\circ$  ( $L/D = 2$ ) for the Stimpson test and  $25^\circ$ – $35^\circ$  for disk tilt test; (3) for #600 surfaces (Figure 8(a)),  $21^\circ$ – $38^\circ$  ( $L/D = 4$ ) and  $23^\circ$ – $40^\circ$  ( $L/D = 2$ ) for Stimpson test and  $19^\circ$ – $32^\circ$  for disk tilt test.

For #200 surfaces, the average sliding angles obtained by the Stimpson test were nearly equal after 90 repetitions (within around  $1^\circ$ ). For #600 surfaces, the average sliding angles obtained by the Stimpson test were nearly equal after

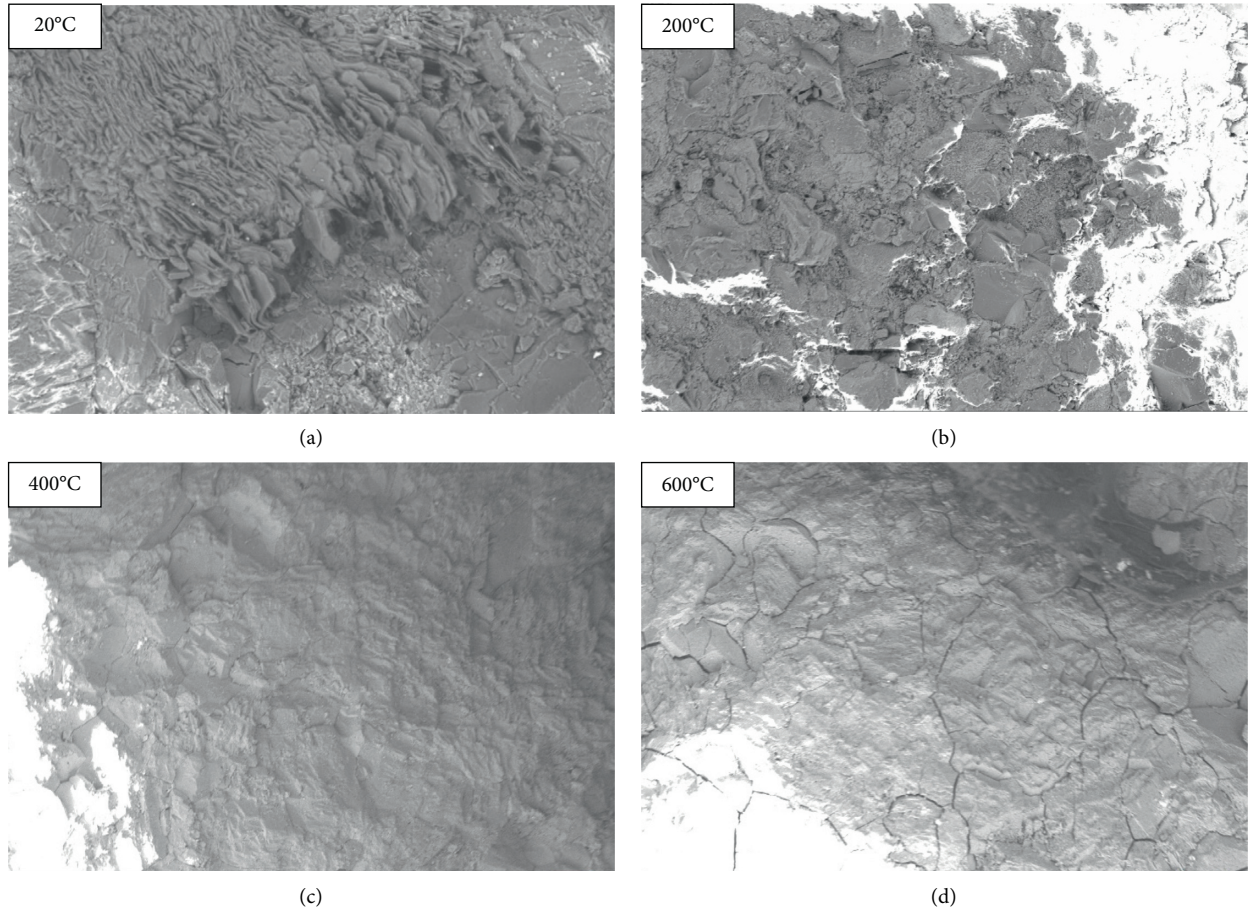


FIGURE 4: SEM images for the marble surfaces after thermal treatments.

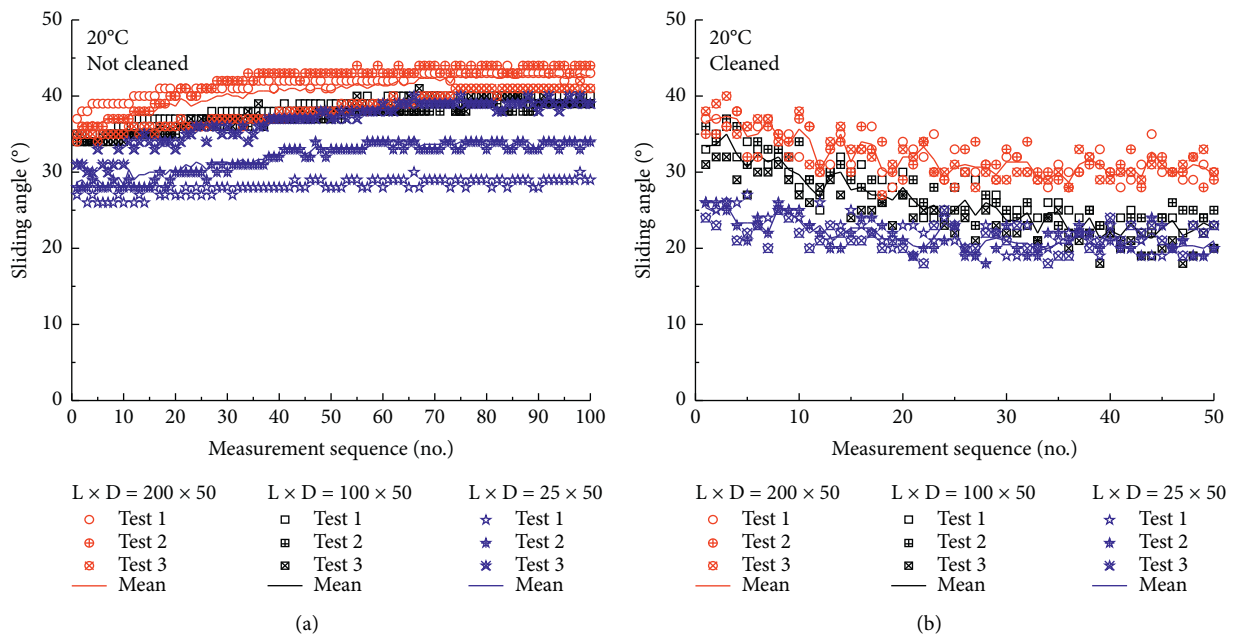


FIGURE 5: Results of tilt tests for the marble surface under room temperature. (a) Not cleaned after each measurement. (b) Cleaned after each measurement.

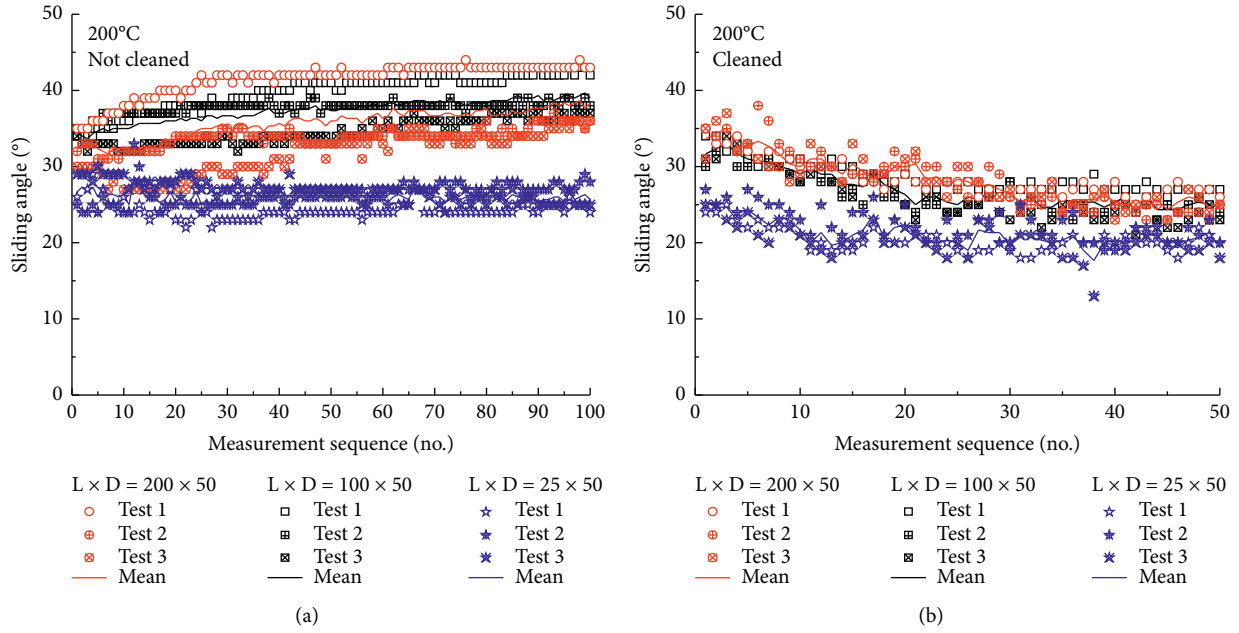


FIGURE 6: Results of tilt tests for the marble after 200°C. (a) Not cleaned after each measurement. (b) Cleaned after each measurement.

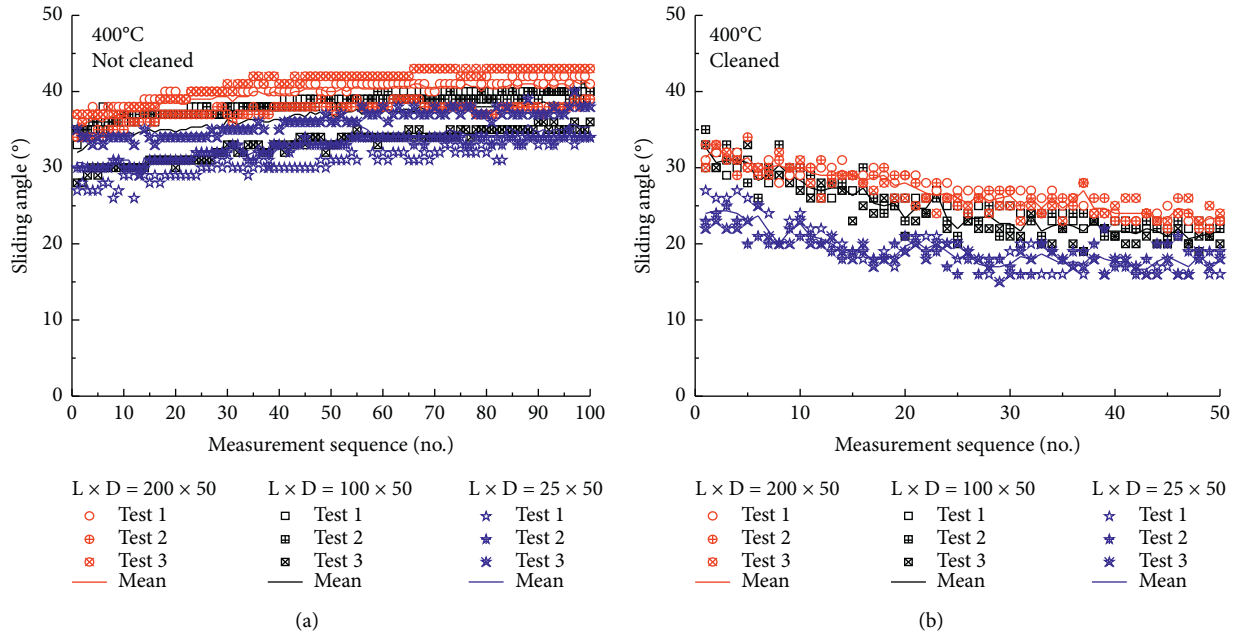


FIGURE 7: Results of tilt tests for the marble after 400°C. (a) Not cleaned after each measurement. (b) Cleaned after each measurement.

40 repetitions. For #400 surfaces, the difference was about 2° throughout the measurements. When cleaned, the distributed range of the sliding angles becomes narrower with the increase of temperatures. After 30 repetitions, the average sliding angles of #200 surfaces obtained by the Stimpson test were approximately equal (Figure 6(b)).

However, the average sliding angles for samples with the length-to-diameter ratio of 4 were higher than samples with the length-to-diameter ratio of 2 for other conditions (Figures 7(b) and 8(b)). Generally, the lower limits of sliding angles under the cleaned condition were smaller than those under the not-cleaned condition.

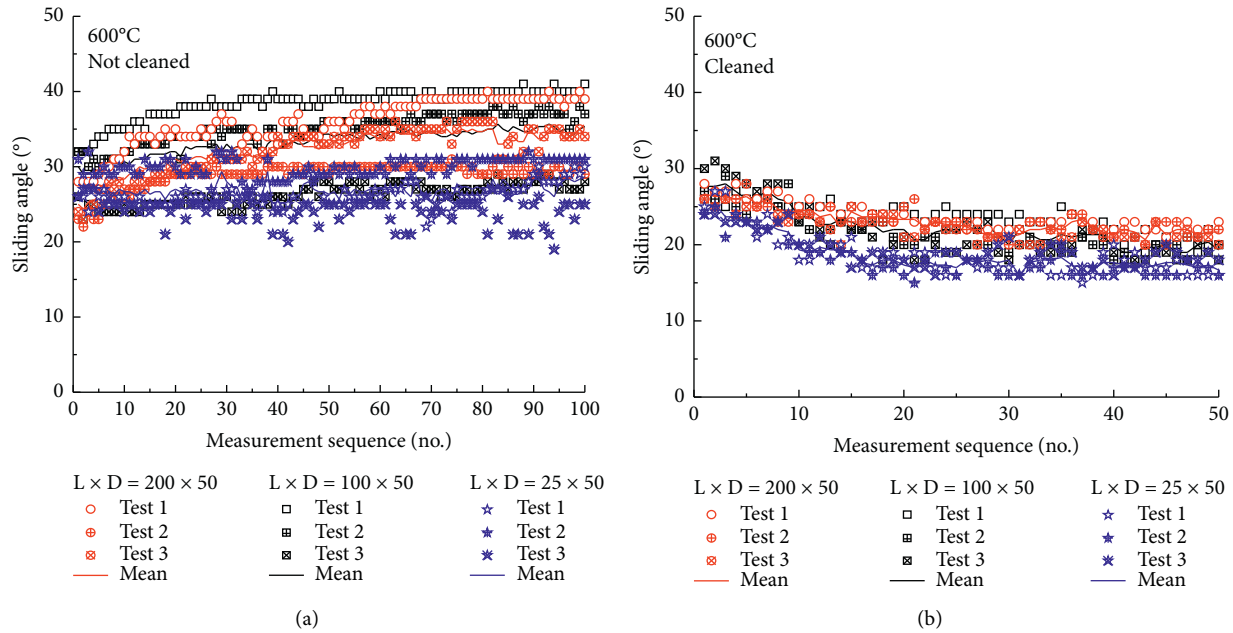


FIGURE 8: Results of tilt tests for the marble after 600°C. (a) Not cleaned after each measurement. (b) Cleaned after each measurement.

## 5. Conclusions

In order to study the effect of temperature on the basic friction angle of the rock surface, the direct shear test and tilt test on samples after 200°C, 400°C, and 600°C were performed by using the Leiyang marble. The surfaces exhibited temperature-dependent properties and tended to be inhomogeneous after exposure to high temperatures. The basic friction angle, determined by the direct shear test, decreased with the increase of temperatures. The Stimpson test on samples with the length-to-diameter ratio of 2 can be used to estimate the basic friction angle within the applied temperature range. Results showed that the disk tilt test tended to consistently underestimate the basic friction angle. Generally, the average sliding angles obtained by the Stimpson test using samples with the length-to-diameter ratio of 4 were higher than those of samples with the length-to-diameter ratio of 2. When the surfaces were not cleaned, the sliding angles generally increased with the increase of measurements. When the surfaces were cleaned, the sliding angles generally decreased with the increase of measurements. The first 20 repetitions have the greatest influence on the sliding angles for both surface conditions. The lower limits of sliding angles under the cleaned condition were smaller than those under the not-cleaned condition.

## Data Availability

The data used to support the findings of this study are available from the corresponding author upon request.

## Conflicts of Interest

The authors declare that they have no conflicts of interest regarding the publication of this paper.

## Acknowledgments

The authors thank Yu Tang, Yu Feng Zhang, and Yong Yi Li for their assistance to perform the tilt tests.

## References

- [1] N. Barton, "Review of a new shear-strength criterion for rock joints," *Engineering Geology*, vol. 7, no. 4, pp. 287–332, 1973.
- [2] R. Ulusay and H. Karakul, "Assessment of basic friction angles of various rock types from Turkey under dry, wet and submerged conditions and some considerations on tilt testing," *Bulletin of Engineering Geology and the Environment*, vol. 75, no. 4, pp. 1683–1699, 2016.
- [3] Z. C. Tang, "Experimental investigation on temperature-dependent shear behaviors of granite discontinuity," *Rock Mechanics and Rock Engineering*, vol. 53, no. 9, pp. 4043–4060, 2020.
- [4] Z. C. Tang and Y. Zhang, "Temperature-dependent peak shear-strength criterion for granite fractures," *Engineering Geology*, vol. 269, Article ID 105552, 2020.
- [5] N. Barton, "The shear strength of rock and rock joints," *International Journal of Rock Mechanics and Mining Sciences & Geomechanics Abstracts*, vol. 13, no. 9, pp. 255–279, 1976.
- [6] S. R. Hencher, "A simple sliding apparatus for the measurement of rock friction," *Discussion. Géotechnique*, vol. 26, no. 4, pp. 641–644, 1976.
- [7] B. Stimpson, "A suggested technique for determining the basic friction angle of rock surfaces using core," *International Journal of Rock Mechanics and Mining Sciences & Geomechanics Abstracts*, vol. 18, no. 1, pp. 63–65, 1981.
- [8] D. M. Cruden and X. Q. Hu, "Basic friction angles of carbonate rocks from Kananaskis country, Canada," *Bulletin of the International Association of Engineering Geology*, vol. 38, no. 59, 1988.
- [9] I. G. Bruce, D. M. Cruden, and T. M. Eaton, "Use of a tilting table to determine the basic friction angle of hard rock samples," *Canadian Geotechnical Journal*, vol. 26, no. 3, pp. 474–479, 1989.

- [10] S. R. Hencher, "Discussion of alejano, gonzalez and muralha," *Rock Mechanics and Rock Engineering*, vol. 45, no. 6, pp. 1137–1139, 2012.
- [11] L. R. Alejano, J. González, and J. Muralha, "Comparison of different techniques of tilt testing and basic friction angle variability assessment," *Rock Mechanics and Rock Engineering*, vol. 45, no. 6, pp. 1023–1035, 2012.
- [12] L. R. Alejano, J. Muralha, R. Ulusay et al., "A benchmark experiment to assess factors affecting tilt test results for sawcut rock surfaces," *Rock Mechanics and Rock Engineering*, vol. 50, no. 9, pp. 2547–2562, 2017.
- [13] H.-S. Jang, Q.-Z. Zhang, S.-S. Kang, and B.-A. Jang, "Determination of the basic friction angle of rock surfaces by tilt tests," *Rock Mechanics and Rock Engineering*, vol. 51, no. 4, p. 989, 2017.
- [14] Z. C. Tang, Q. Z. Zhang, and J. Peng, "Effect of thermal treatment on the basic friction angle of rock joint," *Rock Mechanics and Rock Engineering*, vol. 53, no. 4, pp. 1973–1990, 2020.
- [15] L. R. Alejano, J. Muralha, R. Ulusay et al., "ISRM suggested method for determining the basic friction angle of planar rock surfaces by means of tilt tests," *Rock Mechanics and Rock Engineering*, vol. 51, no. 12, pp. 3853–3859, 2018.
- [16] C. C. Li, N. Zhang, and J. Ruiz, "Measurement of the basic friction angle of planar rock discontinuities with three rock cores," *Bulletin of Engineering Geology*, vol. 78, no. 4, pp. 1–10, 2017.
- [17] N. S. Farrar and D. C. Cawsey, "Discussion: a simple sliding apparatus for the measurement of rock joint friction," *Géotechnique*, vol. 26, pp. 382–386, 1976.
- [18] G. Rong, J. Peng, M. Yao, Q. Jiang, and L. N. Y. Wong, "Effects of specimen size and thermal-damage on physical and mechanical behavior of a fine-grained marble," *Engineering Geology*, vol. 232, pp. 46–55, 2018.
- [19] Z. C. Tang, J. Sun, and J. Peng, "Influence of high temperature duration on physical, thermal and mechanical properties of a fine-grained marble," *Applied Thermal Engineering*, vol. 156, pp. 34–50, 2019.

## Research Article

# Correlations between Geometric Properties and Permeability of 2D Fracture Networks

Xiaolin Wang , Liyuan Yu , and Hanqing Yang 

State Key Laboratory for Geomechanics and Deep Underground Engineering, China University of Mining and Technology, Xuzhou 221116, China

Correspondence should be addressed to Liyuan Yu; [yuliyuan@cumt.edu.cn](mailto:yuliyuan@cumt.edu.cn)

Received 5 October 2020; Revised 20 October 2020; Accepted 7 January 2021; Published 27 January 2021

Academic Editor: Zhi Cheng Tang

Copyright © 2021 Xiaolin Wang et al. This is an open access article distributed under the Creative Commons Attribution License, which permits unrestricted use, distribution, and reproduction in any medium, provided the original work is properly cited.

The equivalent permeability of fractured rock masses plays an important role in understanding the fluid flow and solute transport properties in underground engineering, yet the effective predictive models have not been proposed. This study established mathematical expressions to link permeability of 2D fracture networks to the geometric properties of fractured rock masses, including number density of fracture lines, total length of fractures per square meter, and fractal dimensions of fracture network structures and intersections. The results show that the equivalent permeability has power law relationships with the geometric properties of fracture networks. The fractal dimensions that can be easily obtained from an engineering site can be used to predict the permeability of a rock fracture network. When the fractal dimensions of fracture network structures and intersections exceed the critical values, the effect of randomness of fracture locations is negligible. The equivalent permeability of a fracture network increases with the increment of fracture density and/or fractal dimensions proportionally.

## 1. Introduction

The estimation of equivalent permeability of fractured rock masses plays an important role in many environmental and engineering applications, such as CO<sub>2</sub> sequestration, underground nuclear waste repositories, and geothermal and heat storages [1–4]. The previous studies have revealed that the equivalent permeability of fracture networks is strongly correlated with the geometric properties of fractures, such as fracture length, density, aperture, and orientation [2, 5–8]. Recently, some works have shown that the fractal dimension is an effective tool to describe the geometric properties of fracture networks, and it is quantitatively correlated with the equivalent permeability [9–11].

A number of predictive models have been proposed to calculate the equivalent permeability of both porous and fractured media. In these models, the length of fractures has different types of distributions, such as random distribution [8, 9], power-law distribution [6, 7], and fractal-like tree distribution [12–14]. The lognormal distribution is another important geometric description of the fracture length in

networks, which, however, was not considered in any previous predictive models.

In this study, the lognormal distribution of fracture length is incorporated into the discrete fracture network (DFN) models with different number densities of fracture lines, and the equivalent permeability of each model is calculated via fluid flow simulations. The mathematical expressions that link equivalent permeability to the geometric properties, i.e., connectivity, density, and orientation, are proposed, and their validities are verified by comparing the predicted results with the calculated results of DFNs. The performance of conventional statistical parameters on predicting equivalent permeability of DFNs is compared with that using fractal dimensions.

## 2. DFN Generation and Fluid Flow Simulation

To generate a DFN model using the Monte Carlo method, the following three aspects need to be addressed. First, the geometric parameters (i.e., length, aperture, orientation, and location) of each fracture need to be assigned, assuming that



the fracture length follows a lognormal distribution and the orientation follows a normal distribution, as shown in Table 1. Second, an original model with a side length of 150 m is generated, followed by extractions from the target model with a side length of 100 m from the original model. Thus, the unevenly distributed fractures close to the boundaries are deleted from the model. Because the fluid flow only takes place in the connected fractures, the fracture segments located out of the model, the isolated fracture segments, and the “dead-end” elements of fractures, which are the ends of fractures that are not connected with other fractures and do not contribute to the fluid flow, are deleted from the model. Finally, the mass continuity equations at each fracture intersection are solved utilizing an iteration scheme under a given boundary condition. In the present study, the aperture has a constant value of 0.18 mm for each fracture, and the location of a fracture is randomly and uniformly distributed. Here, a constant value of apertures is taken into account because the present study aims to investigate the relationships between fractal dimensions and hydraulic properties of fracture networks. The number density of fracture lines,  $\rho$ , varies from  $\rho_0$  to  $64\rho_0$ , and for each  $\rho$ , 10 sets of different random numbers are utilized. Here,  $\rho_0$  is the initial number density of fracture lines, which have values of  $0.00075 \text{ m}^{-2}$  and  $0.00025 \text{ m}^{-2}$  for the two fracture sets, respectively. Three examples of the established DFNs and distribution of fracture intersections are shown in Figure 1. For each model, both the horizontal and vertical flows are simulated under a constant horizontal hydraulic gradient (see Figure 1(a)) and a vertical hydraulic gradient (see Figure 1(c)), respectively.

The basic assumptions are made that the fluid flow only occurs in fractures and obeys the cubic law, and the rock matrix is impermeable. The equivalent permeability is calculated under two boundary conditions (horizontal and vertical) with a constant hydraulic gradient of 10 kPa/m. The equivalent permeability is back-calculated using the following equation:

$$Q = A \frac{K}{\mu} \frac{\partial P}{\partial L}, \quad (1)$$

where  $Q$  is the flow rate,  $A$  is the cross-sectional area,  $K$  is the permeability,  $\mu$  is the dynamic viscosity,  $L$  is the fracture length, and  $P$  is the hydraulic pressure.

### 3. Fractal Evaluation

The fractal dimensions of the fracture network structures represented by  $D_f$  and the intersection points represented by  $D_{in}$  are calculated using the box-counting method. Each image of fracture network structures or intersections is constituted by 300 pixels in length and 300 pixels in width, and each pixel has a value of either 1 or 0 (null). An image is covered with square boxes of different dimensions from  $300 \times 300$  pixels (1 box) to  $1 \times 1$  pixel ( $300 \times 300$  boxes). If there is a part of a fracture in a box, this box will be assigned with a value of 1, otherwise 0. A log-log plot of the box count vs. the number of total boxes can be plotted, and the slope

represents the fractal dimension. The process of calculating the fractal dimension of DFNs is described in [10] in detail. The calculated fractal dimensions for three examples are shown in Figure 1. The value of  $D_f$  is always larger than 1, while  $D_{in}$  may have values less than 1 because  $D_{in}$  describes the fractal properties of dispersedly distributed intersection points in a plane, which may have values larger or smaller than 1 depending on the density of points.

### 4. Results and Analysis

Figures 2(a) ~ 2(d) show the relationships between  $K$  and  $\rho_{in}$ ,  $\rho_{seg}$ ,  $d_m$ , and  $d_{in}$ , respectively. Here,  $\rho_{in}$  is the number density of intersections,  $\rho_{seg}$  is the number density of segments,  $d_m$  is the mass density of fractures, and  $d_{in}$  is the number of intersections per meter at the boundary. The connectivity of a DFN, defined as the total number of intersection points divided by the total number of fracture lines [9], can be represented by a function of  $\rho_{in}$  and  $\rho$ . The flow path of a fracture network is strongly influenced by  $\rho_{seg}$  and  $d_m$ . A larger value of  $\rho_{seg}$  or  $d_m$  indicates a denser fracture distribution and a larger number of intersections, resulting in a larger number of flow paths connecting the inlet boundary to the outlet boundary. The orientation of fractures is depicted by  $d_{in}$ . A larger value of  $d_{in}$  at an orientation means a larger number of fractures intersecting with the boundary and a stronger conductivity. For a limit case, when all of the fractures are horizontal,  $d_{in}$  at the horizontal boundaries is larger than 0, whereas  $d_{in}$  in the direction perpendicular to horizontal is 0, resulting in the stronger permeability in the horizontal direction.

The geometric parameters, i.e.,  $\rho_{in}$ ,  $\rho_{seg}$ ,  $d_m$ , and  $d_{in}$ , increase with the increment of  $\rho$ , and  $K$  of DFNs increases with these geometric parameters following power-law functions, as shown in equations (2) ~ (5). When the values of the geometric parameters are small, i.e.,  $\rho_{in} < 10^{-1}$ , the value of  $K$  varies within a large range, which gradually converges to the best-fitted curves when the values of the geometric parameters become large, i.e.,  $\rho_{in} > 10^0$ . This is because when the density of fractures and intersections is small, the location of fractures is significantly influenced by the randomly distributed fracture center point that can have a large dispersion. The effect of randomness of center points on the geometric characters of networks diminishes with increasing fracture density [10]. Although the value of  $K$  is well estimated utilizing the geometric parameters (i.e.,  $\rho_{in}$ ,  $\rho_{seg}$ ,  $d_m$ , and  $d_{in}$ ), it is still a challenging and time-consuming task to obtain their values for a real-fractured rock mass. To facilitate the process, the fractal dimensions,  $D_f$  and  $D_{in}$ , are utilized to represent the distributions of fractures and intersections, respectively. The geometry of a fracture network can be redepicted based on the images of fracture outcrops in a field [15]. Then,  $D_f$  and  $D_{in}$  can be easily calculated using the box-counting method. Figures 2(e) ~ 2(f) exhibit that  $K$  is also correlated with the fractal dimensions following power law functions, as shown in equations (6) ~ (7). All of the calculated data fit equations (2) ~ (7) fairly well with the correlation coefficient  $R^2 > 0.96$  as follows:

TABLE 1: Geometric parameters used for DFN generation.

Set	Fracture length (m)		Orientation (°)		Aperture (mm)	DFN side length (m)	Initial number density, $\rho_0$ ( $m^{-2}$ )
	Avg.	Dev.	Avg.	Dev.			
1	53.6	5	107.77	343.95	0.18	100	0.00075
2	68	8.7	279.75	286.62	0.18	100	0.00025

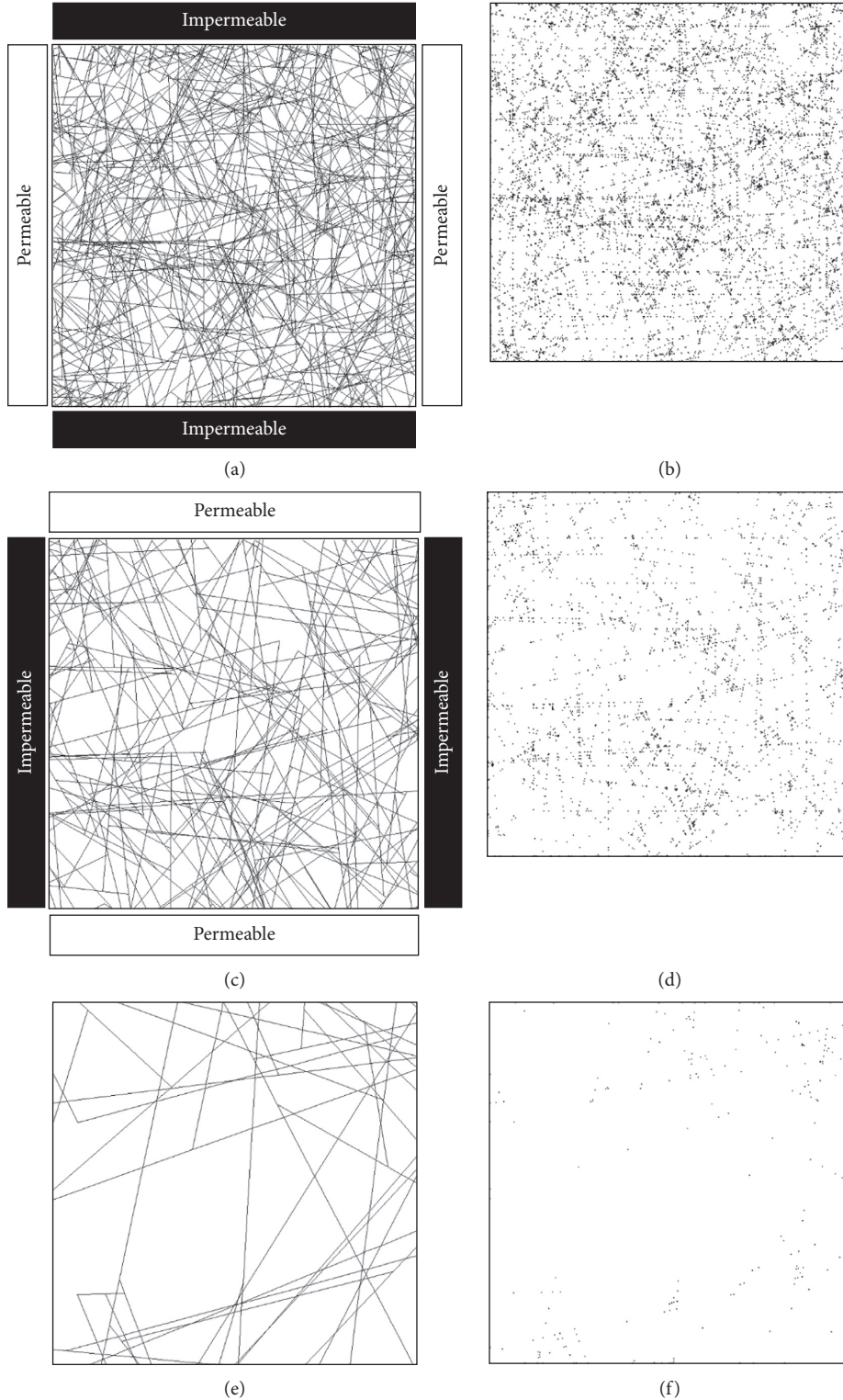


FIGURE 1: Distributions of fractures ((a), (c), and (e)) and intersections ((b), (d), and (f)) in three DFNs with different densities, and the two kinds of boundary conditions applied to DFNs in which the flow directions are perpendicular to each other. (a)  $\rho = 64\rho_0$  and  $D_f = 1.62$ . (b)  $\rho = 64\rho_0$  and  $D_{in} = 1.28$ . (c)  $\rho = 16\rho_0$  and  $D_f = 1.49$ . (d)  $\rho = 16\rho_0$  and  $D_{in} = 0.95$ . (e)  $\rho = \rho_0$  and  $D_f = 1.16$ . (f)  $\rho = \rho_0$  and  $D_{in} = 0.39$ .

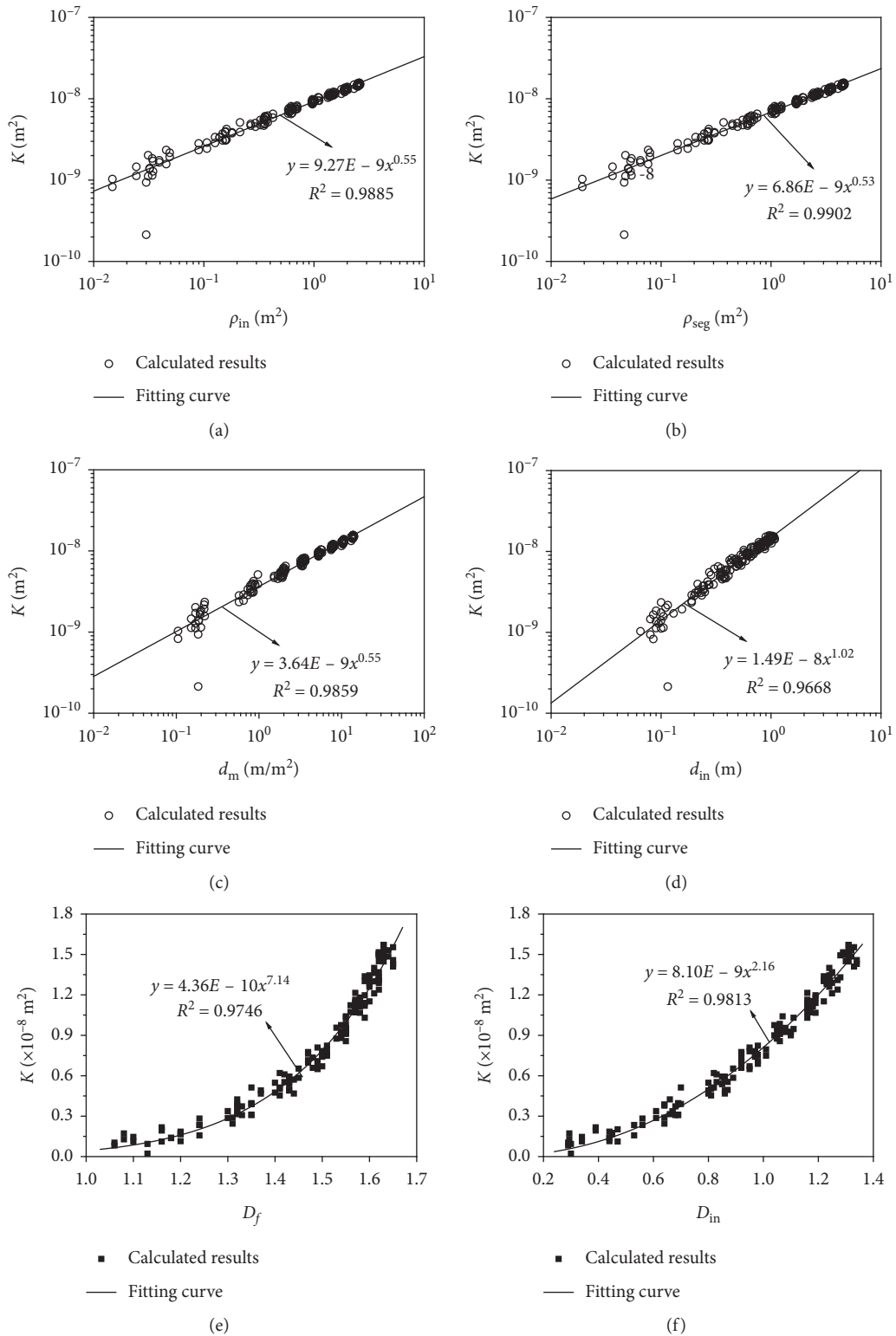


FIGURE 2: Relationships between  $K$  and (a)  $\rho_{in}$ , (b)  $\rho_{seg}$ , (c)  $d_m$ , (d)  $d_{in}$ , (e)  $D_f$ , and (f)  $D_{in}$ , respectively.

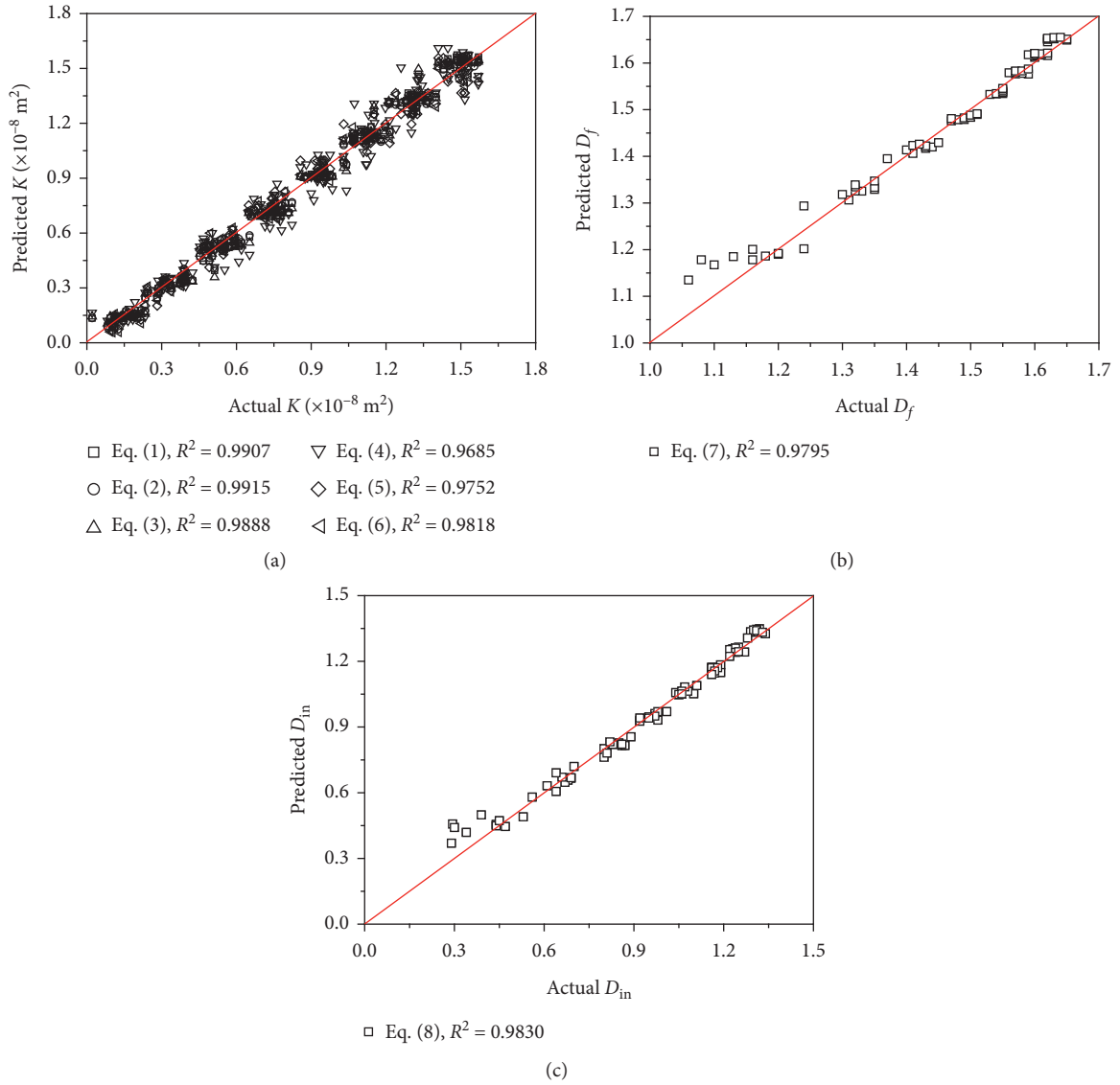


FIGURE 3: Comparisons between predicted and calculated results of (a)  $K$ , (b)  $D_f$ , and (c)  $D_{in}$ . (a) Predicted  $K$  by equations (1)–(6) vs. calculated  $K$ . (b) Predicted  $D_f$  by equation (7) vs. calculated  $D_f$ . (c) Predicted  $D_{in}$  by equation (8) vs. calculated  $D_{in}$ .

$$K = 9.27 \times 10^{-9} \rho_{in}^{0.55}, \quad (2)$$

$$R^2 = 0.9885,$$

$$K = 6.86 \times 10^{-9} \rho_{seg}^{0.53}, \quad (3)$$

$$R^2 = 0.9902,$$

$$K = 3.64 \times 10^{-9} d_m^{0.55}, \quad (4)$$

$$R^2 = 0.9859,$$

$$K = 1.49 \times 10^{-8} d_{in}^{1.02}, \quad (5)$$

$$R^2 = 0.9668,$$

$$K = 4.36 \times 10^{-10} D_f^{7.14}, \quad (6)$$

$$R^2 = 0.9746,$$

$$K = 8.10 \times 10^{-9} D_{in}^{2.16}, \quad (7)$$

$$R^2 = 0.9813.$$

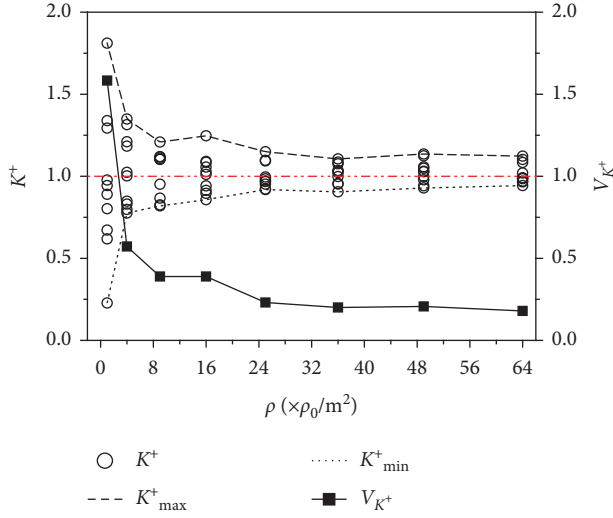


FIGURE 4: Variations in  $K^+$  and  $V_{K^+}$  with varying  $\rho$ .

Substituting equations (2) and (4) into equations (6) and (7), respectively, yields

$$D_f = 1.33d_m^{0.079}, \quad (8)$$

$$R^2 = 0.9790,$$

$$D_{in} = 1.06\rho_{in}^{0.25}, \quad (9)$$

$$R^2 = 0.9830.$$

Equations (8)~(9) imply that  $D_f$  and  $D_{in}$  are also correlated with  $d_m$  and  $\rho_{in}$  following power law functions, with  $R^2 > 0.97$ .

Figure 3 shows the comparisons between the predicted results of  $K$ ,  $D_f$ , and  $D_{in}$  using equations (2)~(9) with the calculated results obtained from flow simulations ( $K$ ) and fractal evaluations ( $D_f$  and  $D_{in}$ ). The results show that the predicted values agree well with the calculated results, and although when  $D_f < 1.15$  and  $D_{in} < 0.4$ , the predicted values of  $D_f$  and  $D_{in}$  are slightly larger than the calculated results, due to the effect of randomness of fracture locations. Therefore, the permeability of a DFN consisting of log-normally distributed fractures can be well estimated using the geometric parameters and fractal dimensions.

Figure 4 shows the variations of  $K^+$  and  $V_{K^+}$  with  $\rho$  varying from  $\rho_0$  to  $64\rho_0$ , in which  $K^+$  and  $V_{K^+}$  are defined as follows:

$$K^+ = \frac{K_v}{K_h}, \quad (10)$$

$$V_{K^+} = K_{\max}^+ - K_{\min}^+, \quad (11)$$

where  $K^+$  is the dimensionless equivalent permeability,  $K_v$  and  $K_h$  are the equivalent permeability of the vertical flow (Figure 1(c)) and horizontal flow (Figure 1(a)), respectively,  $V_{K^+}$  represents the variation in  $K^+$  for different DFNs, and  $K_{\max}^+$  and  $K_{\min}^+$  are the maximum and minimum values of  $K^+$ , respectively.

When  $\rho$  is small, i.e.,  $\rho < 16\rho_0$ ,  $K^+$  is more scattered, and the value of  $V_{K^+}$  is larger, comparing with the cases with a larger  $\rho$ , i.e.,  $\rho > 24\rho_0$ , in which  $K^+$  converges to a smaller range of variations, and the value of  $V_{K^+}$  is smaller.  $K^+$  ranges from 0.23 to 1.81 when  $\rho = \rho_0$  and varies from 0.94 to 1.12 when  $\rho = 64\rho_0$ . The effect of randomness of fracture locations can be neglected when  $\rho > 24\rho_0$ , corresponding to  $D_f > 1.55$  and  $D_{in} > 1.07$ , above which the permeability of a DFN increases with the increment of fracture density and/or fractal dimension.

## 5. Conclusions

This study established a great number of discrete fracture networks (DNFs) with different fracture densities and random numbers for generating the center point and orientation of fractures, in which the length of fractures follows a lognormal distribution. The mathematical expressions were proposed to link the equivalent permeability with the geometric parameters and fractal dimensions that describe the geometric characters of fracture networks. The validity was verified by comparing the predicted results with the calculated results of DFN simulations.

The results show that the equivalent permeability has power law relationships with the geometric properties of DFNs, i.e.,  $\rho_{in}$ ,  $\rho_{seg}$ ,  $d_m$ ,  $d_{in}$ ,  $D_f$ , and  $D_{in}$ . The values of  $D_f$  and  $D_{in}$  can be calculated using the box-counting method to represent  $d_m$  and  $\rho_{in}$  with power law functions. The predicted values of  $K$ ,  $D_f$ , and  $D_{in}$  are consistent with those of the calculated results, indicating that the proposed expressions of  $K$  with the geometric properties of DFNs are reliable. When  $D_f > 1.55$  and  $D_{in} > 1.07$ , the effect of randomness of fracture locations are negligible, and the permeability of a DFN increases with the increment of fracture density and/or fractal dimensions.

The future works will focus on the effect of aperture variation on the equivalent permeability of 2D fracture networks. Besides, we will also study the relationship between the equivalent permeability and fractal dimension of 3D rough fracture networks because the 3D fracture network can better characterize the roughness, orientation, connectivity, and permeability tensor of real-fractured rock masses than 2D fracture networks. Equations (2)~(9) are applicable for 2D fracture networks, whose applicability to 3D fracture networks will be investigated in future works.

## Nomenclature

- $A$ : Cross-sectional area ( $L^2$ )
- $K$ : Equivalent permeability ( $L^2$ )
- $P$ : Hydraulic pressure ( $ML^{-1}T^{-2}$ )
- $K_h$ : Equivalent permeability of horizontal flow ( $L^2$ )
- $K_v$ : Equivalent permeability of vertical flow ( $L^2$ )
- $K^+$ : Dimensionless equivalent permeability
- $V_{K^+}$ : Variation of dimensionless equivalent permeability
- $\mu$ : Dynamic viscosity ( $M/(L \cdot T)$ )
- $\rho$ : Number density of fracture lines ( $L^{-2}$ )
- $\rho_0$ : Initial number density of fracture lines ( $L^{-2}$ )
- $D_f$ : Fractal dimension of fracture network structures

$D_{in}$ : Fractal dimension of fracture intersections  
 $\rho_{in}$ : Number density of fracture intersections ( $L^{-2}$ )  
 $\rho_{seg}$ : Number density of fracture segments ( $L^{-2}$ )  
 $d_m$ : Length of fractures per square meter ( $L \cdot L^{-2}$ )  
 $d_{in}$ : Number of fractures intersecting with the boundary per meter ( $L^{-1}$ ).

## Data Availability

The data used to support the findings of this study are available from the corresponding author upon request.

## Conflicts of Interest

The authors declare that they have no conflicts of interest regarding the publication of this paper.

## Acknowledgments

This study was partially funded by the National Natural Science Foundation of China (Grant no. 51579239).

## References

- [1] A. Baghbanan and L. Jing, "Stress effects on permeability in a fractured rock mass with correlated fracture length and aperture," *International Journal of Rock Mechanics and Mining Sciences*, vol. 45, no. 8, pp. 1320–1334, 2008.
- [2] C. T. O. Leung and R. W. Zimmerman, "Estimating the hydraulic conductivity of two-dimensional fracture networks using network geometric properties," *Transport in Porous Media*, vol. 93, no. 3, pp. 777–797, 2012.
- [3] S.-Q. Yang, Y.-H. Huang, H.-W. Jing, and X.-R. Liu, "Discrete element modeling on fracture coalescence behavior of red sandstone containing two unparallel fissures under uniaxial compression," *Engineering Geology*, vol. 178, pp. 28–48, 2014.
- [4] S.-Q. Yang and H.-W. Jing, "Strength failure and crack coalescence behavior of brittle sandstone samples containing a single fissure under uniaxial compression," *International Journal of Fracture*, vol. 168, no. 2, pp. 227–250, 2011.
- [5] A. Baghbanan and L. Jing, "Hydraulic properties of fractured rock masses with correlated fracture length and aperture," *International Journal of Rock Mechanics and Mining Sciences*, vol. 44, no. 5, pp. 704–719, 2007.
- [6] J.-R. De Dreuzy, P. Davy, and O. Bour, "Hydraulic properties of two-dimensional random fracture networks following a power law length distribution: 1. effective connectivity," *Water Resources Research*, vol. 37, no. 8, pp. 2065–2078, 2001.
- [7] J.-R. De Dreuzy, P. Davy, and O. Bour, "Hydraulic properties of two-dimensional random fracture networks following a power law length distribution: 2. Permeability of networks based on lognormal distribution of apertures," *Water Resources Research*, vol. 37, no. 8, pp. 2079–2095, 2001.
- [8] A. Jafari and T. Babadagli, "Estimation of equivalent fracture network permeability using fractal and statistical network properties," *Journal of Petroleum Science and Engineering*, vol. 92–93, pp. 110–123, 2012.
- [9] A. Jafari and T. Babadagli, "Relationship between percolation-fractal properties and permeability of 2-D fracture networks," *International Journal of Rock Mechanics and Mining Sciences*, vol. 60, pp. 353–362, 2013.
- [10] R. Liu, Y. Jiang, B. Li, and X. Wang, "A fractal model for characterizing fluid flow in fractured rock masses based on randomly distributed rock fracture networks," *Computers and Geotechnics*, vol. 65, pp. 45–55, 2015.
- [11] T. Miao, B. Yu, Y. Duan, and Q. Fang, "A fractal analysis of permeability for fractured rocks," *International Journal of Heat and Mass Transfer*, vol. 81, pp. 75–80, 2015.
- [12] R. Liu, L. Yu, Y. Jiang, Y. Wang, and B. Li, "Recent developments on relationships between the equivalent permeability and fractal dimension of two-dimensional rock fracture networks," *Journal of Natural Gas Science and Engineering*, vol. 45, pp. 771–785, 2017.
- [13] P. Xu, B. Yu, Y. Feng, and Y. Liu, "Analysis of permeability for the fractal-like tree network by parallel and series models," *Physica A: Statistical Mechanics and Its Applications*, vol. 369, no. 2, pp. 884–894, 2006.
- [14] Q. Zheng and B. Yu, "A fractal permeability model for gas flow through dual-porosity media," *Journal of Applied Physics*, vol. 111, no. 2, p. 024316, 2012.
- [15] A. Jafari and T. Babadagli, "Effective fracture network permeability of geothermal reservoirs," *Geothermics*, vol. 40, no. 1, pp. 25–38, 2011.

## Research Article

# Study on Permeability of Deep-Buried Sandstone under Triaxial Cyclic Loads

Mingqiang Sheng <sup>1</sup>, Awei Mabi,<sup>2</sup> and Xigen Lu <sup>2</sup>

<sup>1</sup>School of Civil Engineering and Architecture, Nanchang University, Nanchang 330031, China

<sup>2</sup>School of Human Settlements and Civil Engineering, Nanchang Institute of Science and Technology, Nanchang 330108, China

Correspondence should be addressed to Xigen Lu; 1061807832@qq.com

Received 19 November 2020; Revised 17 December 2020; Accepted 4 January 2021; Published 25 January 2021

Academic Editor: Zhi Cheng Tang

Copyright © 2021 Mingqiang Sheng et al. This is an open access article distributed under the Creative Commons Attribution License, which permits unrestricted use, distribution, and reproduction in any medium, provided the original work is properly cited.

The triaxial cyclic loading and unloading test was carried out on a TAW-2000 rock mechanics to study the permeability characteristics of deep-buried sandstone. This paper analyzed the evolution laws of permeability, elastic modulus, rock damage, dissipated energy, and acoustic emission events of sandstone under different confining pressures. It also introduced the concept of relative strain and further discussed the relationship between relative strain and permeability. The test results showed that the permeability of sandstone under cyclic loading and unloading obviously experienced three stages. At a low strain level, the damage degree of sandstone was low. As a result, both the number of acoustic emission events and the proportion of the dissipated energy density were small. In this stage, with increasing the stress, the permeability decreased. With the increase of the relative strain, the propagation of fissure increased through rock interior and the damage of rock was accumulated. Consequently, the number of acoustic emission events grew slowly, and the proportion of dissipated energy density and the damage variable ( $D$ ) increased gradually. In this stage, the permeability increases. As the axial strain reached the peak strain, the fissures developed into cracks and the rock failure happened. The number of acoustic emission events increased rapidly; both the proportion of the dissipated energy density and the damage variable ( $D$ ) obtain the maximum value. In this stage, the permeability increased greatly. In this study, the point of fissure propagation of rock specimens was used as the point of demarcation. Before the fissures propagated, the permeability increased slowly and it was in accordance with a linear function. After the fissures propagated, the degree of rock damage increased, and the permeability increased in the form of an exponential function. The larger the confining pressure was, the smaller the relative strain corresponding to the point of fissure propagation was.

## 1. Introduction

China is rich in coal resources with the characteristics of the various covered depth of the coal seams. Along with the exhausting shallow resources, the mining depth is increasing with an average rate of 8–25 m per year [1, 2]. Deep mining has already become a trend in the coal industry. Under the high-stress condition, the mechanical characteristics of the coal and rock mass in the deep Earth are easily affected by underground engineering. With groundwater under high pressure, water inrush from rock formations is a serious potential risk during mining activities [3–8].

Deep mining causes the adjustment of the stress state of the coal and rock mass, which further leads to the change of

their mechanical properties. The cyclic loading and unloading test is an effective method to understand the permeability evolution of the coal and rock mass under confining pressure. Many scholars have studied the hydraulic and mechanical properties of the coal and rock mass. For example, according to the seepage properties of sedimentary rocks in the stress-strain process, Peng et al. [9] summarized the relation curve between strain and permeability of rocks. With the permeability and mechanics characteristics test studying on sandstone and granite, Wang et al. [10] studied the evolution law of permeability with confining pressure, seepage pressure, and volumetric strain and established the relation between rock permeability and strain. Kong et al. [11] analyzed the relationship between

permeability and porosity under cyclic loading, based on the experimental study on the gas permeability of sandstone under cyclic loading and unloading. Chen et al. [12] studied the permeability and nonlinear damage characteristics of rock under triaxial load based on RFP software. Yang et al. [13] designed an experiment on the permeability evolution of coal and rock mass under cyclic seepage pressure and discovered the evolutionary characteristics of permeability of coal and rock mass and its relationship with seepage pressure. Generally speaking, previous studies mostly focused on the loading path of rock permeability and its mechanics characteristics.

Deformation and failure of coal and rock mass are damage processes, accompanied by the accumulation, evolution, and dissipation of energy. Peng et al. [14] analyzed the energy mechanism of the evolutionary process of damage of coal and rock mass under various confining pressures and concluded that the energy dissipation of damage increases with the increase of cyclic stress. Meng et al. [15] conducted experimental research on the energy evolution laws of sandstone with different loading rates under uniaxial cyclic loading and unloading. Li et al. [16] studied the energy evolutionary characteristics of granite under different loading and unloading paths and indicated that the ratio of dissipative energy can be used for describing the degree of rock deformation and failure. Li et al. [17] studied the permeability and acoustic emission characteristics of coal under different stress paths and found that the cumulative dissipated energy of coal increases exponentially with the axial effective stress. Cai et al. [18] studied the relationship between acoustic emission  $b$ -value characteristics and rock damage. Based on the study of the permeability evolution law of the damage of coal and rock mass, Zou et al. [19] obtained the relationship between damage characteristics and permeability of granite through the compression test. Zhao et al. [20] used acoustic emission (AE) to obtain the damage and permeability evolution characteristics of rock under stress. Wang et al. [21] conducted cyclic loading and unloading tests on deep coal and rock masses under confining pressure obtained the permeability of coal and rock mass and established its relationship with various mechanical properties of coal and rock mass.

Previous tests, in most cases, mainly focused on the shallow coal and rock mass under cyclic loading and unloading. There is a lack of analysis of permeability characteristics of coal and rock mass with multiparameters in the deep. The coal stratum in the deep coal mine is mainly sandstone. Therefore, taking into account the strong disturbance caused by mining activities, this paper will study the permeability of deep rocks under different confining pressures through the permeability test of cyclic loading and unloading.

## 2. Characteristics of Specimens and Test Methods

**2.1. Sample Preparation.** The testing object is the sandstone collected from 7302 working face of Baodian Coal Mine

(Shandong Province, China) at a depth of 700 m. The vertical bedding direction is densely drilled and sampled. Before selecting the specimens having similar wave speeds and having no large fissures by NM-4B sonic apparatus, all intact cylinder specimens were cored from the same block of sandstone material to a diameter of 50 mm and a length of 100 mm, in accordance with the suggestion by ISRM. The main mineral compositions of the sandstone are quartz and clay minerals, including quartz (52%), ankerite (10%), clay minerals (31%) such as illite and kaolinite, and with minor quantities of plagioclase and Siderite. Water was used as the infiltration medium, and the osmotic pressure difference was 3 MPa. Before the test, the rock sample was saturated with water through the vacuum immersion method.

**2.2. Test Equipment and Method.** TAW-2000 type testing machine, as shown in Figure 1, was used for the triaxial cyclic loading test. The test steps are as follows: (1) in the test process, the confining pressure was firstly loaded to the corresponding confining pressure state using a loading rate of 0.01 MPa/s, and the confining pressures were selected as 5 MPa, 10 MPa, and 15 MPa, respectively. The constant osmotic pressure was 3 MPa; (2) the axial pressure was controlled by displacement. The loading rate was 0.01 mm/min, and the permeability was determined by loading to the initial predetermined value, which is 60% of the predicted peak strength; (3) unloading to hydrostatic pressure at a rate of 0.04 mm/min to complete a cycle; (4) the upper limit stress level of each cycle is increased by 10% of the peak stress of triaxial compression under the same conditions of steps (2) and (3) until the specimen was destroyed. It should be noted that the peak compressive strength of sandstone under confining pressure of 5 MPa, 10 MPa, and 15 MPa were 85 MPa, 150 MPa, and 215 MPa, respectively.

According to the traditional transient method, the permeability can be calculated by the following equation[19]:

$$K = \mu\beta V \frac{\ln(\Delta P_i / \Delta P_f)}{2\Delta t (A/L_s)}, \quad (1)$$

where  $K$  is permeability ( $\text{m}\cdot\text{s}^{-1}$ );  $\mu$  represents the viscosity of water ( $0.001 \text{ Pa}\cdot\text{s}$ );  $\beta$  represents compression coefficient of water ( $4.53 \times 10^{-10} \text{ Pa}^{-1}$ );  $V$  represents the volume of the hydraulic chamber ( $\text{m}^3$ );  $\Delta P_i$  and  $\Delta P_f$  represent initial and final osmotic pressure difference ( $P_a$ ), respectively;  $\Delta t$  is the duration of measuring permeability;  $A$  and  $L_s$  represent the cross-sectional area ( $\text{m}^2$ ) and height ( $\text{m}$ ) of the sample.

The acoustic emissions signals were captured and collected synchronously during the triaxial test process. After the acoustic emission sensor was coated with petrolatum, the pressure was given by the clamping ring to make it closely contacted with the outer wall of the triaxial chamber. The threshold value of acoustic emission was set to 35 dB.

## 3. Results and Analysis

**3.1. Permeability and Stress-Strain.** The mechanical characteristics of the rock specimens under triaxial compression are shown in Figure 2. As we can see from Figure 2, there



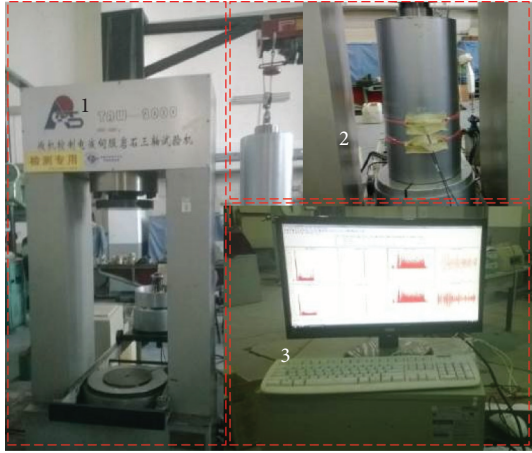


FIGURE 1: TAW-2000 rock mechanics testing system.

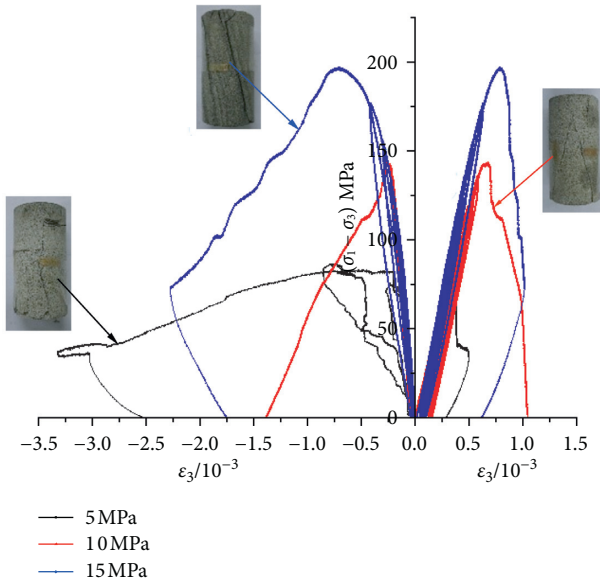


FIGURE 2: Stress-strain curves of rock samples under different confining pressures.

were 4 stages including the initial compression, elastic deformation, plastic yield, and to the post-peak failure state, during the triaxial compression process. A positive correlation can be found between the confining pressure and the peak strength as well as the peak strain. The loading curve deviated from the original loading curve after the specimen was unloaded to zero and then loaded again. During the compaction process, the axial deformation of the rock was slow. After the peak stress occurred and the rock underwent the failure stage and the axial strains increased sharply and obviously. This phenomenon indicates that the deep rocks have characteristics of brittleness which makes the rocks still have residual strength in some degree even after failure.

In order to study the deformation characteristics of the sandstone under cyclic loading and unloading, the evolution of the elastic modulus of the specimen has been recorded. This paper uses the unloading secant modulus to characterize the elastic modulus. Figure 3 shows the rock under

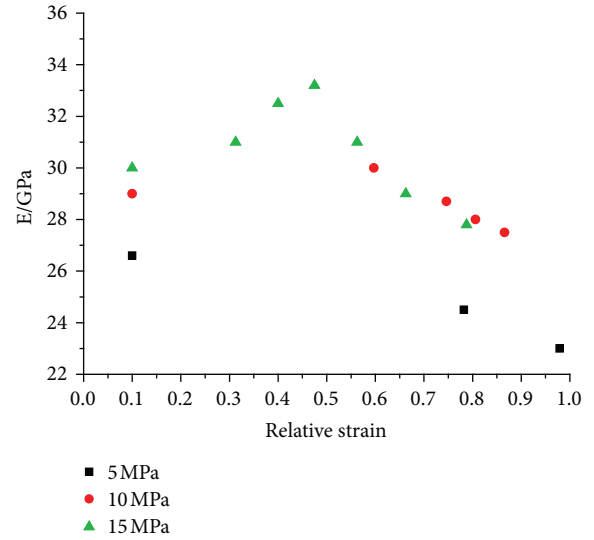


FIGURE 3: Evolution of elastic modulus under different confining pressures.

loading and unloading displays compaction before it enters the yield failure, and with the increase of stress, the elastic modulus of the rock increases first and then decreases. Meanwhile, the elastic modulus is positively associated with confining pressure.

The elastic modulus of the rock continuously changes with stress and strain. The damage variable can be written as follows and can be used to describe the damage degree of the rock under loading and unloading [22].

$$D = 1 - \frac{E_i}{E_0}, \tag{2}$$

$$\varepsilon_\eta = \frac{\varepsilon_i}{\varepsilon_t},$$

where  $D$  is the damage variable;  $E_i$  is the unloading rigidity;  $E_0$  is the initial elastic modulus of the rock, which is also known as the undamaged modulus.  $\varepsilon_n$  is the relative strain, the dimensionless parameters;  $\varepsilon_i$  and  $\varepsilon_t$  are unloading strain and peak strain, respectively. The positive and negative values of  $D$  indicate fracture damage and density damage, respectively.

Figure 4 demonstrates the damage variable ( $D$ ) and the evolution law of the permeability. The horizontal axis represents the relative strain, the ratio of corresponding strain to peak strain. The test indicates that with the increase of the relative strain, the permeability of sandstone decreases first and then increases, and there is a correlation between the permeability and damage variable ( $D$ ). Before the rock deformation gets in the plastic zone, the rock is in the compaction stage (a negative value of  $D$ ), and the permeability decreases. In contrast, after the rock deformation goes into the plastic zone, the rock gets in the stage of expansion (a positive value of  $D$ ), and the permeability increases. When the peak pressure is interrupted, the fissures of the specimen are expanded and the permeability increases rapidly. The permeability at the state of hydrostatic pressure under

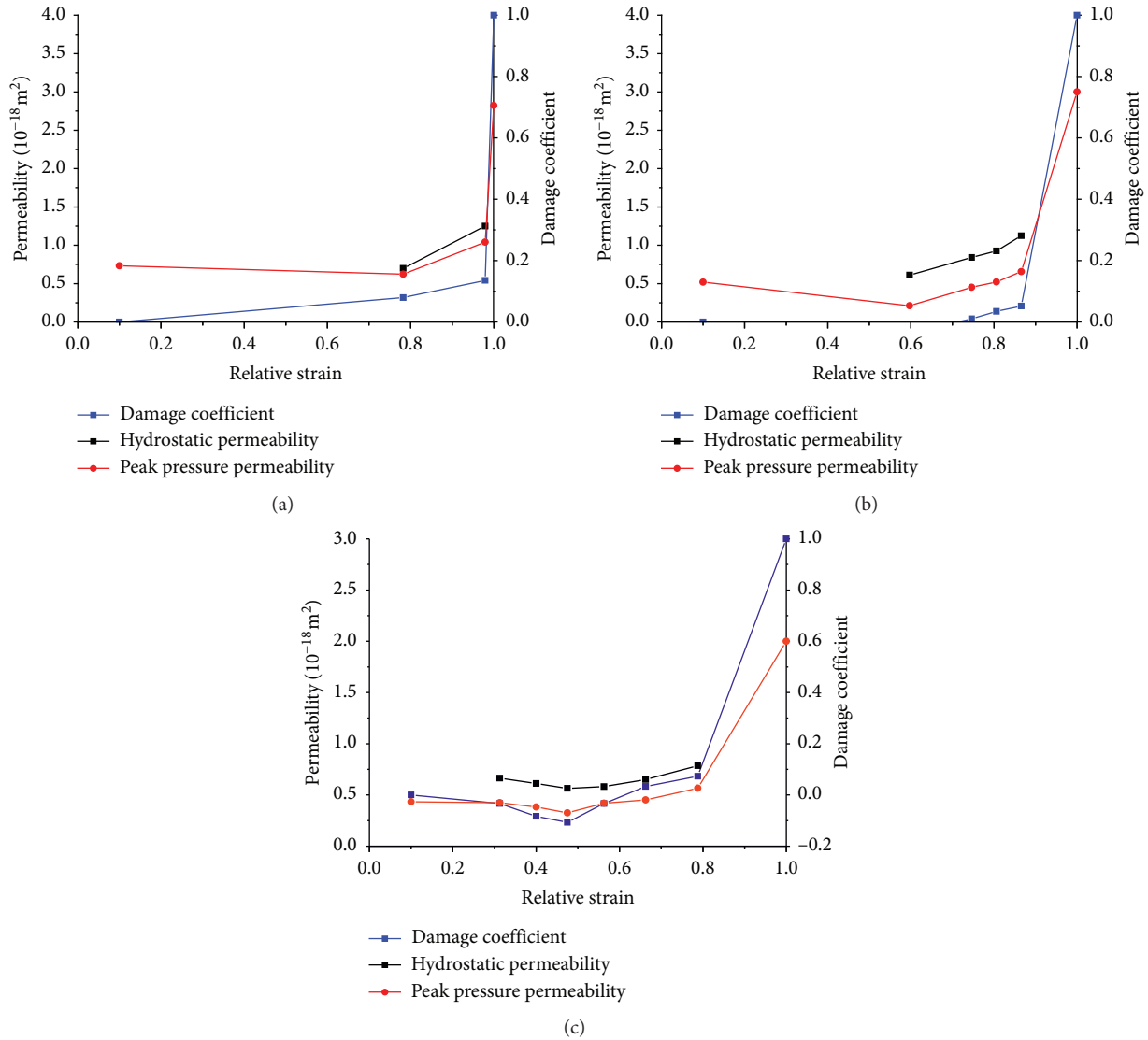


FIGURE 4: Evolution of permeability with damage  $D$  under different confining pressure. (a) Confining pressures 5 MPa. (b) Confining pressures 10 MPa. (c) Confining pressures 15 MPa.

unloading is always higher than the permeability at the state of peak stress. According to the relationship between the damage variable ( $D$ ) and permeability and relative strain, the permeability of rocks under low confining pressure increases at a strain level of about 0.8, and the permeability of rocks under high confining pressure changes at a strain level of 0.45, indicating that the increase in confining pressure will reduce the strain level of rocks to get in the yield stage.

**3.2. Permeability and Energy Characteristics.** When the rock specimen is loaded under triaxial cyclic loads, the test system transfers mechanical energy to the specimen, a proportion of which is converted into elastic energy that is stored in the specimen and can be released entirely under unloading. The rest of the energy is consumed when the plastic deformation and the damage occur in the rock specimen, and it is irreversible. As the energy is consumed in the cyclic loading

test and the dissipated energy of the rock specimen is irreversible, the hysteretic loop can be seen from the stress-strain curve [23]. The area under the unloading stress-strain curve is the elastic energy density ( $U^e$ ), and the area of the hysteresis loop in the loading-unloading stress-strain curve is the dissipated energy density ( $U^d$ ).

$$\begin{cases} U^e = \int_{\varepsilon''}^{\varepsilon'} \sigma_1 d\varepsilon_1, \\ U^d = \int_0^{\varepsilon'} \sigma_1 d\varepsilon_1 - \int_{\varepsilon''}^{\varepsilon'} \sigma_1 d\varepsilon_1, \end{cases} \quad (3)$$

where  $\varepsilon'$  and  $\varepsilon''$  are the initial strain under unloading and the strain of hydrostatic pressure after unloading, respectively.

Based on the energy statistics resulted from different confining pressures given by the cyclic loading and unloading test, with the increase of the relative strain, the elastic energy and dissipated energy of the rock specimen

increase before the peak value appears. Meanwhile, at the plastic yield stage, the dissipated energy continuously increases to the failure point where the peak value appears, and after the rock failure happens, the elastic energy decreases rapidly to a certain level which is considered as the residual elastic energy. With the increase of the confining pressure, the elastic strain energy of the specimen increases gradually and the peak elastic energy, maximum storage energy, and residual elastic energy all increase somewhat. However, the dissipated energy does not increase significantly before the rock failure happens.

The dissipated energy of rock often reflects its damage evolution, and the degree of the dissipated energy density is related to the internal damage of rock. Using the dimensionless parameter ( $k_d$ ), the proportion of dissipated energy can be written as follows:

$$k_d = \frac{U^d}{(U^e + U^d)}. \quad (4)$$

Figure 5 shows the relationship between the change in the proportion of dissipated energy density and the change in the permeability of the specimen under cyclic loading and unloading. From it, we can see (1) before the deformation of the specimen goes into the yield stage, the relative strain is low, the elastic characteristics are good, the dissipated energy density is low, and with the increase of strain, the permeability decreases. (2) when the strain goes into the field stage, the proportion of dissipated energy density grows gradually, the damage happens through rock interior, the main role of stress at this stage is a fracture, and with the increase of stress, the permeability increases slightly. (3) when the specimen reaches the peak value, the proportion of the dissipated energy density obtains the maximum value and the permeability achieves the highest level. There is a good correlation between permeability and the proportion of dissipated energy, indicating that, in the cyclic loading and unloading test, the proportion of dissipated energy can be used to predict the trend of change in permeability.

**3.3. Permeability and Acoustic Emission Characteristics.** Acoustic emission is a phenomenon caused by partial fracture of rock material and rapid release of energy in the form of elastic waves. The signal that the acoustic emission monitor captures and collects is the acoustic emission of rocks [24]. The generation of acoustic emission is related to the internal damage of the rock, and the cumulative acoustic emission events reflect the accumulated damages of the specimen under loading and unloading. Therefore, acoustic emission is important in evaluating the damage development in rocks under loading, and acoustic emission signals are monitored and used to associate different stages of crack development with different stages of the mechanical parameter evolution. Comparative analysis of acoustic emission characteristics and permeability of the specimens can

indicate the evolutionary relationship between acoustic emission and permeability. Figure 6 demonstrates the evolution law of the permeability with the cumulative AE events.

As can be seen from Figure 6,

- (1) With the characteristics of high strength and strong brittleness, at the low strain level, the degree of damage of sandstone under cyclic loading and unloading is low, the number of acoustic emission events is small, and with the increase of stress, the permeability decreases.
- (2) As the strain is close to the yield stage, the number of acoustic emission events increases rapidly under loading, and the acoustic emission signal is less under unloading, indicating that at the yield stage, the plastic zone expands under loading and the damage of rock is closure under unloading. When the strain approaches the peak strain, the rock failure happens; the number of acoustic emission events has the highest increase amplitude, and relatively, the permeability increases rapidly.

## 4. Discussion

Based on the experimental data from the cyclic loading and unloading test on sandstone under different confining pressures, this paper analyzed the evolutionary relationship between permeability and relative strain, damage, energy density characteristics, and acoustic emission characteristics. The research reveals that the evolution law of permeability of the specimens under cyclic loads is roughly the same. Under cyclic loading and unloading, the damage degree of rock affects the permeability. In addition, damage coefficient, energy density characteristics, and acoustic emission characteristics can effectively describe the evolution of permeability with rock damage. Moreover, with the increases in the proportion of dissipated energy density, damage variable ( $D$ ), and the number of acoustic emission events, the permeability increases correspondingly. A case study from the specimen under a confining pressure of 15 MPa can summarize the evolution law of permeability, as shown in Figure 7.

- (1) *The First Stage.* The sandstone specimens go into the elastic compaction stage, the relative strain is low, the degree of rock damage is low, the number of acoustic emission events is small, the proportion of dissipated energy density is small, and with the increase of stress, the permeability decreases.
- (2) *The Second Stage.* The sandstone specimens get into the stage of fissure propagation, the relative strain increases, the propagation of fissure increases through rock interior, the damage of rock is accumulated, the number of acoustic emission events grows slowly, the proportion of dissipated energy

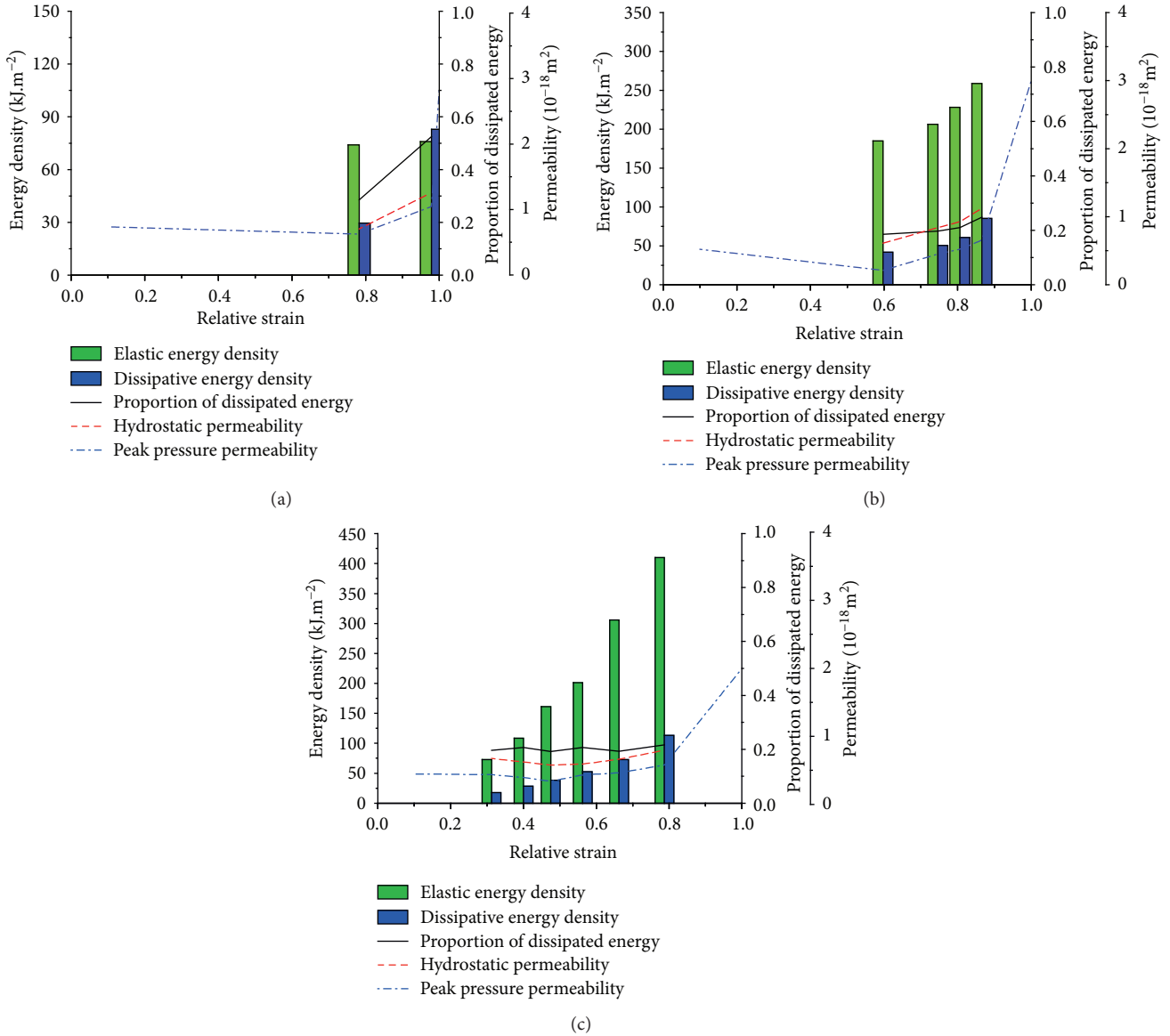


FIGURE 5: Evolution of permeability with energy under different confining pressures. (a) Confining pressures 5 MPa. (b) Confining pressures 10 MPa. (c) Confining pressures 15 MPa.

density, as well as damage variable ( $D$ ) increase gradually, and with the increase of the relative strain, the permeability increases.

- (3) *The Third Stage.* The specimens go into the stage of yield failure, the axial strain reaches the peak strain, the fissures develop into cracks, the rock failure happens, the number of acoustic emission events increases rapidly, the proportion of the dissipated energy density, as well as damage variable ( $D$ ) obtain the maximum value, and the permeability increases greatly.

To sum up, during the compaction stage, the fissures do not propagate and the evolution trend of permeability

decreases insignificantly; during the stage of fissure propagation, the permeability increases slowly and steadily; during the stage of yield failure, after the fissures develop into cracks and even cause macroscopic failure, the permeability increases significantly. There is a certain difference in relative strains which is related to different stages under different confining pressures. The permeability of rocks under low confining pressure increases at a strain level of about 0.8, and the permeability of rocks under high confining pressure changes at a strain level of 0.45, indicating that the increase in confining pressure will reduce the strain level of rocks to get in the yield stage.

Based on the analysis mentioned above, the permeability ( $P$ ) is closely related to the relative strain. The relationship

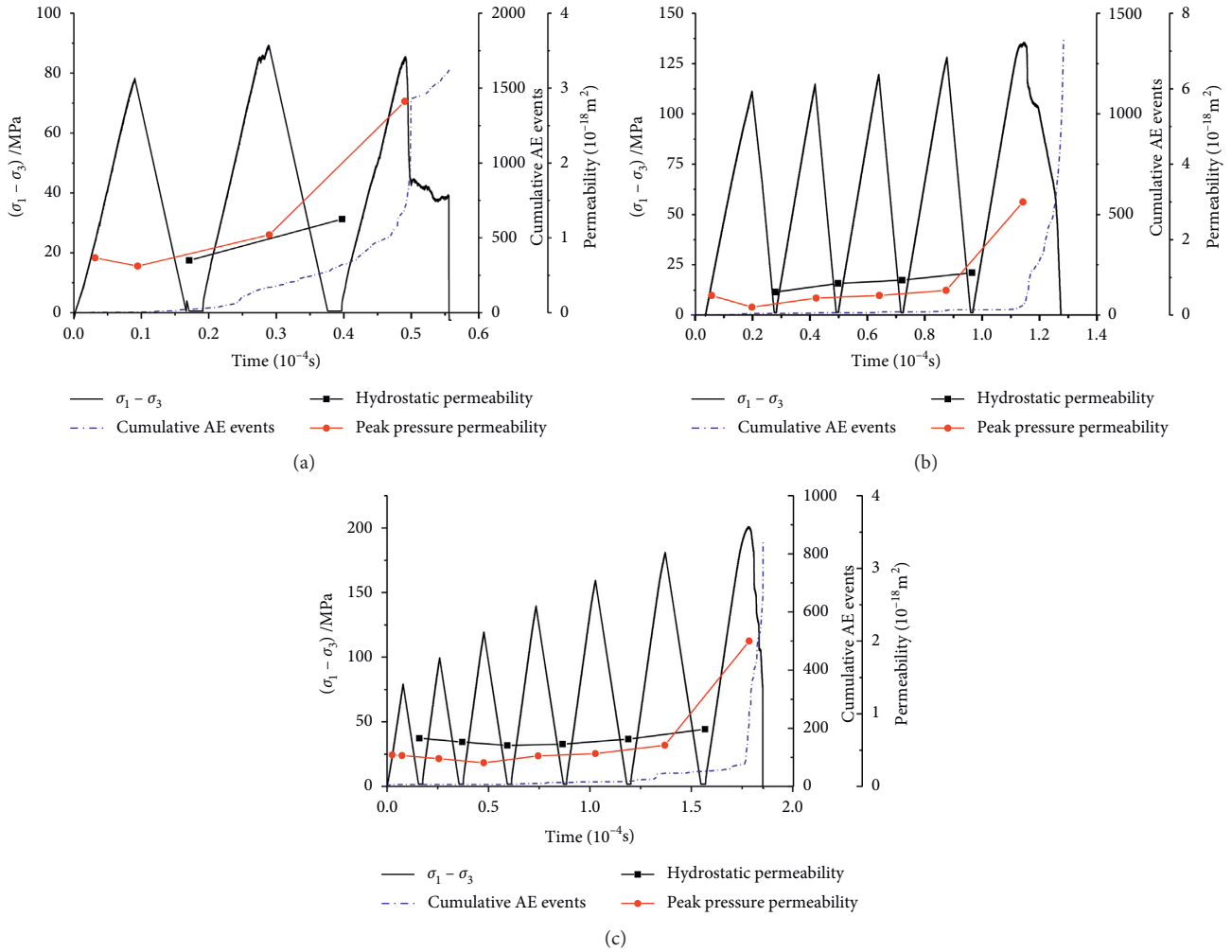


FIGURE 6: Permeability-accumulative AE events-time curves. (a) Confining pressures 5 MPa. (b) Confining pressures 10 MPa. (c) Confining pressures 15 MPa.

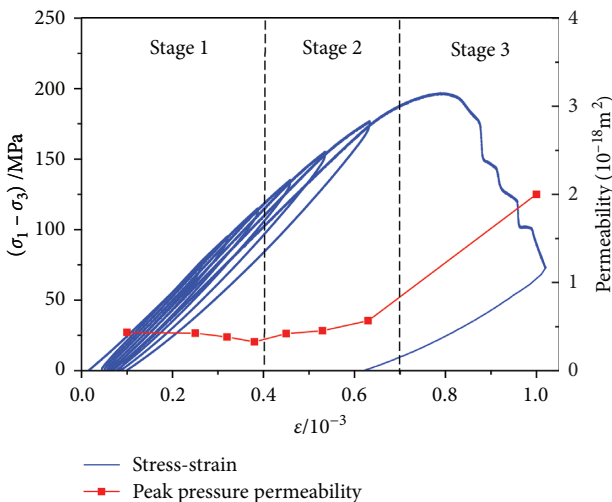


FIGURE 7: Evolution law of permeability.

between permeability and the relative strain under a certain confining pressure can be written as follows [25]:

$$P = \begin{cases} a + b\varepsilon_\eta, & (\varepsilon_\eta \leq \varepsilon_k), \\ me^{n(\varepsilon_\eta - c)}, & (\varepsilon_\eta > \varepsilon_k), \end{cases} \quad (5)$$

where  $a$ ,  $b$ ,  $m$ , and  $p$  are fitting parameters;  $n$  is the evolution rate of permeability;  $\varepsilon_k$  is the relative strain of rock specimen at the stage of fissure propagation.

In this paper, the point of fissure propagation of rock specimens is used as the point of demarcation, and the permeability and relative strain are fitted in sections. The linear function is adopted before the fissures are propagated, and the exponential function is applied after the fissures are propagated. The fitting curve is shown in Figure 8. All the fitting correlation coefficients are relatively high. Therefore, the composite function shown in equation (5) can be used to simply describe the evolution law of permeability of the rock specimens at the stress-strain stage. Before the fissures propagated, the permeability decreases with the lowest rate

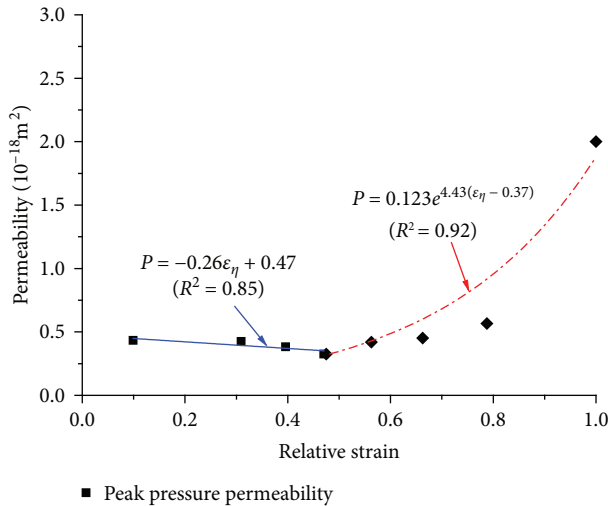


FIGURE 8: Fitting results of permeability and relative strain.

of evolution; however, after the rock specimens go into the yield stage, the permeability increases with the highest rate of evolution.

## 5. Conclusions

- (1) In the process of cyclic loading and unloading, the mechanical damage state of rock affects permeability. The damage coefficient, energy density characteristics, and acoustic emission characteristics can effectively characterize the evolution characteristics of damage and permeability. The proportion of dissipated energy density and damage  $D$  increase step by step, and the number of acoustic emission events increases, so does the permeability.
- (2) In the process of rock cyclic loading and unloading, the permeability shows three obvious stages: low relative strain level stage, permeability decreases with the increase of stress, the relative strain level increases, the internal fracture of rock sample expands, the permeability increases with the increase of relative strain level, the axial strain reaches the peak strain, the fracture expands into the crack, and the permeability increases greatly.
- (3) Taking the crack growth point of the rock sample as the boundary point, the permeability decreases slowly in the form of linear function before crack propagation and increases in the form of exponential function after fracture propagation; the greater the confining pressure is, the smaller the relative strain level corresponding to the fracture growth point is.

## Data Availability

The data used to support the findings of this study can be obtained from the corresponding author upon request.

## Conflicts of Interest

The authors declare that they have no conflicts of interest regarding the publication of this paper.

## Acknowledgments

The authors gratefully acknowledge the financial support of the National Natural Science Foundation of China (52069013).

## References

- [1] H. P. Xie, J. H. Wang, B. H. Shen, J. Z. Liu, and G. Wu, "New idea of coal mining: scientific mining and sustainable mining capacity," *Journal of China Coal Society*, vol. 37, no. 7, pp. 1069–1079, 2012.
- [2] L. Yuan, "Scientific conception of precision coal mining," *Journal of China Coal Society*, vol. 17, no. 42, pp. 1–7, 2017.
- [3] Z. C. Tang and Y. Y. Jiao, "Choosing appropriate appraisal to describe peak spatial features of rock joint profiles," *International Journal of Geomechanics*, vol. 20, no. 4, Article ID 04020021, 2020.
- [4] L. Wei, Q. Yue-ping, Z. Miao-miao, W. Cui-xia, and W. Yaru, "Test study on permeability properties of the sandstone specimen under triaxial stress condition," *Procedia Engineering*, vol. 26, pp. 173–178, 2011.
- [5] J. P. Zou, Y. Y. Jiao, Z. C. Tang, Y. L. Ji, C. Z. Yan, and J. C. Wang, "Effect of mechanical heterogeneity on hydraulic fracture propagation in unconventional gas reservoirs," *Computers and Geotechnics*, vol. 125, Article ID 103652, 2020.
- [6] Z. C. Tang, Q. Z. Zhang, and J. Peng, "Effect of thermal treatment on the basic friction angle of rock joint," *Rock Mechanics and Rock Engineering*, vol. 53, no. 4, pp. 1973–1990, 2020.
- [7] L. Chen, J. F. Liu, C. P. Wang, J. Liu, R. Su, and J. Wang, "Characterization of damage evolution in granite under compressive stress condition and its effect on permeability," *International Journal of Rock Mechanics and Mining Sciences*, vol. 71, pp. 340–349, 2017.
- [8] U. M. Yasidu, Y. Fujii, J.-i. Kodama et al., "Influences of water vapor on roof fall accidents in selected underground coal mines in Malawi," *Advances in Civil Engineering*, vol. 2019, pp. 1–17, Article ID 6243609, 2019.
- [9] S. P. Peng, H. L. Qu, L. P. Luo, L. Wang, and Y. E. Duan, "An experimental study on the penetrability of sedimentary rock during the complete stress-strain path," *Journal of China Coal Society*, vol. 25, no. 2, pp. 113–116, 2000.
- [10] H. L. Wang, W. Y. Xu, and S. Q. Yang, "Experimental investigation on permeability evolution law during course of deformation and failure of rock specimen," *Rock and Soil Mechanics*, vol. 27, no. 10, pp. 1703–1708, 2006.
- [11] Q. Kong, H. L. Wang, S. P. Ran, and Z. N. Lin, "Experimental investigation on relationship between porosity and permeability of sandstone under cyclic loading condition," *Journal of China Three Gorges University (Natural Sciences)*, vol. 37, no. 4, pp. 55–61, 2015.
- [12] X. Chen, J. Yu, C. A. Tang, H. Li, and S. Y. Wang, "Experimental and numerical investigation of permeability evolution with damage of sandstone under triaxial compression," *Rock Mechanics and Rock Engineering*, vol. 50, pp. 1529–1549, 2015.
- [13] D. S. Yang, X. Y. Qi, W. Z. Chen, S. G. Wang, and J. P. Yang, "Anisotropic permeability of coal subjected to cyclic loading and unloading," *International Journal of Geomechanics*, vol. 18, no. 8, pp. 85–93, 2018.
- [14] R. D. Peng, Y. Ju, F. Gao, H. P. Xie, and P. Wang, "Energy analysis on damage of coal under cyclical triaxial loading and unloading conditions," *Journal of China Coal Society*, vol. 39, no. 2, pp. 245–252, 2014.

- [15] Q. Meng, M. Zhang, L. Han, H. Pu, and T. Nie, "Effects of acoustic emission and energy evolution of rock specimens under the uniaxial cyclic loading and unloading compression," *Rock Mechanics and Rock Engineering*, vol. 49, no. 10, pp. 3873–3886, 2016.
- [16] D. Li, Z. Sun, T. Xie, X. Li, and P. G. Ranjith, "Energy evolution characteristics of hard rock during triaxial failure with different loading and unloading paths," *Engineering Geology*, vol. 228, pp. 270–281, 2017.
- [17] Q. Li, Y. Liang, Q. Zou, and Q. Li, "Acoustic emission and energy dissipation characteristics of gas-bearing coal samples under different cyclic loading paths," *Natural Resources Research*, vol. 29, no. 2, pp. 1397–1412, 2020.
- [18] Y. Cai, D. Liu, J. P. Mathews et al., "Permeability evolution in fractured coal - combining triaxial confinement with X-ray computed tomography, acoustic emission and ultrasonic techniques," *International Journal of Coal Geology*, vol. 122, pp. 91–104, 2014.
- [19] H. Zou, J. F. Liu, B. Yu, Z. W. Zhou, and Z. Yue, "Experimental study on mechanical and permeability properties of sandstone with different granularities," *Chinese Journal of Geotechnical Engineering*, vol. 37, no. 8, pp. 1462–1468, 2015.
- [20] Y. Zhao, H. Zhou, J. Zhong, and D. Liu, "Study on the relation between damage and permeability of sandstone at depth under cyclic loading," *International Journal of Coal Science & Technology*, vol. 6, no. 4, pp. 479–492, 2019.
- [21] X. Y. Wang, H. W. Zhou, J. Zhong et al., "Study on energy evolution and permeability characteristics of deep coal damage under triaxial cyclic loading and unloading conditions," *Chinese Journal of Rock Mechanics and Engineering*, vol. 37, no. 12, pp. 2676–2684, 2018.
- [22] J. W. Zhou, X. G. Yang, W. X. Fu et al., "Experimental test and fracture damage mechanical characteristics of brittle rock under uniaxial cyclic loading and unloading conditions," *Chinese Journal of Rock Mechanics and Engineering*, vol. 29, no. 6, pp. 1172–1183, 2015.
- [23] H. P. Xie, *Damage Mechanics of Rocks and Concrete*, pp. 11–25, China University of Mining and Technology Press, Xuzhou, 1998.
- [24] H. Li and H. Li, "Mechanical properties and acoustic emission characteristics of thick hard roof sandstone in Shendong coal field," *International Journal of Coal Science & Technology*, vol. 4, no. 2, pp. 147–158, 2017.
- [25] L. Chen, J. F. Liu, C. P. Wang, J. Liu, R. Su, and J. Wang, "Investigation on damage evolution characteristic of granite under compressive stress condition and its impact on permeability," *Chinese Journal of Rock Mechanics and Engineering*, vol. 33, no. 2, pp. 287–295, 2014.

## Research Article

# Change Detection and Feature Extraction of Debris-Flow Initiation by Rock-Slope Failure Using Point Cloud Processing

Xiaoying He <sup>1</sup>, Zeqing Yu <sup>1</sup>, John M. Kemeny,<sup>2</sup> Ann Youberg <sup>3</sup> and Yunkun Wang <sup>4</sup>

<sup>1</sup>College of River and Ocean Engineering, Chongqing Jiaotong University, Chongqing 400074, China

<sup>2</sup>College of Engineering, University of Arizona, Tucson, AZ 85721, USA

<sup>3</sup>College of Science, University of Arizona, Tucson, AZ 85721, USA

<sup>4</sup>College of Engineering, University of Toronto, Toronto, ON M5S, Canada

Correspondence should be addressed to Xiaoying He; [xiaoyinghe@cqjtu.edu.cn](mailto:xiaoyinghe@cqjtu.edu.cn)

Received 23 November 2020; Revised 14 December 2020; Accepted 29 December 2020; Published 12 January 2021

Academic Editor: Xiaobo Zhang

Copyright © 2021 Xiaoying He et al. This is an open access article distributed under the Creative Commons Attribution License, which permits unrestricted use, distribution, and reproduction in any medium, provided the original work is properly cited.

Our understanding of debris-flow initiation by slope failure is restricted by the challenge of acquiring accurate geomorphic features of debris flows and the structural setting of the rock mass in the remote mountainous terrain. Point cloud data of debris flows in Sabino Canyon, Tucson, Arizona, July 2006, with initiation by joint-controlled rock slope were obtained using multitemporal LiDAR scanning. Topographic changes were detected by comparing historical LiDAR scanning data of this area since 2005 by adopting open-source CloudCompare software. The results showed persistent scour and erosion in the debris flows after 2006. Point cloud data of joint-controlled rock in the initiation zone were generated by the means of photogrammetry using Pix4D software. The joint planes, the dip direction and the dip value of the joint plane, the joint spacing, and the joint roughness were therefore acquired by point cloud processing. Our study contributes a foundation for analyzing the relationship between the rock features, the generation of slope failure, and the initiation of debris flows.

## 1. Introduction

Debris flows that are often initiated in the mountainous terrain and triggered by heavy rainfall are significant geologic hazards that can lead to catastrophic damage across large regions [1–3]. Mitigation and early warning of the hazards posed by the debris flows require an understanding of the mechanisms leading to their initiation [4, 5].

Geologists have long recognized that debris flows were initiated by a slide, debris avalanche, or rockfall from a steep bank ( $>20^\circ$ ), synchronously or lag behind rainfall [1, 6, 7]. The instability of rock slope projected rock fragments directly into the steep upper channels, providing both the initial material and steep gradient for the debris flow, making debris flows heavy in terms of volume and weight and thereby leading to its rapid occurrence [7, 8].

The processes for the mobilization of debris flows from slope failure include the Coulomb failure within the sloping mass, liquefaction, and high pore-fluid pressures of the mass

by the rapid undrained loading of rockslides and the conversion of the landslide translational energy to internal vibrational energy [1, 9, 10]. Gradient, angle of entry of failure into the channel, and the amount of in-channel stored sediment are regarded as the parameters that determine the initiation of debris flows by rock-slope failure [9, 10].

In order to figure out the initiation of debris flows, field observation, empirical models, experimental modeling, statistical and simulation models, and hydromechanical models have been adopted [11, 12]. However, these models are data-dependent. It always requires the estimation of a larger number of parameters, as well as knowledge of the initial conditions and boundary conditions [3]. Particularly for rockslide debris flow, the joints have profound effects on the rock-slope stability [13]. Joint parameters, that is, joint spacing, joint length, joint roughness, and joint orientation, influence the weathering velocity, the size of blocks, the rock strength, and the fissure-fluid pressure distribution during heavy rainfall events [14–16]. Subtle differences in joints can



lead to significant differences in the erodibility and rock-slope stability, thus leading to the initiation of this type of debris flows [17].

However, challenges still exist in obtaining accurate and detailed features of the debris flows and rock mass in a safe way, since the debris flows usually originate in the remote mountainous terrain and/or steep rock slopes [17, 18]. Conventional survey methods present serious limitations for collecting the datasets required for the analysis and modeling of the debris flows. Therefore, technologies like the aerial photography, LiDAR (Light Detection and Ranging), and photogrammetry technologies are applied to extract the data in an unbiased and secure way [2, 19, 20]. Point cloud data generated in these ways could then be processed to extract the necessary parameters for rock-slope failure-initiated debris flows.

In the present work, the historical LiDAR datasets before and after the debris flow event in 2006 in the study area were used for detecting topographic changes. Point cloud data of the rock in initiation zones with joint sets generated by photogrammetry were processed for obtaining the detailed joint parameters. The aim of this research was to demonstrate the effectiveness of the LiDAR and point cloud processing in acquiring the geomorphic features of debris flows and the joint parameters.

## 2. Study Area

**2.1. Setting.** The study area is located on the Santa Catalina Mountains roughly 15 km northeast of Tucson, Arizona, the United States (Figure 1).

The Santa Catalina Mountains are a metamorphic core complex typical of the Basin and Range Province of North America, and the bedrock of the southern half of the range is almost entirely granitic [21]. Elevation ranges from 805 m at the mountain front at Sabino Canyon to 2800 m at Mount Lemmon [22]. The Santa Catalina Mountains are bounded on the south by the low-angle Catalina detachment fault and on the west by the high-angle Pirate fault. Offset along these faults occurred in two separate intervals of deformation and uplift. The first extension along an  $\sim 240^\circ$  azimuth was accompanied by tectonic tilting of an extension-parallel topographic ramp and by antiformal arching along a direction approximately orthogonal to extension. The second extension was oriented more nearly east-west compared to the earlier phase of extension [22].

The climate is semiarid across most of the Santa Catalinas, with mean annual precipitation ranging from 330 mm at the mouth of Sabino Canyon to 750 mm on Mount Lemmon. About 45% of rainfall falls during the summer monsoon season of July through September, typically in convective storms [23].

**2.2. Debris-Flow Description.** In July 2006, a week of extreme precipitation (recurrence interval > 1000 years for 4-day precipitation) in the study area caused 435 slope failures and spawned numerous damaging debris flows [22, 23]. Sabino Canyon, a heavily used recreation area, located at the

southern flank of Santa Catalina Mountains (the drainage area is estimated to be  $89 \text{ km}^2$ ), had the most slope failures (Figure 1) [24]. At least 13 debris flows occurred in this area and resulted in the creation of the steep chutes down to the Sabino Creek. Numerous large boulders were entrained, adding mass to debris flows and compounding damage of the roads, bridges, and structures in Sabino Canyon including the destruction of structures and the roadway, and resulted in closed public access for months [24].

Digital orthophotography orthophotos produced by the Pima Association of Governments' (PAG's) Regional Remote Sensing Program show the debris-flow activities in Sabino Canyon (Figure 2).

There were more than fifty slope failures occurring in lower Sabino Canyon (Figure 2). Many of them aggregated debris-flow tracks and resulted in the creation of the steep chutes down to the Sabino Creek.

Debris flows were joint-controlled and oriented parallel and perpendicular to the extension-related joint sets and geomorphology in a range of settings (joint control on network geometry) [25].

Debris flows were typically initiated on a steep slope before developing into a rapid flow confined by a steep channel and ultimately deposited the material downstream on the Sabino Creek (Figure 3).

The topography of most slope failure surfaces was hollow chute. Colluvium and diluvium on these chutes, that is, debris, had already been removed by rain, flowing along the narrow (<4.5 m wide) and relatively long (about 457 m) chutes, all the way to the canyon bottom (the Sabino Creek). Bedrock was exposed after the debris migration process; therefore, the mean failure depth was consistently about the depth of colluvium and diluvium,  $0.8 \pm 0.4 \text{ m}$  [24].

**2.3. Rock Cliffs in Initiation Zone.** The initiation zone of the debris flows was near vertical bedrock outcrops of the Wilderness Granite [21] and consisted of central core granitic intrusion flanked with a metamorphic core complex on the margins [25]. Steep talus slopes below these outcrops were covered with thin colluvium [24]. Each debris flow had one or multiple initiation points, finally gathered in Sabino Canyon (Figure 4).

The slope failures from July 2006 occurred between elevations of 1220 and 1830 m, and the failure surface in many cases was the bedrock.

Two nearly orthogonal, steeply dipping structural joint sets (WSW-ENE trending and SSE-trending) incised the bedrock into blocks (Figure 5) that mobilized the sediment and contributed to the initiation of the debris flows and also to the enormous potential and kinetic energy of the debris flows, leading to the scouring of material from the hillsides, channels, and downstream channels [23].

## 3. Change Detection of Debris Flows

After the unusual extreme rainfall event in late July 2006, the debris-flow activities in Sabino Canyon subsided, but it never meant being incapable of its recurrence, because of the

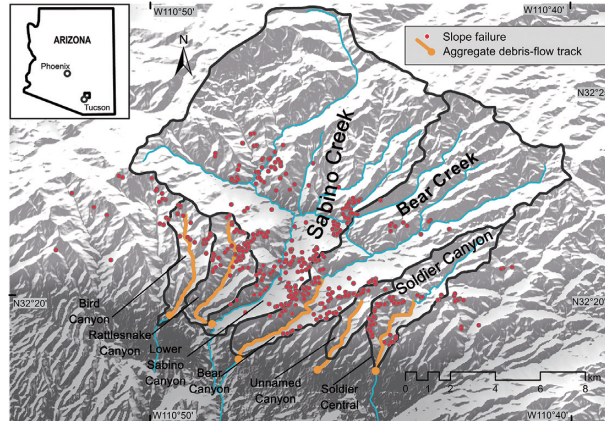


FIGURE 1: Location map showing the position of slope failures and debris flows that occurred in Santa Catalina Mountainous area, Pima County, southern Arizona, in late July 2006.

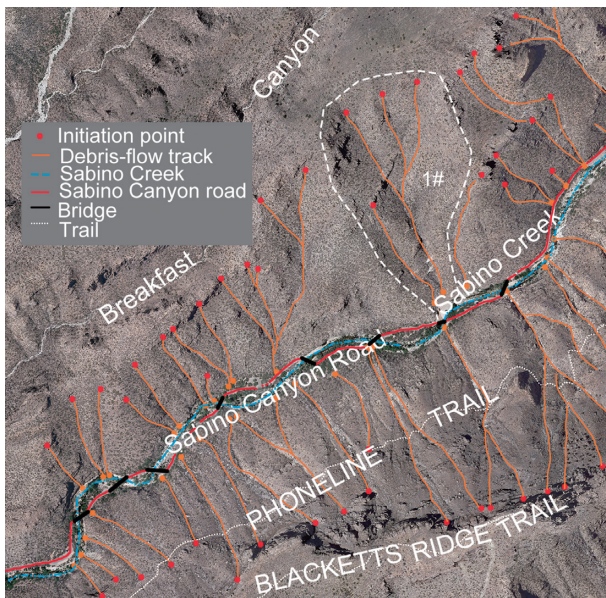


FIGURE 2: Orthophoto of Sabino Canyon collected in 2015 by PAG (2.56 km<sup>2</sup> area with a 15 cm accuracy, edited).



FIGURE 3: Slope failures and debris flows along the east side of Sabino Canyon. Photograph obtained from Magirl, 2009.

unpredictable weather conditions. A little change of topography might attribute to the debris flows [26]. Monitoring the topographic changes in debris-flow areas was important to indicate the likelihood of slope failure and debris flows. LiDAR technology has the potential to precisely identify and quantify the topographic change [27], which has been applied in investigations to rapidly provide detailed topographic models [20, 28]. Therefore, we tried to precisely quantify the change in Sabino Canyon, by processing the point cloud generated from LiDAR scanning.

**3.1. Point Cloud Data Preprocessing.** Four high-resolution LiDAR datasets were collected by the Pima Association of Governments’ (PAG’s) Regional Remote Sensing Program before and after the debris-flow event, in 2005, 2007, 2011, and 2015, which imaged a 2.6 km<sup>2</sup> swath of the ground covered study area.

The datasets were high-density collections (greater than or equal to 1 pulse per square meter (pls/m<sup>2</sup>)). Aggregate nominal pulse density (ANPD) was used to represent the point density of LiDAR datasets measured in the areas of Sabino Canyon Road, where the datasets were relatively flat and unchanged. The ANPDs of LiDAR dataset were 1.6301 pls/m<sup>2</sup>, 2.0517 pls/m<sup>2</sup>, 2.4804 pls/m<sup>2</sup>, and 3.0776 pls/m<sup>2</sup>, respectively. ANPDs of LiDAR data collected in 2007, 2011, and 2015 were up to the minimum acceptable quality level 2 (ANPD ≥ 2.0 pls/m<sup>2</sup>) [29].

The validity of comparing the topographic change of different LiDAR datasets was checked by calculating the error range of *z* values of a different LiDAR database in an area with a perfectly flat level surface, since dust could cause erroneous measurements of LiDAR data. We selected an overlapped ten meters long hard surface road in lower Sabino Canyon Road as the surrogates with a relatively subdued topographic change. The mean difference value ± 1 standard deviation was selected to be an error range (Table 1). A ±0.30 m overall error range was selected to represent the differenced value, which meant that when differentiating the LiDAR datasets, elevation changes less



FIGURE 4: A large chute that passed the debris flows with its multiple, steep talus slope initiation points.



FIGURE 5: Two primary steeply dipping joint sets taken around the Thimble peak. The joint sets marked in the photo are the one along an  $\sim 240^\circ$  azimuth, and the other joint sets are the slope orientation which is nearly east-west azimuth.

than  $\pm 0.3$  m were not considered. Comparison and change detection were performed based on these datasets.

**3.2. Change Detection.** Following the quality testing of the data, we performed the topographic change analysis by means of the open-source CloudCompare software (version 2.11. Alpha, 2019). The CloudCompare software is a 3D point cloud (triangular mesh) editing and processing software, which supports various point cloud processing algorithms and provides a good comparison between the point cloud datasets.

The mesh to mesh distance computation in the CloudCompare is a unique way to compute the signed distances directly between the reference mesh and the compared mesh, which calculates the nearest neighbor Euclidean distance between the two meshes. This is regarded as a reflection of the topographic change.

The three steps that were taken before distance computation are as follows:

- (1) Importing and denoising the point cloud data: LiDAR datasets were imported, respectively, into CloudCompare software to clean the noise by using filtering scale value. We retained the vegetation instead of removing them because of the imprecise vegetation removal at present [30, 31]. Furthermore, the growth rate of the major vegetation in the study area, Saguaro, was less than 0.3 m in 10 years, which could be ignored compared with the accuracy of LiDAR datasets.
- (2) Meshing point cloud data and reconstructing slope surfaces: the extensive point data of each year were meshed by implementing the triangulated meshing tool to generate the triangulated irregular networks (TINs) by reconstructing the 3Dslope surface.
- (3) Registering and computing: two data to be compared were registered by applying the ICP algorithm, which aimed to minimize the Euclidean distance between the two 3D point clouds. The signed distance between every two meshes could be computed after registration to align with the real-life coordinates and for implementing a distance computation algorithm.

The topographic changed maps using the LiDAR data recorded the land surface before and after event is shown in Figure 6, where the previous year was set as reference data and the subsequent year represented a compared data. The positive distance meant that the compared mesh was outside the reference mesh and the negative distance meant that the compared mesh was inside the reference mesh. Color scale referred to the range of signed distance and the bulge on the right of the color scale represented the distribution of computation results. 700 represented the plotting scale, meter.

Compared with the large spatial scale, the change was quite insignificant. Most of the changes between the two meshes were concentrated on a small interval ranging from  $-1$  m to  $1$  m, since the colluvium covered on the slopes was thin ( $<1$  m). In order to clearly observe the topographic change relative to its area, we edited the color scale to concentrate it on an interval ranged from  $-1$  m to  $1$  m to show the primary topographic change (Figure 6). The distance computation results exhibited evident changes before and after the debris-flow events that occurred in 2006, showing an extensive positive change in 2007 compared with 2005. Compared with 2007, a constant negative change occurred later, and a relatively bigger negative change happened during the period from 2007 to 2011 (Figures 6(b) and 6(c)), whereas a relatively inconspicuous change was exhibited from 2011 to 2015 (Figure 6(d)).

The topographic changes in debris-flow areas from 2006 to 2015 are illustrated in Table 2.

Debris-flow events that occurred in 2006 delivered the debris as well as the thin colluvium covered on the slope (around 1 m) from high elevation to low elevation, which exhibited a relatively flat gradient, thereby providing a deposit place for debris flows and leading to positive changes.

TABLE 1: z value difference comparison in areas of data overlap.

Year flown	Range of z difference (m)	Error range (m)	Overall error range (m)
2005	-0.51 to 0.41	$0 \pm 0.28$	
2007	-0.51 to 0.45	$0 \pm 0.27$	
2011	-0.51 to 0.53	$0 \pm 0.26$	$\pm 0.30$
2015	-0.64 to 0.65	$0 \pm 0.27$	

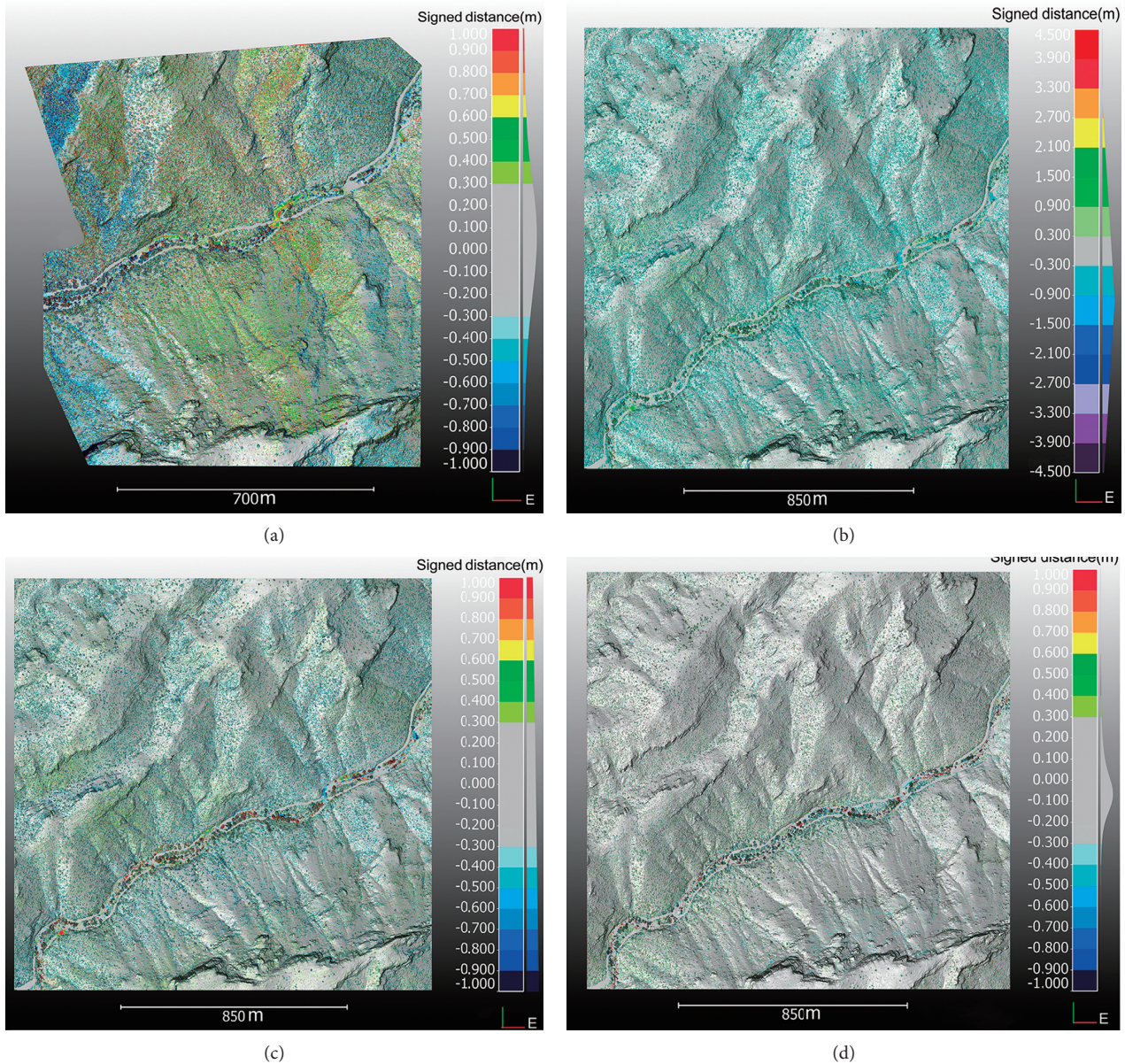


FIGURE 6: The result of distance computation.

Erosion of debris flows took place after 2007 due to the continuous weathering of the bedrock and the velocity of erosion was high during 2007 and 2011 and slowed down after 2011.

The largest and persistent positive or negative distance occurred along the Sabino Creek that was especially concentrated at the snout of the chute of debris flows, which was

because the Sabino Creek provided a natural deposition place for all the debris flows as well as a scour and transportation for the debris.

At the initiation points, the rock cliffs of the debris flow in Sabino Canyon, especially the ones at upper and middle regions, had already reached the ridge, making a gentle gradient of the rock slopes on the initiation points. However,

TABLE 2: Change detection results of debris flows.

No.	Year	Color scale (m)	Topographic changes
(a)	2005–2007	–1.0–1.0	An extensive positive change around 0.3 m to 0.9 m on the slope represents a mass deposition which is almost caused by the debris delivered by the debris flows. Obvious negative changes occurred along the big chutes of debris flows in lower Sabino Canyon, representing strong erosion caused by the scour of debris flows.
(b)	2007–2011	–4.5–4.5	A wide negative change represents continuous weathering and erosion, while a relatively small positive change existed at the lower canyon on its west side, signifying the continuous sediment deposition in that area.
(c)	2007–2011	–1.0–1.0	A more distinct weathering and erosion on the slopes and obvious sediment in the Sabino Creek.
(d)	2011–2015	–1.0–1.0	Positive change around 0.3 m to 0.9 exists on the slope showing a mass deposition caused by the debris delivered by the debris flows. Negative changes occurred along the big chutes of the debris flows in lower Sabino Canyon, representing the strong erosion caused by the scour of the debris flows.

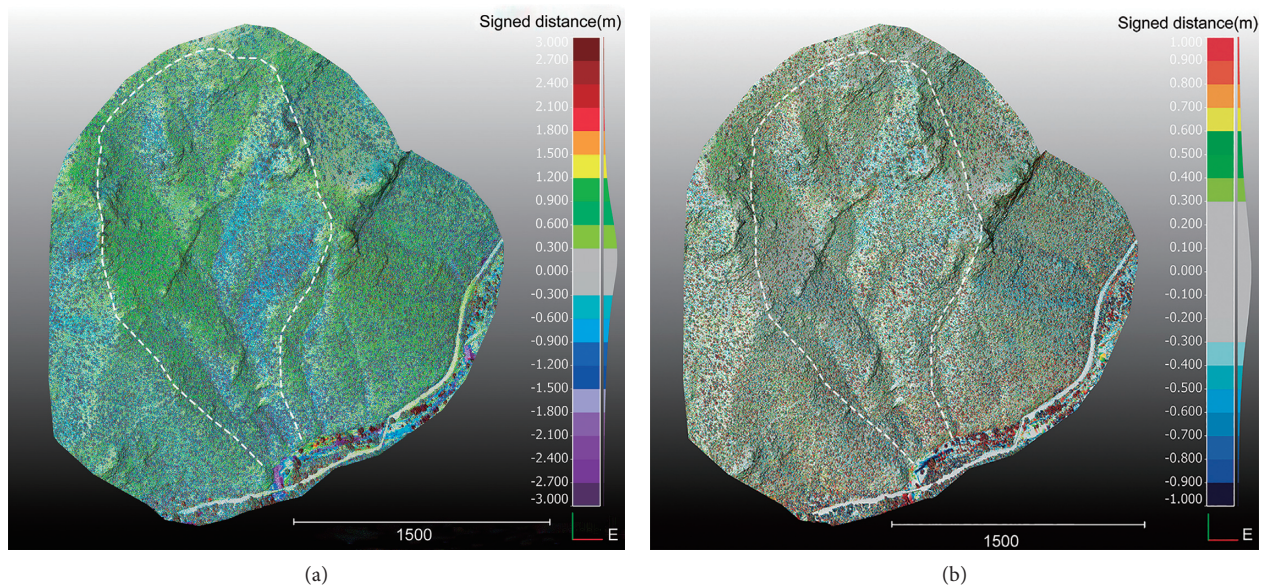


FIGURE 7: The change detection of debris-flow area. (a) The changes in the detection in 1# debris flow from 2007 to 2011. It showed strong erosion in debris-flow chute which ranged from 1.2 m to 1.5 m. A relatively small positive change ranging from 0.3 m to 0.6 m occurred outside the debris flow, representing the deposition on the slope due to the weathering and small pieces of rocks that fell down from the steep initiation points. (b) The changes in the detection in 1# debris flow from 2011 to 2015. It showed inconspicuous change during these 4 years which shows that the debris flow tends to be stable.

the ones located at lower Sabino Canyon had a steeper gradient, which was almost vertical, where most slope failures and debris flows occurred.

To show a more detailed change for all parts of debris flows, we segmented the point cloud in debris flows marked in Figure 2 and compared the change from 2007 to 2015 because of the fragmentary data of that area collected in 2005, as illustrated in Figure 7.

On comparing the changes in the detection results of the data collected in 2011 and those collected in 2007, a more visible change was seen and a stronger erosion occurred at the initiation area at the east side of the chute, about 1.2 m to 1.5 m, but a relatively positive change existed outside the debris-flow area due to probable deposition of the debris (Figure 7(a)). After 2011, the topographic changes seemed to

be slowed down, with a relative change distance  $\pm 1$  m, and mainly concentrated in a range less than 0.3 m (Figure 7(b)).

A noticeable relative visible negative change occurred at the initiation points as well as the chutes of debris flows, which showed the continuously unstable condition of the rocks. A little change in this could cause the probability of the formation of debris flows.

From the field observations, it was found that the bedrock exposed on the steep rock cliffs was quite joint-controlled. Two joint sets incised the bedrock in the study area, which affected both the stability of the rock cliffs and the initiation of the debris flows. However, the historic LiDAR data were comprised of the topographic changes of the debris flows in an unbiased, rapid, and accurate manner from a remote distance. However, it lacked the detailed



FIGURE 8: Point clouds of rock block sample generation by photogrammetry. (a) Rock block samples that were taken at the bottom of the Thimble peak. (b) Point cloud data of the rock block samples generated in Pix4D and segmented in CloudCompare software.

information and accuracy about the characteristics of the rocks in the initiation, which was necessary for analyzing the change of debris flows and the rock cliffs.

#### 4. Joint Features of Rock at Initiation Zone

In the present work, we employed the photogrammetry technology to acquire a point cloud of rock, which has been widely used in geological disaster monitoring [31, 32]. The joint parameters were obtained using the CloudCompare software, which reduced the amount of manual labor involved and enabled us to use a mobile phone combined with a camera instead of the costly 3D laser scanner.

**4.1. Point Cloud Data Generation by Photogrammetry.** A rock block sample, closing to the initiation point of debris-flow chute, is shown in Figure 6(b) containing groups of joint sets selected in a talus rock slope (Figure 8(a)).

166 images were then taken using a mobile phone with the mobile phone built-in WGS 84 (EGM 96 Geoid) coordinate system. Subsequently, the images were uploaded to the photogrammetry Pix4D software (<https://www.pix4d.com/>), and the images were firstly calibrated with a 2.99% relative difference between the initial and optimized internal camera parameters. 62148 key points were then collected per image with an average 0.08 cm/1 cm ground sampling distance (GSD), and 26266.8 of them were matched per calibrated image. Then, the noise was filtered, and the surface smoothed point cloud of the block was densified and generated using the point cloud for processing automatically. The number of 3D densified points was 6203692 and the average density was 1028353 pls/m<sup>2</sup>, which was quite a high quality. Finally, the point cloud data were output with WGS 84/UTM zone 12N (EGM 96 Geoid) coordinate system.

In order to acquire the joint parameters of the rock block, the point cloud file was imported to the CloudCompare software (7,080,405 points), the point cloud data were cleaned, and the vegetation was removed manually using a segmentation tool (4,559,945 points left) (Figure 8(b)).

#### 4.2. Joint Parameters Measurement

**4.2.1. Joint Identification and Joint Orientation.** Joint surfaces can be detected by the means of the CloudCompare software using the “RANSAC Shape Detection” plugin, an interface to the automatic shape detection algorithm proposed by Schnabel et al. [33], which can extract shapes by randomly drawing minimal sets from the point data and constructing corresponding shape primitives.

The normal of the point cloud was computed first and 50,000 was selected as the number of samples per “plane” primitive to detect the joint face based on our cloud density and the size of the joint faces to be detected. 16 planes were detected, and 10 planes were picked up manually by removing those inaccurate distinctly. Accordingly, the joint parameters were measured or calculated. Dip value and dip direction were displayed after segmenting the rock blocks by cross section and converting the normal to dip and dip direction.

Three joint sets were identified (Figure 9), while it was noteworthy that the orientation of the two joint sets detected by RANSAC matched well with the field observations conducted in December 2018. However, the third bedding plane did not match. The reason for this could be the horizontal orientation of the bedding plane, which caused an error between the reality and the field measurement.

Detected results of the joints were compared with the field observation and displayed in Table 3.

**4.2.2. Block Size.** The joint spacing was measured by the distance detection between the joint planes after obtaining the section point cloud of each detection plane using the “Cross Section” tool. Joint density was approximately 1.5 times the SSE-NNW trending joint set compared to the WSW-ENE-trending joint set.

Block size was therefore calculated by computing the joint space and the results are shown in Table 4.

**4.2.3. Joint Roughness.** The normal vector is a three-dimensional parameter that represents a plane, which can be obtained in CloudCompare software. The roughness along a

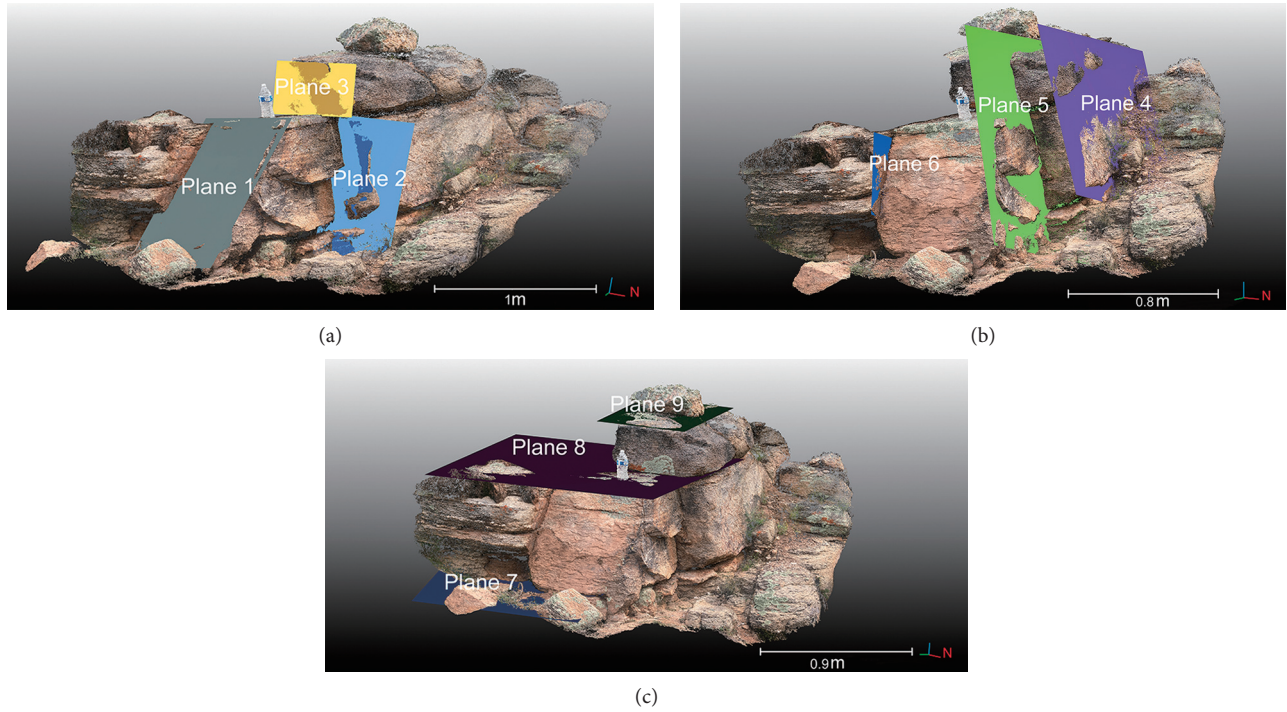


FIGURE 9: Joint sets of sample rock blocks. (a) Joint set 1. (b) Joint set 2. (c) Joint set 3.

TABLE 3: Information of plane detection.

Joint sets	Plane	Point number	Trend (°)	Plunge (°)	Trend (°)		Plunge (°)		Trend angular deviation
					RANSAC	Field	RANSAC	Field	
1	1	562,308	217	70					2.5550
	2	282,536	234	81	231	80	223	82	12.2785
	3	105,497	242	89					5.3921
2	4	367,858	158	68					7.0292
	5	376,927	153	76	155	147	75	72	12.0665
	6	59,363	154	72					17.4691
3	7	237,004	249	19					22.9368
	8	258,733	230	23	233	330	23	22	34.3245
	9	101,392	230	26					26.6021

TABLE 4: Information on joint sets.

Joint sets	Orientation	Joint spacing (m)	Block size (m <sup>3</sup> )
1	SSE-NNW	0.9071	
2	WSW-ENE	0.6167	0.30040
3	/	0.5370	

joint face in different azimuths may help characterize the roughness in a more realistic way, providing insight into the variation in shear strength along different azimuths [26, 34, 35].

In this study, we computed the dip direction and dip value of the orient normal vector of triangles formed by three adjacent points along a detected joint surface by using

simple spherical statistics equations. The mean orient normal of the best-fitting plane was calculated by the calculation of the Fisher mean vector. The standard angular deviation of orientation normal between every polygon and the mean normal vector was assumed to represent the surface roughness.

The orientation of the normal was obtained and was plotted on a stereo net, wherein the scatter plot showed the point dense, and the contour plot displayed the distribution of orient normal (Figure 10).

The standard angular deviation of the orient normal along each detected joint surface could reflect the joint roughness, as shown in Table 2. Accordingly, the bedding planes exhibited the roughest surface, and the exposed joint surfaces were rougher than the fresh ones.

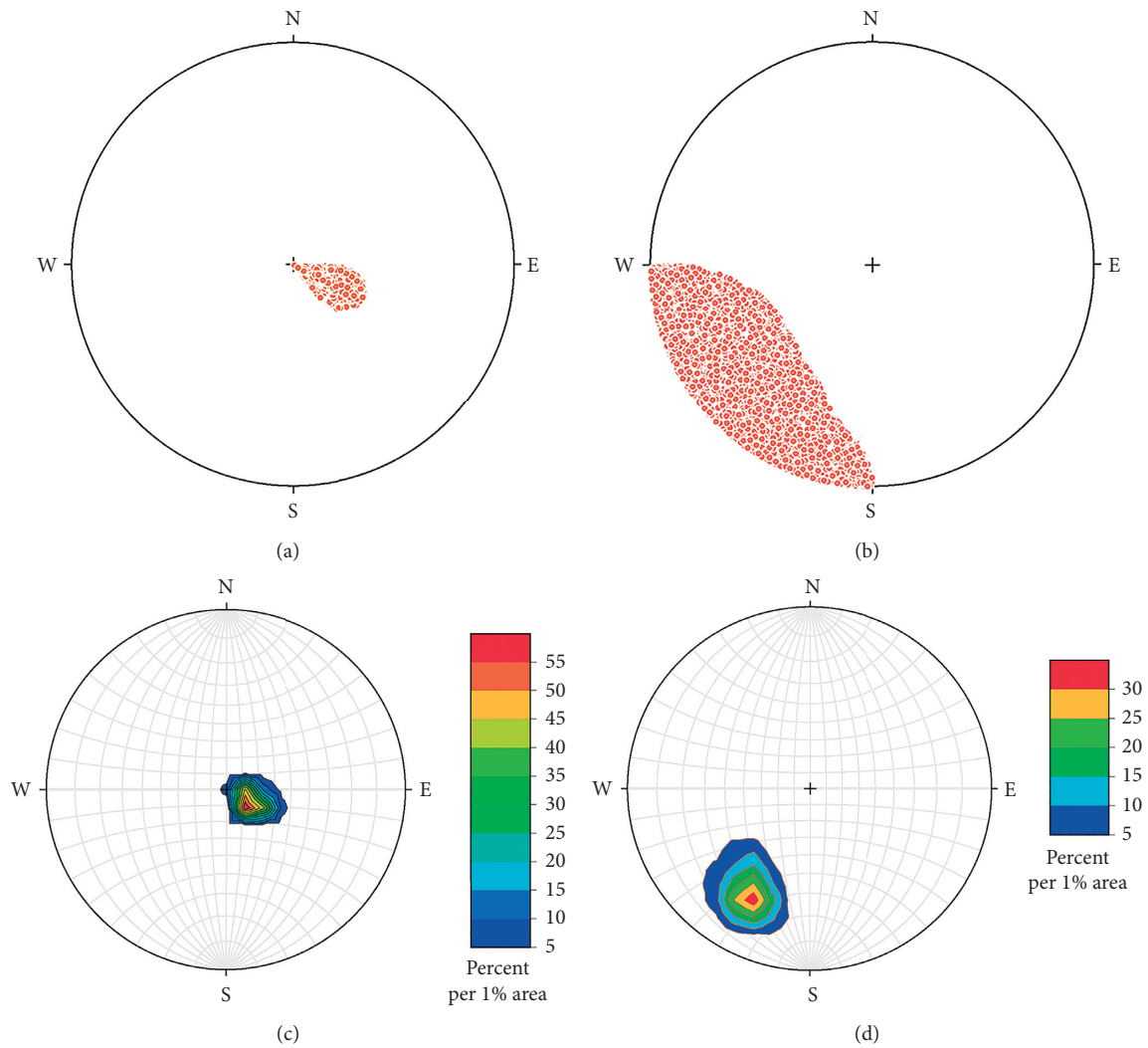


FIGURE 10: Scatter plot and the contour plot of the orient normal to polygons of detected joint sets. (a) Scatter plot of the orient normal to polygons of detected joint set 2 (plane 4). (b) Scatter plot of the orient normal to polygons of detected bedding plane (plane 8). (c) Contour plot of the orient normal to polygons of detected joint set 2 (plane 4). (d) Contour plot of the orient normal to polygons of detected bedding plane (plane 8).

## 5. Discussion and Conclusions

The debris-flow activities in the Sabino Canyon were quite joint-controlled, and the initiation of these debris flows was related to the rock-slope failure. The point cloud data were recorded safely, were unbiased, and could be processed efficiently to exhibit the topographic condition of debris flows and detailed joint characteristics of rock slope in initiate zones. Furthermore, it presented opportunities for establishing a 3D model for further mechanic analysis and simulation. In this study, we showed that the point clouds generated by LiDAR scanning as well as photogrammetry could be processed and then be used not only in the analysis of the topographic changes in the large-scaled debris-flow activities but also in the measurement of the joint parameters of small-scaled rock block.

The LiDAR data of the study area were successfully processed, mapped, and precisely quantified for topographic changes, showing the location of sediment deposition and erosion after the debris-flow events.

Both the topographic change computation of large-scale LiDAR dataset and geometry characteristics obtaining small-scale LiDAR dataset demonstrated the capabilities and huge potential of LiDAR to precisely acquire information and assessment of hazards.

The spacing between the points and the mesh triangles is determined by scanning with different resolutions. High-resolution scanning is required to obtain more accurate data. In addition, the JRC (Joint Roughness Coefficient) is perhaps the most common empirical method for determining the joint roughness; however, visually assigning a JRC value to a joint profile is inherently subjective. The standard angular



deviation between the orient normal of triangles surfaces generated by point and best-fitting plane of the joint faces is able to represent the joint roughness, and the bigger the angular deviation, the bigger the joint roughness.

The results are consistent with the actual situation, representing its feasibility for analyzing the debris flow initiated by rock-slope failure. However, the way to remove the vegetation accurately and to build 3D models of the debris flow initiated by rock slope should be done in future work.

## Data Availability

The data of numerical results used to support the findings of this study can be obtained from the corresponding author upon request.

## Conflicts of Interest

The authors declare that they have no known conflicts of interest that could have appeared to influence the work reported in this paper.

## Acknowledgments

The authors would like to thank the Pima Association of Governments' (PAG's) Regional Remote Sensing Program for providing the laser scanner data for this research. This study was supported by the National Natural Science Foundation of China (51608083 and 41807272) and the Second Tibetan Plateau Scientific Expedition and Research (STEP) Program of China (2019QZKK0902).

## References

- [1] R. M. Iverson, M. E. Reid, and R. G. LaHusen, "Debris-flow mobilization from landslides," *Annual Review of Earth and Planetary Sciences*, vol. 25, no. 1, pp. 85–138, 1997.
- [2] N. Zhang and T. Matsushima, "Numerical investigation of debris materials prior to debris flow hazards using satellite images," *Geomorphology*, vol. 308, pp. 54–63, 2018.
- [3] N. N. Vasu, S. R. Lee, D. H. Lee, J. Park, and B. G. Chae, "A method to develop the input parameter database for site-specific debris flow hazard prediction under extreme rainfall," *Landslides*, vol. 15, no. 8, pp. 1–17, 2018.
- [4] M.-L. Li, Y.-J. Jiang, T. Yang, Q.-B. Huang, J.-P. Qiao, and Z.-J. Yang, "Early warning model for slope debris flow initiation," *Journal of Mountain Science*, vol. 15, no. 6, pp. 1342–1353, 2018.
- [5] M. Hong, S. Jeong, and J. Kim, "A combined method for modeling the triggering and propagation of debris flows," *Landslides*, vol. 17, no. 4, pp. 805–824, 2020.
- [6] F. Imaizumi, R. C. Sidle, S. Tsuchiya, and O. Ohsaka, "Hydrogeomorphic processes in a steep debris flow initiation zone," *Geophysical Research Letters*, vol. 33, no. 10, p. a, 2006.
- [7] O. Hungr, S. Leroueil, and L. Picarelli, "The Varnes classification of landslide types, an update," *Landslides*, vol. 11, no. 2, pp. 167–194, 2014.
- [8] J.-w. Zhou, P. Cui, and X.-g. Yang, "Dynamic process analysis for the initiation and movement of the Donghekou landslide-debris flow triggered by the Wenchuan earthquake," *Journal of Asian Earth Sciences*, vol. 76, pp. 70–84, 2013.
- [9] Q. Xu, X. Fan, and X. Dong, "Characteristics and formation mechanism of a catastrophic rainfall-induced rock avalanche-mud flow in Sichuan, China," *Landslides*, vol. 9, no. 1, pp. 143–154, 2010.
- [10] A. Dufresne and M. Geertsema, "Rock slide-debris avalanches: flow transformation and hummock formation, examples from British Columbia," *Landslides*, vol. 17, no. 1, pp. 15–32, 2020.
- [11] T. Bogaard and R. Greco, "Invited perspectives: hydrological perspectives on precipitation intensity-duration thresholds for landslide initiation: proposing hydro-meteorological thresholds," *Natural Hazards and Earth System Sciences*, vol. 18, no. 1, pp. 31–39, 2018.
- [12] X. Liu, F. Wang, K. Nawnit, X. Lv, and S. Wang, "Experimental study on debris flow initiation," *Bulletin of Engineering Geology and the Environment*, vol. 79, no. 3, pp. 1565–1580, 2020.
- [13] W. G. Pariseau, S. Puri, and S. C. Schmelter, "A new model for effects of impersistent joint sets on rock slope stability," *International Journal of Rock Mechanics and Mining Sciences*, vol. 45, no. 2, pp. 122–131, 2008.
- [14] J. Kemeny, "Time-dependent drift degradation due to the progressive failure of rock bridges along discontinuities," *International Journal of Rock Mechanics and Mining Sciences*, vol. 42, no. 1, pp. 35–46, 2005.
- [15] A. Perrone, R. Vassallo, V. Lapenna, and C. D. Maio, "Pore water pressures and slope stability: a joint geophysical and geotechnical analysis," *Journal of Geophysics and Engineering*, vol. 5, no. 3, pp. 323–337, 2008.
- [16] D. H. Kim, I. Gratchev, and A. Balasubramaniam, "Determination of joint roughness coefficient (JRC) for slope stability analysis: a case study from the Gold Coast area, Australia," *Landslides*, vol. 10, no. 5, pp. 657–664, 2013.
- [17] C. Gregoretti, "The initiation of debris flow at high slopes: experimental results," *Journal of Hydraulic Research*, vol. 38, no. 2, pp. 83–88, 2000.
- [18] H. Liang, S. He, and W. Liu, "Dynamic simulation of rockslide-debris flow based on an elastic-plastic framework using the SPH method," *Bulletin of Engineering Geology and the Environment*, vol. 79, no. 1, pp. 451–465, 2020.
- [19] J. Mah, C. Samson, and S. D. McKinnon, "3D laser imaging for joint orientation analysis," *International Journal of Rock Mechanics and Mining Sciences*, vol. 48, no. 6, pp. 932–941, 2011.
- [20] C. Morino, S. J. Conway, M. R. Balme et al., "Debris-flow release processes investigated through the analysis of multi-temporal LiDAR datasets in north-western Iceland," *Earth Surface Processes and Landforms*, vol. 44, no. 1, pp. 144–159, 2019.
- [21] E. R. Force, "Geology and Mineral Resources of the Santa Catalina Mountains, Southeastern Arizona: a cross-sectional approach," *University of Arizona Center for Mineral Resources, Monograph in Mineral Resource Science*, Tucson, AZ, USA, 1997.
- [22] P. G. Griffiths, C. S. Magirl, R. H. Webb et al., "Spatial distribution and frequency of precipitation during an extreme event: July 2006 mesoscale convective complexes and floods in southeastern Arizona," *Water Resources Research*, vol. 45, no. 7, pp. 217–230, 2009.
- [23] C. S. Magirl, P. G. Griffiths, and R. H. Webb, "Analyzing debris flows with the statistically calibrated empirical model LAHARZ in southeastern Arizona, USA," *Geomorphology*, vol. 119, no. 1-2, pp. 111–124, 2010.

- [24] A. Youberg, M. L. Cline, J. P. Cook, P. A. Pearthree, and R. H. Webb, *Geologic Mapping of Debris-Flow Deposits in the Santa Catalina Mountains, Pima County, Arizona*, Arizona Geology Survey, Tucson, Arizona, 2008.
- [25] J. D. Pelletier, T. Engelder, D. Comeau et al., "Tectonic and structural control of fluvial channel morphology in metamorphic core complexes: the example of the Catalina-Rincon core complex, Arizona," *Geosphere*, vol. 5, no. 4, pp. 363–384, 2009.
- [26] C. Y. Chen and Q. Wang, "Debris flow-induced topographic changes: effects of recurrent debris flow initiation," *Environmental Monitoring & Assessment*, vol. 189, no. 9, p. 449, 2017.
- [27] M. Bremer and O. Sass, "Combining airborne and terrestrial laser scanning for quantifying erosion and deposition by a debris flow event," *Geomorphology*, vol. 138, no. 1, pp. 0–60, 2012.
- [28] J. Adams and J. Chandler, "Evaluation of lidar and medium scale photogrammetry for detecting soft-cliff coastal change," *The Photogrammetric Record*, vol. 17, no. 99, pp. 405–418, 2002.
- [29] The United States Geological Survey, *Lidar Base Specification Version 1.3*, The United States Geological Survey, Reston, Virginia, USA, 2018.
- [30] D. Ma and B. Li, "Vegetation filtering in gully region of loess plateau based on laser scanning point cloud's intensity attenuation model and its terrain construct," *Transactions of the Chinese Society of Agricultural Engineering*, vol. 29, no. 15, pp. 162–171, 2012.
- [31] M. R. James, S. Robson, and M. W. Smith, "3-D uncertainty-based topographic change detection with structure-from-motion photogrammetry: precision maps for ground control and directly georeferenced surveys," *Earth Surface Processes and Landforms*, vol. 42, no. 12, pp. 1769–1788, 2017.
- [32] R. Schnabel, R. Wahl, and R. Klein, "Efficient RANSAC for point-cloud shape detection," *Computer Graphics Forum*, Blackwell Publishing Ltd, vol. 26, no. 2, pp. 214–226, 2007.
- [33] P. Mo and Y. Li, "Estimating the three-dimensional joint roughness coefficient value of rock fractures," *Bulletin of Engineering Geology and the Environment*, vol. 78, no. 2, pp. 857–866, 2019.
- [34] N. Chen, J. Kemeny, Q. Jiang, and Z. Pan, "Automatic extraction of blocks from 3d point clouds of fractured rock," *Computers & Geosciences*, vol. 109, pp. 149–161, 2017.
- [35] K. Marsch, D. Wujanz, and T. M. Fernandez-Steeger, "On the usability of different optical measuring techniques for joint roughness evaluation," *Bulletin of Engineering Geology and the Environment*, vol. 79, no. 2, pp. 811–830, 2020.

## Research Article

# Research on Bearing Theory of Squeezed Branch Pile

Hong-wei Ma <sup>1,2</sup>, Yi-ying Wu <sup>1</sup>, Yu Tong,<sup>1</sup> and Xiao-qiang Jiang<sup>1</sup>

<sup>1</sup>School of Civil Engineering and Architecture, Anhui University of Science and Technology, Huainan 232001, China

<sup>2</sup>State Key Laboratory of Mining Response and Disaster Prevention and Control in Deep Coal Mines, Anhui University of Science and Technology, Huainan, China

Correspondence should be addressed to Hong-wei Ma; [hw\\_ma1984@126.com](mailto:hw_ma1984@126.com)

Received 15 November 2020; Revised 27 November 2020; Accepted 8 December 2020; Published 29 December 2020

Academic Editor: Zhi Cheng Tang

Copyright © 2020 Hong-wei Ma et al. This is an open access article distributed under the Creative Commons Attribution License, which permits unrestricted use, distribution, and reproduction in any medium, provided the original work is properly cited.

Based on the shear displacement method, theoretical research on the load transfer relation of squeezed branch pile is established. In combination with the nonlinear relation of the interaction between piles and soil, the hyperbolic function is used to describe the pile tip, pile skin, and branch. The theoretical method of the load transfer is improved, and the expression of the load transfer coefficient of these three parts is given. Finally, the applicability of the theoretical method is verified by the model test of homogeneous soil and the field test of stratified soil. The verification results show that the theoretical calculation method of the squeezed branch single-pile bearing capacity based on the shear displacement method can better calculate the ultimate load in practical engineering applications.

## 1. Introduction

The squeezed branch pile is a kind of friction-end bearing pile, which is formed by squeezing into an expanded body at a specific position based on the cast-in-place pile. Thanks to the function of the expanded body, the load-bearing system of branch resistance-shaft resistance-tip resistance is helpful to realize the high bearing capacity and low settlement. At present, related applied research and engineering practices have been carried out in many engineering fields, such as large-scale factory projects and infrastructure construction in clay soil areas (Yin et al. [1] and Xiao et al. [2]).

With the development of engineering technology, the research on bearing characteristics of squeezed branch piles has gradually deepened. Yang et al. [3] obtained the bearing characteristics of high bearing capacity and low settlement through comparative tests of large diameter piles on the same site. Li et al. [4] analyzed the working mechanism of squeezed branch piles in actual projects and found that the expanded body has a high contribution to the bearing capacity of the pile foundation. Zhang and Wang [5] verified the aforementioned bearing characteristics by field comparison tests. It is also proposed that the reasonable setting of the expanded body and the selection of the diameter of the

branch have a significant impact on the bearing capacity, Cui and Wang [6], Zhang et al. [7], and Liu et al. [8] verified the excellent application prospect of the squeezed branch pile under different site conditions through the field static load test. The aforementioned studies can prove the good site adaptability of squeezed branch piles. It is of great significance to carry out corresponding theoretical research and practice based on the bearing characteristics of the squeezed branch pile.

Therefore, many scholars have carried out studies mainly on the bearing mechanism and the load-settlement relationship of squeezed branch piles. Liang et al. [9] analyzed the influence of the pile-soil interaction state on the bearing capacity of the pile and proposed a variable section calculation method of pile load-settlement characteristics. Wu et al. [10] proposed a settlement calculation method for squeezed multibranch piles based on the layered summation method. Ju et al. [11] analyzed the pile-soil interaction under load and proposed a revised reference for the design formula of bearing capacity in the code. Gao and Zhu [12] analyzed the characteristics of the load-settlement curve of the squeezed branch piles in actual projects, predicted the ultimate bearing capacity of the squeezed branch piles through the hyperbolic model, and obtained theory results closer to

the measured values. Jiang et al. [13] improved the accuracy of bearing capacity calculation by using the power function-hyperbolic combination model. Other scholars have carried out theoretical research on the bearing characteristics of squeezed branch piles. Liu et al. [14] established the relationship between the bearing capacity and settlement of multistage enlarged piles based on the load transfer law of the pile foundation from top to bottom. The calculation formula is obtained, and the calculation result is more consistent with the measured values. Li et al. [15] combined the load-bearing system of branch resistance-shaft resistance-tip resistance and carried out a nonlinear simplified analysis of the load-settlement characteristics of squeezed branch piles through a segmented displacement coordinated iteration algorithm.

The expanded branch can bear more loads, and the damage of the squeeze branch pile is mainly due to the shear failure of the soil under the branch or the failure of the soil at the pile end, which is different from the conventional bearing capacity design method. The side resistance of the squeezed branch pile is limited by the branch resistance, and the pile foundation will completely fail after the expanded body is damaged. Therefore, this paper establishes the load-settlement calculation theory of squeezed branch pile based on the shear displacement method. Combined with the model test of homogeneous soil and the field test of stratified soil, the calculation theory was verified, respectively. According to the verification results, we can analyze the stress mechanism of the squeezed branch pile.

## 2. Theoretical Analysis

**2.1. Bearing Theory of Pile Foundation by the Shear Displacement Method.** As shown in Figure 1, the bearing theory of the shear displacement method proposes that the soil around the pile undergoes shear deformation with the settlement of the pile, and the shear deformation is transferred from the radius  $r_0$  of the pile to the influence radius  $r_m$ , and equation (1) represents the transfer relationship of shear stress  $\tau(z)$  in the radial direction, and equation (2) represents the elastic relationship between shear stress  $\tau(z)$  and shear strain in the soil at the side of the pile:

$$\tau(z) = \tau_0(z) \frac{r_0}{r_m}, \quad (1)$$

$$\tau(z) = G_s \frac{dw(r)}{dr}. \quad (2)$$

As shown in equations (1) and (2), Randolph and Wroth [16] put forward the influence radius  $r_m = 2.5H\rho_m(1-\nu)$ ;  $H$  is the depth of the calculated section.  $\rho_m$  is the correction coefficient of finite-depth soil;  $\rho_m$  is taken as 1 in the homogeneous soil layer;  $\nu$  is Poisson's ratio of the soil at the side of the pile;  $\tau_0(z)$  is the shear force of the pile-soil contact surface at depth  $z$ ; and  $G_s$  is the shear modulus of the soil.

Combining equations (1) and (2), the displacement of the soil at the side of the pile is obtained by integral:

$$\begin{cases} w(r) = \frac{\tau_0(z)r_0}{G_s} \ln \frac{r_m}{r}, & r_0 \leq r \leq r_m, \\ w(r) = 0, & r \geq r_m. \end{cases} \quad (3)$$

Under the load state, equation (4) takes an element of a single pile for force balance analysis, and the relationship between the pile side displacement  $w(r_0)$  and axial force is shown in equation (5):

$$\frac{dF(z)}{dz} = 2\pi r_0 \tau_0(z), \quad (4)$$

$$\frac{\partial w(r_0)}{\partial z} = \frac{F(z)}{\pi r_0^2 E_p}. \quad (5)$$

As shown in equations (4) and (5),  $F(z)$  is the axial force of the pile section at depth  $z$ ;  $E_p$  is the elastic modulus of the pile.

At the same depth  $z$ , the displacement of the soil at the side of the pile is equal to the pile side displacement. By combining equations (3)–(5), the displacement balance equation can be established as follows:

$$\frac{\partial^2 w(r_0)}{\partial z^2} - \frac{2G_s}{r_0^2 E_p \ln(r_m/r_0)} w(r_0) = 0. \quad (6)$$

The general solution of equation (6) is

$$w = m_1 e^{\alpha z} + m_2 e^{-\alpha z}. \quad (7)$$

As shown in equation (7),  $m_1$  and  $m_2$  are undetermined constants; the calculation method for parameter  $\alpha$  is shown as follows:

$$\alpha = \left( 2G_s \ln(r_m/r_0) \right)^{1/2} r_0^2 E_p^{-1/2}. \quad (8)$$

**2.2. Bearing Theoretical Calculation Model of Squeezed Branch Pile.** Seed and Reese [17] proposed the load-settlement hyperbolic relationship at the end of the pile, and the relationship between the pile tip resistance  $P_b$  and the settlement  $s_b$  is shown as follows:

$$P_b = A \frac{s_b}{a_s + b_s s_b}. \quad (9)$$

In equation (9), the cross-sectional area of the straight hole section  $A = \pi d^2/4$ ,  $d$  is the pile diameter and  $a_s$  and  $b_s$  are the transferred parameters of the pile tip resistance.

As shown in Figure 2, the length of the pile shaft under the  $n$ th expanded body is  $l_n$ . Assuming that the pile tip resistance is  $P_b$  and pile tip settlement is  $s_b$ , and combining the bearing theory of the shear displacement method, the displacement of the section under the  $n$ th expanded body can be obtained as

$$s_n = \cosh(\alpha l_n) s_b + \frac{\sinh(\alpha l_n)}{\alpha A E_p} P_b. \quad (10)$$

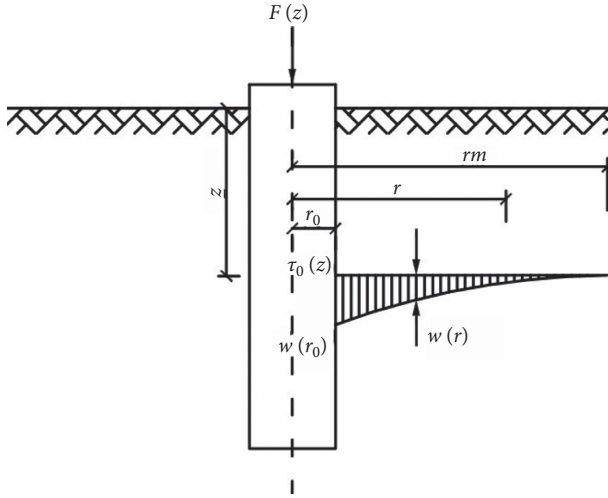


FIGURE 1: Pile-soil shear displacement model.

In equation (10),  $L$  is the pile length and  $E_p$  is the elastic modulus of the pile shaft.

Assuming that the shaft resistance  $f_n$  of the pile shaft varies linearly along the pile body,  $f_n$  can be shown as

$$f_n = \pi d l_n \frac{\tau_n + \tau_b}{2}. \quad (11)$$

In equation (11),  $\tau_n$  is the shear stress at the section under the  $n$ th expanded body and  $\tau_b$  is the shear stress at the pile end.

The shear stress and settlement satisfy the hyperbolic function relationship:

$$\tau_n = \frac{s_n}{a_{fn} + b_{fn}s_n}, \quad (12)$$

$$\tau_b = \frac{s_b}{a_{fb} + b_{fb}s_b}. \quad (13)$$

In the formula,  $a_{fn}$  and  $b_{fn}$  are the transfer parameters of the shear force under the  $n$ th expanded body;  $a_{fb}$  and  $b_{fb}$  are the transfer parameters of the shear force at the pile end.

For nonrigid piles, the pile would be compressed when the pile is loaded. Assuming that the load  $dF$  acts on the microelement  $dz$  of the pile, the static balance relationship of the microelement segment is satisfied as follows:

$$dF = \pi d \frac{s}{a_{fb} + b_{fb}s} dz, \quad (14)$$

$$ds = \frac{F}{E_p A} dz, \quad (15)$$

where  $s$  is the settlement of the microelement section relative to the reference section and  $F$  is the axial force difference of upper and lower sections of the microelement section.

From equations (14) and (15), the differential equation for the axial force transfer of the pile shaft is

$$FdF = \pi d E_p A \frac{s}{a_{fb} + b_{fb}s} ds. \quad (16)$$

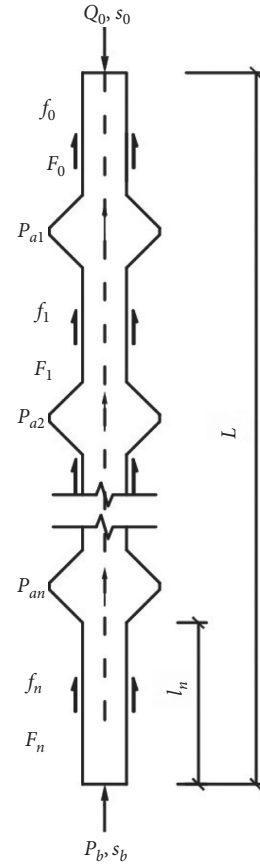


FIGURE 2: Calculation model of the squeezed branch pile.

Combining the initial conditions  $F=0$  and  $s=0$  to integrate equation (16), we get

$$F = \frac{\sqrt{2\pi d E_p A}}{b_{fb}} \sqrt{b_{fb}s - a_{fb} \ln\left(1 + \frac{b_{fb}}{a_{fb}} s\right)}. \quad (17)$$

From the results of the shear displacement of the pile shaft  $l_n$ , it can be seen that the compression of the pile shaft  $l_n$  is

$$s_c^n = s_n - s_b. \quad (18)$$

Therefore, the additional axial force required to provide compression of the pile shaft  $l_n$  is

$$F_n = \frac{\sqrt{2\pi d E_p A}}{b_{fb}} \sqrt{b_{fb}s_c^n - a_{fb} \ln\left(1 + \frac{b_{fb}}{a_{fb}} s_c^n\right)}. \quad (19)$$

Since the rigidity of the expanded body is much greater than the pile shaft, it is assumed that the settlement of each section of the expanded body is equal under the same load. The load-bearing method of the expanded body can be simplified, as the branch resistance acts vertically on the expanded ring area. Same as pile end, the relationship between the branch resistance  $P_{an}$  and the settlement  $s_n$  of the  $n$ th expanded body is shown as follows:

$$P_{an} = A_{pn} \frac{s_n}{a_{pn} + b_{pn} s_{an}}. \quad (20)$$

In equation (20),  $P_a$  represents the branch resistance,  $A_p$  represents the expanded ring area, and  $s_n$  represents the settlement of the  $n$ th expanded body. The annular cross-sectional area of the expanded body  $A_{pn} = \pi(D_n^2 - d^2)/4$ ,  $D_n$  is the diameter of the  $n$ th expanded body, and  $a_{pn}$  and  $b_{pn}$  are the transferred parameters of the branch resistance of the  $n$ th expanded body.

Regarding the  $n$ th expanded body and the pile shaft under the body as an expanded unit, the axial force transmitted to the top of the unit is  $R_n$ :

$$R_n = P_{an} + P_b + f_n + F_n. \quad (21)$$

For the squeezed branch pile with  $n$  expanded units, the calculation process of the squeezed branch pile is shown in Figure 3.

When any set of the pile tip settlement  $s_b$  is given, the corresponding pile top load and pile top settlement can be obtained by the above calculation. Taking any pile top load  $Q$  and the settlement  $s$ ,  $Q_p$  and  $Q_q$  can be determined, where  $Q_p = 10/12Q$ ,  $Q_q = 11/12Q$ ,  $s_p$  is the corresponding settlement of the pile top  $Q_p$ , and  $s_q$  is the corresponding settlement of the pile top  $Q_q$ , where  $\Delta s_1 = s_q - s_p$ ,  $\Delta s_2 = s - s_p$ , any  $Q$  is selected. When  $\Delta s_2 > 2\Delta s_1$ , the ultimate bearing capacity of the pile can be determined to be  $11/12Q$ .

### 2.3. Calculation Parameters

2.3.1.  $a_s$  and  $b_s$ . Randolph and Wroth [18] studied the nonlinear relationship between the pile tip resistance and pile tip settlement:

$$s_b = \frac{P_b(1 - \nu_b)}{2G_b d}. \quad (22)$$

In the formula,  $G_b$  is the shear modulus of the pile-end soil and  $\nu_b$  is Poisson's ratio of the pile-end soil.

Therefore,

$$a_s = \frac{(1 - \nu_b)\pi d}{8G_b}. \quad (23)$$

Janbu [19] gives the ultimate tip resistance  $P_{bu}$  of straight hole piles:

$$P_{bu} = (c_b N_c + q_b N_q) A, \quad (24)$$

$$b_s = \frac{1}{(c_b N_c + q_b N_q)}. \quad (25)$$

In the formula,  $c_b$  is the cohesive force of the pile tip soil,  $q_b$  is the average effective compressive stress on the side of the pile tip plane, and  $N_c$  and  $N_q$  are the bearing capacity coefficients of the pile. The calculation is shown in the following formula, where  $\phi$  is the angle of the failure surface of the pile tip under the ultimate load and the range from soft clay to compact sand is  $60^\circ$  to  $105^\circ$ , where  $\gamma$  is the soil gravity

on the side of the pile and  $\phi$  is the effective internal friction angle of the soil.

$$\begin{aligned} N_c &= (N_q - 1) \cot \phi, \\ N_q &= \left( \tan \phi + \sqrt{1 + \tan^2 \phi} \right)^2 e^{2\phi \tan \phi}. \end{aligned} \quad (26)$$

2.3.2.  $a_f$  and  $b_f$ . The relationship between the shear displacement of the pile side soil and the shear stiffness is given by equation (3). Let  $r = r_0$ , then the shaft resistance transfer parameter  $a_f$  can be shown as

$$a_f = \frac{d}{2G_s} \ln \frac{2r_m}{d}. \quad (27)$$

The shear strength of the pile-soil interface can be shown as

$$\tau_f = k\sigma_v \tan \delta. \quad (28)$$

Therefore,

$$b_f = \frac{R_f}{k\sigma_v \tan \delta}. \quad (29)$$

In the formula,  $R_f$  is the failure ratio, which can be taken as 0.80~0.95 and  $k$  is the horizontal earth pressure coefficient, which can be taken according to Table 1. In Table 1,  $k_0$  is the static earth pressure coefficient,  $k_0 = 1 - \sin \phi$ ,  $\sigma_v$  is the vertical stress of the soil at the calculated height and  $\delta$  is the friction angle of the pile-soil interface.

## 3. Determination of Disk Resistance Function Based on Model Test

### 3.1. Test Sand and Model Pile

3.1.1. *Preparation of Model Piles.* As shown in Figure 4, the model pile is made of aluminum alloy, and the pile end and pile head are sealed with the same material. The pile diameter  $d = 20$  mm, the depth of the pile body into the soil  $L = 500$  mm in the test, the exposed pile head is 50 mm, and the length-to-diameter ratio is 25:1. The inclination angle of the branch surface  $\alpha = 45^\circ$  and a  $\phi 20$  circular hole is left inside. The dimensions are shown in Figure 1(b). According to the different diameters of the expanded body, the piles were divided into 5 groups. The parameters of each group are shown in Table 2.

3.1.2. *Preparation of Test Sand.* Before the test, the natural sand was cleaned and dried first, and then the test sand was screened with a 2.45 mm aperture fine sieve to remove larger particles and impurities. After fixing the position of the model pile with the self-made device, the test sand was filled in six layers, and the filling mass of each layer was controlled to 80 kg. A small vibratory trowel with a vibration frequency of 2840 times/min was used for tamping for 1 min. The compaction state measured by the light penetrometer was of

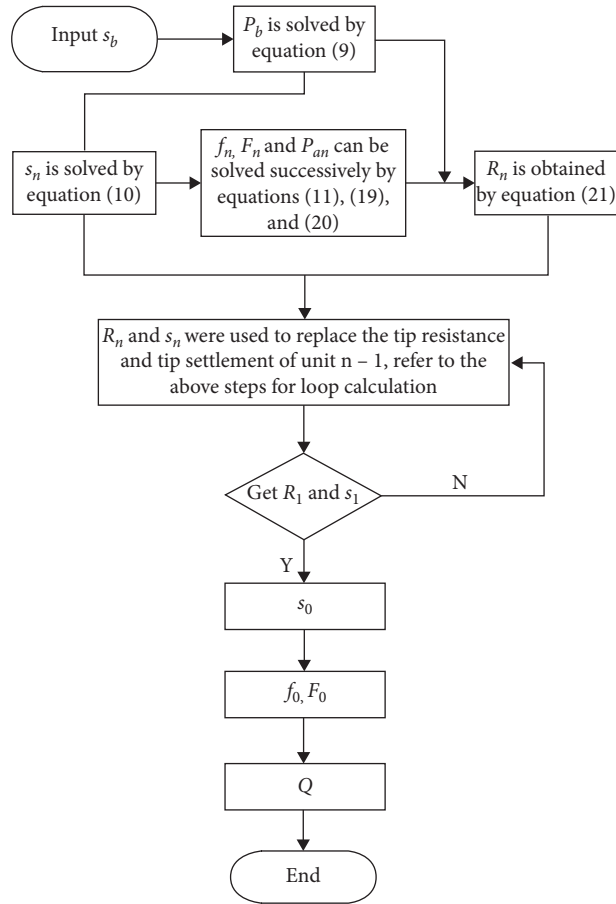


FIGURE 3: The calculation of the bearing capacity of the squeezed branch pile.

TABLE 1: Suggested value of the lateral earth pressure coefficient  $k$ .

Data provider	Working conditions	$k$
Kulhawy [20]	Steel pipe piles, concrete piles or H-shaped steel piles with a smooth surface, and a small settlement	$(0.7\sim 1.2) k_0$
Yang [21]	Driven steel piles in alluvial deposit or fully weathered granite	$(1.2\sim 1.5) k_0$

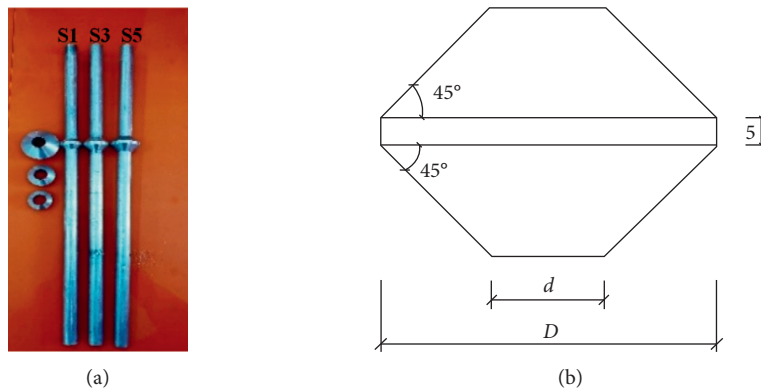


FIGURE 4: The model of the squeezed branch pile. (a) Model pile. (b) Branch bearing.

TABLE 2: The parameters of the model pile.

Group	$D$ (mm)	$h$ (mm)	$l_1$ (mm)	$l_2$ (mm)
S1	40	25	137.5	337.5
S2	45	30	135.0	335.0
S3	50	35	132.5	332.5
S4	55	40	130.0	330.0
S5	60	45	127.5	327.5

medium density and was kept still for 12 hours after the landfill is completed.

### 3.2. Test Loading

**3.2.1. Test Loading Device.** The loading device is shown in Figure 5.

The clearance size of the model box is  $0.8\text{ m} \times 0.6\text{ m} \times 0.58\text{ m}$  ( $L \times W \times H$ ), which meets the test error control requirements. The sidewall of the model box is made of a combination of 12 mm thick plexiglass plate and using an 8 mm thick steel bar hoop for reinforcement, and the bottom is sealed with a 12 mm thick plexiglass plate. During the test, the maximum deformation of the sidewall of the model box was measured to be less than 0.1 mm, and it indicates that the stiffness of the model box did not affect the test results.

The test loading device adopts lever-type loading, and a balance system is designed in the loading system to eliminate the weight of the steel beam and the loading plate. To ensure that the center of the pile is under load, a solid alloy steel ball is used to transmit the force at the position of the pile head.

**3.2.2. Loading Steps and Limit State Determination.** The load of each stage of the test is 0.2 kN. After each stage of loading is completed, the settlement of the model pile is observed every 5 minutes. If the difference between the two adjacent observations is less than 0.01 mm, it means that the stable state is reached and the next level of loading begins. If the corresponding settlement of a certain level of the load exceeds 2 times of the previous level, it means that the load limit state has been reached. We determine the ultimate state of the load from two aspects. One is that the settlement of this stage is more than twice that of the previous stage. The other is that settlement dose not reach a stable state within 1.5 hours. It is determined that the total load to the upper level is the ultimate bearing capacity of the pile.

**3.3. The Load Transfer Coefficients of the Branch Resistance.** The deflections  $\chi(\beta)$  of the branch end load were determined from six groups of indoor model experiments on a small scale. The resistance strain gauges on both sides of the pile body were measured, and the vertical displacement of the pile top was monitored by using a dial indicator.

The layout plan of the axial measuring point is shown in Figure 6.

Determination of resistance load transfer coefficients  $a_p$  and  $b_p$  at the branch:

The load-bearing method at the expanded body is same as the pile end, but it is only affected by the diameter of ball bearing and the interaction between ball bearing and the soil. Therefore, assuming that the branch resistance is equivalently simplified to the tip resistance form, which is shown as follows:

$$P_a = A(\beta^2 - 1) \frac{s_a}{a_p + b_p s_a} = \frac{R_b}{\chi(\beta)}, \quad (30)$$

$$R_b = A \frac{s_a}{a_{sp} + b_{sp} s_a}. \quad (31)$$

In the formula,  $R_b$  is the equivalent tip resistance,  $a_{sp}$  and  $b_{sp}$  are the transfer parameters of ball bearing, the calculation refers to  $a_s$  and  $b_s$ ,  $\chi(\beta)$  is the correct function of the branch resistance, and  $\beta$  is the ratio of the branch bearing diameter to the pile diameter.

From equations (31) and (32), the transfer coefficients  $a_p$  and  $b_p$  of the expanded body can be shown as follows:

$$a_p = (\beta^2 - 1) \chi(\beta) a_{sp}, \quad (32)$$

$$b_p = (\beta^2 - 1) \chi(\beta) b_{sp}. \quad (33)$$

Equation (31) can be transformed into

$$\frac{s_a}{P_a} = \frac{a_p}{A(\beta^2 - 1)} + \frac{b_p}{A(\beta^2 - 1)} s_a. \quad (34)$$

Let  $y = s_a/P_a$  and  $x = s_a$ , then  $y = kx + c$

$$k = \frac{b_p}{A(\beta^2 - 1)}, \quad (35)$$

$$c = \frac{a_p}{A(\beta^2 - 1)}.$$

According to the principle of least squares, it can be obtained

$$k = \frac{\sum_{i=1}^n x_i y_i - n \bar{x} \bar{y}}{\sum_{i=1}^n x_i^2 - n \bar{x}^2} = \frac{l_{xy}}{l_{xx}},$$

$$c = \bar{y} - k \bar{x}, \quad (36)$$

$$\gamma = \frac{l_{xy}}{\sqrt{l_{xx}} \sqrt{l_{yy}}}$$

where,



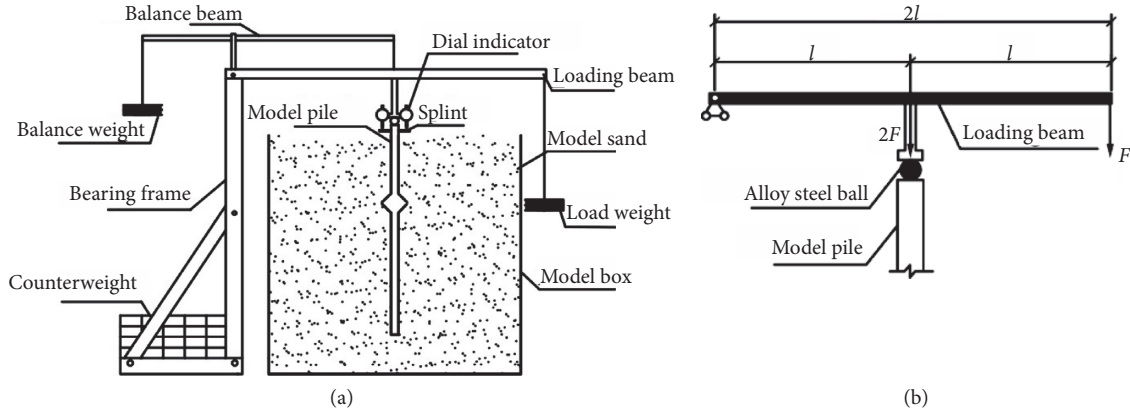


FIGURE 5: Loading device: (a) schematic diagram of loading device and (b) details of loading points.

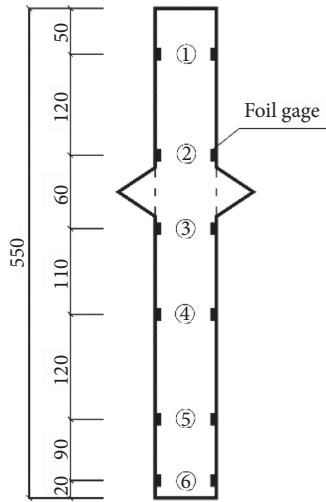


FIGURE 6: The layout plan of the axial measuring point.

$$\bar{x} = \frac{1}{n} \sum_{i=1}^n x_i,$$

$$\bar{y} = \frac{1}{n} \sum_{i=1}^n y_i, \quad (37)$$

$$l_{yy} = \sum_{i=1}^n y_i^2 - n\bar{y}^2.$$

Combining equations (34) and (38), the function  $\chi(\beta)$  is simplified as

$$\chi(\beta) = \frac{kA}{b_{sp}}. \quad (38)$$

The function  $\chi(\beta)$  is determined according to the axial force data of the pile of 6 groups of model pile tests, and the correction function value of the branch resistance is shown in Table 3.

According to the static load test results, multiple groups of  $P_a$  and  $s_a$  in the elastic-plastic state are determined. The parameters  $k$  and  $c$  are obtained according to the least square

method. The correction value  $\chi(\beta)$  of each diameter is obtained by data fitting and shown in Table 3. The obtained empirical formula of the branch resistance correction for each diameter is

$$\chi(\beta) = 0.36\beta^2 - 2.36\beta + 4.20. \quad (39)$$

According to the above calculation and derivation, the transfer parameters of the pile tip resistance, shaft resistance, and branch resistance can be determined.

#### 4. Test Verification and Analysis

**4.1. Theoretical Verification and Comparative Analysis of On-Site Large-Scale Test.** According to Tang [22], field large-scale test data, the length of the No. 1 pile is 2 m, the pile diameter  $d=150$  mm, the diameter of the bell bearing  $D=300$  mm, and the bell bearing is set at 1 m below the top of the pile. The bell bearing is set in dense clay, and the pile tip is in a sandy silt layer. Poisson's ratio of the clay around the pile is 0.25, the sandy silt of the pile tip is 0.3, and the failure angle of the pile tip is  $95^\circ$ , and the physical parameters of the remaining soil layers are shown in Table 4. According to the measured data, and combining the theoretical method of this paper, the comparison of load-settlement between the theoretical curve and the measured curve of the No. 1 pile is shown in Figure 7, and the theoretical and measured values are shown in Table 5.

It can be seen from Figure 6 that the theoretical curve obtained by the calculation method in this paper has a relatively close change trend with the field measured curve. Since the soil under the expanded body has reached an elastoplastic state after rolling at the initial stage of loading, the pile top load increases approximately linearly with the pile top settlement. At the initial stage of loading, the theoretical calculation takes the influence of the elastic state of the pile and soil into account and obtained a slow-change theoretical curve that is more consistent with the actual projects. It can be seen from Table 5 that with the increase of the pile top loading, the relative error between the theoretical value and measured value gradually decreases. In the middle and late loading period, although the theoretical curve and measured value do not completely overlap, they can

TABLE 3: Correction function value of branch resistance.

No.	S1		S2		S3		S4		S5	
	$P_a$ (N)	$s_a$ (mm)	$P_a$ (N)	$s_a$ (mm)	$P_a$ (N)	$s_a$ (mm)	$P_a$ (N)	$s_a$ (mm)	$P_a$ (N)	$s_a$ (mm)
	478	1.80	714	2.61	550	1.50	585	1.38	631	1.20
	630	3.15	895	4.32	746	2.42	797	2.13	862	1.82
	774	5.77	985	5.63	946	3.82	1017	3.22	1101	2.63
	884	8.20	1075	7.54	1047	4.83	1129	3.93	1224	3.13
			1165	10.64	1148	6.15	1243	4.83	1349	3.73

TABLE 4: Basic physical and mechanical parameters of the ground at the test site.

No.	Soil layer	$H$ (m)	$h$ (m)	$E_s$ (MPa)	$\rho$ (g/cm <sup>3</sup> )	$e$	$c$ (kPa)	$\varphi$ (°)
1	Clay	1.7	0~1.6	9.1	1.81	0.64	13.9	23
2	Sandy silt	1.0	1.6~1.8	39	2.1	—	0	25

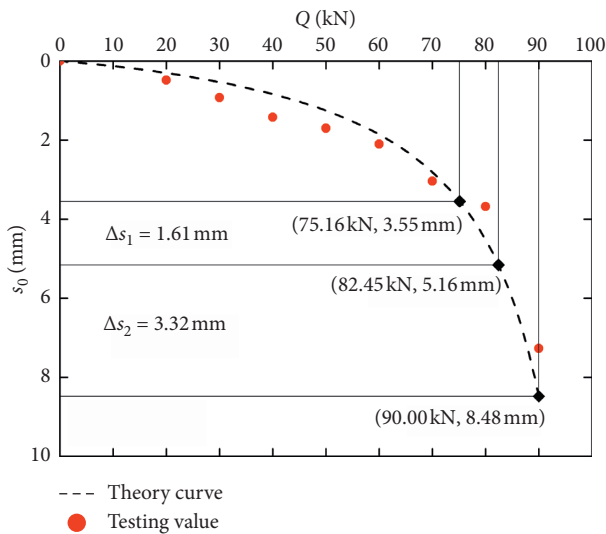


FIGURE 7: Comparison of Q-s curves in the field test.

maintain parallel growth. The relative error can be controlled within 5%. Under the loading limit state, the ultimate calculated bearing capacity of the pile by the theory is 82.45 kN, which is in good agreement with the measured value.

#### 4.2. Theoretical Verification and Comparative Analysis of Indoor Test

**4.2.1. Load-Settlement Relationship.** The same pile tip settlement is given as the small-scale test. According to the theoretical calculation results, the five groups of pile top load-settlement curves with different diameters are shown in Figure 8. Under the same pile top settlement  $s_0$ , the error analysis of the theoretical value and measured value of the pile top load is shown in Figure 9.

As shown in Figure 8, at the initial stage of loading, the theory load of the pile top is lower than the measured value.

When the load on the pile top is small, the pile foundation and the soil at the side of the pile are in an elastic state, and the bearing characteristics of the squeezed branch piles are affected by the pile-soil interaction. The theoretical value and measured value are easy to deviate. With the increase of the load on the pile top, the soil around the pile gradually reaches an elastic-plastic state. By the middle and late loading period, the measured curve and theoretical curve have approximately overlapped. As shown in Figure 9, the influence of the pile-soil interaction state on the bearing capacity of the squeezed branch pile is more important at the beginning. As  $s_0$  increases, the relative error between the theoretical value and measured value gradually decreases. When  $s_0$  exceeds 2 mm, the error of the pile top load under each diameter is less than 5%, and in the middle and late loading period, the theory curves and measured curves maintain a relatively consistent trend, and the errors of the two measured values are mostly close to 0.

The error analysis of the ultimate bearing capacity of each group obtained by theoretical calculation is shown in Table 6. As shown in Table 6, the theoretical ultimate bearing capacity under the load limit state is in good agreement with the actual measured value. The relative error of the ultimate bearing capacity under different diameters is less than 2%, which can be controlled within a reasonable range. Therefore, the ultimate bearing capacity of squeezed branch piles can be predicted based on the actual working conditions and the method described in this article.

**4.2.2. Bearing Strength Analysis.** Taking the S1 ( $D = 40$  mm), S3 ( $D = 50$  mm), and S5 ( $D = 60$  mm) groups of squeezed branch piles as examples, the contribution of each resistance under the same  $s_0$  is shown in Figure 10.

As shown in Figure 10, the theoretical resistance contribution rate is closer to the measured contribution rate under the same settlement. As the branch diameter increases, the coincidence between the measured resistance contribution rate and theoretical contribution rate gradually increases. At the initial stage of loading, the measured resistance contribution rate is in low agreement with the theory result. The contribution rate of each resistance value obtained from the theoretical calculation maintains regular increase or decrease without sudden change. Under the test conditions, the soil at the pile end had been tamped and reached an elastoplastic state, and the contribution rate of the measured resistance value is easily biased due to the influence of the test error. With the increase of top load, when reaching the middle and late loading period, the

TABLE 5: Comparison of the theoretical and measured value.

$s_0$ (mm)	0.48	0.92	1.42	1.70	2.10	3.04	3.68	7.27
Measured value	20.00	30.00	40.00	50.00	60.00	70.00	80.00	90.00
Theoretical value	27.91	42.24	53.13	57.72	63.03	71.79	75.92	87.91
Relative error (%)	39.54	40.81	32.84	15.45	5.05	2.56	-5.09	-2.32

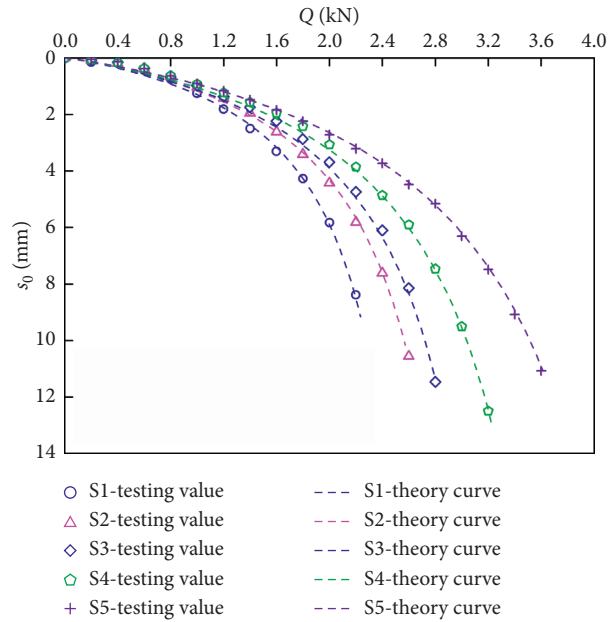


FIGURE 8: Comparison of  $Q$ - $s$  curves between testing value and theory result.

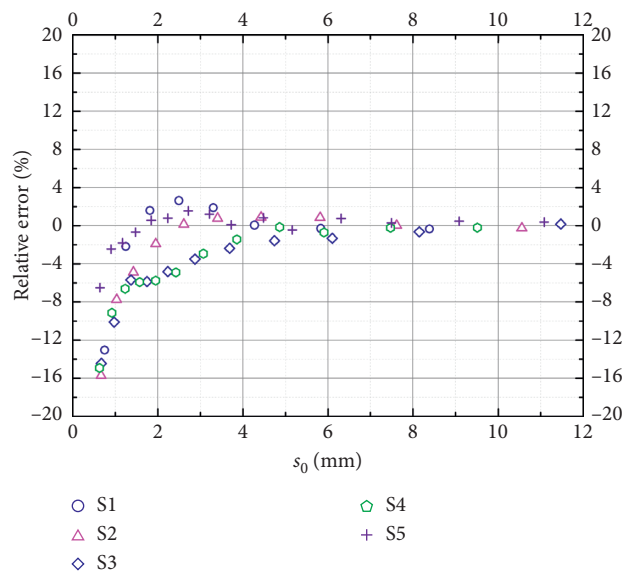


FIGURE 9: Error analysis of the theoretical and measured value.

contribution rate of the measured resistance value and theoretical resistance value shows a coincidence or parallel increase. Based on the relationship between the resistance

contribution rate of each group, the bearing strength of each part of the squeezed branch pile can be reasonably predicted by the theory method in actual projects.

TABLE 6: Error analysis of the ultimate bearing capacity.

Group	Measured value (kN)	Theory value (kN)	Relative error (%)
S1	2.20	2.24	2.00
S2	2.60	2.57	-1.15
S3	2.80	2.80	0.00
S4	3.20	3.22	0.63
S5	3.60	3.61	0.28

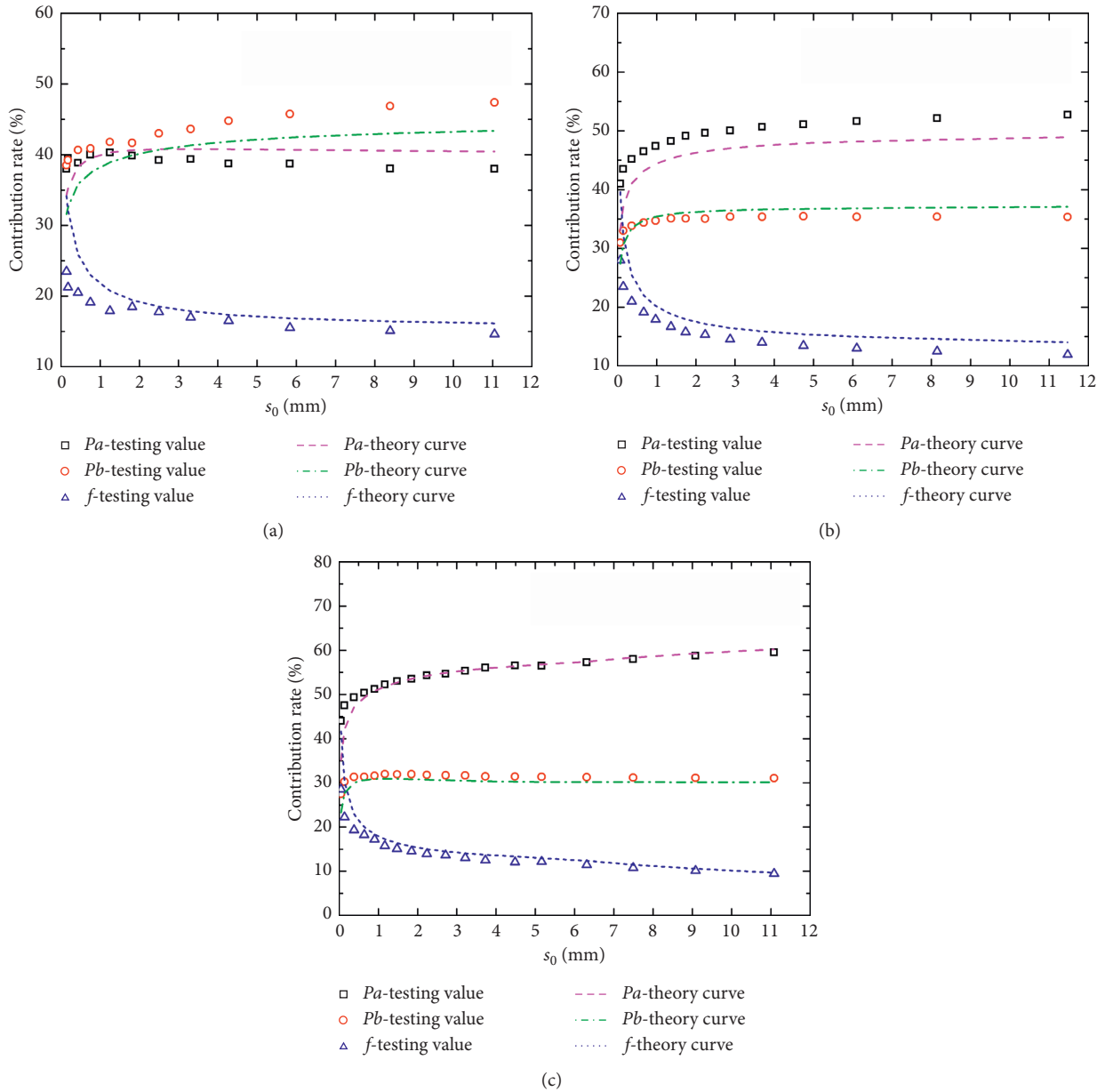


FIGURE 10: The comparison of the bearing capacity contribution: (a) S1, (b) S2, and (c) S3.

## 5. Conclusions

- (1) The calculation theory of pile bearing capacity based on the shear displacement method is established. According to the hyperbolic function relation, the load-settlement relation of pile tip resistance, pile skin resistance, and branch resistance is deduced, reflecting the nonlinear relation between pile and soil, and the theoretical model of the bearing capacity calculation of the single pile of the squeezed branch pile is established.
- (2) Theoretical calculation methods of the load transfer function at the pile tip, pile skin, and branch were given. Theoretical calculation and comparative analysis were combined with the results of the laboratory model test, and the rationality of theoretical calculation was verified.
- (3) The theory of pile bearing capacity has been verified in the homogenized soil model test. The results show that the squeezed branch single pile based on the shear displacement method can reliably predict the ultimate load of the actual project and provide good theoretical support for the design of bearing capacity.

## Data Availability

The data used to support the finding of this study are available from the corresponding author upon request.

## Conflicts of Interest

The authors declare that they have no conflicts of interest.

## Acknowledgments

The authors sincerely thank the School of Civil Engineering and Architecture, State Key Laboratory of Mining Response and Disaster Prevention and Control in Deep Coal Mines, Anhui University of Science and Technology for providing the experimental conditions. This work was supported by the National Natural Science Foundation of China (51408006) and Guangxi Key Laboratory of Geomechanics and Geotechnical Engineering.



## References

- [1] L. Z. Yin, X. G. Fan, and S. J. Wang, "A study on application of squeezed branch pile in clay soil foundation," *Earth and Environmental Science*, vol. 61, no. 1, pp. 1–6, 2017.
- [2] Q. Xiao, D. H. Wang, and J. Xu, "Experimental study on mechanical characteristics of squeezed branch piles for power transmission lines," *Journal of Experimental Mechanics*, vol. 30, no. 1, pp. 124–130, 2015.
- [3] G. L. Yang, S. H. Chen, and Y. L. Lin, "Contrastive experimental study between expanded diameter piles and equal diameter piles," *Journal of Railway Science and Engineering*, vol. 6, no. 2, pp. 34–42, 2009.
- [4] F. Li, H. B. Song, and Y. D. Zhou, "Bearing characteristics of squeezed branch pile," *Journal of Hohai University*, vol. 38, no. 2, pp. 202–205, 2010.
- [5] L. P. Zhang and X. M. Wang, "Comparison on load-bearing character is tics among equal diameter pile, branched pile and branch pile," *Journal of Chang'an University*, vol. 36, no. 5, pp. 37–44, 2016.
- [6] W. Cui and Z. J. Wang, "Field experiment study on the bearing characteristics of squeezed branch pile in loess area," *Applied Mechanics and Materials*, vol. 166–169, pp. 1329–1332, 2012.
- [7] Y. Zhang, P. Chen, and Z. X. Zhao, "Experimental study on squeezed branch pile foundation in soft soil ground," *Chinese Journal of Geotechnical Engineering*, vol. 35, no. S2, pp. 994–997, 2013.
- [8] X. B. Liu, L. H. Chen, Z. Y. Yu, J. X. Hu, and W. Peng, "Experimental study on DX pile performance in frozen soils under lateral loading," *Sciences in Cold and Arid Regions*, vol. 5, no. 5, pp. 608–613, 2013.
- [9] Y. Liang, S. F. Ren, D. X. Geng, and X. ShangGuan, "Research on vertical bearing capacity and settlement algorithm of large diameter and variable cross section Piles," *Journal of East China Jiaotong University*, vol. 26, no. 4, pp. 34–38, 2009.
- [10] Y. H. Wu, G. Zheng, and S. W. Yan, "A settlement prediction method for multi-under-reamed cast-in-situ pile foundation," *Chinese Journal of Geotechnical Engineering*, vol. 5, pp. 528–531, 2000.
- [11] Y. W. Ju, R. W. Liang, X. H. Bai, and S. Y. Zhang, "Experimental study of bearing and deformation behavior of squeezed branch pile and its bearing capacity calculation," *Engineering Mechanics*, vol. 6, pp. 34–38, 2003.
- [12] X. J. Gao and X. R. Zhu, "Forecasting ultimate bearing capacity of single squeezed branch pile by hyperbola method," *Rock and Soil Mechanics*, vol. 9, pp. 1596–1600, 2006.
- [13] J. P. Jiang, G. Y. Gao, and B. H. Gu, "Bearing behaviors and description of Q-s curves of piles with expanded diameter based on power-hyperbola combined model," *Engineering Mechanics*, vol. 27, no. 11, pp. 120–126, 2010.
- [14] G. B. Liu, G. J. Hu, Z. Han, Y. D. Zheng, and R. Y. Zheng, "Model tests on bearing behaviors and calculation of multi-stage expanded piles," *Chinese Journal of Geotechnical Engineering*, vol. 41, no. S2, pp. 149–152, 2019.
- [15] L. X. Li, X. J. Li, and B. Liu, "A simplified nonlinear settlement analysis method for axial loaded squeezed and branch piles," *Chinese Journal of Underground Space and Engineering*, vol. 14, no. 4, pp. 904–911, 2018.
- [16] M. F. Randolph and C. P. Wroth, "Analysis of deformation of vertically loaded piles," *Journal of the Geotechnical Engineering Division*, vol. 104, no. 12, pp. 1465–1488, 1978.
- [17] H. B. Seed and L. C. Reese, "The action of soft clay along friction piles," in *Proceedings of the American Society of Civil Engineers*, pp. 731–754, St. Louis, MO, USA, 1955.
- [18] M. F. Randolph and C. P. Wroth, "An analysis of the vertical deformation of pile groups," *Géotechnique*, vol. 29, no. 4, pp. 423–439, 1979.
- [19] N. Janbu, "Static bearing capacity of friction piles," in *Proceedings of the European Conference on Soil Mechanics and Foundation Engineering*, pp. 479–488, Vienna, Austria, March 1976.
- [20] F. H. Kulhawy, "Limiting tip and side resistance: fact or fallacy?" in *Proceedings of the Symposium on Analysis and Design of Pile Foundations*, San Francisco, CA, USA, October 1984.

- [21] J. Yang, L. G. Tham, P. K. K. Lee, S. T. Chan, and F. Yu, "Behaviour of jacked and driven piles in sandy soil," *Géotechnique*, vol. 56, no. 4, pp. 245–259, 2006.
- [22] S. T. Tang, *Research on bearing mechanism and settlement of single DX pile and DX pile group*, Ph.D. thesis, Beijing Jiaotong University, Beijing, China, 2012, in Chinese.

## Research Article

# Study on Identification of Construction Method for Ultra-Large-Span Tunnel

Xu Chongbang <sup>1,2,3</sup> and Qin Youlin <sup>1,2,3</sup>

<sup>1</sup>Bridge and Tunnel Research Center, Research Institute of Highway Ministry Transport, Beijing 100088, China

<sup>2</sup>National Engineering Laboratory of Bridge Structure Safety Technology, Beijing 100088, China

<sup>3</sup>Research Institute of Highway Ministry of Transport Research and Development Center of Transport Industry of Technologies and Equipments for Intelligent Design, Construction and Maintenance of Underwater Tunnel, Ministry of Transport, Beijing 100088, China

Correspondence should be addressed to Xu Chongbang; xubang-2003@163.com

Received 10 October 2020; Revised 5 December 2020; Accepted 14 December 2020; Published 24 December 2020

Academic Editor: Zhi Cheng Tang

Copyright © 2020 Xu Chongbang and Qin Youlin. This is an open access article distributed under the Creative Commons Attribution License, which permits unrestricted use, distribution, and reproduction in any medium, provided the original work is properly cited.

Although the determination of tunnel construction methods is extremely critical for the construction of ultra-large-span tunnels, the determination of construction methods is still at a qualitative level, which relies on the engineering experience of on-site technicians and lacks rigorous and systematic theoretical basis and technical standards. By means of orthogonal test method, the proper construction method was established for the deep-buried ultra-large-span tunnel where the tunnel excavation span, tunnel surrounding rock strength, and rock integrity coefficient were set as the main control factors. The stability of tunnel surrounding rock under various test conditions was quantified according to the plastic zone properties calculated by the three-factor and five-level orthogonal test model. Meanwhile, the macro form and quantitative method of test combinations under different levels of various factors were proposed to obtain the influence of each factor on the stability of tunnel surrounding rock, and thus the functional relations between various factors and tunnel stability were obtained. On this basis, the identification and the criterion of the ultra-large-span tunnel construction method were established, which can quantitatively reflect the contribution of excavation span of the tunnel, the number of lateral drifts in cross section, surrounding rock strength, and rock integrity coefficient to surrounding rock stability of the tunnel. The construction method calculation results of the Malin tunnel, a practical underground project, are obtained according to the orthogonal test model calculation. Based on the method, Malin tunnel can be constructed safely and efficiently. The research results could provide the theoretical basis for the identification and selection of construction method for ultra-large-span tunnel.

## 1. Introduction

The determination of tunnel construction methods is extremely critical for the construction of ultra-large-span tunnels, which directly affects the construction safety, progress, costs, and the configuration of humans, machines, and materials during construction. Various methods for ultra-large-span tunnel construction have been developed under the influences of many factors including the size of the tunnel section and topographical, engineering geological, and hydrogeological conditions. The commonly used methods include the center diaphragm method (CD

method) [1], center cross diagram method (CRD) [2–6], the double-side drift method [7–9] and the three-stage and seven-step method [10, 11], and other methods derived from these basic methods. In the construction of ultra-large-span tunnels, the determination of construction methods is still at a qualitative level, which relies on the engineering experience of on-site technicians and lacks rigorous and systematic theoretical basis and related technical standards [12].

In common practices, factors considered during selecting construction methods often include (1) project factors, such as overall excavation span of the tunnel, the maximum single excavation span, and auxiliary engineering measures [13], and

(2) geological and environmental factors, such as the properties of surrounding rock (the strength of the surrounding rock and the integrity coefficient of the rock mass) [14–19], groundwater [20], and the in situ stress [21]. In order to ensure the stability of the tunnel after blasting and before the initial support construction, the maximum one-step excavation span of the tunnel, the strength of the surrounding rock, and rock integrity are placed at the top priority. Other factors are generally considered as supplementary grounds for final decision. In this paper, we established the orthogonal test model to determine the proper construction method for the deep-buried ultra-large-span tunnel where the tunnel excavation span, tunnel surrounding rock strength, and rock integrity coefficient were set as the main control factors. Our work aims to establish the evaluation system for selection of construction method and provide theoretical calculation basis for determining the number of lateral drifts in cross section of ultra-large-span tunnels through the quantification of control factors on the stability of surrounding rock during tunnel excavation.

## 2. Orthogonal Test Design

*2.1. The Level of Orthogonal Factors.* In order to elucidate the influence of tunnel span, surrounding rock strength, and rock integrity coefficient on the stability of tunnel surrounding rock, a five-level orthogonal test scheme is designed in this paper. The tunnel span, surrounding rock strength, and rock integrity coefficient are represented by A, B, and C, respectively. The five levels of the three factors are set as follows:

- (1) Factor A: with reference to the drift span, common tunnel span, and ultra-large-span tunnel span in highway tunnels, the five levels of factor A are designed as 6 m, 9 m, 12 m, 15 m, and 18 m, and the tunnel cross section is shown in Figure 1.
- (2) Factor B: factor B is the rock strength, which is divided according to the degree of soft and hard rock. The five levels of factor B are designed as 2 MPa, 10 MPa, 20 MPa, 40 MPa, and 65 MPa. According to the Mohr–Coulomb criterion, the internal friction angle  $\varphi$  and cohesive force  $C$  corresponding to the five levels are listed in Table 1.
- (3) Factor C: the five levels of factor C, which represents the coefficient of surrounding rock integrity, are 0.1, 0.2, 0.4, 0.6, and 0.75. The five levels of factor C in the test are shown in Table 2. The test parameters of the joint plane are selected in accordance with the recommended values of the peak shear strength of the rock discontinuity structural plane in the “Road Tunnel Design Rules” [22], as listed in Table 3.

*2.2. Orthogonal Test Combinations.* According to the orthogonal test design [23], the three-factor and five-level orthogonal test requires a total of 25 tests. The combinations of orthogonal tests are shown in Table 4:

## 3. Calculations and Results

*3.1. Model Size.* In order to eliminate the boundary effect of the tunnel calculation model, the size of the model was determined as 200 m (width)  $\times$  110 m (height). The buried depth of the tunnel was set as 50 m, as the typical depth of deep-buried tunnel. The tunnel structure was placed in the center of the model (Figure 2). The simulated tunnel construction employed a one-step excavation method without considering the role of lining support structure. The stress release rate of the tunnel surrounding rock was defined as 30%.

*3.2. Criterion of Surrounding Rock Instability.* In the experimental calculation model, the surrounding rock was assumed as ideal elastoplastic material, and thus the Mohr–Coulomb constitutive model was used to develop the criterion of surrounding rock instability [22] based on “Road Tunnel Design Rules.” It is assumed that the surrounding rock becomes unstable when plastic zones appear in the surrounding rock at the tunnel arch and the side walls and these zones communicate with each other. Meanwhile, in order to quantify the stability of the tunnel under each simulated condition, the properties of the plastic zone were quantified according to Table 5.

### 3.3. Calculation Results

*3.3.1. Example of Surrounding Rock Stability Analysis.* Here no. 1 A1B1C1 is taken as an example to illustrate the analysis process of surrounding rock stability. In the no. 1 test, there are multiple tensile stress distribution areas in the tunnel vault and arch wall (Figure 3). Plastic zones are found at the joint planes and rock blocks of the tunnel arch and the side walls, which connect each other (Figure 4). Therefore, it can be concluded that the full-face excavation under this three-factor combination is unstable. The quantitative score of the no. 1 test is 1 point.

*3.3.2. Test Results.* According to the conditions of the plastic zone calculated from the 25 sets of experiments, the results of the experimental calculations were quantified according to the quantitative rules. The quantitative statistical results and the tunnel stability are listed in Table 6.

## 4. Identification of Construction Method for Ultra-Large-Span Tunnel

*4.1. Data Processing.* In order to quantitatively analyze the influence of a single factor on the stability of the tunnel, the test data of each group were processed in combinations from a macro perspective to eliminate the impact of other factors based on the same frequency and probability of each level of every factor in the orthogonal test. Factor A is used as an example to explain the detailed process.



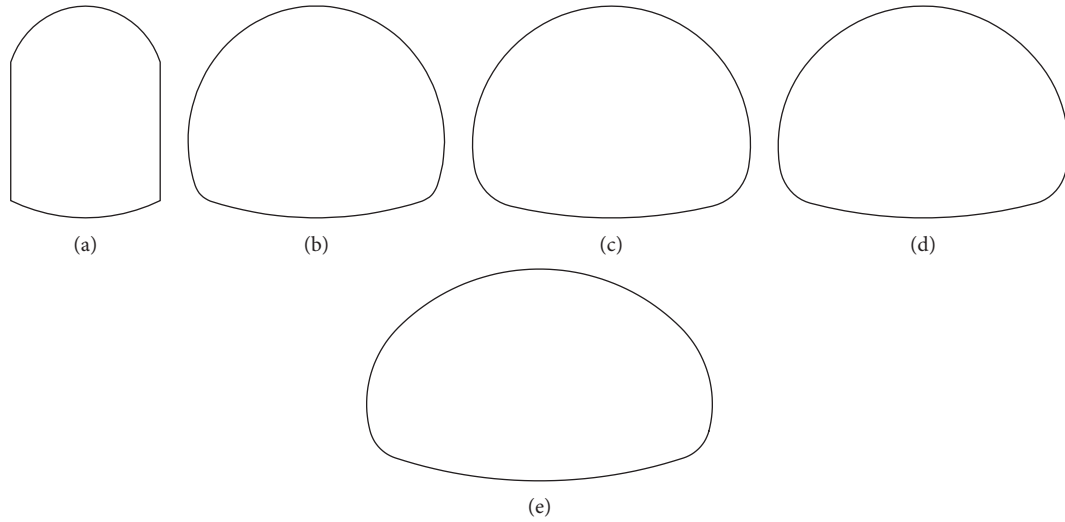


FIGURE 1: Five types of tunnel cross section. (a) With span of 6 m. (b) With span of 9 m. (c) With span of 12 m. (d) With span of 15 m. (e) With span of 18 m.

TABLE 1: Parameter values of each level of factor A.

Level	Compressive strength (MPa)	Internal friction angle $\varphi$ ( $^{\circ}$ )	Cohesive force $C$ (MPa)	Volumetric weight $\gamma$ ( $\text{kN}\cdot\text{m}^{-3}$ )	Elasticity modulus $E$ (GPa)	Poisson's ratio $\mu$
1	2	27.5	1.6	22	1.0	0.3
2	10	37	2.5	22	1.0	0.3
3	20	46.4	4	22	1.0	0.3
4	40	56.6	6	22	1.0	0.3
5	65	63	7.8	22	1.0	0.3

Note. The influences of volumetric weight, elasticity modulus, and Poisson's ratio were not considered.

TABLE 2: Parameter values of each level of factor C.

Level	Number of joint planes	Space of joint plane	Joint inclination angle ( $^{\circ}$ )	Coefficient of surrounding rock integrity
1	4	0.2	0/90/45/135	0.1
2	3	0.3	0/90/45	0.2
3	2	0.4	0/90	0.4
4	2	0.8	0/90	0.6
5	2	1.5	0/90	0.75

TABLE 3: Joint plane parameters.

Internal friction angle $\varphi$ ( $^{\circ}$ )	Cohesive force $C$ (MPa)	Compressive strength (MPa)
15	0.06	0.13

**4.1.1. Combination of Test Conditions.** The levels of factor A are the main study targets. Combining the levels of factor A with the five levels of factor B and factor C obtains the macro form of the test combinations (Table 7). The obtained combinations have the same macro combination of factor B and factor C for each level of factor A. Therefore, on this basis, comparative analysis of the influence of various levels of factor A on tunnel stability can be performed.

**4.1.2. Quantification of the Macro Form of the Test Combinations.** In order to quantify the influence of various factors on the tunnel stability, it is necessary to quantify the macro form of the test combinations. Given that the conditions under the combination are all independent, the linear superposition method is used to define the quantitative scores of factor A under each level to obtain the quantitative index F of tunnel stability under different combinations. The detailed calculation process is as follows:

- The first level of factor A (6 m span): IA = A1B(5)  
C(5) = 1 + 2 + 5 + 6 + 6 = 20.
- The second level of factor A (9 m span): IIA = A2B(5)  
C(5) = 1 + 3 + 5 + 5 + 3 = 17.
- The third level of factor A (12 m span): IIIA = A3B(5)  
C(5) = 1 + 3 + 5 + 3 + 4 = 16.

TABLE 4: Orthogonal test analysis.

No.	Excavation span A	Surrounding rock strength B	Coefficient of surrounding rock integrity C	Code
1	1 (6 m)	1 (2 MPa)	1 (0.1)	A1B1C1
2	1 (6 m)	2 (10 MPa)	2 (0.2)	A1B2C2
3	1 (6 m)	3 (20 MPa)	3 (0.4)	A1B3C3
4	1 (6 m)	4 (40 MPa)	4 (0.6)	A1B4C4
5	1 (6 m)	5 (65 MPa)	5 (0.75)	A1B5C5
6	2 (9 m)	1 (2 MPa)	2 (0.2)	A2B1C2
7	2 (9 m)	2 (10 MPa)	3 (0.4)	A2B2C3
8	2 (9 m)	3 (20 MPa)	4 (0.6)	A2B3C4
9	2 (9 m)	4 (40 MPa)	5 (0.75)	A2B4C5
10	2 (9 m)	5 (65 MPa)	1 (0.1)	A2B5C1
11	3 (12 m)	1 (2 MPa)	3 (0.4)	A3B1C3
12	3 (12 m)	2 (10 MPa)	4 (0.6)	A3B2C4
13	3 (12 m)	3 (20 MPa)	5 (0.75)	A3B3C5
14	3 (12 m)	4 (40 MPa)	1 (0.1)	A3B4C1
15	3 (12 m)	5 (65 MPa)	2 (0.2)	A3B5C2
16	4 (15 m)	1 (2 MPa)	4 (0.6)	A4B1C4
17	4 (15 m)	2 (10 MPa)	5 (0.75)	A4B2C5
18	4 (15 m)	3 (20 MPa)	1 (0.1)	A4B3C1
19	4 (15 m)	4 (40 MPa)	2 (0.2)	A4B4C2
20	4 (15 m)	5 (65 MPa)	3 (0.4)	A4B5C3
21	5 (18 m)	1 (2 MPa)	5 (0.75)	A5B1C5
22	5 (18 m)	2 (10 MPa)	1 (0.1)	A5B2C1
23	5 (18 m)	3 (20 MPa)	2 (0.2)	A5B3C2
24	5 (18 m)	4 (40 MPa)	3 (0.4)	A5B4C3
25	5 (18 m)	5 (65 MPa)	4 (0.6)	A5B5C4

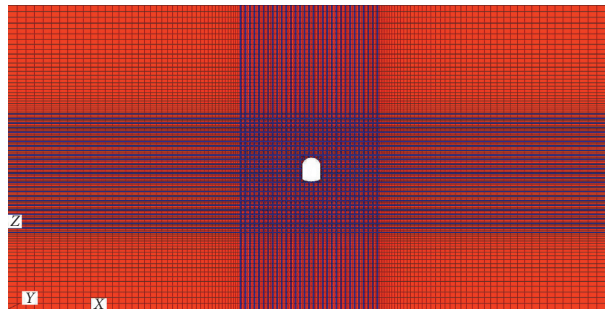


FIGURE 2: Calculation model of no. 1 test.

TABLE 5: Criterion and quantitative standard of surrounding rock stability state.

No.	Conditions of the plastic zone	Stability of surrounding rock	Quantitative score
1	Communicated plastic zones occur in both joint planes and rock blocks	Unstable	1
2	Plastic zones occur in both joint planes and rock blocks, but only communicate in joint planes	Unstable	2
3	Communicated plastic zones only occur in joint planes	Unstable	3
4	Noncommunicated plastic zones occur in both joint planes and rock blocks	Stable	4
5	Noncommunicated plastic zones occur in joint planes	Stable	5
6	No plastic zones occur in both joint planes and rock blocks	Stable	6

(d) The fourth level of factor A (15 m span):  
 $IVA = A4B(5)C(5) = 1 + 3 + 1 + 3 + 5 = 13$ .

(e) The fifth level of factor A (18 m span):  $VA = A5B(5)C(5) = 2 + 1 + 2 + 3 + 5 = 13$ .

4.1.3. *Processing Results.* The data processing of factors B and C is carried out in the same way, and their quantitative index F under various levels is calculated, as listed in Table 8.

As indicated by the range of the stability quantitative index of three factors in Table 8 [24], the strength of the

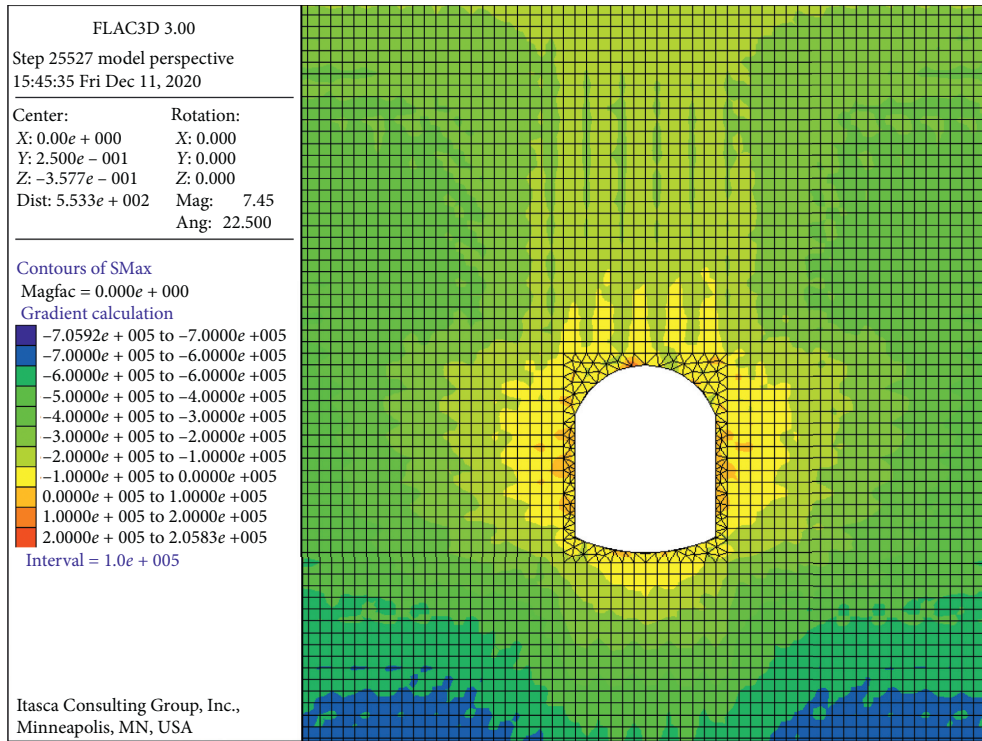


FIGURE 3: Principal stress distribution of surrounding rock.

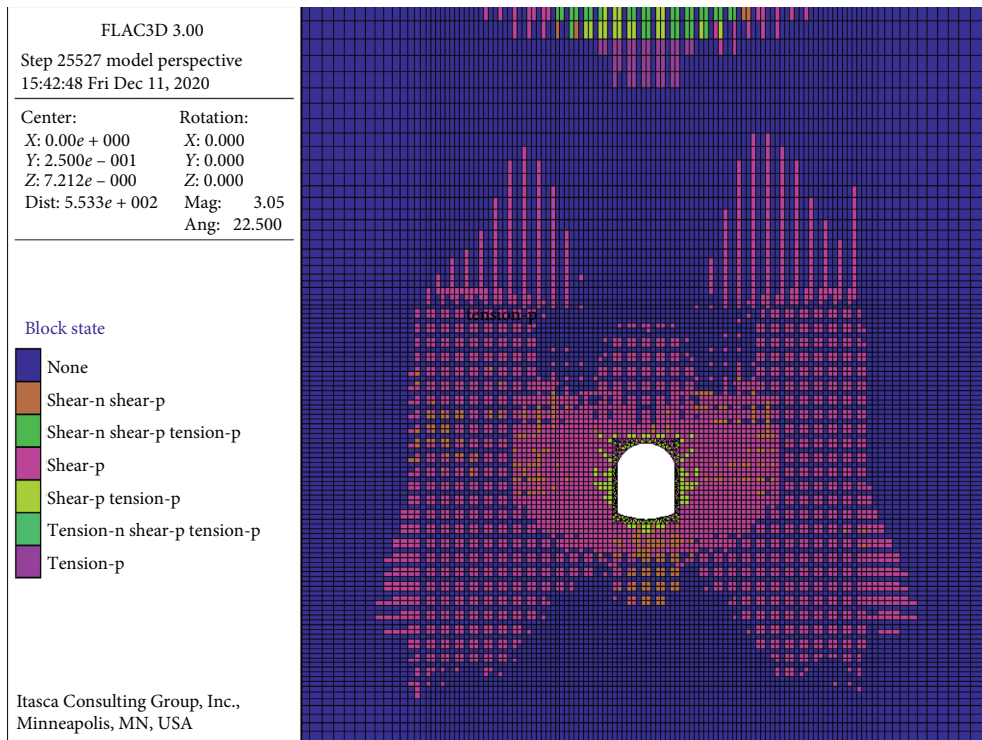


FIGURE 4: Distribution of plastic zone of surrounding rock.

TABLE 6: Quantification of test data and stability index.

Test no.	Test code	Stability	Quantitative score
1	A1B1C1	Unstable	1
2	A1B2C2	Unstable	2
3	A1B3C3	Stable	5
4	A1B4C4	Stable	6
5	A1B5C5	Stable	6
6	A2B1C2	Unstable	1
7	A2B2C3	Unstable	3
8	A2B3C4	Stable	5
9	A2B4C5	Stable	5
10	A2B5C1	Unstable	3
11	A3B1C3	Unstable	1
12	A3B2C4	Unstable	3
13	A3B3C5	Stable	5
14	A3B4C1	Unstable	3
15	A3B5C2	Stable	4
16	A4B1C4	Unstable	1
17	A4B2C5	Unstable	3
18	A4B3C1	Unstable	1
19	A4B4C2	Unstable	3
20	A4B5C3	Stable	5
21	A5B1C5	Unstable	2
22	A5B2C1	Unstable	1
23	A5B3C2	Unstable	2
24	A5B4C3	Unstable	3
25	A5B5C4	Stable	5

TABLE 7: Macro form of test combination at each level of factor A.

No.	Excavation span (A)	Code of test combinations	Macro form of the test combinations
1	1	A1B1C1, A1B2C2, A1B3C3, A1B4C4, A1B5C5	A1B(5)C(5)
2	2	A2B1C2, A2B2C3, A2B3C4, A2B4C5, A2B5C1	A2B(5)C(5)
3	3	A3B1C3, A3B2C4, A3B3C5, A3B4C1, A3B5C2	A3B(5)C(5)
4	4	A4B1C4, A4B2C5, A4B3C1, A4B4C2, A4B5C3	A4B(5)C(5)
5	5	A5B1C5, A5B2C1, A5B3C2, A5B4C3, A5B5C4	A5B(5)C(5)

Note. B(5) represents the combinations of five levels of factor B and C(5) represents the combinations of five levels of factor C.

TABLE 8: Quantitative index value of tunnel stability under different factor levels.

Level of factor	Quantitative index value of tunnel stability F		
	Tunnel span A	Rock strength B	Coefficient of rock integrity C
I	20	6	9
II	17	12	12
III	16	18	17
IV	13	20	20
V	13	23	21
Range	7	17	12

surrounding rock has the most significant impact on tunnel stability, followed by the surrounding rock integrity and the span of the tunnel in decreasing order.

*4.2. The Influence of Main Control Factors on Tunnel Stability.* Based on the stability quantitative index of three factors listed in Table 8, the influence rule of these factors on

tunnel stability can be drawn, as shown in Figures 5–7, respectively.

*4.2.1. Tunnel Span.* According to Figure 5, the tunnel excavation span has a negative correlation with the stability of the surrounding rock. The stability of the tunnel deteriorates with the increase of tunnel span. The relationship between them is expressed as a power function:

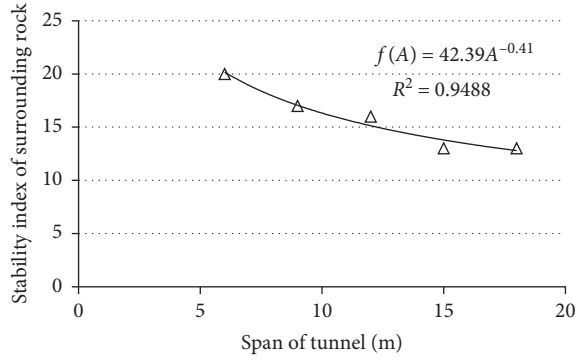


FIGURE 5: Fitting curve between stability index of surrounding rock and span of tunnel.

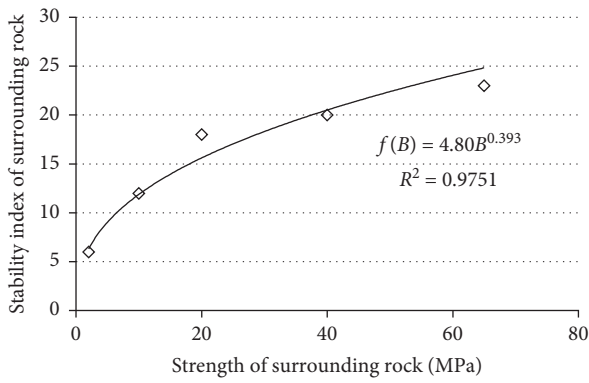


FIGURE 6: Fitting curve between stability index and strength of surrounding rock.

$$f(A) = 42.39A^{-0.41}. \quad (1)$$

4.2.2. *Compressive Strength of Surrounding Rock.* Figure 6 shows a strong positive correlation between surrounding rock strength and tunnel stability. A higher compressive strength of surrounding rock is beneficial for better tunnel stability. Their relation can be expressed as

$$f(B) = 4.80B^{0.393}. \quad (2)$$

4.2.3. *Coefficient of Surrounding Rock Integrity.* The tunnel stability is positively related with the coefficient of surrounding rock integrity, indicating that higher coefficient of surrounding rock integrity contributes to tunnel stability. The relation can be expressed as

$$f(C) = 6.208 \ln(C) + 22.78, \quad (3)$$

where  $f(C) > 0$ ; therefore, the coefficient of surrounding rock C should be greater than 0.03.

4.3. *The Expression of Quantitative Index of Surrounding Rock Stability.* The stability of the surrounding rock of the tunnel is the result of the combined action of the three main control

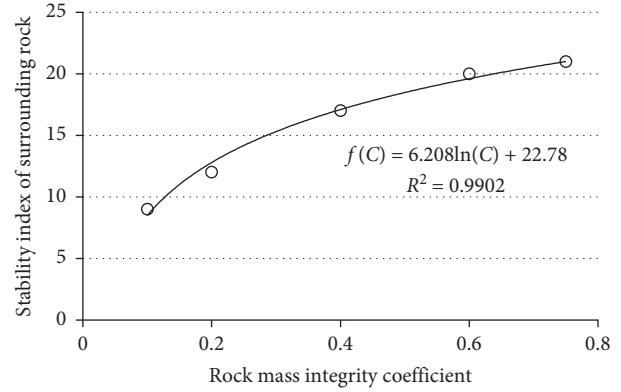


FIGURE 7: Fitting curve between stability index of surrounding rock and rock mass integrity coefficient.

factors. The influences of the main control factors on the stability are interrelated and coupled. This correlation can be expressed by their product and a coefficient  $k$ . Therefore, the tunnel stability after excavation can be quantified as

$$F = kf(A)f(B)f(C). \quad (4)$$

Substituting equations (1)–(3) into equation (4), F can be derived:

$$F = A^{-0.41}B^{0.393}(6.208 \ln(C) + 22.78), \quad (5)$$

where  $k$  is a constant value ( $k = 0.004907$ ).

4.4. *Criterion of Quantification of Surrounding Rock Stability.* Substituting the test calculation parameters (Table 4) into equation (5), the value of the tunnel stability quantitative index F for each test can be obtained (Table 9).

It can be seen from Table 9 that in 25 sets of orthogonal tests, the minimum index is 5.3 and the maximum is 22.3 when the surrounding rock is unstable after tunnel excavation. And the minimum index is 23.8 and the maximum is 51.9 when the surrounding rock of the tunnel remains stable. Therefore, the criteria for stability of surrounding rock can be given as follows:

- (1) If  $F \geq 23$ , the surrounding rock is in stable state.
- (2) If  $F < 23$ , the surrounding rock becomes unstable.

According to this criterion and the quantification rules, the stability index F can be classified as six levels specifically, as listed in Table 10.

#### 4.5. Criterion for Tunnel Construction Method Selection

4.5.1. *One-Step Maximum Excavation Span.* According to equation (5), for a given tunnel surrounding rock, a proper one-step excavation span should be selected to satisfy the index  $F \geq 23$  to ensure the stability of the surrounding rock during excavation. Thus, maximum span  $A_{max}$  of the next-step excavation can be calculated under given surrounding rock properties (strength and integrity coefficient) when assuming that  $F = 23$ , as shown in the following equation:

TABLE 9: Index calculation value of tunnel stability.

Test no.	Test code	Stability	F
1	A1B1C1	Unstable	5.3
22	A5B2C1	Unstable	6.4
6	A2B1C2	Unstable	6.8
11	A3B1C3	Unstable	8.1
21	A5B1C5	Unstable	8.4
16	A4B1C4	Unstable	8.5
18	A4B3C1	Unstable	9.1
23	A5B3C2	Unstable	12.7
14	A3B4C1	Unstable	13.1
2	A1B2C2	Unstable	15.2
17	A4B2C5	Unstable	17.1
7	A2B2C3	Unstable	17.2
12	A3B2C4	Unstable	17.5
10	A2B5C1	Unstable	17.8
19	A4B4C2	Unstable	18
24	A5B4C3	Unstable	22.3
15	A3B5C2	Stable	23.8
13	A3B3C5	Stable	24.6
8	A2B3C4	Stable	25.9
3	A1B3C3	Stable	26.6
20	A4B5C3	Stable	29
25	A5B5C4	Stable	30.9
9	A2B4C5	Stable	36.3
4	A1B4C4	Stable	40.1
5	A1B5C5	Stable	51.9

TABLE 10: Index value and qualitative description of tunnel stability.

F	Unstable state				Stable state	
	<13	[13, 17)	[17, 23)	[23, 26)	[26, 40)	≥40
Description of stability	Extremely unstable	Very unstable	Unstable	Basically stable	Very stable	Highly stable

$$A_{\max} = \left( \frac{B^{0.393} (6.208 \ln(C) + 22.78)}{23} \right)^{2.44} \quad (6)$$

4.5.2. *Determination of the Number of Drifts.* Assuming that the maximum span of tunnel excavation is  $L$  and the number of lateral drifts in the cross section is  $N$ , it can be seen from equation (6) that the number of lateral drifts in the tunnel section should be

$$N \geq \frac{L}{A_{\max}} = \frac{L}{\left( \left( B^{0.393} (6.208 \ln(C) + 22.78) \right) / 23 \right)^{2.44}} \quad (7)$$

Thus,

$$N_{\min} = \frac{L}{\left( \left( B^{0.393} (6.208 \ln(C) + 22.78) \right) / 23 \right)^{2.44}} \quad (8)$$

where  $N_{\min}$  should be integer.

4.5.3. *Bench Division of Tunnel Drift.* After determining the number of lateral drifts, the stability state of the tunnel drift is used as a reference for the necessity of bench cut. It is

recommended to perform bench cut construction in the lateral drifts as instructed by Table 11.

4.6. *Influencing Analysis of Other Factors.* In the construction phase of tunnel engineering, the identification of construction method should consider not only the three crucial factors including tunnel span, rock mass integrity coefficient, and strength of surrounding rock but also the secondary factors such as in situ stress, groundwater, and construction capacity of the subcontractors. The secondary influence factors are restricted by the geological conditions of the tunnel site, which is not universal. Therefore, in the actual tunnel projects, the influence of secondary factors can be revised according to the specific situation of projects, and the influence of secondary factors is reflected by means of revision.

## 5. Case Study

The Malin tunnel is located in Wudang District, Guiyang City. It is a separated two-way six-lane tunnel. The inner outline is a three-center round curved side wall structure. The net area is 123.68 m<sup>2</sup>, the net span is 17.61 m, the net height is 5.0 m, and the flatness ratio is 0.618 (as shown in Figure 8). The designed speed of 100 km/h is tailored, as that

TABLE 11: Stability index value and bench division of tunnel drift.

Description of tunnel stability	Basically stable	Very stable	Highly stable
Bench division	Bench division is necessary and temporary invert should be adopted	Bench division is necessary and temporary invert is not compulsive	Bench division is unnecessary

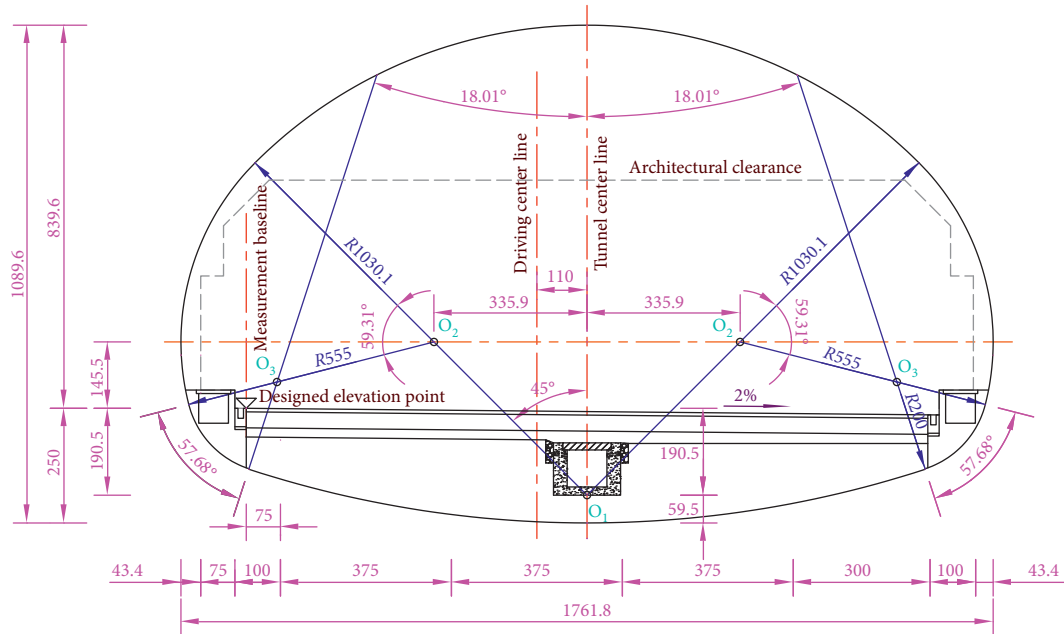


FIGURE 8: Inside outline of Malin tunnel.

TABLE 12: Calculation results of Malin tunnel construction method.

Item	Quantitative index
One-step span	15.9
Overall span	19.9
Number of calculated lateral drift	1.2
Number of determined lateral drift	2.0
Determined one-step excavation span	9.94
Index of surrounding rock stability F	27.81
Stability of surrounding rock	Very stable
Recommended method	CD method



FIGURE 9: Photo of CD method construction in Malin tunnel.

of expressway. The total length of the left tunnel is 745 m, the total length of the right tunnel is 760 m, and the maximum buried depth of the tunnel is about 98.7 m.

The surrounding rock is mainly composed of full-moderately weathered dolomite and dolomitic limestone. The rock grades mainly fall into grade IV and grade V. The grade V surrounding rock is mainly gravel, highly weathered dolomitic limestone, and cataclasite. The self-stability of surrounding rock is poor, so it is not controversial to use the double-side drift method for the grade V rock. Our method is applied to determine the construction method for the grade IV surrounding rock.

According to the survey and design of the Malin tunnel, the excavation span, rock strength, and rock integrity coefficient of grade IV rock are 19.54 m, 25.4 MPa, and 0.69, respectively. The calculation results based on our evaluation system are listed in Table 12.

Therefore, the grade IV surrounding rock section of the Malin tunnel should be constructed using the CD method with two lateral drifts in the cross section. The left and right drifts are divided into upper and lower drifts, and the tunnel construction is implemented with the CD method (Figure 9). The safety and efficiency of the construction process have been verified in the whole construction process.

## 6. Conclusions

In this paper, the orthogonal test method was used to establish a three-factor five-level test model, and the quantitative relationship functions between the three factors and the stability of the surrounding rock of the tunnel were given. The following conclusions can be drawn from this paper:

- (1) The tunnel excavation span is negatively related to the stability of the surrounding rock of the tunnel, which can be described by a power function. The strength of the surrounding rock of the tunnel is positively related to the stability of the surrounding rock of the tunnel and can be described by a power function; the rock integrity coefficient is positively related to the stability of the surrounding rock of the tunnel, and their relationship can be described by a logarithmic function.
- (2) An equation for determining the construction method of ultra-large-span tunnel is constructed, which can quantitatively reflect the contribution of excavation span of tunnel, the number of lateral drifts in cross section, surrounding rock strength, and rock integrity coefficient to surrounding rock stability of tunnel. The research results provide the theoretical basis for the identification and selection of construction method for ultra-large-span tunnel and provide theoretical calculation basis for determining the number of drifts in the cross section.

## Data Availability

The data used to support the findings of this study are available from the corresponding author upon request.

## Conflicts of Interest

The authors declare that they have no conflicts of interest regarding the publication of this paper.

## Acknowledgments

This study was financially supported by the Special Science and Technology Innovation Fund of Research Institute of Highway Ministry of Transport (grant no. 2019-C505) and the Central Public-Interest Scientific Institution Basal Research Fund (grant no. 2020-9032).

## References

- [1] X. Chong-bang, Z.-G. Yang, and H. Wang, "Optimization analysis on construction method of shallow buried large section tunnel," *Highway*, vol. 61, no. 4, pp. 261–264, 2016.
- [2] Y. Hong-wei and W. Wang, "Study of optimal proposal and field test for CRD excavation method of shallow-buried tunnel," *Journal of Railway Science and Engineering*, vol. 15, no. 6, pp. 1509–1515, 2018.
- [3] W. Liang and M.-L. Huang, "Subsidence and deformation control of large-span tunnel in water-bearing unfavorable geological conditions with CRD method," *Chinese Journal of Rock Mechanics and Engineering*, vol. 26, no. 2, pp. 3738–3742, 2007.
- [4] H. Ming-Qi, X.-L. Fu, and L. Yun-chao, "Study on stability control of large-section subsea tunnels in weak strata by CRD construction method," *Chinese Journal of Rock Mechanics and Engineering*, vol. 26, no. 2, pp. 3084–3089, 2007.
- [5] Y.-L. Qi, M.-X. Tang, and H. Cao, "Simulation of CRD construction method in large-section shallowmining subsea tunnel," *Chinese Journal of Underground Space and Engineering*, vol. 10, no. 1, pp. 136–143, 2014.
- [6] X. Shi, J. Zhang, and L. Bao-chen, "A study of the construction sequences of a large-Section shallow-buried unsymmetrical loading tunnel by the CRD Method," *Modern Tunnelling Technology*, vol. 52, no. 3, pp. 193–199, 2015.
- [7] X. Chong-bang, C.-C. Xia, and H.-H. Zhu, "Optimum analysis for construction scheme of multiple-arch tunnel with eight traffic lanes," *Chinese Journal of Rock Mechanics and Engineering*, vol. 28, no. 1, pp. 17–26, 2009.
- [8] G.-H. Zhang, C. Li-Biao, and Q. Shi-Xiong, "On-site supervision measure and analysis of Damaoshan tunnels with large section and small clear-distance," *Rock and Soil Mechanics*, vol. 31, no. 2, pp. 489–496, 2010.
- [9] C. Jian-xun, Y.-bin Luo, and Li Wan, "Research status and challenges of highway tunnel with super long span," *Road Machinery & Construction Mechanization*, vol. 35, no. 6, pp. 36–44, 2018.
- [10] L. Zhi-Qing, C.-L. Ding, and D. Shi-Xue, "Analysis on deformation characteristics of surrounding rock in large section shallow loess tunnels," *Chinese Journal of Underground Space and Engineering*, vol. 10, no. S1, pp. 1623–1628, 2014.
- [11] L. I. Xin-Zhi, L. I. Shu-Cai, and L. I. Shu-Chen, "Ground settlement deformation characteristic study of shallow large-span tunnel in construction process," *Chinese Journal of Rock Mechanics and Engineering*, vol. 30, no. S1, pp. 3348–3353, 2011.
- [12] C. Zuo-Qiang, L. Rui-Hui, and C. Yao, "Study on transformation method of construction method for super-long span



- highway tunnel,” *Science Technology and Engineering*, vol. 20, no. 17, pp. 7059–7065, 2020.
- [13] L. Yan-Yan, Y.-R. Zheng, and N. Kang, “Sensitivity analysis on influencing factors of tunnel stability,” *Chinese Journal of Underground Space and Engineering*, vol. 11, no. 2, pp. 491–498, 2015.
- [14] C.-C. Xia, C. Xiao-xiang, and X. Chong-bang, “Fine description of rock joint combined with block theory and its applications in extra-large cross-section multiple-arch tunnel,” *Chinese Journal of Rock Mechanics and Engineering*, vol. 29, no. 1, pp. 13–20, 2010.
- [15] Z. C. Tang, Q. Z. Zhang, and J. Peng, “Effect of thermal treatment on the basic friction angle of rock joint,” *Rock Mechanics and Rock Engineering*, vol. 53, no. 4, pp. 1973–1990, 2020.
- [16] J. Zou, Y.-Y. Jiao, Z. Tang, Y. Ji, C. Yan, and J. Wang, “Effect of mechanical heterogeneity on hydraulic fracture propagation in unconventional gas reservoirs,” *Computers and Geotechnics*, vol. 125, Article ID 103652, 2020.
- [17] Z. C. Tang and Y. Y. Jiao, “Choosing appropriate appraisal to describe peak spatial features of rock joint profiles,” *International Journal of Geomechanics*, vol. 20, no. 4, Article ID 4020021, 2020.
- [18] Z. C. Tang and Q. Z. Zhang, “Elliptical Hertz-based general closure model for rock joints,” *Rock Mechanics and Rock Engineering*, vol. 55, no. 4, pp. 1945–1956, 2020.
- [19] Z. C. Tang, L. Li, X. C. Wang, and J. P. Zou, “Influence of cyclic freezing-thawing on shear behaviors of rock fracture,” *Cold Regions Science and Technology*, vol. 181, Article ID 103192, 2020.
- [20] H. Hong-Xing, “The influence of excavation method on the stability of surrounding rock in mountain tunnel with rich water,” *Journal of Water Resources and Architectural Engineering*, vol. 18, no. 3, pp. 150–155, 2020.
- [21] X.-M. Han, M.-L. Sun, and L. Wen-Jiang, “Optimization of section shape and support parameters of tunnel under complicated conditions,” *Rock and Soil Mechanics*, vol. 32, no. 1, pp. 725–731, 2011.
- [22] CCCC Second Highway Consultants Co., Ltd., *Guidelines for Design of Highway Tunnels: JTG/T D70-2010*, China Communications Press, Beijing, China, 2010.
- [23] R. Lu-Quan, *Regression Design and its Optimization*, Science Press, Beijing, China, 2009.
- [24] F. Kai-Tai and M. Chang-Xing, *Orthogonal and Uniform Experimental Design*, Science Press, Beijing, China, 2001.

## Research Article

# A Method and Equipment for Continuously Testing the Permeability Coefficient of Rock and Soil Layers

Wei Chen <sup>1</sup>, Datian Cui,<sup>2</sup> Meng Xu,<sup>3</sup> and Rongchao Xu <sup>1</sup>

<sup>1</sup>College of Geosciences and Engineering, North China University of Water Resources and Electric Power, Zhengzhou 450045, China

<sup>2</sup>School of Materials Science and Engineering, North China University of Water Resources and Electric Power, Zhengzhou 450045, China

<sup>3</sup>College of Geology and Info-Physics Engineering, Central South University, Changsha 410083, China

Correspondence should be addressed to Rongchao Xu; rcxirms@126.com

Received 4 November 2020; Revised 30 November 2020; Accepted 8 December 2020; Published 24 December 2020

Academic Editor: Zhi Cheng Tang

Copyright © 2020 Wei Chen et al. This is an open access article distributed under the Creative Commons Attribution License, which permits unrestricted use, distribution, and reproduction in any medium, provided the original work is properly cited.

The water pressure test and steady-flow pumping test are still commonly used for measuring the permeability coefficient of rock and soil strata. Limited by the fact that the average value of the permeability coefficient could be obtained only by this testing method, the accuracy of the experimental results of the permeability coefficient for special rock and soil strata is not good. Therefore, a new on-site testing method and equipment for continuously measuring the permeability coefficient of rock and soil strata is studied in this paper. The method is suitable for water pressure testing in borehole and the steady-flow pumping test. The technical proposal is when the pumping test or water pressure test is carried out, the final water penetration will tend to be a stable value, and then, the high-precision current meter probe will be placed at the bottom of the pumping test hole or water pressure test hole. For the pumping test, the current meter will be lifted uniformly from the bottom of the borehole testing section to the stable water level. Meanwhile, the flow rate of a differential zone of the tested section is continuously detected. For the water pressure test, the current meter will be lifted uniformly from the bottom of the borehole test section to the top of the borehole test section, and the flow rate of the differential section will be continuously detected. Through data analysis and processing, not only the average permeability coefficient of the detected sections can be obtained but also the permeability coefficient of the differential section of the rock and soil stratum can be calculated, respectively. Furthermore, the corresponding relationship between the permeability coefficient and the detected location can be obtained. In view of the abovementioned reasons, the leaking point, the specific position, and the leakage quantity of the detected section could be found out accurately, which will improve the accuracy of the testing results obviously.

## 1. Introduction

The water pressure test and pumping test are common test methods for measuring the permeability coefficient of rock and soil layers [1]. The water pressure test is to isolate a certain length of the borehole test section with special water-stop equipment and then use a fixed water pressure to pressurize water into this section of borehole; water seeps into the rock mass through the cracks around the borehole wall, and eventually, the amount of water seeped will tend to a stable value; according to the water pressure, the length of the test section, and the stable amount of water seeped into

the rock mass, the permeability coefficient of rock mass can be calculated. The stable flow pumping test means that the flow rate and water level are relatively stable in a certain period of time. The permeability coefficient of rock and soil can be calculated by using various theoretical formulas of groundwater flow. However, the two methods have the following disadvantages [2–4]: ① At present, the permeability coefficient obtained by the water pressure test and pumping test is the average value of the rock and soil stratum in a test section. The permeability coefficient of a differential section of the rock and soil stratum in the test section cannot be calculated, the corresponding relationship between the

permeability coefficient and test section cannot be obtained, and the specific location and leakage amount of the leakage point and section cannot be accurately identified. ② The theoretical conditions do not agree with the actual geological conditions. The method of the pressure water test and steady-flow pumping test considers that the seepage water in the test section only distributes in the rock mass between the upper and lower ends of the test section and the two parallel planes perpendicular to the test section. There is no hydraulic connection between the test sections and the bottom of the hole. In fact, they have complex hydraulic connections. In order to overcome the abovementioned problems, the method and equipment of continuous detection of the permeability coefficient of the rock and soil stratum can be used. This method and equipment can not only detect the average permeability coefficient of the test section but also accurately detect the permeability coefficient along the differential section of the rock and soil stratum along the test section, obtain the corresponding relationship between the permeability coefficient and the test section, and accurately find out the leakage point. The specific location and leakage amount of the segment effectively improve the accuracy of the test results.

## 2. Working Principle

**2.1. Differential Water Pressure Test.** The purpose of this scheme is to provide a method of the single-stage differential water pressure test with a high sensitivity and large-range ratio anemometer, as shown in Figure 1. The testing program is to drill the test hole in stages. After the single hole is finished, the hole is washed and the orifice tube is placed, the probe of current meter is put into the bottom of the hole, the single hole orifice is sealed, and the water is supplied to the hole to achieve the specified value. When the water flow in the hole is stable, the stepper motor works and sends the probe slowly and uniformly to the top of the single hole along the axis of the test section from the bottom to top. The probe can measure the velocity of flow at each point along the borehole axis and convert it into flow. The flow of a differential hole section is equal to the difference between the flow of the upper and lower sections of the hole section. The length of the differential test section is measured by using a stepping motor. The pressure is derived from the measured value of the pressure sensor installed at the hole mouth and the static position of groundwater. The permeability of the hole section is calculated according to formula (1) of the pressure water test [5–7]. The absorption rate is calculated, and the distribution map of the test data of the differential pore section along the hole depth is drawn.

$$\Delta q = \frac{\Delta Q}{P \Delta L}, \quad (1)$$

where  $\Delta q$  is the absorption rate of the differential section, Lu;  $\Delta Q$  is the water quantity pressed into rock mass of the differential section,  $m^3$ ;  $P$  is the test pressure; and  $\Delta L$  is the test length of the differential section, m.

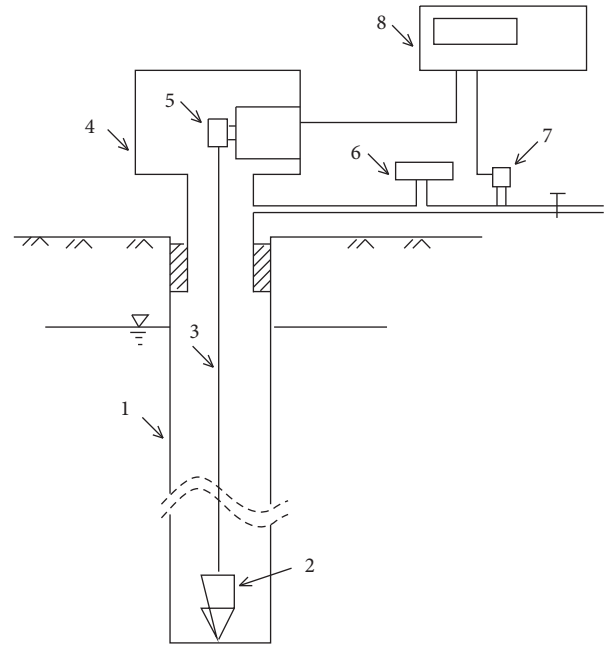


FIGURE 1: Layout plan of the differential water pressure test scheme. 1- drill hole; 2- turbine current meter; 3- electric cable; 4- sealing device; 5- stepper motor; 6- water supply device; 7- pressure sensor; and 8- computer.

**2.2. Differential Steady-Flow Pumping Test.** The steady-flow pumping test is to drill a pumping test hole and several water level observation holes at the designed position, respectively. A pumping system is used to pump water from the pumping test hole to form a stable flow, forming a depressing funnel-shaped groundwater surface centered on the pumping test hole; as shown in Figure 2, when the water flow is assumed to flow horizontally, the cross section of seepage through the hole should be a series of concentric cylindrical surfaces. The pumping quantity  $Q$  is measured, and the distance between the observation hole and the axis of the pumping test hole are  $r_1$  and  $r_2$ , respectively. The average  $K$  value and differential  $\Delta K$  value of the soil layer can be obtained by Darcy's law [1, 8, 9].

Now, a cross section is taken around the axis of the pumping test hole. The distance between the cross section and the center of the pumping test hole is  $r$ , and the height of the water surface is  $h$ . Then, the cross section area  $A$  is

$$A = 2\pi r h, \quad (2)$$

where  $A$  is the cross-section area,  $m^2$ ;  $r$  is the distance between the cross section and the center of the pumping test hole, m; and  $h$  is the water surface height, m.

Assuming that the hydraulic gradient is constant and equal to the gradient of the groundwater level line at this point,

$$i = \frac{dh}{dr}, \quad (3)$$

where  $i$  is the hydraulic gradient at the cross section.

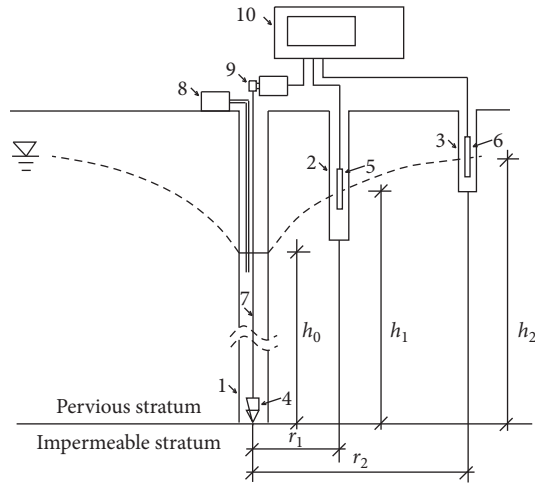


FIGURE 2: Schematic diagram of continuous detection by the steady-flow pumping test. 1- pumping test hole; 2- observation borehole I; 3- observation borehole II; 4- turbine current meter; 5- water level monitor ①; 6- water level monitor ②; 7- electric cable; 8- pumping device; 9- stepper motor; and 10- computer.

According to Darcy's law, the amount of water pumped from the well per unit time is

$$Q' = Aki = 2\pi rh \cdot k \frac{dh}{dr}, \quad (4)$$

where  $Q$  is the amount of water pumped from the pumping test hole per unit time,  $m^3$ ;  $k$  is the permeability coefficient,  $cm/s$ .

The integral equation (3) is

$$Q' \int_{r_1}^{r_2} \frac{dr}{r} = 2\pi k \int_{h_1}^{h_2} h dh. \quad (5)$$

Then,

$$k = \frac{Q'}{\pi} \frac{\ln(r_2/r_1)}{(h_2^2 - h_1^2)}, \quad (6)$$

$$\Delta k = \frac{h_0}{\Delta h} \frac{\Delta Q'}{\pi} \frac{\ln(r_2/r_1)}{(h_2^2 - h_1^2)}, \quad (7)$$

where  $\Delta k$  is the permeability coefficient of a differential section,  $cm/s$ ;  $\Delta Q'$  is the amount of water drawn from pumping test hole of the differential section in the unit time,  $m^3$ .

A probe of the current meter is placed at the bottom of the pumping test hole and lifted from the bottom of the test hole to the stable water level uniformly. It continuously detects the flow of the differential section. Two water level monitors are used to detect the flow from the bottom of the hole to the stable water level test section, and two water level monitors, which are, respectively, placed in observation hole I and II, are used to check the water level  $h_1$  and  $h_2$ ; By computer system analysis and processing, the distribution of the permeability coefficient of the rock and soil stratum along the depth of the pumping test hole can be obtained.

### 3. Hardware Design

**3.1. Hardware Composition Design.** The structure of the system is shown in Figure 3 [10–16]. The system consists of four sensors and a host computer. The host computer is mainly composed of an 80C196 single-chip computer system, input channel (sensor, interface circuit, and keyboard), output channel (monitor, printer, and data transponder), and so on. The sensors include a current meter probe, water level monitor, displacement sensor, and pressure sensor. Among them, the current meter probe measures the flow velocity along the axis of the borehole and converts it into an electric pulse signal which passes through the signal line in the cable and the photoelectric isolator and sends it to the microcomputer system; the pressure sensor measures the water pressure, and the water level monitor measures the water level of the observation hole and converts it into an analog signal which passes through the signal line and photoelectric isolation and sends it to the microcomputer system. The computer processes and analyses the above-mentioned signals to get the distribution of absorption rate or permeability coefficient of rock and soil along the borehole range and displays and prints them.

**3.2. Interface between the Sensor and MCU.** The analog sensor signal is a 4–20 mA DC current signal. The analog signal can be directly connected with the A/D conversion circuit integrated in the 80C196 single-chip computer through the interface. Its interface is composed of an isolator, I/V converter, low-pass filter, protection circuit, and reference voltage. The analog current signal of 4–20 mA is input into the interface circuit through an electromagnetic isolator. It is converted into 1–5 V DC voltage by the I/V converter. After the interference signal is removed by using the low-pass filter, it is fed to the A/D port of the single-chip computer [11–14].

The pulse sensor is a high-frequency pulse signal, which is transformed into a regular negative-tip pulse signal by phase-sensitive rectification, coupled by a photoelectric isolator, differential circuit, and monostable trigger, and then transformed into a standard rectangular wave. The 80C196 microcontroller reads the corresponding port data at the set time interval [11–14].

### 4. Software Design

This software adopts 80C196KB single-chip computer  $c$  language for modular structure program design and sets dozens of subprograms. The main program part of the flow chart is shown in Figure 4 [12–16]. The software can be divided into the following main modules by function. (1) data acquisition module- completing the flow rate data at the flow meter and the data of the test hole depth provided by the servo motor and the collection of various signs; (2) test module- completing the test according to the water pressure test and pumping test procedures; (3) data processing module- calculating the flow distribution data along the axis of the test hole; process and analyze the data according to

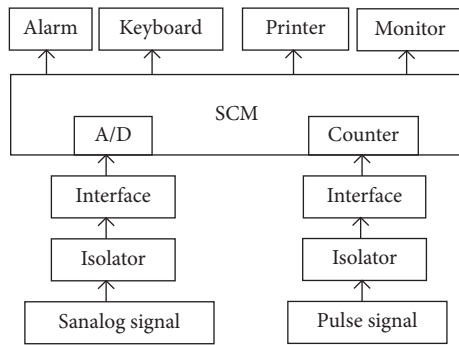


FIGURE 3: Host computer schematic diagram of continuous detection by the steady-flow pumping test.

Darcy’s law and related calculation formulas, and obtain the permeability coefficient along the axis of the test hole; and (4) data printing module- the curves and tables required for printing.

**5. Simulation Test and Discussion**

The porous pumping test is carried out at a certain site. The pumping hole belongs to the diving integrity hole. The pumping hole depth is 15.2 meters, the groundwater level is 2 meters deep, and the water level drops 3.2 meters after pumping. The distance between observation hole I and II from the center of the pumping test hole is observed,  $r_1$  and  $r_2$  are 4.3 m and 10 m, respectively, and the water levels in observation hole I and II are 12.45 m and 12.72 m, respectively, and the permeability coefficient calculated according to formula (6) is 5.23 m/d. Then, the current meter probe is uniformly raised upward from the bottom of the pumping test hole (15.2 m below the ground) to the stable water level (5.2 m below the ground). After data processing and analysis, the distribution curves of pumping capacity and permeability coefficient with pumping hole depth are obtained, as shown in Figure 5. The test results show that ① the permeability coefficient is not a fixed value with the change of the hole depth, but fluctuates within a large range; the minimum is 0.48 m/d and the maximum is 24.66 m/d; ② the section with small permeability coefficient can be judged as an impervious section, and the section with large permeability coefficient can be judged as a leakage point or section, such as points A, B, C, and D in Figure 5; and ③ the corresponding relationship between the permeability coefficient and test section is obtained, and the specific location and leakage amount of the leakage point and section are found accurately, which effectively improves the accuracy of test results.

The water pressure test was carried out at a certain fractured rock mass site. The depth of the test hole was 15 m, the depth of the pressurized water test section was 5–15 m, the test pressure was 1.0 MPa, and the water flow was 31.6 L/min. The absorption rate is 6.32 Lu according to formula (1). Then, the current meter probe is uniformly raised upward from the bottom of the water pressure test hole (15.0 m below the ground) to the top of the water pressure test hole (5.0 m below the ground). After data processing and

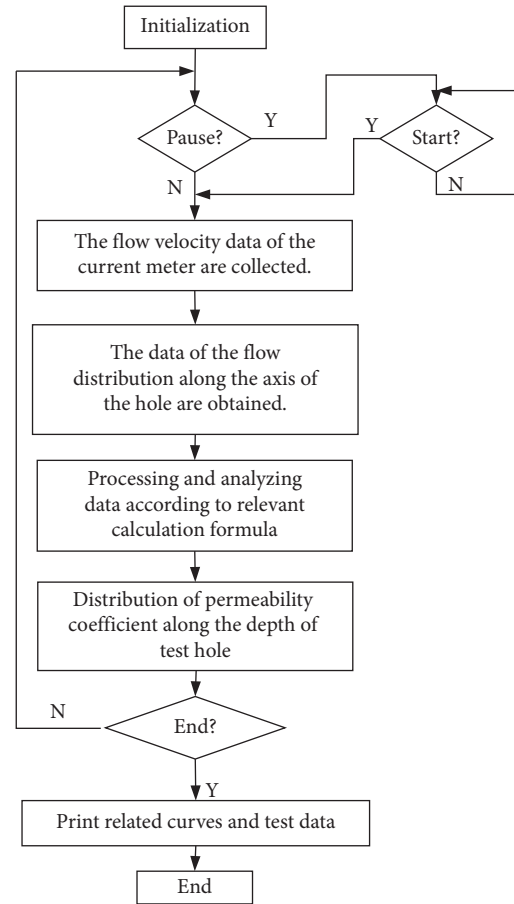


FIGURE 4: Main program flowchart.

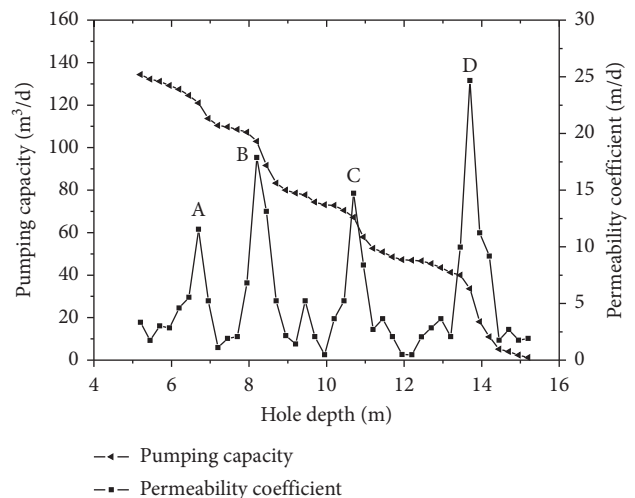


FIGURE 5: Distribution curves of the pumping capacity and permeation coefficient with the pumping hole depth.

analysis, the distribution curves of pressurized water flow and absorption rate with water pressure test hole depth are obtained, as shown in Figure 6. The test results show that ① the absorption rate is not a fixed value with the change of the hole depth, but fluctuates within a large range, the minimum is 1.32 Lu, and the maximum is 43.32 Lu; ② the section with

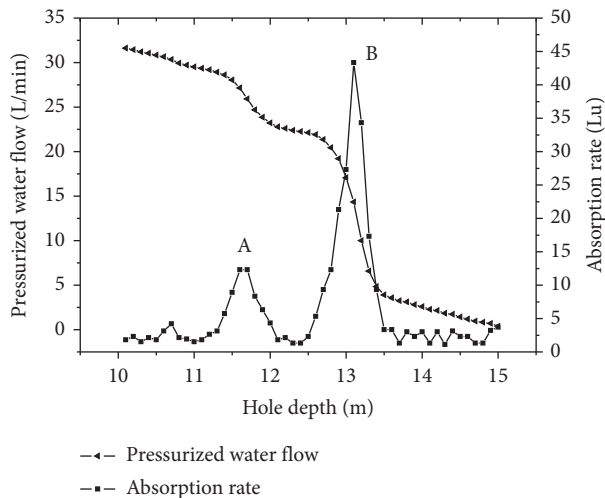


FIGURE 6: Distribution curves of pressurized water flow and absorption rate with the pumping hole depth.

small absorption rate can be judged as an impervious section, and the section with large absorption rate can be judged as a leakage point or section, such as points A and B in Figure 6; and ③ the corresponding relationship between the absorption rate and test section is obtained, and the specific location and leakage amount of the leakage point and section are found accurately, which effectively improves the accuracy of test results.

## 6. Conclusions

- (1) This paper studies a method and equipment for continuously detecting the permeability coefficient of the rock soil layer. This method is suitable for the drilling water pressure test and steady-flow pumping test and introduces the test principle, equipment hardware, and software design.
- (2) The method and equipment can continuously detect the flow of the differential section of rock and soil strata in the test section. After the data analysis and processing, the method and the device can not only obtain the average permeability coefficient of the test section but also get the microsegment permeability coefficient of the test section; meanwhile, the corresponding relationship between the permeability coefficient and the test section is obtained, the leakage point, the specific position of the section, and the leakage amount are accurately found, and the precision of the test result is effectively improved.
- (3) The test results show that ① the permeability coefficient or absorption rate varies with the depth of the hole, sometimes not a fixed value, but fluctuates within a large range; ② the section with small permeability or absorption rate can be judged as impervious, while the section with large permeability coefficient or absorption rate can be judged as a leakage point and section; and ③ according to the corresponding relationship between permeability or

absorption rate and the test section, the leakage point, the specific position of the section, and the leakage amount can be accurately found.

## Data Availability

The figure data used to support the findings of this study are included within the article.

## Conflicts of Interest

The authors declare that they have no conflicts of interest.

## References

- [1] N. Men, Y. W. Sun, and J. S. Bo, "Study of permeability coefficient in pumping test on steady flow in completely penetrating well," *Advanced Materials Research*, vol. 379, pp. 362–365, 2012.
- [2] S. R. Paiva, L. A. Lima, and F. Maria Raquel, "Analysis on determination of hydraulic conductivity for steady flow in fully pumping tests," *Railway Investigation & Surveying*, vol. 83, no. 4, pp. 1165–1170, 2010.
- [3] O. Banton and L. M. Bangoy, "A new method to determine storage coefficient from pumping test recovery data," *Groundwater*, vol. 34, no. 5, pp. 772–777, 2010.
- [4] Q. Fan, Z. Wang, J. Xu, M. Zhou, Q. Jiang, and G. Li, "Study on deformation and control measures of columnar jointed basalt for baihetan super-high arch dam foundation," *Rock Mechanics and Rock Engineering*, vol. 51, no. 8, pp. 2569–2595, 2018.
- [5] Q. Wang and H. Zhan, "The effect of intra-wellbore head losses in a vertical well," *Journal of Hydrology*, vol. 548, pp. 333–341, 2017.
- [6] Q. Wang and H. Zhan, "Intrawellbore kinematic and frictional losses in a horizontal well in a bounded confined aquifer," *Water Resources Research*, vol. 53, no. 1, pp. 127–141, 2017.
- [7] H. P. Patra, S. K. Adhikari, and S. Kunar, "Aquifer parameters, pumping test and the yield," *Springer Hydrogeology*, pp. 159–181, 2016.
- [8] X. Wang and A. Xiong, *Advanced Fluid Mechanics*, Huazhong University of Science and Technology Press, Wuhan, China, 2003.
- [9] W. Li, A. Englert, and H. Vereecken, "Inference of 3-D hydraulic conductivity from flowmeter and pumping-test data," in *Proceedings of the AGU Fall Meeting Abstracts*, San Francisco, CA, USA, May 2007.
- [10] F. Kohlbeck and A. Alvarez, "A method to determine the formation constants of leaky aquifers, and its application to pumping test data," *Groundwater*, vol. 29, no. 3, pp. 425–429, 2010.
- [11] M. Xu, P. Zhen-Bin, and C. Xun, "Design of detection system for differential water pressure," *Transducer & Microsystem Technologies*, vol. 30, no. 1, pp. 76–78, 2011.
- [12] Q. Fan, C. Huang, and X. Jiang, "Intelligent grouting control method and system for hydropower engineering," *Journal of Hydraulic Engineering*, 2018.
- [13] Y. Fan and X. F. Wu, "The design of intelligent pressure detection and alarm system," *Advanced Materials Research*, vol. 961, no. 4, 2014.
- [14] M. Xu, *The Development and Research of a New Intelligent Grouting and Pressurized Water Detection System*, Central South University, Changsha, China, 2010.

- [15] C. Wei, M. Xu, and J.-Q. He, "Study of grouting on-line detecting system based on SCM," *Instrument Technique & Sensor*, 2010.
- [16] W. Chao, L. Xu, and M. Xu, "Design and experimentation of grouting pressure automatic control system on PLC," *Journal of Central South University*, vol. 44, no. 10, pp. 4055–4062, 2013.

## Research Article

# Structural Mechanical Characteristics and Instability Law of Roof Key Block Breaking in Gob-Side Roadway

Xinfeng Wang <sup>1,2,3</sup>, Mingyuan Lu,<sup>1</sup> Yuhao Gao,<sup>1</sup> Wenbo Luo,<sup>3</sup> and Wengang Liu<sup>1,2</sup>

<sup>1</sup>College of Environment and Resources, Xiangtan University, Xiangtan, Hunan 411105, China

<sup>2</sup>Key Laboratory of Safety and High-Efficiency Coal Mining, Ministry of Education (Anhui University of Science and Technology), Huainan, Anhui 232001, China

<sup>3</sup>Hunan Key Laboratory of Geomechanics and Engineering Safety, College of Civil Engineering and Mechanics, Xiangtan University, Xiangtan, Hunan 411105, China

Correspondence should be addressed to Xinfeng Wang; wangxinfeng110@126.com

Received 27 October 2020; Revised 23 November 2020; Accepted 3 December 2020; Published 15 December 2020

Academic Editor: Xiaobo Zhang

Copyright © 2020 Xinfeng Wang et al. This is an open access article distributed under the Creative Commons Attribution License, which permits unrestricted use, distribution, and reproduction in any medium, provided the original work is properly cited.

The influence of mining on the upper section of working face leads to the fracture of the lateral key block of the roof. From the goaf to the coal body, a group of “left-middle-right” key blocks are formed. According to the three different spatial position structure relations formed by roadway and broken key block in practical engineering, the mechanical causes of broken structure of key block in roof of roadway along goaf are analyzed. FLAC<sup>3D</sup> is used to simulate and analyze the deformation characteristics and stress state of key block structure model before and after roadway excavation, and the mechanical characteristics and instability mechanism of key block sliding and breaking under three spatial structure modes are obtained. With the help of the mathematical model of material mechanics, the structural mechanical behavior of key block model of roof before and after roadway excavation and the temporal and spatial evolution law of unloading and breaking are studied. The results show that the complex influence factors of mining disturbance and low strength of the weak rock mass will weaken the internal balance of “masonry beam” structure. When the roadway is located below the fracture line of the key block, the middle key block will rotate and lose stability with the side hinge joint of the goaf as the axis; when the roadway is located in the fracture line of the key block, it is easy for the middle key block to slide and lose stability; when the roadway is located outside the fracture line of the key block, the middle key block is in the state of complete collapse, the mechanical transmission mechanism of the surrounding rock in the vertical direction is weakened, and the surrounding rock is the most stable.

## 1. Introduction

China’s energy system is characterized by rich coal, poor oil, and less gas, which determines that coal is still the main energy carrier that supports China’s industrial development and economic construction for a long time. With the gradual reduction of mineral resources reserves and the gradual destruction of geological and ecological environment, green mining, precise mining, efficient utilization, and intelligent development have become an important guarantee for coal resources development and sustainable development [1, 2]. Academician He and academician Xie have pointed out that there is a strong demand for the development and utilization of deep coal resources under the situation of energy output

rising, mining intensity increasing, and mining depth expanding. However, due to the particularity and complexity of deep underground engineering environment, it is still difficult to meet the needs of deep mining to study the deformation and failure mechanism and mechanical evolutionary mechanism of deep rock mass [3–5]. Therefore, it is a direct way and effective measure to solve the problem by vigorously studying the mechanical behavior and dynamic response law of deep rock mass disaster and promoting the new mining system and mining technology.

With the in-depth discussion of Chinese scholars, gob-side roadway has become the key research object of efficient mining of coal resources because of its reasonable design method, small amount of roadway excavation, and high coal



recovery rate. The use of gob-side roadway not only significantly improves the mine production efficiency, but also opens up the direction for the strategic concept of green mining and precise mining in China. However, in view of the complex and diverse mining geological conditions of underground coal and the multifield coupling of “three high and one disturbance” of deep excavation rock mass, how to realize the safety and stability control of gob-side roadway excavation is still facing many challenges.

The problem of asymmetric deformation and failure of roof in the roadway was studied by Xie. The influencing factors of the overall instability of the surrounding rock bearing structure were proposed. The mechanical model of the deep beam structure with strong mining asymmetric anchorage was established, and the stress distribution characteristics of the anchored beam structure and the cooperative bearing machine were analyzed [6, 7]. Based on the coordinated deformation model, the stability control technology of gob-side roadway retaining in fully mechanized top coal caving face was proposed by using roof presplitting blasting method [8]. Combined with the geological engineering background of fully mechanized top coal caving face, the stress state and failure characteristics of the filling body beside the roadway along goaf were studied by Feng [9]. The structural model of roof fracture of secondary gob-side roadway retaining was established by Kan, and the mechanical evolutionary law and stability control technology of overlying rock deformation and failure of secondary gob-side roadway retaining were revealed [10]. The basic roof of gob-side roadway was divided into three types of fracture by Wang, and the relative difference relationship and evolutionary law of surrounding rock stress and coal pillar pressure were analyzed with the help of numerical software [11]. Through the concrete dynamic analysis of the movement mode of the key block of the “masonry beam” formed by the hard basic roof in the western mining area, the relationship between the extrusion pressure and the inclination angle of key block and the mechanical response characteristics of the key block instability were revealed by Liu [12]. Based on the study of roof breaking law of close distance coal seam group, He has pointed out that the greater the roof damage, the greater the probability of S-R instability. The judgment basis depending on the dynamic variable of collapse pressure and anti extrusion strength attenuation of “masonry beam” hinge point was given [13]. Based on the theory of fracture mechanics, the influence factors of the fracture instability of the cantilever beam were analyzed by Yang. The inclination angle and length of the crack were the key factors causing the fracture and instability of the cantilever beam [14]. Based on the finite difference principle and material failure criterion, the elastic-plastic constitutive model of the primary failure of the basic roof was established by He. The dynamic fracture characteristics of the whole process of the basic roof breaking evolution were analyzed from the aspects of roof breaking position, breaking sequence, and breaking state [15].

The above research provides a generalized model of the broken structure of the key block for the roadway along the goaf, and the mechanical mechanism between the roof of the “masonry beam” structure and the coal mass in the goaf below, the instability process, and the determination method of the key block are given. However, the space-time relationship and mechanical response mechanism of roadway along goaf and upper key block have not been systematically integrated. Based on the theory of “masonry beam” key block, this paper focuses on three kinds of spatial relationship between gob-side roadway and upper layer key block breaking: roadway is located under the fracture line of key block, roadway is located inside the fracture line of key block, and roadway is located outside the fracture line of key block. The structural model of roof key block fracture is established, and the mechanical causes of key block fracture structure are analyzed. Through three-dimensional numerical simulation and theoretical analysis, the mechanical mechanism and deformation law of roof key blocks are revealed under three kinds of spatial structure states, and the judgment basis for the optimal selection of space-time position of gob-side roadway and upper broken key block and disaster prevention and control is provided.

## 2. Analysis of Spatial Structure Model of Roof Key Block Breaking in Gob-Side Roadway

During the mining process of coal body in the upper section working face, the coal edge supporting the basic roof in the direction of side goaf changes from elastic state to plastic failure state, resulting in a large amount of bending deformation [16]. With the continuous influence of dynamic pressure and the continuous advance of the working face, the overlying strata structure is destroyed, forming a group of three key blocks, namely, the right key block, the middle key block, and the left key block. The spatial structure model is shown in Figure 1.

The direct roof of the upper working face gradually collapses with the mining of the lower coal body, and the basic roof breaks at the bearing fulcrum of both ends of the rock beam. The right key block is completely compacted on the gangue pile of the upper section working face and forms an articulated relationship with the adjacent fractured rock beams [16]. The stress analysis of the middle key block is shown in Figure 2; the middle key block is squeezed with adjacent rock beam under the action of left and right horizontal extrusion force  $T$ , and the shear forces  $Q_A$  and  $Q_C$  on the contact angle make it stable in the vertical direction. Taking the left hinge joint as the axis, it rotates and sinks to the right goaf direction, showing a stepped subsidence structure.

In Figure 2,  $T_a$  and  $T_c$  are the squeezing forces of adjacent rock beams, kN;  $G_b$  is the self-weight stress, kN;  $q_1$  is the supporting load of coal body and direct roof, kN/m;  $q_0$  is the overburden load, kN/m;  $Q_A$  and  $Q_C$  are the shear forces of rock beam, kN;  $l_1$  is the supporting load length, m;  $l_0$  is the rock block length, m;  $h_0$  is the depth of stratum, m; and  $\theta$  is the middle key block angle.

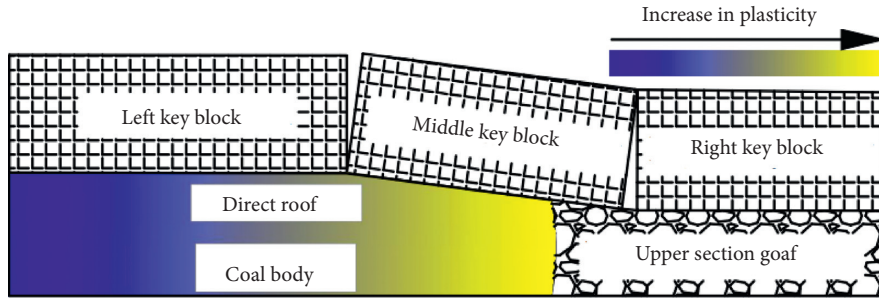


FIGURE 1: Schematic diagram of key block fracture structure model.

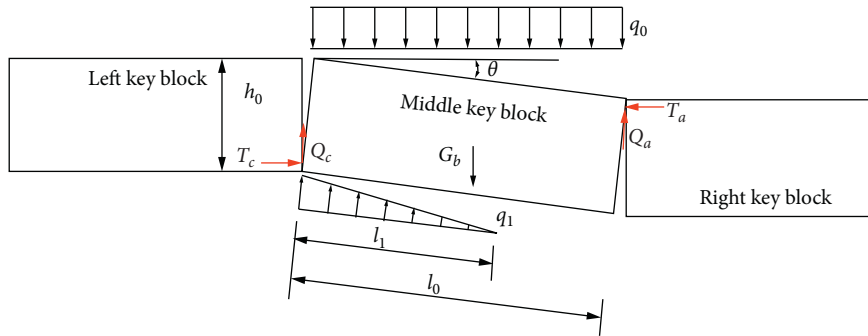


FIGURE 2: Stress analysis of the middle key block.

### 3. Mechanical Cause Analysis of Space Structure Broken by Key Blocks

Based on the analysis of key stratum theory, a large amount of coal mining results in a large area of goaf, which is accompanied by “three zones” of roof. Because the soft cushion held by the key layers of each layer will weaken the mechanical transmission capacity of the overlying strata in the vertical direction, the multiple groups of “masonry beam” structure formed in the vertical direction of the fracture zone will also play a certain supporting role on the underlying rock layer, which makes it difficult for the mechanical response mechanism of the lowest basic roof to show an obvious upward trend with the increase of the working face buried depth. Therefore, the movement structure of the lowest sub-key layer of the key block is not affected by the migration of overlying strata, but only determined by its own mechanical characteristics and rock properties, and its movement characteristics will play a key role in restricting the direct roof below and the pressure bearing state of the coal body.

The condition of the key block rotating instability is that the extrusion force at the hinge point is greater than the anti extrusion strength; that is, the hinge joint strength of the key block cannot support the transmission force of adjacent rock beams [17, 18]; the expression is

$$T > a \cdot \eta \cdot \sigma_c. \quad (1)$$

In (1),  $a$  is contact area of hinge point,  $m^2$ ;  $\eta$  is extrusion strength coefficient of contact surface; and  $\sigma_c$  is extrusion strength of contact surface, MPa.

$$h + h_1 \leq \frac{0.15\sigma_c}{\rho g} \left( i^2 - \frac{2}{3}i \cdot \sin \theta + \sin^2 \theta \right). \quad (2)$$

In (2),  $h$  is thickness of coal seam,  $m$ ;  $h_1$  is thickness of immediate roof,  $m$ ;  $\sigma_c$  is extrusion strength, MPa;  $i$  is rock mass fragmentation;  $\theta$  is dip angle;  $\rho$  is rock mass density,  $kg/m^3$ ; and  $g$  is acceleration of gravity,  $N/kg$ .

When the right key block in the upper section gradually sinks, it will drive the middle key block to rotate towards the goaf and fracture. Before the two key blocks reach the initial balance, the rotation angle of the middle key block increases gradually, and the fracture boundary on both sides is rotated to form hinge joint.

For the hard roof rock mass of shallow deep mine, when the antiextrusion strength of the hinge point is greater than the horizontal extrusion pressure, a stable key block structure of “masonry beam” is formed. Even if the roadway along the goaf is excavated in the lower coal body, the hinge point can still maintain a relatively stable self-balance state without breaking. However, in the deep soft rock roadway, the hinge point is often in the postfailure stage. The main reasons for the fracture of the hinge point are as follows: On the one hand, the coal seam group composed of multilayer coal body is distributed from the top to the bottom of the deep mine. The basic roof of this coal seam is located in the influence area of the floor damage when the upper coal mining disturbance occurs, the integrity of the upper part of the basic roof and even the whole rock beam is damaged, and the bearing capacity and stability are greatly reduced [13]. On the other hand, the roof rock layer in the “three soft” coal seam in deep mine is relatively soft, and the compressive strength of rock mass is greatly reduced, which makes the

judgment conditions of rotary deformation and instability of surrounding rock reduced. It is difficult for the “masonry beam” to form a stable hinge point, and the rock movement continuously causes subsidence and is gradually compacted on the supporting body below. The supporting load provided by the support body increases gradually, which causes the key block to evolve from the rotary instability to the limit equilibrium state, until the overburden structure is balanced again.

In the limit equilibrium state of the deep soft rock roof, the mechanical properties and integrity of the rock at the hinge joints on both sides are poor, so it is difficult to provide enough shear force and extrusion force. Therefore, the coal body and direct roof under the middle key block are the main supporting loads to maintain the structural stability. When the roadway is excavated under the basic roof, the redistribution of coal stress will seriously affect the supporting force of overlying strata, break the limit equilibrium state, and lead to S-R instability of the key broken block. The load generated by the “given deformation” state will directly act on the surrounding rock of the roadway until a new equilibrium is reached.

#### 4. Analysis of Breaking and Instability Characteristics of Key Roof Blocks in Gob-Side Roadway Based on Numerical Simulation

*4.1. Establishment of Numerical Model.* After the excavation of underground coal and rock mass, the roof of gob-side roadway is damaged, which leads to the deformation and fracture of the upper key block. The spatial position relationship between gob-side roadway and key block can be divided into three types: the roadway is located under the fracture line of the key block, the roadway is located inside the fracture line of the key block, and the roadway is located outside the fracture line of the key block [11]. The stress-strain characteristics of surrounding rock caused by three kinds of roadway layout are analyzed using FLAC<sup>3D</sup> numerical simulation software, and the spatiotemporal evolution process of key block failure is explored.

The model size is divided into 150 m × 30 m × 50 m, and the three-dimensional numerical analysis model as shown in Figure 3 is established. The displacement constraint boundary is set on the left and right sides of the model, the bottom of the model is fixed as the full constraint boundary, the corresponding displacement constraint boundary is set at the top of the model synchronously, and the vertical uniform load is applied above the model. The model is divided into five groups of strata from bottom to top, which represent basic floor, immediate floor, coal body, immediate roof, and basic roof. The basic roof is divided into three groups every 50 m along the  $x$ -axis direction, including the left key block, the middle key block, and the right key block. The Mohr-Coulomb constitutive yield criterion is used to reveal the evolutionary process of dynamic failure of surrounding rock. The rock mechanical parameters selected by simulation are shown in Table 1.

This model mainly highlights the manifestation of the force exerted on the roadway surrounding rock by the breaking key block, so it simplifies the basic overlying strata model. An in situ stress load of 20 MPa was applied in the area with a height of 50 m. In the right side of the model, the null model is established to simulate the goaf, and large deformation is used to simulate the caving characteristics of roof strata. The interface between the left key block, the middle key block, and the right key block is established to simulate the crack and hinge joint of the “masonry beam” structure. After calculating the balance of the goaf model, the 4 m × 3 m gob-side roadway is excavated according to the space position of the roadway and the key block fracture line, as shown in roadway ①, roadway ②, and roadway ③ in Figure 3. Meanwhile, the 4 m narrow coal pillar is reserved for roadway protection.

*4.2. Stress Distribution Characteristics of Key Block Fracture.* The vertical stresses of overburden space structure before and after excavation of three kinds of gob-side roadways are analyzed, which are located under the fracture line of the key block, inside the fault line of the key block, and outside the fault line of the key block. The stress evolutionary nephogram is shown in Figures 4–6.

Before roadway excavation, the middle key block, the left key block, and the right key block jointly form the stepped sinking structure of “masonry beam.” The key blocks of model ① and model ② belong to oblique overlapping state, while the key blocks of model ③ are in horizontal compaction state. The influence range of supporting pressure on coal wall side is smaller and more stable than the former two models.

After the roadway excavation, the maximum vertical support pressure of coal pillar is about 35 MPa when it is directly below the fracture line of key block, The value is about 31 MPa when it is located inside the fracture line of the key block, and the minimum value is about 13 MPa when it is far away from the action range of the key block. With the different space position of roadway layout, the support pressure of coal pillar decreases obviously. It can be seen that the spatial position relationship between the middle key block and the gob-side roadway is the key factor affecting the surrounding rock stability of gob-side roadway. When the roadway is located at any position below the key block, it will show different stress characteristics. The deformation of surrounding rock is the macroscopic manifestation of the corresponding supporting pressure caused by different shapes of the middle key block.

The right part of the middle key block of model ① is compacted on the gangue pile in the goaf, and the plastic stress increases. The supporting load on the left end point is completely borne by the coal pillar. The large span and inclination angle produced by the oblique overlapping state of the middle key block lead to the obvious stress concentration phenomenon in the left bottom corner and right top corner of the coal pillar, for which it is easy to cause the single inclined plane shear failure of the coal pillar. In addition, the left hinge joint plays a role of mechanical

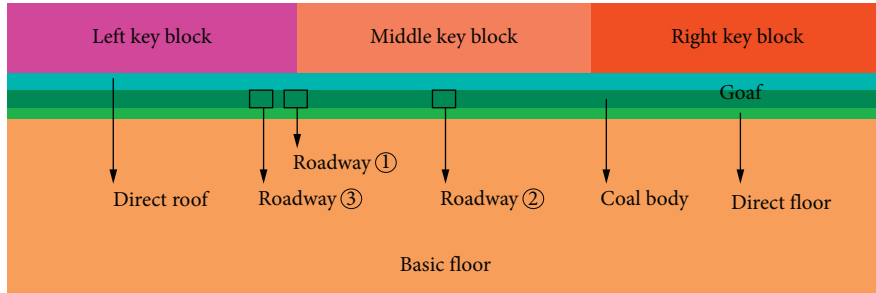


FIGURE 3: Numerical analysis model.

TABLE 1: Parameters of rock mechanics.

Classification	$B$ (GPa)	$S$ (GPa)	$C$ (MPa)	$f$ (°)	$T$ (MPa)
Right key block	5.65	5.25	8.0	30.5	7.6
Middle key block	5.65	5.25	8.0	30.5	7.6
Left key block	5.65	5.25	8.0	30.5	7.6
Immediate roof	0.65	0.62	6.0	25.6	5.4
Coal body	0.25	0.62	6.0	30.0	2.0
Immediate floor	0.53	0.41	6.0	25.6	5.3
Basic floor	4.80	4.60	5.0	20.0	6.0

transmission in the process of roadway excavation, which drives the left coal mass to produce a large range of stress increasing area and causes the roof subsidence and bottom heave. When the mining disturbance scope of the working face gradually expands, there is a hidden danger of S-R instability in the middle key block, which will lead to a large amount of direct roof caving and single inclined plane shear failure of coal pillar.

The left side of the middle key block of model ② is located on the solid coal, bearing the maximum supporting load, and the right side is mainly balanced by the extrusion friction of hinge joint, forming a relatively stable triangular support structure, which plays a certain supporting role for roadway excavation. As the supporting point of the upper rock beam, the coal pillar guides the support pressure to transfer to the deep coal body, resulting in a large range of stress increasing area at the coal wall side of the roadway. Because the coal pillar is located directly below the middle key block, the stress increase area in the middle of the coal pillar will be generated due to the splitting effect, which aggravates the risk of “left bottom corner middle right top corner” breakthrough failure of coal pillar. At the same time, because the whole roadway is enveloped by the middle key block and the stress increasing area under the two sides is connected at the floor, the superimposed pressure will have a strong impact on the floor. Therefore, for this kind of space structure roadway, attention should be paid to the floor pressure relief and support measures to alleviate the damage of superimposed pressure.

In model ③, when the goaf is formed, there is no supporting load under the hinge joint on the left side of the broken roof, so it is difficult to support the inclined overlapping stable structure depending on the shear force at the hinge point, so as to completely lose the stability and make it compacted on the gangue pile in the goaf to produce plastic

stress peak value. For the coal body, the force is only the reverse force produced by the left key block when resisting the sliding instability of the broken roof, and when the hinge joint is completely destroyed, the reverse force will disappear. Therefore, the surrounding rock stress of the roadway is the minimum, the displacement is also the minimum, and the surrounding rock state is the most stable. However, such key blocks will cause severe roof disturbance when roof cutting occurs, accompanied by obvious energy release and abnormal ground pressure. Therefore, special attention should be paid to the safety of personnel and equipment near the working face at that time.

*4.3. Deformation Instability Characteristics of Key Block Fracture.* Through dynamic observation and analysis of the surrounding rock displacement changes of the three roadway models after excavation, the displacement evolution nephogram is obtained, as shown in Figure 7. After the excavation of roadway, the plastic failure characteristics of coal pillar radial expansion and axial compression are obvious. The surrounding rock of roadway generally presents the deformation evolution characteristics of concave corner, convex side line, from square to X shape. Due to the oblique eccentric load action of the middle key block of model ① and model ② and the left horizontal thrust action of the middle key block of model ③, the surrounding rock of roadway presents the evolution trend of oblique deformation, and the deformation amount decreases gradually.

The displacement curve is drawn with the maximum unbalanced force operation sequence in FLAC<sup>3D</sup> simulation as abscissa and the displacement of two sides of roadway, roof, and floor as ordinate, as shown in Figure 8.

According to the analysis in Figure 8, the displacement curves of coal wall side of roadway ① and roadway ② are approximately equal, which is consistent with the phenomenon of coal wall side support pressure shown in Figures 4 and 5. The displacement of side and roof of coal pillar shows corresponding numerical changes due to different supporting pressure. The floor heave curve of roadway ② is slightly higher than that of roadway ①. Compared with the stress distribution nephogram in Figures 4 and 5, it can be seen that the floor pressure stress areas of roadway ① are, respectively, limited under the coal wall and coal pillar, and the floor pressure stress areas of two sides of roadway ② have a penetrating and overlapping effect, which causes the

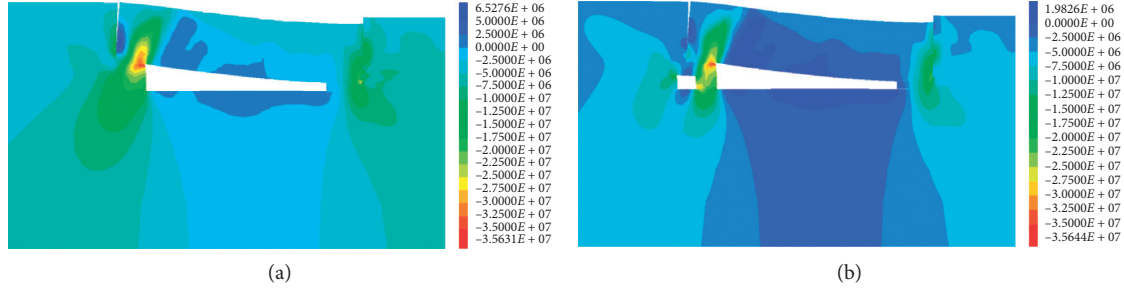


FIGURE 4: Vertical stress distribution map of overburden structure before and after excavation when roadway is under the fracture line of key block. (a) Before roadway excavation (unit: Pa). (b) After roadway excavation (unit: Pa).

floor heave to increase. Comprehensive analysis of the deformation displacement curve of surrounding rock at different positions of the roadway shows that the displacement of surrounding rock of roadway ③ is the smallest, and no obvious deformation occurs on the whole.

## 5. Mechanical Evolutionary Law of Roof Key Block Breaking in Gob-Side Roadway

**5.1. Mechanical Model Analysis of Key Block Structure before Roadway Excavation.** Based on the above-mentioned structural characteristics of “masonry beam,” the mechanical model of the key block in the roof of gob-side entry is constructed. Considering that the thickness of overlying strata in deep mine working face is relatively large, usually more than 800 m, the difference of overburden load caused by rotation subsidence of key block can be ignored, and the force exerted by overlying strata on the key block is approximately uniform load in vertical direction. With the rotation and subsidence of the key block in the middle position, the collapsed rock layer is gradually compacted on the direct roof and coal body below, resulting in the increasing of the supporting force of coal and rock mass, and the bearing structure gradually reaches the limit equilibrium state. The direct roof and coal body change from original rock state to goaf from elastic deformation to plastic yield until plastic failure. The supporting effect of surrounding rock on the key block is nonuniform load, which shows a linear decreasing trend approximately.

The stress model of the key block in Figure 2 is improved to the “masonry beam” optimization model as shown in Figure 9, and then the stress status of the key block is analyzed. In Figure 9, the shear force and compression force on both sides evolve into four hinge bearings, which are omitted because the self-weight is smaller than the load of overlying strata. This model is a one-time statically indeterminate model; the model is further refined and decomposed to form the radial force model of “masonry beam” shown in Figure 10 and the axial force model of “masonry beam” shown in Figure 11. Then, the improved radial force model of masonry beam and the axial force model of masonry beam are solved, respectively, and the radial force  $F_{AY}$ ,  $F_{CY}$  and axial force  $F_{AX}$ ,  $F_{CX}$  of rock beam model are obtained.

The radial force model of “masonry beam” in Figure 10 is analyzed, and the equilibrium condition is obtained.

$$\left\{ \begin{array}{l} \sum F_X = 0 \Rightarrow F_{CX} + \int_0^{l_0} q_0 \sin \theta dx = F_{AX} \\ \Rightarrow F_{CX} + q_0 l_0 \sin \theta = F_{AX}, \\ \sum F_Y = 0 \Rightarrow F_{CY} + F_{AY} + \frac{1}{2} q_1 l_1 = q_0 l_0 \cos \theta \\ \Rightarrow F_{CY} + F_{AY} = q_0 l_0 \cos \theta - \frac{1}{2} q_1 l_1, \\ \sum M_O = 0 \Rightarrow q_0 l_0 \cos \theta \cdot \frac{1}{2} l_0 \cos \theta \\ = F_{AY} l_0 + \int_0^{l_1} \left( q_1 - \frac{q_1}{l_1} x \right) x dx = F_{AY} l_0 + \frac{1}{6} q_1 l_1^2. \end{array} \right. \quad (3)$$

After solving, the results are as follows:

$$\left\{ \begin{array}{l} F_{AY} = \frac{1}{2} \cos^2 \theta q_0 l_0 - \frac{1}{6} q_1 \frac{l_1^2}{l_0}, \\ F_{CY} = q_0 l_0 \cos \theta \left( 1 - \frac{1}{2} \cos \theta \right) - \frac{1}{2} q_1 l_1 \left( 1 - \frac{1}{3} \frac{l_1}{l_0} \right). \end{array} \right. \quad (4)$$

In (3) and (4),  $F_X$  is the force characteristic in  $X$  direction, kN;  $F_Y$  is the force characteristic in  $Y$  direction, kN;  $M_O$  is the moment at the hinge point  $O$  between the middle key block and the left key block, kN·m;  $F_{CX}$  is the axial force of the left key block along the middle key block, kN;  $l_0$  is the rock block length, m;  $q_0$  is the overburden load, kN/m;  $F_{AX}$  is the axial force of the right key block along the middle key block, kN;  $\theta$  is the inclination angle of beam;  $F_{CY}$  is the radial force at the hinge joint between the middle key block and the left key block, kN;  $F_{AY}$  is the radial force at the hinge joint between the middle key block and the right key block, kN;  $q_1$  is the supporting load provided by the direct roof and coal body below, kN/m; and  $l_1$  is the length of direct roof and coal body below, m.

The axial force model of “masonry beam” structure in Figure 11 is analyzed, and the equilibrium condition is obtained.

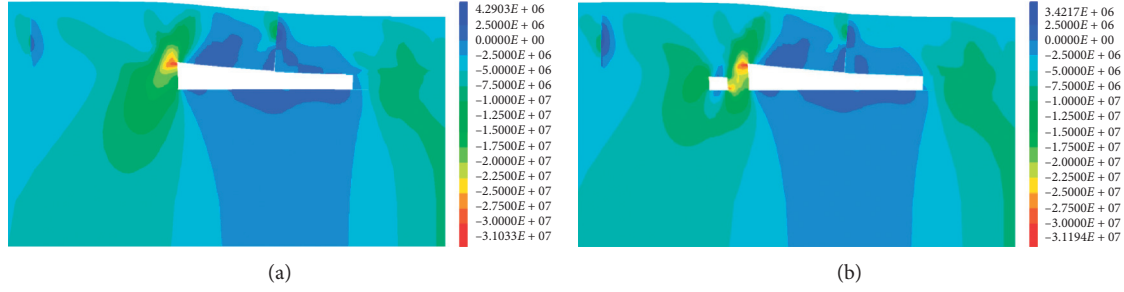


FIGURE 5: Vertical stress distribution map of overburden structure before and after excavation when roadway is located in the fracture line of key block. (a) Before roadway excavation (unit: Pa). (b) After roadway excavation (unit: Pa).

$$\begin{cases} F_{CX} + q_0 \sin \theta x + F_N(x) = 0, \\ \varepsilon(x) = \frac{\sigma}{E} = \frac{F_N(x)}{EA} = \frac{F_{CX}}{EA} - \frac{q_0 \sin \theta x}{EA}, \\ \Delta L(x) = \int_0^x \varepsilon(x) dx = \frac{F_{CX}}{EA} x - \frac{q_0 \sin \theta}{EA} \frac{x^2}{2}. \end{cases} \quad (5)$$

When  $x$  is equal to the total length of  $l_0$ , we get

$$\Delta L(l_0) = \frac{F_{CX} l_0}{EA} - \frac{q_0 \sin \theta}{EA} \frac{l_0^2}{2} = 0. \quad (6)$$

After further solution,

$$\begin{cases} F_{CX} = -\frac{1}{2} q_0 l_0 \sin \theta, \\ F_{AX} = -\frac{1}{2} q_0 l_0 \sin \theta + q_0 l_0 \sin \theta = \frac{1}{2} q_0 l_0 \sin \theta. \end{cases} \quad (7)$$

In (5)–(7),  $x$  is the axial length variable of the beam,  $m$ ;  $F_N(x)$  is the axial force function about  $x$ ;  $\varepsilon(x) = (\sigma/E)$  is a function of Hooke's law about  $x$ ;  $E$  is the elastic modulus, Pa;  $A$  is the cross-sectional area of the bar,  $m^2$ ; and  $\Delta L(x)$  is the elongation function about  $x$ .

The definition of radial force  $F_{AY}$ ,  $F_{CY}$  and axial force  $F_{AX}$ ,  $F_{CX}$  in the material mechanics model is the hinge support reaction force to maintain the stability of the structure. In practical engineering problems, they are the mechanical framework of the coupling of extrusion force  $T$  and shear force  $Q$ , as shown in

$$\begin{cases} F_{AY} = Q_A + T_A \sin \theta, \\ F_{CY} = Q_C + T_C \sin \theta, \end{cases} \quad (8)$$

$$\begin{cases} F_{AX} = T_A \cos \theta, \\ F_{CX} = T_C \cos \theta. \end{cases} \quad (9)$$

The shear force  $Q$  is nominally generated by the friction resistance of axial force  $F_X$  at the hinge point, but it is not equal in the field measurement value, which means that the shear force  $Q$  is affected by many factors such as the strength of the contact surface at the hinge point, rock properties, and hydrogeological conditions.

According to the mathematical analysis, when the middle key block reaches the limit equilibrium state, the mechanical properties of the rock at the hinge point are poor, and the friction mechanical connection between the shear stress and the extrusion force is weak, which can be regarded as separate force. In the same underground engineering environment, when the limit equilibrium state is destroyed due to mining disturbance, according to (4) and (8), the shear force  $Q_A$ ,  $Q_C$  at the hinge point of the middle key block is mainly affected by the support load  $q_1$  and the inclination angle  $\theta$ . According to (7) and (9), extrusion forces  $T_C$  and  $T_A$  are only affected by inclination angle  $\theta$ . In practical engineering, the cause of structural instability is usually the excavation of gob-side roadway, which directly leads to the decrease of support load  $q_1$  and the redistribution of stress state of the middle key block. With the gradual decrease of support load  $q_1$ , the shear force  $Q_A$  and  $Q_C$  will increase, and the increase range of  $Q_C$  is greater than that of  $Q_A$ . However, due to the weak nature of rock, the shear force provided by it is far less than the shrinkage of support load  $q_1$  amplitude reduction. Therefore, the middle key block rotates to the horizontal direction, the inclination angle  $\theta$  decreases, the extrusion pressures  $T_C$  and  $T_A$  produce synchronous attenuation, and the key block breaking shows a sinking trend, for which it is easy to cause instability.

**5.2. Evolution Law of Key Block Breaking and Instability after Roadway Excavation.** Tunnel excavation leads to stress unloading of surrounding rock, resulting in secondary distribution of initial equilibrium stress field. With shear dilatancy failure of internal weak structural plane, surrounding rock quickly presents yield state and gradually loses bearing capacity [19], which leads to secondary subsidence of broken key block. The migration and subsidence trend of key broken block after three groups of model roadway excavation is shown in Figure 12.

According to the previous calculation formula of mine stress and strata control theory [20], the width of limit equilibrium zone of roadway side is

$$x_0 = \frac{mA}{2tg\varphi_0} \ln \left( \frac{k\gamma H + (C_0/tg\varphi_0)}{(C_0/tg\varphi_0) + (P_x/A)} \right). \quad (10)$$

In (10),  $m$  is the mining thickness of coal seam,  $m$ ;  $A$  is the side pressure coefficient;  $tg\varphi$  is the friction coefficient;  $k$  is

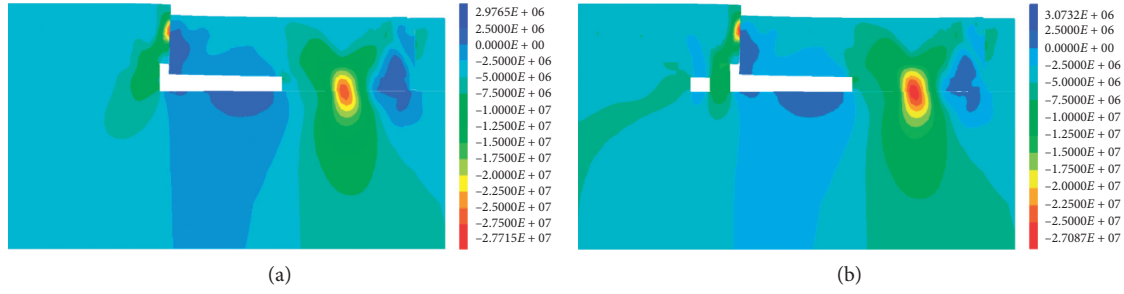


FIGURE 6: Vertical stress distribution map of overburden structure before and after excavation when roadway is located outside the fracture line of key block. (a) Before roadway excavation (unit: Pa). (b) After roadway excavation (unit: Pa).

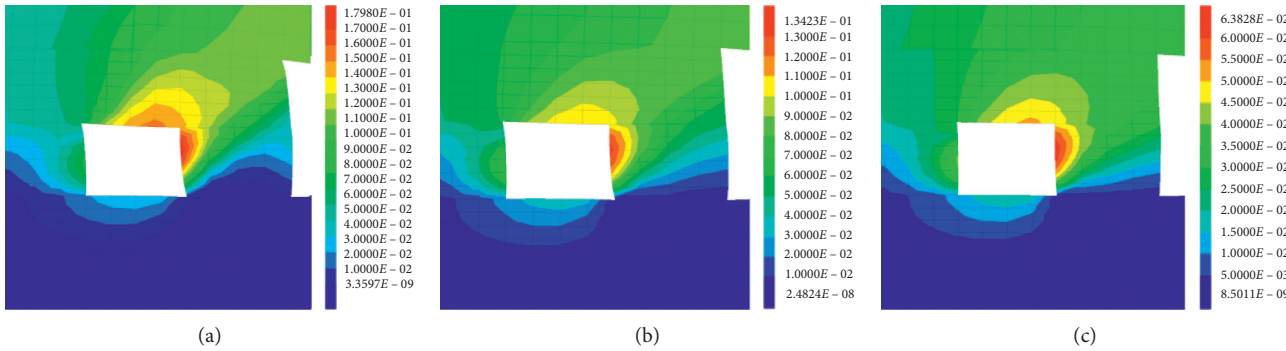


FIGURE 7: Cloud chart of surrounding rock displacement evolution after excavation of three roadway models. (a) Roadway ① (unit: m). (b) Roadway ② (unit: m). (c) Roadway ③ (unit: m).

the stress concentration factor;  $H$  is the buried depth of roadway,  $m$ ;  $\gamma$  is the average bulk density of rock stratum,  $\text{kN/m}^3$ ;  $C_0$  is the cohesion between coal seam and roof rock, MPa; and  $P_x$  is the support resistance, MPa.

After analysis, the width of the vertical projection plastic zone of the roadway relative to the horizontal plane of the roof is obtained as follows:

$$L = x_0 + l + 4. \quad (11)$$

In (11),  $L$  is the width of plastic zone,  $m$ ;  $x_0$  is the width of limit equilibrium zone,  $m$ ; and  $l$  is the width of roadway,  $m$ .

Therefore, in the area of  $L = x_0 + l + 4$  under the roof, due to the plastic failure of coal, the supporting force provided by the coal body to the roof decreases, and the stress state of the broken key block is redistributed. The main manifestation is that the mechanical behavior at the hinge joint changes, and, with the S-R instability, the surrounding rock of the roadway produces a lot of deformation.

Before the roadway is excavated, the broken key block is in the limit equilibrium state. It is assumed that the load acting on the key block is decreasing nonuniform load. When the gob-side roadway is excavated under the broken key block, the bearing capacity of the direct roof and coal body will be directly reduced, and the supporting load will be attenuated, which will lead to the secondary subsidence of the broken key block. According to the different subsidence of three groups of model breaking key blocks shown in Figure 12, it is concluded that when the roadway is under the fracture line of key broken block, the

attenuation effect on supporting load is the largest. When the roadway is located in the fracture line of the key block, the attenuation effect on the supporting load is moderate. When the roadway is located outside the fracture line of the key block, the attenuation of the supporting load on the broken roof is almost zero. That is,  $\Delta q_1(\text{model ①}) > \Delta q_1(\text{model ②}) > \Delta q_1(\text{model ③})$ .

According to the first kind of situation, when the roadway is located near the fracture line of the left key block and the middle key block, the pressure relief state generated in the  $L$  area will directly act on the hinge joint position. The supporting load  $q_1$  of the left hinge point of the middle key block decreases sharply,  $Q_C$  gradually increases and drives the increase of  $Q_A$  slowly, the extrusion pressure  $T$  decreases, the hinge point loses stability, and the right hinge point of the middle key block suffers from the left stress state. The effect of state change is small, and it is still stable. Therefore, the rotation instability of the middle key block takes the hinge point in the direction of the right goaf as the axis, the load generated by the left rotary subsidence directly acts on the  $L$  area, which makes the surrounding rock of the roadway produce a large amount of displacement, and the narrow coal pillar and coal body cannot bear the sinking load of the basic roof. Therefore, the side support structure of the coal pillar is required to provide enough support resistance within the effective time to make the middle key block reach the level balance state again.

In the second case, the roadway is all located under the middle key block, and the existence of  $L$  area attenuates

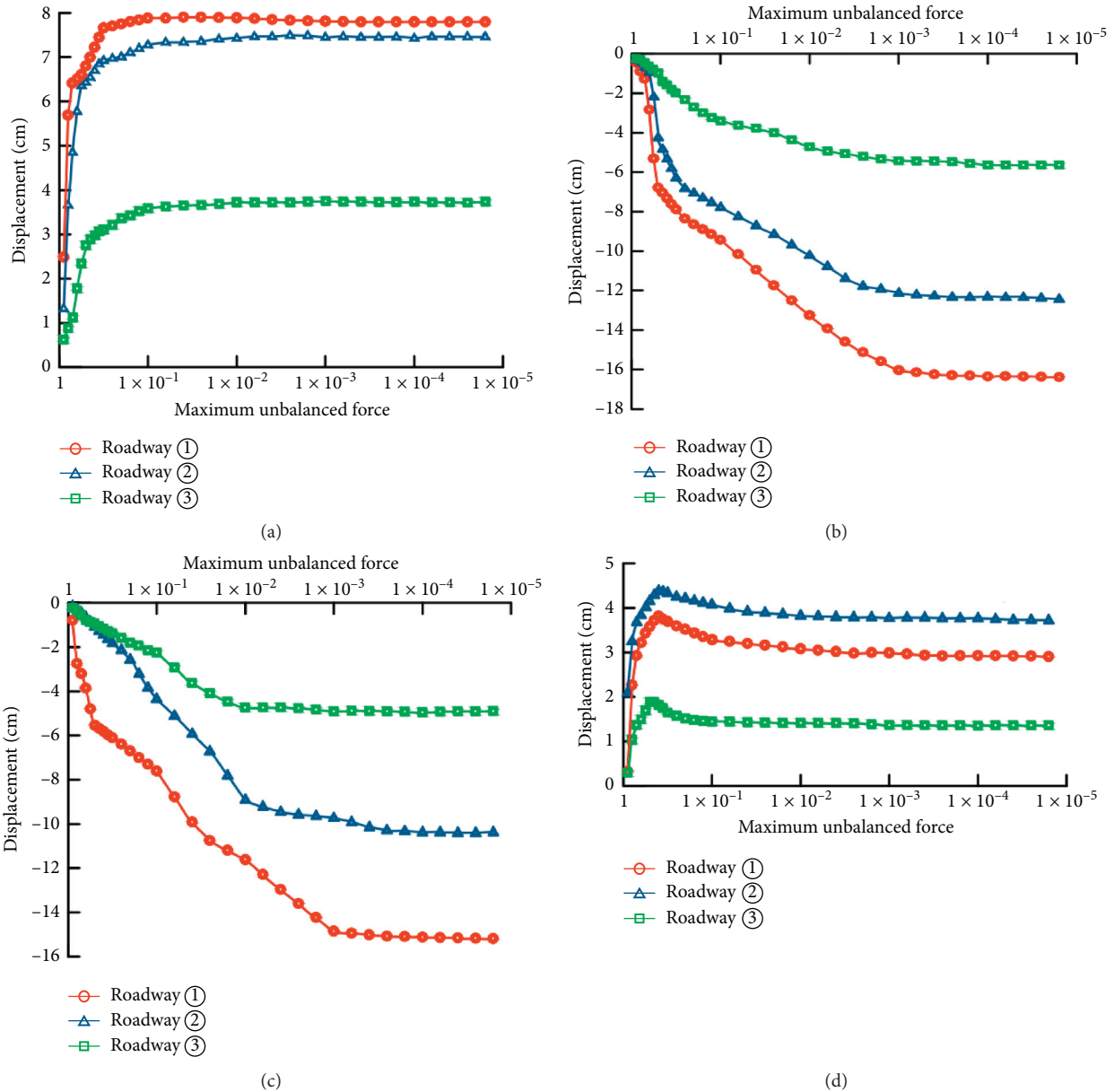


FIGURE 8: Displacement curve of measuring points at different positions of roadway. (a) Displacement curve of coal wall side measuring point in roadway. (b) Displacement curve of coal pillar side measuring point in roadway. (c) Displacement curve of roadway roof measuring point. (d) Displacement curve of roadway floor measuring point.

the supporting force. The attenuation center is approximately taken as the center line of the vertical direction of the middle key block. The support load  $q_1$  decreases, and  $Q_C$  and  $Q_A$  increase correspondingly. The middle key block sinks, and the support pressure is applied to the left coal body. Therefore, the angle  $\theta$  of the middle key block decreases, the extrusion pressure  $T$  decreases, it is difficult for the two hinge joints to maintain the original equilibrium state, and the key block in the middle is sliding and unstable. Due to the pressure produced by its sliding and the subsidence acting on the coal below, the surrounding rock of the roadway will lose its stability and deformation along with a large range of plastic zone. Therefore, in the process of roadway excavation and

support, it is necessary to pay attention to the overall supporting measures of surrounding rock to provide a wide range of supporting force to maintain the structural balance.

In the third kind of situation, the roadway is located outside the fault line of the left key block and the middle key block. For the deep soft rock roadway, the strength of the hinge point is low. When the goaf is formed, it will be destroyed due to the large in situ stress, so that the key block in the middle is completely crushed on the gangue pile, and it is difficult to form a triangular support structure. In this space state, the support pressure of coal body is the minimum. The function of  $L$  area is mainly in the active range of the left key block; when the support load  $q_1$  decreases, it is



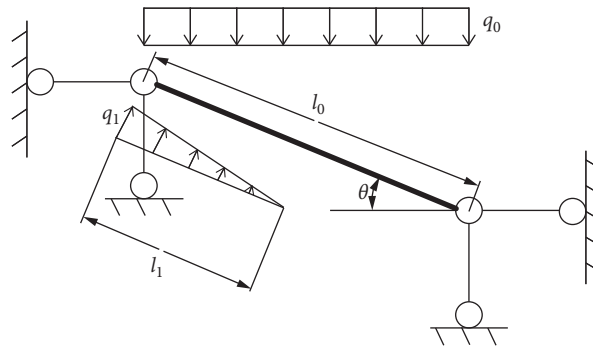


FIGURE 9: Optimization model of "masonry beam."

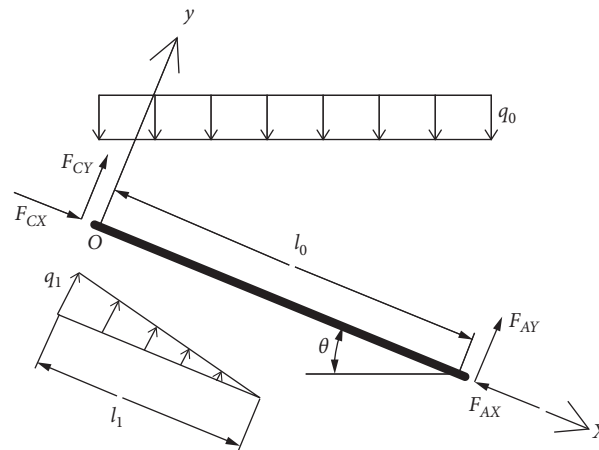


FIGURE 10: Radial force model of "masonry beam."

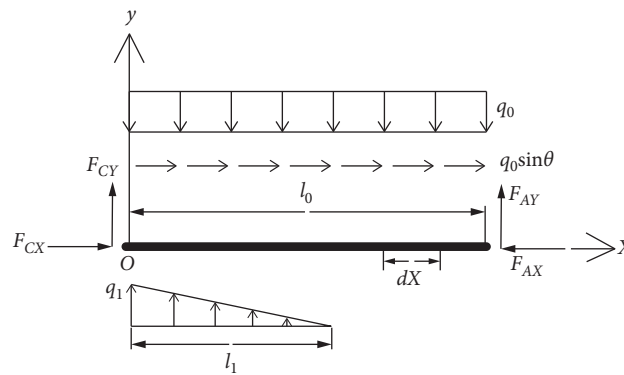


FIGURE 11: Axial force model of "masonry beam."

only affected by the bearing pressure of left key block, which is not enough to cause S-R instability deformation of the left key block, so the roadway is the most stable in this spatial position.

For the first and second types of structural mechanics models, the state load of "given deformation" caused by breaking key block will directly act on the surrounding rock of roadway, and its size is related to the angle of  $\theta$ . With the decrease of  $\theta$  angle, S-R instability will occur in the middle key block, and the load on coal body will increase gradually. When  $\theta = 0$ , the middle key block will

lose the role of friction shear force, the self-gravity and all the load of overlying strata will be borne by the coal below, it will be difficult for the surrounding rock of roadway to maintain stable state, and the support is difficult. Therefore, it is necessary to support the surrounding rock of roadway as soon as possible after the roadway excavation and before the decrease of  $\theta$ , so as to enhance the stability of surrounding coal, reduce the attenuation amplitude of support load, and restore the balance of large structure within the controllable range of surrounding rock displacement.



FIGURE 12: Subsidence trend chart of key block broken after roadway excavation based on three groups of models (from top to bottom, model ①, model ②, model ③).

For the third kind of structural mechanics model, the supporting force at the hinge point of the middle key block is mainly provided by the side coal pillar of the goaf, the load of the left key block is mainly borne by the coal mass that has not been mined, the influence of  $l$  area on the left key block and the right key block is small, the surrounding rock pressure and displacement of roadway are the minimum, and the structure is most stable.

## 6. Conclusions

- (1) The stability of the key block of “masonry beam” is directly related to the compressive strength of rock mass at the hinge point. The roof of deep soft rock roadway is easily affected by the mining disturbance of the upper coal body and the low strength of rock mass itself, resulting in the lower  $\sigma_c$  of basic roof. If the compressive strength at the hinge point is unable to withstand the extrusion force generated by the rotation of key block, the shear force provided by the hinge point is very weak, and the surrounding rock will gradually sink until the supporting load is enough to maintain the balance of “masonry beam” structure.
- (2) The spatial relationship between the roadway and key block can be divided into three types: the roadway is located below the fracture line of key block, the roadway is located inside the fracture line of key block, and the roadway is located outside the fracture line of key block. When the roadway is located below the fracture line of key block, the support pressure at the side of coal pillar is the largest. When the roadway is located inside the fracture line of key block, the support pressure of the coal pillar side is slightly lower than that of the former, but both of them have the risk of single inclined plane shear failure. Moreover, the support pressure range of coal wall side of such roadway is the largest, and the stress superposition area appears in the floor, which leads to a large-scale bottom drum. When the roadway is located outside the fracture line of broken roof, the stress of surrounding rock is the minimum.
- (3) The shear forces  $Q_A$  and  $Q_C$  at the hinge point of the middle key block are mainly affected by the support load  $q_1$  and the inclination angle  $\theta$ , while the extrusion forces  $T_C$  and  $T_A$  are only affected by the inclination angle  $\theta$ . With the decrease of support load  $q_1$ , the shear stresses  $Q_A$  and  $Q_C$  increase, and the increase range of  $Q_C$  is greater than that of  $Q_A$ . However, due to the weak mechanical properties and low strength of the rock, the shear force provided by the rock is far less than the reduction range of the support load  $q_1$ , which makes the broken roof rotate to the horizontal direction, the inclination angle  $\theta$  decreases, the extrusion pressures  $T_C$  and  $T_A$  produce synchronous attenuation, and the broken roof shows a sinking trend as a whole, for which it is easy to slide and lose stability.
- (4) The mechanical evolutionary law of S-R instability of the key block is obtained by analyzing the stress state and deformation characteristics of the key block under three kinds of spatial positions. When the roadway is located below the fracture line of key block, the coal wall and coal pillar cannot provide enough support for the hinge joint, which makes the surrounding rock rotate unstably with the hinge point of the goaf side as the axis. When the roadway is located in the fracture line of key block, the surrounding rock bears the maximum support pressure, and it is easy for the hinge joint on both sides to slide and lose stability when the extrusion pressure decreases. According to these two kinds of roadway layout, the stress superposition caused by concentrated load should be avoided reasonably in effective time, and the surrounding rock of roadway should be reinforced and supported. When the roadway is located outside the fracture line of key block, the middle key block is in the state of complete collapse, the mechanical transmission mechanism of surrounding rock in the vertical direction is weakened, and the surrounding rock is the most stable.

## Data Availability

The data used to support the findings of this study are included within the article.

## Conflicts of Interest

The authors declare that they have no conflicts of interest regarding the publication of this paper.

## Acknowledgments

This study was financially supported by the National Natural Science Foundation of China (51904266); Key Laboratory of Safety and High-Efficiency Coal Mining, Ministry of Education (Anhui University of Science and Technology) (JYBSYS2018203); High-Level Talent Gathering Project in Hunan Province (2019RS1059); and Hunan Key Laboratory of Geomechanics and Engineering Safety (16GES10).

## References

- [1] S. M. Wang, Q. Sun, J. W. Qiao et al., "Geological guarantee of coal green mining," *Journal of China Coal Society*, vol. 45, no. 01, pp. 8–15, 2020.
- [2] L. Yuan, "Scientific problem and countermeasure for precision mining of coal and associated resources," *Journal of China Coal Society*, vol. 44, no. 01, pp. 1–9, 2019.
- [3] M. C. He, H. P. Xie, S. P. Peng et al., "Study on rock mechanics in deep mining engineering," *Chinese Journal of Rock Mechanics and Engineering*, vol. 24, no. 16, pp. 2803–2813, 2005.
- [4] H. P. Xie, "Research framework and anticipated results of deep rock mechanics and mining theory," *Advanced Engineering Sciences*, vol. 29, no. 02, pp. 1–16, 2017.
- [5] H. P. Xie, "Research review of the state key research development program of China: deep rock mechanics and mining theory," *Journal of China Coal Society*, vol. 44, no. 05, pp. 1283–1305, 2019.
- [6] S. R. Xie, Q. Zhang, D. D. Chen et al., "Research and application of asymmetric anchorage deep beam bearing structure model in gob-side entry retaining roof," *Journal of Mining & Safety Engineering*, vol. 37, no. 02, pp. 298–310, 2020.
- [7] S. R. Xie, H. Pan, D. D. Chen et al., "Stability analysis of integral load-bearing structure of surrounding rock of gob-side entry retention with flexible concrete formwork," *Tunnelling and Underground Space Technology*, vol. 103, pp. 1–11, 2020.
- [8] X. Shi, H. Jing, J. Ning, Z. Zhao, and J. Zhu, "Stability control of gob-side entry retaining in fully mechanized caving face based on a compatible deformation model," *Computer Modeling in Engineering & Sciences*, vol. 124, no. 1, pp. 315–343, 2020.
- [9] G. R. Feng, Y. Q. Ren, P. F. Wang et al., "Stress distribution and deformation characteristics of roadside backfill body for gob-side entry of fully-mechanized caving in thick coal seam," *Journal of Mining & Safety Engineering*, vol. 36, no. 06, pp. 1109–1119, 2019.
- [10] J. G. Kan, J. K. Wu, N. Zhang et al., "Structure stability analysis and control technology of surrounding rock of the secondary gob-side entry retaining," *Journal of Mining & Safety Engineering*, vol. 35, no. 05, pp. 877–884, 2018.
- [11] H. S. Wang, S. G. Li, X. Z. Zhang et al., "Analysis on stability of narrow coal pillar influenced by main roof fracture structure of gob-side roadway," *Coal Science and Technology*, vol. 42, no. 02, pp. 19–22, 2014.
- [12] Y. Y. Liu, X. M. Song, D. F. Zhu et al., "Dynamic structural mechanical behavior and response characteristics of large key blocks," *Rock and Soil Mechanics*, vol. 41, no. 03, pp. 1019–1028, 2020.
- [13] S. S. He, S. R. Xie, B. H. Song et al., "Breaking laws and stability analysis of damage main roof in close distance hy-pogynous seams," *Journal of China Coal Society*, vol. 41, no. 10, pp. 2596–2605, 2016.
- [14] D. F. Yang, L. F. Zhang, M. Chai et al., "Study of roof breaking law of fully mechanized top coal caving mining in ultra-thick coal seam based on fracture mechanics," *Rock and Soil Mechanics*, vol. 37, no. 07, pp. 2033–2039, 2016.
- [15] F. L. He, W. R. He, D. D. Chen et al., "First fracture structure characteristics of main roof plate considering elastic-plastic deformation of coal," *Journal of China Coal Society*, vol. 45, no. 08, pp. 2704–2717, 2020.
- [16] J. Zhang, X. H. Duan, and Y. Liu, *Research and Application of Surrounding Rock Characteristics and Support Technology of Complex High Stress Soft Rock Roadway*, Coal Industry Press, India, 2014, in Chinese.
- [17] M. G. Qian, X. X. Miao, and F. L. He, "Analysis of key block in the structure of voussoir beam in longwall mining," *Journal of China Coal Society*, vol. 19, no. 06, pp. 557–562, 1994.
- [18] M. G. Qian and P. W. Shi, *Mining Pressure and Strata Control*, China University of Mining and Technology Press, Xuzhou, China, 2003, in Chinese.
- [19] W. G. Qiao, W. J. Song, Q. B. Meng et al., *Failure Mechanism and Support Technology of Deep High Stress Soft Rock Roadway*, Wuhan University Press, Wuhan, China, 2017, in Chinese.
- [20] C. J. Hou and N. J. Ma, "Coal stress and limit equilibrium zone study on two sides of coal roadway," *Journal of China Coal Society*, vol. 04, pp. 21–29, 1989, in Chinese.

## Research Article

# Experimental Study on the Temperature Field of Cold Region Tunnel under Various Groundwater Seepage Velocities

Shiding Cao <sup>1</sup>, Taishan Lu <sup>2,3</sup>, Bo Zheng <sup>4</sup>, and Guozhu Zhang <sup>2,3</sup>

<sup>1</sup>Shenzhen Transportation Design & Research Institute Co., Ltd., Shenzhen 518000, China

<sup>2</sup>Institute of Geotechnical Engineering, Southeast University, Nanjing 210096, China

<sup>3</sup>Jiangsu Key Laboratory of Urban Underground Engineering & Environmental Safety, Southeast University, Nanjing 210096, China

<sup>4</sup>Southwest Research Institute Co., Ltd of C. R. E. C., Chengdu, Sichuan 611731, China

Correspondence should be addressed to Taishan Lu; 230189653@seu.edu.cn

Received 16 October 2020; Revised 14 November 2020; Accepted 2 December 2020; Published 11 December 2020

Academic Editor: Zhi Cheng Tang

Copyright © 2020 Shiding Cao et al. This is an open access article distributed under the Creative Commons Attribution License, which permits unrestricted use, distribution, and reproduction in any medium, provided the original work is properly cited.

Groundwater seepage significantly affects the temperature field of a cold region tunnel. Laboratory model tests are carried out to evaluate its effects, yielding four main results. First, groundwater seepage can increase tunnel air temperature and decrease the thickness and length of the tunnel insulation layer. Second, groundwater seepage and tunnel ventilation exert a coupling effect on the surrounding rock temperature. This effect is related to the surrounding rock depth. Third, the influence of the groundwater seepage velocity on the temperature of the interface between the lining and surrounding rock demonstrates a spatial difference, and the groundwater seepage leads to an uneven temperature distribution at the interface between the lining and surrounding rock. Furthermore, under groundwater seepage, the shape and size of the tunnel cross section have significant effects on the interface temperature. Fourth, the cold region tunnel has an antifreezing capability that is mainly related to the frost heaving of the surrounding rock and the groundwater seepage velocity. This capability should be fully utilized in the design of cold region tunnels. The experimental data presented can be used to verify the reliability of the theoretical calculation model for tunnel temperatures in cold regions.

## 1. Introduction

Half of the world's land area is covered by transient permafrost, seasonal frozen soil, or permafrost [1, 2]. Cold region tunnels have been increasingly built in recent years but freezing damage to such tunnels threatens their structural and operational safety [3–6]. Aiming to solve the problem of freezing damage to cold region tunnels, investigations on their temperature field have increased. For example, Lai et al. [7] used dimensionless parameters and perturbation methods to approximate the temperature distribution of the surrounding rock of cold region tunnels. Zhang et al. [8] proposed an analytical solution for heat conduction in tunnels, considering both composite medium and time-dependent boundary conditions. Lai et al. [9] derived the governing equations for the coupled problems of

seepage, temperature, and stress fields, with consideration of the ice-water phase change. Zhang et al. [10–12] derived an element calculation formula for the thermo-hydro coupling model to explore how different construction seasons, initial temperatures, and thermal insulation thicknesses affect the temperature field of cold region tunnels. Tan et al. [13–15] used the “three-zone” model to derive the governing equation for the temperature field of surrounding rock. The airflow inside the tunnel and the heat convection between the air and lining were simulated using the k-s turbulence model and the wall function. Li et al. [16] established a water-thermal coupling mathematical model for permafrost to determine the optimal thickness of the tunnel insulation layer. Yan et al. [17] performed a numerical investigation on the influences of different ventilation velocities on the design parameters of the thermal insulation layer.

The above theoretical studies demonstrate the complexity of tunnel heat transfer in cold regions. Model tests can also be used to study the temperature field of the cold region tunnel. Feng et al. [18] developed a cold region tunnel model consisting of a refrigeration system, a circulation system, and a temperature control system with a 1:25 geometric reduced scale to study the temperature field and frost heave force of cold region tunnels and the reliability of thermal insulation layers. Zhang et al. [19] investigated the effects of the heat released during construction and of boundary temperatures on the temperature field of surrounding rock in permafrost tunnels using a model experiment with a 1:26.83 geometric reduced scale. Speeding up construction and installing insulation layers effectively weakened the negative effects of thermal disturbance during construction and of boundary temperatures. Zeng et al. [20] explored the influences of inlet airflow temperatures and mechanical ventilation on the temperature distribution of surrounding rock via a model test with a 1:30 geometric reduced scale under ventilation conditions. They found that mechanical ventilation in the positive ventilation direction adversely affects the freezing damage to cold region tunnels. Liu et al. [21] built a tunnel model with a 1:37 geometric reduced scale to explore the distribution of the temperature field and the expansion law of frost front under different inlet airflow temperatures and wind speeds.

Groundwater seepage has significant effects on the temperature field of the surrounding rock in cold region tunnels [9, 13, 22–24]. The frozen depth of cold region tunnels is significantly affected by the seepage velocity [9]. However, the above model tests did not consider its effects on the temperature field of cold region tunnels. In this paper, heat transfer model tests of cold region tunnels experiencing groundwater seepage are carried out. The model test results are used to analyze the distribution characteristics of the temperature field and to reveal the gradual freezing process of cold region tunnels under groundwater seepage. The results are also used to analyze the causes of freezing damage to cold region tunnels and to thereby provide a basis for its prevention and control.

## 2. Model Test

*2.1. Investigating the Freezing Damage to a Prototype Tunnel.* The freezing damage (shown in Figure 1) to two highway tunnels, one in the Inner Mongolia Autonomous Region and the other in Hebei Province, is investigated.

The highway tunnel from the Inner Mongolia Autonomous Region is a separated tunnel that is 3,960 m long on the left and 3,915 m long on the right, and the width of each tunnel is 12 m. The average wind speed is 1.2 m/s, and the mean annual temperature is  $-2.6^{\circ}\text{C}$ . The yearly frost-free period lasts for approximately 95 days. The frost penetration depth is 3 m. The tunnel was opened to traffic in November 2012. In January 2013, the average temperature in was below  $-25^{\circ}\text{C}$ , and a large number of leakages and extensive road ice occurred in the tunnel.

The highway tunnel from Hebei Province is a separated tunnel that is 2,946 m long on the left and 2,992 m long on the right, and the width of each tunnel is 12 m. The average wind speed is 2.4 m/s, and the mean annual temperature is  $3.2^{\circ}\text{C}$ . The yearly frost-free period lasts for approximately 120 days. The frost penetration depths of the entrance and exit of the tunnel are 1.4 m and 2 m, respectively. In January 2016, the tunnel experienced extreme cold weather. The average temperature in January 2016 was close to  $-25^{\circ}\text{C}$ . Freezing damage, such as leakage and water freezing, occurred in the tunnel.

Based on the freezing damage to two highway tunnels in the Inner Mongolia Autonomous Region and Hebei Province, a model test is conducted to investigate the distribution of the tunnel temperature field and the mechanism of freezing damage under various groundwater seepage velocities.

### 2.2. Similarity Criteria for the Prototype and Model Tunnels.

The transient heat transfer in the concrete lining and surrounding rock of the tunnel prototype is governed by Fourier's law in the polar coordinates [25], as shown in the following equation:

$$\frac{\partial T_p}{\partial t_p} = \alpha_p \left( \frac{\partial^2 T_p}{\partial r_p^2} + \frac{1}{r_p} \frac{\partial T_p}{\partial r_p} \right), \quad r_p > \xi_p, \quad (1)$$

where subscript  $p$  indicates the tunnel prototype,  $T$  is the temperature,  $r$  is the distance from the center of the tunnel,  $t$  is the time,  $\alpha$  is the thermal diffusivity, and  $\xi$  is the inner radius of the tunnel lining.

The transient heat transfer in the concrete lining and surrounding rock of the tunnel model is governed by Fourier's law in the polar coordinates, as shown in the following equation:

$$\frac{\partial T_m}{\partial t_m} = \alpha_m \left( \frac{\partial^2 T_m}{\partial r_m^2} + \frac{1}{r_m} \frac{\partial T_m}{\partial r_m} \right), \quad r_m > \xi_m, \quad (2)$$

where subscript  $m$  indicates the tunnel model.

According to similarity theory [18, 21], the heat transfer similarity criteria can be defined as follows:

$$\pi_1 = \frac{\alpha t}{r^2}, \quad (3)$$

$$\pi_2 = \frac{Q}{TC},$$

where  $\pi_1$  and  $\pi_2$  are the heat transfer similarity criteria,  $Q$  is the latent heat of the phase change due to groundwater freezing, and  $C$  is determined as follows:

$$c = \frac{\alpha}{\lambda}. \quad (4)$$

Based on equation (3), the following similarity relationships of temperature and time can be obtained:

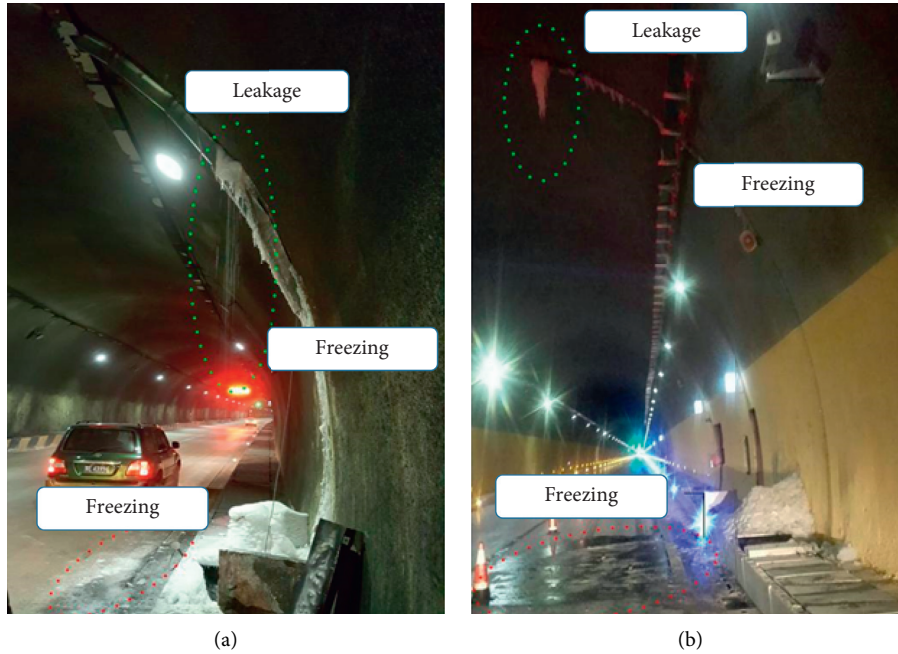


FIGURE 1: Freezing damage to tunnels in (a) the Inner Mongolia Autonomous Region and (b) Hebei Province.

$$\frac{T_p}{T_m} = \frac{Q_p}{Q_m} \frac{C_m}{C_p}, \quad (5)$$

$$\frac{t_p}{t_m} = \frac{\alpha_m}{\alpha_p} \frac{r_p^2}{r_m^2}.$$

The groundwater seepage in the rock surrounding the tunnel can be modeled as a homogeneous flow in a medium with an effective porosity [26]. The groundwater seepage velocities of the tunnel prototype and tunnel model can be obtained using Darcy's law, as shown in the following equation, respectively:

$$\nu_p = -K_p \frac{\partial u_p}{\partial r_p}, \quad (6)$$

$$\nu_m = -K_m \frac{\partial u_m}{\partial r_m},$$

where  $\nu$  is the groundwater seepage velocity,  $u$  is the water head, and  $K$  is the hydraulic conductivity.

The water head of the tunnel model is the same as that of the tunnel prototype. Based on equation (6), the following similarity relationship for groundwater seepage velocity can be obtained:

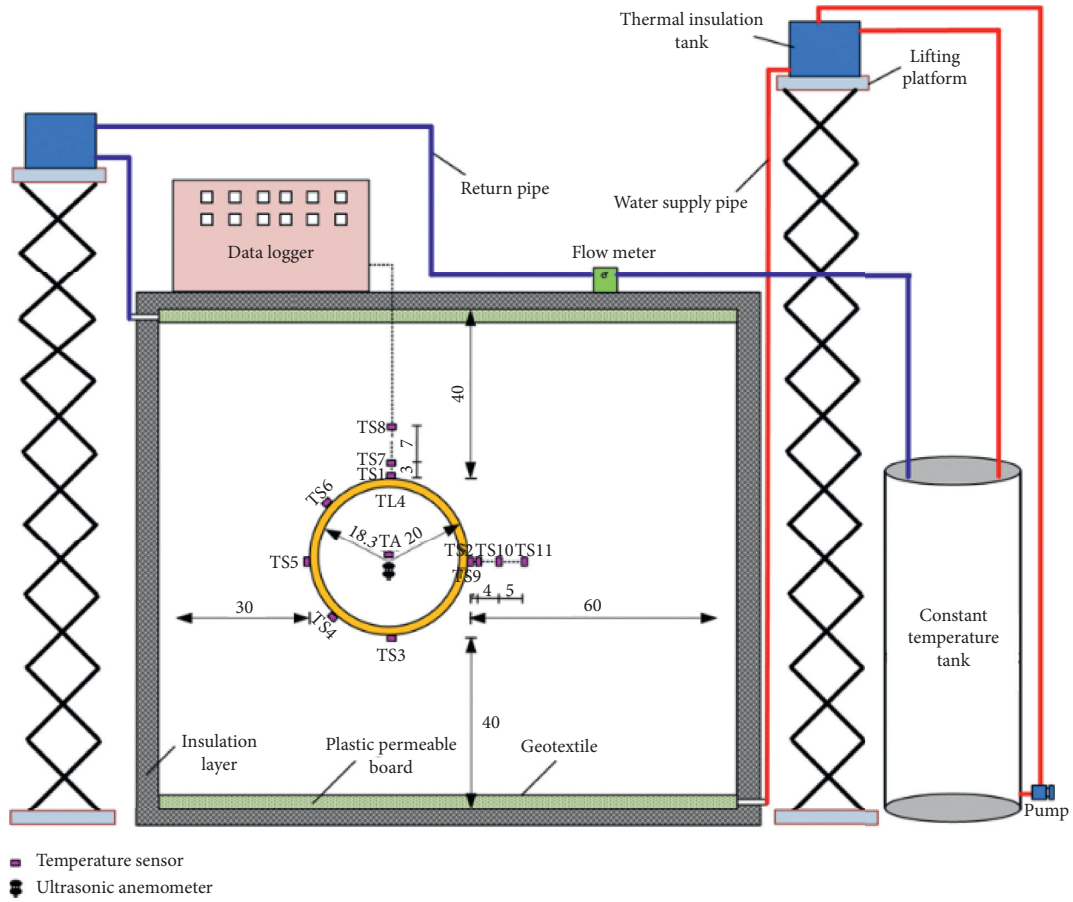
$$\frac{\nu_p}{\nu_m} = \frac{K_p}{K_m} \frac{r_m}{r_p}. \quad (7)$$

Considering the research results of previous tunnel heat transfer model tests [16, 18–21] and previous test conditions [22, 23], a geometric similarity ratio of 1 : 30 between the tunnel model and tunnel prototype is selected. According to equations (5) and (7), similarity ratios of 1:1, 1:900, and 30:1 for temperature, time, and velocity, respectively, are obtained.

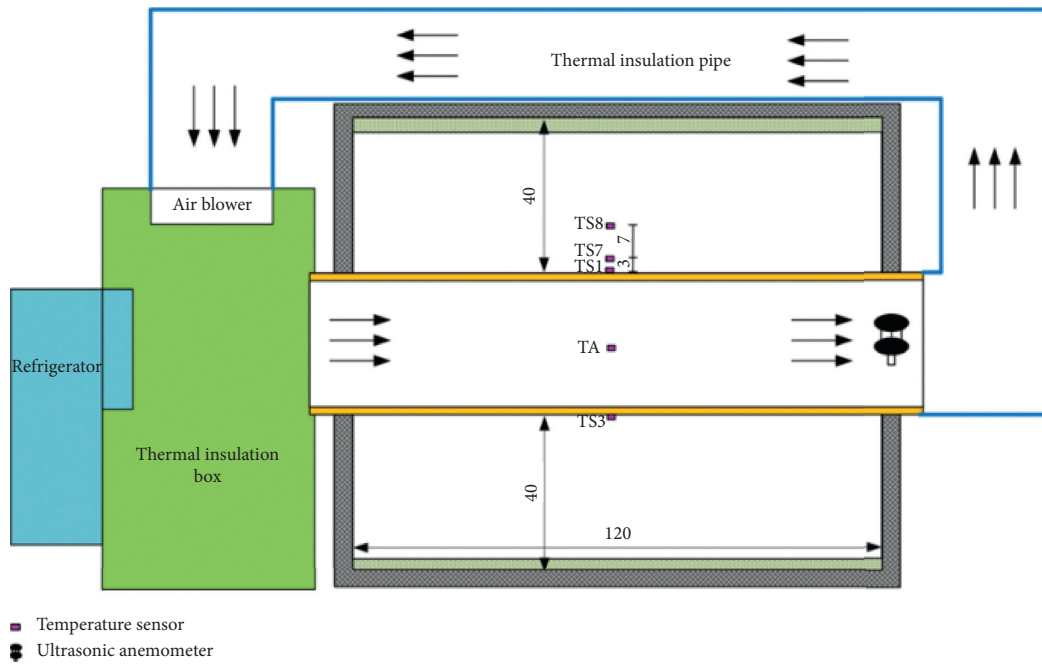
**2.3. Model Test Design.** Figure 2 describes the design of the cold region tunnel model test under the conditions of tunnel ventilation and groundwater seepage. In the model test, the fractured rock mass is considered to be a homogeneous medium with an effective porosity [26], the groundwater seepage in the tunnel surrounding rock is modeled as a homogeneous flow in a homogeneous medium with an effective porosity, and the sand soil is used to simulate the tunnel surrounding rock. Constant water head tests are used to simulate the groundwater seepage field of the tunnel surrounding rock, and water with a constant inlet temperature is used to simulate the underground temperature field. All of the tests have the same inlet temperature which is 13°C. To ensure a uniform groundwater seepage field, groundwater seepage occurs from bottom to top. The groundwater seepage velocity is controlled by adjusting the water head difference. Cold airflow is blown into the tunnel through the closed circulation ventilation ducts to freeze the groundwater in the tunnel surrounding rock, and the wind speed variation is controlled by changing the voltage applied to the air blower. The temperatures of the surrounding rock, tunnel lining, and air in the tunnel are measured by temperature sensors. The wind speed is measured by using an ultrasonic anemometer, and the groundwater seepage velocity is measured by using a liquid mass flow meter.

**2.4. Model Test Apparatus and Materials.** Figure 3 presents the apparatus of the laboratory model test, which consists of the tunnel model box, the tunnel ventilation system, the groundwater seepage system, and the measuring system.

Table 1 summarizes the model test equipment and devices.



(a)



(b)

FIGURE 2: Model test design: (a) cross section and (b) vertical section.

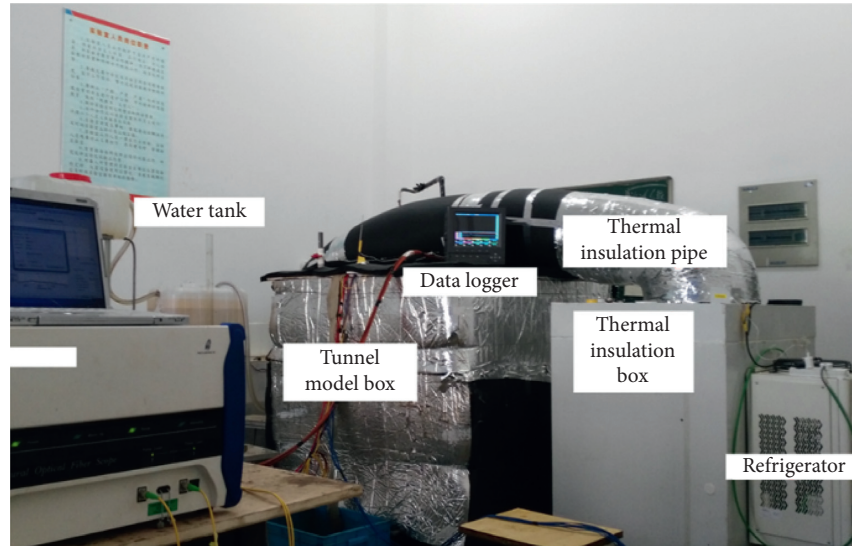


FIGURE 3: Model test setup.

TABLE 1: Model test equipment and devices.

Item	Specification
Constant temperature tank	Heating power is 6 kW, volume is 1,000 L
Pump	Water head is 9 m, flow velocity is 30 L/min
Thermal insulation tank	Volume is 18 L
Air blower	Maximum wind speed is 4 m/s
Temperature sensor	Resistance temperature detector (HSRTD-3-100-A) with an accuracy of $\pm 0.15^\circ\text{C}$
Flow meter	Liquid mass flow meter (DMF-1-1-A) with a precision of $\pm 0.2\%$ , measurement scope is 0–40 kg/h
Ultrasonic anemometer	Measurement scope is 0–40 m/s, accuracy is 0.01 m/s
Refrigerator	Refrigerating power is 2 kW, minimum temperature is $-30^\circ\text{C}$

**2.4.1. Tunnel Model.** The tunnel model consists of a  $1.4\text{ m} \times 1.2\text{ m} \times 1.2\text{ m}$  stainless steel box and a 1.8 m concrete tube with an outer diameter of 40 cm and a thickness of 2 cm. The concrete tube, which has a circular cross section, is made of cement, sand, gravel, and water in a ratio of 1:2.4:3.6:0.65. Sand is used in the test. The sand-raining method is used to fill the tunnel model with sand from the Yangtze River, the density and thermal conductivities of which are  $2.05\text{ g/cm}^3$  and  $1.58\text{ W/(m}\cdot^\circ\text{C)}$ , respectively. To minimize the heat transfer boundary effect, a 5-cm thick thermal insulation layer is installed around the outer surface of the stainless steel box. The plastic permeable boards are installed at the top and bottom of the stainless steel box to ensure that the groundwater seepage spreads over the surrounding rock. The permeable plastic boards are wrapped with geotextile to prevent the groundwater seepage from carrying away the sand.

**2.4.2. Tunnel Ventilation System.** The ventilation system consists of a refrigerator, an air blower, a thermal insulation box, and a thermal insulation pipe. The thermal insulation pipe connects the air blower, the thermal insulation box, and the concrete tube to form closed circulation ventilation ducts. The air blower is installed on the top of the thermal insulation box, and the refrigerator is installed in the thermal insulation box. The air inside the refrigerator can be cooled to  $-30^\circ\text{C}$ , and the airflow velocity in the ducts can reach 4 m/s.

**2.4.3. Groundwater Seepage System.** The groundwater seepage system consists of a constant temperature water tank, a pump, two thermal insulation water tanks, two lifting platforms, a water supply pipe, and a return pipe. The water supply pipe and return pipe connect the constant temperature water tank, the thermal insulation water tanks, the pump, and the stainless steel box to form a closed circulation system. Both thermal insulation water tanks are placed on the lifting platforms. The groundwater seepage velocity is controlled by adjusting the height difference between the two thermal insulation water tanks.

**2.4.4. Measuring System.** To monitor the temperature variations in the air, surrounding rock, and the interface between the tunnel lining and surrounding rock, a temperature monitoring cross section is installed in the middle of the model box. The platinum resistance temperature sensor TA is installed in the center of the concrete tube to monitor the temperature of the airflow. The platinum resistance temperature sensors TS7 to TS11 are installed in the sand to monitor the temperature variation of the surrounding rock temperature field at different positions and depths. The platinum resistance temperature sensors TS1 to TS6 are installed on the concrete tube surface, equally spaced along the cross section, to monitor the temperature variation of the interface between the tunnel lining and surrounding rock.



The wind speed is monitored using an ultrasonic anemometer that is placed at the tunnel exit. Finally, the liquid mass flow meter is connected to the water return pipe of the groundwater seepage system.

**2.5. Model Test Strategy.** Two factors are considered in the model test, namely, wind speed and groundwater seepage velocity. Zhang et al. [22] presented a systematic study of the heat transfer in tunnels under groundwater seepage. Groundwater seepage velocities of less than 0.864 m/d had negligible effects on the temperature field of the surrounding rock. Thus, groundwater seepage velocities of 0, 0.923 and 2.743 m/d are chosen for this model. The average wind speed of the tunnel in the Inner Mongolia Autonomous Region and in Hebei Province is 2.2 m/s and 2.4 m/s, respectively. Thus, wind speeds of 0.606, 1.002, and 2.398 m/s are chosen for this model. Table 2 presents the model test strategy. The experiment time of each test is different, as groundwater seepage can prevent the surrounding rock from freezing. Hence, the time that the temperature of surrounding rock down to 0°C varies with groundwater seepage velocities. The experiment times of 11.5, 23, and 32.5 h for groundwater seepage velocities of 0, 0.923, and 2.743 m/d, respectively, are chosen for this model. These experiment times can guarantee a part of the surrounding rock around the lining will freeze.

### 3. Results and Discussion

**3.1. Effect of Groundwater Seepage on the Tunnel Air Temperature.** Figure 4 presents the variations in tunnel air temperature over time under the effects of groundwater seepage and ventilation in the model test. Specifically, it shows that the air temperature in the tunnel decreases. Furthermore, the air temperature reduction rate decreases over time, and the temperature curve fluctuates every 12 h due to the deicing of the refrigeration equipment. Figure 4 also shows that groundwater seepage velocity and wind speed have significant influences on tunnel air temperature. Figure 5 presents the variations in tunnel air temperature for various groundwater seepage velocities at different wind speeds after cooling for 11.5 h. In Figure 5, the air temperature in the tunnel increases almost linearly as the groundwater seepage velocity increases. Furthermore, the effect of groundwater seepage velocity on air temperature in the tunnel is related to wind speed. The lowest air temperature in the tunnel is  $-22.55^{\circ}\text{C}$  under a groundwater seepage velocity of 0 m/s and a wind speed of 0.606 m/s. The highest air temperature in the tunnel is  $-14.58^{\circ}\text{C}$  under a groundwater seepage velocity of 2.743 m/d and a wind speed of 2.398 m/s. Thus, the higher the groundwater seepage velocity and wind speed are, the higher the air temperature is in the tunnel.

The above analysis shows that groundwater seepage has a significant effect on the air temperature in a tunnel. The higher the groundwater seepage velocity is, the higher the air temperature is in the tunnel. Low air temperature in a tunnel may induce tunnel freezing damage. The thickness and length of the tunnel insulation layer are determined by the

TABLE 2: Model test strategy.

Test no.	Groundwater seepage velocity (m/d)	Wind speed (m/s)
1		0.606
2	0	1.002
3		2.398
4		0.606
5	0.923	1.002
6		2.398
7		0.606
8	2.743	1.002
9		2.398

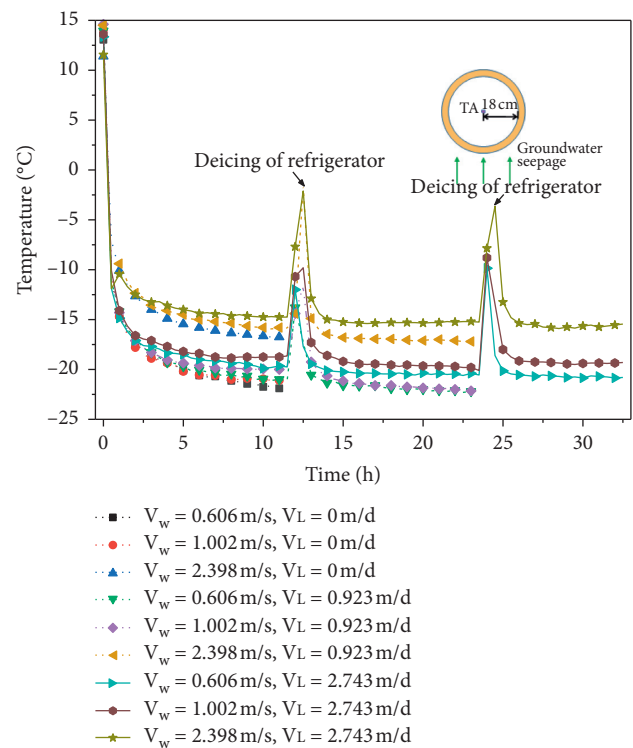


FIGURE 4: Variations in the tunnel air temperature over time.

air temperature in the tunnel. Specifically, the lower the air temperature is in the tunnel, the thicker and longer the tunnel insulation layer needs to be to avoid freezing damage. It can be speculated that groundwater seepage has a significant influence on the thickness and length of the tunnel insulation layer in cold regions, causing it to thin and short. Thus, the influence of groundwater seepage should be considered when designing the insulation layers of cold region tunnels.

**3.2. Effect of Groundwater Seepage on the Surrounding Rock Temperature.** Figure 6 presents the variations in the surrounding rock temperature over time under the influence of groundwater seepage and ventilation in the model test. Specifically, it shows that the surrounding rock temperature at TS9, TS10, and TS11 decreases. The cooling rates and amplitudes of the surrounding rock temperature differ significantly between TS9, TS10, and TS11. The cooling rate

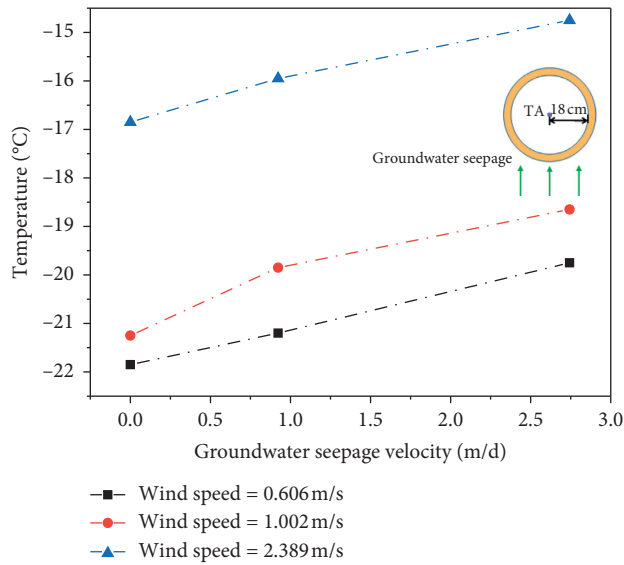


FIGURE 5: Variations in the tunnel air temperature after 11.5 h of cooling.

and amplitude of the surrounding rock temperature are related to the depth of the tunnel surrounding rock, the groundwater seepage velocity, and the wind speed. The cooling rate and amplitude of the surrounding rock temperature at the TS9 monitoring point are the largest and those at the TS11 monitoring point are the smallest. Thus, the deeper the tunnel surrounding rock is, the lower the cooling rate and amplitude of the tunnel surrounding rock temperature are. Lower groundwater seepage velocities and higher wind speeds lead to greater cooling rates and amplitudes of the surrounding rock temperature. The influence of groundwater seepage and tunnel ventilation on the surrounding rock temperature field is related to the depth of the surrounding rock. The increase in wind speed has a strong influence on the temperature field at TS9 and TS10 but a weak influence on that at TS11. Figure 6 also shows that the wind speed has the most significant influence on the surrounding rock temperature field when the groundwater seepage velocity is 0.923 m/d but has the least significant influence on the surrounding rock temperature field when the groundwater seepage velocity is 0 m/d. This can be explained by the coupling effect of groundwater seepage and tunnel ventilation.

Figure 7 presents the variations in the surrounding rock temperature drops under groundwater seepage velocities at different wind speeds after 11.5 h of cooling. It also shows that the temperature drops in the tunnel surrounding rock decrease as the groundwater seepage velocity increases. The temperature drops differ at TS9, TS10, and TS11 under different wind speeds. The temperature drop at TS11 at different wind speeds decreases linearly as the groundwater seepage velocity increases. At wind speeds of 0.606 m/s and 1.002 m/s, the temperature drops at TS9 and TS10 decrease linearly as the groundwater seepage velocity increases. At a wind speed of 2.398 m/s and groundwater seepage velocity under 0.923 m/d, the temperature drops at TS9 and TS10 slowly decrease as the groundwater

seepage velocity increases. At a wind speed of 2.398 m/s and groundwater seepage velocity over 0.923 m/d, the temperature drops at TS9 and TS10 sharply decrease as the groundwater seepage velocity increases.

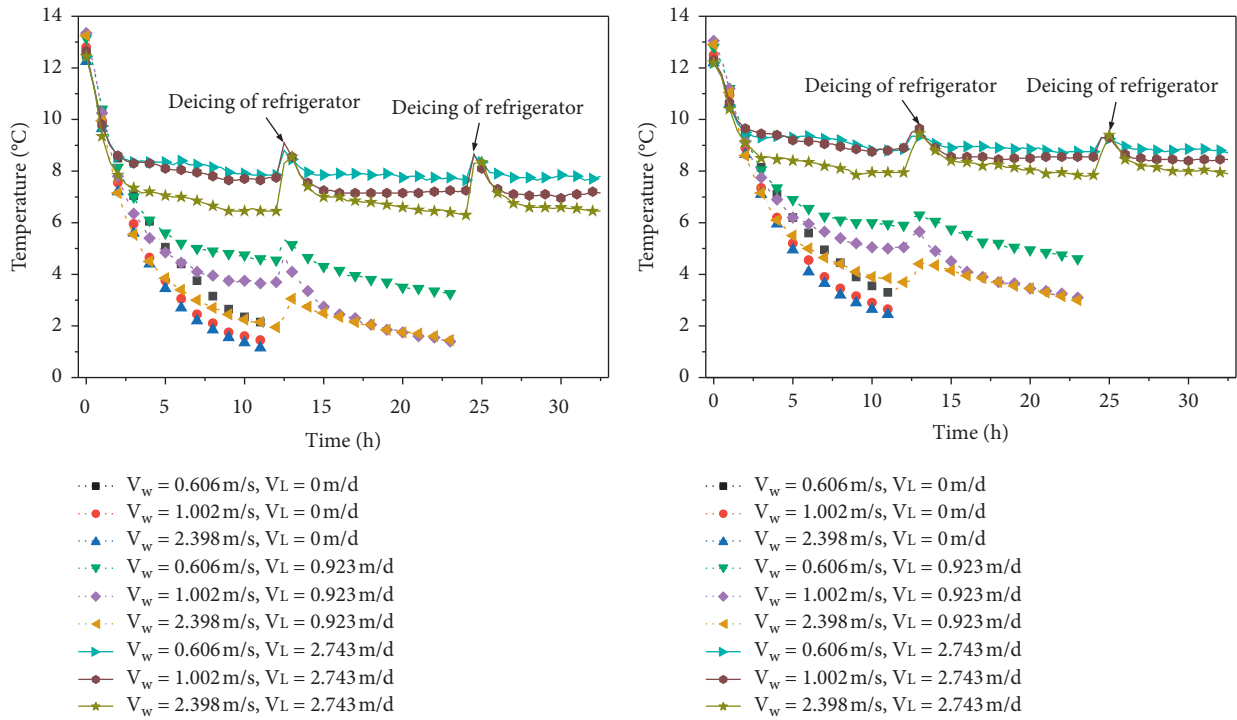
The above analysis shows that groundwater seepage and tunnel ventilation have a coupling effect on the surrounding rock temperature. Specifically, higher groundwater seepage velocities and lower wind speeds lead to higher surrounding rock temperatures. Thus, the coupling influence of groundwater seepage and tunnel ventilation should be considered when designing the insulation layers of cold region tunnels.

### 3.3. Effect of Groundwater Seepage on the Temperature at the Interface between the Lining and Surrounding Rock.

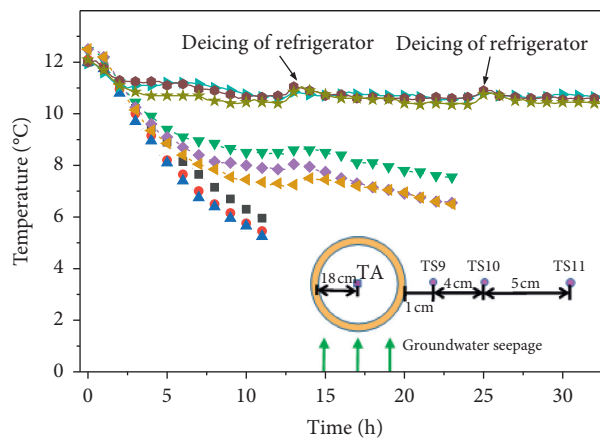
Figure 8 presents the temperature variation over time at the interface between the lining and surrounding rock under the influence of groundwater seepage and ventilation in the model test. It shows that the interface temperatures of TS1, TS3, TS4, TS5, and TS6 decrease over time when groundwater seepage and ventilation are considered in the model test. Groundwater seepage has a significant effect on the interface temperature. The effect is related to the location of the monitoring points. Therefore, the cooling rates and amplitudes of the interface temperature for TS1, TS3, TS4, TS5, and TS6 differ significantly. The groundwater seepage has the most significant effects on measuring points TS3 and TS4 and has the least significant effects on measuring points TS1 and TS6. Wind speed also has a significant effect on the interface temperature. The effect is related to the groundwater seepage velocity. These results indicate that groundwater seepage and tunnel ventilation have a coupling effect on the interface temperature and that this coupling effect is related to the interface location.

Figure 9 shows the variations in the temperature drops at TS1, TS3, TS4, TS5, and TS6 with groundwater seepage velocity under tunnel ventilation after 11.5 h of cooling. It shows that the temperature drops at TS3 and TS4 upstream of the groundwater seepage field decrease as the groundwater seepage velocity increases. However, the temperature drops at TS1 and TS6 downstream of the groundwater seepage field increase as the groundwater seepage velocity increases from 0 to 0.923 m/d. Furthermore, the temperature drops at TS1 and TS6 decrease as the groundwater seepage velocity increases from 0.923 to 2.743 m/d. The smallest temperature drop occurs at TS3 (upstream of the groundwater seepage field), and the largest temperature drop occurs at TS1 (downstream of the groundwater seepage field) under groundwater seepage. These results indicate that groundwater seepage leads to an uneven temperature distribution at the interface between the lining and surrounding rock and that tunnel ventilation enhances this uneven distribution.

Figure 10 presents the temperature differences between TS3, TS5, and TS6. The temperature at TS3 is higher under groundwater seepage than those at TS5 and TS6. The interface temperature upstream of the groundwater field is higher than that downstream. Figure 10 also shows that the temperature difference between TS3 and TS6 increases as the groundwater



(a) (b)



(c)

FIGURE 6: Variations in the surrounding rock temperature over time.

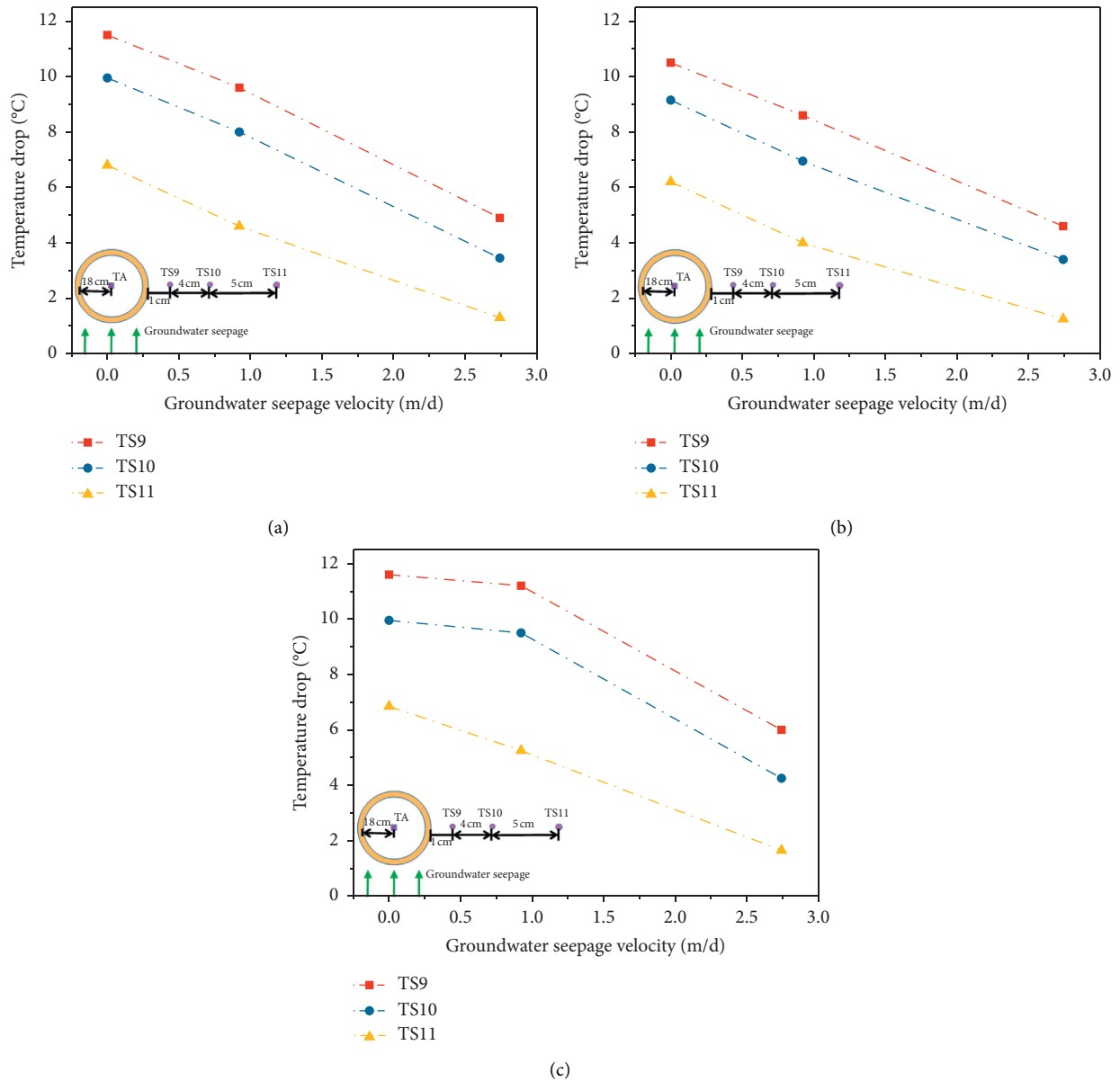


FIGURE 7: Variations in the surrounding rock temperature drop at different groundwater seepage velocities after 11.5 h of cooling. Average wind speed of (a) 0.606 m/s, (b) 1.002 m/s, and (c) 2.398 m/s.

seepage velocity increases. Thus, the higher the groundwater seepage velocity is, the higher the temperature difference is between TS3 and TS6. The temperature difference between TS3 and TS5 increases as the groundwater seepage velocity increases from 0 to 0.923 m/d and decreases as the groundwater seepage velocity increases from 0.923 to 2.743 m/d. Groundwater seepage has a great effect on the interface temperature. This effect has a spatial difference. Thus, both the shape and size of the cross section of the tunnel significantly affect the interface temperature under groundwater seepage.

**3.4. Effect of Groundwater Seepage on the Freezing Damage to Cold Region Tunnels.** The tunnel drainage system is located between the lining and the surrounding rock.

Monitoring points TS3, TS5, and TS6 are located at the top, middle, and foot of the tunnel drainage system, respectively. The temperatures at TS3, TS5, and TS6 determine the antifreezing ability of cold region tunnels. Therefore, the higher the temperatures at TS3, TS5, and TS6 are, the stronger the antifreezing capability of the tunnel in cold regions is. Figure 8 shows that when the groundwater seepage velocity is 0 m/d, the measuring points TS3, TS5, and TS6 freeze synchronously. If the tunnel surrounding rock is free of frost heaving, cold region tunnels may not need a thermal insulation layer. When the groundwater seepage velocity is 0.923 m/d, the monitoring point TS6 freezes first. The interface then gradually freezes from TS6 to TS5 along the circumferential direction of the tunnel section. This explains why

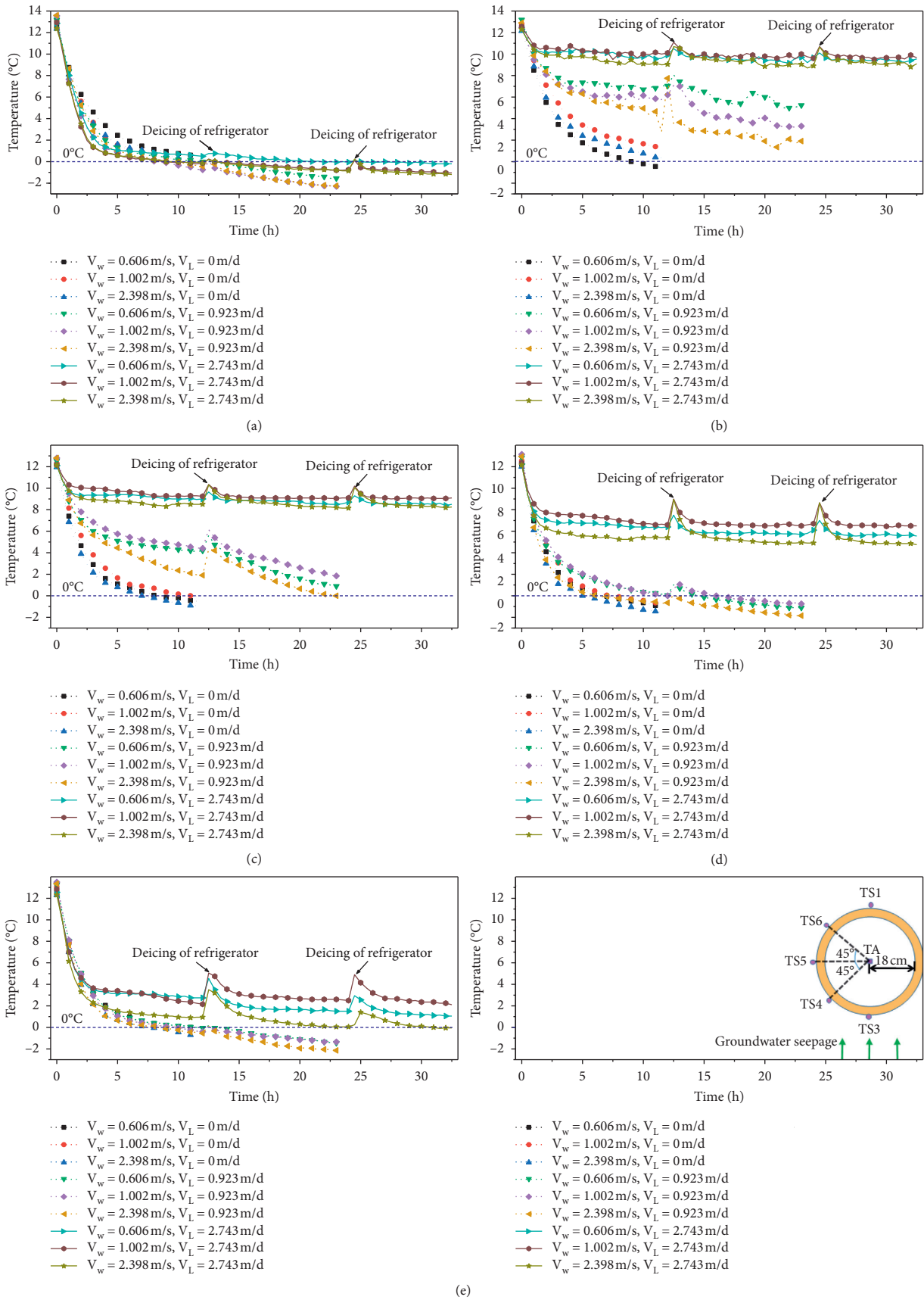


FIGURE 8: Variations in the temperature at the interface between the lining and the surrounding rock: (a) TS1, (b) TS3, (c) TS4, (d) TS5, and (e) TS6.

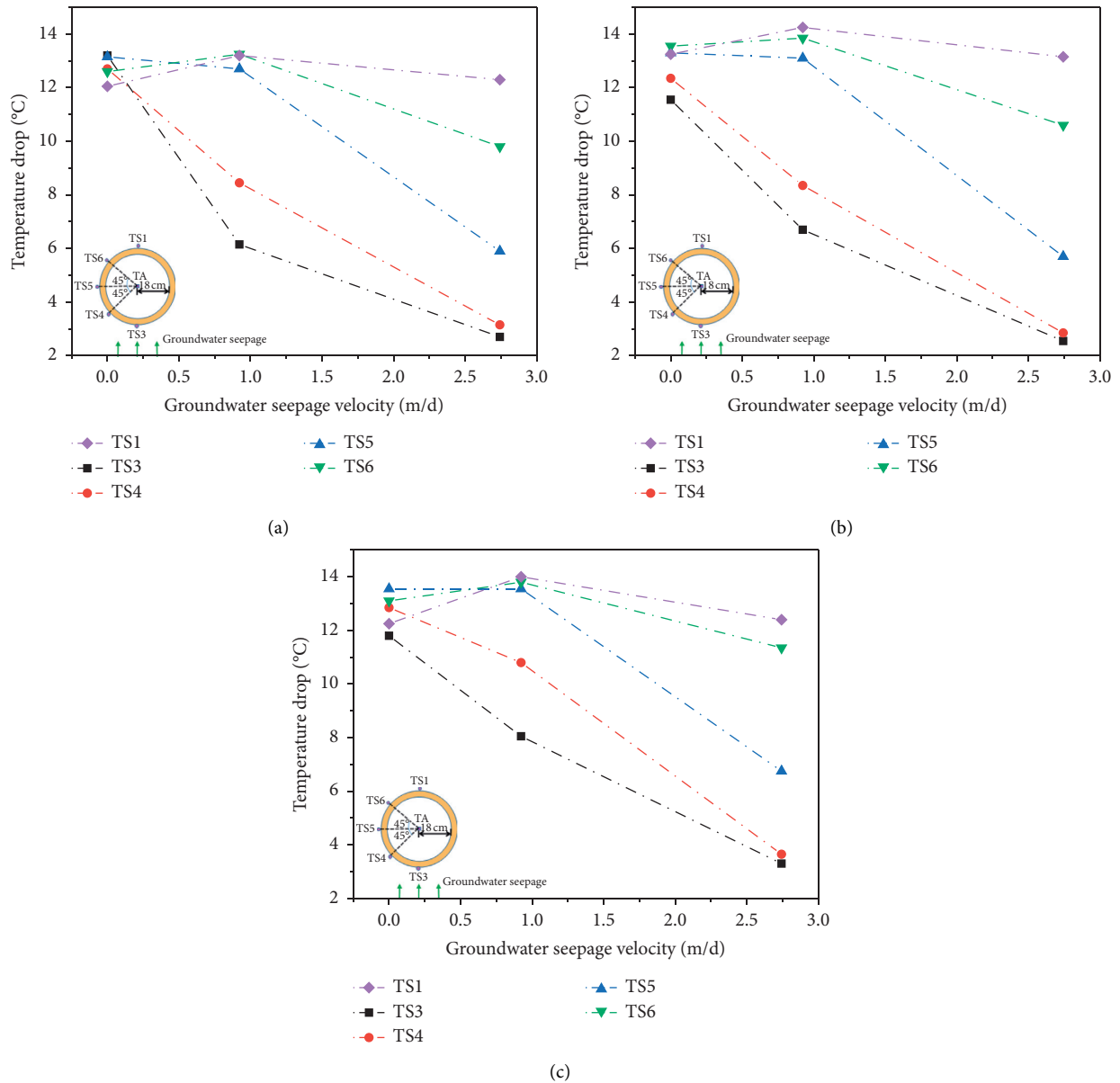


FIGURE 9: Variations in the surrounding rock temperature drop at different groundwater seepage velocities after 11.5 h of cooling. Average wind speed of (a) 0.606 m/s, (b) 1.002 m/s, and (c) 2.398 m/s.

cold region tunnels suffer tunnel lining leakage and road icing. The results of the model test reveal the cause of tunnel lining leakage and road icing. To avoid tunnel leakage in cold region tunnels, a thermal insulation layer should be properly designed and a heating device should be installed in its longitudinal drainage pipe when the groundwater seepage velocity is low. When the groundwater seepage velocity is 2.743 m/d, the monitoring point at TS6 freezes but the monitoring points at TS3 and TS5 do not. Furthermore, their temperatures do

not decrease significantly as cooling time increases. Therefore, the tunnel has good antifreezing capability when the groundwater seepage velocity is high. This good antifreezing capability should be fully utilized. Furthermore, the foot of the tunnel drainage system should be strengthened against freezing via an insulation layer and heating device.

The above analysis demonstrates that cold region tunnels have an antifreezing capability that is mainly related to the frost heaving of the surrounding rock and the groundwater seepage

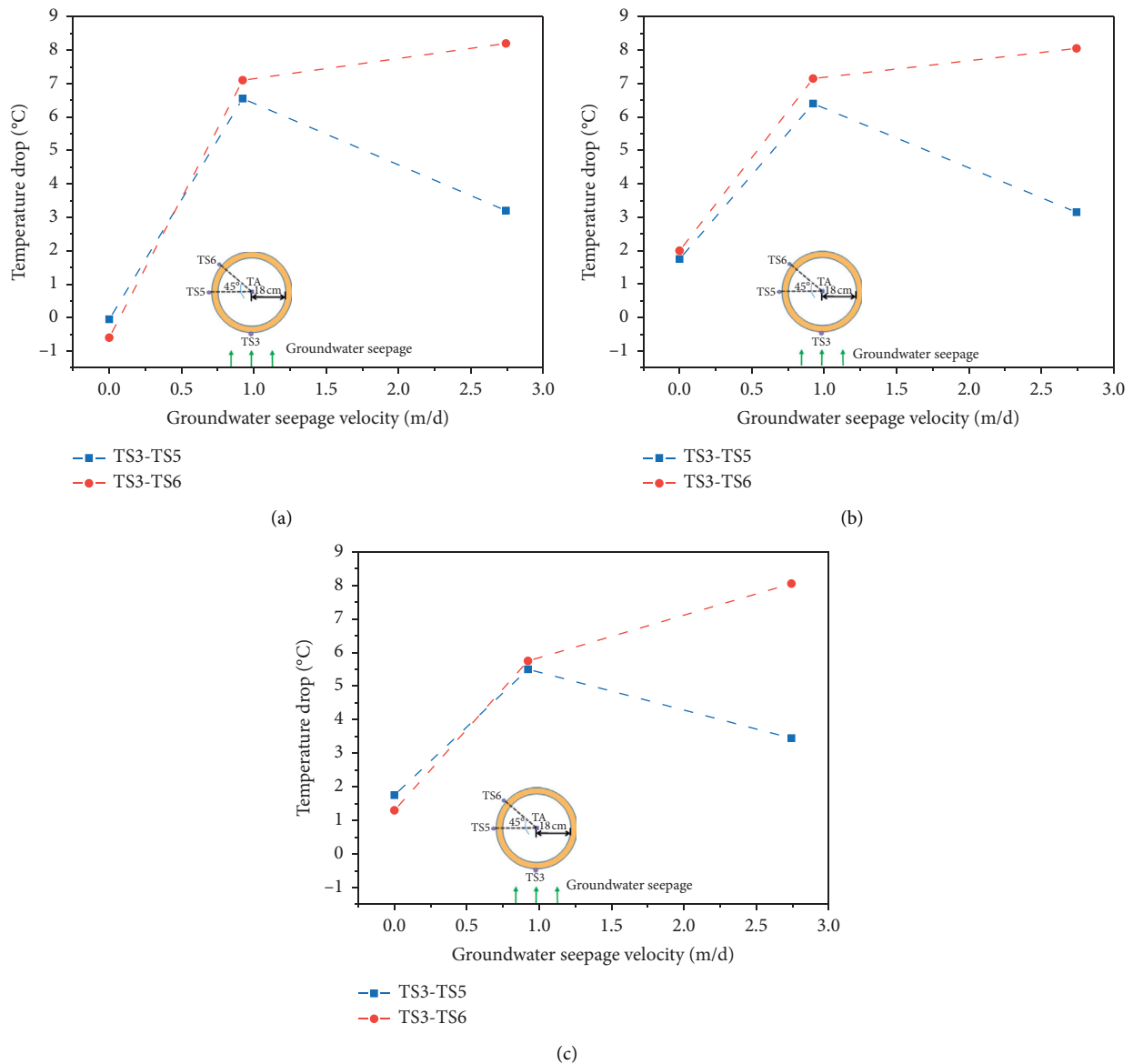


FIGURE 10: Relationships between the temperature differences at TS5, TS6, and TS3 and groundwater seepage velocity. Average wind speed of (a) 0.606 m/s, (b) 1.002 m/s, and (c) 2.398 m/s.

velocity. This antifreezing capability should be fully utilized in the antifreezing design of cold region tunnels.

#### 4. Conclusions

A systematic study on the temperature field of cold region tunnels is presented in which a model test that considers the coupling effects of groundwater seepage and tunnel ventilation is conducted. The effects of groundwater seepage on the air temperature in the tunnel, the surrounding rock temperature, the temperature at the interface between the lining and surrounding rock, and the freezing damage of the tunnel in cold regions are studied. The following four main conclusions are drawn.

First, groundwater seepage has a significant effect on the air temperature in the tunnel. The higher the groundwater

seepage velocity, the higher the air temperature in the tunnel. Groundwater seepage has a significant influence on the thickness and length of the tunnel insulation layer in cold regions. The thickness and length of the tunnel insulation layer can decrease under groundwater seepage.

Second, groundwater seepage and tunnel ventilation have a coupling effect on the surrounding rock temperature. Higher groundwater seepage velocity and lower wind speed lead to higher surrounding rock temperature. The influence of groundwater seepage and tunnel ventilation on the surrounding rock temperature field is related to the depth of the surrounding rock.

Third, groundwater seepage leads to an uneven temperature distribution at the interface between the lining and surrounding rock. The tunnel ventilation further enhances this uneven temperature distribution. The groundwater

seepage and tunnel ventilation have a coupling effect on the interface temperature. This coupling effect is related to the interface location. The influence of the groundwater seepage velocity on the interface temperature has a spatial difference. The shape and size of the cross section of the tunnel have a significant influence on the interface temperature under groundwater seepage.

Fourth, cold region tunnels have an antifreezing capability that is mainly related to the frost heaving of the surrounding rock and the groundwater seepage velocity. The antifreezing capability of the tunnel should be fully utilized in the antifreezing design of cold region tunnels.

## Data Availability

The data used to support the findings of this study are available from the corresponding author upon request.

## Conflicts of Interest

The authors declare that they have no conflicts of interest.

## Acknowledgments

This study was supported by the Key Laboratory of Geotechnical and Underground Engineering of Ministry of Education, Tongji University (No. KLE-TJGE-B1605), the Key Laboratory of Rock Mechanics and Geohazards of Zhejiang Province (No. ZJRM-2018-Y-01), and the Sichuan Science and Technology Program (No. 2018GZ0359).

## References

- [1] S. Li, M. Zhang, W. Pei, and Y. Lai, "Experimental and numerical simulations on heat-water-mechanics interaction mechanism in a freezing soil," *Applied Thermal Engineering*, vol. 132, pp. 209–220, 2018.
- [2] S. Li, M. Zhang, Y. Tian, W. Pei, and H. Zhong, "Experimental and numerical investigations on frost damage mechanism of a canal in cold regions," *Cold Regions Science and Technology*, vol. 116, pp. 1–11, 2015.
- [3] S. Shen, C. Xia, J. Huang, and Y. Li, "Influence of seasonal melt layer depth on the stability of surrounding rock in permafrost regions based on the measurement," *Natural Hazards*, vol. 75, no. 3, pp. 2545–2557, 2015.
- [4] K.-J. Jun, Y.-C. Hwang, and C.-Y. Yune, "Field measurement of temperature inside tunnel in winter in Gangwon, Korea," *Cold Regions Science and Technology*, vol. 143, pp. 32–42, 2017.
- [5] Q. Ma, X. Luo, Y. Lai, F. Niu, and J. Gao, "Numerical investigation on thermal insulation layer of a tunnel in seasonally frozen regions," *Applied Thermal Engineering*, vol. 138, pp. 280–291, 2018.
- [6] X. Zhao, X. Yang, H. Zhang, H. Lai, and X. Wang, "An analytical solution for frost heave force by the multifactor of coupled heat and moisture transfer in cold-region tunnels," *Cold Regions Science and Technology*, vol. 175, 2020.
- [7] Y. M. Lai, S. Y. Liu, Z. W. Wu, and W. Yu, "Approximate analytical solution for temperature fields in cold regions circular tunnels," *Cold Regions Science and Technology*, vol. 34, no. 1, pp. 43–49, 2002.
- [8] G. Zhang, C. Xia, M. Sun, Y. Zou, and S. Xiao, "A new model and analytical solution for the heat conduction of tunnel lining ground heat exchangers," *Cold Regions Science and Technology*, vol. 88, pp. 59–66, 2013.
- [9] Y. M. Lai, Z. W. Wu, Y. L. Zhu, and L. N. Zhu, "Nonlinear analysis for the coupled problem of temperature, seepage and stress fields in cold-region tunnels," *Tunnelling and Underground Space Technology*, vol. 13, no. 4, pp. 435–440, 1998.
- [10] X. Zhang, J. Xiao, Y. Zhang et al., "Study of the function of the insulation layer for treating water leakage in permafrost tunnels," *Applied Thermal Engineering*, vol. 27, no. 2–3, pp. 637–645, 2007.
- [11] X. Zhang, Y. Lai, W. Yu, and S. Zhang, "Non-linear analysis for the freezing-thawing situation of the rock surrounding the tunnel in cold regions under the conditions of different construction seasons, initial temperatures and insulations," *Tunnelling and Underground Space Technology*, vol. 17, no. 3, pp. 315–325, 2002.
- [12] X. Zhang, Y. Lai, W. Yu, and Y. Wu, "Forecast analysis for the re-frozen of Feng Huoshan permafrost tunnel on Qing-Zang railway," *Tunnelling and Underground Space Technology*, vol. 19, no. 1, pp. 45–56, 2004.
- [13] X. Tan, W. Chen, H. Tian, and J. Cao, "Water flow and heat transport including ice/water phase change in porous media: numerical simulation and application," *Cold Regions Science and Technology*, vol. 68, no. 1–2, pp. 74–84, 2011.
- [14] X. Tan, W. Chen, G. Wu, and J. Yang, "Numerical simulations of heat transfer with ice-water phase change occurring in porous media and application to a cold-region tunnel," *Tunnelling and Underground Space Technology*, vol. 38, pp. 170–179, 2013.
- [15] X. Tan, W. Chen, D. Yang et al., "Study on the influence of airflow on the temperature of the surrounding rock in a cold region tunnel and its application to insulation layer design," *Applied Thermal Engineering*, vol. 67, no. 1–2, pp. 320–334, 2014.
- [16] S. Li, F. Niu, Y. Lai, W. Pei, and W. Yu, "Optimal design of thermal insulation layer of a tunnel in permafrost regions based on coupled heat-water simulation," *Applied Thermal Engineering*, vol. 110, pp. 1264–1273, 2017.
- [17] Q. Yan, B. Li, Y. Zhang, J. Yan, and C. Zhang, "Numerical investigation of heat-insulating layers in a cold region tunnel, taking into account airflow and heat transfer," *Applied Sciences*, vol. 7, no. 7, p. 679, 2017.
- [18] Q. Feng, B.-S. Jiang, Q. Zhang, and G. Wang, "Reliability research on the 5-cm-thick insulation layer used in the Yuximolegai tunnel based on a physical model test," *Cold Regions Science and Technology*, vol. 124, pp. 54–66, 2016.
- [19] X. Zhang, Z. Zhou, J. Li, Y. Zhou, and F. Han, "A physical model experiment for investigating into temperature redistribution in surrounding rock of permafrost tunnel," *Cold Regions Science and Technology*, vol. 151, pp. 47–52, 2018.
- [20] Y. Zeng, K. Liu, X. Zhou, and L. Fan, "Tunnel temperature fields analysis under the couple effect of convection-conduction in cold regions," *Applied Thermal Engineering*, vol. 120, pp. 378–392, 2017.
- [21] L. Liu, Z. Li, X. Liu, and Y. Li, "Frost front research of a cold-region tunnel considering ventilation based on a physical model test," *Tunnelling and Underground Space Technology*, vol. 77, pp. 261–279, 2018.
- [22] G. Zhang, Y. Guo, Y. Zhou et al., "Experimental study on the thermal performance of tunnel lining GHE under groundwater flow," *Applied Thermal Engineering*, vol. 106, pp. 784–795, 2016.
- [23] G. Zhang, S. Liu, X. Zhao et al., "The coupling effect of ventilation and groundwater flow on the thermal performance



- of tunnel lining GHEs,” *Applied Thermal Engineering*, vol. 112, pp. 595–605, 2017.
- [24] Q. Hu, R. Shi, Y. Hu et al., “Method to evaluate the safety of tunnels through steeply inclined strata in cold regions based on the sidewall frost heave model,” *Journal of Performance of Constructed Facilities*, vol. 32, 2018.
- [25] H. Cai, P. Li, and Z. Wu, “Model test of liquid nitrogen freezing-temperature field of improved plastic freezing pipe,” *Journal of Cold Regions Engineering*, vol. 34, no. 1, 2020.
- [26] S. E. A. Gehlin and G. Hellström, “Influence on thermal response test by groundwater flow in vertical fractures in hard rock,” *Renewable Energy*, vol. 28, no. 14, pp. 2221–2238, 2003.

## Research Article

# Analysis of Rock $\beta$ -Dynamic Parameters and the Stability of Earthquake Dangerous Rocks Based on PFC

Yun Tian <sup>1</sup>, Lin-feng Wang <sup>1</sup>, Biao Zeng <sup>2</sup>, and Hong-hua Jin <sup>2</sup>

<sup>1</sup>Key Laboratory of Geological Hazards Mitigation for Mountainous Highway and Waterway, Chongqing Municipal Education Commission, Chongqing Jiaotong University, Chongqing 400071, China

<sup>2</sup>School of Transportation, Southeast University, Nanjing 210096, China

Correspondence should be addressed to Lin-feng Wang; wanglinfeng@cqjtu.edu.cn

Received 11 October 2020; Revised 20 November 2020; Accepted 26 November 2020; Published 9 December 2020

Academic Editor: Zhi Cheng Tang

Copyright © 2020 Yun Tian et al. This is an open access article distributed under the Creative Commons Attribution License, which permits unrestricted use, distribution, and reproduction in any medium, provided the original work is properly cited.

Mesoparameters of rock materials are the main factors affecting the macromechanical properties of dangerous rock slopes. Based on the principle of particle flow and synthetic rock mass technology (SRM), the influence of mesoparameters on macromechanical properties is investigated by calibrating mesoparameters of rock materials at depth for a rock sequence in Beichuan Qiang Autonomous County, Sichuan Province, China. By combining these parameters with conventional and dynamic cycle triaxial tests, sensitivity analysis of rock  $\beta$ -parameters was completed. As a result, the reliability of mesoparameters in the simulation of dangerous rocks is strengthened, providing a basis to examine the failure mechanism of earthquake dangerous rocks in this region. Results indicate that, in the triaxial test, sandstone failed in tension, and brittleness gradually weakened as confining pressure increased. Mudstone recorded shear failure, and the characteristic value of brittle attenuation showed a V-shaped change with increasing confining pressure. Under cyclic loading, cracks had a degrading effect on the damping ratio ( $\beta$ ) and the damping coefficient ( $C$ ) of sandstone. Mudstone recorded relatively low  $\beta$  and low brittleness whilst sandstone had high  $\beta$  and high brittleness. In rock materials,  $\beta_n$  is more sensitive than  $\beta_s$  in mechanical properties. When the value of the  $\beta_n$ -parameter was between 0.2 and 0.3 and the value of the  $\beta_s$ -parameter was between 0.2 and 0.6, rock brittleness was more stable, and the reflected macroscopic mechanical properties were the most authentic. By using a deepened mesoparameter trial adjustment method, the failure mode of the Particle Flow Code (PFC) dangerous rock model near provincial highway 205, simulated under conditions for the Wenchuan earthquake, indicated a tensile fracture-horizontal slip failure. The simulated failure mode was consistent with that of real dangerous rocks, with the failure trend being concentrated between the first and the third layer of the rock mass.

## 1. Introduction

Sichuan Province, China, located in the Helan-Liupan-Longmen-Hengdun Mountain seismic zone, experiences frequent earthquakes and rockslides. In this area, earthquake-induced rock slope instability often occurs, resulting in significant economic and property loss. Dangerous rock slopes have been identified as the main formation resulting in earthquake-type slope collapse disasters. Rock masses are generally cut by different structural planes. When the main control structural plane is located at the rear of the dangerous rock block, it gradually penetrates the rock mass until the mass breaks under the action of multiple factors. Under this condition, the dangerous rock block becomes unstable

and is destroyed. Although previous investigations have predominantly examined instability and failure of dangerous rocks, studies examining the stability of dangerous rocks in earthquake areas are typically based on the principle of particle flow; reliable rock material mesoparameter calibration methods are urgently needed. This area of research has become one of the main research areas and technical challenges in this field [1, 2]. From the perspective of rock materials, the discrete element method has become important to solve critical rock simulation technology, and the key condition to determine the reliability of the method is the selection of mesoparameters in the model.

For seismic slopes, Chen [3] deduced the chain development process of dangerous rocks in the Three Gorges

Reservoir area. From the perspective of geomorphology, they revealed the influence of rock cavern weathering on the stability of dangerous rock slopes, proposing the dangerous rock chain pattern development. Based on fracture mechanics and damage mechanics, Tang et al. [4, 5] discussed the sequence of dangerous rock caving on a cliff with a weak base, establishing a calculation method for the time of dangerous rock caving. Yan et al. [6] used the QUIVER code to realize the response analysis of earthquake gentle slopes, identifying slope response and sliding displacement law under the action of an earthquake. The movement characteristics of dangerous rock slopes under different seismic conditions were simulated by Huang et al. [7] using the discontinuous deformation analysis (DDA) method. The influence of seismic loads on the movement characteristics of dangerous rock mass collapse blocks was shown using the DDA method. Zhao et al. [8] used particle flow PFC2D software to dynamically simulate the instability process of rock slopes, revealing the influence of the distribution of weak structural planes on the instability and failure of rock slopes. Tang et al. [9] used a two-dimensional discrete element simulation to study the formation mechanism of the Caoling landslide in 1941.

For studies of rock materials, Cong et al. [10] proposed that the macroscopic mechanical characteristics of materials are closely related to microscopic parameters. These parameters can be combined with marble indoor loading and unloading tests to determine the mesoparameters suitable for rock materials (such as marble). He et al. [11] comparatively analyzed the damping characteristics of sandstone, conglomerate, and glutenite under different stress paths, highlighting the evolution of the damping ratio ( $\beta$ ) and the damping coefficient ( $C$ ) with the number of cycles. The influence of fractures on rock mechanical properties proposed by Huang et al. [12] has important practical significance for the engineering stability of fractured rock masses. In addition, strength, deformation parameters, and failure modes of rock materials with discontinuous, non-parallel double fissures were analyzed in detail. The mesoparameters of PFC2D numerical sandstone samples from the mesolevel aspects of displacement, crack evolution, and distribution were studied by Zhou et al. [13]. Tang and Zhang [14–16] studied the shear behavior of rock fractures from the perspective of temperature and provided new ideas for the stability evaluation of surrounding rock in temperature-dependent underground engineering. Tang and Jiao [17] also proposed that, in the contact behavior of rock joints, the three-point peak (3PP) standard seems to be the most appropriate method to identify the contour peaks of rock joints. Zou et al. [18] used the extended finite element method (XFEM) to simulate the propagation of hydraulic fractures in heterogeneous reservoirs. They proposed that the hard blocks in the reservoir promote the growth of hydraulic fractures, but limit the growth of fracture widths.

As the majority of previous investigations considered the two-dimensional particle flow method, dangerous rock slope simulation technology lacks reliability due to insufficient factors being considered, resulting in low applicability of earthquake dangerous rock simulation technology in

earthquake areas. Furthermore, the mechanical characteristics and mesoscopic parameters of rock materials need further evaluation. In particle flow rock material simulation, the parallel bond contact model is generally used to assign values to the contact between rock particles. Since Poisson's ratio  $\mu$ , elastic modulus  $E^*$ , stiffness ratio  $k^*$ , and other mesoparameters will directly affect the macromechanical properties of rock materials under numerical tests, they have become the main objects considered in the trial adjustment processes [19–25]. However, under the dynamic action of a rock slope, the damping ratio ( $\beta$ ) is an important parameter that affects the dynamic response of a rock [11]. This influence on the macromechanical properties of rock materials has generally been overlooked in previous investigations. Therefore, our study includes crack tracking, strength attenuation index (brittleness characteristics), and  $\beta$ -dynamic parameter analysis on the basis of traditional parameter adjustment methods. By selecting different mesoparameters from previous studies, we investigated normal critical damping ratio  $\beta_n$  and shear critical damping ratio  $\beta_s$  for sensitivity analysis. As a result, rock mesoparameters that can better reflect true materials are obtained, providing a strong basis for simulating the seismic damage of dangerous rocks and analyzing the stability of earthquake dangerous rocks.

## 2. Mechanical Behavior of Rock Materials

### 2.1. Sample Equipment and Sample Preparation

**2.1.1. Sample Equipment.** Mudstone and sandstone mechanical tests in this study were performed on a RMT-150C rock mechanics test system (Figure 1) which can realize automatic data collection and processing. The maximum axial load of the testing machine is 1000 kN, the vibration frequency is 0.2–2 Hz, the specimen size is  $\Phi$  (50 × 100)–(100 × 300) mm, the maximum three-axis confining pressure is 100 MPa, the confining pressure rate is 0.001–1 MPa/s, the displacement measurement range is  $\pm 50$  mm, and the strain measurement range is  $\pm 0.01$ . The source vibration wave can be sine wave, triangle wave, square wave, oblique wave, etc.

**2.1.2. Sample Preparation.** One set of mudstone and three sets of sandstone (Figure 2) were used in this investigation. The static mechanics test was divided into one set of mudstone specimens (No. A) and one set of sandstone specimens (No. B). The dynamic test was divided into one group of conventional sandstone specimens (No. C) and one group of fractured sandstone specimens (No. D) (Figure 3). Rock samples were collected from dangerous rock on Provincial Highway 205 in Beichuan Qiang Autonomous County. The test sample was a cylinder with a diameter of 50 mm and a height of 100 mm. The error range was controlled within  $\pm 2$  mm, meeting the requirement of a 2:1 height-to-diameter ratio specified by the International Society of Rock Mechanics. The cutting position of the cracked sandstone was set as the top central axis; the cutting depth was 50 mm, and the gap width was 2 mm.



FIGURE 1: The RMT-150C rock mechanics test system.

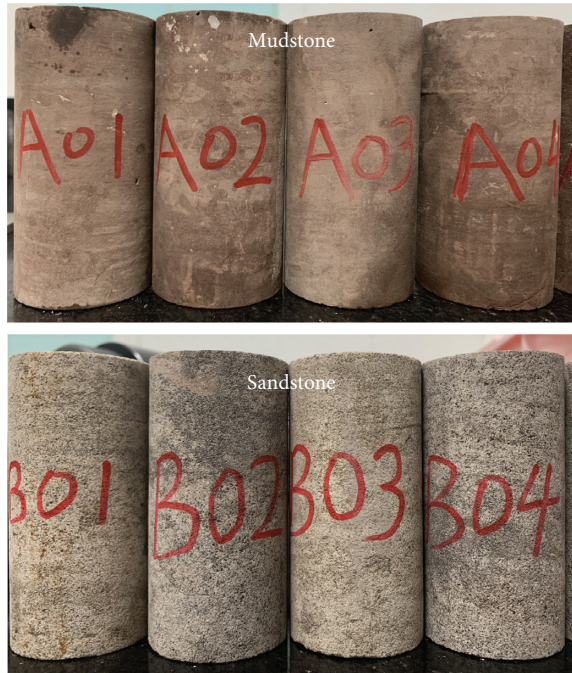


FIGURE 2: Conventional triaxial rock specimens.

## 2.2. Mechanics Test Plan

**2.2.1. Conventional Triaxial Test.** The conventional triaxial test is an important step for adjusting the mesoparameters of PFC3D and determining the rationality of the particle flow

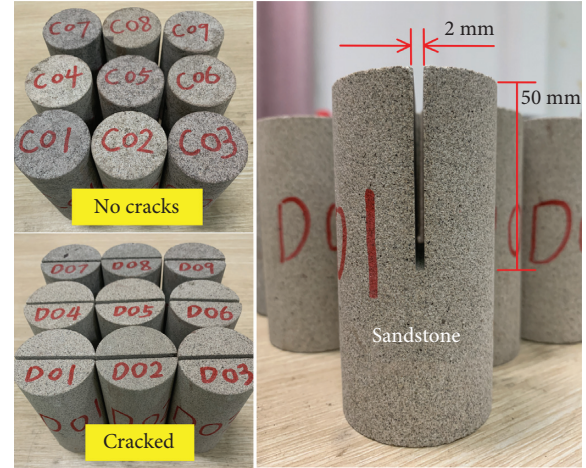


FIGURE 3: Triaxial circulation sandstone samples.

method. This test was carried out at a room temperature of about 25°C. The loading test adopts axial strain control; the loading rate was 0.02%/min, the maximum stress was set to 150 kN, and the axial load was continuously applied under four confining pressures (2 MPa, 4 MPa, 6 MPa, and 8 MPa) until the rock sample failed. The strength criterion of the conventional triaxial test followed the Mohr–Coulomb strength criterion [26, 27]. The failure mechanism was that the material experiences shear failure under the action of normal stress. The maximum shear stress  $\tau_m$  it bears was determined by the cohesion and the angle of internal friction, expressed as

$$\tau_m = c + \sigma \tan \varphi, \quad (1)$$

where  $c$  is the cohesive force,  $\sigma$  is the normal stress on the shear failure surface, and  $\varphi$  is the internal friction angle. In order to further reflect the brittleness of the rock, we examined the mechanical index that characterizes the strength attenuation behavior of rock samples after the peak [28]. The specific algorithm was as follows:

$$D_s = \frac{\sigma_1^P - \sigma_r}{\sigma_1^P} = \frac{\Delta\sigma}{\sigma_1^P}, \quad (2)$$

$$\Delta\sigma = \sigma_1^P - \sigma_r, \quad (3)$$

where  $D_s$  is the intensity attenuation coefficient and the value range is [0, 1];  $\Delta\sigma$  is the intensity attenuation value;  $\sigma_1^P$  is the peak intensity; and  $\sigma_r$  is the residual intensity.

**2.2.2. Dynamic Cycle Triaxial Test.** The dynamic cycle triaxial test was used to study the dynamic mechanical characteristics of the rock samples under three-dimensional stress. The test simulates not only the static stress state of the rock on-site, but also the actual seismic effect. This test provides a reference for studying the dynamic parameters of sandstone and the dynamic stability of dangerous rocks. In the cyclic loading process of an ideal elastic material, the stress and strain time history of the elastic body is synchronized. Rock is a typical inhomogeneous material, with

different levels of cracks, pores, and other microscopic defects distributed throughout. The cement interface between mineral particles is also a relatively weak surface. The area of the hysteresis loop can reflect the amount of energy consumed in the cyclic loading process. Under ideal elasticity, the vibration damping ratio  $\beta$  can be calculated according to the area of the hysteresis loop; the average slope of the hysteresis loop reflects the magnitude of the dynamic elastic modulus  $E_d$  (Figure 4) [29].

The values of damping ratio  $\beta$ , damping coefficient  $C$ , and  $E_d$  can be calculated as follows [30]:

$$\beta = \frac{A}{(4\pi/A_s)}, \quad (4)$$

$$C = \frac{A}{\pi X^2 \omega}, \quad (5)$$

$$E_d = \frac{\sigma_{d \max}}{\varepsilon_{d \max}}, \quad (6)$$

where  $A$  is the area of the hysteresis loop ABCDA;  $A_s$  is the area of triangle AOE;  $X$  is the amplitude of vibration;  $\omega$  is the angular frequency of vibration;  $\sigma_{d \max}$  is the maximum axial dynamic stress of the hysteresis loop; and  $\varepsilon_{d \max}$  is the maximum axial dynamic strain of the hysteresis loop. As dangerous rocks in this area are mainly composed of sandstone, this cyclic test was only conducted on sandstone samples. Confining pressures were 2 MPa, 4 MPa, and 6 MPa, and the vibration frequency was 1 Hz; the loading rate was 60 kN/min. The loading process was divided into six stages of cyclic loading: (1) when the hoop load reached the predetermined confining pressure, the first stage was loaded from 0 to 20 kN and then loaded cyclically between 0 and 20 kN at a frequency of 1 Hz 30 times and then unloaded to 0. (2) The second stage was loaded from 0 to 40 kN, loaded cyclically from 0 to 40 kN at a frequency of 1 Hz 30 times, and finally unloaded to 0. Stages 3 to 6 continued in this format until 120 kN was used in stage 6. During the step-by-step loading process, if the test piece was damaged, the test ended.

### 2.3. PFC Mechanical Test

**2.3.1. Numerical Three-Axis Servo Test.** In this study, the PFC3D simulated triaxial test was used to conduct microscopic failure analysis and mesoparameter calibration on two kinds of rocks. The entire three-axis numerical simulation loads the sample by specifying the top and bottom wall boundary constraint speeds, determining the stress and strain state of the sample through the built-in FISH function of PFC3D. The established loading model is shown in Figure 5. According to the real triaxial test, the model generates particles in a cylindrical wall with a height of 10 m and a diameter of 5 m. In preliminary model calculations, it was found that if the particles are generated according to the actual gradation, the number of particles will reach 1 million. However, the existing calculation conditions cannot complete the numerical analysis of such a large number of

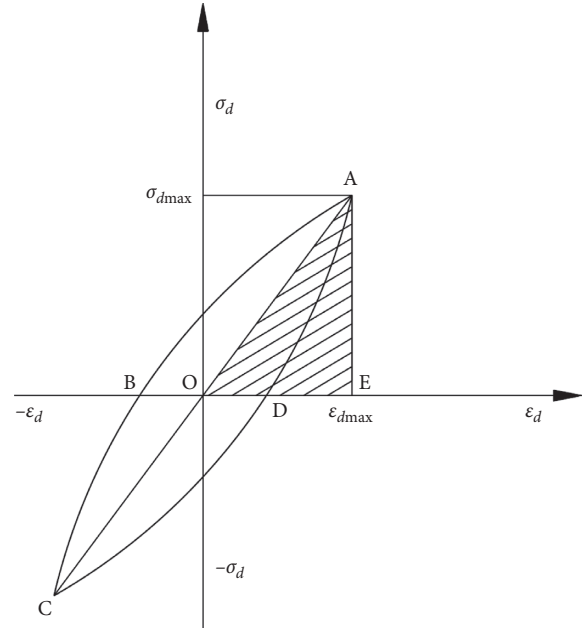


FIGURE 4: Dynamic stress-strain hysteresis loop.

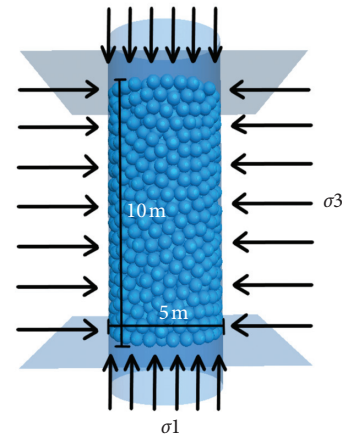


FIGURE 5: Schematic diagram of the numerical three-axis loading model.

particles. In this case, after considering the impact of the particle size effect on the test results [31], the radius of the particles is appropriately expanded, and the radius is 0.2–0.25 m. The purpose of setting the sample size in this way is to keep the particle size of the numerical triaxial sample and the numerical slope model at the same size (that is, the unit is m). At the same time, it not only improves the calculation efficiency, but also does not affect the accuracy of the simulation results. Under the condition of constant confining pressure, the upper and lower loading plates moved towards each other at a speed of 10 mm/min until the specimen was broken. The stress-strain curve was automatically recorded throughout the process. In addition, the confining pressure was loaded according to the amount of 2 MPa, 4 MPa, 6 MPa, and 8 MPa in the indoor test. Finally, the overall project view and flowchart of the analysis steps is shown in Figure 6.

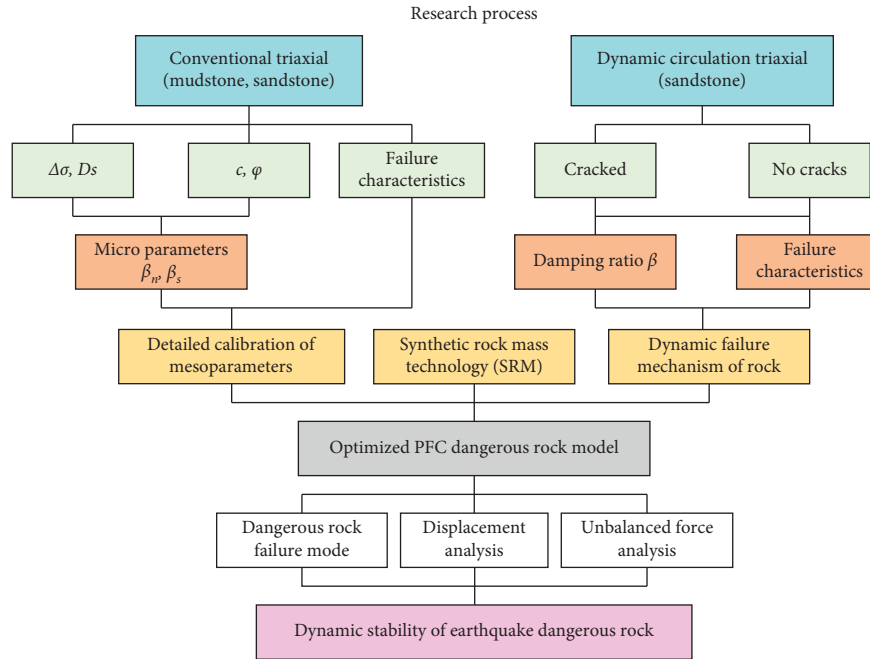


FIGURE 6: Research flowchart.

## 2.4. Mechanical Test Analysis

**2.4.1. Conventional Triaxial Test Analysis.** The macro-mechanical properties of sandstone and mudstone under the two triaxial test methods are shown in Table 1. Comparison of results under the two methods indicates that cohesion  $c$  and the friction angle  $\varphi$  were essentially consistent. Among these, the cohesive force error was controlled within 0–0.02 MPa, and the friction angle error was controlled within  $0.3^{\circ}$ – $0.4^{\circ}$ , thereby preliminarily determining the rationality of the microscopic parameters.

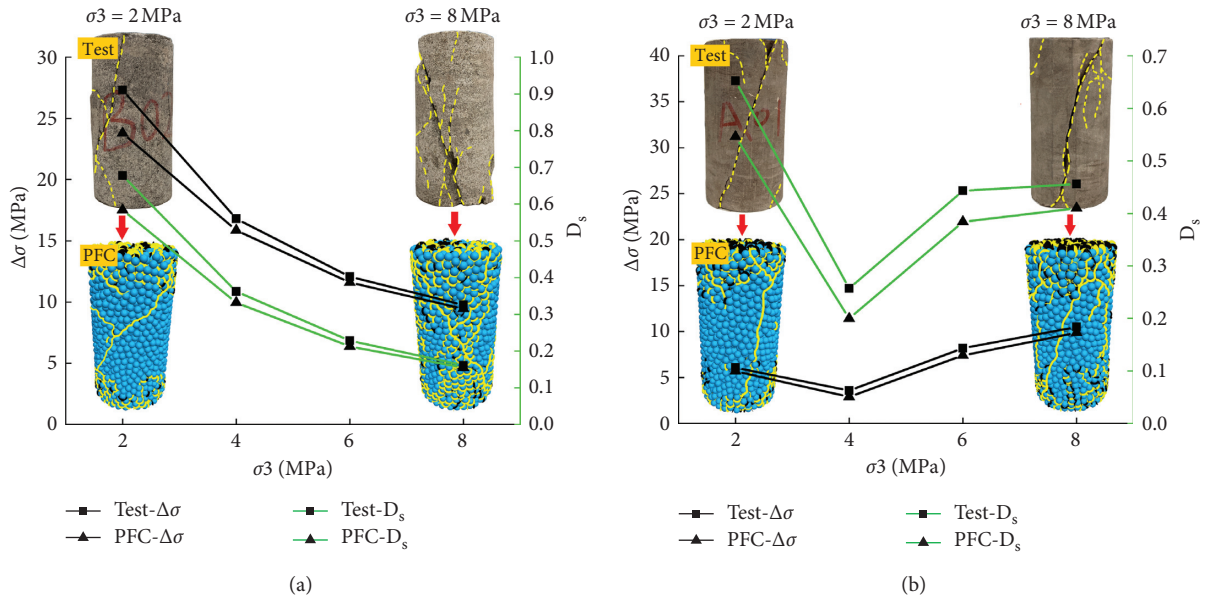
In the process of the numerical triaxial test, the damaged contact links were expressed in the form of disc joints (DNF\_disk), thereby forming damage cracks. The change law of strength attenuation value  $\Delta\sigma$ , strength attenuation coefficient  $D_s$ , and failure characteristics of the two rock samples is shown in Figure 7. With an increase of confining pressure,  $\Delta\sigma$  for sandstone recorded a gradual trend of decrease, consistent with the findings of Zuo et al. [26]. The  $D_s$  curve for sandstone recorded an obvious sharp decline (0.67 to 0.37) after a confining pressure of 2 MPa, after which the decline continued more slowly. This result indicates that the brittleness of sandstone gradually weakens with an increase of confining pressure, and the weakening ability of brittleness increases after a confining pressure of 2 MPa is reached.  $\Delta\sigma$  and  $D_s$  mudstone curves recorded a V-shaped change with increasing pressure (Figure 7(b)). When the curve dropped to a 4 MPa confining pressure,  $\Delta\sigma$  and  $D_s$  increased at the same time, by 7.05 MPa and 0.15, respectively; after 6 MPa, the rate of increase declined. This result indicates that, under a low confining pressure, due to large initial porosity, the brittleness of mudstone initially weakens and ductility is enhanced. Mudstone brittleness then increases, and ductility decreases at a high confining pressure.

Finally, the difference in  $\Delta\sigma$  and  $D_s$  between the two rocks is due to the difference in initial porosity and initial pore water content between sandstone and mudstone. It can be said that, under the same external conditions, the strength of mudstone is generally smaller than that of sandstone, and the initial porosity and initial pore water ratio are also greater than those of mudstone. Therefore, when the confining pressure of mudstone continues to increase, the pores will be compacted in the middle, the pore water will be discharged, and a new arrangement and combination of rock particles will be formed inside the rock. This makes the strength decay curve different from sandstone.

Analysis of the partial failure characteristics of the two rock samples shows that the failure mode of sandstone is a tensile failure; mudstone has a shear failure. There were numerous tensile cracks in the microscopic joints of the sandstone, with tensile fractures causing the main damage among individual grains. When the confining pressure was 2 MPa, mesocracks were generated from the bottom of the sandstone which gradually developed towards the top. Due to the low confining pressure, macroscopic shear cracks did not penetrate the top, and the top mesocracks developed slowly. When the confining pressure was 8 MPa, the bottom crack gradually expanded to the top, forming a penetrating macroscopic shear crack. The sandstone samples failed under this confining pressure; the number of cracks gradually increased as the confining pressure increased, finally forming rock failure characterized by a multiple crack staggered development. Mudstone specimens mostly recorded shear cracks in the microscopic joints, with the majority of fractures occurring between particles being shear failures. Under a confining pressure of 2 MPa, a single shear failure was recorded for the mudstone,

TABLE 1: Comparison of rock mechanics characteristics.

	Method	$\sigma_3$ (MPa)	$\sigma_1 - \sigma_3$ (MPa)	$\sigma_1$ (MPa)	$\sigma_r$ (MPa)	$c$ (MPa)	$\varphi$ ( $^\circ$ )
Mudstone	Test	2	9.3	11.3	3.2	1.32	32.53
		4	13.95	17.95	10.36		
		6	19.46	25.46	11.28		
		8	24.06	32.06	13.55		
	PFC	2	11.52	13.66	3.98	1.35	32.81
		4	14.18	18.18	11.28		
		6	19.81	25.81	12.41		
		8	23.97	31.97	14.09		
Sandstone	Test	2	41.31	43.31	15.00	8.14	38.42
		4	47.41	51.41	31.61		
		6	53.86	59.86	41.79		
		8	60.42	68.42	51.66		
	PFC	2	41.01	43.01	17.22	8.16	38.7
		4	47.57	51.57	31.71		
		6	53.87	59.87	42.27		
		8	61.13	69.13	51.68		

FIGURE 7: Comparison of rock attenuation value  $\Delta\sigma$ , attenuation coefficient  $D_s$ , and failure characteristics. (a) Sandstone. (b) Mudstone.

having fewer shear failure cracks and being characterized by obvious brittleness. The mudstone sample also recorded a few tension cracks from the base upwards. When the confining pressure increased to 8 MPa, microscopic cracks at the base and top gradually increased, propagating towards the middle. At this time, shear failure of mudstone cracks increased and became more obvious. The failure characteristics and strength attenuation law of the two kinds of rocks in the indoor test and the PFC test were basically the same, adhering to the law proposed by Chen [32]. Therefore, rationality of the material mesoscopic parameters was further verified.

**2.4.2. Triaxial Cyclic Loading Test and  $\beta$ -Parameter.** The sandstone cyclic triaxial test dynamic stress-strain curve and its failure characteristics (Figure 8) indicate that, under the

action of dynamic circulation, the peak stress intensity of the sandstone was obviously lower than that of the conventional triaxial. This result indicates that the compressive strength of the sandstone was weakened under dynamic load. Sandstone without cracks has instantaneous elastic deformation at the moment of loading, and its strain value is generally between 0 and 0.2%; the strain value of sandstone with cracks is between 0 and 0.1%. Under a certain confining pressure, sandstone gradually exhibits obvious creep properties as load applied by stepwise loading increases. Eventually, under the action of the last level of load, the sandstone appeared to be destroyed by an accelerated creep stage. Our results indicate that as the confining pressure increased, the number of loading levels also increased. As the confining pressure increased from 0 to 6 MPa, the axial load increased when creep failure occurred. As the increase of confining pressure

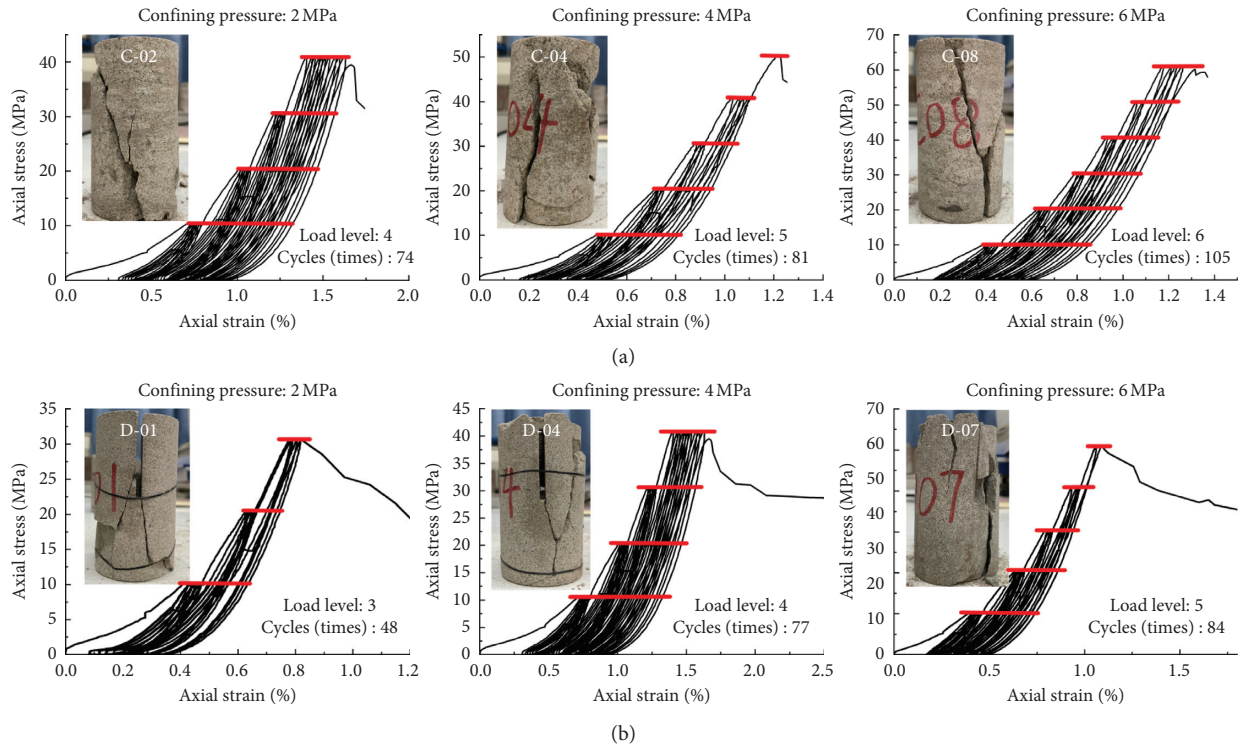


FIGURE 8: Cyclic triaxial dynamic stress-strain curve and failure characteristics. (a) Sandstone without cracks. (b) Sandstone with cracks.

improved the compressive strength of the sandstone, the occurrence of cracks resulted in the axial strain of the sandstone to increase. Under a confining pressure of 2 MPa, the number of cycles of sandstone with fractures was 36 times lower than that of sandstone without fractures, and the maximum peak stress declined by 10 MPa (25%). At a confining pressure of 4 MPa, the number of cycles of sandstone with fractures was reduced by four times compared with sandstone without fractures, and the maximum peak stress was reduced by 10 MPa (20%). At a confining pressure of 6 MPa, the number of cycles of sandstone with fractures was 31 times lower than that of sandstone without fractures, and the maximum peak stress declined by 10 MPa (16.7%). This result indicates that while the confining pressure increased, the yield strength of sandstone with fractures was one lower than that of sandstone without fractures, and it was more prone to failure under dynamic loads.

Analysis of failure characteristics indicates that sample C-02 has low confining pressure, low compressive strength, and low creep, and the sample is accompanied by partial tensile failure and primarily shear failure. As the confining pressure increased, the number of cycles increased stepwise and creep increased. Samples C-04 and C-08 recorded obvious simultaneous effects of tension and shear. In addition, tensile crack penetrated the entire sample, intersecting with the shear crack to form a Y-shaped crack in C-08. Results for cracked sandstone (Figure 8(b)) indicate that, when the low confining pressure is cyclically loaded, the

crack expands outwards in the form of a tensile crack along with the reserved fracture, finally intersecting with the shear crack and failing.

In the cyclic loading stage, the damping ratio  $\beta$  and the damping coefficient  $C$  of the rock sample changed, and the condition of the cracks will affect  $\beta$  and  $C$  of the sandstone. By using equations (4) and (5),  $\beta$  and  $C$  were calculated. In order to facilitate the analysis of the influence of cracks on damping parameters, two sets of hysteresis loops with different cracks under a high confining pressure of 6 MPa were selected to calculate  $\beta$  and  $C$ . Finally, the relationship between the damping parameters of the two sets of sandstone samples and the number of cycles was calculated (Figure 9).

Results in Figure 9 indicate that, under the same confining pressure, the damping coefficient  $C$  increases linearly with an increase in the number of cycles, and it is not affected by the increase of the load amplitude. In addition, the damping coefficient  $C$  of sandstone with fractures is five times lower than that of sandstone without fractures. The damping ratio  $\beta$  noticeably fluctuates under the action of cyclic loading with a confining pressure of 6 MPa, gradually decreasing as the number of cycles increases. The  $\beta$  of fractured sandstone is generally 0.1% lower than that of sandstone without fractures. Under a higher confining pressure, the damping coefficient  $C$  varies with cycle times in the opposite direction to the damping ratio  $\beta$ . This law is consistent with the results of Zhou [29], indicating that cracks have a degrading effect on the damping coefficient  $C$  of sandstone.



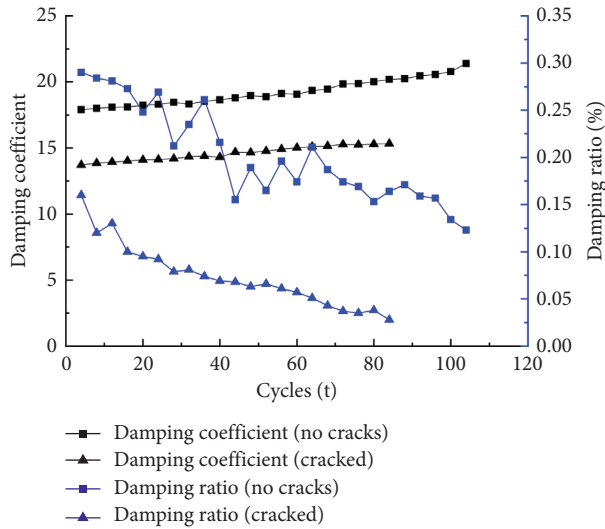


FIGURE 9: A 6 MPa confining pressure on the sandstone damping coefficient, the damping ratio, and the number of cycles.

2.4.3.  $\beta$  Mesoparameter Sensitivity Analysis. Results in Section 2.4.1 indicated that the attenuation value and attenuation coefficient of mudstone were relatively low in numerical experiments; results for sandstone were relatively high. This is because during the trial adjustment of the mesoparameters, those that affect rock brittleness mainly depend on the critical damping ratio  $\beta$ . The critical damping of mudstone is relatively low, and its brittleness is low in numerical tests; as the critical damping of sandstone is relatively high, it is therefore more brittle. Based on these conclusions, the following sensitivity analysis of  $\beta$ -mesoparameters of sandstone and mudstone was carried out.

(1)  $\beta_n$ -parameter sensitivity analysis: during the numerical triaxial test, under a constant confining pressure of 8 MPa with other bonding mesoparameters unchanged, normal critical damping ratio  $\beta_n$  of 0, 0.1, 0.2, 0.3, 0.4, 0.5, 0.6, 0.7, 0.8, 0.9, and 1.0 was used. Under different  $\beta_n$  values, the stress-strain curves of mudstone and sandstone materials were calculated (Figure 10).

Results indicate that  $\beta_n$  has an important influence on the peak strength of deviatoric stress of mudstone and sandstone. When  $\beta_n$  had a value of 0 to 1.0, the stress-strain curves of the two materials recorded an obvious “three-segment” distribution, and the curve trend was different. For mudstone, the increase of  $\beta_n$  resulted in peak deviatoric stress and residual stress to increase; results for strain recorded no significant influence. When  $\beta_n$  was 0, 0.1, 0.5, 0.6, 0.7, 0.8, and 1.0, the peak deviatoric stress of mudstone was the largest, being 10–12 MPa larger than the peak deviatoric stress under actual mudstone parameters. This result demonstrates that the value of  $\beta_n$  has an amplifying effect on the peak deviatoric stress of mudstone. When the  $\beta_n$  value was 0.2 and 0.3, the peak deviatoric stress and initial deviatoric stress of mudstone were moderate and consistent with the deviatoric stress under actual parameters, and the difference range was within 2 MPa. This indicates that the mesoscopic parameters of mudstone under  $\beta_n$  are the closest to the actual effect. When the  $\beta_n$  value was 0.4 and 0.9, the

strength of mudstone material was the lowest, and the peak deviatoric stress and initial deviatoric stress were 10–12 MPa lower than the actual value. The  $\beta_n$  value has a degrading effect on the strength of mudstone, and the initial deviatoric stress direction is abnormal, making the initial deviatoric stress value negative.

For sandstone, an increase in  $\beta_n$  reduced overall peak deviatoric stress and residual stress. The peak strain fluctuated slightly under different  $\beta_n$  values, and peak strain was the largest when  $\beta_n$  was 0.3. Considering the strength range, when  $\beta_n$  was 0.1, 0.4, and 0.9, the peak deviatoric stress of sandstone was the largest, being 5–6 MPa larger than the peak deviatoric stress under actual sandstone parameters, and the initial deviatoric stress was also larger than the actual one. This result indicates that the  $\beta_n$  value has an amplification effect on the peak deviatoric stress of sandstone, and the amplification value was within 10–12 MPa. When  $\beta_n$  was 0.2 and 0.3, the initial deviatoric stress and peak deviatoric stress of sandstone were closest to the actual value. Although the error was within 2 MPa, the strain was larger than the actual value. When adjusting these parameters, it is recommended that after these values are tested and adjusted, other mesoparameters need to be considered to continue to improve the strain calibration. When  $\beta_n$  was 0.5, 0.6, 0.7, and 1.0, the peak deviatoric stress was too small. In the same way, the  $\beta_n$  parameter under this condition had a degrading effect on sandstone and, with abnormal initial conditions, it is not recommended to be used in parameter sensitivity test adjustments.

For the process of judging whether the particle flow rock material is close to the real material, only using the peak stress and the values of  $c$  and  $\varphi$  as the judgment basis is not recommended. Rock ductility and brittleness should also be considered. Based on this, we also considered the sensitivity of  $\beta$ -parameters under the intensity attenuation value and intensity attenuation coefficient. The influence of  $\beta_n$  parameter on material brittleness (Figure 11) indicates that, within the range 0–0.3, the strength attenuation value of sandstone is 12–15 MPa larger than that of mudstone, and a slight upward “U”-shaped fluctuation occurs with the attenuation coefficient. Here, the  $\beta_n$ -parameter has little effect on the strength attenuation value and attenuation coefficient of the two materials, that is, the brittleness and ductility of the material remain unchanged. When  $\beta_n$  increased to 1.0, the intensity attenuation value and attenuation coefficient significantly fluctuated as the damping ratio increased. The attenuation value of sandstone increased to 42.24 MPa when  $\beta_n$  had a value of 0.4, and the attenuation coefficient increased to 0.68. At this time, the mudstone attenuation value did not fluctuate. This result indicates that the  $\beta_n$  value greatly improved the brittleness of the two kinds of rocks, and sandstone was more sensitive. When  $\beta_n$  reached 0.5, the attenuation value of sandstone significantly dropped to 22.19 MPa (the attenuation coefficient dropped to 0.52); the attenuation value of mudstone began to increase to 25.63 MPa, and the attenuation coefficient decreased. Although this result shows that  $\beta_n$  at this moment had greatly improved the ductility of sandstone and decreased its brittleness, its sensitivity to mudstone was not high. By

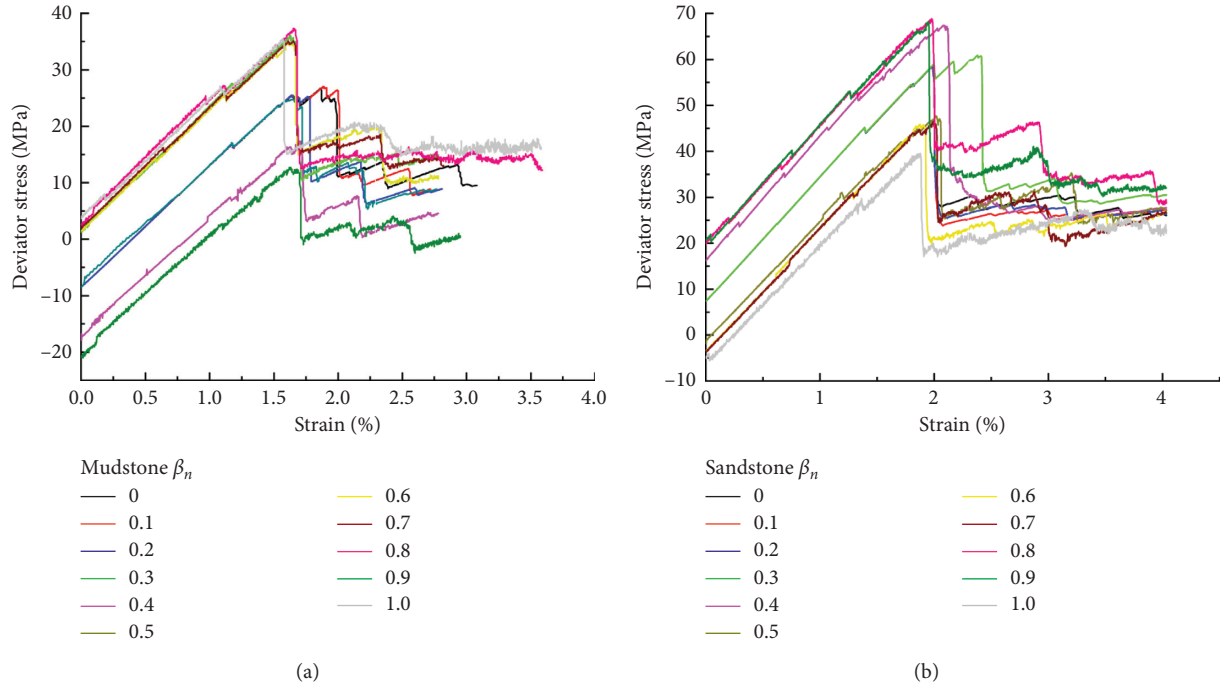


FIGURE 10: Two kinds of rock stress-strain curves under different  $\beta_n$ . (a) Mudstone. (b) Sandstone.

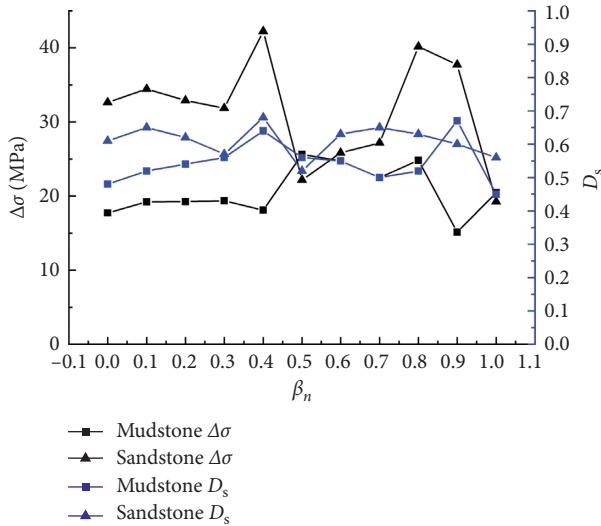


FIGURE 11: Intensity attenuation  $\Delta\sigma$  and intensity attenuation coefficient  $D_s$  of the two rocks under different  $\beta_n$ .

taking all of our results into consideration, brittleness of the two rock materials was relatively stable when the  $\beta_n$  value was 0–0.3 and the parameter value ranged between 0 and 1.0. At the same time, the trial adjustment of the  $\beta_n$ -parameter between 0.2 and 0.3 was closer to the actual value, and the macroscopic mechanical properties were more stable.

(2)  $\beta_s$ -parameter sensitivity analysis: as for the sensitivity analysis of the normal critical damping ratio  $\beta_n$ , confining pressure was maintained at 8 MPa and other bonding meso-parameters were unchanged during  $\beta_s$ -parameter sensitivity analysis. The shear critical damping ratio  $\beta_s$  was taken as 0, 0.1, 0.2, 0.3, 0.4, 0.5, 0.6, 0.7, 0.8, 0.9, and 1.0 (Figure 12).

As seen in Figure 12, the peak deviatoric stress of mudstone and sandstone materials did not significantly change with an increase in  $\beta_s$ , and it was consistent with the deviatoric stress under the actual macroscopic test. This result indicates that the shear damping ratio had no great influence on the macroscopic yield strength of the two materials, and there was no need to consider its influence on the peak deviatoric stress during the mesoscale trial adjustment. The influence of  $\beta_s$ -parameter on material brittleness is shown in Figure 13.

$\beta_s$ -parameter had a certain influence on the brittleness of the two rock materials. For mudstone, the strength attenuation value and attenuation coefficient showed a “wave-shaped” change as  $\beta_s$  increased. When  $\beta_s$  was 0.1, the maximum attenuation value and attenuation coefficient reached 19.33 MPa and 0.54, respectively, and the minimum attenuation value and attenuation coefficient were 15.1 MPa and 0.43 when  $\beta_s$  was 0.7, respectively. In the process of parameter trial adjustment, the range can be set within 0.1~0.7, and the selection was based on the strength attenuation coefficient obtained from the indoor test. For sandstone, as  $\beta_s$  increased, the strength attenuation curve recorded an “arch” change. When the  $\beta_s$  value was 0.2, the brittleness of sandstone increased from 0.53 to 0.65 before remaining stable; when  $\beta_s$  was 0.6, brittleness decreased to 0.53. According to the attenuation coefficient obtained from the indoor test, it was observed that the  $\beta_s$ -parameter was within the range of 0.2 to 0.6 as a reasonable and sensitive test adjustment range. At this time, brittleness of the sandstone material was closest to the real material.

2.4.4. Mesoparameter Calibration. Based on the above quantitative and qualitative analysis, the final meso-parameters of mudstone and sandstone materials are shown

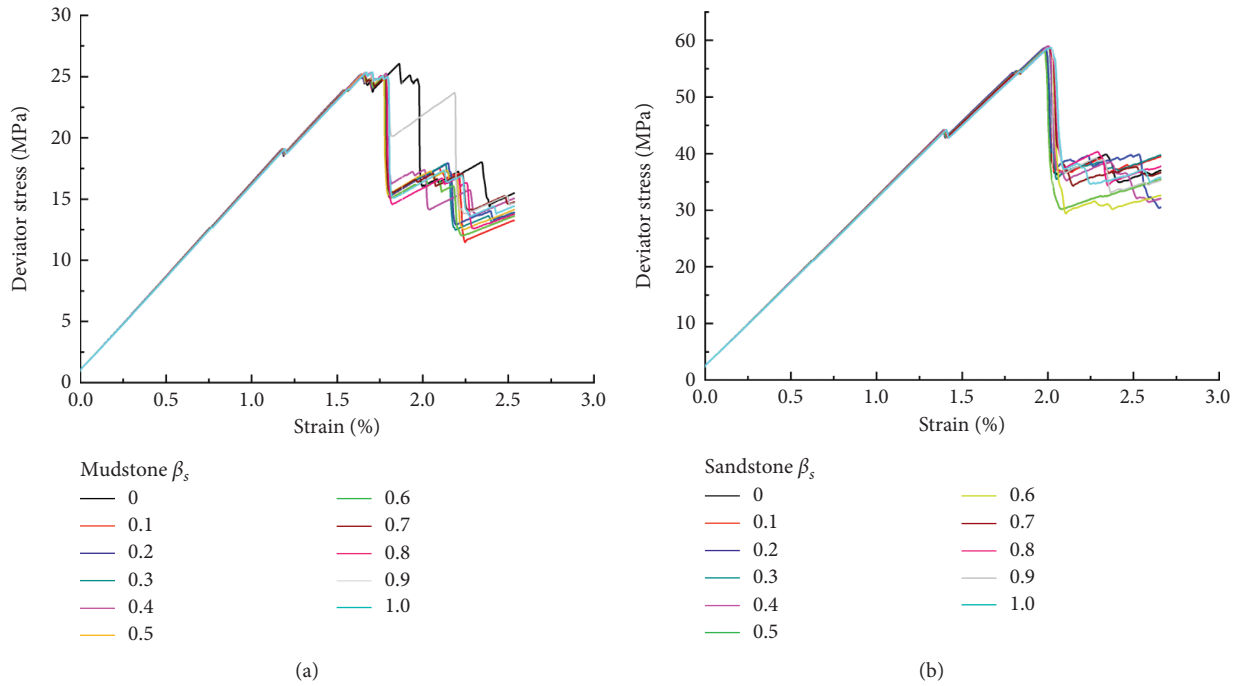


FIGURE 12: Mudstone (a) and sandstone (b) stress-strain curves under different  $\beta_s$  values.

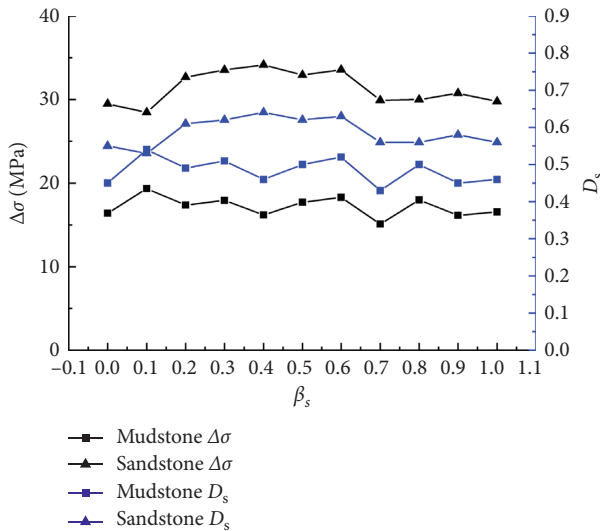


FIGURE 13: Intensity attenuation  $\Delta\sigma$  and intensity attenuation coefficient  $D_s$  of the two rocks under different  $\beta_s$  values.

in Table 2. With reference to previous studies [33, 34], the structure of surface mesoparameters (Table 3) was confirmed.

### 3. Dangerous Rock Model

**3.1. Model Establishment.** In this study, we used a typical steep slope of dangerous rock on Provincial Highway 205, Beichuan Qiang Autonomous County, Sichuan Province, China (Figure 14), as a case study. The 2008 Wenchuan Earthquake in Sichuan caused a series of instabilities, resulting in the collapse of dangerous rocks posing a

significant threat to the safe operation of the provincial highway and nearby residents. After a detailed geological survey, the steep slope of dangerous rock (about 23 m high) was restored. The upper rock mass is composed of feldspar sandstone with good integrity, about 16 m high, with a natural bulk density of  $24.7 \text{ kg/m}^3$  and a fracture toughness of  $26.0 \text{ MPa m}^{1/2}$ ; the lower rock mass is mudstone with poor integrity, being about 7 m high with a natural bulk density of  $25.3 \text{ kg/m}^3$ . The fracture penetration rate is 25%, and four sandstone layers were identified in the rock mass, including two main control structural planes. According to the chain law of rock slope [35], the external macrochain was called the No. 1 chain, and the internal macrochain was the No. 2 chain. Each macrochain contains four microchains, and the dangerous rock masses are numbered from bottom to top (the first chain was 1-1, 1-2, 1-3, and 1-4, and the second chain was 2-1, 2-2, 2-3, and 2-4).

According to survey results of on-site dangerous rocks, reasonable generalizations were made for this investigation. PFC3D was used to establish a particle flow model for dangerous rock slopes in three dimensions (Figure 15). Here, the formation of the rock joint surface adopted artificial synthetic rock mass technology [36], and the linear parallel bond model was selected as the internal contact model of the rock; the smooth-joint contact model was the contact model of the joint surface between the rocks.

The seismic model under the coupling action of transverse waves and longitudinal waves has an amplifying effect on stability, and the probability of both acting at the same point at the same time is small. It was therefore decided to use the first 20 s acceleration curve (Figure 16) of the real EW transverse wave monitored in Wolong during the

TABLE 2: Mesoscopic parameters of sandstone and mudstone materials.

Lithology	$d$ (mm)	$P$ ( $\text{kg} \cdot \text{m}^{-3}$ )	$E_c$ (GPa)	$Kc^*$	$\mu$	$\lambda$	$K^*$	$E_b$ (GPa)	$\sigma_c$ (MPa)	$c$ (MPa)	$\beta_n$	$\beta_s$
Mudstone	0.24	3100	2	1.0	0.8	1.00	1.0	20	18	28	0.2	0.2
Sandstone	0.26	3000	3	1.0	0.6	1.01	1.0	30	20	35	0.3	0.6

TABLE 3: Mesoscopic parameters of the structural plane.

Structural plane type	$sj\_kn$ ( $\text{N} \cdot \text{m}^{-1}$ )	$sj\_ks$ ( $\text{N} \cdot \text{m}^{-1}$ )	$sj\_mu$	$sj\_c$ (MPa)	$sj\_phi$ ( $^\circ$ )
Horizontal structure plane	10	1	0.7	0.3	10
Vertical structure plane	10	1	0.3	0	8

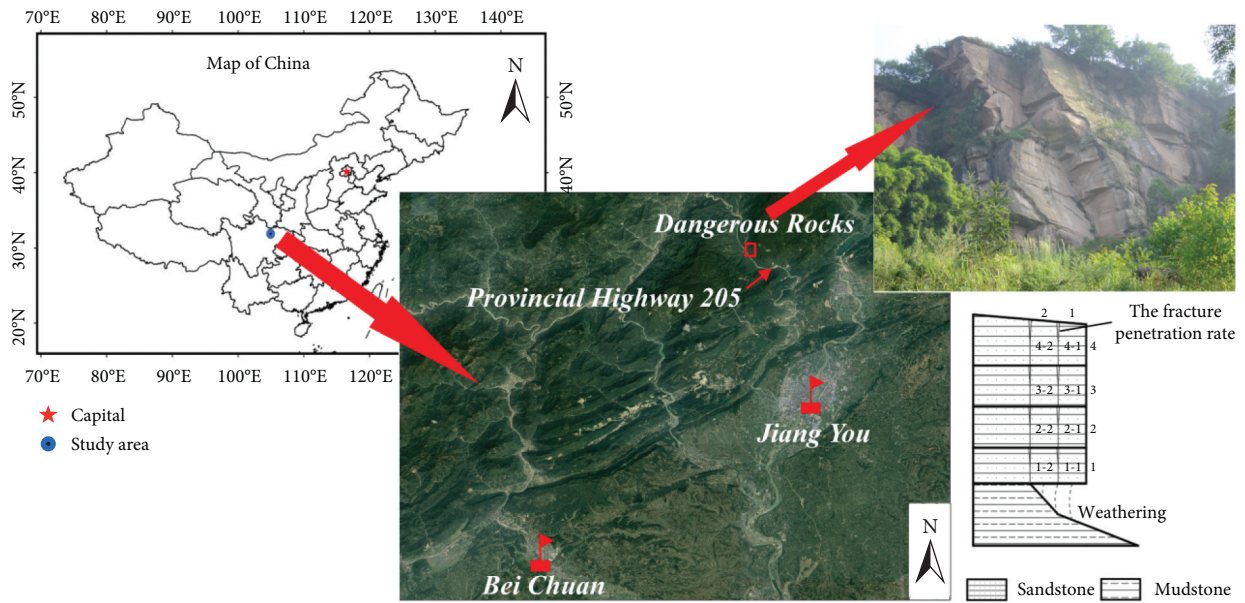


FIGURE 14: Damaged rock on Provincial Highway 205, Beichuan Qiang Autonomous County, Sichuan Province, China.

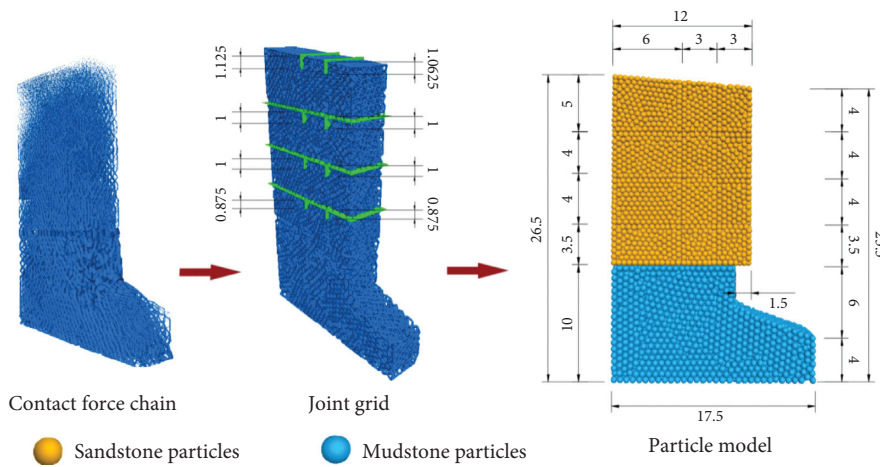


FIGURE 15: Slope force chain and joint grid layout (unit: m).

Wenchuan earthquake as the seismic input. When applying seismic action, in order to prevent seismic waves from reflecting at the boundary of the model, a viscous boundary

condition is required [37]. In PFC3D, this was achieved by setting dampers in the normal and tangential directions of the two sides and the bottom boundary of the model, as

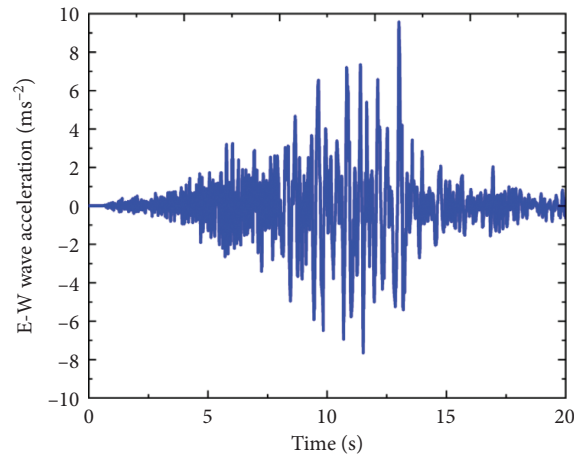


FIGURE 16: E-W wave acceleration-time history curve.

shown in Figure 17. During the loading process, seismic acceleration was transformed into boundary acceleration, resulting in the model particles to vibrate.

### 3.2. Seismic Damage Analysis of Dangerous Rock Model

**3.2.1. Failure Mode Analysis.** The destruction process of the dangerous rock model under a 20 s earthquake is shown in Figure 18. Model results indicate that, between a seismic shear wave time of 0 and 6 s, the rock mass did not undergo significant deformation or damage. At the same time, crack development in the lower mudstone was not recorded and slope stability was generally good. Comparison with the particle velocity cloud map indicated that the maximum particle movement velocity was concentrated on the bottom rock mass 1-1 and rock mass 1-2 at 3 s. At 6 s, the maximum particle velocity was transferred to the second and third layers of rock, indicating that, before the rock mass was destroyed, the failure trend was concentrated between the first and third layers. When calculation time reached 9 s, the seismic acceleration curve gradually peaked (see Figure 8). Here, the internal structural surface contact model of Nos. 1-1, 2-2, and 3-2 dangerous rocks was locally fractured, and cracks in rock mass 1-2 gradually developed. Approximately 10 s later, the 1-2 rock mass fractured. In addition, the top rock layer began to move, accompanied by the fracture of the smooth joint model between the layers. The particle velocity at this moment was the largest relative to the velocity at other moments, and the failure trend was concentrated between the first and third rock mass layers. When the earthquake rupture time was 11.5 s, the internal vertical rock mass fell outward as a whole, colliding with the external vertical rock mass, being pulled apart. Because of this movement, fissures between the rock masses were further enlarged. In addition, due to gravity and seismic action of the upper rock mass, particles in the lower mudstone base began to disintegrate. At 20 s, due to the interaction of adjacent rock blocks at the bottom under the earthquake, the top rock block (No. 4-1) broke locally. As this rock block was located on the lower rock mass, it therefore fluctuated with the earthquake. At the

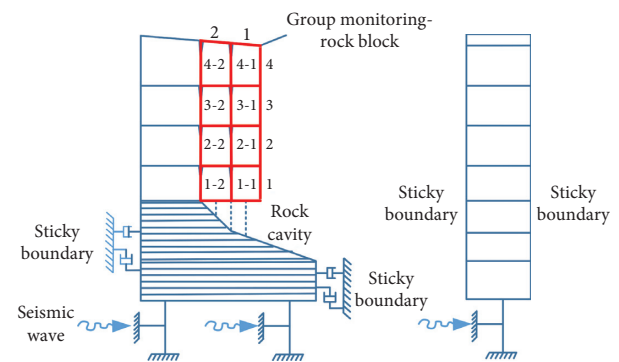


FIGURE 17: Boundary conditions for the dynamic calculation.

same time, the rest of the rock masses, except for No. 4-2, had a tendency to bulge outwards as a whole. However, based on the support of the upper and lower rock masses, no rock mass collapse occurred. In summary, the dangerous rock of Provincial Highway 205 in the high-intensity area will undergo slight instability failure under the action of a traverse EW-wave 20 s strong earthquake, and the failure mode will be a tensile fracture-horizontal slip failure.

In order to further verify the rationality of the rock material mesoparameters and the seismic damage of the PFC dangerous rock model, we introduced two other dangerous rock failure maps in the area (Figure 19). It can be seen that after the Wenchuan earthquake, the failure mode of the real dangerous rock was basically consistent with the failure mode of the earthquake simulated in our study.

**3.2.2. Displacement Analysis.** Monitoring the vertical and horizontal displacement of the rock block in this study provides further information on the failure mode and stability of the rock block. Model displacement in the vertical  $z$ -direction and horizontal  $y$ -direction (Figure 20) indicate that there is no sign of rock collapse or falling during the earthquake action period; the displacement value was recorded to be very small. Negative vertical displacement (distributed between 0 and 0.4 m) and

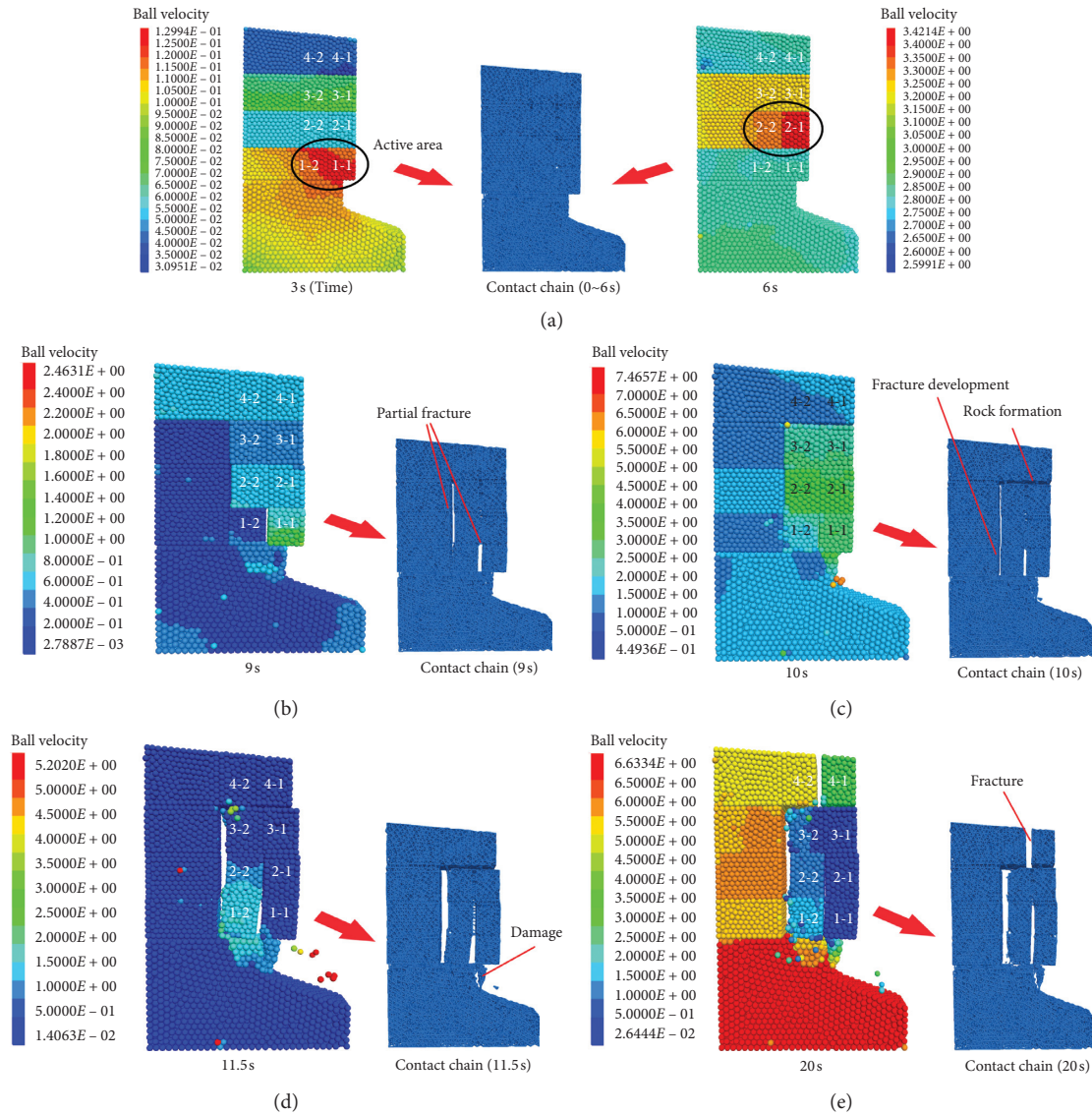


FIGURE 18: The failure process of the dangerous rock model under different earthquake durations. (a) 0~6 s, (b) 9 s, (c) 10 s, (d) 11.5 s, and (e) 20 s.

positive horizontal displacement (distributed between 0 and 1.2 m) values indicate that the failure characteristics of the model in the vertical and horizontal directions are small, and the impact of earthquakes in the horizontal direction is relatively large. No vertical displacement change was recorded between 0 and 9 s in the calculation time. In addition, the particles of each rock block all have horizontal  $y$ -direction displacement fluctuations with the action of shear waves, and the amplitude of the fluctuations increases as seismic action time extended. During this period, there was also no sign of damage to the slope, indicating a stable state. After 8.5 s, displacement of each rock block in Model 1 fluctuated with a small frequency in the vertical direction before slowly declining after 11 s. At this time, horizontal displacement to the right gradually increased, with a maximum value of 1.2 m distributed in the top rock block No. 4-1. After the calculation, displacement in both directions of the 1-1 rock block continued to increase, and the vertical and

horizontal displacement curves of the remaining rock blocks tended to be flat. Results in Figure 18 indicate that the rock block was damaged and fractured during this period. Although the mudstone base cracked and stability gradually decreased, caving and rolling failure did not occur. Based on the damage trend, it can be judged that rock blocks 4-1 and 1-1 will be the most likely to fall. It should be noted that the vertical displacements of No. 1-2 and No. 3-2 rock masses are large, possibly due to adjacent rock masses colliding and squeezing each other, resulting in surface rock mass particles to break and fall off.

**3.2.3. Analysis of Unbalanced Force of the Rock Block.** By analyzing the failure modes of various slope models under earthquake conditions, it is accepted that the dynamic interaction of rock blocks is an important factor causing rock

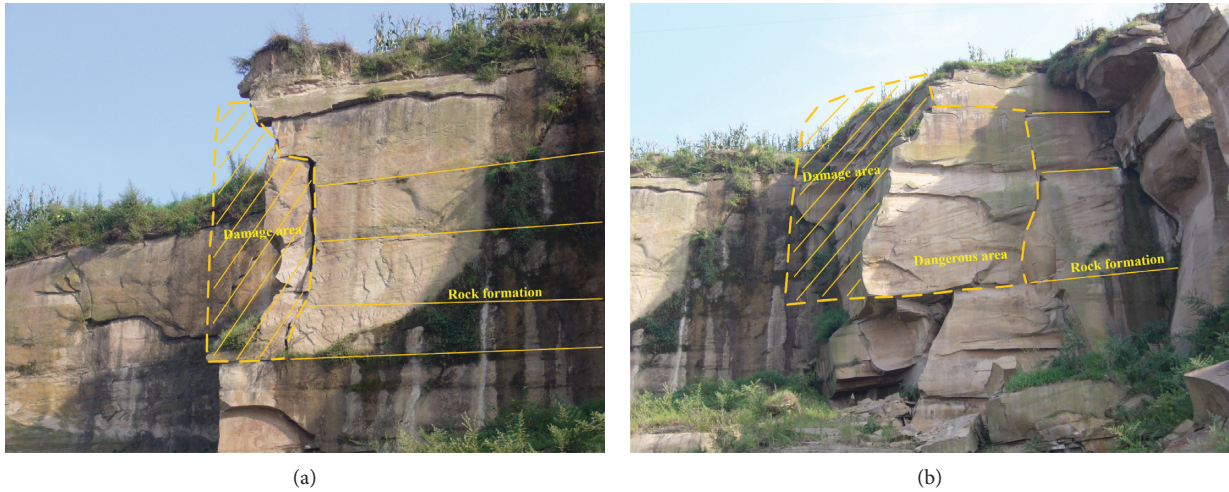


FIGURE 19: On-site destruction of #3 and #4 dangerous rock slopes. (a) #3. (b) #4.

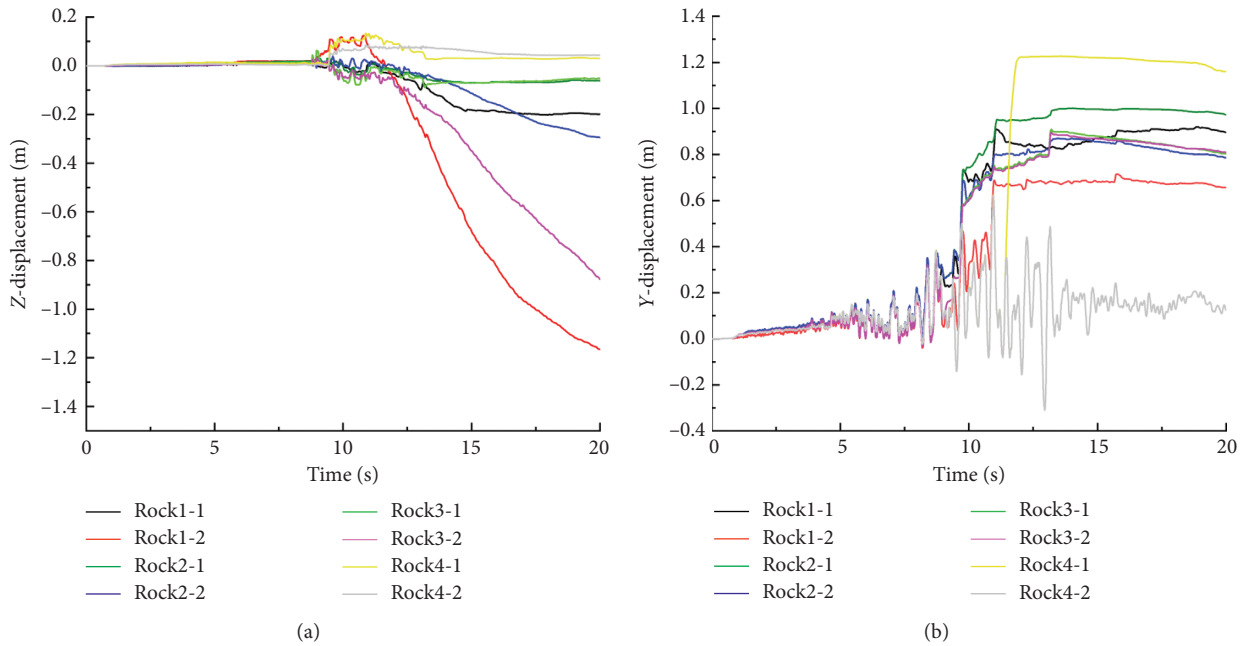


FIGURE 20: Time history curve of model displacement. (a) Vertical  $z$ -direction displacement. (b) Horizontal  $y$ -direction displacement.

mass collapse. In PFC, the unbalanced force of the particle not only represents the size of the contact force chain around the particle but also includes the tension and compression of the interlayer load and adjacent rock blocks. Therefore, the unbalanced force in each rock block can represent the magnitude and direction of the load on each rock block. The unbalanced force fluctuation curve of each rock block, obtained using *in situ* monitoring, is shown in Figure 21. In the vertical  $z$ -direction, the rock mass unbalanced force

predominantly fluctuates between 8 and 13 seconds. This wave phenomenon is caused by rocks caving and colliding with each other. The vertical upward peak unbalanced force generated by the fracture was 230 kN, generated by rock block 4-1; the vertical downward peak unbalanced force was 350 kN, generated by rock blocks 1-2 and 3-2. The maximum horizontal  $y$ -direction unbalanced force was distributed in rock blocks 1-2, and the peaks were concentrated in the maximum seismic acceleration interval. It can be seen that

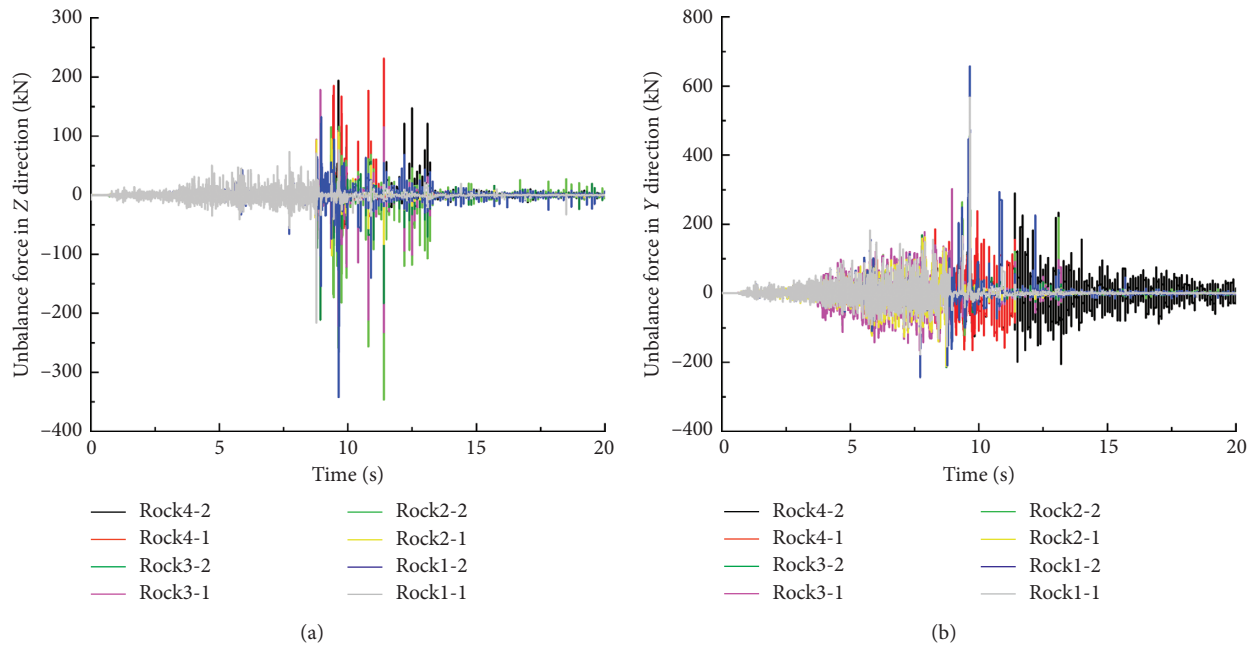


FIGURE 21: Time history curve of unbalanced force. (a) Vertical z-direction. (b) Horizontal y-direction.

collisions of Nos. 4-1, 1-2, and 3-2 rock blocks are the most violent under the action of an earthquake, especially rock block 1-2.

#### 4. Conclusions

Based on the principle of discrete element particle flow, we conducted an in-depth analysis of the mechanical characteristics and mesoparameters ( $\beta$ -parameters) of rock materials through dynamic and static triaxial tests of sandstone and mudstone. Findings from this investigation enhance the reliability of rock material mesoparameter calibration technology. Furthermore, a more realistic and reliable dangerous rock model compared to previous studies was presented, with seismic stability analysis undertaken. Conclusions from this study are as follows:

- (1) The brittleness of sandstone gradually weakened with an increase in confining pressure, with brittleness weakening more severely after a confining pressure of 2 MPa. In addition, the characteristic value of mudstone brittleness attenuation recorded a V-shaped change with increasing confining pressure. Under low confining pressure, the brittleness of mudstone was preferentially weakened and ductility was enhanced. Under high confining pressure, the brittleness of mudstone was enhanced and ductility decreased. During the PFC numerical three-axis test, mudstone particles were recorded to undergo shear failure and the sandstone particles underwent tensile failure. The failure characteristics of the two types of rocks in the PFC numerical test are in accordance with results from an indoor test.
- (2) Fissures have a degrading effect on  $\beta$  and  $C$  of sandstone. When the rock fails, the dynamic

compressive strength of sandstone with cracks is one lower than that of sandstone without cracks. The peak stress of the compressive strength of the former is reduced by 16.7%~25% compared with the latter. This finding indicates that sandstone, especially sandstone with many cracks, is more prone to damage under dynamic load. Under the same confining pressure, the damping coefficient increases linearly with the increase of the number of cycles, and it is not affected by the increase of the loading amplitude. The damping coefficient of sandstone with fractures is generally lower than that of sandstone without fractures by a factor of five.

- (3) During the trial adjustment of mesoparameters, the peak deviatoric stress and  $c - \varphi$  value are not the only criteria for judging the authenticity of materials. The effect of material brittleness is equally important to mesoparameters and cannot be ignored. In addition, the mesoparameters of rock brittleness mainly depend on the damping ratio  $\beta$ . Mudstone has a relatively low  $\beta$  and low brittleness whereas sandstone has a high  $\beta$  and high brittleness. In rock materials,  $\beta_n$  is more sensitive than  $\beta_s$ . The value of the  $\beta_n$ -parameter was between 0.2 and 0.3, and the value of  $\beta_s$ -parameter was between 0.2 and 0.6. Rock brittleness was more stable and the reflected macroscopic mechanical properties were more realistic. With an increase of  $\beta_s$ ,  $\Delta_s$  and  $D_s$  of mudstone indicated “wave-shaped” changes. In contrast, sandstone recorded “arch” changes.
- (4) After an in-depth analysis of mesoparameters, the failure mode of the PFC dangerous rock model of Provincial Highway 205 under the simulated Wenchuan earthquake was a tensile fracture-horizontal



slip failure. The simulated failure mode was basically consistent with results recorded for the real dangerous rock. Combined with displacement analysis, the failure trend was concentrated between the first layer to the third layer of the rock mass. The failure characteristics of the model in the vertical and horizontal directions were small, and the horizontal influence was relatively large. In addition, the dangerous rock did not eventually collapse and fall in a large area. It is judged that rock blocks 4-1 and 1-1 are likely to fall in the later stage of an earthquake. Combined with analysis of the unbalanced force, collisions of rock blocks 4-1, 1-2, and 3-2 are the most violent under the action of the earthquake, especially rock block 1-2.

### Data Availability

The table and figure data used to support the findings of this study are available from the corresponding author upon request.

### Conflicts of Interest

The authors declare that they have no conflicts of interest.

### Acknowledgments

This work was financially supported by the National Key Research and Development Project (2016YFC0802203), National Natural Science Foundation (51678097), Science and Technology Research Project of Chongqing Municipal Education Commission (KJQN201800706), and the General Project of Chongqing Natural Science Foundation (cstc2020jcyj-msxmX0218). The authors would like to express their gratitude to EditSprings (<https://www.editsprings.com/>) for the expert linguistic services provided.

### References

- [1] L. F. Wang, H. M. Tang, and F. Tang, "Three-dimensional stability analysis of complex gently inclined rock mass slope," *China Journal of Highways*, vol. 31, pp. 57–66, 2018.
- [2] A. Azzon, G. La Barbera, and A. Zanietti, "Analysis and prediction of rockfalls using a mathematical model," *International Journal of Rock Mechanics and Mining Sciences and Geomechanics Abstracts*, vol. 32, pp. 709–724, 1995.
- [3] H. K. Chen, "Geomorphological Interpretation of the chain law of dangerous rocks in the three gorges reservoir area," *Journal of Chongqing Jiaotong University (Natural Science Edition)*, vol. 27, pp. 91–94, 2008.
- [4] H. M. Tang, H. K. Chen, and L. F. Wang, "Study on mechanism of dangerous rock caving on rocky steep slope," *Metal Mine*, vol. 392, pp. 40–45, 2009.
- [5] H. M. Tang, H. K. Chen, and L. F. Wang, "Dangerous base collapsed cliff on a dangerous base," *Geotechnical Engineering*, vol. 3, pp. 205–210, 2010.
- [6] G. Z. Yan, C. Jie, and S. Yu, "Earthquake response and sliding displacement of submarine sensitive clay slopes," *Engineering Geology*, vol. 227, pp. 69–83, 2017.
- [7] X. F. Huang, Y. B. Zhang, and X. Q. Zhao, "Preliminary discussion on the movement characteristics of dangerous rock collapse under earthquake conditions," *Rock and Soil Mechanics*, vol. 38, pp. 583–592, 2017.
- [8] K. Zhao, Y. W. Zeng, and C. Zeng, "Stability analysis of rock slope with weak structural surface based on particle flow method," *Science Technology and Engineering*, vol. 18, pp. 97–102, 2018.
- [9] C.-L. Tang, J.-C. Hu, M.-L. Lin, R.-M. Yuan, and C.-C. Cheng, "The mechanism of the 1941 Tsaoling landslide, Taiwan: insight from a 2D discrete element simulation," *Environmental Earth Sciences*, vol. 70, no. 3, pp. 1005–1019, 2013.
- [10] Y. Cong, Z. Q. Wang, and Y. R. Zheng, "Experimental study on microscopic parameters of brittle materials based on particle flow theory," *Chinese Journal of Geotechnical Engineering*, vol. 37, pp. 1031–1040, 2015.
- [11] M. M. He, N. Li, and W. S. Chen, "Damping ratio and damping coefficient of rock under different cyclic loading conditions," *Rock and Soil Mechanics*, vol. 38, pp. 2531–2538, 2017.
- [12] Y. H. Huang, S. Q. Yang, and Y. Ju, "Experimental study on mechanical behavior of rock-like materials containing pre-existing intermittent fissures under triaxial compression," *Chinese Journal of Geotechnical Engineering*, vol. 38, pp. 1212–1220, 2016.
- [13] J. Zhou, Y. X. Wang, and Y. F. Zhou, "Macro-micro evolution mechanism on sandstone failure in triaxial compression test based on PFC2d," *Journal of China Coal Society*, vol. 42, pp. 76–82, 2017.
- [14] Z. C. Tang and Y. B. Zhang, "Temperature-dependent peak shear-strength criterion for granite fractures," *Engineering Geology* 2020, vol. 269, Article ID 105552, 2020.
- [15] Z. C. Tang, Q. Z. Zhang, and J. Peng, "Effect of thermal treatment on the basic friction angle of rock joint," *Rock Mechanics and Rock Engineering*, vol. 53, no. 4, pp. 1973–1990, 2020.
- [16] Z. C. Tang, "Experimental investigation on temperature-dependent shear behaviors of granite discontinuity," *Rock Mechanics and Rock Engineering*, vol. 53, no. 9, pp. 4043–4060, 2020.
- [17] Z. Tang and Y. Jiao, "Choosing appropriate appraisal to describe peak-spatial features of rock-joint profiles," *International Journal of Geomechanics*, vol. 20, no. 4, Article ID 4020021, 2020.
- [18] J. Zou, Y.-Y. Jiao, Z. Tang, Y. Ji, C. Yan, and J. Wang, "Effect of mechanical heterogeneity on hydraulic fracture propagation in unconventional gas reservoirs," *Computers and Geotechnics* 2020, vol. 125, Article ID 103652, 2020.
- [19] L. J. Wang, *Numerical Analysis on Characteristics of Reinforced Soil Retaining Wall Based on Particle Flow Code*, Chongqing Jiaotong University, Chongqing, China, 2019.
- [20] J. J. Tian and J. S. Sun, "Influence of spring and sticky kettle parameters on deformation features in particle flow numerical simulation of rock creep," *Safety and Environmental Engineering*, vol. 26, pp. 202–206, 2019.
- [21] Y. H. Huang and S. Q. Yang, "Particle flow simulation of macro- and meso- mechanical behavior of red sandstone containing two pre-existing non-coplanar fissures," *Chinese Journal of Rock Mechanics and Engineering*, vol. 33, pp. 1644–1653, 2014.
- [22] S. C. Wu, Y. Zhou, and B. Gao, "Study of unloading tests of rock burst and pfc3d numerical simulation," *Chinese Journal of Rock Mechanics and Engineering*, vol. 29, pp. 4082–4088, 2010.

- [23] L. Jin and Y. W. Zeng, "Refined simulation for macro-and meso-mechanical properties and failure mechanism of soil-rock mixture by 3D DEM," *Chinese Journal of Rock Mechanics and Engineering*, vol. 37, pp. 1540–1550, 2018.
- [24] Y. B. Deng, Y. P. Yang, and D. D. Shi, "Refinement and application of variable particle-size methods in 3D discrete element modelling for large-scale problems," *Chinese Journal of Geotechnical Engineering*, vol. 39, pp. 62–70, 2017.
- [25] G. Zheng, X. S. Cheng, and Y. Diao, "Discrete element simulation and redundancy analysis of excavation collapse," *Rock and Soil Mechanics*, vol. 35, pp. 573–583, 2014.
- [26] J. P. Zuo, Y. Cheng, and J. W. Zhang, "Failure behavior and strength characteristics of coal-rock assembly under different confining pressures," *Journal of China Coal Society*, vol. 41, pp. 2706–2713, 2016.
- [27] J. F. Labuz and A. Zang, "Mohr-coulomb failure criterion," *Rock Mechanics and Rock Engineering*, vol. 45, no. 6, pp. 975–979, 2012.
- [28] J. Peng, G. Rong, and M. Cai, "Determination of residual strength of rocks by a brittle index," *Rock and Soil Mechanics*, vol. 26, pp. 403–408, 2015.
- [29] J. B. Zhou, *Research on Dynamic Stability of Cracked Structure Rock Mass and Seismic Reinforcement in Strong Earthquake Zone*, Chengdu University of Technology, Chengdu, China, 2012.
- [30] J. Xu, Q. S. Li, and G. L. Li, "Experimental research on damping parameters of rock under cyclic loading," *Chinese Journal of Rock Mechanics and Engineering*, vol. 29, pp. 1036–1041, 2009.
- [31] X. H. Cheng, "Discrete element analysis for size effects of coarse-grained soils," *Rock and Soil Mechanics*, vol. 30, pp. 287–292, 2009.
- [32] Y. Chen, *Study on Deformation Failure Behaviors and Non-linear Models for Rocks under the Influence of Mining Disturbance*, China University of Mining and Technology, Xuzhou, China, 2018.
- [33] K. Bian, J. Liu, and X. J. Hu, "Study on failure mode and dynamic response of rock slopes with intermittent joints and intermittent joints under earthquake action," *Rock and Soil Mechanics*, vol. 39, pp. 3029–3037, 2018.
- [34] X. J. Hu, K. Bian, and P. C. Li, "Particle flow simulation of seismic dynamic failure process of horizontal thick layered rock slope," *Chinese Journal of Rock Mechanics and Engineering*, vol. 36, pp. 2156–2168, 2017.
- [35] H. K. Cheng and H. M. Tang, "Chained mechanism and moving routine for perilous rock toavalanche in the area of the three gorges reservoir of China," in *Proceedings of China Association for Science and Technology*, pp. 501–506, Beijing, China, January 2006.
- [36] Z. Cui and Q. Sheng, "Numerical modelling of structural effect of equivalent mechanical parameters of fractured rock mass," *Rock and Soil Mechanics*, vol. 39, pp. 3830–3840, 2018.
- [37] X. T. Zhou, Q. Sheng, and X. L. Leng, "Viscous artificial boundary for seismic dynamic time-history analysis with granular discrete element method and its application," *Chinese Journal of Rock Mechanics and Engineering*, vol. 36, pp. 928–939, 2009.

## Research Article

# Application of Digital Image Correlation Technique for the Damage Characteristic of Rock-like Specimens under Uniaxial Compression

Jing Chai,<sup>1,2</sup> Yongliang Liu ,<sup>1</sup> YiBo OuYang,<sup>1</sup> Dingding Zhang,<sup>1,2</sup> and Wengang Du<sup>1</sup>

<sup>1</sup>School of Energy, Xi'an University of Science and Technology, Xi'an, Shaanxi 710054, China

<sup>2</sup>Western Key Laboratory of Mine Mining and Disaster Prevention, Ministry of Education, Xi'an University of Science and Technology, Xi'an, Shaanxi 710054, China

Correspondence should be addressed to Yongliang Liu; [yliu.xust@gmail.com](mailto:yliu.xust@gmail.com)

Received 1 August 2020; Revised 29 October 2020; Accepted 2 November 2020; Published 7 December 2020

Academic Editor: Zhi Cheng Tang

Copyright © 2020 Jing Chai et al. This is an open access article distributed under the Creative Commons Attribution License, which permits unrestricted use, distribution, and reproduction in any medium, provided the original work is properly cited.

The damage and degradation are the main influence factors of the instability of rock mass engineering. In this paper, the damage and deformation characteristics of the rock-like samples are investigated under the uniaxial compression test, and the advanced digital image correlation (DIC) device is devoted to full-field deformation data acquisition on the sample surface. Based on the full-field deformation data, a new damage variable is proposed by the principal strain standard deviation to characterize the uniaxial compression damage process of the rock-like samples. The results show that the newly presented damage variable can be utilized for the quantitative characterization of the sample damage. According to the characteristics of the damage variable, the damage evolution process of the rock-like specimens under uniaxial compression can be divided into four stages: initial damage closure stage, linear elastic damage stage, elastic-plastic damage stage, and plastic damage stage. From the stress-strain curve, the cut-off point from elastic to plastic deformation of the rock-like specimen is also the turning point from micro to macro damage; after the point, the apparent initial damage starts to occur on the sample surface; furthermore, the damage of the specimen is accelerated in the plastic damage stage. When the overall damage variable reaches 0.5 or the damage variable of strain localization zone reaches 0.8, the macro crack forms, and the bearing capacity of the rock-like specimen decreases rapidly. The findings are of great significance to the prediction of the damage process of rock mass engineering by digital image correlation.

## 1. Introduction

With economic development in China, the construction of geotechnical engineering, such as dams, bridges, tunnels, and mining engineering, is in the ascendant. The damage and degradation of rock mass engineering are serious under complex occurrence conditions and stress environments. To assess the stability of rock engineering in real time, methods such as monitoring and identifying the damage, maintenance, and reinforcement of the critical region are utilized increasingly. They are critical for ensuring the safe and stable operation of rock engineering.

To reveal the failure mechanism of rock mass, the damage and degradation process of rock-like materials has been studied recently by many scholars with the theory of

fracture mechanical behaviors, such as crack propagation, damage evolution process, and degradation and stability evaluation. A 0-1 variable scalar was initially established by Walsh to describe the damage evolution process of rock [1]. The concept of damage variable  $D$  was proposed by Krajcinovic for the first time [2]; then, a generality damage model was presented by Horii based on the previous research results, which made an important contribution to the quantitative description of damage evolution of rock and other solid materials [3].

In the aspect of rock damage constitutive models, considering the joint geometry and mechanical properties of rock mass [4, 5], the deformation characteristics of jointed rock mass with different parameters under uniaxial, triaxial, and cyclic loads were studied, and the damage constitutive

model of jointed rock mass under different loads was established [6–10]. Considering the influence of the occurrence environment on the deformation and damage process of rock [11, 12], the damage constitutive models of rock under the conditions of the freeze-thaw cycle, high temperature, and moisture were studied [13–17]. These studies have laid a solid foundation for mastering the law of damage and failure of rock.

With the popular application of acoustic emission, X-ray, computed tomography (CT), scanning electron microscopy (SEM), and so forth in rock mechanics, the researchers gradually integrate them with the damage theory and try to describe the damage process of rock mass from the micro and macro scale.

Under the loading, the internal defects of rock develop and form damage. In the process, the acoustic emission phenomenon is apparent. AE is very popularly utilized to detect the macro damage of rock. The damage state of rock under different loading conditions can be reflected by the spatial evolution characteristics of AE events [18, 20]. To investigate the damage evolution process of rock, scholars combined the acoustic emission energy [20, 21], events counts [20, 22], ringing counts [22, 23], and other characteristic parameters with the damage theory, establishing new damage variables characterizing the damage evolution law of rock.

The CT and SEM are widely used to identify the mesoscopic and microscopic damage characteristics and propagation process of rock cracks [23, 24]. Based on the principle of CT, a method of establishing the damage variable was put forward by CT number [25]. Compared with Bellonoi's and Lemaitre's formula, it can be applied to a wider range and reveal the damage mechanism of rock and concrete well. The damage variable based on the damaged area, such as crack and pore, is defined with the CT image processing technology [26], for instance, gray-level analysis and image segmentation technology, providing a feasible method for quantitative analysis of rock damage evolution. To investigate the damage process of rock, the volumetric porosity [27, 28] and accumulated plastic strain [29] are utilized to establish the damage variable combining the SEM. The mechanical behavior relationship between the micro and macro damage mechanisms of rock materials was investigated by observing the whole deformation and failure process with SEM [30].

As an advanced optical testing method, DIC is also combined with damage theory to evaluate the deformation and failure of rock. The shear strain, maximum shear strain variation coefficient, the gray-scale variation, and so forth obtained by DIC were used to propose the damage variable. The maximum shear strain, extracted on the samples with DIC, was used to establish a damage variable, which was utilized to describe the deformation and damage process of marble and slate with holes [31]. The gray-scale variation in the deformation process of the rock sample was studied by Ma, and the relationship between the gray-scale variation and the damage was established to describe the damage evolution process of samples [32]. The strain localization process of coal samples was investigated by Wang et al.; the

maximum shear strain variation coefficient was presented by extracting the surface shear strain [33]. The changes of strain gradient responding to loading were observed in the flat dog-bone specimens tensile tests with DIC [34]. DIC technique can be utilized to describe the evolution of damage in rock materials.

Compared with CT, SEM, and AE, DIC has the typical advantages of large test range, lower cost, high precision, full-field observation, and so forth. As an advanced non-destructive monitoring method, DIC has been widely used in the field of rock mechanics. Up to now, there are few researches on the evolution of rock-like samples damage by DIC. In this paper, based on the advantage of full-field strain measurement, the damage variable was defined with the main strain standard deviation for investigating the damage evolution process of rock-like samples. The findings are of great significance to the prediction of damage deterioration of rock engineering.

## 2. Experimental Setup and Specimen Preparation

**2.1. 3D-DIC Setup.** Digital image correlation (DIC) is a rising optical measurement technology in recent years. Due to the unique advantages, such as noncontact measurement, full-field strain and displacement data extracting, and high precision, it has been widely used. In this paper, the ARAMIS-3D commercial full-field strain test system of the GOM group is used. It is mainly composed of an industrial camera, digital image correlation calculation software, and calibration system.

**2.1.1. Principle of 3D-DIC.** The 3D-DIC is developed from 2D-DIC. It is a 3D deformation measurement method that integrates the computer binocular stereo vision and 2D-DIC related matching technology. Based on the principle of binocular stereo vision, the system needs to be calibrated to obtain the internal and external parameters of the camera before the test. Usually, the process is that the two cameras of a certain angle to each other take several photos of the calibration plate with different attitudes. As shown in Figure 1(a), take the point  $P(X_W, Y_W, Z_W)$  on the sample surface in the world coordinate system  $O(X_W, Y_W, Z_W)$  as an example, respectively, and the point  $P$  is imaged at points of  $P_1(U_1, V_1)$  and  $P_2(U_2, V_2)$  in the image plane of the left and right cameras, respectively. From the knowledge of stereo vision [35], when the internal and external parameters of left and right cameras are known, the image coordinate  $P(U, V)$  is uniquely determined for any given 3D space point  $P(X_W, Y_W, Z_W)$ , and the 3D coordinate of the point is also to be reverse-calculated. As a result, the 3D coordinate of point  $P$  is determined in the world coordinate system  $(X_W, Y_W, Z_W)$ .

The coordinate in the left and right images of the same point on the sample will be identified by binocular stereo vision technology when the 3D-DIC begins measurement. At the same time, the 2D digital image correlation technology is utilized to match the deformed and undeformed images of the sample. Note that the deformed image will be

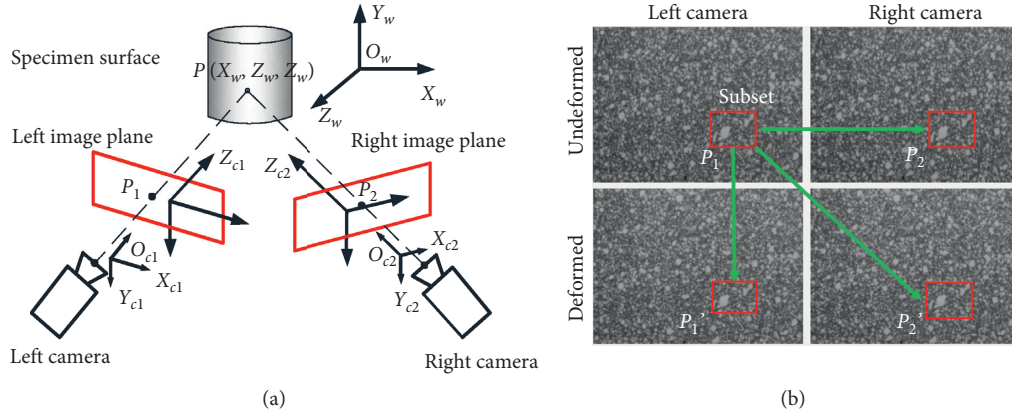


FIGURE 1: 3D-DIC measurement principle. (a) Binocular stereo vision principle. (b) Three-dimensional displacement calculation.

divided into some small grids named subsets in the matching process. It will be used to evaluate the correlation of deformed images. Generally, the correlation of subsets is calculated by the normalized covariance cross-correlation function shown in formula (1), where  $f(x, y)$  and  $G(x, y)$  represent the gray distribution of the subregion of the

reference image and the target image, respectively. The points of the subregion center in the two images are completely matched when the correlation coefficient  $C$  is up to 1, and, also, the reference subregion is completely correlated with the target subregion:

$$C = \frac{\sum_{i=-M}^M \sum_{j=-M}^N [f(x_i, y_j)] [g(x'_i - y'_j) - g_m]}{\sqrt{\sum_{i=-M}^M \sum_{j=-m}^N [f(x_i, y_j) - f_m]^2} \cdot \sqrt{\sum_{i=-M}^M \sum_{j=-m}^N [g(x'_i, y'_j) - g_m]^2}} \quad (1)$$

In 3D-DIC deformation measurement, the matching procedure of image before and after deformation in the left and right cameras is represented by Figure 1(b). Point  $P(X_w, Y_w, Z_w)$  in space is imaged on points  $P_1(u_1, v_1)$  and  $P_2(u_2, v_2)$  on the left and right cameras, respectively, before deformation. After deformation, point  $P$  is moved to  $P'(X_w, Y_w, Z_w)$ , and the points  $P_1(u_1, v_1)$  and  $P_2(u_2, v_2)$  on the image plane of left and right cameras are imaged, respectively. The correlation function of equation (1) is used to calculate the correlation of images. The image subregion of the right camera before deformation will be taken as the reference subregion. To confirm the point  $P$  in the deformed image, the subregion with the highest correlation between the deformed image and the reference image will be matched. The displacement from  $P'$  to  $P$  could be obtained by the three-dimensional coordinate. Repeat the above process for all pixels in the image, and then the three-dimensional displacement field of the sample surface can be obtained. After the displacement is smoothed, the corresponding strain field can be obtained by differential calculation.

**2.1.2. 3D-DIC Image Acquisition Method.** As shown in Figure 2, the ARAMIS 3D-DIC image acquisition system is mainly composed of two COMS industrial cameras, two fixed-focus lenses with a focal length of 50 mm, two high-brightness blue-light sources without stroboscopic light, and a computer with data acquisition. The resolution of COMS is

4096 × 3000. During the test, the sample should be filled with camera vision as much as possible.

DIC collects two photos per second during the uniaxial compression of rock-like samples. The subset is 19 pixels and the spacing is 16 pixels in the data processing stage. The actual length of each pixel is calculated to be 0.5 mm/pixel in the experiment. A ROI (region of interest) 40 mm wide × 80 mm high is set on the specimens to obtain the data strain and displacement.

## 2.2. Sample Preparation and Test Procedure

**2.2.1. Sample Preparation.** Based on the parameters of sandstone in the field, three kinds of rock-like samples were made with quartz sand, iron powder, barite powder, gypsum, and alcohol rosin solution. Quartz sand accounts for 30% of the total weight of rock-like materials. Gypsum content is the ratio of gypsum to total materials. 40 g alcohol is needed for every 1000 g of rock-like materials. The binder concentration is the ratio of rosin to rosin and alcohol solution weight, and the weight of barite powder and iron powder is 70% of the total similar material weight. In order to summarize the damage evolution law of the rock-like material under uniaxial compression, the three kinds of samples with different proportions were made. The mechanical parameters of rock-like sample and the field sandstone are shown in Table 1. The contents of iron powder, alcohol rosin

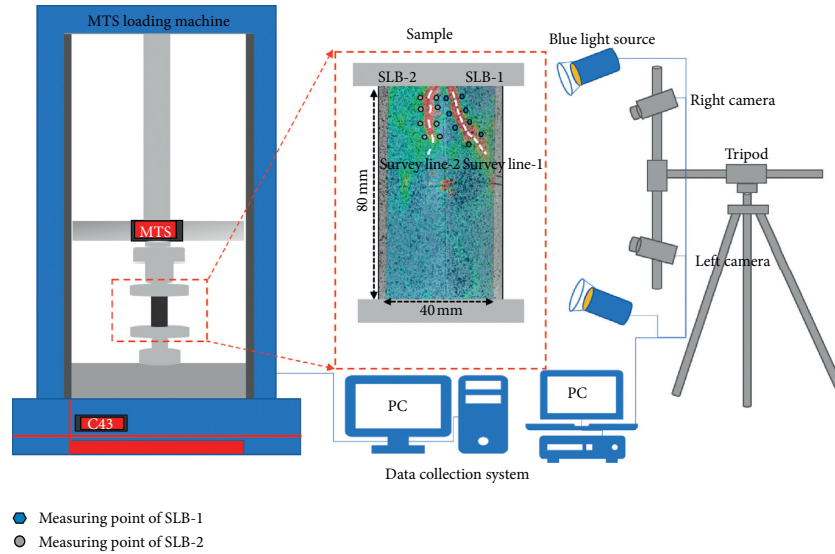


FIGURE 2: Test system diagram.

TABLE 1: Proportion and mechanical parameters of the sample.

Number	A (%)	B (%)	C (%)	D (MPa)	Density ( $g \cdot cm^3$ )	UCS (MPa)	E (GPa)	$\sigma_t$ (MPa)	Poisson's ratio	Brittleness (%)
S1	20	25	8	6.0	2.07	2.63	3.06	0.19	0.17	7.2
S2	35	25	6	4.0	2.18	2.31	2.87	0.17	0.15	7.3
S3	30	20	8	2.0	2.04	2.14	6.26	0.15	0.19	7.0
	Field sandstone				2.32	27.5	35.31	1.93	0.21	7.0

solution, gypsum, and the forming pressure of the material are represented by  $A$ ,  $B$ ,  $C$ , and  $D$ . A high-accuracy electronic scale of  $0.01 g$  was utilized to weight the material, such as iron powder, barite powder, quartz sand, rosin, and alcohol. To ensure the homogeneity of the samples, the material will be fully stirred and then loaded into the mold and formed on the universal testing machine according to the set forming pressure. Finally, according to the standard for test methods of engineering rock mass (GB/T 50266-2013) [36], the cylindrical standard specimens with a height of 100 mm and a diameter of 50 mm are produced.

**2.2.2. Test Procedure.** The uniaxial compression experiment was conducted by the high-precision MTS electrohydraulic servo testing machine with a range of 50 kN. For the principle of DIC, the sample's surface needs to make some speckle of a diameter of about 1 mm with black and white paint before the test. After the speckle was made, placing the sample on the MTS, the angle of the sample is adjusted to present the speckled surface in the field of vision of two cameras. The loading mode of MTS is displacement control; the loading rate and the sampling frequency are set separately as 1 mm/min and 2 Hz, respectively. Meanwhile, to conveniently compare the data, the acquisition rate of the camera is also set to 2 pieces per second, and the devices start to measure at the same time.

### 3. Failure Characteristics of Rock-like Samples

**3.1. Typical Stress-Strain Curve of Rock Sample.** The stress-strain curves of S1, S2, and S3 are shown in Figure 3.

As shown in Figure 3, the UCS (Uniaxial Compressive Strength) of samples S1, S2, and S3 is around 2.5 MPa. The stress of the sample drops rapidly after reaching the peak value.

Brittleness is an important parameter for evaluating rock-like materials. At present, it is usually evaluated by the tension-compression ratio, and the smaller the ratio, the stronger the brittleness of the rock [37]. The tension-compression ratio of natural rock is approximately 2.9% to 8.3% [38]. According to the relevant parameters of S1–S3 in Table 1, the tension-compression ratio of rock-like sample is from 5.9% to 7.1%, so the brittleness of the rock-like sample in this paper is similar to natural rock. The rock-like material selected in the experiment has good performance to simulate the rock.

**3.2. Failure Characteristics of Rock Samples.** In this section, taking S1 as an example, the deformation and failure modes of rock-like samples are analyzed. In the test, the specimen S1 first produced macro cracks from the right side of the specimen top. With the continuous increase of stress, the left side of the specimen also produced an X-shaped crack intersecting the right side, and the final specimen presented

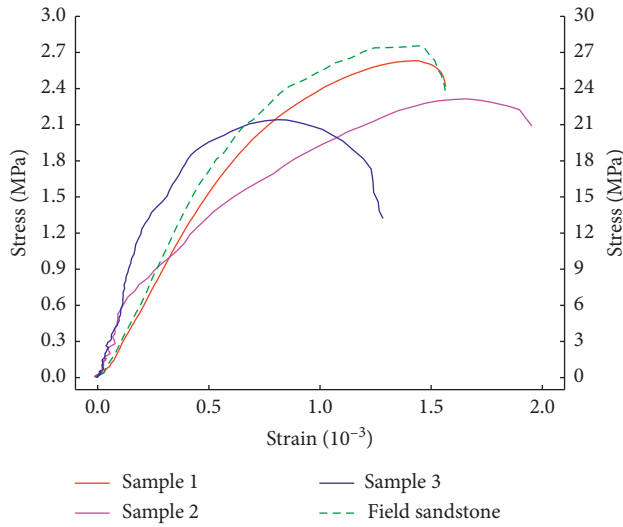


FIGURE 3: Stress-strain curve of uniaxial compression.

an X-shaped failure. The characteristics main strain and displacement were analyzed by selecting 10-key-point nephogram of ROI on the sample S1. Figure 4 is the main strain evolution cloud diagram of ROI (region of interest) on the sample surface before the peak stress of S1, S2, and S3.

To analyze the failure characteristics of the specimen, measure points located at both sides of the strain localization band (SLB) are evenly arranged, which are to extract the data of the main strain and displacement in the loading process in the axial (Y direction) and radial (X direction) directions of the sample.

From the results obtained in Table 2, before the peak stress up to  $0.3\sigma_c$ , there is a small strain concentration point scattered sporadically on the surface of the sample S1. When the peak stress is between  $0.4\sigma_c$  and  $0.6\sigma_c$ , the points of strain concentration on the surface of the specimen increase and gradually develop into a short strain localization band; with the further increase of stress, the strain localization band continues to grow and connect, forming a relatively clear strain localization band.

When the stress reaches  $0.6\sigma_c$ , two more obvious X-shaped strain localization bands are formed at the upper end of the sample. When the stress increases from  $0.7\sigma_c$  to  $\sigma_c$ , the X-type strain localization band in the upper part of the specimen continues to extend to the lower part of the specimen, the width increases gradually, and the localization bands in other positions are gradually connected into a network, staggered distribution. When the peak stress is reached, two obvious strain localization bands are formed on the surface of the upper end of the specimen, the position is consistent with the failure crack shape of the specimen, and the strain concentration degree of the localization band on the right side of the upper end is greater than that on the left side.

Four measuring points were arranged separately on both sides of S1 localization bands 1 and 2, as shown in Figure 2. The displacement, extracted, respectively, in X and Y directions of the points, was utilized to describe the failure

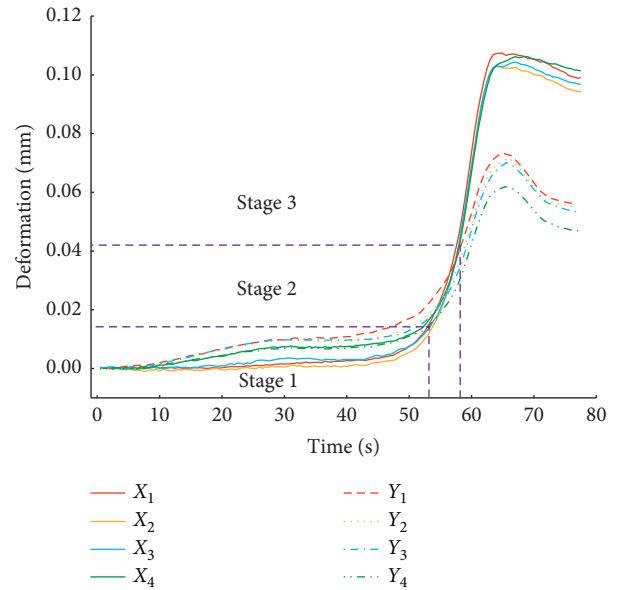


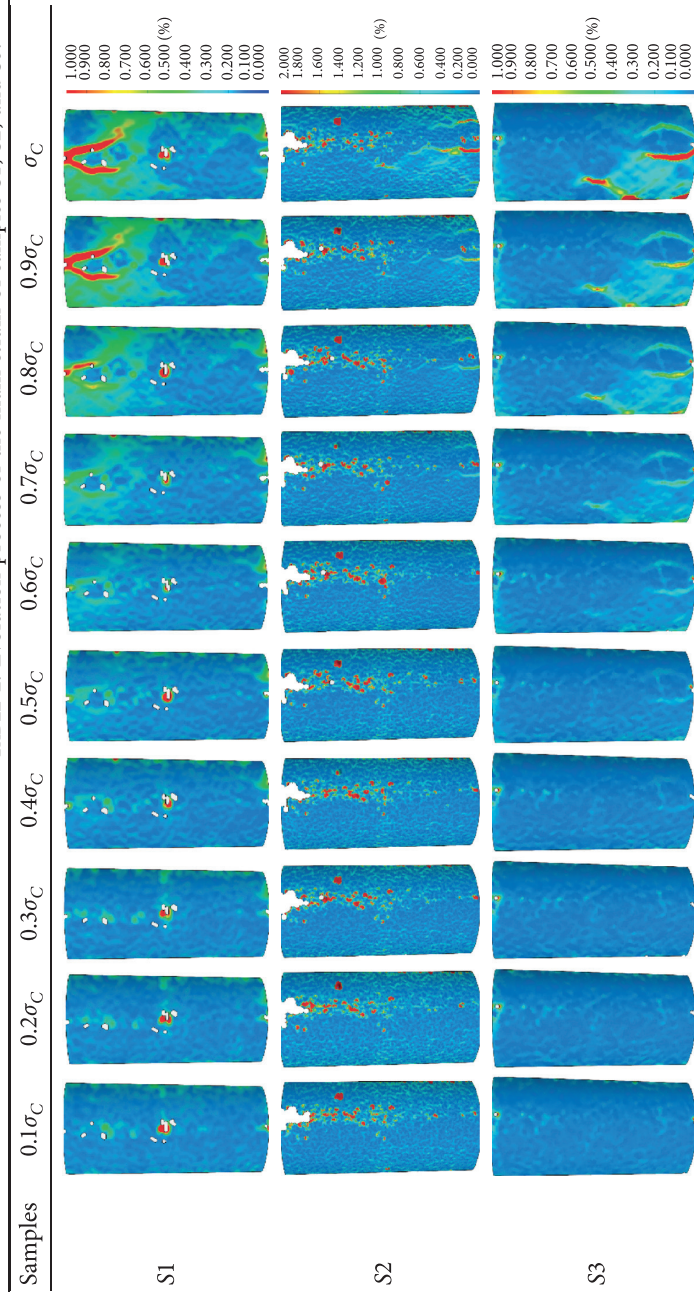
FIGURE 4: Displacement evolution of measuring point in SLB1.

mode of samples. The type of crack is determined by the relative value of the axial and radial displacement of the measuring points on both sides of the strain localization zone in this paper. When the radial deformation of the sample is greater than the axial deformation, it is a tensile crack; and when it is not greater than the axial deformation, it is a shear crack. The results are shown in Figures 4 and 5. Note that the downward compression displacement of the sample is positive.

As shown in Figure 4, the deformation of S1 localized band 1 can be divided into three stages. In the first stage, the axial (Y direction) displacement of localized band 1 is larger than that of radial (X direction) displacement before the specimen is loaded for 53 s, and the strain localization is mainly shear deformation. In the second stage, the specimen is loaded with 53 s–56 s, and the axial and radial displacements of the specimens increase rapidly until the radial and axial displacements are the same. In the third stage, after 59 s of loading, the radial displacement of the specimen is obviously larger than that of the axial displacement, and the macroscopic crack occurs. The cracks formed in the strain localization band 1 of the specimen are mainly subjected to shear crack.

As shown in Figure 5, the displacement evolution of the measuring points on both sides of the strain localization zone 2 can also be divided into three stages. Stage 1 is 53 s before loading, and the axial displacement of localization zone 2 is larger than that of radial displacement, which is shear deformation. In the second stage, the specimen was loaded with 53 s–63 s, and the radial displacement of the localized zone 2 was larger than that in the axial direction, which was tensile deformation. In stage 3, after the specimen was loaded for 63 s, the tensile displacement of localization band 2 further increased, which led to the failure of the sample. Therefore, the crack in the localized band 2 is the first shear, and then tension formed.

TABLE 2: Evolution process of the main strain of samples S1, S2, and S3.





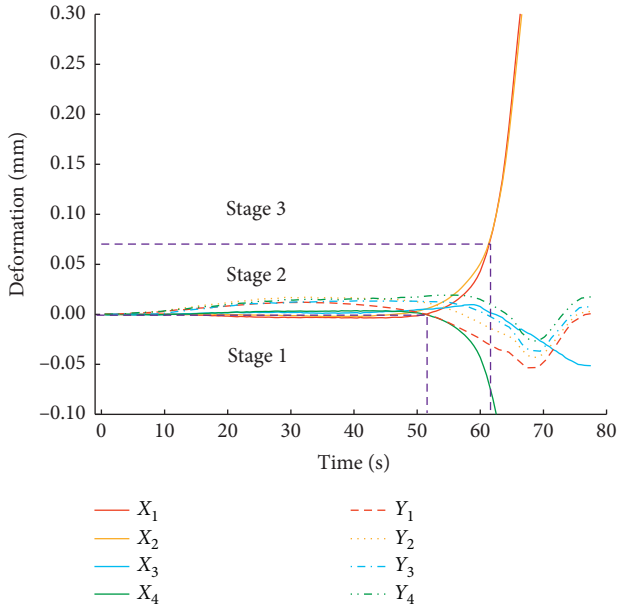


FIGURE 5: Displacement evolution of measuring point in SLB2.

#### 4. Damage Assessment of Rock-like Samples Based on 3D-DIC

**4.1. Establishment of Damage Variables.** In the field of rock mechanics, defining new damage variables combining the parameters obtained from DIC with the damage theory is a key factor to describe the damage mechanism of materials.

According to the damage theory, the original damage variable is represented by the reduction of the effective bearing area. So the initial damage variable can be defined as in formula (2).

$A_d$  is the defect area on the effective bearing area, and  $A$  is the effective bearing area.

$$D = \frac{A_d}{A}. \quad (2)$$

In this paper, the standard deviation of the main strain is introduced into the formula of the damage variable.  $S$  is the standard deviation of the main strain when the damaged area reaches  $A_d$ , and  $S_{\max}$  is the main strain when the damaged area reaches  $A_d$ . Then formula (2) can be rewritten as

$$D = \frac{S_i}{S_{\max}}. \quad (3)$$

$S_i$  is the standard deviation of the main strain on each measuring line in formula (3), as shown in the following formula:

$$S_i = \sqrt{\frac{1}{n-1} \sum_{1}^n (X_i - \bar{X})^2}. \quad (4)$$

In formula (4),  $n$  is the number of statistical points,  $X_i$  is the principal strain of ( $i$ ) statistical points at any time, and  $\bar{X}$

is the average value of the principal strain on the measuring line.

The load was stopped when the load decreased to 20% of the peak load during the experiment. As a result, the specimen was not completely damaged and the damage variable did not reach 1.

**4.2. Data Extraction Method.** A clear evolution nephogram of the displacement field and strain field in the process of specimen loading can be obtained with DIC technology. Strain and displacement data in all directions, by setting an ROI area on the measuring area and arranging lines and measuring points in the ROI area, can be extracted at any time in the process of sample loading. The maximum, minimum, and average strain data of the ROI region can also be obtained utilizing the statistical function of the software of DIC.

The ROI region is determined according to the research objective. Arranging the measuring line and point according to the location of SLB in the ROI area on the sample, the strain data can be extracted.

At the moment before the macro and micro cracks appear in sample S1, there are many clear SLBs on the surface. The two SLBs of the sample are named SLB1 and SLB2. Measuring lines 1 and 2 are arranged along the propagation direction of SLB1 and SLB2, respectively. Strain data in the measuring lines are extracted to analyze the evolutionary relationship between the sample S1 stress-strain curve and SLB1 and SLB2 damage variables. The measuring line and point arrangement in the ROI area of sample S1 are shown in Figure 2.

#### 4.3. Damage Characteristics of Rock-like Sample

**4.3.1. Whole Damage Analysis of Sample.** In this section, the damage evolution processes of S1, S2, and S3 specimens were compared and analyzed with their stress-strain curve. As shown in Figure 6, taking S1 as an example, five key points O, A, B, C, and D were taken from the stress-strain curve of sample S1 for analysis. The damage evolution process of S1 specimen under uniaxial compression before peak stress can be divided into four stages.

- (1) The samples in the stage of OA have uniform deformation. The microfissure and micropore in the samples are gradually compacted under the loading, and the damage variable tends to 0, which is the initial damage closure stage.
- (2) The microfissure and micropores had been compacted in the AB stage of sample deformation, and the deformation of the samples has entered the stage of linear elasticity. At this time, the internal micro damage of the specimen developed gradually, which was the stage of linear elastic damage. In this stage, the damage variable of apparent was still small, and the damage degree of the specimen was low. The deformation of the specimen changed from linear elastic to nonlinear elastic when the specimen was

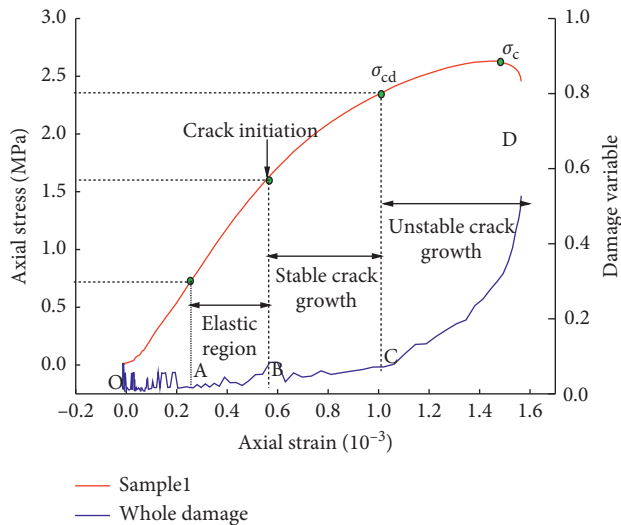


FIGURE 6: The relationship between whole damage variable and loading curve of sample S1.

loaded to point B. The damage of the specimen increased and the damage variable began to evolve.

- (3) The BC segment of sample deformation was the elastic-plastic stage. The segment microfissure developed stably, the damage of the specimen gradually evolved from the inside and outside to the surface, and the apparent damage variable gradually increased, which also is the elastic-plastic damage stage.
- (4) Point C is the critical point of the deformation of the sample from elastic-plastic to plastic. The fissure initiated and developed rapidly in the CD segment. Meanwhile, the damage variable increased quickly. It was the plastic damage stage, in which the specimen gradually develops from micro to macro failure. When the loading is up to the peak stress (point D), the macro cracks appeared, the whole damage variable of the specimen reached 0.528, and the bearing capacity decreased rapidly.

In the OA segment, the damage variable of the S1 sample fluctuated a little, which was caused by the error caused by the DIC system noise. It did not affect the whole damage evolution trend of the sample S1.

As shown in Figure 7, when the loading of the specimen S1 reached the peak stress, the whole damage value was 0.528, which was a little small. The main reason is that the deformation of the specimen is nonuniform, leading to appearance of strain concentration area. The strain is more than the other regions in the area. So, the maximum principal strain is located in the strain localization zone, and  $S_{\max}$  is larger, resulting in the whole damage of the specimen becoming smaller.

The failure of brittle materials, such as rock, is usually due to the inhomogeneous deformation of the specimen caused by the internal defects of the rock mass. The strain localization zone usually appears in the location of inhomogeneous deformation and where deformation is large and

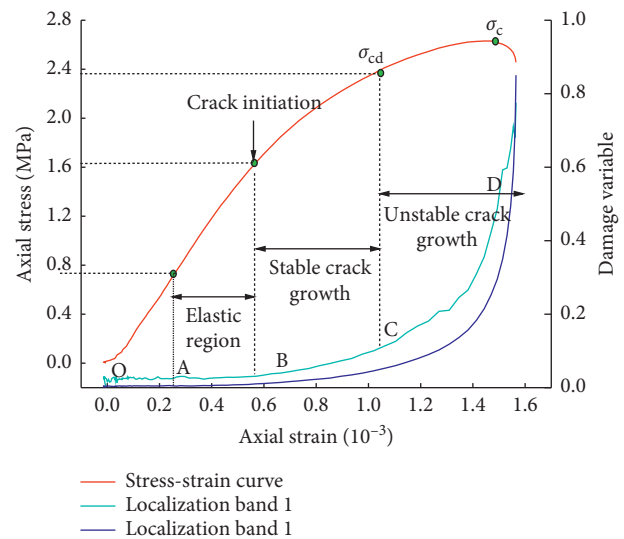


FIGURE 7: The relationship between damage variable and loading curve of SLB1.

easy to produce macro cracks, which leads to the whole failure of the specimen.

In this section, the damage evolution law of the whole ROI area was analyzed with DIC, which was the whole trend of the sample damage. However, the deformation of the specimen is nonhomogenous, as mentioned above, where the deformation of SLB is larger than the other zone. Therefore, to more carefully investigate the damage process of the specimen, the damage evolution process of the SLB was analyzed by the main strain distribution nephogram of the specimen S1 before the appearance of macroscopic crack.

**4.3.2. Damage Evolution Analysis of SLB.** As shown in Figure 2, measuring lines 1 and 2 are arranged, respectively, for obtaining the principal strain and maximum standard deviation of the principal strain at the SLBs of sample S1. The data will be used for calculating the damage variable with equation (3).

It can be seen from Figure 7 that the damage evolution process of SLB1 and SLB2 can also be divided into four stages: the OA segment is the initial damage closure stage and is also the micro cracks compaction stage of the specimen. Meanwhile, the apparent damage is small, about 0.005.

The AB segment is in the stage of linear elastic damage. The specimen is elastically deformed and the micro cracks propagate initially. At the same time, the sample's damage develops from the inside to the surface and evolves on the surface. It increases approximately linearly for the damage variables of SLB1 and SLB2, up to 1.3 and 3.6 times, respectively. The BC segment is an elastic-plastic damage stage. In this stage, the micro cracks develop steadily, and the damage variable of SLB1 and SLB2 increases quickly, up to 1.8 and 2.45 times. The damage of SLB1 and SLB2 is larger than the whole sample. The CD segment is the plastic damage stage. The microfractures rapidly unstably develop and connect to each other. The damage variables of SLB1 and

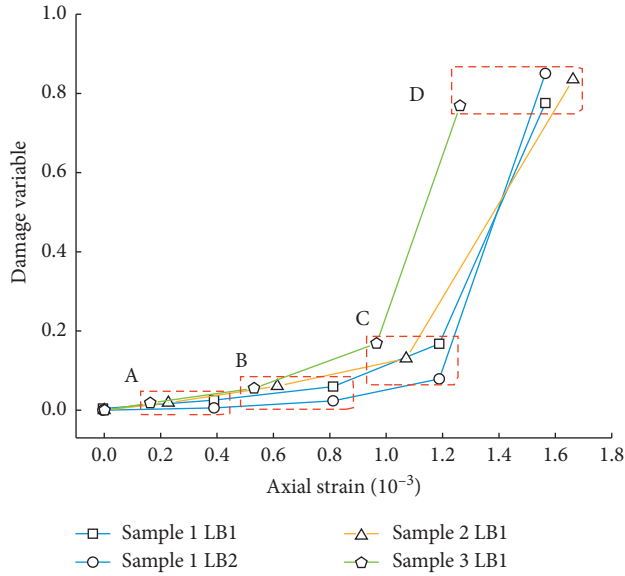


FIGURE 8: Damage evolution characteristic curve of SLB of specimens S1, S2, and S3.

SLB2 are exponentially increased by 9.7 and 3.6 times larger than point C, respectively. It reaches the maximum value at point D before the specimen failure.

The principal strains of S2 and S3 for analyzing damage were also obtained with DIC. The damage variable of the characteristic point of the stress-strain curve is obtained from the whole and SLB of specimens S1, S2, and S3. It is shown in Figures 8 and 9, and more detailed data are shown in Table 3. It can be seen from Figure 8 that, before point C, the damage of SLB of the rock-like specimen is about 0.2, and after reaching the point D, it is about 0.8. The damage of the specimen in the on-line elastic stage is small, and the failure of the specimen in the yield stage is accelerated, and the larger macro failure is formed when the peak stress is reached.

It can be seen from Figure 9 that the whole damage of the sample highly increases in the CD segment. The damage variable of points C to D increases from 0.2 to 0.5 and the macro cracks and failure appeared in the stage. It could be illustrated that the rock-like specimen is stable before reaching the yield stress, and the damage in the yield phase is the main reason for the failure of the specimen. It is more than 60% of the total damage of the sample. The damage in the AB and BC segments is about 40% of the total of the sample, developed slowly, which has little impact on the stability of the sample.

Based on DIC obtained strain data, the damage variable defined with the standard deviation of principal strain can describe effectively the damage process of the specimen by analyzing the damage evolution process of S1, S2, and S3. The damage evolution process of the samples can be divided into four phases at prepeak stress: initial damage closure stage, linear elastic damage stage, elastic-plastic damage stage, and plastic damage stage, corresponding to the compression stage, linear elastic stage, elastic-plastic stage, and yield stage of the stress-strain curve. The damage

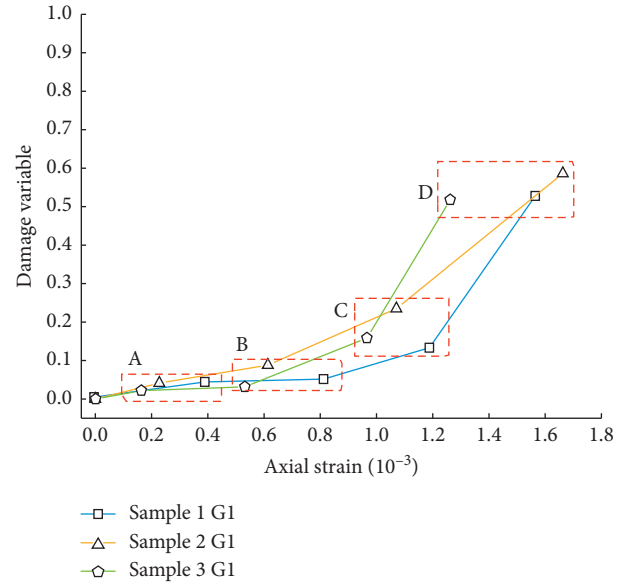


FIGURE 9: Damage evolution characteristic curve of whole specimens S1, S2, and S3.

TABLE 3: Evolution process of damage variable of samples S1–S3.

Sample	Damage	A	B	C	D	Damage variation		
						AB	BC	CD
S1	Global	0.044	0.052	0.133	0.528	0.182	1.558	2.970
	1	0.026	0.060	0.168	0.776	1.308	1.800	3.619
	2	0.005	0.023	0.079	0.851	3.600	2.435	9.772
	$\epsilon/10^{-3}$	0.390	0.812	1.188	1.565	—	—	—
S2	Global	0.041	0.088	0.235	0.586	1.146	1.670	1.494
	1	0.019	0.061	0.130	0.835	2.250	1.145	5.410
	$\epsilon/10^{-3}$	0.228	0.614	1.071	1.663	—	—	—
	Global	0.022	0.032	0.159	0.518	0.455	3.969	2.258
S3	1	0.018	0.055	0.169	0.769	2.072	2.043	3.560
	$\epsilon/10^{-3}$	0.164	0.532	0.966	1.262	—	—	—

propagation of the specimen is a process from inside to outside. The characteristic point B, from linear elastic to nonlinear elastic deformation of the specimen, is the key point from internal to external damage evolution. Then, the damage of the specimen gradually evolves from internal to apparent scale.

## 5. Conclusions

- (1) Using DIC technology to extract displacement data, through analyzing the displacement evolution of both sides of S1 SLB, it is shown that the position of S1 SLB1 is a shear crack, and the position of SLB2 is tensile crack. The failure mechanism of the sample is shear failure first and then tensile failure. The deformation failure mode of the specimen can be explained quantitatively with DIC.
- (2) The whole field strain is obtained by DIC measurement technology, and the damage variable based on the standard deviation of principal strain is

established. The damage evolution process of rock-like specimens can be divided into four stages: initial damage closure stage, linear elastic damage stage, elastic-plastic damage stage, and plastic damage stage. It is verified that the damage variable proposed can well describe the deformation and damage process of the specimen.

- (3) The deformation of rock-like samples is inhomogeneous. The damage of the SLB zone is greater than that of the whole. The damage of rock-like samples is mainly concentrated in the yield stage. When the overall damage of rock-like samples reaches about 0.5 or the damage of the SLB zone reaches about 0.8, the failure of samples will occur soon. The description of the rock damage process with SLB damage is more effective.

### Data Availability

The data used to support the findings of this study are included within the article.

### Conflicts of Interest

The authors declare that they have no conflicts of interest regarding the publication of this paper.

### Acknowledgments

This study was financially supported by the National Natural Science Foundation of China (51174280) and the National Natural Science Foundation of China Youth Fund (51804244).


### References

- [1] J. B. Walsh, "The effect of cracks on the compressibility of rock," *Journal of Geophysical Research*, vol. 70, no. 2, pp. 381–389, 1965.
- [2] D. Krajcinovic and M. A. G. Silva, "Statistical aspects of the continuous damage theory," *International Journal of Solids and Structures*, vol. 18, no. 7, pp. 551–562, 1982.
- [3] H. Horii, Nemat, S. Nasser, and M. F. Ashby, "Brittle failure in compression: splitting faulting and brittle-ductile transition," *Philosophical Transactions of the Royal Society of London. Series A, Mathematical and Physical Sciences*, vol. 319, no. 1549, pp. 337–374, 1986.
- [4] Z. C. Tang, "Experimental investigation on temperature-dependent shear behaviors of granite discontinuity," *Rock Mechanics and Rock Engineering*, vol. 53, no. 9, pp. 4043–4060, 2020.
- [5] Z. C. Tang and Y. Zhang, "Temperature-dependent peak shear-strength criterion for granite fractures," *Engineering Geology*, vol. 269, Article ID 105552, 2020.
- [6] G. Li, F. Ma, G. Liu, H. Zhao, and J. Guo, "A strain-softening constitutive model of heterogeneous rock mass considering statistical damage and its application in numerical modeling of deep roadways," *Sustainability*, vol. 11, no. 8, p. 2399, 2019.
- [7] H. Liu and L. Zhang, "A damage constitutive model for rock mass with nonpersistently closed joints under uniaxial compression," *Arabian Journal for Science and Engineering*, vol. 40, no. 11, pp. 3107–3117, 2015.
- [8] G. Wu, K. Wang, M. Zhao, Z. Nie, and Z. Huang, "Analysis of damage evolution of sandstone under uniaxial loading and unloading conditions based on resistivity characteristics," *Advances in Civil Engineering*, vol. 2019, Article ID 286819, 12 pages, 2019.
- [9] Z. C. Tang and Q. Z. Zhang, "Elliptical hertz-based general closure model for rock joints," *Rock Mechanics and Rock Engineering*, 2020.
- [10] Z. C. Tang, Q. Z. Zhang, and J. Peng, "Effect of thermal treatment on the basic friction angle of rock joint," *Rock Mechanics and Rock Engineering*, vol. 53, no. 4, pp. 1973–1990, 2020.
- [11] J. F. Yang, L. Li, and H. J. Lian, "Experimental investigation of the effects of water content on the anisotropy of mode I fracture toughness of bedded mudstones," *PLoS One*, vol. 15, no. 8, Article ID e0237909, 2020.
- [12] J. F. Yang, L. Li, and H. J. Lian, "Experimental evaluation of the influences of water on the fracture toughness of mudstones with bedding," *Advances in Materials Science and Engineering*, vol. 2019, Article ID 5693654, 16 pages, 2019.
- [13] K. Bian, J. Liu, W. Zhang, X. Zheng, S. Ni, and Z. Liu, "Mechanical behavior and damage constitutive model of rock subjected to water-weakening effect and uniaxial loading," *Rock Mechanics and Rock Engineering*, vol. 52, no. 1, pp. 97–106, 2019.
- [14] D. Lei, H. Lin, Y. Chen, R. Cao, and Z. Wen, "Effect of cyclic freezing-thawing on the shear mechanical characteristics of nonpersistent joints," *Advances in Materials Science and Engineering*, vol. 2019, Article ID 9867681, 14 pages, 2019.
- [15] J. Zhang, H. Deng, J. Deng, and H. Guo, "Influence of freeze-thaw cycles on the degradation of sandstone after loading and unloading," *Bulletin of Engineering Geology and the Environment*, vol. 79, no. 4, pp. 1967–1977, 2020.
- [16] Z. L. Wang, H. Shi, and J. G. Wang, "Mechanical behavior and damage constitutive model of granite under coupling of temperature and dynamic loading," *Rock Mechanics and Rock Engineering*, vol. 51, no. 10, pp. 3045–3059, 2018.
- [17] Z. C. Tang, L. Li, X. C. Wang, and J. P. Zou, "Influence of cyclic freezing-thawing treatment on shear behaviors of granite fracture under dried and saturated conditions," *Cold Regions Science and Technology*, vol. 181, Article ID 103192, 2021.
- [18] D. X. Li, E. Y. Wang, X. G. Kong et al., "Damage precursor of construction rocks under uniaxial cyclic loading tests analyzed by acoustic emission," *Construction and Building Materials*, vol. 206, no. 6, pp. 169–178, 2019.
- [19] S.-Q. Yang and H.-W. Jing, "Strength failure and crack coalescence behavior of brittle sandstone samples containing a single fissure under uniaxial compression," *International Journal of Fracture*, vol. 168, no. 2, pp. 227–250, 2011.
- [20] Z. Zhang, R. Zhang, H. Xie, J. Liu, and P. Were, "Differences in the acoustic emission characteristics of rock salt compared with granite and marble during the damage evolution process," *Environmental Earth Sciences*, vol. 73, no. 11, pp. 6987–6999, 2015.
- [21] C. A. Tang and X. H. Xu, "Evolution and propagation of material defects and kaiser effect function," *Journal of Seismological Research*, vol. 13, no. 2, pp. 203–213, 1990, in Chinese.
- [22] Z. Jia, H. Xie, R. Zhang et al., "Acoustic emission characteristics and damage evolution of coal at different depths under triaxial compression," *Rock Mechanics and Rock Engineering*, vol. 53, no. 5, pp. 2063–2076, 2020.

- [23] Z. Cui and W. Han, "In Situ Scanning electron microscope (SEM) observations of damage and crack growth of shale," *Microscopy and Microanalysis*, vol. 24, no. 2, pp. 107–115, 2018.
- [24] X. Y. Wu, P. Baud, and T.-F. Wong, "Micromechanics of compressive failure and spatial evolution of anisotropic damage in Darley Dale sandstone," *International Journal of Rock Mechanics and Mining Sciences*, vol. 37, no. 1, pp. 143–160, 2000.
- [25] G. S. Yang, D. Y. Xie, and C. Q. Zhang, "The quantitative analysis of distribution regulation of CT values of rock damage," *Chinese Journal of Rock Mechanics and Engineering*, vol. 17, no. 3, pp. 279–285, 1998, in Chinese.
- [26] G. S. Yang and H. Liu, "Study on the rock damage characteristics based on the technique of CT image processing," *Journal of China Coal Society*, vol. 32, no. 5, pp. 463–468, 2007, in Chinese.
- [27] Q. S. Zhang, G. S. Yang, and J. X. Ren, "New study of damage variable and constitutive equation of rock," *Chinese Journal of Rock Mechanics and Engineering*, vol. 22, no. 1, pp. 30–34, 2003, in Chinese.
- [28] X. J. Li, X. H. Ni, and Z. D. Zhu, "Statistical damage model for marble under uniaxial compression based on SEM testing scheme," *Journal of Hydroelectric Engineering*, vol. 34, no. 5, pp. 119–123, 2015, in Chinese.
- [29] H. Jia, W. Xiang, and M. Krautblatter, "Quantifying rock fatigue and decreasing compressive and tensile strength after repeated freeze-thaw cycles," *Permafrost and Periglacial Processes*, vol. 26, no. 4, pp. 368–377, 2015.
- [30] X. H. Ni, Z. D. Zhu, J. Zhao, D. W. Li, and X. T. Feng, "Meso-damage mechanical digitalization test of complete process of rock failure," *Rock and Soil Mechanics*, vol. 30, no. 11, pp. 3283–3290, 2009, in Chinese.
- [31] Y. Y. Cao, S. P. Ma, X. Wang, and Z. Y. Hong, "A new definition of damage variable for rock material based on the spatial characteristics of deformation fields," *Advanced Materials Research*, vol. 146, no. 4, pp. 865–868, 2010.
- [32] S. P. Ma, S. J. Liu, and Y. H. Zhao, "Gray correlation of digital images from loaded rock specimen surface to evaluate its damage evolution," *Chinese Journal of Rock Mechanics and Engineering*, vol. 25, no. 3, pp. 590–595, 2006, in Chinese.
- [33] X. B. Wang, W. T. Hou, Y. S. Pan, and W. Dong, "Experiments of strain localization processes of coal specimens in uniaxial compression based on the digital image correlation method," *Journal of China Coal Society*, vol. 43, no. 04, pp. 984–992, 2018, in Chinese.
- [34] G. Yang, Z. Cai, X. Zhang, and D. Fu, "An experimental investigation on the damage of granite under uniaxial tension by using a digital image correlation method," *Optics and Lasers in Engineering*, vol. 73, no. 4, pp. 46–52, 2015.
- [35] F. P. Zhu, D. Y. Kong, Y. Gong et al., "The measurement of tensile mechanical properties of high-strength steel using three-dimensional digital image correlation," *Chinese Quarterly of Mechanics*, vol. 39, no. 2, 2018, in Chinese.
- [36] GBT 50266-2013, *Standard for Test Methods of Engineering Rock Mass*, China Planning Press, Beijing, China, 2013, in Chinese.
- [37] Q. Li, M. Chen, Y. Jin, and B. Zhang, "Indoor evaluation method for shale brittleness and improvement," *Chinese Journal of Rock Mechanics and Engineering*, vol. 31, no. 8, pp. 1681–1685, 2012, in Chinese.
- [38] H. Wang, S. Yu, H. Li, R. Ren, L. Tang, and W. Zhu, "Ultrasound fracturing of brittle solids with an internal crack based on 3d-ILC method," *Chinese Journal of Rock Mechanics and Engineering*, vol. 39, no. 5, pp. 938–948, 2020, in Chinese.

## Research Article

# Estimation of the Occurrence Time of Thaumasite Sulfate Attack on Tunnel Lining Concrete

Chongbang Xu,<sup>1,2</sup> Xiaojing Gao ,<sup>1,2</sup> Xuefeng Li,<sup>1,2</sup> and Kaishun Zhang<sup>3</sup>

<sup>1</sup>Bridge and Tunnel Research Center, Research Institute of Highway Ministry of Transport, Beijing 100088, China

<sup>2</sup>Research Institute of Highway Ministry of Transport Research and Development Center of Transport Industry of Technologies and Equipments for Intelligent Design, Construction and Maintenance of Underwater Tunnel, Ministry of Transport, Beijing 100088, China

<sup>3</sup>The 5th Engineering Co. Ltd. of China Railway 11th Bureau Group, Chongqing 400037, China

Correspondence should be addressed to Xiaojing Gao; [xiaojing.gao1990@foxmail.com](mailto:xiaojing.gao1990@foxmail.com)

Received 26 October 2020; Revised 9 November 2020; Accepted 12 November 2020; Published 26 November 2020

Academic Editor: Zhi Cheng Tang

Copyright © 2020 Chongbang Xu et al. This is an open access article distributed under the Creative Commons Attribution License, which permits unrestricted use, distribution, and reproduction in any medium, provided the original work is properly cited.

The thaumasite sulfate attack (TSA) on tunnel concrete structure has been reported increasingly in the past decades. Previous investigations on the formation of thaumasite were focused on identifying the deterioration products and reaction mechanisms, while the occurrence time of TSA on tunnel concrete structures was not reported. A highway tunnel exposed to TSA was reported in the present study. The development of tunnel diseases and results of experimental tests conducted in the tunnel and in the laboratory were analyzed to investigate the occurrence time of TSA on concrete. Results revealed that the thaumasite was formed in a range of 18 to 36 months after the construction of Dugongling tunnel. The preconditions for the formation of thaumasite on tunnel concrete structures are available in Shanxi Province, China, due to the special conditions of stratum lithology and climate. The compositions of corrosion products of lining concrete under TSA varied for site studies and for laboratory tests. Site investigations on TSA on tunnel lining concrete should be paid more attention in further research.

## 1. Introduction

The rapid economic development urges the construction of high-speed transportation in China. Due to the different environment and geological conditions, there exist various geologic hazards. Some of the hazards are related to the rock masses (including the discontinuities) [1–5], and others are related to the engineering structures (such as the concrete). Sulfate attack has a significant effect on the long-term durability of concrete, which has been largely studied in the concrete industry. The formation of sulfate can generate expansion, cracking, spalling, loss of strength, and severe degradation. Generally, conventional sulfate attack on cement-based materials refers to the formation of corrosion products including ettringite and gypsum [6]. However, thaumasite sulfate attack (TSA) is another type of sulfate attack, which is greatly different from other sulfate attack types and has been widely investigated over the past years [7–10].

Thaumasite,  $\text{Ca}_6[\text{Si}(\text{OH})_6]_2[(\text{SO}_4)_2(\text{CO}_3)_2] \cdot 24\text{H}_2\text{O}$ , is a naturally occurring mineral and can be artificially synthesized in the laboratory under proper conditions. As a special form of sulfate attack, the thaumasite is typically formed according to the sulfate ions reacting with calcium silicate hydrates (C-S-H) gel in hydrated paste. Excessive thaumasite formation transforms cementitious material into a mushy, noncohesive gray-white mass without any binding, resulting in a loss of strength on cement-based materials [8]. Compared with the ordinary type of sulfate attack, TSA leads to more serious damage to concretes or mortars and has been increasingly reported [11].

Given the danger of TSA on concrete structure, the composition, mechanism, and influencing factors were widely investigated. There are two different formation mechanisms of TSA. One is the direct formation, and the thaumasite is formed through the reaction among C-S-H, calcite, unbound sulfate ions, and moisture [12–14]. For the

indirect formation, the thaumasite is formed through the reaction among ettringite which forms first, C-S-H, carbonate, and water [15]. In the presence of carbonates in the cement-based materials with abundance of water in a low-temperature environment, the formation of thaumasite will occur [16–18]. Results of field and laboratory tests show that the extent of TSA depends on multiple critical factors including type and concentration of sulfate, change of temperature, relative humidity, type of cement, inclusion of limestone materials, and type and dosage of supplementary cementitious materials [19]. The cool and wet conditions provided in underground buildings and tunnels are favourable to the formation of thaumasite, which result in increasing reports about TSA damaged concrete structures in tunnels [10].

TSA on the tunnel concrete lining can cause the degradation of concrete material and a decrease in the integral bearing capacity, and the reduced safety reliability of the tunnel structure after degradation [20, 21]. The occurrence of TSA has been reported for tunnel concrete structures in Germany, Norway, Switzerland, China, Korea, and Austria [22–25]. Field studies in tunnels were conducted to investigate the mechanisms of thaumasite formation, reaction processes of TSA, and mineralogical composition of damaged concrete materials. Tunnels are considered as the important structure of transportation infrastructure. Due to the implementation of the China Western Development Strategy, an increasing number of road and railway tunnels under the condition of complicated geology are being constructed. Erosive substances, for instance, gypsum and anhydrite widely exist in the formations of Western China [26]. The special stratum in Western China may increase the occurrence of TSA on tunnel concrete structures. The severity of concrete deterioration is related to the risk of failure of the construction and to the costs of repair. The costs for tunnel renovations are extremely high. It is important to understand the deterioration processes of tunnel concrete structure and determine the occurrence time of thaumasite in order to initiate protective countermeasures against TSA.

In this research, the instance of a tunnel concrete structure suffered from TSA in Western China was introduced. The damage of this tunnel was observed for a long time, and experimental tests in the tunnel environment and in the laboratory were conducted to investigate the occurrence time of TSA on the tunnel concrete. X-ray powder diffraction (XRD) and Fourier Transform Infrared (FTIR) spectroscopy were applied to identify and quantitatively analyze the compositions of concrete corroded by sulfate attack.

## 2. Overview of the Tunnel Project

Dugongling tunnel is located in Pingshun County, Shanxi Province, China, with a design velocity of 80 km/h. The tunnel is a double-route tunnel and the distance between the two route is 27 m. The total length of the left tunnel and the right tunnel are 2474 m and 2515 m, respectively. The maximum buried depth of tunnel is approximately 231 m. The pile numbers of the left tunnel and the right tunnel are

from ZK 33 + 226 to ZK 35 + 700 and from YK 33 + 227 to YK 35 + 742. A curved section with 3 centers of circles was adopted to construct the inner contour of the tunnel, as shown in Figure 1. The net width of the tunnel is 10.25 m.

**2.1. Hydrogeological Conditions.** The strata of Dugongling tunnel are mainly composed of loessial silt and gravelly soil of Quaternary Holocene ( $Q_4^{d1+p1}$ ), mudstone of Benxi formation in the Middle Carboniferous ( $C_2b$ ), and marlstone and limestone of the upper Majiagou formation in the Middle Ordovician ( $O_2S^1$  and  $O_2S^2$ ) [27]. The marlite stratum contains irregular gypsum. In order to obtain the distribution of marlite rock containing gypsum, the composition of minerals in rock which was drilled from the tunnel surrounding rock were analyzed, as shown in Figure 2. Total 225 rock samples taken from 121 tunnel sections were measured. The measured results show that the composition of tunnel surrounding rocks are calcite, quartz, dolomite, plagioclase, potash feldspar, gypsum, and anhydrite. The percentage of gypsum and anhydrite in sample of tunnel surrounding rock can be as large as 90%. Among the 225 rock samples, there are 67 rock samples containing anhydrite. Among the 121 tunnel sections, it is found that the surrounding rock in 42 tunnel sections containing anhydrite. The distribution of these sampled tunnel sections containing anhydrite is discontinuous. Considering the complexity of formation lithology, it can be concluded that the development of gypsum rock in the longitudinal direction of Dugongling tunnel is irregular.

The area of Dugongling tunnel belongs to midtemperate semiarid continental climate. The temperature and rainfall of Pingshun County, where the Dugongling tunnel is located, were measured from 2013 to 2017 and from 2010 to 2017, respectively. The average temperature of every month is shown in Figure 3. The temperatures of three months were recorded between 5 to 15°C which are favorable to the occurrence of thaumasite. The average rainfall of every month is shown in Figure 4 which indicates that rainfall mainly accumulates between May and September. The annual rainfall of 582 mm can provide abundant water for sulfate attack on tunnel concrete structures. The main type of groundwater of tunnel area contains carbonate fracture, karst water and perched water, which directly affect the moisture content of surrounding rock.

**2.2. Tunnel Disease Conditions.** In addition to the softening and swelling characteristics, the gypsum rock presented significantly corrosive characteristics on tunnel reinforced concrete, as shown in Figure 5. When the groundwater flows through gypsum strata, it carries a lot of sulfate ions which react with hydrated calcium aluminate to form ettringite. This poses a sulfate attack on the tunnel concrete structures and leads to corrosion expansion, strength loss, reduction of structural bearing capacity and damage on tunnel concrete structures.

The occurrence of thaumasite form of sulfate attack on concrete requires a source of sulfate, carbonate, abundance of water, and low temperature [9]. Considering the formation lithology and hydrogeology of Dugongling tunnel,

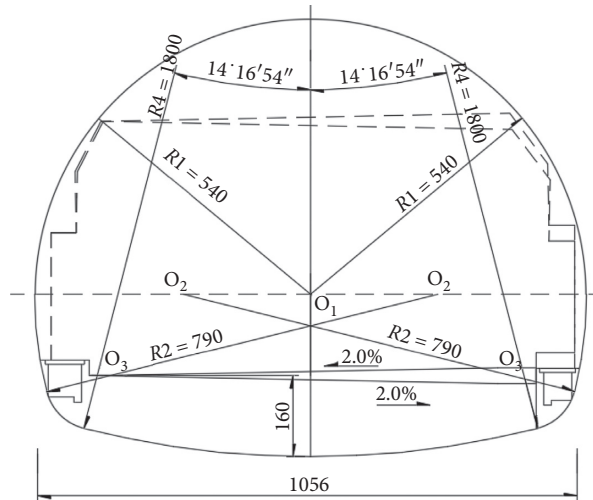


FIGURE 1: Typical cross-section for Dugongling tunnel (unit: cm).

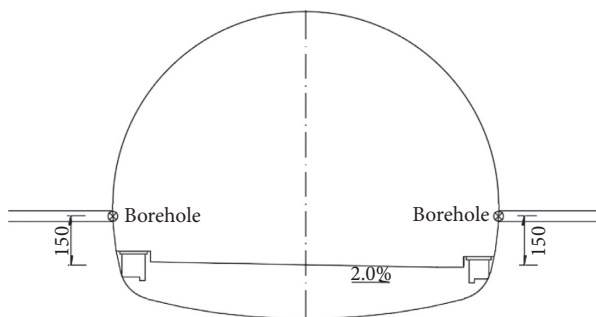


FIGURE 2: Core selection scheme and field photo.

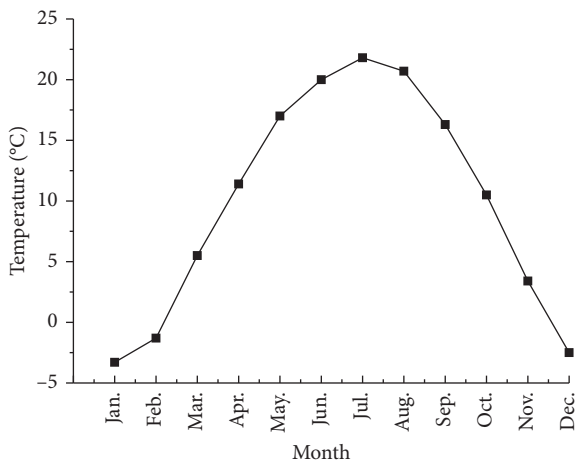


FIGURE 3: Temperature of Dugongling tunnel site.

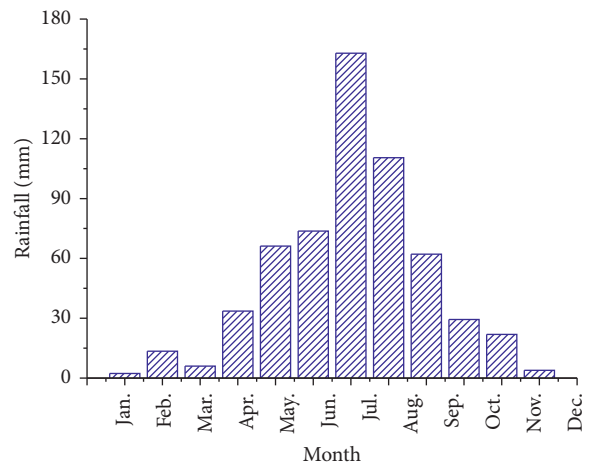


FIGURE 4: Rainfall of Dugongling tunnel site.

the preconditions for TSA are present in this tunnel. Excessive thaumasite formation transforms tunnel lining concrete into a pulpy and noncohesive gray-white mass, which leads to serious damage to tunnel concrete structures.

The construction of Dugongling tunnel was started in March 2010 and completed in December 2011. Tunnel damages such as lining cracks and cable trench movement

gradually appeared after the tunnel has been constructed, as shown in Figure 6(a). The length of the damaged tunnel is 1447 linear meters after about 5 years from the completion of tunnel. Tunnel damages, such as lining cracks, spalling, and swelling deformation, continued to develop in the process of tunnel renovations, as shown in Figure 6(b). The exposed humid concrete of initial lining behaves like soft pulp, which





FIGURE 5: Corrosion of tunnel lining concrete.

indicated that the strength of concrete decreases significantly.

The XRD test was performed to determine the composition of the corroded concrete which behaves like soft pulp. From Figure 7, the main composition of the corrosion products collected from the damaged lining concrete are gypsum, calcite, ettringite, thaumasite, quartz, and dolomite. It is found that the TSA occurred on the tunnel lining concrete.

### 3. Estimate the Occurrence Time of TSA by Development of Tunnel Diseases

Considering the preconditions for TSA, it is found that the TSA on the lining concrete of a tunnel section will not occur until the construction of this tunnel cross-section has been finished. Two sections of Dugongling tunnel were selected to estimate the occurrence time of TSA on concrete structures based on the development of tunnel diseases and the construction dates of tunnel cross-sections.

The main development of tunnel diseases is as follows:

- (1) Longitudinal cracks of secondary tunnel lining (Figure 8) occurred in the left tunnel at sections from ZK 34 + 935 to ZK 35 + 180 and in the right tunnel at sections from YK 34 + 800 to YK 35 + 005 in March 2012.
- (2) In December 2012, longitudinal cracks and floor heave appeared on pavement in the left tunnel at sections from ZK 35 + 260 to ZK 35 + 300. Cracking of secondary tunnel lining were continuously developing in the right tunnel (Figure 9) at sections from YK 34 + 810 to YK 34 + 840 and from YK 34 + 955 to YK 34 + 985.
- (3) In November 2013, tunnel diseases, such as lining cracking, floor heave, and movement of cable duct, became serious in the left tunnel (Figure 10) at sections from ZK 34 + 300 to ZK 34 + 400 and from ZK 34 + 700 to ZK 35 + 550, in the right tunnel at sections from YK 34 + 450 to YK 34 + 650 and from

YK 34 + 700 to YK 35 + 250. The tunnel structures suffered from severe damage and led to the Dugongling tunnel closing.

Based on the development of tunnel diseases, two assumptions were made:

- (1) The occurrence time of thaumasite formation in tunnel lining concrete was ranging from December 2012 to November 2013 because the tunnel concrete structures were seriously damaged during that time.
- (2) The section ZK 35 + 260 in the left tunnel and the section YK 34 + 820 in the right tunnel were selected as the typical sections to predict the occurrence time of TSA on tunnel lining concrete.

In March 2010, the construction of Dugongling tunnel started from the entrance and exit. In December 2011, the construction was finished in the middle of the tunnel. The construction time of Dugongling tunnel is 21 months. The average construction speed is 119 m/month, and the average construction speed of the left tunnel or the right tunnel is 59.5 m/month. The distance between the typical section ZK 35 + 260 in the left tunnel and tunnel portal is 440 m, and the distance between the typical section YK 34 + 820 in the right tunnel and tunnel portal is 992 m. The construction dates of the typical sections ZK 35 + 260 in the left tunnel and YK 34 + 820 in the right tunnel were finished in November 2010 and June 2011, respectively.

Based on the dates when TSA appeared and the constructions of the typical sections of tunnel were finished, the occurrence time of TSA on tunnel lining concrete for section ZK 35 + 260 and YK 34 + 820 are in a range of 25–36 months and in a range of 18–30 months, respectively, as shown in Table 1. The earliest time that TSA appeared on Dugongling tunnel was selected as 18 months. Results of the composition of tunnel surrounding rock show that the distribution of gypsum rock varies with the tunnel section. Also, the natural water content of tunnel surrounding rock is different for different tunnel sections. Therefore, the time of TSA on lining concrete varies with the tunnel section. In order to reduce the error between the actual time and the



FIGURE 6: Photos of different damage degrees for Dugongling tunnel. (a) Initial damage of tunnel lining. (b) Further damage of tunnel lining.

estimated time, a wide range of time was selected. The minimum and maximum value of the occurrence time of TSA on the two tunnel sections were selected and the occurrence time of TSA on Dugongling tunnel was estimated as a range of 18 to 36 months after the tunnel section has been built up.

#### 4. Estimate the Occurrence Time of TSA by Experimental Tests

Experimental tests were conducted in the tunnel and in the laboratory to investigate the occurrence time of TSA on tunnel lining concrete. The mix proportion and materials of concrete tested in the tunnel environment are the same as those of Dugongling tunnel lining concrete, as shown in Table 2. A P·O type 42.5 Portland cement, limestone sand, and limestone with diameter ranging from 5 to 10 mm, and polycarboxylate superplasticizer were used to prepare concrete specimen in the experimental study. The mix ratios

of cement to coarse and fine aggregate was 1:2.3:2.6, respectively. The  $w/c$  ratio was 0.5.

*4.1. Experimental Test in Tunnel.* The concrete paste were cast into a mould with dimensions of  $100 \times 300 \times 400$  mm (Figures 11(a) and 11(b)) and stored at a moist environment for 24 h. After that, the concrete together with the mould were cured under the standard conditions of  $20 \pm 2^\circ\text{C}$  with a relative humidity less than 95%. After curing, the concrete was cut into cube specimens with dimensions of  $100 \times 100 \times 100$  mm. The concrete specimens were soaked in a plastic box which contained gypsum rock and water obtained from the tunnel drainpipe (Figure 11(c)). The gypsum rock was the waste slag rock from tunnel excavation, in which the percentage of gypsum was larger than 90%. The plastic box was put in the tunnel to keep the actual environmental temperature.

The appearance of concrete samples was carefully observed every two months. Obvious corrosion was not

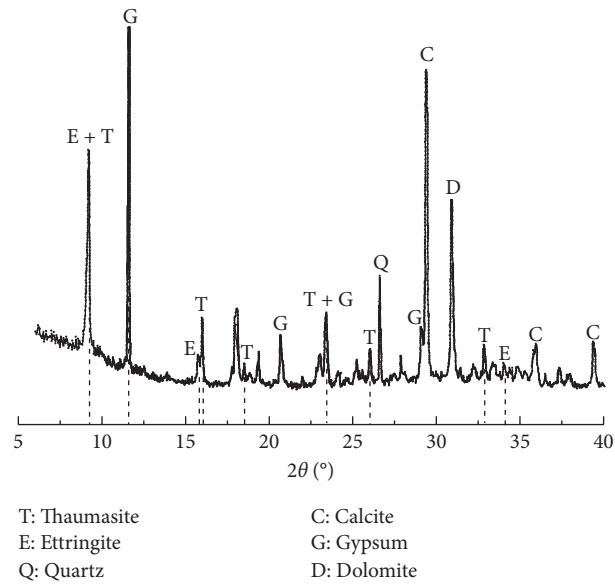


FIGURE 7: XRD pattern of tunnel lining concrete under TSA.



FIGURE 8: Longitudinal cracks of secondary tunnel lining.



(a)

(b)

FIGURE 9: Tunnel diseases in December 2012. (a) Floor heave. (b) Longitudinal cracks on pavement.



FIGURE 10: Tunnel diseases in November 2013. (a) Lining cracking. (b) Movement of cable duct.

TABLE 1: Information of the two typical damaged tunnel sections.

Typical sections	Finished date of construction	Occurrence date of TSA	Occurrence time of TSA
ZK 35 + 260	Nov. 2010	From Dec. 2012 to Nov. 2013	Ranging from 25 to 36 months
YK 34 + 820	Jun. 2011	From Dec. 2012 to Nov. 2013	Ranging from 18 to 30 months

TABLE 2: Concrete mix proportion scheme (kg/m<sup>3</sup>).

Cement	Water	Admixture (limestone powder)	Coarse aggregate	Fine aggregate	Superplasticizer
374	190	48	864	974	5.64

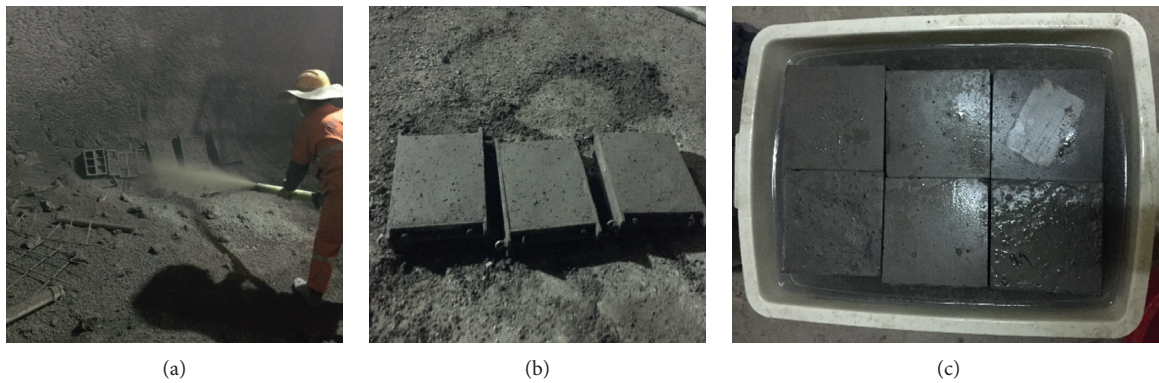


FIGURE 11: Preparation and maintenance of concrete specimens in tunnel environment.

observed on the concrete appearance after 10 months (Figure 12(a)), while phenomena including local separation and spalling were observed after 16 months and 20 months, as shown in Figures 12(b) and 12(c).

FTIR was used to identify the composition of corrosion products of concrete under sulfate attack. The FTIR spectra of immersion samples for 16 months and 20 months are shown in Figure 13.  $[\text{SiO}_6]$ ,  $\text{CO}_3^{2-}$ , and  $\text{SO}_4^{2-}$  are the characteristic peaks of thaumasite. Typically, the variation peaks at  $500\text{ cm}^{-1}$ ,  $670\text{ cm}^{-1}$ , and  $750\text{ cm}^{-1}$  band are attributed to the characteristic peaks of  $[\text{SiO}_6]$  in thaumasite [28]. The peaks of  $\text{CO}_3^{2-}$  occur at  $875\text{ cm}^{-1}$  and  $1425\text{ cm}^{-1}$ .

The vibration peaks of  $\text{SO}_4^{2-}$  are at bonds of  $1140\text{ cm}^{-1}$ ,  $1120\text{ cm}^{-1}$ , and  $600\text{ cm}^{-1}$  [29].  $[\text{AlO}_6]$  is the characteristic peak of ettringite  $\text{Ca}_6[\text{Al}(\text{OH})_6]_2(\text{SO}_4)_3 \cdot 26\text{H}_2\text{O}$ , indicating that aluminium is coordinated with six hydroxyls. The peaks of  $[\text{AlO}_6]$  occur at  $450\text{ cm}^{-1}$  and  $850\text{ cm}^{-1}$ , corresponding to the bending vibration and stretching vibration of  $[\text{AlO}_6]$  [30]. From Figure 13, the band at approximately  $500\text{ cm}^{-1}$  band revealed that thaumasite was formed on the damaged concrete surface after 20 months. Composition of deterioration products were shown in Table 3 based on the FTIR analysis, which revealed that the time when TSA on tunnel concrete occurred was in a range of 16 to 20 months.

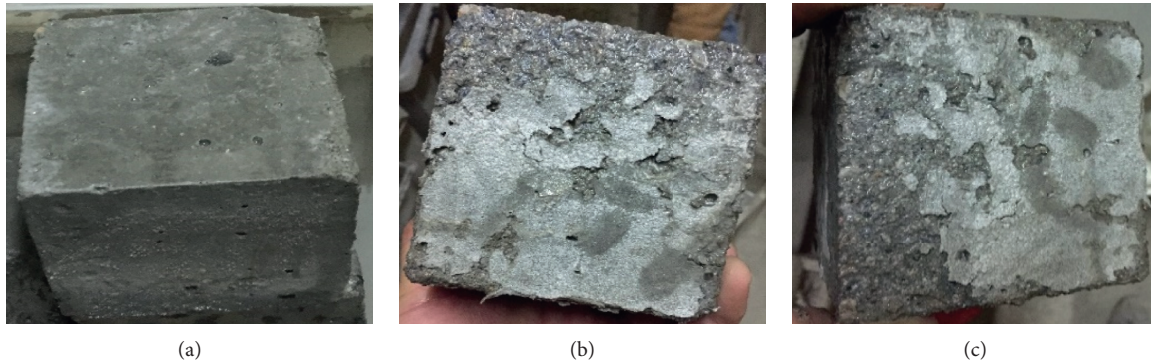


FIGURE 12: Appearance observation of corroded concrete in tunnel environment. (a) 10 months. (b) 16 months. (c) 20 months.

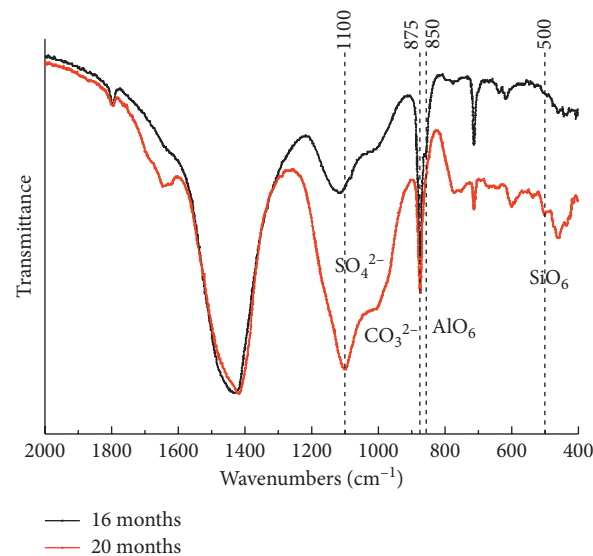


FIGURE 13: FTIR spectrum of concrete suffered from sulfate attack in tunnel environment.

TABLE 3: Components of corrosion products of damaged concrete.

Sample	Quartz (%)	Plagioclase (%)	Microcline (%)	Calcite (%)	Thaumasite	Dolomite	Gypsum	Ettringite (%)
TSA-16	21	21	12	33	—	—	—	13
TSA-20	28	16	7	29	6%	6%	—	8

**4.2. Laboratory Test.** Laboratory tests were conducted to investigate the TSA on lining concrete in China Building Materials Academy. To accelerate the speed of sulfate attack on concrete, 10 percent of magnesium sulfate was added in the concrete materials to provide  $\text{SO}_4^{2-}$  which is the pre-condition for TSA. Concrete specimens were cast into a mould with dimensions of  $100 \times 100 \times 100$  mm and stored at a moist environment for 1 day. After that, the concrete specimens were soaked in the water under the conditions of  $5 \pm 1^\circ\text{C}$ .

The appearance of all concrete specimens was carefully observed every month. The damage of the specimens under sulfate attack at 6, 9, and 11 months was representative. Images of the concrete specimens immersing in water after

6, 9, and 11 months are shown in Figure 14. From the appearances of the concrete exposed to the water containing sulfate ions for 9 months and 11 months, visible cracking and spalling occurred on the surface of the concrete specimens, respectively.

XRD was carried out to analyze the compositions of corrosion products of concrete under sulfate attack after 6 months, 9 months, and 11 months. Figure 15 shows the XRD test results. From Figure 15(a), the deterioration materials generated on the damaged surface of concrete after 6 months were mainly composed of ettringite, portlandite, calcite, C2S, C3S, and C4AF. Figure 15(b) showed that the compositions of the main corrosion products of concrete exposed to sulfate ions after 9 months were quartz, calcite,

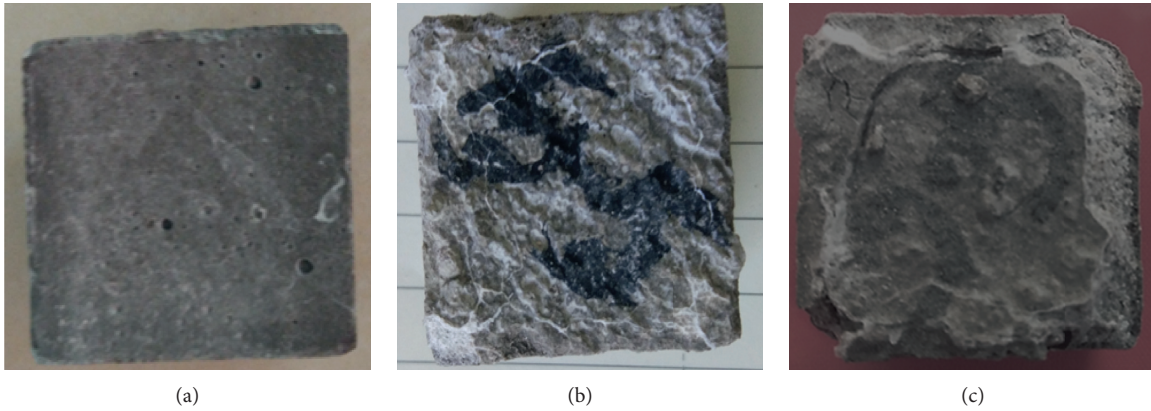


FIGURE 14: Appearance of corroded concrete specimens exposed to sulfate ions in the laboratory. (a) 6 months. (b) 9 months. (c) 11 months.

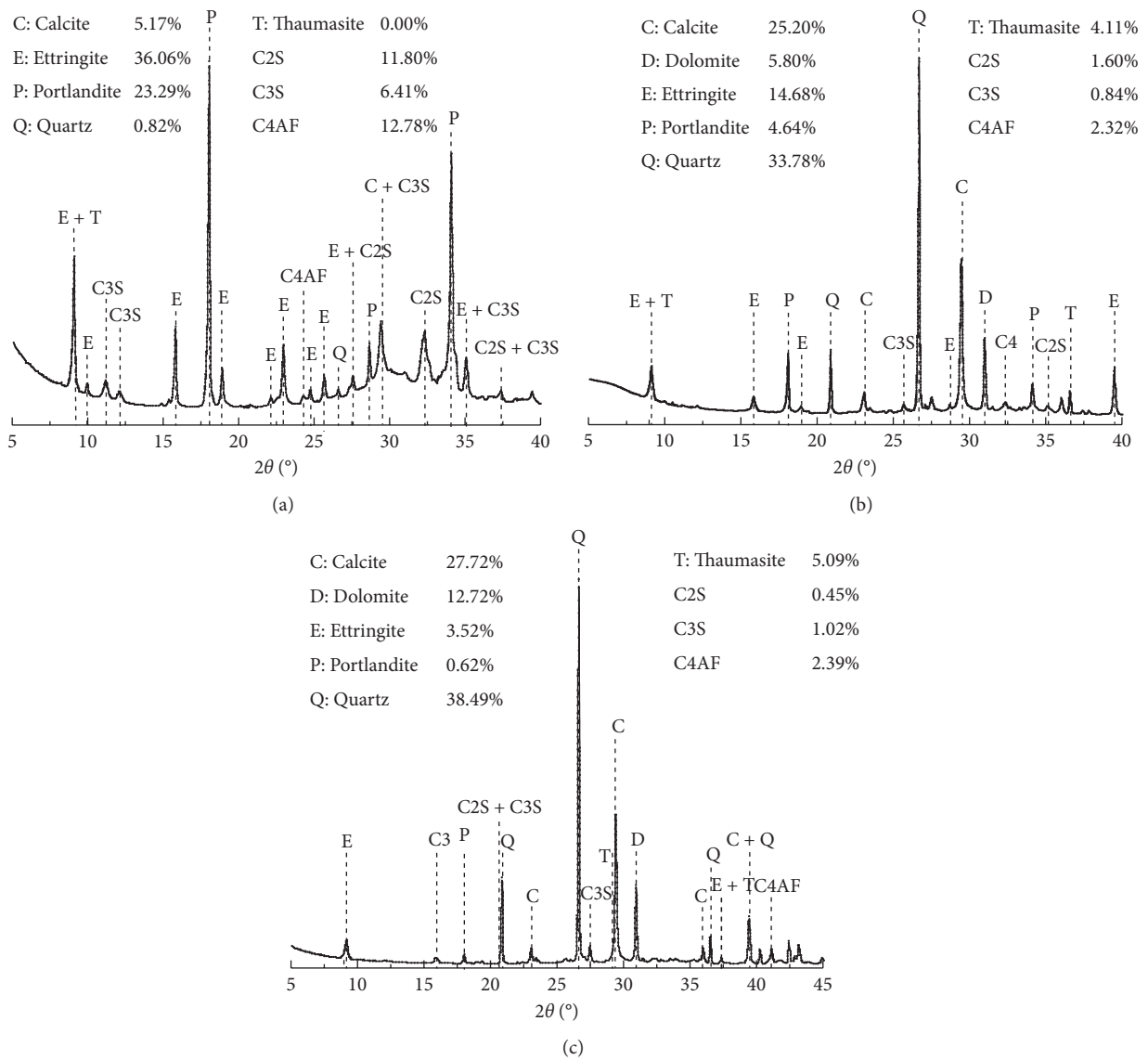


FIGURE 15: XRD patterns of concrete specimens exposed to sulfate ions in the laboratory. (a) 6 months. (b) 9 months. (c) 11 months.

ettringite, portlandite, and thaumasite. Results in Figures 15(a) and 15(b) showed that the content of ettringite decreased and the content of thaumasite increased after 9 months compared to the corresponding content after 6 months, suggesting that the thaumasite was formed from ettringite. From Figure 15(c), the content of quartz was greater than the contents of the other deterioration products, revealing that quartz was the main production of TSA on the lining concrete. From Figure 15, the content of ettringite and portlandite decreased with an increase in generation of thaumasite, indicating that ettringite and portlandite were the reactants of TSA. XRD results in Figure 15 indicated that the time when laboratory concrete exhibit TSA was ranging from 6 months to 9 months in present research.

### 5. Estimate the Occurrence Time of TSA on Dugongling Tunnel Concrete

Results of experimental tests in Figure 15 showed that the occurrence time of TSA on concrete ranged from 6 months to 9 months. The 10 percent of magnesium sulfate in concrete accelerated the corrosion of concrete for laboratory tests. It is reasonable that the time determined by corrosion tests in the laboratory was shorter than that obtained from the analysis of tunnel diseases. Results of corrosion tests proved the rationality of the time estimated by tunnel diseases.

Results of experimental tests shown in Figure 13 indicated that the time when TSA occurred was in a range of 16 to 20 months. The time determined by experimental tests at the tunnel and the time estimated by tunnel disease overlaps by two months. The concretes tested in the tunnel were totally immersed in the engineering water. However, it is not clear if the tunnel lining concretes were totally contacted with the underground water in the actual tunnel engineering environment. Considering the potential influence of immersion conditions, the average of 16 and 20, namely, 18 months were considered as the time that TSA occurred on experimental concrete. Meanwhile, taking the complexity of the stratum lithology of tunnel site into consideration, a wide range of time, 18–36 months, was determined as the occurrence time of TSA on tunnel concrete structure.

The occurrence time of TSA on Dugongling tunnel lining concrete was in a range of 18 to 36 months by considering the development of tunnel disease and results of experimental tests.

### 6. Conclusions

In this study, the occurrence time of TSA on Dugongling tunnel lining concrete was estimated based on the development of tunnel diseases and experimental corrosion tests conducted in the tunnel and in the laboratory. The main conclusions of this research were obtained as follows:

- (1) Gypsum rock existing in stratum, lower temperatures (lower than 15°C), and seasonal precipitation can provide preconditions for TSA in Shanxi Province, China. The occurrence time of TSA on

Dugongling tunnel lining concrete was in a range of 18 to 36 months.

- (2) The typical tunnel diseases which occurred before the formation of thaumasite on Dugongling tunnel lining concrete were cracking and local expansion. The tunnel lining structures were seriously damaged with the spalling of concrete and floor heave, corresponding to the thaumasite form of sulfate attack.
- (3) Results of laboratory corrosion tests indicated that the route for thaumasite formation was indirect, and ettringite acted as the precursor for thaumasite formation. Quartz, calcite, and dolomite were the productions of TSA, ettringite, and portlandite were the reactants of TSA.

### Data Availability

The data used to support the findings of this study are available from the corresponding author upon request.

### Conflicts of Interest

The authors declare no conflicts of interest.

### Acknowledgments

This work was financially supported by the Central Public-Interest Scientific Institution Basal Research Fund (Grant no. 2020-9032), the Special Science and Technology Innovation Fund of Research Institute of Highway Ministry of Transport (Grant no. 2019-C505), and the Science and Technology Project of Department of Transportation of Shanxi Province (Grant no. 2017-1-6).

### References

- [1] Z. C. Tang, Q. Z. Zhang, and J. Peng, "Effect of thermal treatment on the basic friction angle of rock joint," *Rock Mechanics and Rock Engineering*, vol. 53, no. 4, pp. 1973–1990, 2020.
- [2] J. Zou, Y.-Y. Jiao, Z. Tang, Y. Ji, C. Yan, and J. Wang, "Effect of mechanical heterogeneity on hydraulic fracture propagation in unconventional gas reservoirs," *Computers and Geotechnics*, vol. 125, Article ID 103652, 2020.
- [3] Z. C. Tang and Y. Y. Jiao, "Choosing appropriate appraisal to describe peak spatial features of rock joint profiles," *International Journal of Geomechanics*, vol. 20, no. 4, Article ID 04020021, 2020.
- [4] Z. C. Tang and Q. Z. Zhang, "Elliptical hertz-based general closure model for rock joints," *Rock Mechanics and Rock Engineering*, vol. 20, 2020.
- [5] Z. C. Tang, L. Li, X. C. Wang, and J. P. Zou, "Influence of cyclic freezing-thawing on shear behaviors of rock fracture," *Cold Regions Science and Technology*, vol. 181, 2020.
- [6] J. Q. Ma, "Application of shotcrete linings under sulfate attack environments," *Advanced Materials Research*, vol. 233-235, pp. 2061–2067, 2011.
- [7] K.-L. Ma, G.-C. Long, and Y.-J. Xie, "Railway tunnel concrete lining damaged by formation of gypsum, thaumasite and sulfate crystallization products in southwest of China,"

- Journal of Central South University*, vol. 19, no. 8, pp. 2340–2347, 2012.
- [8] N. Crammond, “The occurrence of thaumasite in modern construction—a review,” *Cement and Concrete Composites*, vol. 24, no. 24, pp. 393–402, 2002.
- [9] G. Collett, N. J. Crammond, R. N. Swamy, and J. H. Sharp, “The role of carbon dioxide in the formation of thaumasite,” *Cement and Concrete Research*, vol. 34, no. 9, pp. 1599–1612, 2004.
- [10] B. Ma, X. Gao, E. A. Byars, and Q. Zhou, “thaumasite formation in a tunnel of bapanxia dam in western China,” *Cement and Concrete Research*, vol. 36, no. 4, pp. 716–722, 2006.
- [11] M. Wu, Y. Zhang, Y. Ji, W. She, L. Yang, and G. Liu, “A comparable study on the deterioration of limestone powder blended cement under sodium sulfate and magnesium sulfate attack at a low temperature,” *Construction and Building Materials*, vol. 243, Article ID 118279, 2020.
- [12] M. E. Gaze and N. J. Crammond, “The formation of thaumasite in a cement:lime:sand mortar exposed to cold magnesium and potassium sulfate solutions,” *Cement and Concrete Composites*, vol. 22, no. 3, pp. 209–222, 2000.
- [13] N. J. Crammond, “The thaumasite form of sulfate attack in the UK,” *Cement and Concrete Composites*, vol. 25, no. 8, pp. 809–818, 2003.
- [14] J. Bensted, “Thaumasite-direct, woodfordite and other possible formation routes,” *Cement and Concrete Composites*, vol. 25, no. 8, pp. 873–877, 2003.
- [15] S. Köhler, D. Heinz, and L. Urbonas, “Effect of ettringite on thaumasite formation,” *Cement and Concrete Research*, vol. 36, no. 4, pp. 697–706, 2006.
- [16] J. Aguilera, S. Martínez-Ramírez, I. Pajares-Colomo, and M. T. Blanco-Varela, “Formation of thaumasite in carbonated mortars,” *Cement and Concrete Composites*, vol. 25, no. 8, pp. 991–996, 2003.
- [17] A. Skaropoulou, K. Sotiriadis, G. Kakali, and S. Tsvivilis, “Use of mineral admixtures to improve the resistance of limestone cement concrete against thaumasite form of sulfate attack,” *Cement and Concrete Composites*, vol. 37, pp. 267–275, 2013.
- [18] Y. Luo, C. Wang, Z. Fang, L. Xiao, and Q. Zeng, “The TSA degradation process of cement-based materials in the electrical field environment,” *Construction and Building Materials*, vol. 206, pp. 703–716, 2019.
- [19] M. M. Rahman and M. T. Bassuoni, “Thaumasite sulfate attack on concrete: mechanisms, influential factors and mitigation,” *Construction and Building Materials*, vol. 73, pp. 652–662, 2014.
- [20] A. Neville, “The confused world of sulfate attack on concrete,” *Cement and Concrete Research*, vol. 34, no. 8, pp. 1275–1296, 2004.
- [21] P. Fredrik, F. D. Glasser, and J. Marchand, “Durability of concrete-degradation phenomena involving detrimental chemical reactions,” *Cement and Concrete Research*, vol. 38, no. 2, pp. 226–246, 2008.
- [22] E. Freyburg and A. M. Berninger, “Field experiences in concrete deterioration by thaumasite formation: possibilities and problems in thaumasite analysis,” *Cement and Concrete Composites*, vol. 25, no. 8, pp. 1105–1110, 2003.
- [23] P. Hagelia, R. G. Sibbick, N. J. Crammond, and C. K. Larsen, “Thaumasite and secondary calcite in some Norwegian concretes,” *Cement and Concrete Composites*, vol. 25, no. 8, pp. 1131–1140, 2003.
- [24] M. Romer, L. Holzer, and M. Pfiffner, “Swiss tunnel structures: concrete damage by formation of thaumasite,” *Cement and Concrete Composites*, vol. 25, no. 8, pp. 1111–1117, 2003.
- [25] F. Mittermayr, A. Baldermann, C. Kurta et al., “Evaporation - a key mechanism for the thaumasite form of sulfate attack,” *Cement and Concrete Research*, vol. 49, pp. 55–64, 2013.
- [26] M. Lei, L. Peng, C. Shi, and S. Wang, “Experimental study on the damage mechanism of tunnel structure suffering from sulfate attack,” *Tunnelling and Underground Space Technology*, vol. 36, pp. 5–13, 2013.
- [27] N. Liu, N. Li, C. Xu, G. Li, Z. Song, and M. Yang, “Mechanism of secondary lining cracking and its simulation for the dugongling tunnel,” *Rock Mechanics and Rock Engineering*, vol. 53, no. 10, pp. 4539–4558, 2020.
- [28] S. M. Torres, C. A. Kirk, C. J. Lynsdale, R. N. Swamy, and J. H. Sharp, “Thaumasite-ettringite solid solutions in degraded mortars,” *Cement and Concrete Research*, vol. 34, no. 8, pp. 1297–1305, 2004.
- [29] F. Abubaker, C. Lynsdale, and J. Cripps, “Investigation of concrete-clay interaction with regards to the thaumasite form of sulfate attack,” *Construction and Building Materials*, vol. 67, pp. 88–94, 2014.
- [30] Q. Zeng, C. Wang, Y. Luo, C. Yu, Q. Huang, and C. Luo, “Effect of temperatures on TSA in cement mortars under electrical field,” *Construction and Building Materials*, vol. 162, pp. 88–95, 2018.



## Research Article

# Experimental Study on Mechanical Properties of Deep Buried Granite under Different Confining Pressures

Jun Zhao <sup>1,2</sup> and Tan Zhang<sup>1</sup>

<sup>1</sup>School of Civil Engineering and Architecture, Anhui University of Science and Technology, Huainan, Anhui 232001, China

<sup>2</sup>School of Civil Engineering, Jiangxi University of Engineering, Xinyu, Jiangxi 338000, China

Correspondence should be addressed to Jun Zhao; [jzhao\\_rsm@163.com](mailto:jzhao_rsm@163.com)

Received 29 October 2020; Revised 3 November 2020; Accepted 15 November 2020; Published 26 November 2020

Academic Editor: Zhi Cheng Tang

Copyright © 2020 Jun Zhao and Tan Zhang. This is an open access article distributed under the Creative Commons Attribution License, which permits unrestricted use, distribution, and reproduction in any medium, provided the original work is properly cited.

Brittle failure of hard rock poses a serious threat to the stability of surrounding rock in deep underground engineering. In order to study the deformation and failure characteristics of deep buried granite under high confining pressure cyclic loading and unloading, MTS815 electro-hydraulic servo rock test system was used to conduct cyclic loading and unloading tests under confining pressures of 15 MPa, 35 MPa, 45 MPa, and 55 MPa, and the corresponding stress-strain curves and deformation failure characteristic curves were obtained. The experimental results show the follows: (1) under the same confining pressure, the peak strength, crack initiation stress, crack damage stress, and Poisson's ratio of the specimens under cyclic loading and unloading are larger than those under conventional triaxial loading and unloading, and the unloading elastic modulus is smaller than that, under conventional triaxial compression; (2) the results show that, under different confining pressures, the granite samples show obvious brittle failure characteristics, the elastic modulus and crack initiation stress increase first and then decrease with the confining pressure, the peak strength and crack damage stress of the samples increase linearly with the confining pressure, and Poisson's ratio increases first and then remains unchanged with the confining pressure; (3) under the two kinds of stress conditions, the macroscopic failure of the samples is mainly shear failure. The deformation and failure law of granite samples revealed in this study has significant reference value for the selection of rock mass mechanical model of surrounding rock stability of underground engineering, the formulation of surrounding rock support countermeasures, and the evolution law of mechanical parameters with damage variables.

## 1. Introduction

With the rapid development of the world economy, there has been a rapid increase in demand for energy extraction and underground space development for human survival and development, leading to the large-scale development of human engineering activity in deep underground areas with high stress [1–3]. These deep underground projects inevitably encounter a common problem: the surrounding rock mass stability of deep underground structures or structures under high geo-stress. Compared with shallow (low geo-stress) rock mass, deep rock mass is the carrier of direct interaction between deep resources and underground space development. At depth, the nonlinear behavior of rock mass

materials is more prominent, and the in situ stress state of the rock mass and the role of ground stress environment have become more prominent. High stress and large magnitude disasters induced by different engineering activity methods turn out to be more significant [4]. When a cavern is excavated in deep hard rock, the rock mass undergoes complex stress path adjustments due to the interaction of layering, segmental excavation, and excavation between adjacent caverns. The same part of the rock mass is repeatedly subjected to a hoop stress increase and a radial stress decrease (in the direction of the excavation's free face). Once the stress exceeds the ultimate bearing capacity of the surrounding rock itself, a large number of stress-type brittle failures (such as spalling, splitting, and stress-type rock

burst) may occur, posing a great threat to the surrounding rock stability of underground engineering project and the personal safety of the field technicians. Therefore, examining the deformation and destruction mechanism of deep buried hard rocks under cyclic loading and unloading not only is of great theoretical value but also provides significant engineering guidance.

Many scholars at home and abroad have examined the mechanical properties of deeply buried hard rocks under complex stress paths. Research methods include indoor tests, in situ damage characterization observations, theoretical methods, and numerical simulations, while studies range in scale, covering indoor rock specimens to in situ single chambers to giant cave clusters.

Huang et al. [5] and Martin and Chandler [6, 7] proposed a CWFS model for deep rocks by analyzing the results of indoor tests on a large number of granite mechanical properties. Yang et al. [8], Yin et al. [9], and Yin et al. [10] conducted a large number of cyclic loading and unloading tests on Jinping deep-buried marble specimens and investigated influence factors such as the rate of unloading confining pressure, initial damage, and unloading path on damage characteristics to establish a unified strain energy criterion for homogeneous isotropic hard rocks. Feng et al. [11] examined the Jinping Underground Laboratory Phase 2 deep buried tunnel using digital borehole equipment and proposed a data evaluation method for digital borehole observations based on a rock mass integrity index for analyzing the fracturing process of deep buried hard rock subdivisions. Due to the complexity of stress conditions and uncertainty of the geological and construction conditions at the site, indoor small-scale mechanical tests are still one of the primary methods of studying the mechanical properties of deeply buried hard rocks. The repeated cyclic loading and unloading processes experienced by deep rocks under the influence of multi-step/multistage excavations have been simulated by numerous researchers with cyclic loading and unloading tests to study the evolution of rock mechanical properties during this process. For instance, Li et al. [12] studied the mechanical characteristics of sandstone by uniaxial cyclic loading and unloading test combined with micro-mechanical means. Ming-Qing and Cheng-Dong. [13] and Zhang et al. [14] conducted uniaxial cyclic loading and unloading tests on marble with different specimen categories under the confining pressures of 40 MPa. Zhang et al. [15] investigated the destruction mechanism of rocks containing veins in landslide-slip zones under uniaxial cyclic loading and unloading. Wang et al. [16] investigated the strength and deformation characteristics as well as estimated the elastic parameters of Jinping marble under uniaxial compression cyclic loading and unloading. Hao-Ran et al. [17] studied the damage characteristics of saline rock under multistage cyclic loading and unloading at 5, 10, 15, and 20 MPa confining pressure. Rui-Dong et al. [18] studied the damage evolution characteristics of coal under triaxial cyclic loading and unloading at 10, 15, and 20 MPa confining pressure. Yang et al. [19] studied the evolution of energy consumption ratio of sandstone under axial cyclic

loading at 10, 20, and 30 MPa confining pressure. Tang et al. [20] studied the shear strength characteristics of rock mechanics.

In general, the majority of such studies employ uniaxial cyclic loading and unloading tests on soft rocks with relatively low strength, while the confining pressure is low in the triaxial cyclic loading and unloading experimental studies. The high and low confining pressure cyclic replacement environment of deep buried rocks during excavation has not been examined, which makes controlling the surrounding rock mass stability deeply buried or underground structures under high geo-stress difficult. Therefore, further study of the deformation and damage characteristics of hard rocks under various confining pressures and cyclic loading and unloading conditions is an important engineering requirement for deep rock engineering construction.

In this paper, by conducting conventional triaxial and cyclic loading and unloading tests on deep fine-medium grained granite from a hydropower station in Sichuan using a MTS 815 rock testing system at the Institute of Rock and Soil Mechanics, Chinese Academy of Sciences, the strength, deformation, and damage fracture characteristic parameters under low confining pressure to high confining pressure (0~50 MPa) and cyclic loading and unloading are investigated. The influence of confining pressure on the deformation and damage characteristics of deep-buried hard rocks is analyzed to provide an indoor test basis for excavation support of the deep underground caverns.

## 2. Test Conditions and Schemes

*2.1. Lithological Conditions and Specimen Preparation.* Granitic specimens were sourced from the upper drainage corridor of the underground powerhouse of a hydropower station in Sichuan Province. Specimens were obtained from a depth of 320~500 m. The following observations are made from the results of SEM scanning (Figure 1) and thin section identification (Table 1). The mineral particle size of the granite is concentrated around 0.3~4.5 mm, and the mineral components are primarily quartz (40%), feldspar (50%), and mica (a minor amount) (Table 1). These specimens are classified as fine-medium grained granite and diorite. Because of the high quartz content, the granite commonly undergoes brittle failure. In situ ground measurements show that the maximum principal stress of the cavern in sampling location is 16~38 MPa. In addition, there is slight rock-core diskling in the drilled core (Figure 1); hence, the granite in the test is from a hard rock-high stress environment.

*2.2. Granite Specimens.* According to International Society for Rock Mechanics (ISRM) specifications recommended methods [21], the granite core collected on-site (with a diameter of 70~72 mm) was further processed into 50 mm diameter and 100 mm high specimens (Figure 1). In order to reduce the discreteness of the test results, the acoustic velocity of these specimens was measured in the laboratory, and specimens with significant differences in acoustic velocity were rejected.



Granite specimens

FIGURE 1: Rock core and granite specimens.

TABLE 1: Mineral content and grain size of granite specimens.

Name of mineral	Content (%)	Grain size (mm)
Quartz (Qtz)	36	0.30~5.12
K-feldspar (Kfs)	5	0.35~3.13
Biotite (Bt)	12	0.20~1.26
Zircon (Zrn)	2	0.05~0.12

**2.3. Test Schemes and Procedures.** The test was divided into conventional triaxial and triaxial cyclic loading and unloading tests under confining pressures of 15, 35, 45, and 55 MPa. The test schemes are shown in Table 2. Each confining pressure corresponds to one set of tests with three specimens in each set. All tests were performed under triaxial stress conditions using a MTS 815 rock testing system housed at the Institute of Rock and Soil Mechanics, Chinese Academy of Sciences. The test process in this study included the following steps. First, in order to determine the axial compression design value of the cyclic loading and unloading test (80% of the maximum principal stress difference), the peak strength (the maximum principal stress difference) under different confining pressures was obtained using the conventional triaxial compression test; then, the specimen was preloaded to 0.5 kN so that the pressure head is in full contact with the specimen; next, the confining pressure and axial stress were applied to the desired level at a rate of 0.05 MPa/s; after that axial force was applied to 80% of the maximum principal stress difference at a rate of 0.01 MPa/s while confining pressure was constant, and the axial force was released (unloaded) to 5 kN at a rate of 0.25 kN/s. After repeating the process five times, the specimens were loaded until failure.

### 3. Analysis of Test Results

**3.1. Conventional Triaxial Test.** Figure 2 shows the stress-strain curves under the conventional triaxial test at 0, 15, 35, 45, and 55 MPa confining pressure. Under various confining pressures, the peak strength, Poisson's ratio, and elastic modulus obtained according to Figure 3 are listed in Table 3. Under various confining pressures, granite specimens immediately show a significant stress drop with increasing strain after reaching the peak strength, and the peak strain ranges from 0.65% to 1.19% (less than 3%) (Figure 2). According to the classification in the literature [22], the

specimens experience brittle failure. According to the data in Table 3, we plot the relation curves between peak strength, elastic strength, Poisson's ratio, and confining pressure for the conventional triaxial tests (Figure 4). The peak specimen strength increases linearly with confining pressure (Figure 4(a)). The elastic modulus increases first and then decreases with confining pressure, and under a confining pressure of 45 MPa, the elastic modulus reached a maximum 61.3 GPa (Figure 4(b)). When confining pressure is less than 25 MPa, Poisson's ratio increases with confining pressure. When the confining pressure is greater than 25 MPa, Poisson's ratio is  $19.6 \times 10^{-2}$  (Figure 4(b)).

**3.2. Cyclic Loading and Unloading Test.** In the cyclic loading and unloading test, the elastic modulus is calculated using the mean unloading elastic modulus. The unloading elastic modulus ( $E_{ur}$ ) equals the slope at two intersecting points of the hysteresis loop:

$$E_{ur} = \frac{\Delta(\sigma_1 - \sigma_3)}{\Delta\varepsilon_1}, \quad (1)$$

where  $\Delta(\sigma_1 - \sigma_3)$  is the increment of axial stress at both ends of the hysteresis loop;  $\sigma_1$  is the axial stress;  $\sigma_3$  is the confining pressure; and  $\Delta\varepsilon_1$  is the increment of axial strain at both ends of the hysteresis loop.

According to the ratio of lateral strain to axial strain during unloading and reloading, Poisson's ratio ( $\mu$ ) under this cyclic loading and unloading is obtained, which is called the ratio of lateral strain increment and axial strain increment at the two intersection points of the hysteresis loop:

$$\mu = \frac{\varepsilon_{3u} - \varepsilon_{3s}}{\varepsilon_{1u} - \varepsilon_{1s}}, \quad (2)$$

where  $\varepsilon_{3u} - \varepsilon_{3s}$  is the lateral strain increment at the two intersection points of the hysteresis loop and  $\varepsilon_{1u} - \varepsilon_{1s}$  is the axial strain increment at the two intersection points of the hysteresis loop.

Figure 3 shows the stress-strain curves of the specimens tested under the confining pressures of 0, 35, 45, and 55 MPa. With increasing confining pressure, the plastic deformation stage of the granite increases, and the axial stress-strain curves of the granite specimen under cyclic loading and unloading are concavely curved and closely arranged (Figure 3). At the beginning of cyclic loading and unloading, five hysteresis loops are generated. The area of the hysteresis loops increases with the hysteresis loop. In the lateral stress-strain curve, the hysteresis loop area also increases; however, the shape of the hysteresis loop is convex. Rock specimens under cyclic loading and unloading immediately show significant stress drop after reaching the peak strength, and the peak strain ranges from 0.56% to 1.24% (less than 2.6%), which is brittle failure [23, 24].

The peak strength of specimens is listed in Table 4, and the curve of peak strength vs. confining pressure is plotted (Figure 5(a)). The unloaded elastic modulus and Poisson's ratio are obtained according to equations (1) and (2) and Figure 4 (Tables 5 and 6). In addition, the curves of unloaded elastic modulus vs. Poisson's ratio and confining pressure

TABLE 2: Test schemes.

Name of test	Confining pressure (MPa)	Specimen
Conventional triaxial test	0	JZ-0-1, JZ-0-2, JZ-0-3
	15	JZ-15-1, JZ-15-2, JZ-15-3
	35	JZ-35-1, JZ-35-2, JZ-35-3
	45	JZ-45-1, JZ-45-2, JZ-45-3
	55	JZ-55-1, JZ-55-2, JZ-55-3
Triaxial cyclic loading and unloading test	0	XHJ-0-1, XHJ-0-2, XHJ-0-3
	15	XXJ-15-1, XHJ-15-2, XHJ-15-3
	35	XHJ-35-1, XHJ-35-2, XHJ-35-3
	45	XHJ-45-1, XHJ-45-2, XHJ-45-3
	55	XHJ-55-1, XHJ-55-2, XHJ-55-3

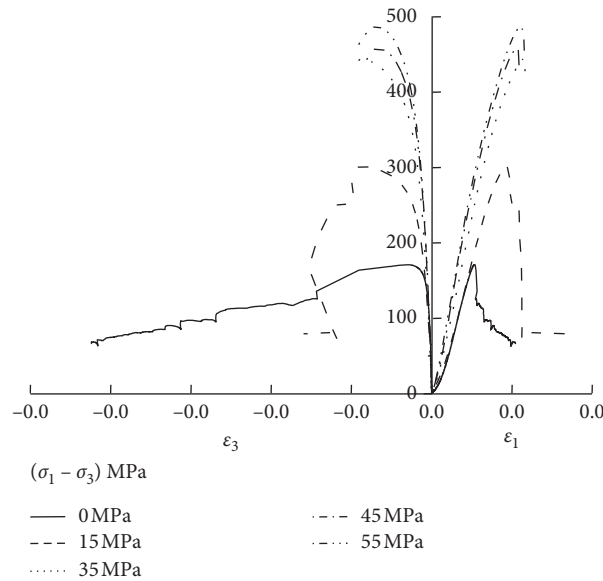


FIGURE 2: Stress-strain curves for conventional triaxial tests.

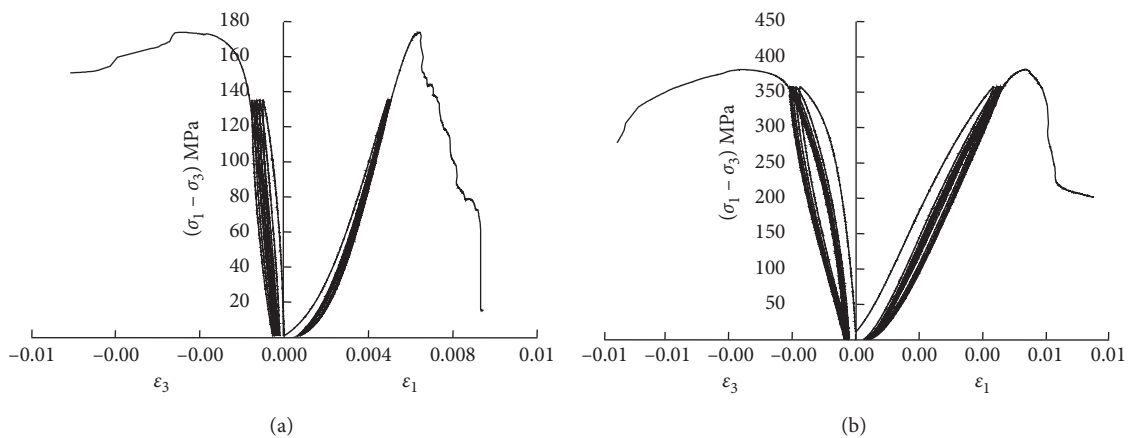


FIGURE 3: Stress-strain curves of triaxial cyclic loading and unloading tests with varying confining pressures. (a) The confining pressure is 0 MPa. (b) The confining pressure is 30 MPa.

are plotted according to the data in Tables 5 and 6 (Figure 5(b)). Under cyclic loading and unloading, the peak strength of specimens increases with increasing confining pressure (Figure 5). Peak strength is linearly related to

confining pressure in general, which is the same as the relationship between peak strength and confining pressure under conventional triaxial conditions. The elastic modulus increases first and then decreases with confining pressure.

TABLE 3: Conventional triaxial peak strength under various confining pressures.

Confining pressure (MPa)	Peak strength (MPa)	Axial peak strain ( $10^{-3}$ )	Elastic modulus (GPa)	Poisson's ratio ( $10^{-2}$ )
0	171.1	5.3	41.4	7.1
15	330.3	11.4	38.0	13.1
35	504.3	14.1	52.3	26.2
45	523.2	12.7	68.1	19.9
55	566.1	10.3	56.1	23.2

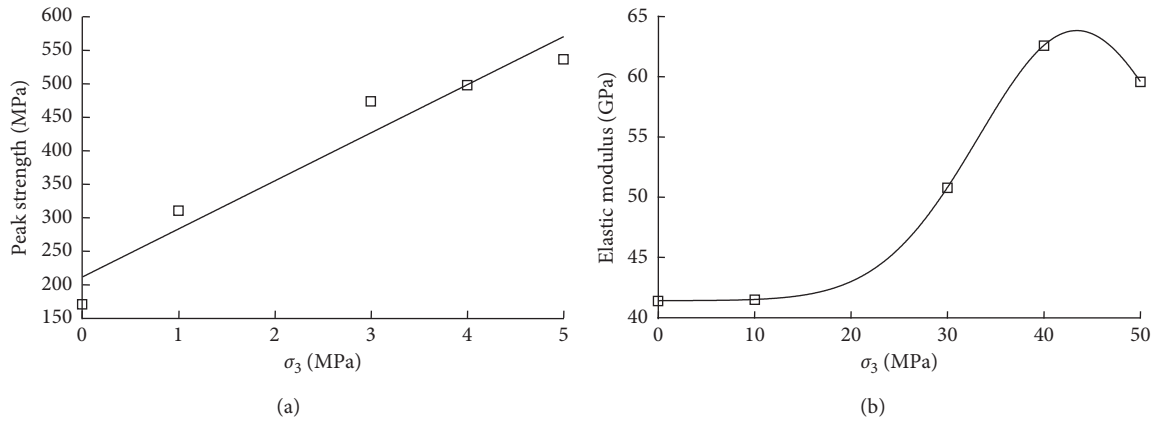


FIGURE 4: Relationship between peak strength, elastic strength, Poisson's ratio, and confining pressure in conventional triaxial tests. (a) Peak strength vs. confining pressure. (b) Elastic modulus vs. confining pressure.

TABLE 4: Peak strength of cyclic loading and unloading under different confining pressures.

Confining pressure (MPa)	Peak strength (MPa)	Axial peak strain ( $10^{-3}$ )
0	171.8	5.9
15	362.0	7.9
35	425.3	12.3
45	554.1	12.9
55	585.9	14.1

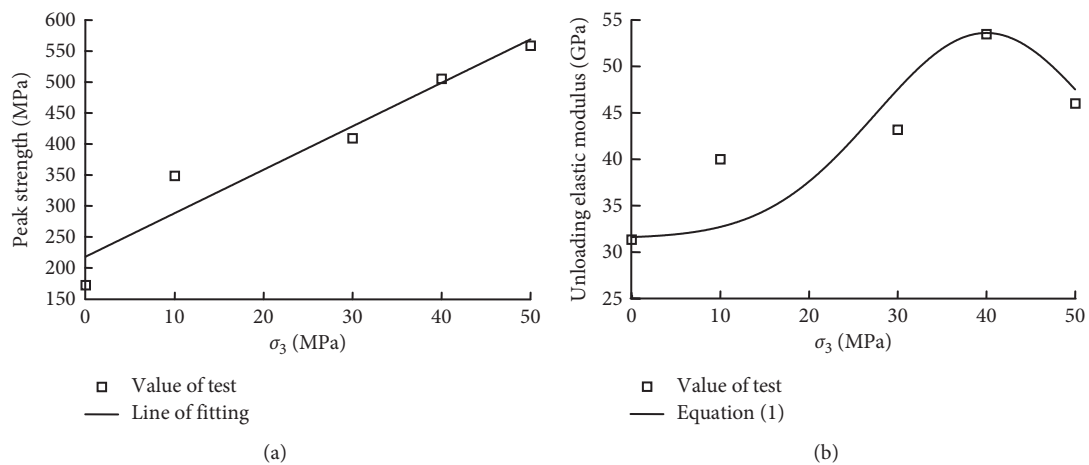


FIGURE 5: Relationships between peak strength, unloading elastic modulus, Poisson's ratio, and confining pressure under cyclic loading and unloading. (a) Peak strength vs. confining pressure. (b) Unloading elastic modulus vs. confining pressure.

TABLE 5: Unloading elastic modulus of hysteresis loops under various confining pressures.

Category of confining pressure (MPa)	Unloading elastic modulus (GPa)					Average
	Hysteresis loop 1	Hysteresis loop 2	Hysteresis loop 3	Hysteresis loop 4	Hysteresis loop 5	
0	32	31	31	31	32	32
15	46.2	43.1	41.3	42.3	41.1	40.1
35	46.9	47.6	48.9	46.2	48	42.1
45	60.1	58	58.6	59	49.6	55.9
55	51.6	49.9	51.1	51.1	52	52.6

TABLE 6: Poisson's ratio of hysteresis loops under various confining pressures.

Category of confining pressure (MPa)	Poisson's ratio ( $10^{-2}$ )					Average
	Hysteresis loop 1	Hysteresis loop 2	Hysteresis loop 3	Hysteresis loop 4	Hysteresis loop 5	
0	17.3	19.8	21.1	22.6	23.2	21.0
15	29.1	30.2	30.1	29.5	31.2	28.6
35	41.3	42.0	44.3	44.6	44.3	42.3
45	29.1	29.2	29.1	28.1	27.9	26.5
55	21.3	21.3	21.5	21.3	21.6	21.3

Under a confining pressure of 45 MPa, the elastic modulus reaches a maximum of 52.2 GPa. Poisson's ratio also increases first and then decreases with confining pressure under cyclic loading and unloading. Under a confining pressure of 35 MPa, the elastic modulus reaches a maximum of  $36.3 \times 10^{-2}$ . In a single specimen, the axial strain increment of the hysteresis loops slightly increases with the hysteresis loop under cyclic loading and unloading. For instance, under a confining pressure of 35 MPa, the strain increment of the hysteresis loops are  $8.01 \times 10^{-3}$ ,  $8.12 \times 10^{-3}$ ,  $8.33 \times 10^{-3}$ ,  $8.34 \times 10^{-3}$ , and  $8.08 \times 10^{-3}$ , respectively; however, the axial stress increment remains nearly unchanged. Therefore, the unloading elastic modulus is slightly reduced or almost same. Due to the fact that the granite is taken from a tight hard rock under high geo-stress, the loading and unloading hysteresis loop is long and narrow, and the accretion effect of the rock density is limited under the cyclic loading and unloading stress path.

The variation range of Poisson's ratio gradually decreases, and this trend becomes more significant under high confining pressure. For instance, under a confining pressure of 45 MPa, Poisson's ratio of hysteresis loops 1 to 5 are  $27.5 \times 10^{-2}$ ,  $29.3 \times 10^{-2}$ ,  $27.8 \times 10^{-2}$ ,  $25.8 \times 10^{-2}$ , and  $27.8 \times 10^{-2}$ , respectively. This is because the damage of specimens under cyclic loading and unloading increases with increasing hysteresis loops, which causes the hoop strain to increase with increasing damage. Since the inhibiting ability of the hoop strain is poor under low confining pressure, Poisson's ratio increases significantly with the hysteresis loop under low confining pressure. However, the high confining pressure has a stronger ability

to restrain hoop strain. As a result, Poisson's ratio changes less under high confining pressure cycles.

#### 4. Comparative Analysis of Conventional Triaxial and Cyclic Loading and Unloading Tests

*4.1. Mechanical Parameters.* Under the same confining pressure, the peak strength of specimens in the cyclic loading and unloading tests is generally larger than the corresponding specimens in conventional triaxial tests, which is caused by the greater degree of microfracture closure in the rock under cyclic loading and unloading than under conventional triaxial testing, resulting in greater frictional strength under loading and unloading. The unloading elastic modulus of specimens in the cyclic loading and unloading tests is generally smaller than those in conventional triaxial tests, due to the fact that the hysteresis loop under cyclic loading and unloading is convex. Furthermore, Poisson's ratio of specimens in the cyclic loading and unloading tests is larger than those in conventional triaxial tests because compared to the conventional triaxial unidirectional loading process repeated loading and unloading of the rock specimen under cyclic loading and unloading intensifies the closure, extension, and aggregation of the pre-existing fractures in the specimen, as well as the formation of induced fractures and increases the damage degree. There is a significant cumulative damage effect under cyclic loading and unloading on the mechanical properties of such rocks, indicating that we must consider the effect of cracking on rock mass mechanical parameters caused by cumulative damage under

stage excavation when we analyze the surrounding rock mass stability of underground structures under high geostress.

**4.2. Volumetric Strain Characteristics.** The similarities and differences in volumetric strain characteristics of specimens under conventional triaxial and cyclic loading and unloading tests with the deviatoric stress-volume strain curves at 50 MPa confining pressure are discussed. Under the two stress paths, the curves can be divided into two parts, the volume decrease stage and volume increase stage. That is, when the external load is small, microcracks inside the rock close gradually with increasing external load; hence, the rock volume decreases. When the external load is greater than critical load, microcracks inside the rock splay gradually with increasing external load, causing rock volume to increase until failure. Under the conventional triaxial and cyclic loading and unloading paths, points A and B represent the demarcation points of the two stages, respectively (namely, the maximum point of volume strain). Under the same conditions, the relative increment from the deviatoric stress at the inflection point of volume strain to the peak deviatoric stress in the conventional triaxial test is 0.22 (the difference between the peak deviatoric stress and the deviatoric stress at the inflection point of volume strain/the deviatoric stress at the inflection point of volume strain), while the corresponding increment in the cyclic loading and unloading test is only 0.18. In contrast to the conventional triaxial test, the cumulative damage of specimens in the cyclic loading and unloading test under the same volume strain is larger, restricting the specimen from bearing a larger load increment after reaching the peak volume strain, indicating that, under the same conditions, the bearing potentials of hard surrounding rocks that have undergone multiple stress adjustments are much smaller than those of hard surrounding rocks that have experienced fewer stress adjustments after an external load exceeds its damage stress. Therefore, it is necessary to systematically analyze the stress evolution law and damage degree of the hard surrounding rock under the condition of high stress layered or segmented excavation to estimate its bearing potential and select reasonable reinforcement means and timing.

**4.3. Crack Initiation Stress and Crack Damage Stress.** The volumetric strain is the sum of the elastic volumetric strain and the crack volumetric strain. When the volumetric strain is positive, the volume is decreasing. In the elastic stage, the total volumetric strain increment is equal to the elastic volumetric strain increment. At this moment, the initial crack is closed, and the initial crack volumetric strain is equal to the volumetric shrinkage of the initial crack closure. When the specimen enters the crack growth stage, the volumetric strain increment of the crack propagation is contained in the total volumetric strain increment, so the total volumetric strain increment is less than the elastic strain increment. Hence, the crack volumetric strain curve inclines toward the negative direction and there is an inflection point. The axial stress level corresponding to this

inflection point is the crack stress. When the load increases continuously, the volume deformation of the rock shifts from compression to expansion, and an inflection point will appear in the volumetric strain curve. The axial stress level corresponding to this inflection point is the damage stress. In the conventional triaxial test results, stress values corresponding to the inflection points of the axial strain-volumetric strain curve and the axial strain-crack volumetric strain curve are the initial stress and damage stress, respectively (Figure 6). In the cyclic loading and unloading test results, the stress value corresponding to the inflection point of the axial strain-crack volumetric strain first loading curve on the stress-strain curve is the initial stress, and the stress value corresponding to the inflection point of the axial strain-volumetric strain of the final loading curve on the stress-strain curve is the damage stress (Figure 6). The initial stress and damage stress of specimens under various confining pressures in conventional triaxial and cyclic loading and unloading tests are obtained (Table 7).

According to the data in Table 6, the curves among the crack initiation stress, damage stress, and confining pressure are further plotted (Figure 7). Under conventional triaxial and cyclic loading and unloading tests, the crack initiation stress of the specimen increases first and then decreases with confining pressure (Figure 7). Under a 35 MPa confining pressure, the crack initiation stress reaches 139.4 MPa and 240.5 MPa, respectively. Under the two stress paths, the crack damage stress of the specimens increases linearly with confining pressure. From the slope of the fitting curve, we can see that the crack damage stress increment of specimens in the cyclic loading and unloading tests is generally larger than that in conventional triaxial tests. When the external load is less than the crack damage stress, the closure degree of microfractures in the rock under cyclic loading and unloading is greater than that under conventional triaxial loading. The contact area of microfractures in the rock under cyclic loading and unloading is greater than that under conventional triaxial loading. Therefore, the frictional strength under cyclic loading and unloading is greater than that under conventional triaxial loading, which causes the crack initiation stress and crack damage stress of specimens in the cyclic loading and unloading tests to be generally larger than those in conventional triaxial tests under the same confining pressure.

**4.4. Macrofailure Characteristics.** The macrofailure characteristics of specimens under different confining pressures in the conventional triaxial test are shown in Figure 8. The macrofracture behavior of the granite specimen is shear fracture. Under a 0 MPa confining pressure, there are three primary tensile cracks accompanied by a few secondary cracks, and the damage is relatively serious. Under a 15 MPa confining pressure, a tension-shearing crack intersects the specimen surface, the amount of secondary cracks decreases, and only a few cracks exist. Under a 35~55 MPa confining pressure, only one complete shear crack passes through the upper and lower surfaces of the granite, showing a wedge shape from 45° to 65° with no secondary cracks. Under cyclic

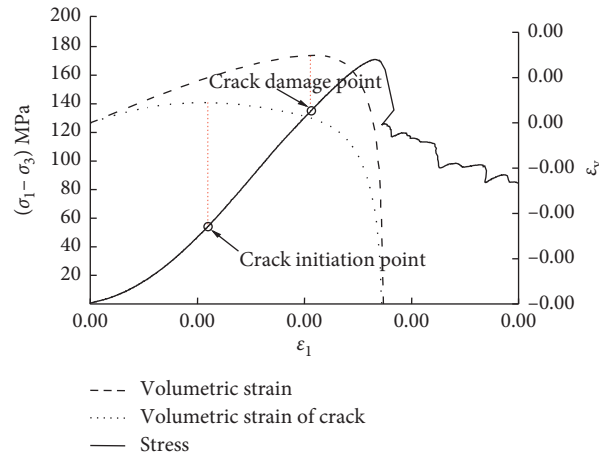


FIGURE 6: Determination of crack initiation stress and crack damage stress.

TABLE 7: Crack initiation stress and crack damage stress under various confining pressures.

Confining pressure (MPa)	Conventional triaxial test		Cyclic loading and unloading test	
	Crack initiation stress (MPa)	Crack damage stress (MPa)	Crack initiation stress (MPa)	Crack damage stress (MPa)
0	58.2	125.1	58.3	132.3
15	75.6	167.9	128.6	181.6
35	98.3	291.5	258.6	322.1
45	89	339.2	142.2	376.2
55	87.2	360.2	140.2	449.5

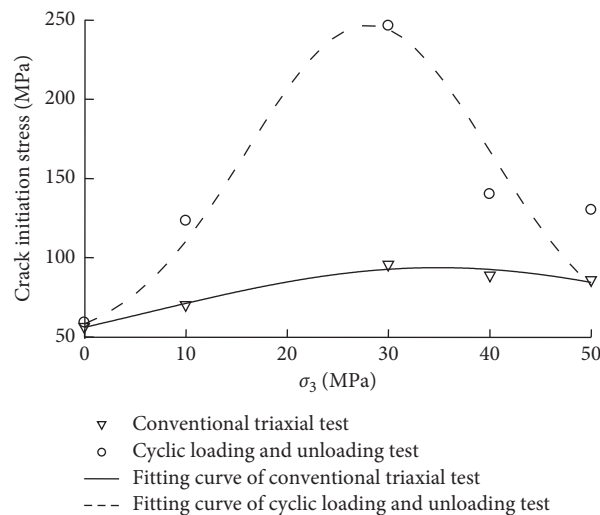


FIGURE 7: Relationship between crack initiation stress, crack damage stress, and confining pressure.

loading and unloading, when the confining pressure is 0 MPa, the damage to the specimen was relatively serious. Most specimens experience damage with a few shear cracks; however, different from the conventional triaxial test, shear cracks with complete transfixion were dominant under 15, 35, and 55 MPa confining pressures, accompanied by a few secondary cracks. Under a 45 MPa confining pressure, there exists a mesh of cracks dominated by shear cracks with

complete transfixion and supplemented by a secondary shear crack. Moreover, tension cracks are present. Since most of the microcracks in the rock are oblique cracks and a few of the microcracks are transverse cracks, some of the oblique cracks in the rock will slip and expand with increasing axial stress under low confining pressure, which causes tensional stress to concentrate and partial tensional cracks to appear. Under high confining pressure, due to the



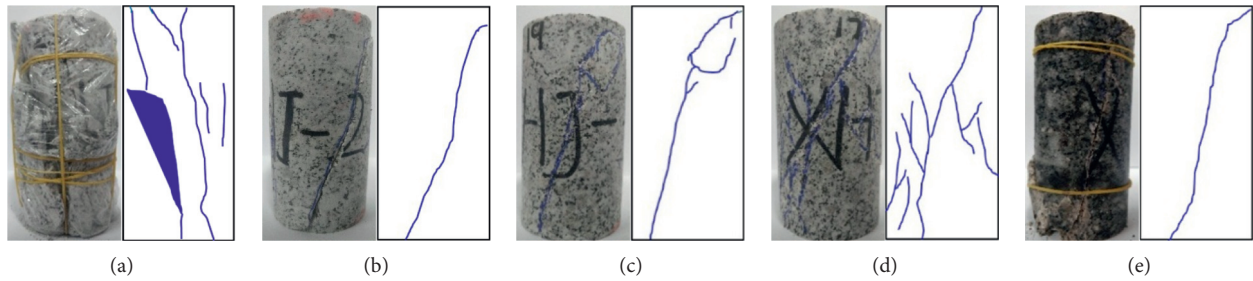


FIGURE 8: Failure characteristics of specimens under various confining pressures.

fact that the tensional stress is less than or equal to the external confining pressure on the rock, these oblique cracks can only develop along the original crack direction and finally connect to form a shear crack running through the upper and bottom portions of the specimen.

In general, under the high stress paths, macroscopic failure of the granite specimens is primarily shear failure, indicating that the supporting measures for deep failure of the complete surrounding rock in the deep-buried underground cavern under high ground stress should be primarily designed to prevent shear failure. Reducing the loose cave surrounding rock and increasing the number of systematic bolts with reasonable distance and length is an effective measure to enhance surrounding rock shear strength.

## 5. Conclusions

In order to study the deformation and failure characteristics of deeply buried granite under high confining pressure triaxial cyclic loading and unloading, we carried out conventional triaxial and cyclic loading and unloading tests on the granite specimens under the various confining pressures, obtained corresponding stress-strain curves as well as characteristics of macroscopic deformation and failure, and comparatively studied the similarities and differences in the deformation and failure laws.

The primary conclusions are as follows:

- (1) Under the two stress paths, the peak strength of the specimens linearly increases with increasing confining pressure. The elastic modulus increases first and then decreases. Under a certain confining pressure, the elastic modulus reaches the maximum value. When the confining pressure is less than a certain value, Poisson's ratio increases with increasing confining pressure. When confining pressure is greater than the value, Poisson's ratio remains unchanged or decreases with confining pressure. The crack initiation stress increases first and then decreases with confining pressure, while the crack damage stress increases linearly with confining pressure.
- (2) Under the same confining pressure, the peak strength, crack initiation stress, crack damage stress, and Poisson's ratio of specimens in the cyclic loading and unloading tests are generally larger than those in conventional triaxial tests, while the unloading

elastic modulus is smaller than that in conventional triaxial tests. The results reveal that cyclic loading and unloading has a significant strengthening effect on the frictional strength of rock and has a significant cracking effect on deformation parameters.

- (3) The macroscopic failure characteristics of the specimens under conventional triaxial and cyclic loading and unloading tests were slightly different with varying confining pressure. Specimens under low confining pressure primarily undergo shear failure, accompanied by a few of tensile cracks and secondary cracks. Under high confining pressure, only one complete shear crack passes through the upper and bottom surfaces of the specimen. Results show that the supporting measures for deep failure of the complete surrounding rock in the deep underground cavern in the sampling location should be primarily designed to prevent shear failure.

## Data Availability

The datasets generated for this study are available from the corresponding author upon request.

## Conflicts of Interest

The authors declare that they have no conflicts of interest.

## Authors' Contributions

Jun Zhao completed the test of hard rock under triaxial and cyclic loading and unloading stress paths. Tan Zhang completed the establishment, solution, and manuscript of the macroscopic failure characteristics of the samples under conventional triaxial and cyclic loading and unloading tests.

## Acknowledgments

This work was financially supported by the National Natural Science Foundation of China (51979268).

## References

- [1] X. Heping, F. Gao, and J. Yang, "Research and development of rock mechanics in deep ground engineering," *Chinese Journal of Rock Mechanics and Engineering*, vol. 34, no. 11, pp. 2161–2178, 2015.

- [2] H. Man-chao, X. He-ping, and P. Su-ping, "Study on rock mechanics of deep mining engineering," *Chinese Journal of Rock Mechanics and Engineering*, vol. 24, no. 16, pp. 2803–2813, 2005, <https://www.researchgate.net/scientific-contributions/Y-D-Jiang-2084506269>.
- [3] M.-Y. Wang, Z.-P. Zhou, Q. Qi-Hu et al., "Tectonic, deformation and failure problems of deep rock mass," *Chinese Journal of Rock Mechanics and Engineering*, vol. 25, no. 3, pp. 448–455, 2006.
- [4] X. Heping, "Research framework and anticipated results of deep rock mechanics and mining theory," *Engineering Science and Technology*, vol. 49, no. 2, pp. 1–16, 2017.
- [5] Y.-H. Huang, S.-Q. Yang, W.-L. Tian, W. Zeng, and L.-Y. Yu, "An experimental study on fracture mechanical behavior of rock-like materials containing two unparallel fissures under uniaxial compression," *Acta Mechanica Sinica*, vol. 32, no. 3, pp. 442–455, 2016.
- [6] C. D. Martin and N. A. Chandler, "The progressive fracture of lac du bonnet granite," *International Journal of Rock Mechanics and Mining Sciences and Geomechanics Abstracts*, vol. 31, no. 6, pp. 643–659, 1994.
- [7] C. D. Martin, "Seventeenth Canadian geotechnical colloquium: the effect of cohesion loss and stress path on brittle rock strength," *Canadian Geotechnical Journal*, vol. 34, no. 5, pp. 698–725, 1997.
- [8] T. H. Yang, P. Jia, W. H. Shi, P. T. Wang, H. L. Liu, and Q. L. Yu, "Seepage-stress coupled analysis on anisotropic characteristics of the fractured rock mass around roadway," *Tunnelling and Underground Space Technology*, vol. 43, pp. 11–19, 2014.
- [9] Z. Q. Yin, Z. X. Hu, Z. D. Wei et al., "Assessment of blasting-induced ground vibration in an open-pit mine under different rock properties," *Advances in Civil Engineering*, vol. 2018, Article ID 4603687, 10 pages, 2018.
- [10] Z. Yin, W. Chen, H. Hao et al., "Dynamic compressive test of gas-containing coal using a modified split hopkinson pressure bar system," *Rock Mechanics and Rock Engineering*, vol. 53, pp. 815–829, 2019.
- [11] X.-T. Feng, H.-S. Guo, C.-X. Yang, and S.-J. Li, "In situ observation and evaluation of zonal disintegration affected by existing fractures in deep hard rock tunneling," *Engineering Geology*, vol. 242, pp. 1–11, 2018.
- [12] G. Li, Z. Jiang, C. Lv, C. Huang, G. Chen, and M. Li, "Instability mechanism and control technology of soft rock roadway affected by mining and high confined water," *International Journal of Mining Science and Technology*, vol. 25, no. 4, pp. 573–580, 2015.
- [13] Y. Ming-Qing and S. Cheng-Dong, "Experimental study on strengthening of marble specimen in cyclic loading of uniaxial or pseudo-triaxial compression," *Chinese Journal of Solid Mechanics*, vol. 29, no. 1, pp. 66–72, 2008.
- [14] S. Zhang, S. F. Cox, and M. S. Paterson, "The influence of room temperature deformation on porosity and permeability in calcite aggregates," *Journal of Geophysical Research*, vol. 99, no. 8, pp. 15761–15815, 1994.
- [15] J. J. Zhang, W. B. Standifird, J.-C. Roegiers, and Y. Zhang, "Stress-dependent fluid flow and permeability in fractured media: from lab experiments to engineering applications," *Rock Mechanics and Rock Engineering*, vol. 40, no. 1, pp. 3–21, 2007.
- [16] B. Wang, J.-B. Zhu, Y. Ai-Qing, and J. Hu, "Experimental study on mechanical properties of jinning marble under loading and unloading stress paths," *Chinese Journal of Rock Mechanics and Engineering*, vol. 27, no. 10, pp. 2138–2145, 2008.
- [17] L. Hao-Ran, Y. Chun-He, L. Yu-Lin et al., "Damage evolution and characteristics of ultrasonic velocity and acoustic emission for salt rock under triaxial multilevel loading test," *Chinese Journal of Rock Mechanics and Engineering*, vol. 35, no. 4, pp. 682–691, 2016.
- [18] P. Rui-Dong and J. Yang, W. Peng, "Energy analysis on damage of coal under cyclical triaxial loading and unloading conditions," *Journal of China Coal Society*, vol. 39, no. 2, pp. 245–252, 2014, [https://www.researchgate.net/profile/Feng\\_Gao27https://www.researchgate.net/profile/Heping\\_Xie3](https://www.researchgate.net/profile/Feng_Gao27https://www.researchgate.net/profile/Heping_Xie3).
- [19] X.-B. Yang, H.-M. Cheng, L. Jia-Qi et al., "Energy consumption ratio evolution law of sandstones under triaxial cyclic loading," *Rock and Soil Mechanics*, vol. 40, no. 10, pp. 3751–3757, 2019.
- [20] Z. C. Tang, Q. Z. Zhao, and J. Peng, "Effect of thermal treatment on the basic friction angle of rock joint," *Rock Mechanics and Rock Engineering*, vol. 53, no. 4, pp. 1973–1990, 2020.
- [21] Z. T. Bieniawski and M. J. Bernede, "Suggested methods for determining the uniaxial compressive strength and deformability of rock materials," *International Journal of Rock Mechanics and Mining Sciences*, vol. 16, no. 2, pp. 135–140, 1979.
- [22] X. Shu-Fang and Y. Shu-Bi, *Rock Mechanics*, Geological Publishing House, Beijing, China, 1986.
- [23] Y. Ming-qing, S. Cheng-dong, and X. Tao, "Loading or unloading process in axial direction and young's modulus of rock specimen," *Chinese Journal of Geotechnical Engineering*, vol. 23, no. 5, pp. 588–592, 2001.
- [24] Z. Ze-Qi, S. Qian, L. Xian-lun, and Z. Zhang, "Study on crack initiation mechanism of three gorges granite," *Chinese Journal of Rock Mechanics and Engineering*, vol. 26, no. 12, pp. 2570–2575, 2007.

## Research Article

# Effects of Different Conditions of Water Cooling at High Temperature on the Tensile Strength and Split Surface Roughness Characteristics of Hot Dry Rock

Hanbo Cui , Jupeng Tang , and Xintong Jiang 

School of Mechanics and Engineering, Liaoning Technical University, Fuxin, Liaoning 123000, China

Correspondence should be addressed to Jupeng Tang; tangjupeng@lntu.edu.cn

Received 23 September 2020; Revised 30 October 2020; Accepted 7 November 2020; Published 25 November 2020

Academic Editor: Zhi Cheng Tang

Copyright © 2020 Hanbo Cui et al. This is an open access article distributed under the Creative Commons Attribution License, which permits unrestricted use, distribution, and reproduction in any medium, provided the original work is properly cited.

To investigate the effects of the different conditions of water cooling at high temperature on the tensile strength and split surface roughness characteristics of hot dry rock in the Songliao Basin, the physical characteristics, tensile strength, and split surface roughness of granite under different conditions of water cooling at high temperature were studied. In addition, the relationship between tensile strength and split surface roughness under different conditions of water cooling at high temperature was established. The results showed the following: (1) as the rock temperature increased, the number of water injection cycles increased or the water injection temperature decreased, the mechanical properties of the specimen weakened, and the roughness of the split surface increased. The threshold for the effect of the rock temperature on the split surface roughness of granite was 300°C. At 400°C, the tensile strength greatly decreased. At 600°C, the tensile strength, height mean square error (MSE), fluctuation difference, roughness coefficient, and roughness profile index of the specimen were 0.21, 2.51, 2.57, 8.92, and 1.06 times those at 100°C, respectively. After five heating-cooling cycles, the tensile strength, height MSE, fluctuation difference, roughness coefficient, and roughness profile index of the specimen were 0.57, 1.33, 1.49, 1.29, and 1.01 times those after one cycle, respectively. (2) The roughness angle calculated using the root mean square of the first derivative of the profile was always greater than that derived using the roughness profile index. In addition, the higher the temperature, the lower the water temperature, the more high-temperature-water cooling cycles, the greater the difference between the above two calculations. (3) When the tensile strength varies, the factors affecting the variation in the height MSE and surface roughness were in the following descending order: rock temperature, number of heating-cooling cycles, and water temperature. In addition, the higher the tensile strength, the lower the roughness coefficient. This study is expected to provide a reference for the selection of different conditions of water cooling at high temperature for thermal recovery in the Songliao Basin.

## 1. Introduction

The enhanced geothermal system (EGS) is a technology used for the development of hot dry rock (HDR) by fracturing a reservoir via artificial fracturing and extracting the heat for use from the heat exchange between water and HDR (MIT [1]). The HDR temperature is the primary factor in selecting the location of EGS thermal recovery and determining the production prospects and operating cost of the target area. As water acts as a heat transmission fluid, water temperature is an important control parameter for thermal recovery. The number of water injection circulation cycles at high

temperatures is also closely related to the lifespan of a reservoir. Therefore, understanding the relationships between the temperature of the target area, the water injection temperature, and the number of water circulation cycles performed at high temperatures with the physical and mechanical properties of granite, which are important for the high-quality production of the EGS, is valuable.

In recent years, many numerical simulations have studied the relationship between the injection-production conditions and EGS. Jing et al. [2], Vogt et al. [3], and Zhao et al. [4] discovered that the initial temperature of a reservoir is closely related to the EGS production capacity, and the

higher the temperature is, the better the heat production efficiency is. With the development of thermal recovery, when the temperature of the reservoir decreases to a certain level, the production capacity also decreases. Xin et al. [5] found that the fracture number, fracture bifurcation, and fracture connectivity of the fracturing area determine the final temperature production, net power generation, and thermal recovery rate. Fox et al. [6] and Kazemi et al. [7] demonstrated that as the production capacity decreased, the heat production efficiency was significantly reduced; production should be stopped until the heat energy is restored; and HDR experienced multiple cycles of water cooling at high temperatures during this period. Bataillé et al. [8] and Gong et al. [9] noted a certain correlation between the temperature of the injected fluid and the production capacity. Some researchers have experimentally investigated the physical and mechanical properties of rock in high temperature conditions. Gautam et al. [10] conducted uniaxial tensile and microscopic tests of granite after naturally cooling from high temperatures and established the relationship between the thermal damage and the tensile strength. Shen et al. [11, 12] performed a cooling shock treatment on perforated granite using a calcium chloride solution. They found that when the temperature was above 550°C, as the fluid was injected, obvious macrofractures appeared around the injection hole of the rock, and the lower the refrigerant temperature, the more pronounced the macrofractures. In addition, the higher the rock temperature, the greater the drop in the wave velocity, apparent resistivity, and peak stress. Hu et al. [13] explored the fracture characteristics of granite subjected to tensile failure using different cooling methods. Isaka et al. [14] investigated the mechanical properties of granite under natural cooling and water cooling and found that the deterioration of the rock under water cooling was much higher than that under natural cooling. Zhao [15] noted that at real-time high temperatures, the tensile strength of granite decreases with increasing temperatures. Li and Ju [16] conducted tests on the mechanical properties of granite after several thermal cycles and discovered that most of the mechanical property loss of granite after high-temperature cycles occurred within five thermal cycles. Hosseini [17] found that as the number of high temperature natural cooling cycles increased, the longitudinal wave velocity and tensile strength of the rock decreased significantly.

In addition, some researchers have investigated rock roughness and discussed the correlations between the roughness and the mechanical properties. Ficker [18] evaluated the rock surface roughness using the root mean square (RMS) height. Zeng et al. [19] determined that tensile fracture was a main component of fractures in low-permeability reservoirs. Grasselli and Egger [20] investigated the relationship between the joint roughness coefficient (JRC) and the tensile fracture propagation pattern. Zhang et al. [21] qualitatively examined the relationship between the tensile strength of split granite and the roughness of the split surface. Diaz et al. [22] suggested that the fracture roughness affects the heat production efficiency of an EGS. Tang and Zhang [23] applied shear tests to simulate the

internal fracture structure of a deep, high-temperature rock body to explore the relationship between the temperature and surface roughness of a specimen. Li et al. [24] found that the roughness of the rock surface will affect the liquid nitrogen cryogenic quenching process. Tang et al. [23, 25–27] conducted uniaxial compression tests and shear tests on rocks after heat treatment at 20–800°C and analyzed the effects on several key parameters. As the temperature rises, the concerning parameters exhibit different change rules: the basic friction angle, the uniaxial compressive strength, and the joint roughness coefficient of granite decrease nonlinearly; the cohesion and internal friction angle exhibit a reverse S-shape changing trend; the peak shear strength increases linearly below 400°C and decreases nonlinearly at 400–800°C. The changing of rock mechanical properties and joint surface roughness parameters is related to the dehydration process and the uneven expansion of mineral grains. It is also pointed out [27] that the three-point peak criterion is the most suitable evaluation standard for rock joints.

Numerical simulations of EGS thermal recovery have mainly been performed to study the heat production efficiency, and the investigation of high-temperature granite has focussed on the physical and mechanical properties of rock after natural cooling or at real-time high temperatures. However, there are few studies on the effects of water cooling at high temperatures or cyclic water cooling at high temperatures on the physical and mechanical properties of rock using HDR as the research substrate. In addition, many tensile fractures usually form in low-permeability strata during the thermal recovery process. Different conditions of water cooling at high temperature can cause large differences in the roughness of a fracture surface, which affects the flow path and heat transfer process and changes the heat production efficiency.

Currently, optical and mechanical methods exist for measuring the roughness of a structural surface. The optical methods consist of a laser transmitter–receiver and a digital simulation system, which can measure the three-dimensional (3D) spatial morphology of a structural surface. Although the optical method has a high measurement speed and accuracy, its shortcomings include a small measurement range of the height difference and a very high cost, which limit it to measuring laboratory-fixed specimens within a short distance. The mechanical method consists of a contact probe, driving device, and digital simulation system, which can only be employed for two-dimensional measurements. The application range of the mechanical method is also limited to laboratory-fixed specimens. Therefore, building a low-cost, flexible, and accurate instrument for 3D roughness measurements is necessary.

Based on the above factors, to investigate the effects of different conditions of water cooling at high temperature on the physical and mechanical properties as well as the roughness characteristics of the split surface of HDR, we employed HDR production in the Songliao Basin as the research background to conduct a Brazilian disc test on specimens under different conditions of water cooling at high temperature. A self-developed roughness profilometer was used to measure the roughness of the split surface to

study the effects of the rock temperature, water temperature, and number of heating-cooling cycles performed on the physical characteristics (apparent morphology and mass loss rate), mechanical properties (tensile strength), and split surface roughness properties (height difference parameters, including the height mean square error (MSE) and fluctuation difference, and texture parameters, including the roughness coefficient, roughness profile index, and roughness angle). We have established a relationship between the mechanical parameters and roughness coefficient (tensile strength-height MSE and tensile strength-roughness coefficient) of different conditions of water cooling at high temperature. This study can provide a reference for the selection of different conditions of water cooling at high temperature at the geothermal field in the Songliao Basin.

## 2. Overview of the Tests

**2.1. Geological Background.** The Songliao Basin spans Inner Mongolia, Heilongjiang, Jilin, and Liaoning. Under the influence of geological tectonic movements, faults at the basin basement notably developed, and there is frequent volcanic activity, as well as multiple geothermal anomalies (Zhang et al. [28]). Three main types of heat sources exist in the geothermal field: mantle convection, magma intrusion, and the decay of radioactive elements inside the rock mass. Under the combined action of the three sources, the geothermal flux is in the range of 51.5–90.0 mW/m<sup>2</sup>. The average geothermal gradient is 5.7°C/100 m. The total amount of HDR resources is  $0.62 \times 10^6$  g/cm<sup>3</sup> EJ (Li [29]). The upper part of the target stratum is mainly composed of epimetamorphic rock series and granite, and the lower part is mainly composed of hypometamorphic rock series and gneissic granite. The overlying mudstone caprocks can ensure the storage of thermal energy, and the Songhua River system is located near a geothermal field. Based on these factors, the geothermal field in the Songliao Basin has reasonable prospects for geothermal development.

**2.2. Specimen Preparation.** The northern Songliao Basin was selected as the target area for sampling. The specimens appeared to be greyish white with a density between 2.71 g/cm<sup>3</sup> and 2.99 g/cm<sup>3</sup>. The main mineral compositions include quartz, black or white mica, potash feldspar, plagioclase, pyroxene, and hornblende, as shown in Table 1. A coring machine, cutting machine, and grinding machine were used to machine and polish the specimens. The specimen dimensions were  $\phi 50$  mm  $\times$  25 mm with height and diameter errors of <3 mm. A total of 16 sets of tests were performed, and each set included three specimens.

**2.3. Test Design.** Table 2 shows the design of the tests.

- (1) Different heating temperatures: the HDR was dense, impermeable high-temperature rock buried at a depth of 3–10 km. The rock body contained no water or water vapour, and the temperature was often in the range of 150–650°C (Zhao et al.

[4]). Based on current research findings (Zhang et al. [30], Zhao et al. [31], Zhang et al. [32], and Yang et al. [33]) and the future development of HDR, the specimens were heated to 100°C, 200°C, 300°C, 400°C, 500°C, or 600°C. That is, the heating temperature was 100–600°C, the water temperature was 20°C, and one water cooling cycle was performed at a high temperature.

- (2) Different water temperatures: the water temperature of the Songhua River ranges between 1°C and 25°C. Considering the rise in the water temperature during injection, water temperatures of 1°C, 20°C, 40°C, 60°C, and 80°C were selected for the test. That is, the water temperature was 1–80°C, the specimen temperature was 300°C, and one water cooling cycle was performed at a high temperature.
- (3) The number of heating-cooling cycles: considering the number of cycles of water injection and heat recovery, the number of water cooling cycles at high temperatures was one, two, three, four, or five. That is, the number of heating-cooling cycles was 1–5 (Fox et al. [6] and Li and Ju [16]), the specimen temperature was 300°C, and the water temperature was 20°C.

The test contents included the cyclic water cooling at a high temperature test, the Brazilian disc test, and the roughness test. Following the “Regulation for Testing the Physical and Mechanical Properties of Rock” [34], adjustments were made according to the test conditions. The test process is shown in Figure 1.

- (1) Measurement of specimens in the natural state: a balance was used to measure the mass, and a Vernier caliper was used to measure the height and diameter.
- (2) Heating and water cooling processes under different test protocols, specifically shown in Figures 2(a) and 2(b).
  - (a) Different heating temperatures: an electric stove was used to heat the specimens to the set temperatures (100–600°C) at a rate of 30°C/min. To ensure even heating inside and outside the specimen, the specimens were kept at a constant temperature for 4 h (Yan et al. [35]) and then placed in an alkali aggregate reaction chamber and water-cooled for 4 h (at a water temperature of 20°C, the test showed that, after water cooling for 4 h, the temperatures of the specimens all decreased to approximately 20°C, indicating that no more heat transferred between the water and the specimen, and the specimen was saturated).
  - (b) Different water temperatures: the specimen was heated to 300°C, kept at 300°C for 4 h, and then water-cooled for 4 h (the water temperature was kept at 1–80°C).
  - (c) The number of heating-cooling cycles: the specimen was kept at 300°C for 4 h and then cooled in 20°C water for 4 h. This process was repeated 1–5 times. In addition, ice was added to

TABLE 1: Mineral composition.

Colour	Mineral composition				
	Quartz White transparent, etc.	Mica Black and white, etc.	Potash feldspar White and red, etc.	Plagioclase, etc. White and grey, etc.	Pyroxene and hornblende Black and brown
Chemical composition	SiO <sub>2</sub> , etc.	KAl <sub>2</sub> (AlSi <sub>3</sub> O <sub>10</sub> )(OH) <sub>2</sub> and Fe, etc.	K(AlSi <sub>3</sub> O <sub>8</sub> ), etc.	Na(AlSi <sub>3</sub> O <sub>8</sub> ) and Ca (Al <sub>2</sub> Si <sub>2</sub> O <sub>8</sub> ), etc.	(Na, Ca) <sub>2</sub> (Mg, Fe, Al) <sub>5</sub> and [(Si, Al) <sub>4</sub> O <sub>11</sub> ] <sub>2</sub> (OH) <sub>2</sub>
Content (%)	26.1	8.9	36	25.2	3.8
Particle size (mm)	0.1–2.1	0.35–1.2	0.75–4	2–2.5	—
Coefficient of thermal expansion (1/°C)	5.5 × 10 <sup>-7</sup>	2.2 × 10 <sup>-5</sup>	(5~6) × 10 <sup>-6</sup>	(6.5~7.5) × 10 <sup>-6</sup>	—

Note. The thermal expansion coefficient of mineral composition comes from the network.

TABLE 2: Test scheme.

Test specimen	Heating temperature (°C)	Water temperature (°C)	The number of heating-cooling cycles (times)	Heating time (h)	Water-cooled time (h)
C1	100	20	1	4	4
C3	200	20	1	4	4
C5	300	20	1	4	4
C6	400	20	1	4	4
C7	500	20	1	4	4
C8	600	20	1	4	4
W1	300	1	1	4	4
W2	300	20	1	4	4
W3	300	40	1	4	4
W4	300	60	1	4	4
W5	300	80	1	4	4
P1	300	20	1	4	4
P2	300	20	2	4	4
P3	300	20	3	4	4
P4	300	20	4	4	4
P5	300	20	5	4	4

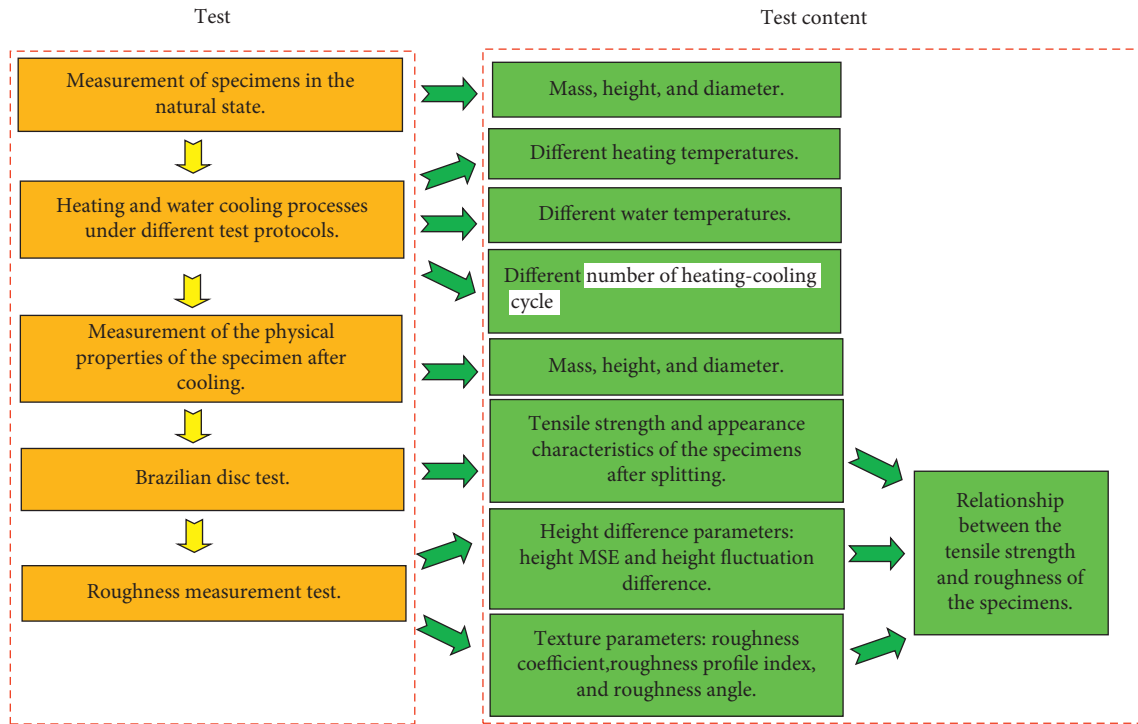


FIGURE 1: Test process.

cool the water to keep the water temperature consistent. An infrared thermometer was used to monitor the water temperature.

- (3) Measurement of the physical properties of the specimen after cooling: the mass, height, and diameter of the specimen under different conditions of water cooling at high temperature were measured, and changes in the appearance characteristics of the specimen were observed.
- (4) Brazilian disc test: thin steel wires were placed as pads on the upper and lower tension surfaces of the

specimen. The specimen was then placed on a press. Experiments revealed that when the loading rate is 0.5 MPa/s, the mass loss rate is the smallest. Therefore, the test was conducted at a loading rate of 0.5 MPa/s until the specimen was damaged. The tensile strength was recorded as specifically shown in Figure 2(c).

- (5) Roughness measurement test: a dial gauge was fixed on a slide rail. After it was split, the specimen was placed on the base, and the horizontal positions of the slide rail and the specimen were adjusted. The

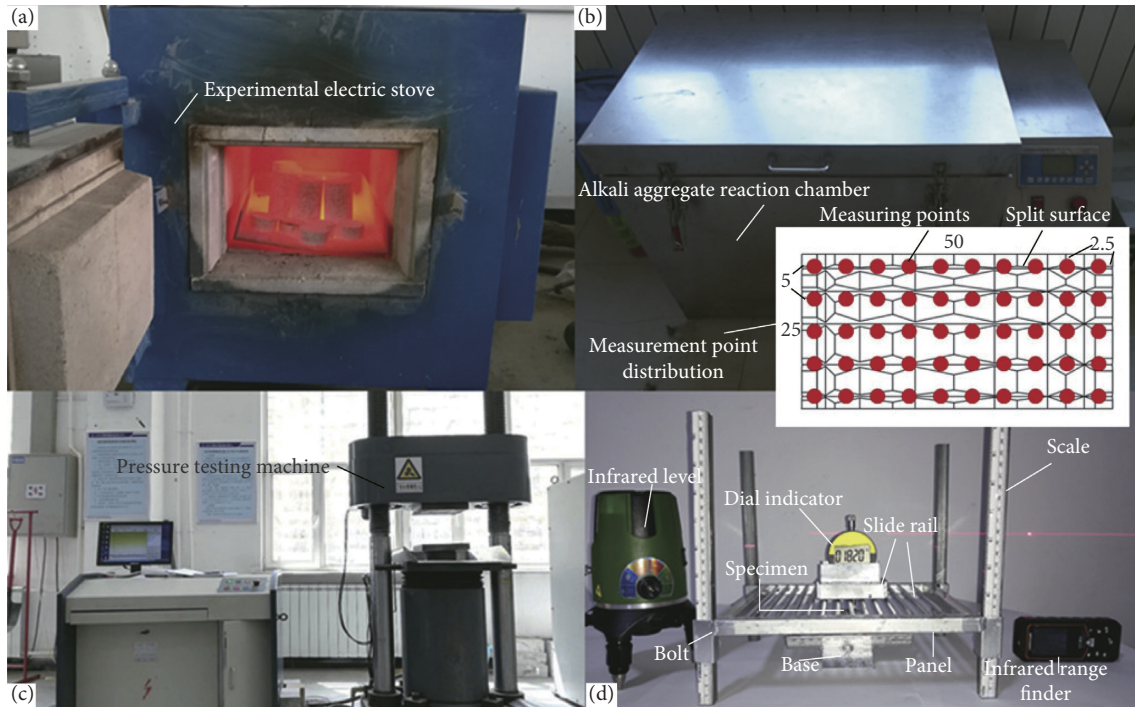


FIGURE 2: Test content. (a) Heating. (b) Cooling. (c) Brazilian disc test. (d) Roughness measurement.

vertical height of the panel was adjusted with nuts. The horizontal angles of the panel and the specimen were measured and levelled with an infrared level. The slide rail was pushed to perform measurements at different measuring points (an infrared range-finder was used to ensure the slide accuracy). The experiment revealed particle shredding during the splitting process. Particle shredding often occurred at the edge of the splitting surface. To minimize the effect of the side of the probe and particle shredding at the edge of the splitting surface, all shredded particles were collected and glued together. The contour sampling method was used to determine the spacing between measuring points, with the measuring points being 2.5 mm from the edge. The specific arrangement of measuring points is shown in Figure 2(d)

**2.4. Test Equipment.** The test equipment parameters are listed in Table 3.

**2.5. Verification of the Accuracy of the Roughness Tester.** To verify the accuracy of the homemade roughness tester, a portable roughness tester was used to measure each specimen. The results showed that the two testers yielded similar measurement results, indicating that the homemade tester was reliable. The verification results are shown in Figure 3.

### 3. Test Results and Analysis

**3.1. Variation Pattern of Appearance Characteristics in Specimens under Different Conditions of Water Cooling at**

*High Temperatures.* With a temperature of 300°C or three heating-cooling cycles, the roughness of the split surface significantly increased. When the temperature reached 500°C or four heating-cooling cycles, the colour of the specimen changed significantly. Adjusting the water temperature did not notably change the appearance of the specimen.

Figures 4(a) and 4(b) show the appearance characteristics of the specimens after splitting under different conditions of water cooling at high temperature. As shown in Figure 4(a), when the temperature was between 100°C and 200°C, the appearance of the specimen changed only slightly from the natural state. The surface was greyish white with localized black spots. When the temperature was between 300°C and 400°C, the colour became lighter, and there were fewer black spots. When the temperature reached 500°C–600°C, the HDR changed from a reddish brown colour to a black-grey colour, and white crystals were locally generated. As the water temperature changed, the colour of the specimen did not change significantly. When the number of heating-cooling cycles reached four or five, the number of black spots decreased substantially, and the appearance turned from a grey-white colour to white.

Figures 4(a) and 4(b) show that all specimens had penetrating fractures in the radial direction after splitting under different conditions of water cooling at high temperature. The split surface was generally parallel to the plane defined by two thin steel wires. However, the roughness of the split surface differed. When the temperature was between 100°C and 200°C, the penetrating fractures were relatively close together. When the temperature was between 300°C and 600°C, the split surface was uneven, and even if it was pieced together, a few gaps remained. As the temperature rose, the split surface became rougher. Varying the



TABLE 3: Test equipment.

Function	Device	Remarks
Weighing	Electronic balance	Error 0.01 g
Heating	SX2-14-13 experimental electric stove	Room temperature to 1250°C
Cooling	JKS automatic alkali aggregate reaction chamber	1–100°C
Achieving constant temperature	101-1 electrothermal blowing dry box	Room temperature to 300°C
Brazilian disc test	YAW-microcomputer controlled electrohydraulic servopressure testing machine	Weighing range 10 t
Roughness measurement	Roughness profilometer	Micrometre (accuracy 0.001 mm)
		Infrared level (accuracy 0.1 mm)
		Infrared range finder (accuracy 0.1 mm)

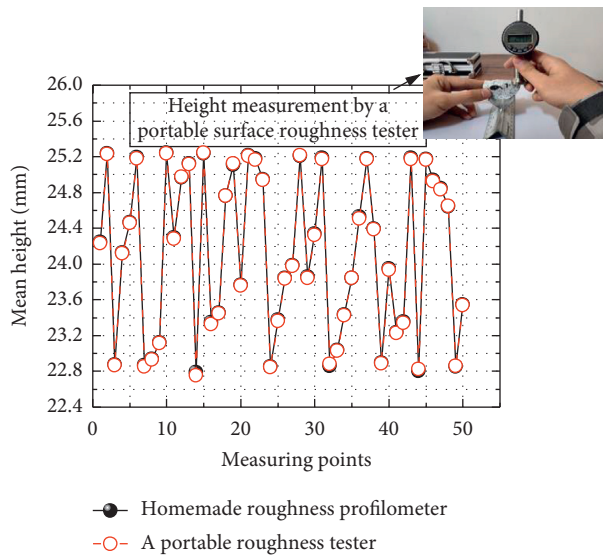


FIGURE 3: Verification of the accuracy of the homemade roughness tester.

water temperature did not noticeably change the roughness of the fracture surface. When the number of heating-cooling cycles went from one to two, the roughness of the fracture surface did not change significantly. After three cycles, the roughness significantly increased. Therefore, the factors that influenced the appearance characteristics of the specimens, from strongest to weakest, were the temperature of HDR, the number of water injection circulation cycles performed at high temperatures, and the water injection temperature. The different conditions of water cooling at high temperature experienced by the thermal recovery area can be deduced from the changes in the appearance characteristics.

**3.2. Variation Pattern of the Mass of the Specimen under Different Conditions of Water Cooling at High Temperatures.** When the temperature rose, the water temperature decreased or the number of water injection circulation cycles increased and the mass loss rate increased. When the temperature was between 300°C and 500°C or at least two water injection cycles occurred, the mass loss rate increased substantially.

To better characterize the mass change rate of the specimens subjected to different conditions of water cooling at high temperature, the mass loss rate ( $Q$ ) is introduced and expressed as in the following equation.

$$Q = \frac{m_0 - m_1}{m_0} \times 100\%, \quad (1)$$

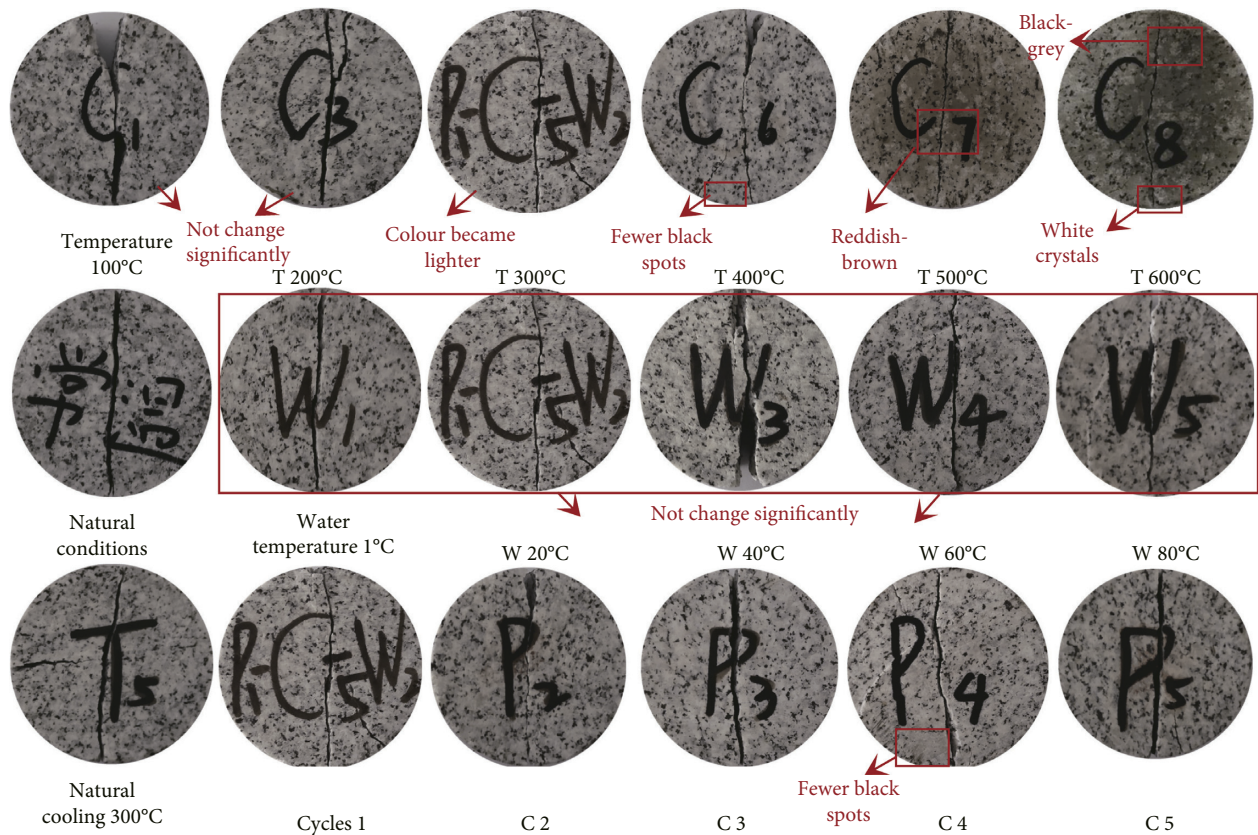
where  $Q$  is the mass loss rate (%),  $m_0$  is the mass of the specimen in a natural state (g), and  $m_1$  is the mass of the specimen after the test (g).

Figure 5 shows the variation pattern of the mass loss rate for the specimens under different conditions of water cooling at high temperature. An examination of the effect of temperature on the mass loss rate of the specimens indicated that the effect of a high temperature on the mass loss rate of the specimens was not significant when the temperature was between 100°C and 300°C. When the temperature reached 400°C, the mass showed a large decrease, with a loss rate of 0.2075%. At 600°C, the mass loss rate reached 0.2822%. Therefore, an increase in temperature increased the mass loss rate of the specimen.

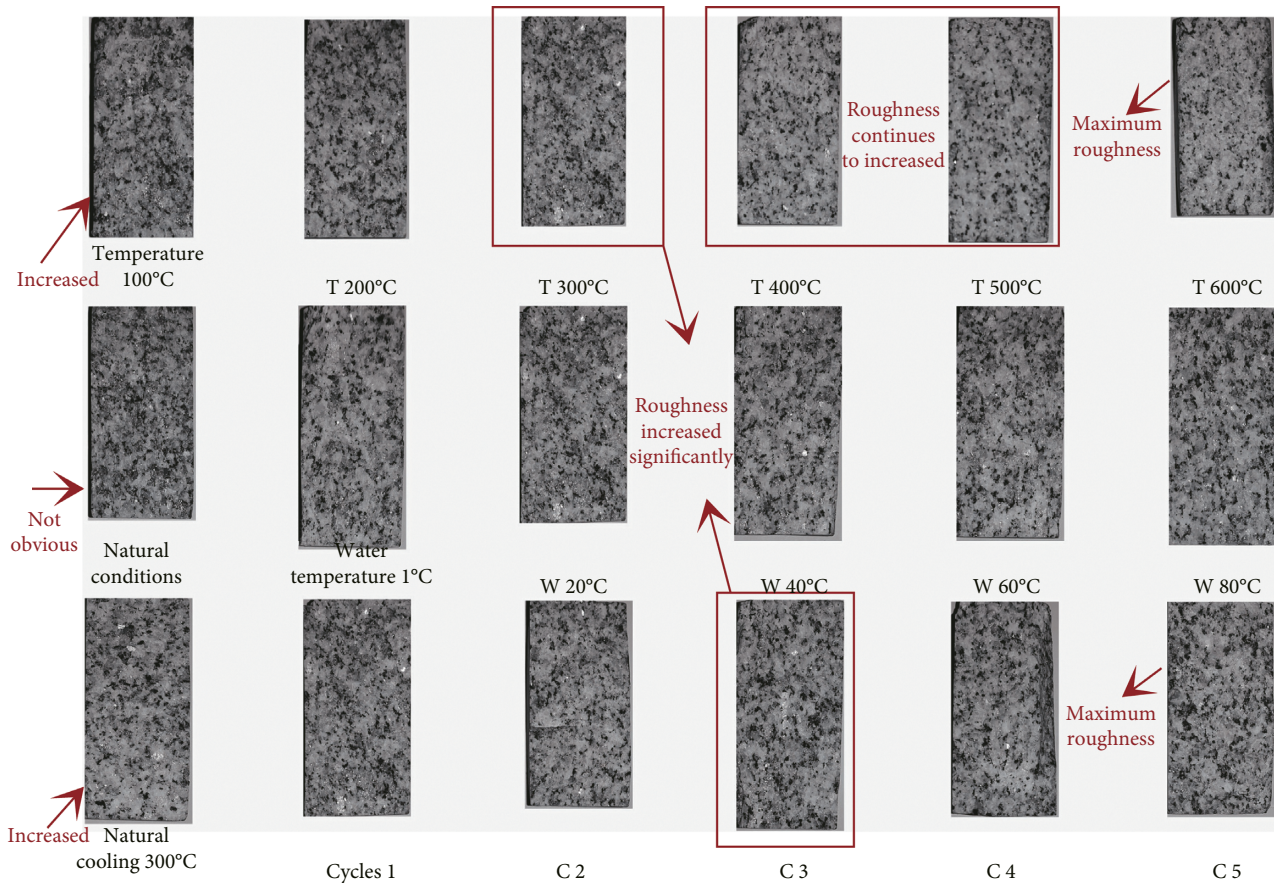
An examination of the effect of the water temperature on the mass loss rate of specimens revealed that at a water temperature of 1°C, the mass loss rate of the specimens was approximately 0.1313%. When the water temperature reached 80°C, the mass loss rate decreased to 0.0962%. Therefore, an increase in the water temperature can reduce the mass loss of the specimens to some extent.

The effect of the number of heating-cooling cycles performed on the mass loss rate of the specimens was investigated. The mass loss of the specimen occurred mainly at the initial stage of the water injection cycle. After two heating-cooling cycles were performed, the mass loss rate of the specimen was approximately 0.1855%. As the number of water injection cycles increased, the mass loss rate of the specimen increased, but the magnitude of the loss decreased. After five cycles, the loss rate was approximately 0.2204%.

**3.3. Variation Pattern of the Tensile Strength of Specimens under Different Conditions of Water Cooling at High Temperatures.** When the temperature rose, the water temperature decreased or the number of water circulation cycles increased and the tensile strength of the specimen decreased. When the temperature was 400°C or at least two water



(a)



(b)

FIGURE 4: Appearance characteristics of the specimens after splitting under different conditions of water cooling at high temperature. (a) Front view. (b) Side view.

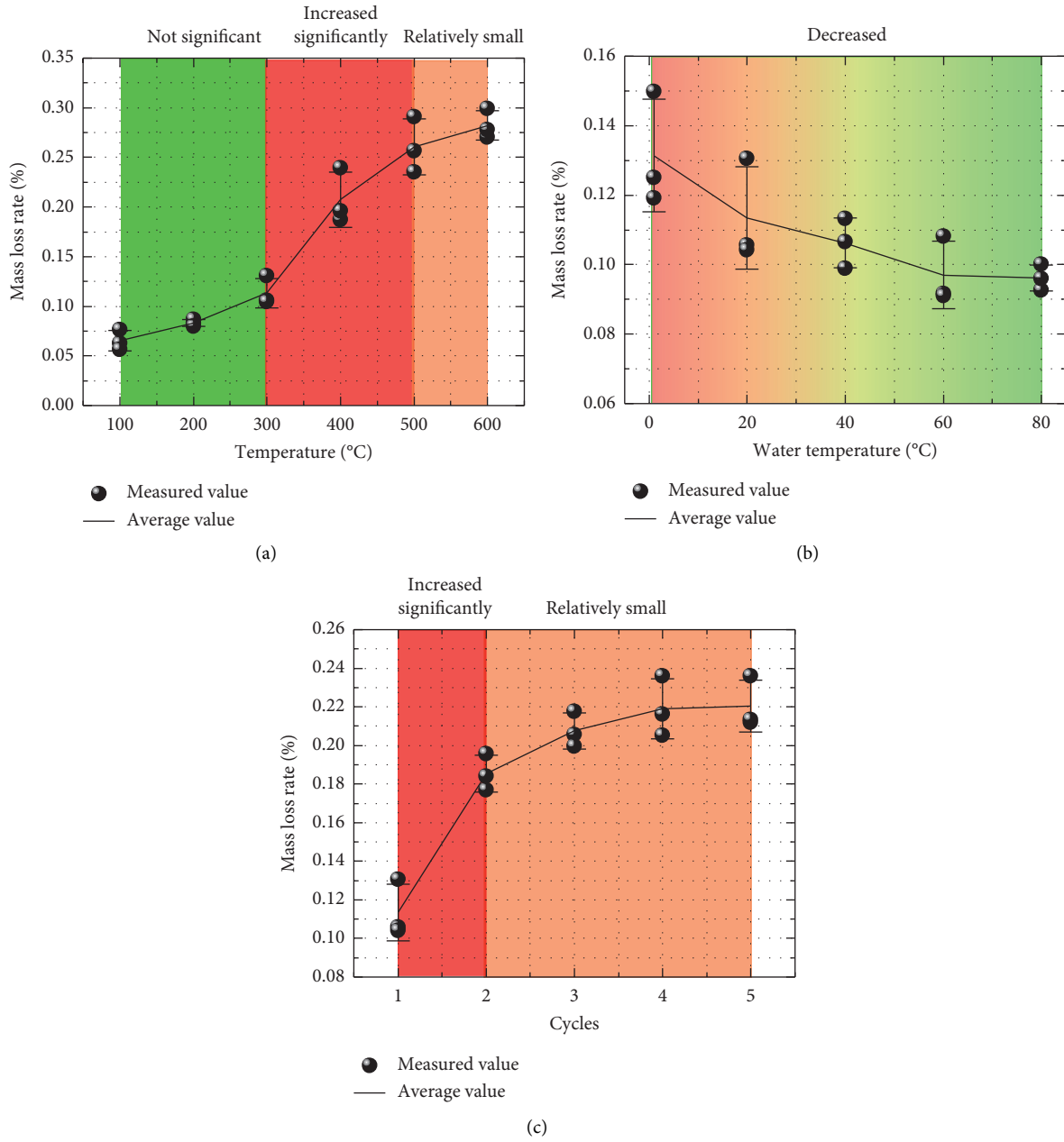


FIGURE 5: Mass loss rate of specimens subjected to different conditions of water cooling at high temperatures. (a) HDR temperature. (b) Water temperature. (c) The number of heating-cooling cycles.

injection cycles occurred, the tensile strength of the specimen significantly decreased.

In the thermal recovery process, many tensile fractures usually form in low-permeability strata. Note that the tensile strength ( $\sigma_t$ ) of the specimen under different conditions of heating-cooling cycles has a certain reference value for studying the fracture initiation and propagation patterns in the target area. The tensile strength is calculated by the following equation.

$$\sigma_t = \frac{2P}{\pi dt}, \quad (2)$$

where  $\sigma_t$  is the tensile strength (MPa),  $P$  is the ultimate load (kN),  $d$  is the specimen diameter (mm), and  $t$  is the specimen thickness (mm).

Figure 6 shows how the tensile strength of the specimens varied under different conditions of water cooling at high temperature. An examination of the effect of temperature on the tensile strength of the specimens revealed that temperature had a relatively small effect on the tensile strength of the specimens between 100°C and 300°C. As the temperature rose, the tensile strength decreased slightly; the resulting pattern is similar to that found by Xi and Zhao [36]. At 400°C, the decrease was the most marked at 51.08%. As

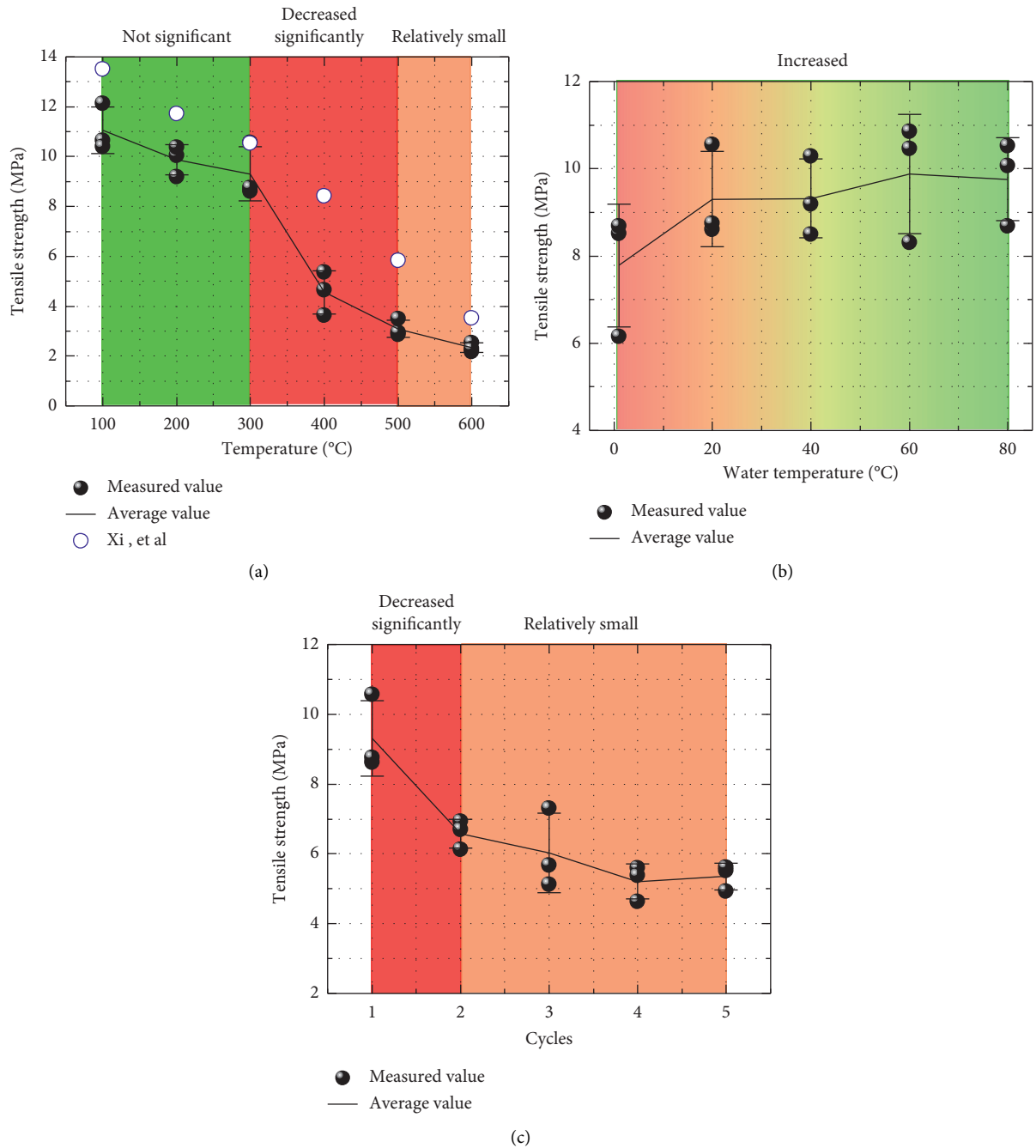


FIGURE 6: Tensile strength of the specimens under different conditions of water cooling at high temperatures. (a) HDR temperature. (b) Water temperature. (c) The number of heating-cooling cycles.

the temperature continued to rise, the loss slightly decelerated. At 600°C, the tensile strength of the specimen was approximately 21.27% of that at 100°C. Thus, the higher the temperature in the target area is, the lower the tensile strength of the rock mass during the water injection cooling process and the higher the possibility that tensile failure will occur.

The effect of the water temperature on the tensile strength of the specimens was examined next. At water temperatures of 1°C, 20°C, 40°C, 60°C, or 80°C, the tensile strength of the specimens was 7.78 MPa, 9.30 MPa,

9.32 MPa, 9.87 MPa, or 9.76 MPa, respectively. As the water temperature increased, the specimen tensile strength increased. Therefore, low-temperature water injection can accelerate rock fracturing.

The effect of the number of heating-cooling cycles performed on the tensile strength of the specimen was investigated. It was found that at the initial stage of high-temperature water circulation, the tensile strength decreased significantly; the decrease reached approximately 29.32% after two cycles. As the number of cycles increased, the strength loss increased. The tensile strength after five cycles

was approximately 57.47% of that after one cycle. Exposure to multiple water circulation cycles therefore raised the probability of new tensile fractures forming in the rock strata.

**3.4. Variation Pattern of the Height Difference Parameters of the Specimens Subjected to Different Conditions of Water Cooling at High Temperatures.** The variation pattern of the height difference parameters (the height MSE and undulation difference) of the split surfaces of the specimens for various water cooling scenarios under high temperature conditions shows that the value of each parameter increased as the temperature or the number of heating-cooling cycles increased, while the values decreased as the water temperature increased.

The height difference parameters mainly include two amplitude parameters (mean height and height MSE) and the fluctuation difference. These parameters describe the height distribution and variation characteristics of the fracture morphology and are important factors that affect the flow path of a fluid-working medium in the fracture. The amplitude parameters can reflect the uniformity of the distribution of the fluctuation pattern on the split surface, where the average height ( $Z_u$ ) is expressed in equation (3), and the height MSE ( $Z_A$ ) is expressed in equation (4).

$$Z_u = \frac{1}{n} \sum_{i=1}^n Z_i, \quad (3)$$

where  $Z_u$  is the average height (mm),  $n$  is the number of measuring points, and  $Z_i$  is the height of the  $i$ th measuring point (mm).

$$Z_A = \sqrt{\frac{1}{n-1} \sum_{i=1}^n (Z_i - Z_u)^2}, \quad (4)$$

where  $Z_A$  is the height MSE.

Figure 7 shows the variation pattern of the height MSE of the split surface of the specimens under different conditions of water cooling at high temperature. The effect of the HDR temperature on the height MSE of the specimen split surface was investigated first. When the temperature varied between 100°C and 200°C, the height MSE varied only slightly. As the temperature increased from 200°C to 500°C, the height MSE increased significantly. When the temperature was between 500°C and 600°C, the effect of temperature on the height MSE was smaller. The height MSE of the specimens at a high temperature of 600°C was approximately 2.51 times that at 100°C.

The effect of water temperature on the height MSE of the specimen split surfaces was investigated next. The lower the water temperature was, the larger the height MSE was. The height MSE at a water temperature of 1°C was approximately 1.22 times that at 80°C.

The effect of the number of heating-cooling cycles performed on the height MSE of the specimen split surface was also investigated. The findings revealed that as the number of heating-cooling cycles increased, the height MSE

increased gradually, and the variation rate of the height MSE was relatively small for the first three cycles and increased notably, by approximately 11.39%, after four cycles. The height MSE after five cycles was 1.33 times that after one cycle.

The split surface of rock can be considered to be composed of “large” fluctuations in various regions, with a “small” roughness of these fluctuations, that is, the split surface is formed by the superposition of bumps (depressions) of different sizes. The fluctuation difference is the height difference between the relatively high bumps and the relatively low depressions. This is an important factor that affects the roughness of a split surface. The fluctuation difference between the highest bump and the lowest depression ( $T_Z^2$ ) is calculated as shown in equation (5). Because choosing only one set of maximum and minimum value points would generate some randomness, we selected five high bumps and five low depression points to calculate the fluctuation difference ( $T_Z^{10}$ ), as detailed in equation (6).

$$T_Z^2 = |Z_H| - |Z_C|, \quad (5)$$

where  $T_Z^2$  is the fluctuation difference between the highest bump and the lowest depression (mm),  $Z_H$  is the height of the highest bump (mm), and  $Z_C$  is the height of the lowest depression (mm).

$$T_Z^{10} = \frac{1}{5} \left[ \sum_j^5 |Z_{Hj}| - \sum_j^5 |Z_{Cj}| \right], \quad (6)$$

where  $T_Z^{10}$  is the fluctuation difference between the five bumps and five depressions (mm),  $Z_{Hj}$  is the height of the  $j$ th highest bump (mm), and  $Z_{Cj}$  is the height of the  $j$ th lowest depression (mm).

Figure 8 shows the variation pattern of the height fluctuation difference in the split surfaces of the specimens under different conditions of water cooling at high temperature. The effect of the rock temperature on the fluctuation difference in the split surfaces of the specimens was investigated. The height fluctuation difference approximately linearly increased with an increase in temperature. The height fluctuation difference at 600°C was approximately 2.57 times that at 100°C.

The examination of the effect of water temperature on the height fluctuation difference in the split surface of the specimens indicated that as the water temperature decreased, the height fluctuation difference gradually increased, and at 1°C, it was approximately 1.22 times that at 80°C.

The effect of the number of heating-cooling cycles performed on the height fluctuation difference of the specimen split surfaces was then investigated. As the number of cycles increased, the height fluctuation difference of the specimens gradually increased. After four cycles, the height fluctuation difference had increased significantly by approximately 17.85%. The height fluctuation difference after five cycles was approximately 1.49 times that after one cycle.

The above results indicate that the parameters of the height difference of the split surfaces were highly correlated

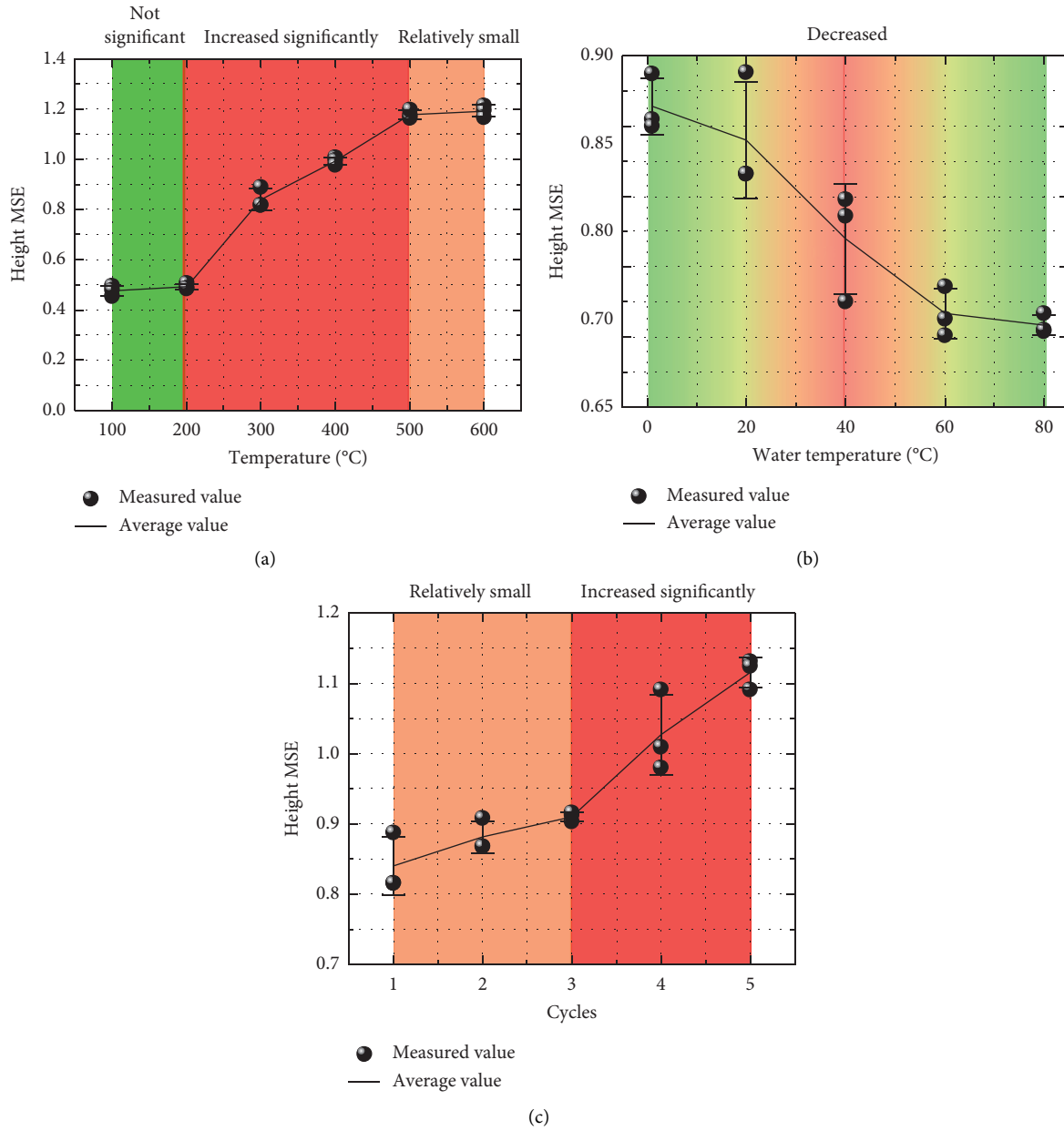


FIGURE 7: Height MSE of the specimen split surface under different conditions of water cooling at high temperatures. (a) HDR temperature. (b) Water temperature. (c) The number of heating-cooling cycles.

with the different conditions of water cooling at high temperature. The height MSE and fluctuation difference on the split surface increased as the rock temperature or the number of heating-cooling cycles increased, while it gradually decreased as the water temperature increased. When considering the effect of the fracture height difference parameters on thermal recovery, their effect on the flow path should be considered first. The increase in the height difference parameters will cause the formation of a few dominant seepage channels in the target rock mass. Fluid injection into these dominant paths reduces the effective heat exchange area and simultaneously causes problems, such as fluid short-circuit and flow loss, which further affect the heat production efficiency. Therefore, the effect of

different conditions of water cooling at high temperature on the height difference parameters is worthy of attention.

*3.5. Variation Pattern of Specimen Texture Parameters under Different Conditions of Water Cooling at High Temperatures.* The variation pattern of the texture parameters (roughness coefficient, roughness profile index, and roughness angle) of the specimen split surfaces for various water cooling scenarios under high temperature conditions reveals that the values of the various texture parameters increased as the rock temperature or number of heating-cooling cycles increased, while the values slightly decreased as the water temperature increased.

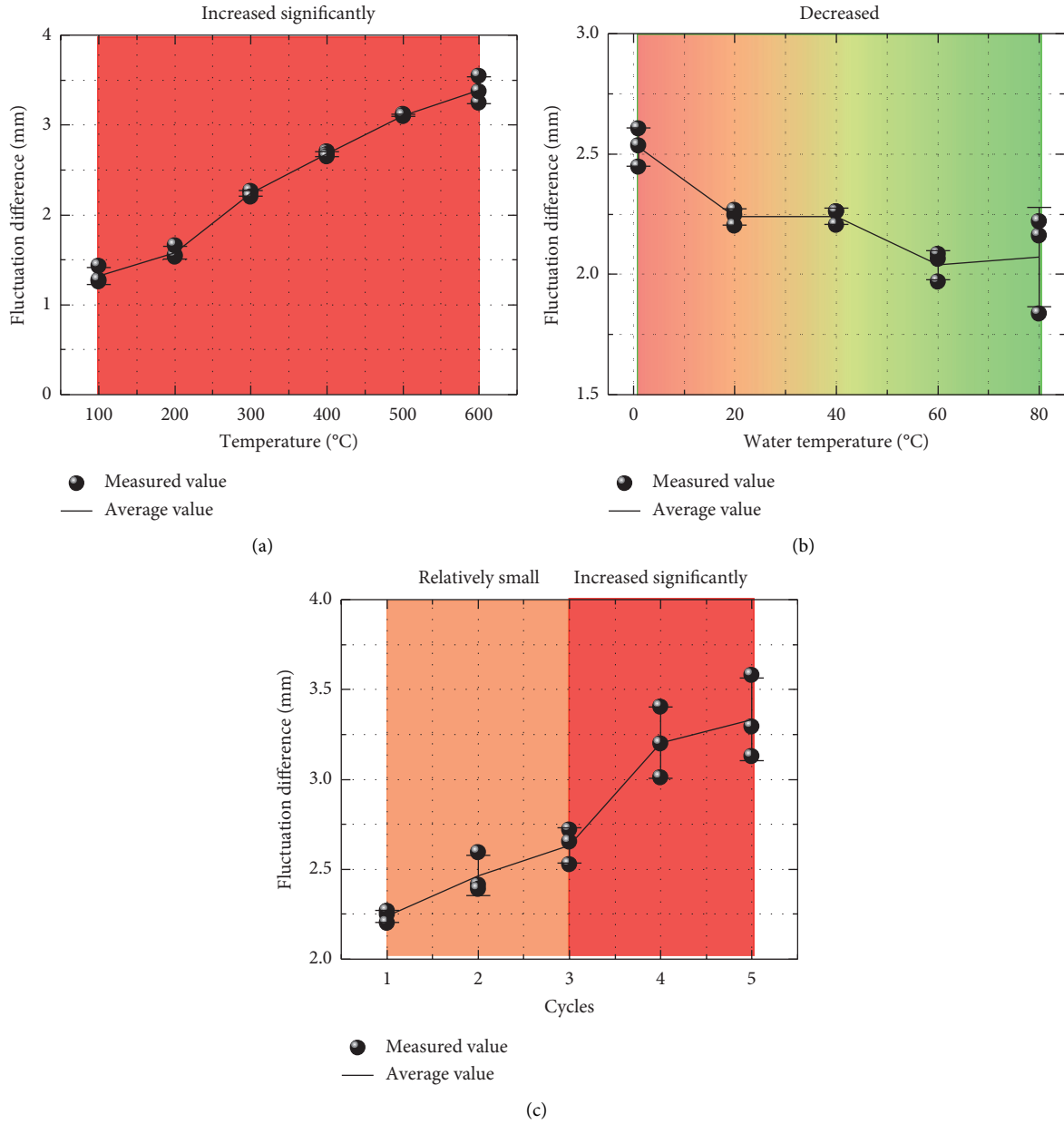


FIGURE 8: Height fluctuation difference in the split surfaces of specimens under different conditions of water cooling at high temperatures. (a) HDR temperature. (b) Water temperature. (c) The number of heating-cooling cycles.

The texture parameters mainly include the roughness coefficient, roughness profile index, and roughness angle, which are the statistics and statistical functions that describe the curve characteristics of the structural surface topography. In 1973, Barton [37] was the first researcher to propose the use of JRC to evaluate the roughness of the structural surface of a rock mass and successively employed the shear test, inclination test, and Brazilian disc test to calculate the roughness coefficient of a structural surface from the empirical formula. Based on Barton’s 10 standard curves, we investigated the variation pattern of the roughness coefficient of a split surface under different conditions of water cooling at high temperature. The RMS of the first derivative

of the profile of the split surface ( $Z_s$ ) is expressed in equation (7), and the roughness coefficient of the split surface is shown in equation (8).

$$Z_s = \sqrt{\frac{\sum_{i=1}^{n-1} (Z_i - Z_{i+1})^2}{(n-1)\Delta s^2}}, \quad (7)$$

where  $Z_s$  is the RMS of the first derivative of the profile of the split surface,  $Z_{i+1}$  is the height of the  $(i+1)^{th}$  measuring point (mm), and  $\Delta s$  is the spacing between two measuring points (mm).

$$JRC = 32.2 + 32.471gZ_s, \quad (8)$$

where JRC is the roughness coefficient.

Figure 9 shows the variation pattern of the roughness coefficient of the specimen split surfaces under different conditions of water cooling at high temperature. The effect of the rock temperature on the roughness coefficient of the specimen split surfaces was investigated. Between 100°C and 200°C, the temperature had a minimal effect on the roughness coefficient. As the temperature rose, the roughness coefficient increased significantly at 300°C to 7.18 times that at 200°C. As the temperature continued to increase, the rate of the increase in the roughness coefficient decreased. The roughness coefficient at a high temperature of 600°C was approximately 8.92 times that at 100°C.

The effect of water temperature on the roughness coefficient of the specimen split surface was investigated next. As the water temperature decreased, the roughness coefficient gradually increased. The roughness coefficient at a water temperature of 1°C was approximately 1.57 times that at 80°C.

The effect of the number of heating-cooling cycles performed on the roughness parameters of the specimen split surfaces was then investigated. With an increasing number of cycles, the roughness coefficient of the specimen gradually increased. The roughness coefficient of the specimen with five cycles was approximately 1.29 times that with one cycle.

The ratio of the profile length to the baseline length is referred to as the roughness profile index ( $R_p$ ). The roughness profile index is a quantitative parameter that uses a statistical method to characterize the roughness patterns of specimens, as shown in the following equation.

$$R_p \approx \frac{\sum_{i=1}^{n-1} \sqrt{\Delta s^2 + (Z_i - Z_{i+1})^2}}{\Delta s(n-1)}, \quad (9)$$

where  $R_p$  is the roughness profile index.

Figure 10 shows the variation pattern of the roughness profile index of the specimen split surfaces under various water cooling at high temperature conditions. An examination of the effect of rock temperature on the roughness profile index of the specimen split surfaces revealed that at temperatures between 100°C and 200°C, the roughness profile index varied only slightly. When the temperature reached 300°C, the roughness profile index rose significantly by approximately 1.88%. The roughness profile index of the specimen at a temperature of 600°C was approximately 1.06 times that at 100°C.

An examination of the effect of water temperature on the roughness profile index of the specimen split surface revealed that the roughness profile indices were 1.0241, 1.0254, 1.0177, 1.0138, and 1.0141 as the water temperature varied from 1°C to 80°C. The roughness profile index decreased slightly with an increase in water temperature.

The effect of the number of heating-cooling cycles performed on the roughness profile index of the specimen split surface was examined next. The findings revealed that as the number of water injection cycles increased, the roughness profile index increased. The roughness profile index obtained with five cycles was approximately 1.01 times that with one cycle.

The total mechanical properties of the structural surface are mainly controlled by relatively large bumps, and the inclination that characterizes a single bump on the structural surface is referred to as the roughness angle ( $i$ ). The roughness angle is a commonly employed index for describing the texture characteristics of a structural surface and is a core parameter used for studying the hydraulic properties of rough fractures. The roughness angle can be obtained in terms of  $R_p$  and  $Z_S$ , as detailed in the following equations, respectively.

$$i_{R_p} = \arccos\left(\frac{1}{R_p}\right), \quad (10)$$

$$i_{Z_S} = \arctan(Z_S), \quad (11)$$

where  $i_{R_p}$  is the roughness angle obtained in terms of  $R_p$  (°), and  $i_{Z_S}$  is the roughness angle obtained in terms of  $Z_S$  (°).

The variation pattern of the roughness angle was the same as the variation patterns of the roughness coefficient and roughness profile index. Figure 11 shows the variation pattern of the roughness angle of the specimen split surface under different conditions of water cooling at high temperature. The effect of rock temperature on the roughness angle of the specimen split surface was investigated first. The findings indicate that the roughness angle varied little at temperatures between 100°C and 200°C. When the temperature was 300°C, the roughness angle significantly increased, and the roughness angles calculated in terms of  $R_p$  and  $Z_S$  were 12.7824° and 12.9166°, respectively, for a difference of 0.1292°. When the temperature reached 600°C, the calculated values were 20.0512° and 20.3715°, for a difference of 0.3203°. As the temperature changed, the roughness angle calculated with  $R_p$  was always smaller than that calculated with  $Z_S$ ; this pattern became starker as the temperature increased.

An examination of the effect of the water temperature on the roughness angle of the specimen split surface revealed that at a water temperature of 1°C, the roughness angles calculated using  $R_p$  and  $Z_S$  were approximately 12.4181° and 12.5517°, respectively, for a difference of 0.1336°. At a water temperature of 80°C, the calculated values were 9.5056° and 9.5571°, for a difference of 0.0515°. The lower the water temperature, the higher the roughness angle of the specimen, and the larger the roughness angle difference calculated by  $R_p$  and  $Z_S$ .

The effect of the number of heating-cooling cycles performed on the roughness angle of the specimen split surface was examined last. As the number of water injection cycles increased, the roughness angle increased. The roughness angles calculated using  $R_p$  and  $Z_S$  after five cycles were 15.2228° and 16.2101°, respectively, which was the greatest difference between the two methods.

When studying the effect of fracture texture parameters on the heat transfer efficiency, the significance of the variation in the texture parameters for the heat transfer process should be understood. When the texture parameters become more extreme, the effective heat exchange area increases, and the fluid flow carries more heat to improve the thermal



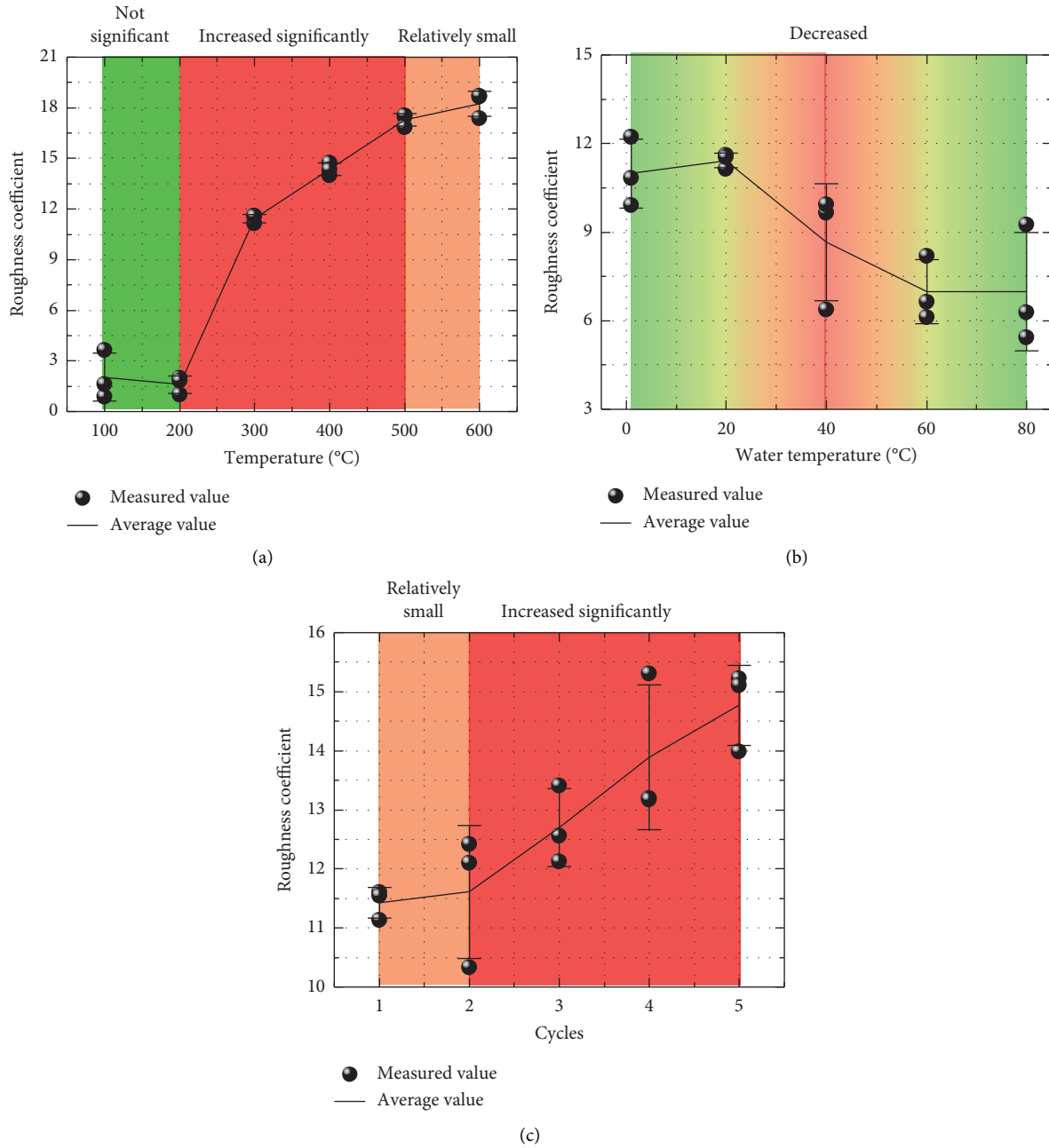


FIGURE 9: Roughness coefficient of the split surface of specimens under different conditions of water cooling at high temperatures. (a) HDR temperature. (b) Water temperature. (c) The number of heating-cooling cycles.

recovery performance. The different conditions of water cooling at high temperature are important factors in the texture parameters of the split surface. The texture parameters continuously increased as the temperature increased, the cycle number increased, or the water temperature decreased. Therefore, studying the effect of different conditions of water cooling at high temperature on the fracture texture parameters is valuable.

**3.6. Relationship between the Tensile Strength and Roughness of the Specimens.** The morphological parameters of the fracture surface are related to the injection conditions at high

temperatures and the stress environment at the time of fracture. Therefore, it is important to establish a relationship between the split surface height MSE, height variation, and tensile strength of the specimen under different water circulation conditions.

Figures 12(a)–12(c) and 13(a)–13(c) show the relationships between the tensile strength and height MSE and between the tensile strength and roughness coefficient under different conditions of water cooling at high temperature, respectively. Under different temperature conditions, different water temperature conditions, and different numbers of water circulation cycles, there are certain correlations between

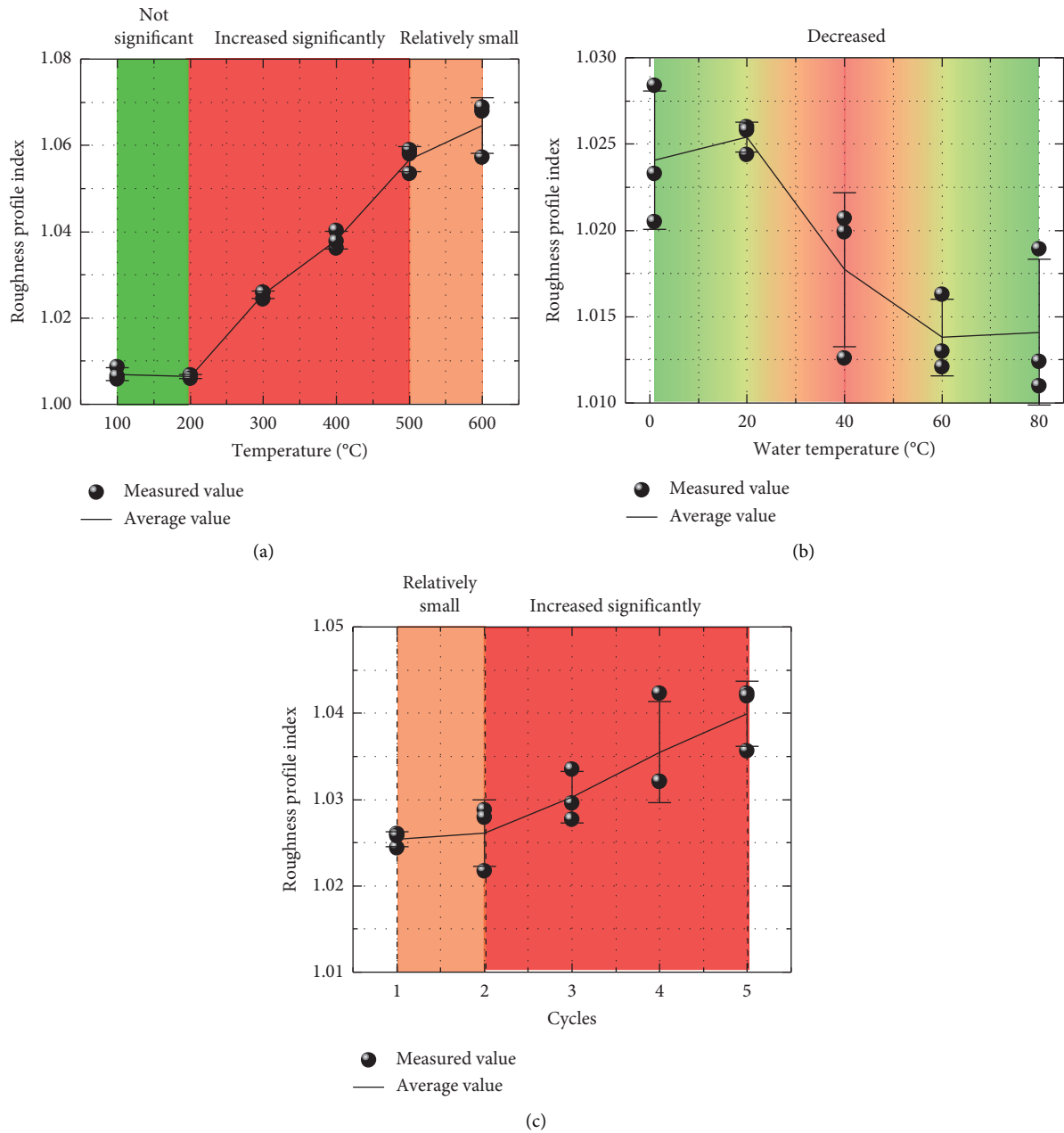


FIGURE 10: Roughness profile index of the specimen split surface under different conditions of water cooling at high temperatures. (a) HDR temperature. (b) Water temperature. (c) The number of heating-cooling cycles.

the tensile strength and height MSE and between the tensile strength and roughness coefficient. Under the same water temperature and the same number of water circulation cycles but different temperatures, the height MSE and roughness coefficient significantly decreased with the increase in tensile strength. Under same temperature but different water temperatures and different numbers of water circulation cycles, the height MSE and roughness coefficient still decreased with the increase in tensile strength, but the decrease was obviously weaker. The fractures inside the rock have different sizes and states, such as open or closed. Under different fracture states, the tensile strength had a different effect on the specimen,

resulting in a different capacity to withstand a splitting load. A high rock body temperature, a low water temperature, and an increasing number of water circulation cycles can all promote the development of fractures inside the rock, aggravating the degree of fracture. The split surface roughness coefficient is the most intuitive index for describing the degree of fracture inside a rock body. The higher the roughness coefficient is, the more severe the fracture, the lower the capability to withstand tensile strength, and vice versa. Temperature changes had the most profound impact on the thermal fracture of the rock, followed by the number of water circulation cycles and the temperature of the injected water. Therefore, it is highly

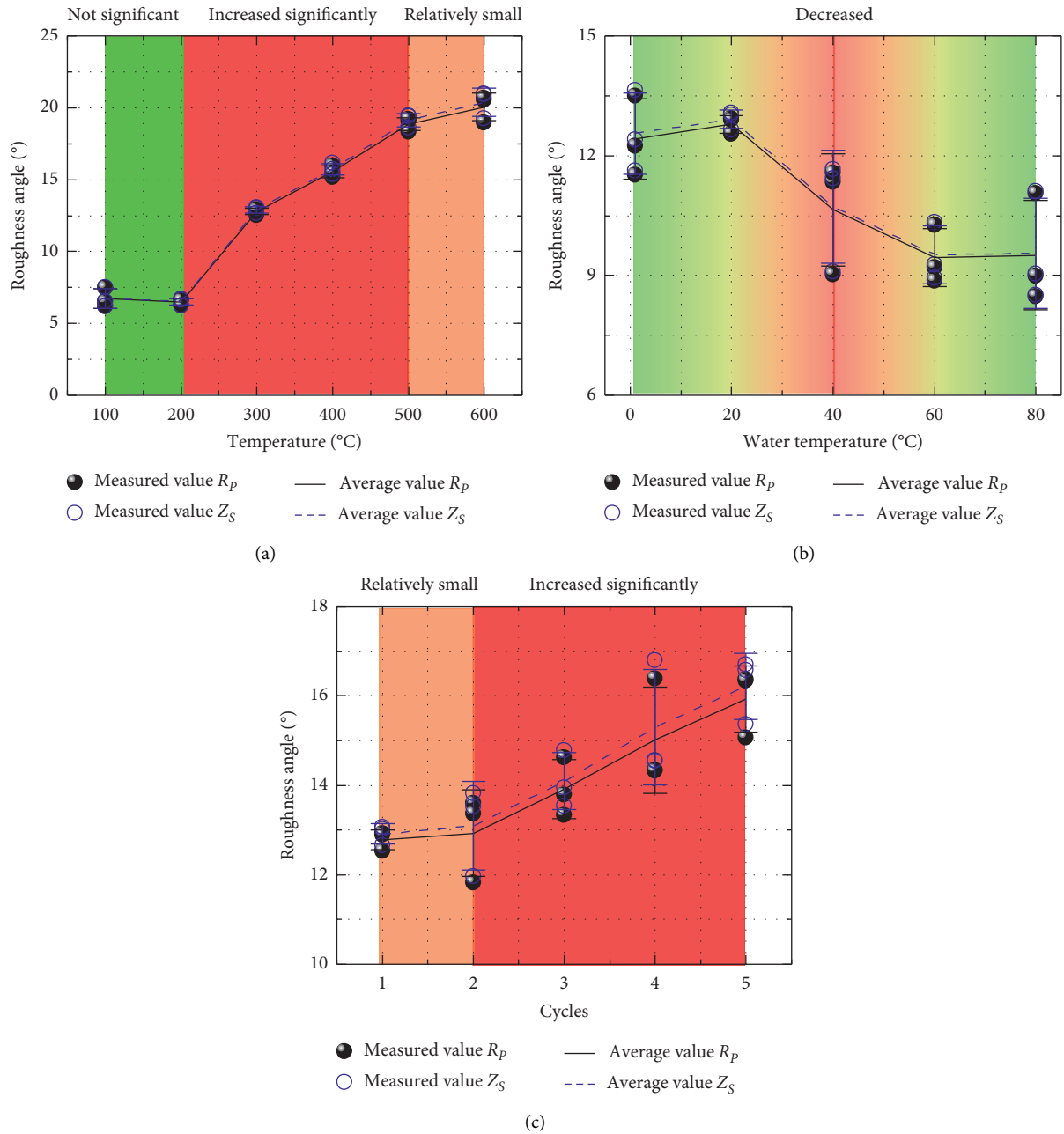


FIGURE 11: Roughness angle of the split surface of the specimen under different conditions of water cooling at high temperatures. (a) HDR temperature. (b) Water temperature. (c) The number of heating-cooling cycles.

feasible to use tensile strength to evaluate the split surface roughness of rock.

3.7. Summary of Test Rules. The rules obtained in this article are summarized, and the conclusions are shown in Table 4.

#### 4. Discussion

The mechanisms related to the physical, mechanical, and split surface roughness characteristics of the granite under different high temperature-cooling conditions are discussed according to the patterns obtained from the tests.

The granite in the target area contains a variety of mineral components, with variations in the content between the components and large differences in the thermal expansion coefficients. Therefore, the mineral components of the rock deform differently under the influence of different high temperature-cooling conditions. The rock as a whole constrains its components to some extent. The part of the rock that expands is compressed, while the part that contracts is elongated. Therefore, an internal force is caused by thermal stress under high temperature conditions. As the temperature rises, the maximum thermal stress usually occurs at the boundary of the rock. When this value is

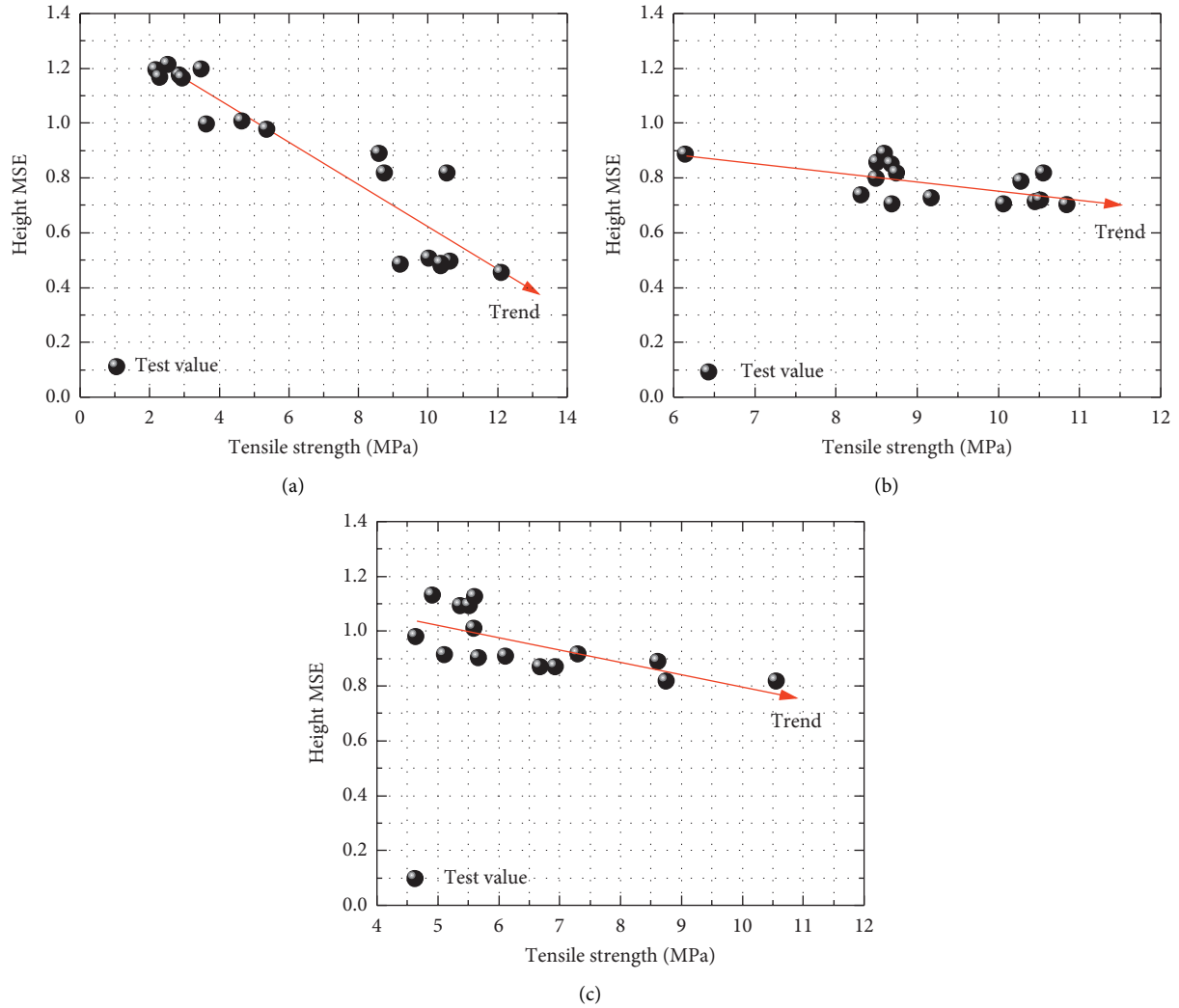


FIGURE 12: The relationship between the tensile strength and the height MSE. (a) HDR temperature. (b) Water temperature. (c) The number of heating-cooling cycles.

reached or exceeded, fractures occur at the interparticle connections near the boundary and, in turn, form microfractures that propagate into the interior of the rock. The continuous increase in temperature also triggers the phenomenon of thermal stress concentration in some parts of the rock, causing the fractures to extend, intersect, become dense, and coalesce to form a network of microfractures, a phenomenon known as thermal cracking. This process is reflected in the physical and mechanical properties of the rock as the occurrence of fracture and the decay of the mechanical strength, and it is reflected in the split surface as an increase in the roughness.

Water cooling of a rock at high temperatures increases the degree of thermal cracking of the rock. If the high temperature and water cooling processes of the rock are considered as a whole, the water cooling process significantly increases the difference between the temperature fields inside the rock and those at the boundary, which is equivalent to a secondary thermal shock effect on the rock. Thus, the thermal stresses in the rock can be divided into those

generated by high temperatures and those formed by the secondary thermal shock of cooling. Assuming that the rock consists of multiple finite units, each of which has only two mineral components, this paper modifies the formula of Zhu et al. [38] and proposes formulas (12)–(15) for the thermal stresses in a process that involves multiple heating-water cooling cycles.

The thermal stresses generated by high temperatures can be calculated as follows:

$$\sigma_{1ij} = \frac{(\gamma_1 - \gamma_2)\Delta T_{1ij}E_1E_2}{E_1 + E_2}. \quad (12)$$

The thermal stresses generated by the secondary thermal shock of water cooling can be calculated as follows:

$$\sigma_{2ij} = E_{ij}\xi_{ij} = \frac{E_{ij}\gamma_{ij}\Delta T_{2ij}}{1 - 2\mu_{ij}}. \quad (13)$$

The total thermal stresses generated by a single heating-water cooling cycle can be calculated as follows:

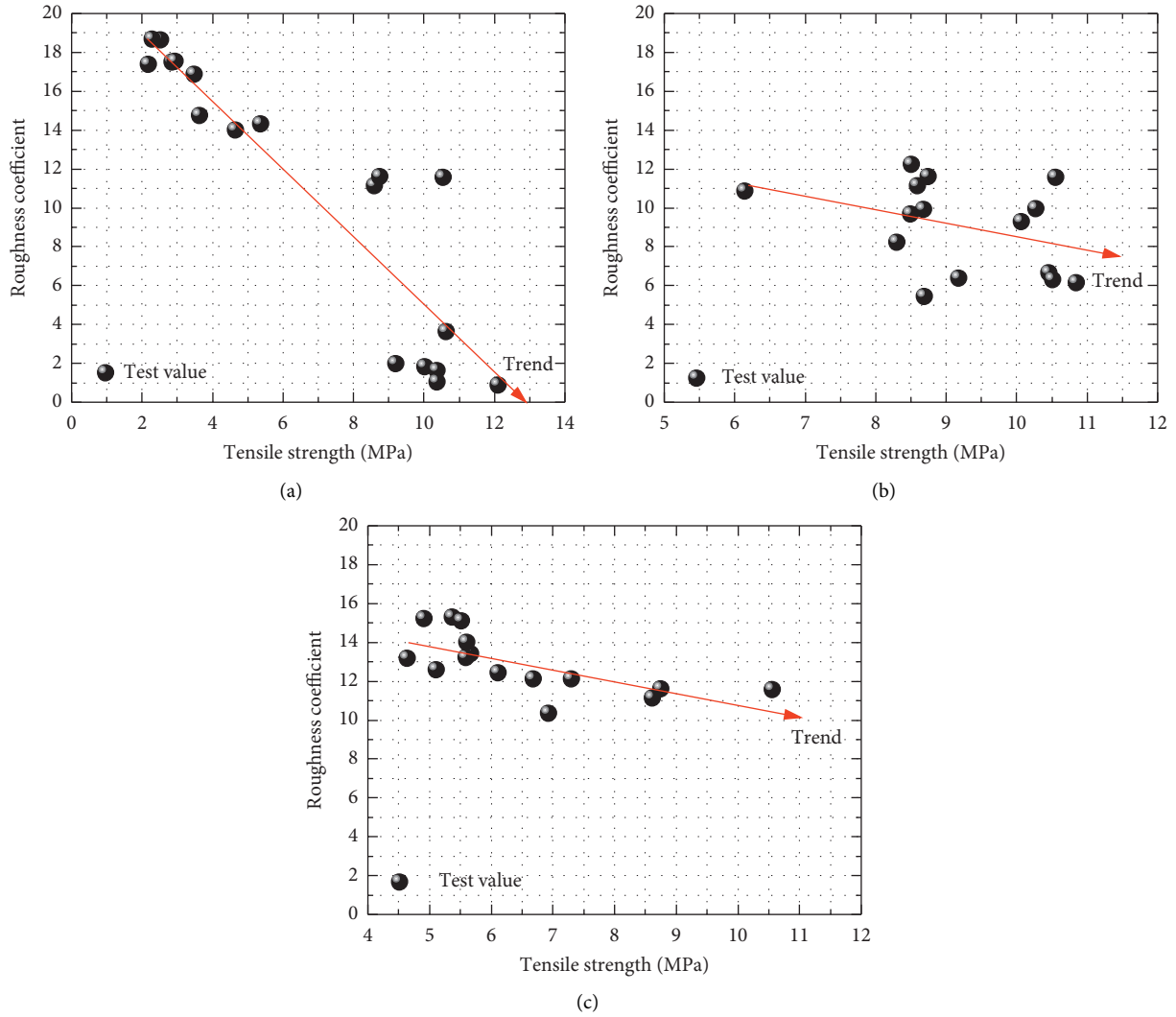


FIGURE 13: The relationship between the tensile strength and the roughness coefficient. (a) HDR temperature. (b) Water temperature. (c) The number of heating-cooling cycles.

$$\sigma_{ij} = \sigma_{1ij} + \sigma_{2ij}. \tag{14}$$

The total thermal stresses generated by multiple heating-water cooling cycles can be calculated as follows:

$$\sigma_{\text{sum}} = \sum_{k=1}^n (\sigma_{ij})_k, \tag{15}$$

where 1, 2, and  $ij$  denote mineral 1, mineral 2, and the  $ij^{\text{th}}$  unit, respectively;  $\gamma_1$ ,  $\gamma_2$ , and  $\gamma_{ij}$  are the volumetric thermal expansion coefficients ( $1/^\circ\text{C}$ ) of mineral 1, mineral 2, and the  $ij^{\text{th}}$  unit, respectively;  $\Delta T_{1ij}$  and  $\Delta T_{2ij}$  are the temperature differences ( $^\circ\text{C}$ ) of the  $ij^{\text{th}}$  unit caused by high temperatures and the secondary thermal shock of water cooling, respectively;  $E_1$ ,  $E_2$ , and  $E_{ij}$  are the elastic moduli (GPa) of mineral 1, mineral 2, and the  $ij^{\text{th}}$  unit, respectively;  $\mu_{ij}$  is Poisson's ratio of the  $ij^{\text{th}}$  unit;  $n$  is the number of heating-cooling cycles (taken as 5); and  $k$  denotes the  $k^{\text{th}}$  heating-cooling cycle.

The above formulas indicate that the thermal cracking of a rock is related to the temperature difference of each unit. The larger the temperature difference, the more pronounced the differential expansions of different mineral components of the rock. Therefore, with a higher temperature of the rock and a lower temperature of the water, the temperature difference between the high-temperature rock and the water flow becomes larger to increase the degree of thermal cracking, the roughness of the split surface, and the loss of the tensile strength. In addition, multiple high temperature water cooling cycles further increase the thermal stress generated in the rock, aggravating the degree of thermal cracking.

Our investigation of the specific cooling conditions, with consideration of the above principles and the experimental phenomena, resulted in the following findings. When the temperature was  $100\text{--}200^\circ\text{C}$ , the thermal cracking stress of the rock was not reached; so, there was no obvious thermal cracking phenomenon, and none of the characteristics of the

TABLE 4: Summary of test rules.

Influencing factors	Variable interval	Height difference parameters			Texture parameters			Tensile strength and height MSE	Tensile strength and roughness coefficient
		Tensile strength	Height MSE fluctuation difference	Height difference	Roughness coefficient	Roughness profile index	Roughness angle		
Rock temperature	100–200°C	Not significant	Not significant	Not significant	Not significant	Not significant	Not significant	Decreased significantly	
	200–300°C	significant	significant	Increased significantly	significant	Not significant	Not significant		
	300–400°C	Decreased significantly	Increased significantly	Increased significantly	Increased significantly	Increased significantly	Increased significantly		
	400–500°C	significantly	significantly	significantly	significantly	significantly	significantly		
Maximum	500–600°C	Relatively small	Relatively small	Relatively small	Relatively small	Relatively small	Relatively small	Decreased significantly	
	Minimum	600°C	100°C	100°C	100°C	100°C	100°C		
	600°C	600°C	600°C	600°C	600°C	600°C	600°C		
Water temperature	1–20°C	Increased	Decreased	Decreased	Decreased	Decreased	Decreased	Relatively small decrease	
	20–40°C	Increased	Decreased	Decreased	Decreased	Decreased	Decreased		
	40–60°C	Increased	Decreased	Decreased	Decreased	Decreased	Decreased		
The number of heating-cooling cycles	60–80°C	Decreased	Decreased	Decreased	Decreased	Decreased	Decreased	Relatively small decrease	
	Minimum	80°C	80°C	80°C	80°C	80°C	80°C		
	Maximum	1°C	1°C	1°C	1°C	1°C	1°C		
The number of heating-cooling cycles	1-2 times	Increased significantly	Decreased significantly	Decreased significantly	Decreased significantly	Decreased significantly	Decreased significantly	Relatively small decrease	
	2-3 times	Increased significantly	Decreased significantly	Decreased significantly	Decreased significantly	Decreased significantly	Decreased significantly		
	3-4 times	Increased significantly	Decreased significantly	Decreased significantly	Decreased significantly	Decreased significantly	Decreased significantly		
	4-5 times	Increased significantly	Decreased significantly	Decreased significantly	Decreased significantly	Decreased significantly	Decreased significantly		
	Minimum	1 time	5 times	1 time	5 times	1 time	5 times		
Maximum	5 times	1 time	5 times	1 time	5 times	1 time	5 times		

specimen changed significantly. Multiple indices of the 100°C specimen were slightly lower than those of the 200°C specimen, which is speculated to be attributed to the difference of the natural rock itself. The loss of mass of the specimen between 100°C and 200°C was mainly due to the loss of free water. When the rock was heated to 300–400°C, the internal water in the bound form (crystalline water and bound water) underwent a bursting phenomenon (Deng et al. [39]) and was converted to free water, which was then consumed by evaporation, contributing to the loss of mass in the rock and leading to the creation of a large number of microfractures. The influx of external free water into the interior of the rock accelerated the propagation of microfractures. When the rock temperature continued to increase to 500°C, the heating-cooling process significantly increased the temperature difference between the interior and exterior of the rock, leading to an increase in the total thermal stress, which promoted further extension and propagation of the thermal cracking in the rock. As a result, its mechanical properties continued to decrease, the roughness of the split surface continued to increase, and at this point, there was a loss of structural water in the rock. When the temperature reached 600°C, the amplitude of variation in the mechanical indices and the roughness index of the split surface of the specimen decreased because high temperatures also increase the size of pores in rock, and large pores can absorb the energy generated by thermal stress, inhibit the deformation of particles, and thus prevent the formation of cracks to some extent. However, an increase in porosity also leads to a decrease in the ability of a rock to resist thermal cracking. Therefore, the influence of the pore structure on the properties of a rock after high temperature heating is two-sided. Based on observations of the surface of the specimen, when the temperature was between 500°C and 600°C, the edge particles fell off, leading to further loss of the rock mass. In addition, a higher temperature and a larger number of heating-cooling cycles led to a more pronounced degree of thermal cracking of the rock. Meanwhile, microparticles flowed out of the rock with water from the fractures, which is another important factor causing a loss of the specimen mass. The use of high-temperature water injection can inhibit the generation of thermal cracking of the rock and reduce the outflow of microparticles from the pores, thus preventing particles from clogging the fractures and affecting the efficiency of the water-rock heat exchange process.

The heat transfer mode is another important factor that cannot be ignored in HDR development. When the temperature is low, the granite has a dense structure, and the internal heat transfer is dominated by intermatrix heat transfer. As the temperature increases, a large number of fractures appeared in the rock, and consequently, the heat transfer process of the rock is affected by both intermatrix heat transfer and matrix-water thermal convection. The test results show that when the water temperature was close to 1°C, there was an abnormal phenomenon that the roughness index of the split surface of each group of specimens was lower than that at a water temperature of 20°C. This is because during the cooling process, ice cubes were

continuously added to the water to ensure that the water temperature was close to 1°C. This practice increased the dynamic viscosity of the water, leading to a significant decrease in the flow rate of water in the fractures, inhibiting the flow path of water in the rock, reducing the area of heat exchange between the rock and the water, and eventually resulting in a decrease in the degree of cracking of the rock and a relatively small roughness index of the split surface.

The variation in mineral parameters in the rock under high temperature water cooling was also a factor to be considered. At room temperature, the interior of the rock is mainly composed of quartz, mica, potash feldspar, plagioclase, pyroxene, and hornblende, with the contents of quartz, mica, and feldspar accounting for approximately 96%. Therefore, the granite in its natural state is greyish white, with black spots, i.e., biotite. When the temperature increased to 300–400°C, the quartz crystal burst and the crystal state changed; the colour changed from transparent to white, so the rock also changed from greyish white to white, while the biotite lost crystalline water under high temperature conditions, so the number of black spots of the specimen was greatly reduced. When the rock was heated to 500°C, the ferrous ions in the ferrous oxides contained in plagioclase were converted to ferric ions, causing some areas of the specimen to appear reddish brown. When the temperature continued to rise to 600°C, the specimen surface turned blackish grey because the surface changed from smooth to rough, and the presence of white crystals was due to the repetitive phase change of the quartz at 573°C (Shen et al. [40]). The multiple high temperature water cooling cycles reduced the temperature of quartz crystal bursting. Therefore, the variation pattern of mineral parameters in the rock can be determined by the change in the appearance characteristics of the specimen.

In summary, the high temperature-cooling conditions affect the HDR development to some extent by notably changing the physicomaterial properties, thermal cracking morphology, and fracture surface roughness characteristics of the rock. How to fracture rock and use the rough surface of fractures for water flow and heat transfer will be the focus of future research.

## 5. Conclusions

This was an experimental study of the physical and mechanical properties and the split surface roughness characteristics of granite after water cooling at high temperatures under different conditions of water cooling at high temperature. The following conclusions can be drawn.

- (1) When the rock temperature rose, the water temperature dropped or the number of heating-cooling cycles increased and the mass loss rate of the specimen increased. The rise in the temperature and the increase in the number of water cooling cycles changed the appearance (colour) of the specimen. Therefore, different conditions of water cooling at high temperature experienced by the thermal

recovery area can be deduced from changes in the appearance characteristics.

- (2) By increasing the rock temperature, increasing the number of heating-cooling cycles, or decreasing water injection temperature, the mechanical properties of the specimen became weaker, and the values of the roughness gradually increased. The different conditions of water cooling at high temperature that influenced the physical and mechanical properties and the roughness characteristics of the rock in the thermal recovery area, from most to least important, were the temperature of the target area, the number of water injection cycles, and the water injection temperature. By selecting high-temperature reservoirs as the target areas for drilling and adopting low-temperature water injection and multiple cold-water circulation cycles, rock strata can be fractured to improve the permeability of reservoirs.
- (3) Under different water cooling conditions, the tensile strength was negatively correlated with the roughness index. When the tensile strength changes, the impact on the roughness was in the descending order of the target area temperature, the number of water circulation cycles, and the water temperature. Thus, tensile strength can be used as an indicator for evaluating the surface roughness under different conditions of water cooling at high temperature.

### Data Availability

The data used to support the findings of this study are available from the corresponding author upon request.

### Conflicts of Interest

The authors declare that there are no conflicts of interest.

### Acknowledgments

This research was supported by the National Natural Science Foundation of China (51874165), the Liaoning Province "Xingliao Talent Program" (XLYC1902106), and the National Key R&D Program of China (2016YFC0600901).

### References

- [1] MIT, *The Future of Geothermal Energy-Impact of Enhanced Geothermal Systems (EGS) on the United States in the 21st Century, An Assessment by an MIT-Led Interdisciplinary Panel*, Massachusetts Institute of Technology, Boston, MA, USA, 2006.
- [2] Y. Jing, Z. Jing, J. Willis-Richards, and T. Hashida, "A simple 3-D thermoelastic model for assessment of the long-term performance of the Hijiori deep geothermal reservoir," *Journal of Volcanology and Geothermal Research*, vol. 269, pp. 14–22, 2014.
- [3] C. Vogt, G. Marquart, C. Kosack, A. Wolf, and C. Clauser, "Estimating the permeability distribution and its uncertainty at the EGS demonstration reservoir Soultz-sous-Forts using the ensemble Kalman filter," *Water Resources Research*, vol. 48, no. 8, pp. 8517–8531, 2012.
- [4] Y. Zhao, Z. Wan, and J. Kang, *Introduction to Geothermal Development of High Temperature Rock Mass*, Science Press, Beijing, China, 2004.
- [5] Y. Xin, L. Zhuang, and Z. Sun, "Numerical investigation on the effects of the fracture network pattern on the heat extraction capacity for dual horizontal wells in enhanced geothermal systems," *Geomechanics and Geophysics for Geo-Energy and Geo-Resources*, vol. 6, no. 2, pp. 533–552, 2020.
- [6] D. B. Fox, D. Sutter, K. F. Beckers et al., "Sustainable heat farming: modeling extraction and recovery in discretely fractured geothermal reservoirs," *Geothermics*, vol. 46, pp. 42–54, 2013.
- [7] A. Kazemi, S. Mahbaz, A. Dehghani-Sani, M. Dusseault, and R. Fraser, "Performance evaluation of an enhanced geothermal system in the Western Canada sedimentary basin," *Renewable and Sustainable Energy Reviews*, vol. 113, Article ID 109278, 2019.
- [8] A. Bataill , P. Genthon, M. Rabinowicz, and B. Fritz, "Modeling the coupling between free and forced convection in a vertical permeable slot: implications for the heat production of an enhanced geothermal system," *Geothermics*, vol. 35, no. 5-6, pp. 654–682, 2006.
- [9] B. Gong, H. Liang, S. Xin, and K. Li, "Effect of water injection on reservoir temperature during power generation in oil fields," in *Proceedings of the 36th Workshop on Geothermal Reservoir Engineering*, Stanford, CA, USA, January 2011.
- [10] P. K. Gautam, A. K. Verma, M. K. Jha, P. Sharma, and T. N. Singh, "Effect of high temperature on physical and mechanical properties of Jalore granite," *Journal of Applied Geophysics*, vol. 159, pp. 460–474, 2018.
- [11] Y. Shen, X. Hou, J. Yuan, and C. Zhao, "Experimental study on temperature change and crack expansion of high temperature granite under different cooling shock treatments," *Energies*, vol. 12, no. 11, 2019.
- [12] Y. Shen, X. Hou, J. Yuan et al., "Thermal deterioration of high-temperature granite after cooling shock: multiple-identification and damage mechanism," *Bulletin of Engineering Geology and the Environment*, vol. 7, pp. 1–14, 2020.
- [13] X. Hu, X. Song, Y. Liu, Z. Cheng, J. Ji, and Z. Shen, "Experiment investigation of granite damage under the high-temperature and high-pressure supercritical water condition," *Journal of Petroleum Science and Engineering*, vol. 180, pp. 289–297, 2019.
- [14] B. Isaka, R. Gamage, T. Rathnaweera, M. Perera, D. Chandrasekharam, and W. Kumari, "An influence of thermally-induced micro-cracking under cooling treatments: mechanical characteristics of Australian granite," *Energies*, vol. 11, no. 6, 2018.
- [15] Z. Zhao, "Thermal influence on mechanical properties of granite: a microcracking perspective," *Rock Mechanics and Rock Engineering*, vol. 49, no. 3, pp. 747–762, 2015.
- [16] B. Li and F. Ju, "Thermal stability of granite for high temperature thermal energy storage in concentrating solar power plants," *Applied Thermal Engineering*, vol. 138, pp. 409–416, 2018.
- [17] M. Hosseini, "Effect of temperature as well as heating and cooling cycles on rock properties," *Journal of Mining and Environment*, vol. 8, no. 4, pp. 631–644, 2017.
- [18] T. Ficker, "Rock joint coefficients and their computerized classification," *International Journal of Mining Science and Technology*, vol. 29, no. 5, pp. 701–709, 2019.



- [19] L. Zeng, J. Qi, and Y. Wang, "Origin type of tectonic fractures and geological conditions in low-permeability reservoirs," *Acta Petrolei Sinica*, vol. 28, no. 4, pp. 52–56, 2007.
- [20] G. Grasselli and P. Egger, "Constitutive law for the shear strength of rock joints based on three-dimensional surface parameters," *International Journal of Rock Mechanics and Mining Sciences*, vol. 40, no. 1, pp. 25–40, 2003.
- [21] W. Zhang, Q. Sun, S. Hao, J. Geng, and C. Lv, "Experimental study on the variation of physical and mechanical properties of rock after high temperature treatment," *Applied Thermal Engineering*, vol. 98, pp. 1297–1304, 2016.
- [22] M. Diaz, K. Y. Kim, S. Yeom, L. Zhuang, S. Park, and K.-B. Min, "Surface roughness characterization of open and closed rock joints in deep cores using X-ray computed tomography," *International Journal of Rock Mechanics and Mining Sciences*, vol. 98, pp. 10–19, 2017.
- [23] Z. C. Tang and Y. Zhang, "Temperature-dependent peak shear-strength criterion for granite fractures," *Engineering Geology*, vol. 269, p. 105552, 2020.
- [24] R. Li, Z. Huang, X. Wu, P. Yan, and X. Dai, "Cryogenic quenching of rock using liquid nitrogen as a coolant: investigation of surface effects," *International Journal of Heat and Mass Transfer*, vol. 119, pp. 446–459, 2018.
- [25] Z. C. Tang, "Experimental investigation on temperature-dependent shear behaviors of granite discontinuity," *Rock Mechanics and Rock Engineering*, vol. 53, no. 9, pp. 4043–4060, 2020.
- [26] Z. C. Tang, Q. Z. Zhang, and J. Peng, "Effect of thermal treatment on the basic friction angle of rock joint," *Rock Mechanics and Rock Engineering*, vol. 53, no. 4, pp. 1973–1990, 2020.
- [27] Z. Tang and Y. Jiao, "Choosing appropriate appraisal to describe peak-spatial features of rock-joint profiles," *International Journal of Geomechanics*, vol. 20, no. 4, Article ID 04020021, 2020.
- [28] C. Zhang, S. Zhang, S. Li et al., "Geothermal characteristics of the Qiabuqia geothermal area in the Gonghe basin, North-eastern Tibetan Plateau," *Chinese Journal of Geophysics-Chinese Edition*, vol. 61, no. 11, pp. 4545–4557, 2018.
- [29] Y. Li, "Preliminary study on EGS geothermal resources evaluation and exploration in Song-Liao basin," Master thesis, Jilin University, Changchun, China, 2017.
- [30] F. Zhang, J. Zhao, D. Hu, F. Skoczylas, and J. Shao, "Laboratory investigation on physical and mechanical properties of granite after heating and water-cooling treatment," *Rock Mechanics and Rock Engineering*, vol. 51, no. 3, pp. 677–694, 2017.
- [31] Y. Zhao, Z. Feng, Y. Zhao, and Z. Wan, "Experimental investigation on thermal cracking, permeability under HTHP and application for geothermal mining of HDR," *Energy*, vol. 132, pp. 305–314, 2017.
- [32] W. Zhang, T.-K. Guo, Z.-Q. Qu, and Z. Wang, "Research of fracture initiation and propagation in HDR fracturing under thermal stress from meso-damage perspective," *Energy*, vol. 178, pp. 508–521, 2019.
- [33] R. Yang, Z. Huang, Y. Shi, Z. Yang, and P. Huang, "Laboratory investigation on cryogenic fracturing of hot dry rock under triaxial-confining stresses," *Geothermics*, vol. 79, pp. 46–60, 2019.
- [34] Ministry of Land and Resources of the People's Republic of China, *DZ/T 0276-2015 Regulation For Testing the Physical and Mechanical Properties of Rock*, Standards Press of China, Beijing, China, 2015.
- [35] Z. Yan, H. Zhu, T. Deng, L. Zeng, J. Yao, and J. Qiang, "Experimental study on longitudinal wave characteristics of tuff, granite and breccia after high temperature," *Chinese Journal of Geotechnical Engineering*, vol. 28, no. 11, pp. 2010–2014, 2016.
- [36] B. Xi and Y. Zhao, "Experimental research on mechanical properties of water-cooled granite under high temperatures within 600°C," *Chinese Journal of Rock Mechanics and Engineering*, vol. 29, no. 5, pp. 892–898, 2010.
- [37] N. Barton, "Review of a new shear-strength criterion for rock joints," *Engineering Geology*, vol. 7, no. 4, pp. 287–332, 1973.
- [38] Y. Zhu, J. Yu, H. Gao, G. Li, X. Zhou, and X. Zheng, "Effect of water cooling on microscopic damage and dynamic properties of high-temperature granite," *Explosion and Shock Waves*, vol. 39, no. 8, pp. 1–12, 2019.
- [39] L. Deng, X. Li, Y. Wu et al., "Study on mechanical damage characteristics of granite with different cooling methods," *Journal of China Coal Society*, 2020.
- [40] Y. Shen, X. Hou, J. Yuan, S. Wang, and C. Zhao, "Thermal cracking characteristics of high temperature granite suffering from different cooling shocks," *International Journal of Fracture*, vol. 225, pp. 153–168, 2020.

## Research Article

# Response Analysis of Deep Foundation Excavation and Dewatering on Surface Settlements

Xian Li,<sup>1</sup> Tingguo Zhou,<sup>1</sup> Yixian Wang ,<sup>1</sup> Junling Han,<sup>1</sup> Yanqiao Wang,<sup>1</sup> Fang Tong,<sup>1</sup> Delong Li,<sup>2</sup> and Jinmei Wen<sup>3</sup>

<sup>1</sup>School of Civil Engineering, Hefei University of Technology, Hefei 230009, China

<sup>2</sup>Nanjiang Hydrogeology and Engineering Geology Team of Chongqing Bureau of Geology and Minerals Exploration, Chongqing 401146, China

<sup>3</sup>No. 208 Hydrogeology and Engineering Geology Team of Chongqing Bureau of Geology and Minerals Exploration, Chongqing Institute of Geological Hazard Prevention Engineering Exploration and Design, Chongqing 400700, China

Correspondence should be addressed to Yixian Wang; wangyixian2012@hfut.edu.cn

Received 7 August 2020; Revised 19 October 2020; Accepted 20 October 2020; Published 10 November 2020

Academic Editor: Zhi Cheng Tang

Copyright © 2020 Xian Li et al. This is an open access article distributed under the Creative Commons Attribution License, which permits unrestricted use, distribution, and reproduction in any medium, provided the original work is properly cited.

Accurate prediction of surface settlements is a primary concern when deep excavations were carrying out under the water table in urban environments for the safety of the work site. The sedimentation deformation due to deep excavation of foundation pit and dewatering occurs as a result of coupling action of the two factors. The study is aimed at revealing the coupling ground response to the two factors and developing empirical correlations for estimating ground deformations. Taking a deep foundation pit of a metro station as an example, surface settlement estimations were calculated by analytical formulas and numerical models. The settlement results by analytical formulas under excavation and dewatering conditions were added linearly to the total settlements. And three-dimensional coupling numerical models were established by applying commercial software (GMS and MIDAS) to investigate the interaction impact of excavation and dewatering on the sedimentation deformation. Comparing with monitoring data, numerical simulation results match well with the monitoring data. Furthermore, an empirical surface subsidence correlation equation was developed by the polynomial fitting to illustrate the effect contribution on the total surface settlement of foundation excavation and dewatering.

## 1. Introduction

Deep underground constructions built below the water table are inevitable in the urban region with the continuous city development. Due to the influence of groundwater, foundation pit dewatering becomes an auxiliary project that must be carried out in the process of deep excavation. A major concern for the urban deep excavations is the induced deformations in the surrounding soil and the subsequent impact on adjacent structures [1–5]. Erroneous estimates of sedimentation deformations may result in either large construction costs due to excessive ground support or damage to the surrounding structures due to inadequate excavation support. The factors such as construction technique,

dewatering, and soil type have significant influences on the predicted deformations [6, 7].

Most of the main theories about settlement caused by excavation are based on the total stress method proposed by Peck based on curve-fitting of an enormous amount of field monitoring results [8–11]. The monitoring data show that the calculation results underestimate the actual settlement. Differences between measurements and theoretical predictions could be attributed to the effect of dewatering. The dewatering process can cause the depressurization of aquifers triggering the changes in effective stresses. When water is extracted from an aquifer, the effective stresses on the soil mass within it increase causing land subsidence [12–15]. Significant results have been achieved in land subsidence research, but the main factors causing land

subsidence are excavation and dewatering [16–18]. Based on the linear superposition of the settlement caused by excavation and dewatering, the total surface settlement can be simply obtained but the interaction between stress release and groundwater level drop is ignored.

Taking a deep foundation pit of a metro station as an example, this paper is aimed at investigating the interaction response to surface settlement of deep foundation and dewatering. The total linear superposition settlements were calculated by analytical formulas under excavation and dewatering conditions. And three-dimensional coupling numerical models were established by commercial software (GMS and MIDAS) to obtain the response on the groundwater level, effective stresses, and the displacement of excavation and dewatering. Then, the two predicted surface settlement results were compared with the monitoring data to verify the validity of the two methods.

## 2. Materials

**2.1. Project Description.** The metro station foundation pit is located at the area of central China with the size of 120 m × 15 m × 22.4 m (length × width × depth). There is a river that goes round the west and south side of the station foundation pit with the minimum distance of 24 m. The main structure of the shield shaft section is only 4.5 m away from the river bank. On the northwest side of the foundation pit is a hotel named building 1. The main building of this hotel has 29 floors, and the five-storey building is pile foundation with the minimum distance of 10.7 meters away from the foundation pit. And the southeast side is a shopping mall named building 2 with 18 floors and the minimum distance of 10 meters. Its foundations are all pile foundations. The northeast side is building 3 with 6 floors. The location of the engineering site is shown in Figure 1.

The metro station foundation pit is mainly located in the alluvial-diluvial silty clay, silty soil, and fine sand layer with poor stability. The possibility of liquefaction exists in the fine sand layer, which has certain influence on the working process. The detailed geological profile of the site is shown in Figure 2.

The deep foundation excavation process was divided into five stages, namely, stage I, stage II, stage III, stage IV, and stage V, each with an excavation depth of 1.4 m, 2.7 m, 4.5 m, 6.4 m, and 7.4 m, respectively. Each excavation floor level was 24.1 m, 21.4 m, 16.9 m, 10.6 m, and 3.2 m. The foundation pit dewatering was carried out along with the excavation stage, ensuring that the groundwater table was 0.5 m below the bottom of the foundation pit. The initial groundwater level was 23 m. Foundation pit dewatering was not required during stage I of foundation excavation because the bottom of the foundation pit is higher than the groundwater level. The dewatering process started from stage II of foundation excavation which was divided into four stages of foundation dewatering.

**2.2. Monitoring of Settlements.** Before the construction process of the station foundation pit, pumping wells were set

parallel along the side line of the foundation pit. In order to make the surrounding soil surface settlement and groundwater level meet the requirements of the design specifications, a steel ruler water level gauge SWJ-90-50 recording foundation was arranged between adjacent pumping wells along the length of the foundation pit. During the dewatering process, the water level near the pumping well fluctuated. Trimble DiNi03 electronic level was set at a vertical interval of 5 m along the center line of the foundation pit to measure surface subsidence (see Table 1); at the same time, inspections of surface subsidence were carried out on building 1, building 2, and building 3. The layout map of various measuring points is given in Figure 3.

There were many monitoring points on the site, represented by DB-1, JCJ-6, JCJ-9, and JCJ-15 observation points. The ground surface settlement values of the DB-1, JCJ-6, JCJ-9, and JCJ-15 settlement monitoring groups were selected to display the effect of the deep foundation excavation process on the control of surrounding environment deformation (see Figure 4). The settlement of each measuring point gradually increased over time, and the settlement rate reached its maximum 25 days prior to construction. The settlement values measured at the nearest monitoring point (DB-1) to the foundation pit were the largest value. The results of the other three monitoring points showed the similar flat trends of the settlement values. The greater the self-weight stress of the building next to the monitoring point was, the greater the monitored settlement values were.

## 3. Settlement Estimation

**3.1. Settlement Estimation by Analytical Formulas.** During the construction of deep foundation pits below the water table, in order to prevent damages such as foundation pit collapse and surge in the pit, the groundwater level should be lowered to 0.5 m below the bottom of the foundation pit before construction.

A cone of depression was formed which caused decrease of groundwater pressure between soils and increase in effective stress between soil particles. In the process of foundation pit dewatering, groundwater moves slowly in laminar flow, and the dewatering curve is distributed symmetrically along the pumping well. Dupuit formula is introduced as the dewatering depression curve equation as follows [19]:

$$y^2 = (l + h)^2 + \left[ H^2 - (l + h)^2 \right] \frac{\ln(x/r)}{\ln(R/r)}, \quad (1)$$

where  $x$  is the horizontal distance from the center of the well axis;  $l$  is the length of the water filter pipe of the dewatering well;  $r$  is the radius of the pumping well;  $h$  is the vertical distance from the partially penetrating well to the aquifer; and the full penetrating well  $h = 0$ , and the radius of dewatering influence is  $R$ .

During the dewatering process, there is air inside the unsaturated zone, and the pore water will be tensioned. The balanced differential equation and stress differential equation of the soil particles and pore water can be combined to

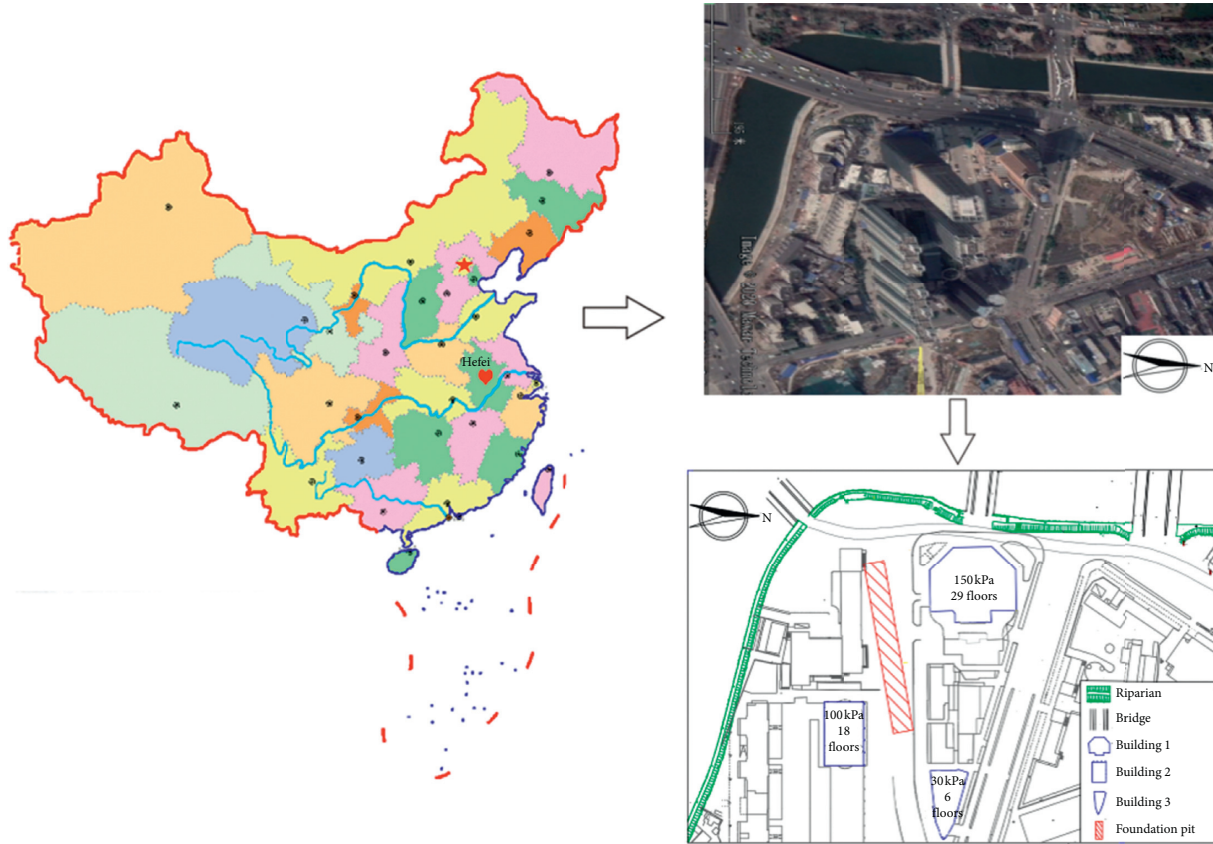


FIGURE 1: The location of the project site.

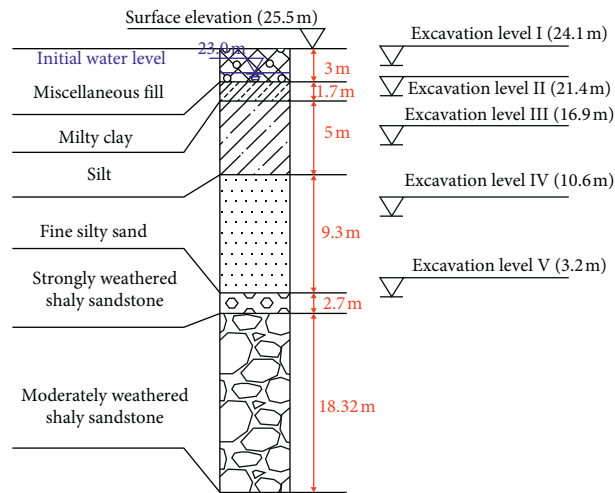


FIGURE 2: Detailed geological profile of the site.

obtain a unified effective stress equation applicable to unsaturated soil and saturated soil [20]:

$$\sigma' = (\sigma - u_a) + S_e(u_a - u_w),$$

$$S_e = \frac{(S - S_r)}{(1 - S_r)} = \frac{(\theta - \theta_r)}{(\theta_s - \theta_r)}, \quad (2)$$

$$\tau = u_a - u_w.$$

In the formula,  $S_e$  and  $S_r$  are the effective saturation and residual saturation of the soil, respectively;  $\theta_s$  and  $\theta_r$  are the saturated volumetric water content and residual volumetric water content, respectively;  $\tau$  is the matrix suction, measured by unsaturated soil triaxial apparatus and pressure plate instrument. When the effective volume saturation  $S_e$  is equal to 1, the equation returns to the effective stress equation of saturated soil.

TABLE 1: Monitoring equipments.

Number	Monitor items	Equipment	Measuring accuracy (mm)	Frequency
1	Surface settlement	Trimble DiNi03	1.0	Once/3 days
2	Groundwater level	SWJ-90-50	5.0	Once/3 days
3	Building settlement	Trimble DiNi03	1.0	Once/3 days

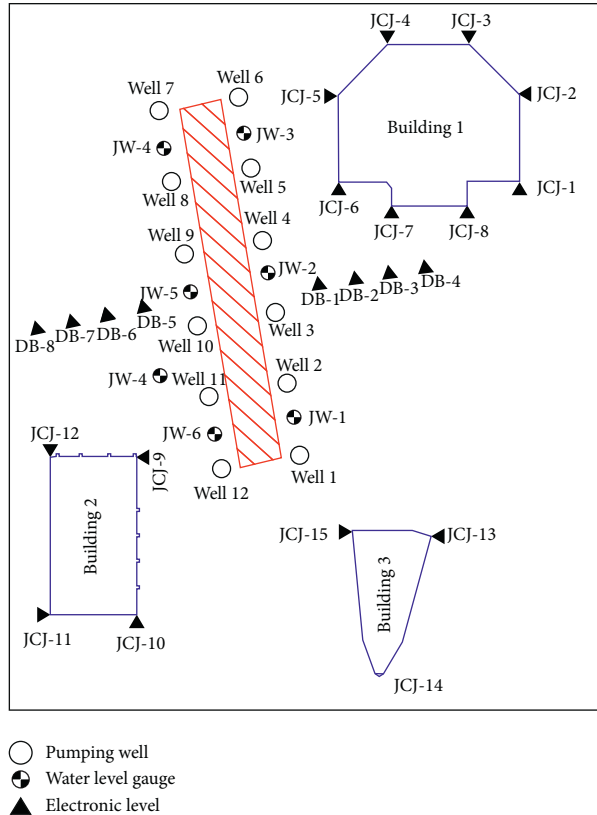


FIGURE 3: Monitoring point layout map.

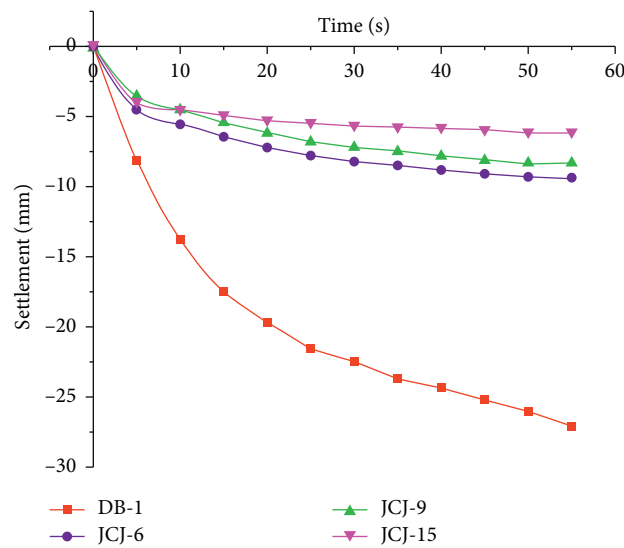


FIGURE 4: Settlement values of monitoring points.

TABLE 2: The physical and mechanical parameters of the soil layer.

Name	Thickness $H$ (m)	Elastic modulus $E$ (MPa)	Cohesion $c$ (kPa)	Friction angle $\varphi$ ( $^{\circ}$ )	Poisson's ratio $\nu$	Permeability $k$ (m/d)
Miscellaneous fill	3.1	8	15	10	—	0.05
Silty clay	1.7	12	10	24	0.35	0.01
Silt	5	10	—	—	0.3	1
Strongly weathered argillaceous sandstone	2.7	53	50	26	0.24	1
Moderately weathered argillaceous sandstone	—	50	130	33	0.23	1

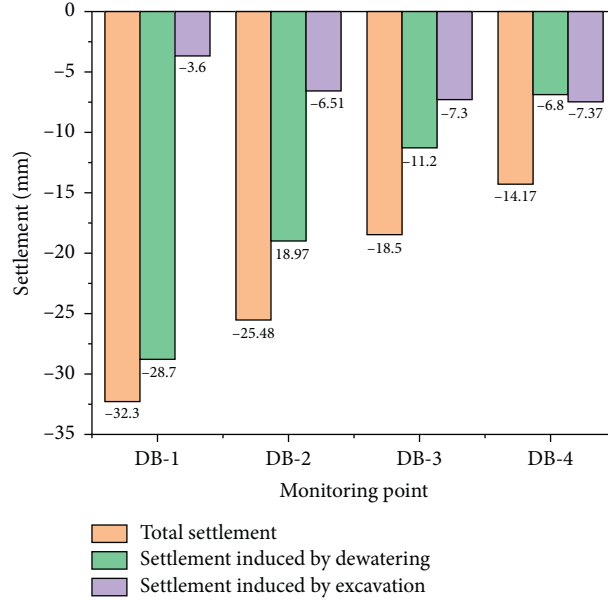


FIGURE 5: Theoretical calculation of surface settlement.

Effective soil stress in the area above the water level did not change before excavation, and the effective stress of the soil in the unsaturated area changed as follows:

$$\Delta\sigma'_1 = \gamma_w(H - y) + (S_e - 1)\tau. \quad (3)$$

For saturated soil, the pores between soil particles are completely filled with water, and the drop of groundwater level causes the pore water pressure decreasing. The equation returns to the saturated soil effective stress equation, and the effective stress change value is the water pressure decrease:

$$\Delta\sigma'_2 = \gamma_w(H - y). \quad (4)$$

Surface settlements caused by dewatering can be calculated by the layerwise summation method as follows:

$$s = \sum_{i=1}^n s_i = \sum_{i=1}^n \frac{\Delta\sigma'_i}{E_i} h_i. \quad (5)$$

In the formula,  $s$  is the surface settlements which caused dewatering;  $s_i$  is the surface settlements of layer  $i$ ;  $E_i$  is the soil elastic modulus of layer  $i$ ; and  $h_i$  is the thickness of layer  $i$ .

According to the layerwise summation formula, the effective stress of the soil in the dry soil area has not changed, so in dry soil, area  $s_1 = 0$ .

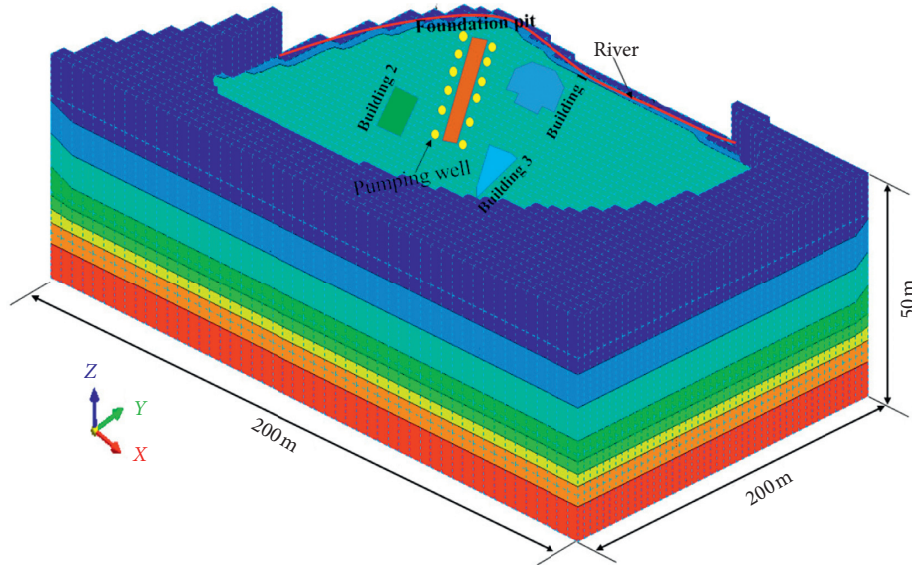
Settlement of the soil layer in the unsaturated zone is as follows:

$$s_2 = \sum_{i=1}^n \frac{\gamma_w(H - y) + \tau(S_e - 1)}{E_i} h_i. \quad (6)$$

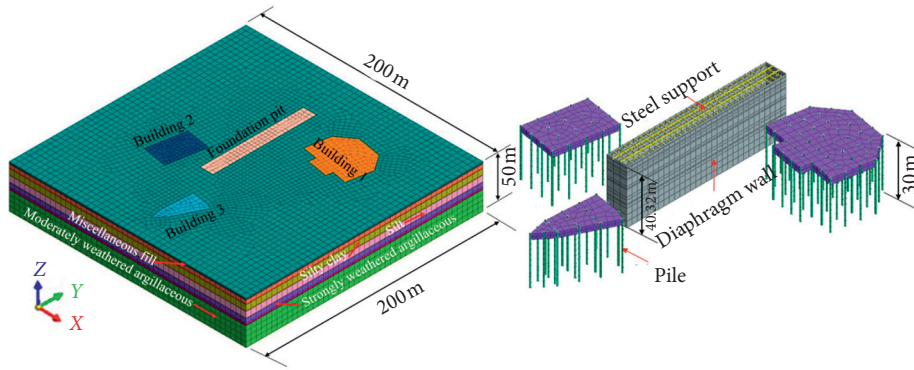
Settlement of soil layer in saturated zone is as follows:

$$s_3 = \sum_{i=1}^n \frac{\gamma_w(H - y)}{E_i} h_i. \quad (7)$$

The excavation of the foundation pit leads to soil unloading which breaks the balance of the self-weight stress in the excavation area and ground settlement. According to the empirical formula formed by the Rayleigh distribution function, the amount of ground settlement caused by foundation pit excavation is calculated as follows [8]:

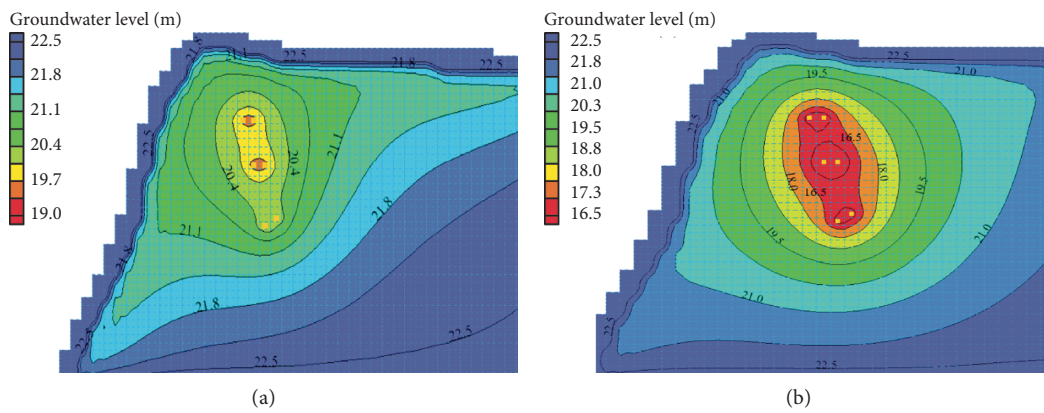


(a)



(b)

FIGURE 6: Meshing of numerical models.



(a)

(b)

FIGURE 7: Continued.

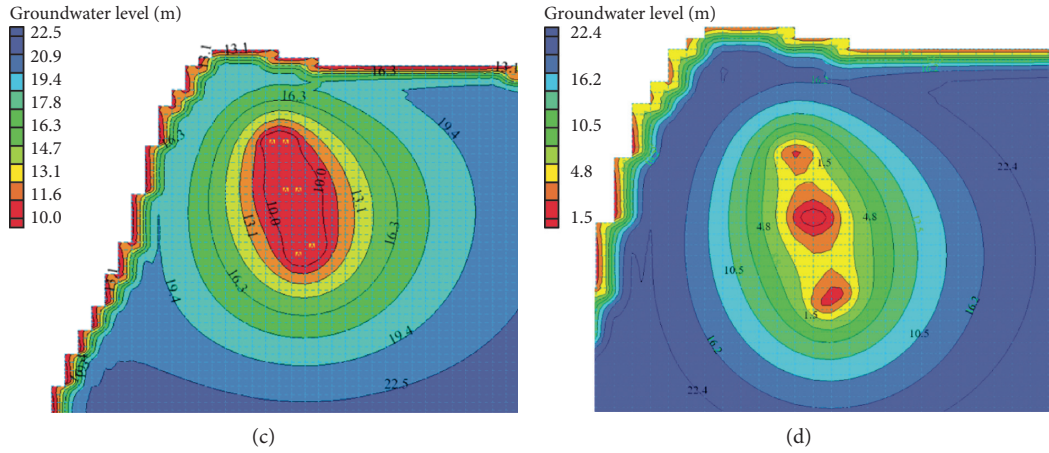


FIGURE 7: Contours of groundwater level after each dewatering stage. (a) After the first stage of dewatering. (b) After the second stage of dewatering. (c) After the third stage of dewatering. (d) After the fourth stage of dewatering.

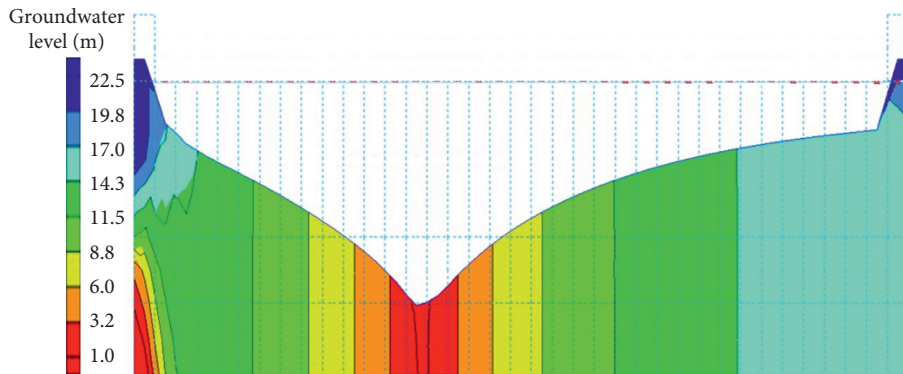


FIGURE 8: The profile of the groundwater table after the fourth dewatering stage.

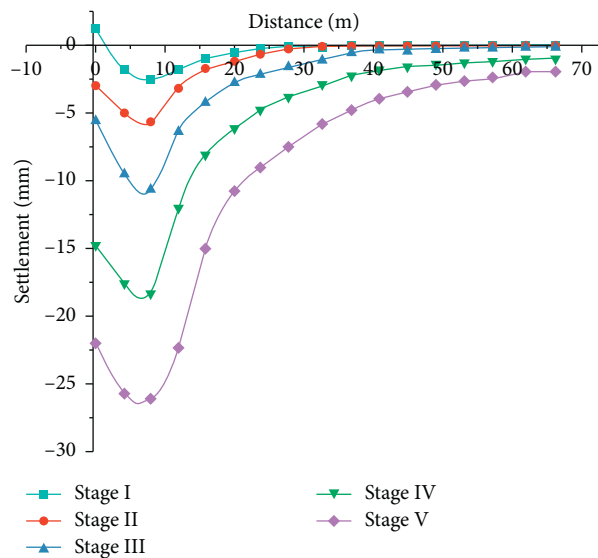


FIGURE 9: Surface settlement curve.



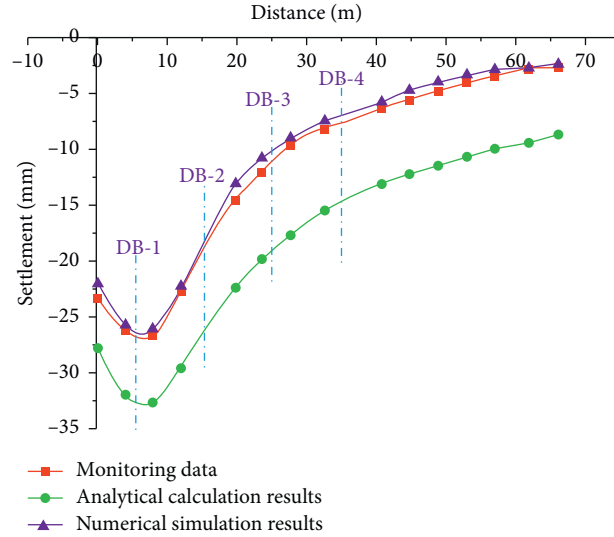


FIGURE 10: Comparison between different settlement values.

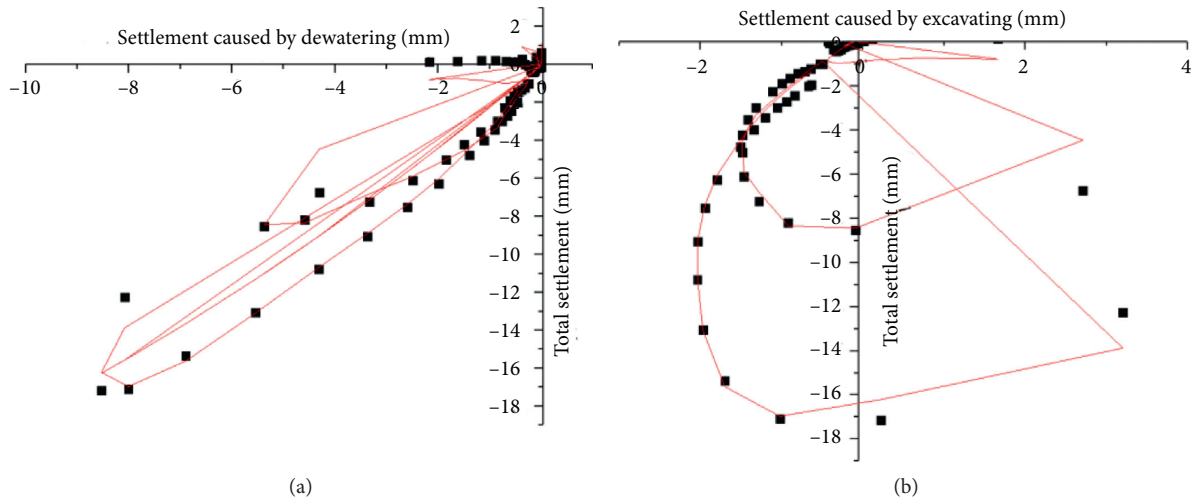


FIGURE 11: Fitted curve between the total settlement and settlement caused by dewatering and excavation.

$$s_4 = s_{vm} \cdot \frac{(d/H) + 0.75}{0.9} \cdot \exp\left\{-\frac{[(d/H) + 0.75]^2}{4.5}\right\},$$

$$s_{vm} = \alpha s_{hm},$$

$$s_{hm} = k_\delta H,$$

(8)

where  $d$  is the distance from the excavation point to the center of the foundation pit;  $H$  is the excavation depth;  $s_{vm}$  is the maximum settlement of the foundation pit excavation;  $s_{hm}$  is the maximum deformation of the enclosure;  $\alpha$  is the empirical coefficient; and  $k_\delta$  is the proportional coefficient. The two settlements are superimposed and summed to estimate the amount of ground settlement caused by the dewatering and excavation of the foundation pit. And the settlement caused by excavation and dewatering is the sum of the above:

$$s = s_1 + s_2 + s_3 + s_4. \quad (9)$$

The physical and mechanical parameters of the soil layer are shown in Table 2. The geotechnical parameters were determined by the conventional testing [21–23].

The calculated results by analytical formulas are shown in Figure 5. The DB series of monitoring points are distributed symmetrically along the foundation pit, which can better indicate the law of surface settlement. From Figure 5, dewatering is the major factor triggering the surface settlements. The maximum settlements occurred at DB-1 point, accounting for 88.9% of the total subsidence. The distances to the foundation pit from DB-1 point to DB-4 point increased. As the monitoring point was farther away from the foundation pit, the slower the decline rate of groundwater level was, the smaller the change of effective stress of soil layer was, resulting in smaller proportion of dewatering contributing to surface settlement.

**3.2. Settlement Estimation by Numerical Models.** In this paper, three-dimensional coupling numerical models were established by applying commercial software (GMS and MIDAS) to investigate the interaction impact of excavation and dewatering on the sedimentation deformation (see Figure 6). The width of the river is about 30 ~ 80 m, and the elevation of the river bottom is about 5 ~ 6 m. The calculated parameters adopted the value as shown in Table 2.

Figure 7 indicates the evolution of groundwater level after each stage of dewatering. In the dewatering process, the groundwater level was distributed in a funnel shape with the dewatering well near the foundation pit as the center. The farther the distance from the center of the foundation pit is, the smaller the drop of groundwater level is (see Figure 8).

Figure 9 shows the simulated surface settlements at each excavation stage. During the first excavation of the foundation pit, the excavation depth was 1.4 m, and the supporting structure was not completed at this time. Due to the unloading effect of the soil, the foundation was uplifted. The settlement curve is distributed as a “spoon” shape from the horizontal distance of the excavation center of the foundation pit. The settlement value increased with the increase of distance from the foundation pit at the distance ranging from 0 to 8 m. However, the values of settlement decreased with the increase of distance from the foundation pit when the distance was greater than 8 m. The accumulated settlement of five excavations reaches the maximum at the fifth stage of excavation, which is 26.1 mm.

**3.3. Comparison of Results between Calculated Results and Settlement Monitoring Data.** Figure 10 shows the comparison between calculated results and settlement monitoring data. The numerical simulation results obtained from a fluid-solid coupling model matched well with the monitoring data than the analytical calculation results, which suggested that the impact of excavation and dewatering on surface settlement cannot simply be added together. As the groundwater level dropped, the effective stress in the soil increased which changed the porosity of the soil and indirectly changed the state of water movement. However, the analytical calculation method directly superimposes the settlement caused by dewatering and excavation, which did not consider the interaction between water and soil leading to the larger result than the monitored data.

## 4. Discussion and Conclusions

This paper used analytical formulas and numerical models to simulate surface settlements of a deep foundation pit of a metro station aimed at investigating the interaction response to surface settlement of deep foundation and dewatering. The conclusions are as follows:

- (1) The ground settlement caused by the construction of the foundation pit was distributed as a “spoon” shape centered on the foundation pit, which is proportional to the depth of the excavation. At a distance of 6.1 m from the center of the foundation pit, the settlement reached the maximum value of 26.1 mm.

Analytical calculation results showed that the surface subsidence is mainly caused by dewatering. As the distance from the monitoring location to the center of the foundation pit was getting further, the lower the groundwater level falls, the smaller the effective stress change of the soil layer, which decreases the influence contribution of dewatering to the surface settlement.

- (2) The numerical simulation results obtained from a fluid-solid coupling model matched well with the monitoring data than the analytical calculation results, which suggested that the impact of excavation and dewatering on surface settlement cannot simply be lineally added together. Therefore, an empirical surface subsidence correlations equation was developed by the polynomial fitting to illustrate the effect contribution on the total surface settlement of foundation excavation and dewatering (as shown in Figure 11). The total settlement can be expressed by dewatering settlement and excavation settlement as follows:

$$z = -0.08x^2 + 0.93x + 0.01y^2 + 1.101y + 0.015, \quad (10)$$

where  $z$  represents the total settlement value,  $x$  is the settlement caused by dewatering, and  $y$  is the excavation settlement; the value of  $R^2$  after fitting adjustment is 0.999, so the fitted equation can be considered accurate.

## Data Availability

The data of numerical results used to support the findings of this study can be obtained from the corresponding author upon request.

## Conflicts of Interest

The authors declare that they have no conflicts of interest.

## Acknowledgments

This research work was funded by the National Natural Science Foundation of China (51774107 and 42077249), the Open Program of State Key Laboratory of Explosion Science and Technology, Beijing Institute of Technology (KFJJ19-02M), and the Fundamental Research Funds of the Housing and Construction Department of Anhui Province (2013YF-27).

## References

- [1] J. H. Kihm, J. M. Kim et al., “Three-dimensional numerical simulation of fully coupled groundwater flow and land deformation due to groundwater pumping in an unsaturated fluvial aquifer system,” *Journal of Hydrology*, vol. 335, no. 1-2, pp. 1-14, 2007.
- [2] C. C. Faunt, M. J. Sneed, and J. T. Brandt, “Water availability and land subsidence in the Central Valley, California, USA,” *Hydrogeology Journal*, vol. 24, no. 3, pp. 675-684, 2016.

- [3] M. Traum and I. Adiyaman, "The influence of clay zones on land subsidence from groundwater pumping," *Ground Water*, vol. 51, no. 1, pp. 51–57, 2013.
- [4] D. L. Galloway and T. J. Burbey, "Review: regional land subsidence accompanying groundwater extraction," *Hydrogeology Journal*, vol. 19, no. 8, pp. 1459–1486, 2011.
- [5] C. R. Jesús, "Settlements around pumping wells: analysis of influential factors and a simple calculation procedure," *Journal of Hydrology*, vol. 548, pp. 225–236, 2018.
- [6] D. Roy and K. E. Robinson, "Surface settlements at a soft soil site due to bedrock dewatering," *Engineering Geology*, vol. 107, no. 3–4, pp. 109–117, 2009.
- [7] E. Pujades, E. Vázquez-Suñé, J. Carrera, and A. Jurado, "Dewatering of a deep excavation undertaken in a layered soil," *Engineering Geology*, vol. 178, pp. 15–27, 2014.
- [8] R. B. Peck, "Deep excavations and tunneling in soft ground," in *Proceedings of the 7th International Conference on Soil Mechanics and Foundation Engineering*, Scientific Research Publishing, Mexico, USA, August 1969.
- [9] E. H. Y. Leung and C. W. W. Ng, "Wall and ground movements associated with deep excavations supported by cast in situ wall in mixed ground conditions," *Journal of Geotechnical and Geoenvironmental Engineering*, vol. 133, no. 2, pp. 129–143, 2007.
- [10] P. Guo and X. Gong, "Displacement and force analyses of braced structure of deep excavation considering unsymmetrical surcharge effect," *Computers and Geotechnics*, vol. 113, pp. 103–102, 2019.
- [11] H. Di, H. Guo, S. Zhou, J. Chen, and L. Wen, "Investigation of the axial force compensation and deformation control effect of servo steel struts in a deep foundation pit excavation in soft clay," *Advances in Civil Engineering*, vol. 2019, no. 6, 16 pages, Article ID 5476354, 2019.
- [12] M. Budhu and I. B. Adiyaman, "Mechanics of land subsidence due to groundwater pumping," *International Journal for Numerical and Analytical Methods in Geomechanics*, vol. 34, no. 14, pp. 1459–1478, 2010.
- [13] J. C. Ni, W. C. Cheng, and L. Ge, "A case history of field pumping tests in a deep gravel formation in the Taipei Basin, Taiwan," *Engineering Geology*, vol. 117, no. 1–2, pp. 17–28, 2011.
- [14] H. A. Loáiciga, "Consolidation settlement in aquifers caused by pumping," *Journal of Geotechnical and Geoenvironmental Engineering*, vol. 139, no. 7, pp. 1191–1204, 2013.
- [15] J. Pacheco-Martínez, M. Hernandez-Marín, T. J. Burbey et al., "Land subsidence and ground failure associated to groundwater exploitation in the Aguascalientes Valley, México," *Engineering Geology*, vol. 164, pp. 172–186, 2013.
- [16] A. Jayeoba, S. A. Mathias, S. Nielsen, V. Vilarrasa, and T. I. Bjørnarå, "Closed-form equation for subsidence due to fluid production from a cylindrical confined aquifer," *Journal of Hydrology*, vol. 573, pp. 964–969, 2019.
- [17] C. W. W. Ng, Y. Hong, G. B. Liu, and T. Liu, "Ground deformations and soil-structure interaction of a multi-propped excavation in Shanghai soft clays," *Géotechnique*, vol. 62, no. 10, pp. 907–921, 2012.
- [18] Y. M. A. Hashash, A. Osouli, and C. Marulanda, "Central artery/tunnel project excavation induced ground deformations," *Journal of Geotechnical and Geoenvironmental Engineering*, vol. 134, no. 9, pp. 1399–1406, 2008.
- [19] J. Bear, *Hydraulics of Groundwater*, Vol. 5, McGraw-Hill International Book, New York, NY, USA, 1979.
- [20] S. Longtan, Q. Yalong, G. Xiaoxia et al., "The validation of the effective stress principle of unsaturated soils," *Chinese Journal of Underground Space and Engineering*, vol. 14, no. 6, pp. 1476–1483, 2018.
- [21] S. D. Mohammadi, M. R. Nikoudel, H. Rahimi, and M. Khamehchiyan, "Application of the dynamic cone penetrometer (DCP) for determination of the engineering parameters of sandy soils," *Engineering Geology*, vol. 101, no. 3–4, pp. 195–203, 2008.
- [22] M. Wang and W. Wan, "A new empirical formula for evaluating uniaxial compressive strength using the Schmidt hammer test," *International Journal of Rock Mechanics and Mining Sciences*, vol. 123, Article ID 104094, 2019.
- [23] M. Wang, W. Wan, and Y. Zhao, "Experimental study on crack propagation and the coalescence of rock-like materials with two preexisting fissures under biaxial compression," *Bulletin of Engineering Geology and the Environment*, vol. 79, no. 6, pp. 3121–3144, 2020.

## Research Article

# Stability Analysis of Jointed Rock Slope by Strength Reduction Technique considering Ubiquitous Joint Model

Ruili Lu,<sup>1</sup> Wei Wei ,<sup>2,3</sup> Kaiwei Shang,<sup>4</sup> and Xiangyang Jing<sup>4</sup>

<sup>1</sup>Changjiang Institute of Technology, Wuhan 430212, China

<sup>2</sup>School of Civil Engineering, Wuhan University, Wuhan 430072, China

<sup>3</sup>Rock Mechanics in Hydraulic Structural Engineering, Ministry of Education, Wuhan 430072, China

<sup>4</sup>Chengdu Engineering Corporation Limited, Chengdu 610072, China

Correspondence should be addressed to Wei Wei; [weiwei\\_276@whu.edu.cn](mailto:weiwei_276@whu.edu.cn)

Received 4 August 2020; Revised 22 September 2020; Accepted 5 October 2020; Published 2 November 2020

Academic Editor: Zhi Cheng Tang

Copyright © 2020 Ruili Lu et al. This is an open access article distributed under the Creative Commons Attribution License, which permits unrestricted use, distribution, and reproduction in any medium, provided the original work is properly cited.

In order to study the failure mechanism and assess the stability of the inlet slope of the outlet structure of Lianghekou Hydropower station, the strength reduction method considering the ubiquitous joint model is proposed. Firstly, two-dimension numerical models are built to investigate the influence of the dilation angle of ubiquitous joints, mesh discretization, and solution domain size on the slope stability. It is found that the factor of safety is insensitive to the dilation angle of ubiquitous joints and the solution domain size but sensitive to the mesh discretization when the number of elements less than a certain threshold. Then, a complex three-dimension numerical model is built to assess the stability of the inlet slope of the outlet structure of Lianghekou Hydropower station. During the strength reduction procedure, the progressive failure process and the final failure surface of the slope are obtained. Furthermore, the comparison of factors of safety obtained from strength reduction method and analytical solutions indicates that the effect of vertical side boundaries plays an important role in the stability of jointed rock slope, and the cohesive force is the main contribution to the resistant force of vertical side boundaries.

## 1. Introduction

The stability of jointed rock slopes for mining, hydraulic, and hydroelectric engineering is crucial for the safety of engineering work [1]. To prevent and reduce the occurrence of instability of rock slope, the stability and deformation of rock slopes during and after excavation at different scenarios are analyzed [2–12]. For slope stability analysis, the limit equilibrium method (LEM) is widely used by engineers and researchers. Usually, slope stability was evaluated by LEM in two dimensions [13]. However, the 2D limit equilibrium analyses simplify the problem into plane strain conditions without considering the true three-dimensional characteristics of slope [14]. Therefore, many researchers improved a number of 3D limit equilibrium methods for slope stability analysis based on extensions of corresponding methods [3, 15–21], which are beneficial for stability assessment of slope with complex failure surfaces.

Although researchers made many improvements to the 3D limit equilibrium method, there are still some limitations when analyzing the stability of rock slopes. Firstly, the limit equilibrium method did not take into account the stress and deformation of the rock slope. Secondly, the failure surface of the slope was predefined by engineers. Thirdly, many assumptions on the internal force distributions were used to simplify the governing equations to solve the factor of safety. In addition, the evolution process of the failure surface could not be simulated using LEM.

The strength reduction method (SRM) based on the finite element method or finite difference method can overcome those limitations of LEM in the stability analysis of slope. This method was firstly proposed by Zienkiewicz et al. [22] to analyze the stability of the slope. Recently, many researchers [23–27] improved this method. Cheng et al. [28] compared SRM with LEM and found that generally, the two methods will give a similar factor of safety (FOS).

Tschuchnigg et al. [29] further discussed the influence of plasticity flow rule and mesh discretization on the FOS. The SRM method was also applied to assess the stability of practical rock slope engineering. Using the strength reduction FEM, Jiang et al. [30] analyzed the stability of the left abutment slope of Jinping-I hydropower station during the period of construction and assessed the effect of shear-resistance tunnels. Zhang et al. [31] proposed a method combining fracture mechanics and the SRM to simulate the fracture behavior in a jointed rock slope and assessed the slope stability. Schneider-Muntau et al. [32] introduced a strength reduction method for the barodetic material model and presented the comparison of the results of slope stability calculated using an elastoplastic material model (Mohr-Coulomb) with the results of an analytical analysis according to Bishop are presented. Nevertheless, most of these studies focused on either homogeneous soil or rock slopes with predefined failure surface. As a natural geological material, in actuality, rock mass contains various randomly or non-randomly geological discontinuities of different sizes, persistence, and toughness. Moreover, different from the circular failure surface of homogeneous soil slope, the rock slope is prone to failure along the discontinuities. Generally, the failure surface of the rock slope is constituted with located discontinuities, such as faults, and random discontinuities, such as joints. In this case, the failure surface of rock slope cannot be predefined and part of it should be searched during the process of strength reduction. In this study, the strength reduction finite element analysis considering ubiquitous joint model is adopted to assess the stability of jointed rock slope. Firstly, the strength reduction method considering the ubiquitous joint model are presented. Then, one example of 2D slope containing a set of ubiquitous joints is adopted to investigate the effect of mesh discretization, dilation angle, and domain size on the failure mechanism and the stability of slope. Finally, the proposed strength reduction method is adopted to analyze the failure mechanism and the stability of the inlet slope of outlet structure of Lianghekou Hydropower station.

## 2. Methodology

**2.1. The Ubiquitous Joint Model.** The ubiquitous joint model [33] is a modified Mohr-Coulomb model considering the presence of the orientation of weak planes. The criterion for failure on the weak planes, whose orientation is given, consists of a composite Mohr-Coulomb envelope with tension cutoff. The position of a stress point on the latter envelope is controlled again by a nonassociated flow rule for shear failure and an associated rule for tension failure. The procedure of implementing the ubiquitous joint model is as follows:

Step 1: Calculate the stresses using the Mohr-Coulomb model. The stresses corresponding to the elastic guess for the current step is analyzed firstly for general failure, and relevant plastic corrections are made using the Mohr-Coulomb model. The resulting stress component, labeled as  $\sigma_{ij}^O$  is then examined for failure on the weak plane.

Step 2: The resulting stress  $\sigma_{ij}^O$  is then examined for failure on the weak plane. If the stress violates the composite yield criterion along the weak plane, then the tensor of stress corrections is calculated and added to  $\sigma_{ij}^O$  to yield new stress values, denoted as  $\sigma_{ij}^N$ .

Step 3: If the stress  $\sigma_{ij}^O$  is in the envelope of composite yield criterion along the weak plane, no plastic flow along the weak plane takes place, and the new stress  $\sigma_{ij}^N$  is equal to  $\sigma_{ij}^O$ .

The detailed procedure for implementing the ubiquitous joint model refers to the section of constitutive models in the manual of FLAC software.

**2.2. Strength Reduction Principle.** In the strength reduction method, the factor of safety (FOS) is defined as the ratio between the actual shear strength and the reduced shear strength for the fault, joints, and intact rock when the slope arrives at a critical state. When implementing the strength reduction procedure, the reduced shear strength parameters, cohesive force  $c_r$ , and the friction angle  $\varphi_r$  are obtained by the following:

$$\begin{aligned} c_r &= \frac{c}{\text{SRF}}, \\ \varphi_r &= \tan^{-1}\left(\frac{\tan \varphi}{\text{SRF}}\right), \end{aligned} \quad (1)$$

where SRF is the strength reduction factor (SRF),  $c$  and  $\varphi$  are the actual shear strength parameters. In the strength reduction procedure, the reduced shear strength decreases gradually until the slope arrives at the critical state, and the corresponding SRF is equal to the FOS.

The solution procedure of the SRM considering the ubiquitous joint model is as follows:

Step 1: An initial value of the SRF is selected and the reduced shear strength parameters of faults, joints, and intact rock are calculated by equation (1).

Step2: Implement numerical calculation for the slope using reduction shear strength parameters. If the slope fails, the SRF is regarded as the FOS.

Step3: The SRF increases with an increment gradually. Go back to step 2 until the slope fails.

**2.3. Failure Criterion of the Slope.** There are three widely used failure criteria for assessing the stability of the slope, namely, numerical nonconvergence criterion [24, 34], the criterion of plastic yield zone connection [35–37], and displacement mutation criterion [38, 39], respectively. Regarding the first criterion, the failure state of the slope is determined by the convergence condition. However, for the stability analysis of a complex 3D slope model, the convergence condition is influenced by many factors, such as element type, yield condition, constitution model, and convergence precision, which may terminate the computation early [40]. The second criterion states that when the plastic yield zones coalesce from the foot to the top of the slope during strength

reduction, the slope will be in a failure state. For the third criterion, the displacement of some monitoring points on the slope surface is firstly recorded during the strength reduction procedure. The inflection point of the curves of displacement versus the SRF is considered as a failure state of slope and the corresponding SRF is equal to the FOS. Compared with the abovementioned criteria, the displacement mutation criterion is selected in the following analyses because of its clear physical concept and numerical tractability.

### 3. Verification and Analysis of Influencing Factor

**3.1. Problem Description and Mesh.** A rock slope with a slope angle of  $45^\circ$  is selected a case study, as shown in Figure 1. In the slope, ubiquitous joints with a dip angle  $\beta = 30^\circ$  are taken into account. The slope dimensions are shown in Figure 1. The mechanical parameters for rock and the joint materials are shown in Table 1. It is noted that the ubiquitous joints drew in Figure 1 are schematic. Hence, the spacing between lines does not represent the actual spacing of joints. The mesh discretization for this slope is shown in Figure 2, which contain 1875 zones and 1976 grid points.

**3.2. Influence of Dilation Angle of Joints.** The definition of the dilation angle of joints is an important issue when using the strength reduction technique considering ubiquitous joints. To study this issue, five different dilation angles are adopted to investigate the effect of flow rule, namely,  $0^\circ$ ,  $5^\circ$ ,  $10^\circ$ ,  $15^\circ$ , and  $20^\circ$ . The horizontal displacement of a monitoring point at the crest of the slope, shown in Figure 2, is recorded during the strength reduction procedure. Figure 3 shows the curves of horizontal displacement of the monitor point versus the strength reduction factor (SRF) for the cases with different nonassociated flow rules. One can observe that the horizontal displacement increases with the increase of the SRF. Moreover, the curves obtained by five dilation angles are approximately the same when the SRF is no more than 1.26 but separated from each other when the SRF is larger than 1.26. According to the displacement mutation criterion, the FOS of those five dilation angles is the same and is equal to 1.26. The results indicate that the FOS is insensitive to the dilation angle of the joints.

Figure 4 illustrates the evolution of incremental shear strains during the SRM when the dilation is equal to  $20^\circ$ . Since the shear strain rate around the failure surface is much larger than other regions of the slope, in the following analysis, the center of the zone of incremental shear strain can be defined as the failure surface of the slope. It can be seen from Figure 4 that the failure surface firstly occurs at the toe of the slope. With the increase of the SRF, the failure surface propagated toward the crest of the slope gradually and passed through the whole slope when the SRF arrived at 1.26, as shown in Figure 4(c).

**3.3. Influence of Mesh Discretization.** It is well known that the element type, the mesh discretization, and the

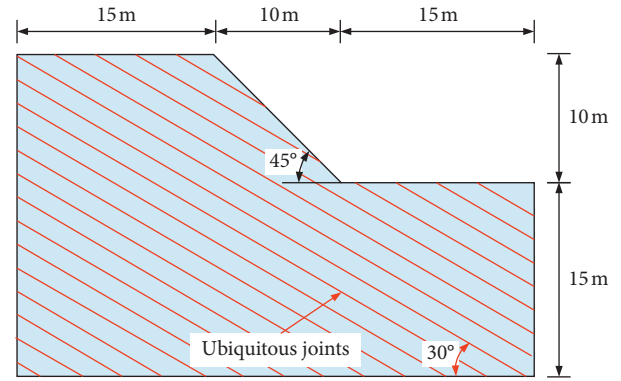


FIGURE 1: The schematic of the 2D slope and its dimension.

TABLE 1: Geotechnical parameters of the numerical model.

Type	Parameter	Value
Rock	Unit weight, $\gamma$ (kN/m <sup>3</sup> )	26
	Elastic modulus, $E$ (GPa)	10
	Poisson's ratio, $\nu$	0.25
	Cohesion, $c_r$ (kPa)	2000
	Friction angle, $\varphi_r$ ( $^\circ$ )	45
Joint	Cohesion, $c_j$ (kPa)	6.7
	Friction angle, $\varphi_j$ ( $^\circ$ )	28

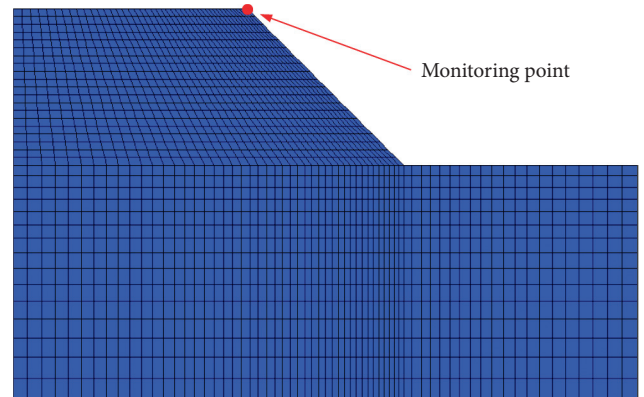


FIGURE 2: The mesh discretization and the layout of the monitoring point of the 2D slope.

convergence tolerations have a significant impact on the FOS. In order to study the mesh dependency, the same model as shown in Figure 1 is used, but nine types of mesh discretization from coarse to very fine are defined. Their number of elements are 169, 300, 469, 675, 919, 1200, 1519, 1875, 2700, and 4219, respectively. From a practical point of view, the coarse and very fine mesh are not realistic, but these two extreme cases are included to show the effect of the mesh influence.

Figure 5 compares the curves of the FOS versus the horizontal displacement of the monitoring point for the cases with different mesh discretization. It is observed that the horizontal displacement increases with the increase of the SRF. Moreover, the curves obtained by different mesh discretization are approximately the same when SRF is no

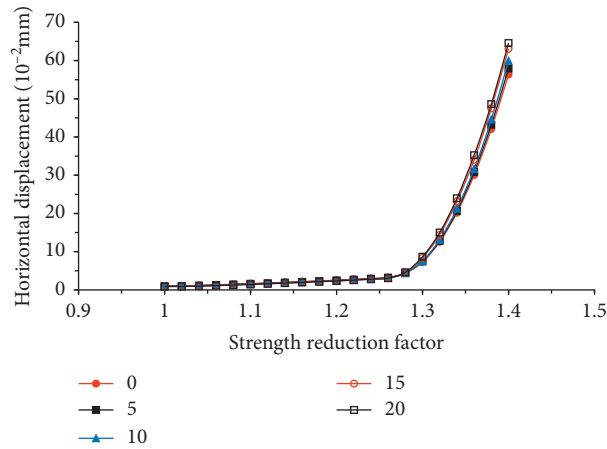


FIGURE 3: The curves of horizontal displacement versus the SRF with different dilation angles.

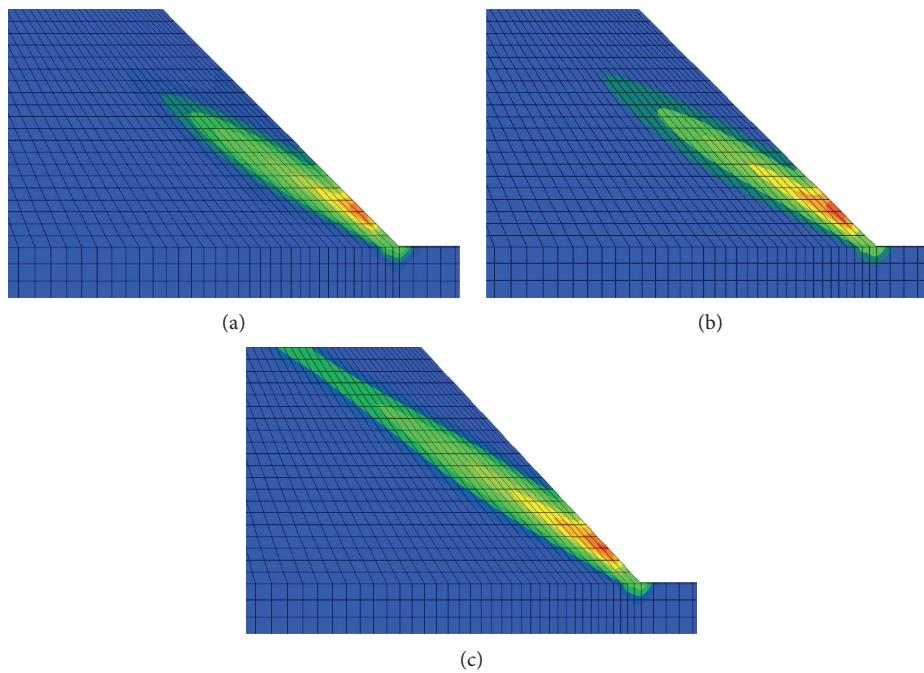


FIGURE 4: Varying failure mechanism during a SRM with dilation  $\psi = 20^\circ$ , (a) SRF = 1.10, (b) SRF = 1.20, (c) SRF = 1.26.

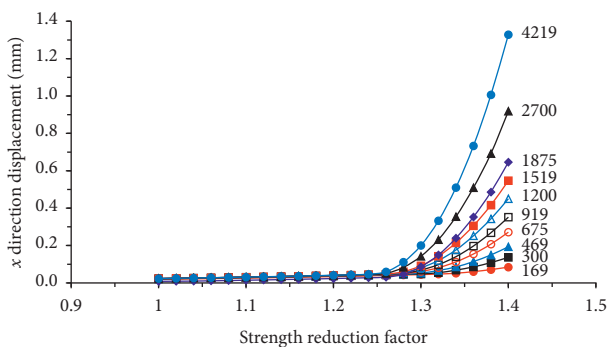


FIGURE 5: The curves of horizontal displacement versus the SRF with different element numbers.

more than 1.24 but separated from each other when SRF is larger than 1.24. In order to investigate the effect of mesh discretization on the factors of safety, the curve of the FOS versus the number of elements is illustrated in Figure 6. It is seen from Figure 6 that the mesh discretization has a significant impact on the FOS. With the increase of the number of elements, the FOS decreases until the number of elements is equal to 2800, which indicates that the FOS is insensitive to the mesh discretization when the number of elements is over a certain threshold.

Figure 7 shows the contour of incremental shear strains obtained from three types of mesh discretization. It is found that the mesh discretization has a significant influence on the distribution of incremental shear strains. For a very coarse

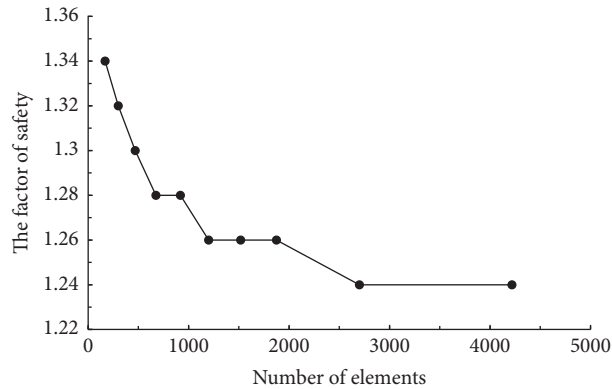


FIGURE 6: Factor of safety obtained by SRM with different element numbers.

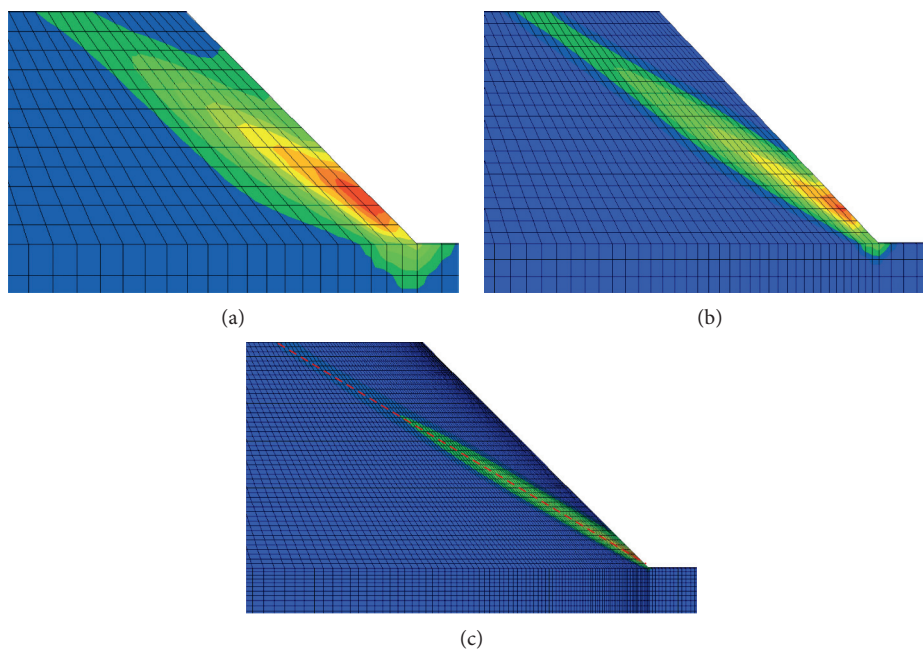


FIGURE 7: Incremental shear strains for different mesh discretization, (a)  $n = 675$ , (b)  $n = 1875$ , (c)  $n = 4219$ .

mesh, shown in Figure 7(a), the zone of incremental shear strains is wider and the failure surface does not pass through the toe of the slope. However, for a very fine mesh, shown in Figure 7(c), the zone of increment shear strain is narrow and the failure surface is clearly defined.

It also can be observed from Figure 7(c) that the central plane of the zone of incremental shear strains, namely, the failure surface, is a plane. It means that the failure mode of the slope is the plane failure mode that is somehow different from that of a homogeneous slope in which the failure surface is a circle failure mode. Therefore, there is an analytical solution to this 2D ubiquitous joints rock slope and the FOS is 1.20. As discussed above, when the mesh discretization is fine enough, the FOS obtain from SRM is 1.24, which is close to the analytical solution. Therefore, it is reasonable to assess the ubiquitous jointed rock slope using the proposed method.

**3.4. Influence of Domain Size.** In order to assess the size effect of the calculation domain in the strength reduction method, a length factor  $d$ , which quantifies the distance from initial boundaries to extended boundaries of the slope, is introduced and shown in Figure 8. In this study, six different cases of  $d$  are considered, namely 5 m, 15 m, 25 m, 35 m, 45 m, and 55 m. In the strength reduction procedure, the mesh discretization of the initial region of the slope is the same as that in Figure 2. Figure 9 illustrated the displacement of the monitoring point evolving with the SRF. It is clear that the curves obtained by six cases are nearly the same when the SRF is no more than 1.26 but separated from each other when SRF is larger than 1.26. According to the displacement mutation criterion, the FOS of those six cases is the same and the value is 1.26. It also indicates that the FOS is insensitive to the calculation domain size.



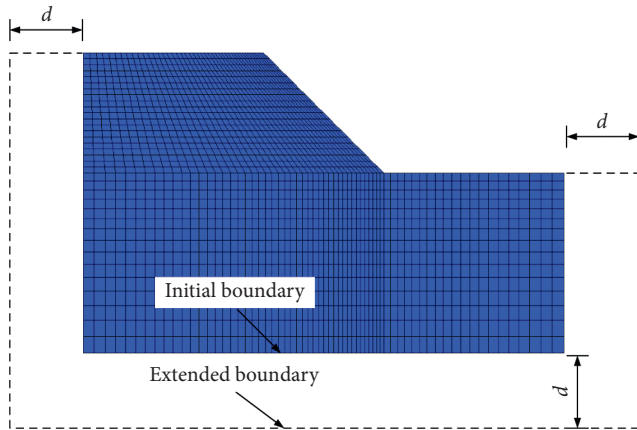


FIGURE 8: The schematic of extended boundaries.

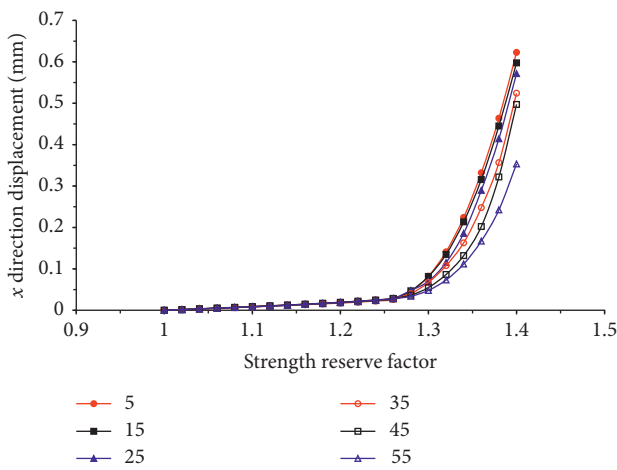


FIGURE 9: The curves of horizontal displacement versus the SRF with different domain sizes.

## 4. Engineering Application

**4.1. Project Description.** The Lianghekou Hydropower station is located on the middle reach of Yalongjiang River, 10 kilometers northern of Yajiang, Sichuan province, China. In this project, a 295 m height gravelly clay-cored rockfill dam is constructed to form a reservoir. In order to fulfill the flood discharging capability of the reservoir, four outlet structures are built, including a tunnel-spillway, deep hole flood discharging tunnel, emptying tunnel, and rotation-flow shaft flood discharging tunnel. The inlet slopes of these four outlet structures are excavated as a whole, which results in a massive engineering slope with 606 m height and 1200 m length, as shown in Figure 10. A typical geological profile 8–8 of the slope is shown in Figure 11. The rock of the slope is composed of deep grey and medium-thick layer metamorphism siltstone, silty slate, and sericite slate. This slope is a typical antidip layered slope and the orientation of the bedding plane is  $200^{\circ} \sim 210^{\circ} \angle 65^{\circ} \sim -75^{\circ}$  (dip direction/dip angle). Besides the bedding plane, the other three sets of joints are developed in the slope and their orientation is  $130^{\circ} \sim 150^{\circ} \angle 10^{\circ} \sim 45^{\circ}$  (J3),  $90^{\circ} \sim 120^{\circ} \angle 70^{\circ} \sim 90^{\circ}$  (J4),  $90^{\circ} \sim 120^{\circ} \angle 10^{\circ} \sim 30^{\circ}$  (J6), respectively. These joints are rigid structural plane

without filling. In addition, as shown in the geological profile 8–8, a large number of faults are developed. Most of these faults are compressive faults which developed along the bedding plane, including f1, f2, f3, f4. Below the 3050 m platform, two main faults are detected, namely, Fault f1 and Fault f13-04. As shown in Figures 10 and 11, the F1, with the occurrence  $180^{\circ} \angle 40^{\circ} \sim 60^{\circ}$ , runs through the entire engineering slope and outcrops above the inlet of the shaft flood discharging tunnel. The f13-04, with the orientation  $10^{\circ} \angle 30^{\circ}$ , outcrops at the step between elevation 2790 m and elevation 2815 m. According to the spatial distribution of faults, a huge potential failure region sliding along the fault f13–04 is observed, where the fault f1 form the back boundary and the fourth set of joints (J4) developed ubiquitously form the two vertical side boundaries of the block. After the completion of the excavation, fault fb13–04 will be exposed on the excavated surface, which will deteriorate the stability of the slope drastically.

**4.2. Description of Numerical Model and Material Property.** Different from the displacement finite element analysis, the strength reduction method focuses on assessing the failure mechanism and the stability of slope rather than obtaining the distribution of displacement and stresses in the slope. Therefore, the potential failure region is the region of great concern during the strength reduction procedure. In order to simplify the numerical model, the terrain in the potential failure region shown in Figure 10 is consistent with the real terrain in the project site, while the terrain around the potential failure region is simplified. The three-dimension numerical model for strength reduction procedure is shown in Figure 12. In this model, the lowest left corner is used as the origin of the  $x$ - $y$  plane, and the  $z$ -axis begins at an elevation of 2540 m. The size of the slope model is 840 m length in the  $x$  direction, 1000 m width in the  $y$ -direction, and 700 m height in the  $z$  direction. The numerical model is made up of 174944 gridpoints and 214823 zones. The two main faults (f1 and f13–04) and the fourth set of joints (J4) are considered in this model. The grid of potential failure region is shown in Figure 12. The mechanical parameters from the recommended values of the designer [41] are listed in Table 2.

**4.3. Results.** For the potential failure domain, the key block is composed of fault f1, fault f13–04, and the fourth set of joints (J4). It is noted that the fourth set of joints is ubiquitous in the slope and their locations are undetermined. The proposed SRM method is used to search for the locations of J4 forming the key block and determine the factor of safety of the key block. Two monitoring points M1 and M2, shown in Figure 12, are selected to record the displacement for different strength reduction factors. The curves of  $y$ -direction displacement of monitor points versus the strength reduction factor are illustrated in Figure 13. It can be seen that the  $y$ -direction displacement of three monitoring points is roughly proportional to the SRF. However, when the SRF increases to 1.36, the displacement curves of M1 and M2 start to deviate from the linear relationship between

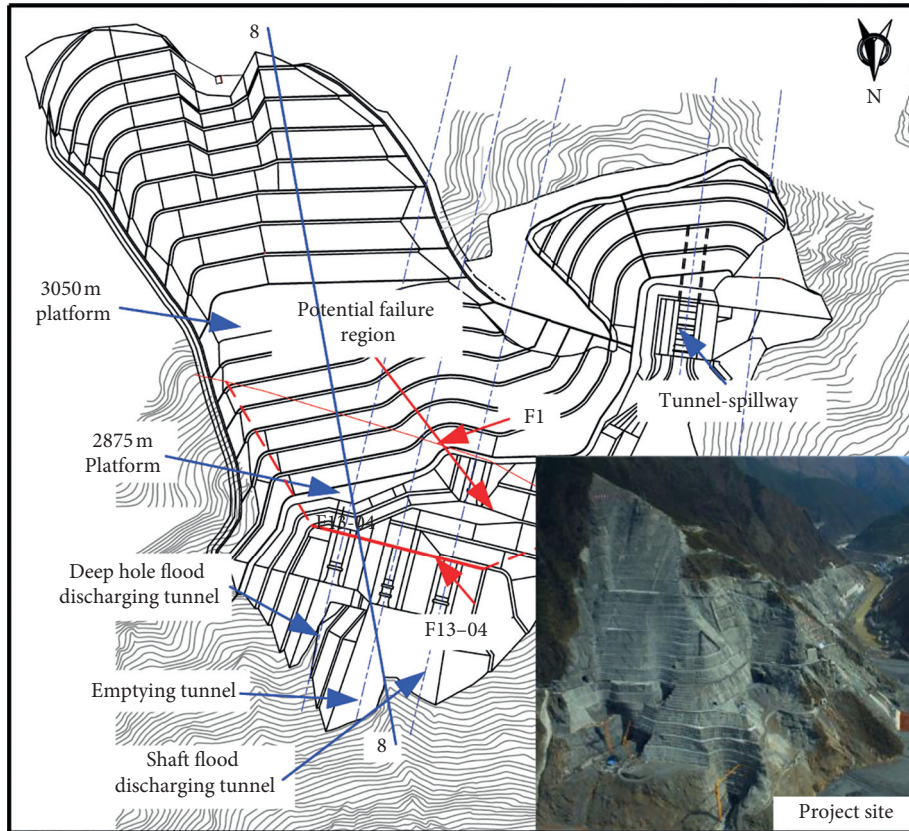


FIGURE 10: The layout of the inlet slope of outlet structures.

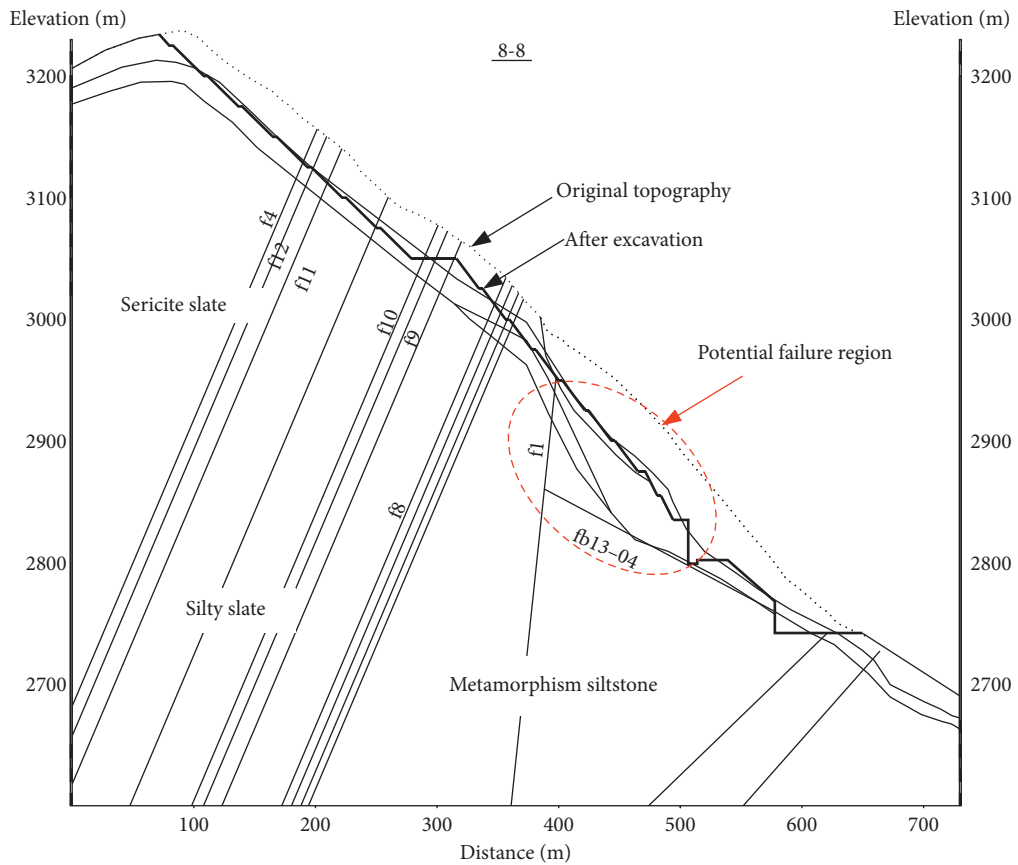


FIGURE 11: Typical section to show the potential failure block.

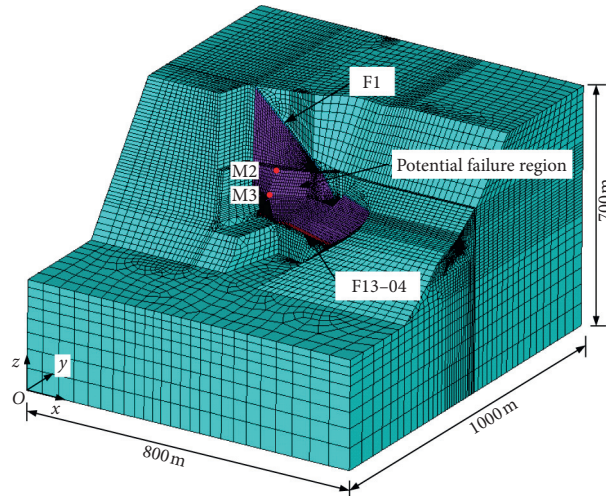
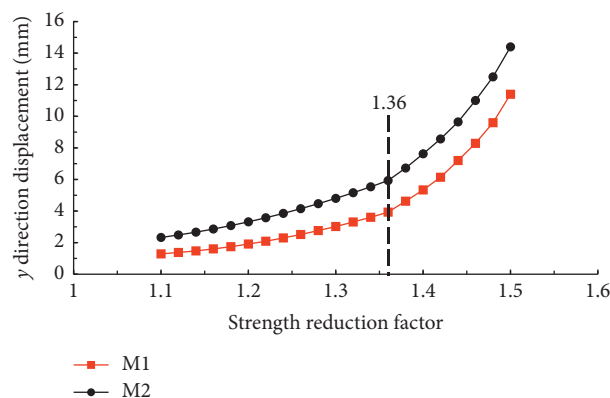


FIGURE 12: The 3D numerical model of the slope.

TABLE 2: Geotechnical parameters for strength reduction procedure.

Type	Deformation modulus $E$ (GPa)	Unit weight $\gamma$ (kN/m <sup>3</sup> )	Poisson's ratio $V$	Cohesion $c_r$ (kPa)	Friction angle $\varphi_r$ (°)
Metamorphism siltstone in heavily unloading zone	1.8	26.0	0.37	113	26.6
Metamorphism siltstone in slightly unloading zone	4.5	26.5	0.32	600	36.9
Thick layered metamorphism siltstone	8.0	26.8	0.27	1250	47.5
f1	0.45	25	0.32	25	12.7
f13-04	0.45	25	0.32	113	23.2
The fourth set of joints	—	—	—	125	27.7

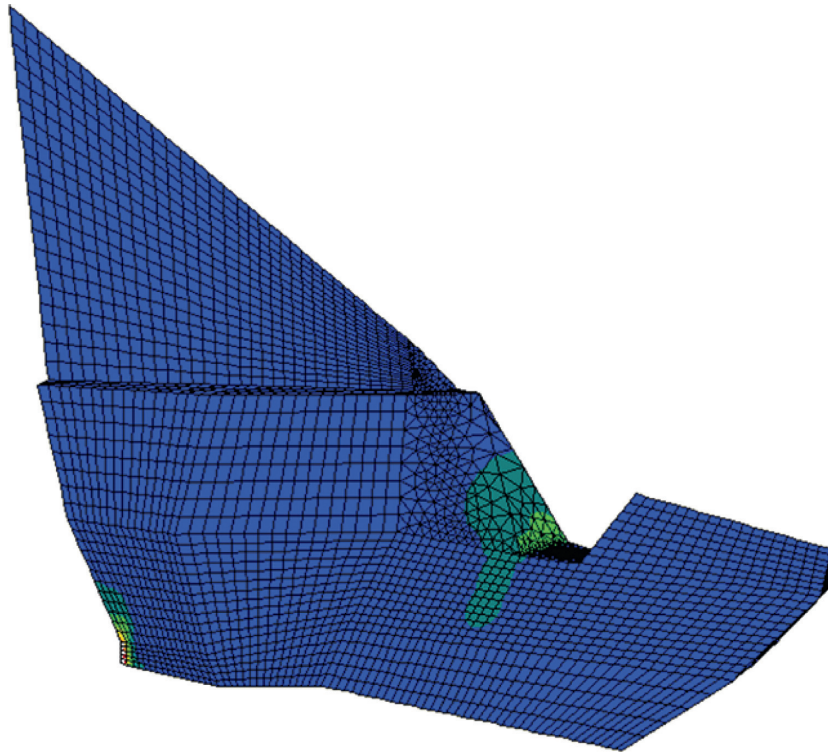
“—” denote that the joint does not possess the property.

FIGURE 13:  $y$ -direction displacement versus the SRF.

displacements and SRF. Therefore,  $\text{SRF} = 1.36$  can be considered as a catastrophic failure point and the FOS of the slope.

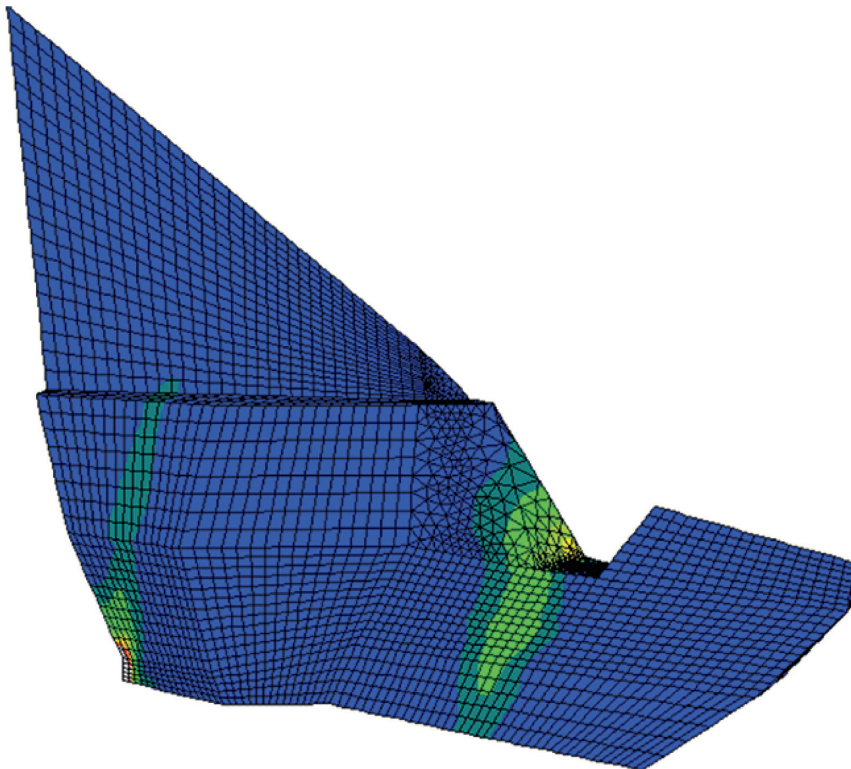
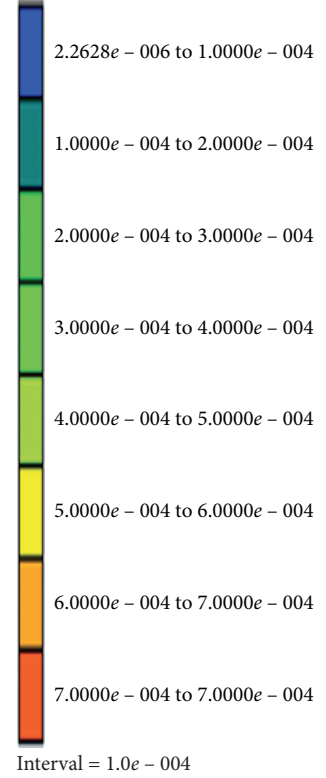
The progressive failure process is investigated during the procedures of reducing the shear strength of the fourth set joints, Fault f13-04, and Fault f1. Figure 14 shows the

evolution of the zone of incremental shear strain in the block at different SRF stages. Figure 15 illustrates the evolution of the plastic yield zone in the block during the process of strength reduction. In Figure 15, the yield state “None” refers to the elastic state of the zone and the “u: shear-n” indicates that the zone is in shear failure along the joints currently. As



(a)

Contour of shear strain increment  
Magfac = 0.000e + 000  
Gradient calculation



(b)

Contour of shear strain increment  
Magfac = 0.000e + 000  
Gradient calculation

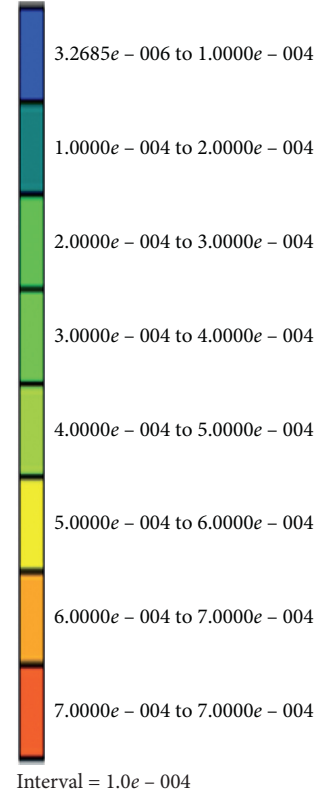


FIGURE 14: Continued.

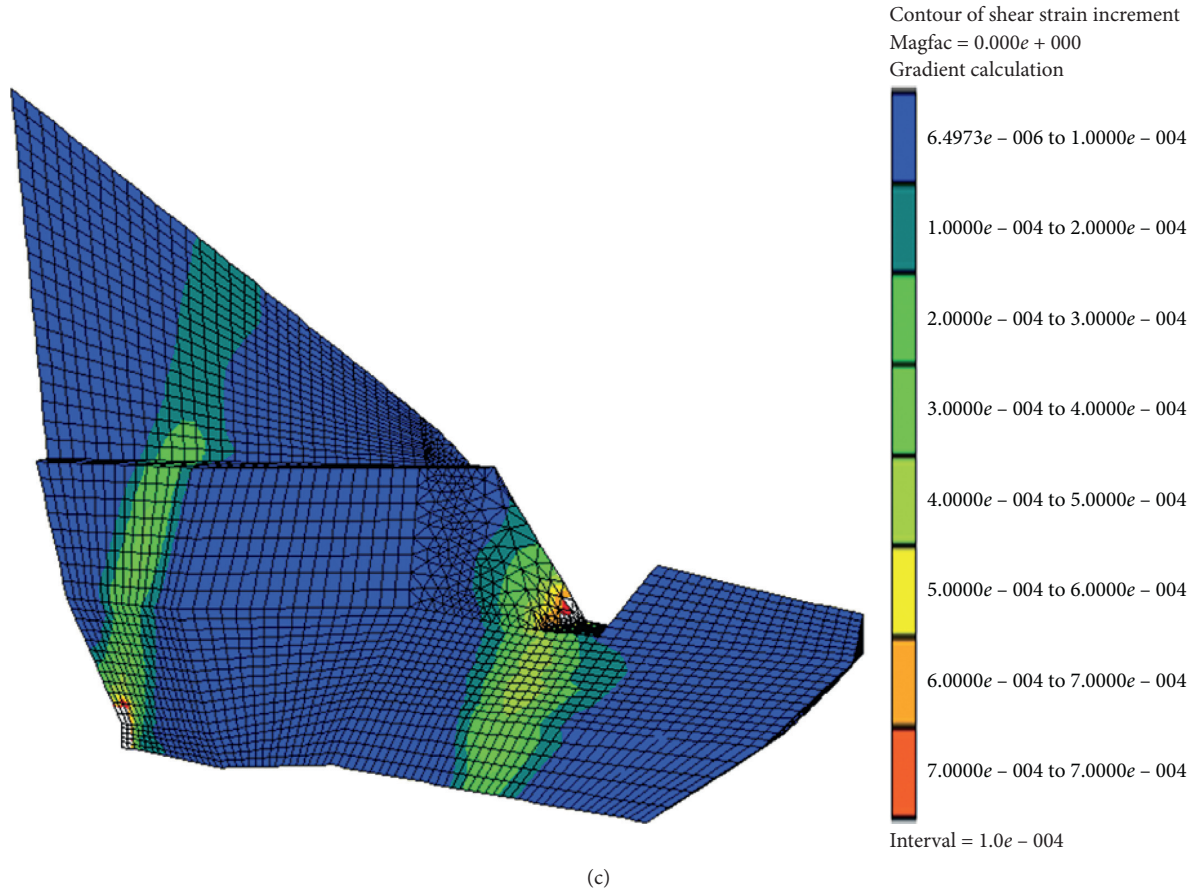


FIGURE 14: Evolution of incremental shear strain of the potential failure region with the SRF, (a) SRF = 1.10, (b) SRF = 1.26, (c) SRF = 1.36.

we can see from Figures 14 and 15, for the case that SRF is equal to 1.1, the zone of incremental shear strain and the plastic zone initiate at the left side of the outcrop of Fault f13-04 and the middle of the inlet of rotation-flow shaft flood discharging tunnel. As the SFR increases, the zone of incremental shear strain propagates along the strike of the fourth set of joints. When the SRF increases to 1.26, the plastic zone and the zone of incremental shear strain propagate through the inlet of the rotation-flow shaft flood discharging tunnel. When the SRF increases to 1.36, the plastic zone propagates through the whole potential failure region and becomes the vertical side boundaries of a new failure block.

As a comparison, the solution obtained by the LEM is also proposed. According to the failure surface obtained by the SRM, the vertical side boundaries and sliding surface of the failure block is illustrated in Figure 16. The areas of sliding surface, left side boundary, and right side boundary are  $A_s = 10,389 \text{ m}^2$ ,  $A_l = 4909 \text{ m}^2$ , and  $A_r = 605 \text{ m}^2$ , respectively. The volume of the failure block is  $V = 32,500 \text{ m}^3$ . If the

resistant force of two vertical side boundaries is ignored, the FOS can be determined as follows:

$$\text{FOS} = \frac{f_r}{f_s}, \quad (2)$$

$$\begin{aligned} f_r &= A_s c_s + \gamma V \cos(\theta) \tan(\varphi), \\ f_s &= \gamma V \sin(\theta), \end{aligned} \quad (3)$$

where  $\theta$  is the dip angle of bottom sliding surface,  $c_s$ ,  $\varphi$  is cohesion and friction angle of bottom sliding force,  $\gamma$  is the unit weight of the potential failure block. The FOS obtained by equation (2) is 1.10, which is far less than the FOS obtained SRM. Obviously, the difference between the two safety factors is attributed to the effect of the two vertical side boundaries. This indicates that the two vertical side boundaries have a significant impact on the stability of the jointed rock slope, and ignoring the effect of the vertical side boundaries will lead to underestimation of the stability of the slope.

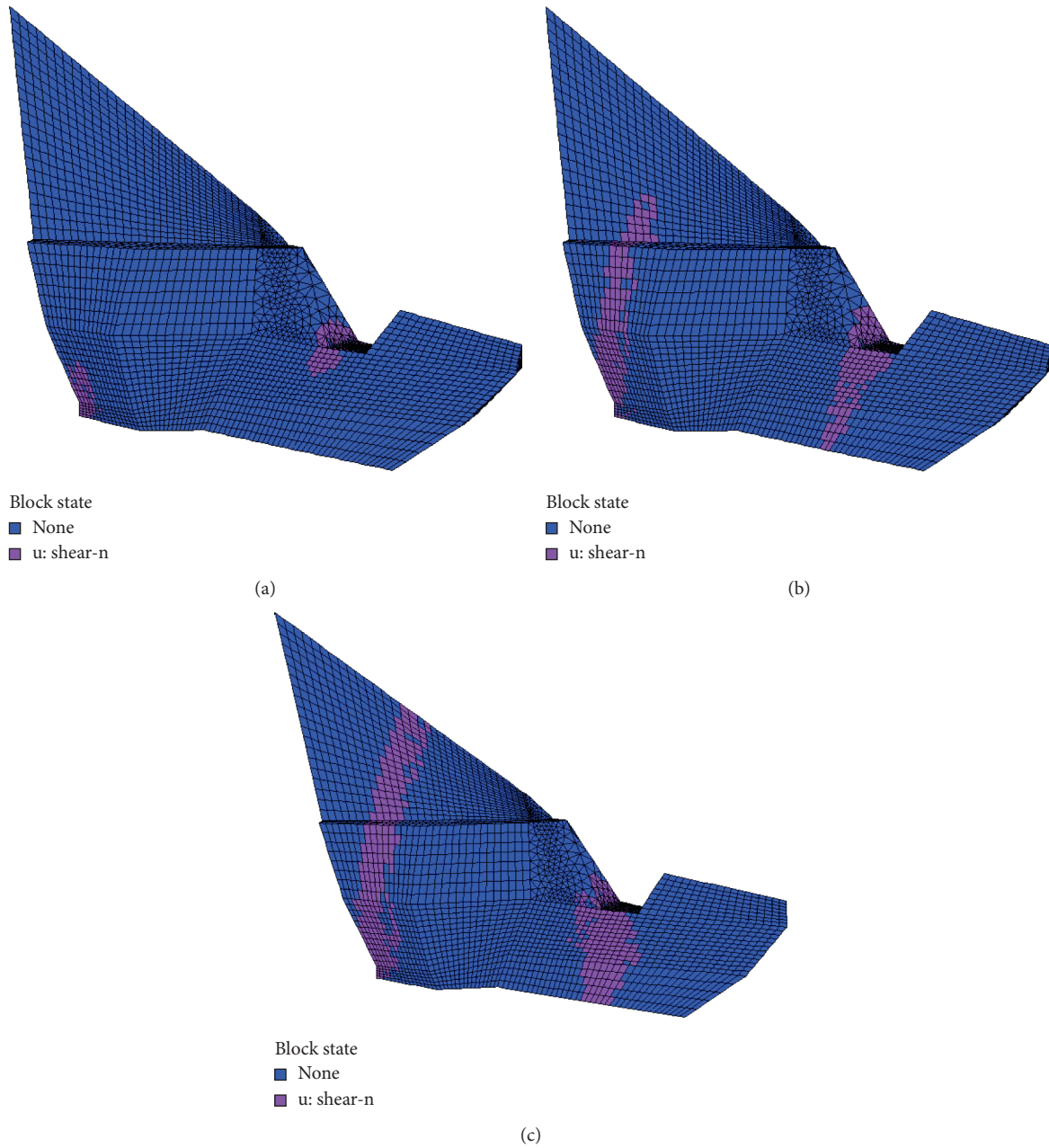


FIGURE 15: Evolution of the plastic zone of the potential failure region with the SRF, (a) SRF = 1.10, (b) SRF = 1.26, (c) SRF = 1.36.

The resistant force of the vertical side boundaries consists of two parts, namely, the cohesive force and the frictional force acting on the vertical side boundaries. For the limit equilibrium method, it is impossible to obtain the magnitude and distribution of the normal force of the vertical side boundaries. Therefore, the FOS is calculated only considering the effect of the cohesive force of vertical side boundaries. Assuming that the direction of the cohesive force of the vertical side boundaries is along the sliding direction of the potential failure block, the resistant force  $f_r$  can be modified as follows:

$$f_r = A_s c_s + A_l c_j + A_r c_j + \gamma V \cos(\theta) \tan(\varphi), \quad (4)$$

where  $c_j$  is the cohesion of the fourth set of joints. The FOS considering the cohesion force of the vertical boundaries is 1.27, which is 0.17 more than the FOS obtained in the case that the effect of vertical side boundaries is ignored and 0.09 less than the FOS obtained from the SRM. This result indicates that the cohesive force is the main contribution to the resistant force of the vertical side boundaries, while the frictional force has a slight influence on the stability of the slope.

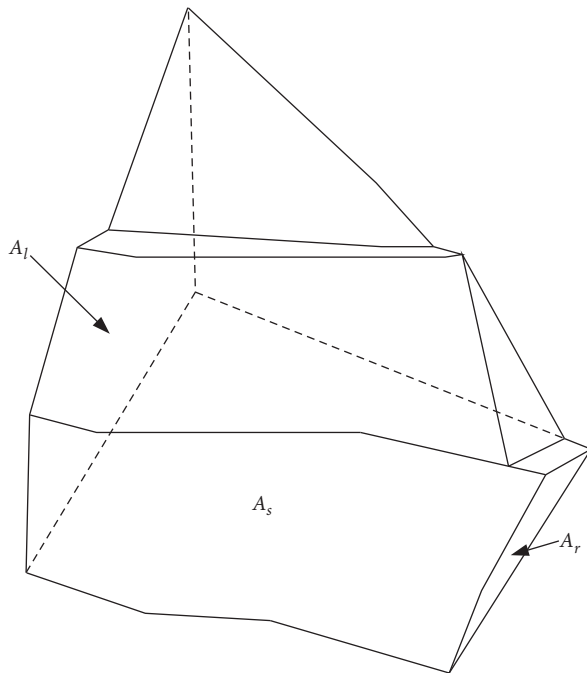


FIGURE 16: The schematic of the failure block for LEM analysis.

## 5. Conclusions

The purpose of this paper is to provide a methodology to analyze the stability of the jointed rock slope by strength reduction method considering the ubiquitous joint model. In order to verify the proposed method, several two-dimension models are built to investigate the effect of the dilation angle of joints, mesh discretization, and boundary size of the numerical model on the stability of the jointed rock slope. The numerical results show that the factor of safety is insensitive to the dilation angle of the joints and the boundary size of the numerical model. For the influence of mesh discretization size, the width of the zone of incremental shear strain and the factor of safety are sensitive to the size of the element. When the number of elements increases to a certain threshold, the factor of safety will not be affected by the mesh discretization.

The stability of the inlet slope of the outlet structure of Lianghekou Hydropower station has been investigated using the proposed method. The stability of this slope is controlled by the huge potential failure region formed by fault f13–04, fault f1, and the fourth set of joints (J4). The final failure block is searched during the strength reduction procedure and the factor of safety is 1.36. In order to investigate the effect of vertical side boundaries, the factor of safety of the final failure block is calculated by the LEM in two different cases. The results show that the effect of the vertical side boundaries plays an important role in the stability of the jointed rock slope and the cohesive force is the dominant contribution to the resistant force of vertical side boundaries.

## Data Availability

The data used to support the findings of this study are included within the article.

## Conflicts of Interest

The authors declare that they have no conflicts of interest.

## Acknowledgments

The work reported in this paper has received financial support from National Key R&D Program of China (nos. 2019YFC0605001 and 2018YFC1505005), the National Natural Science Foundation of China (no. 42077253) and the Guiding Project of Scientific Research Plan of Hubei Science and Technology Department (No. B2020408). These supports are gratefully acknowledged.

## References

- [1] T. Chen, J. Deng, N. Sitar et al., "Stability investigation and stabilization of a heavily fractured and loosened rock slope during construction of a strategic hydropower station in China," *Engineering Geology*, vol. 221, pp. 70–81, 2017.
- [2] N. Chen, J. Kemeny, Q. Jiang, and Z. Pan, "Automatic extraction of blocks from 3D point clouds of fractured rock," *Computers & Geosciences*, vol. 109, pp. 149–161, 2017.
- [3] Q. Jiang, Y. Sun, B. Yi, T. Li, and F. Xiong, "Inverse analysis for geomaterial parameter identification using Pareto multiobjective optimization," *International Journal for Numerical and Analytical Methods in Geomechanics*, vol. 42, no. 14, pp. 1698–1718, 2018.
- [4] J. Yang, J. Cai, C. Yao, P. Li, Q. Jiang, and C. Zhou, "Comparative study of tunnel blast-induced vibration on tunnel surfaces and inside surrounding rock," *Rock Mechanics and Rock Engineering*, vol. 52, no. 11, pp. 4747–4761, 2019.
- [5] W. Wei, Q. Zhao, Q. Jiang, and G. Grasselli, "Three new boundary conditions for the seismic response analysis of geomechanics problems using the numerical manifold method," *International Journal of Rock Mechanics and Mining Sciences*, vol. 105, pp. 110–122, 2018.
- [6] W. Wei, Q. Zhao, Q. Jiang, and G. Grasselli, "A new contact formulation for large frictional sliding and its implement in the explicit numerical manifold method," *Rock Mechanics and Rock Engineering*, vol. 53, no. 1, pp. 435–451, 2020.
- [7] B. Wang, C. Yao, J. Yang et al., "Numerical simulation of macro-meso mechanical behaviours of sandstone containing a single open fissure under uniaxial compression," *European Journal of Environmental and Civil Engineering*, vol. 22, no. 1, pp. s99–s113, 2018.
- [8] Y. Sun, J. Huang, W. Jin, S. W. Sloan, and Q. Jiang, "Bayesian updating for progressive excavation of high rock slopes using multi-type monitoring data," *Engineering Geology*, vol. 252, pp. 1–13, 2019.
- [9] Z. C. Tang, "Experimental investigation on temperature-dependent shear behaviors of granite discontinuity," *Rock Mechanics and Rock Engineering*, vol. 53, no. 9, pp. 4043–4060, 2020.
- [10] Z. C. Tang and Y. Y. Jiao, "Choosing appropriate appraisal to describe peak spatial features of rock joint profiles," *International Journal of Geomechanics*, vol. 20, no. 4, Article ID 04020021, 2020.
- [11] Z. C. Tang, Q. Z. Zhang, and J. Peng, "Effect of thermal treatment on the basic friction angle of rock joint," *Rock Mechanics and Rock Engineering*, vol. 53, no. 4, pp. 1973–1990, 2020.
- [12] J. Zou, Y.-Y. Jiao, Z. Tang, Y. Ji, C. Yan, and J. Wang, "Effect of mechanical heterogeneity on hydraulic fracture propagation

- in unconventional gas reservoirs,” *Computers and Geotechnics*, vol. 125, Article ID 103652, 2020.
- [13] G. Sun, H. Zheng, and W. Jiang, “A global procedure for evaluating stability of three-dimensional slopes,” *Natural Hazards*, vol. 61, no. 3, pp. 1083–1098, 2012.
- [14] Q. Jiang and C. Zhou, “A rigorous method for three-dimensional asymmetrical slope stability analysis,” *Canadian Geotechnical Journal*, vol. 55, no. 4, pp. 495–513, 2018.
- [15] R. H. Chen and J. L. Chameau, “Three-dimensional limit equilibrium analysis of slopes,” *Géotechnique*, vol. 33, no. 1, pp. 31–40, 1982.
- [16] L. Lam and D. G. Fredlund, “A general limit equilibrium model for three-dimensional slope stability analysis,” *Canadian Geotechnical Journal*, vol. 30, no. 6, pp. 905–919, 1993.
- [17] Z. Chen, X. Wang, C. J.-H. Haberfield, and Y. Wang, “A three-dimensional slope stability analysis method using the upper bound theorem,” *International Journal of Rock Mechanics and Mining Sciences*, vol. 38, no. 3, pp. 369–378, 2001.
- [18] H. Yin, “A three-dimensional rigorous method for stability analysis of landslides,” *Engineering Geology*, vol. 145–146, pp. 30–40, 2012.
- [19] X. P. Zhou and H. Cheng, “Analysis of stability of three-dimensional slopes using the rigorous limit equilibrium method,” *Engineering Geology*, vol. 160, pp. 21–33, 2013.
- [20] Q. Jiang, W. Wei, N. Xie, and C. Zhou, “Stability analysis and treatment of a reservoir landslide under impounding conditions: a case study,” *Environmental Earth Sciences*, vol. 75, no. 1, pp. 1–12, 2016.
- [21] Q. Jiang and C. Zhou, “A rigorous solution for the stability of polyhedral rock blocks,” *Computers and Geotechnics*, vol. 90, pp. 190–201, 2017.
- [22] O. C. Zienkiewicz, C. Humpheson, and R. W. Lewis, “Associated and nonassociated visco-plasticity and plasticity in soil mechanics,” *Géotechnique*, vol. 25, no. 4, pp. 671–689, 1975.
- [23] T. Matsui and K.-C. San, “Finite element slope stability analysis by shear strength reduction technique,” *Soils and Foundations*, vol. 32, no. 1, pp. 59–70, 1992.
- [24] D. V. Griffiths and P. A. Lane, “Slope stability analysis by finite elements,” *Géotechnique*, vol. 49, no. 3, pp. 387–403, 1999.
- [25] E. M. Dawson, W. H. Roth, and A. Drescher, “Slope stability analysis by strength reduction,” *Géotechnique*, vol. 49, no. 6, pp. 835–840, 1999.
- [26] H. Zheng, D. F. Liu, and C. G. Li, “Slope stability analysis based on elasto-plastic finite element method,” *International Journal for Numerical Methods in Engineering*, vol. 64, no. 14, pp. 1871–1888, 2005.
- [27] D. V. Griffiths and R. M. Marquez, “Three-dimensional slope stability analysis by elasto-plastic finite elements,” *Géotechnique*, vol. 57, no. 6, pp. 537–546, 2007.
- [28] Y. M. Cheng, T. Lansivaara, and W. B. Wei, “Two-dimensional slope stability analysis by limit equilibrium and strength reduction methods,” *Computers and Geotechnics*, vol. 34, no. 3, pp. 137–150, 2007.
- [29] F. Tschuchnigg, H. F. Schweiger, and S. W. Sloan, “Slope stability analysis by means of finite element limit analysis and finite element strength reduction techniques. Part I: numerical studies considering nonassociated plasticity,” *Computers and Geotechnics*, vol. 70, pp. 169–177, 2015.
- [30] Q. Jiang, Z. Qi, W. Wei, and C. Zhou, “Stability assessment of a high rock slope by strength reduction finite element method,” *Bulletin of Engineering Geology and the Environment*, vol. 74, no. 4, pp. 1153–1162, 2015.
- [31] K. Zhang, P. Cao, J. Meng, K. Li, and W. Fan, “Modeling the progressive failure of jointed rock slope using fracture mechanics and the strength reduction method,” *Rock Mechanics and Rock Engineering*, vol. 48, no. 2, pp. 771–785, 2015.
- [32] B. Schneider-Muntau, W. G. Medicus, and W. Fellin, “Strength reduction method in Barodesy,” *Computers and Geotechnics*, vol. 95, pp. 57–67, 2018.
- [33] Itasca Consulting Group Inc, *FLAC3D: Fast Lagrangian Analysis of Continua in 3 Dimensions, User Manual (Version 3.0)*, Itasca Consulting Group Inc., Minneapolis, MN, USA, 2005.
- [34] K. Ugai, “A method of calculation of total safety factor of slope by elasto-plastic FEM,” *Soils and Foundations*, vol. 29, no. 2, pp. 190–195, 1989.
- [35] M. T. Luan, Y. J. Wu, and T. K. Nian, “A criterion for evaluating slope stability based on development of plastic zone by shear strength reduction FEM,” *Journal of Disaster Prevention and Mitigation Engineering*, vol. 23, no. 3, pp. 1–8, 2003.
- [36] J. H. Deng, J. B. Wei, and H. Min, “3D stability analysis of landslides based on strength reduction (I): back analysis for the shear strength of sliding soils,” *Rock Soil Mechanics*, vol. 6, pp. 896–900, 2004.
- [37] H. Zheng, D. F. Liu, and C. G. Li, “On the assessment of failure in slope stability analysis by the finite element method,” *Rock Mechanics and Rock Engineering*, vol. 41, no. 4, pp. 629–639, 2008.
- [38] S. Y. Zhao, Y. R. Zheng, and W. Z. Deng, “Stability analysis on jointed rock slope by strength reduction FEM,” *Chinese Journal of Rock Mechanics and Engineering*, vol. 22, no. 2, pp. 254–260, 2003.
- [39] Y. R. Zheng, S. Y. Zhao, and C. J. Deng, “Development of finite element limit analysis method and its applications in geotechnical engineering,” *China Engineering Science*, vol. 8, no. 12, pp. 39–61, 2006.
- [40] K. Zhang, P. Cao, and R. Bao, “Progressive failure analysis of slope with strain-softening behaviour based on strength reduction method,” *Journal of Zhejiang University Science A*, vol. 14, no. 2, pp. 101–109, 2013.
- [41] Institute of Chengdu Investigation and Design of National Electrical Power, *Report of Selecting Dam Site for Lianghekou Hydropower Station: Engineering Geological Condition*, Institute of Chengdu Investigation and Design of National Electrical Power, Chengdu, China, 2013, in Chinese.



## Research Article

# Constitutive Model of Swelling Gypsum Rock

Chongbang Xu,<sup>1,2,3</sup> Xiaojing Gao ,<sup>1,2,3</sup> Kaishun Zhang,<sup>4</sup> Zhiguo Liu,<sup>4</sup> and Fan Zhao<sup>4</sup>

<sup>1</sup>Bridge and Tunnel Research Center, Research Institute of Highway Ministry of Transport, Beijing 100088, China

<sup>2</sup>National Engineering Laboratory of Bridge Structure Safety Technology, Beijing 100088, China

<sup>3</sup>Research Institute of Highway Ministry of Transport Research and Development Center of Transport Industry of Technologies and Equipments for Intelligent Design, Construction and Maintenance of Underwater Tunnel, Ministry of Transport, Beijing 100088, China

<sup>4</sup>The 5th Engineering Co., Ltd. of China Railway 11th Bureau Group, Chongqing 400037, China

Correspondence should be addressed to Xiaojing Gao; [xiaojing.gao1990@foxmail.com](mailto:xiaojing.gao1990@foxmail.com)

Received 3 August 2020; Revised 19 September 2020; Accepted 22 September 2020; Published 8 October 2020

Academic Editor: Zhi Cheng Tan

Copyright © 2020 Chongbang Xu et al. This is an open access article distributed under the Creative Commons Attribution License, which permits unrestricted use, distribution, and reproduction in any medium, provided the original work is properly cited.

Swelling of soft rock, such as gypsum rock, is one of the major threats in tunnel engineering, causing structure damages such as floor heave and inward movement of sidewalls during construction and operation. It is of practical significance to study the swelling mechanical behavior of such rocks by tests. Swelling strain tests and swelling stress tests were performed by swelling test apparatus to study the variation of swelling strain with time and the swelling stress-strain relationship for gypsum rock samples, respectively. Three stages of the swelling strain on the time-strain curve of gypsum rock samples were noticed, which are defined as rapid swelling stage, slow swelling stage, and steady stage. And it was further found that the swelling strain caused in the slow swelling stage is of 76% of the total swelling strain. A constitutive model is proposed to describe the stress-strain relationship in swelling considering the swelling deformation and swelling pressure. The proposed model was verified using test data, which shows good agreements in describing the relationship between swelling strain and swelling stress, also in the conditions of maximum swelling strain and maximum swelling stress under lateral restraint situations.

## 1. Introduction

A growing number of road and railway tunnels in complex geological conditions are being constructed with the implementation of the China Western Development Strategy, which are considered as the important structure of transportation infrastructure. There are large amounts of formations containing swelling rocks, such as gypsum and anhydrite, widespread in Western China [1]. The swelling of rocks causes severe problems in tunnel engineering, such as floor heave, inward movement of sidewalls, and destruction of tunnel linings [2]. The swelling behavior of rocks was usually investigated in laboratory condition. Most laboratory experiments or theoretical analyses on the swelling characteristics of a shield tunnel in swelling rock are under certain hypotheses which have not been verified in actual situation. Currently, it is impossible to predict the swelling behavior of an actual geotechnical project due to our limited

knowledge of the processes involved in the swelling of rock and of the geological, mineralogical, chemical, hydraulic, and mechanical controls of the swelling [3]. Historically, swelling rock studies have been largely concentrated on swelling mechanism [4,5] and factors affecting the swelling [6–9]. Several swelling tests are available on the variation of swelling deformation [10, 11] and swelling constitutive relationship [12–19], which help geotechnical engineers to understand the swelling behavior of rock well.

The swelling of gypsum rocks is a major threat in tunnel engineering, causing serious damage to tunnels and producing high additional costs during tunnel construction and operation. Steiner et al. [20] proposed brittle failure of the anhydrite rock after tunnel excavation to be a major process leading to rock swelling. Liu et al. [21] studied the swelling characteristics of gypsum rock and obtained the relationships between swelling stress and water absorption also initial dry density. Gypsum rocks immersed by fresh water

within different times were investigated according to softening tests by Ren et al. [22]. The variations of uniaxial compressive strength, shear strength, elastic modulus, and Poisson's ratio of gypsum rocks with increasing immersion time were analyzed. The factors influencing the swelling characteristics of swelling rock were investigated [23, 24]; it was found that the density and the initial moisture content of rock significantly affected the swelling characteristics of rock.

Huder and Amberg [25] conducted experiments to investigate the swelling characteristics of swelling rock; a relation between normal stress and normal swelling strain was developed. Based on the experimental results of Huder and Amberg [25], Grob [26] proposed a mathematical model for relating final swelling strain to stress, the swelling strain decreases with logarithm of stress, and maximum swelling occurs when there is a minimum normal stress acting on the specimen. The one-dimensional mathematical model of Grob was expanded to three-dimensional constitutive law by Wittke-Gattemann and Wittke [27]. Einstein [28] examined the available swelling models in the literature and concluded that, although the swelling deformation due to chemical changes may be adequately predicted using available models, but time-dependent swelling models need to be developed from a fundamental knowledge of swelling mechanism. Miao et al. [29] proposed the humidity field theory which provided theories foundation for constitutive model of swelling rock. Based on the humidity stress field theory, Chen et al. [30] carried out swelling tests on anhydrite rock mass and proposed a time-dependent swelling constitutive model, and Yu et al. [31] proposed a physical equation to describe a tunnel's mechanical responses in swelling rock. Most of the swelling constitutive models were developed based on the swelling tests and theoretical analysis, while the condition of rock tested in swelling tests is different from that in actual situation. Up to now, no common opinion is offered about the applicability of constitutive laws with which the swelling phenomena of rocks can be described. A swelling model considering the swelling behavior in engineering is needed to solve actual problems.

Swelling characteristics of gypsum rock varies as diagenesis environment and occurrence varies. Swelling strain tests were conducted to investigate the variation of swelling strain with time for gypsum rock. Based on the results of swelling strain test, swelling stress tests under conditions of controlling the swelling strain were carried out to study the swelling stress-strain relationship for gypsum rock. A formula describing the swelling potential of rock was proposed by introducing virtual swelling stress and virtual swelling strain. A swelling constitutive model was developed and verified using three sets of experimental data from the present research and literature.

## 2. Swelling Test

**2.1. Materials.** The gypsum rock blocks, taken from the surrounding rock of Dugongling tunnel in Shanxi Province, China, were used to prepare the samples of swelling tests. The gypsum rock blocks were transported to the laboratory

and processed into the samples with 50 mm diameter and 36 mm height. The powder of natural gypsum rock passing sieve number 500 was used to test the mineralogical composition of gypsum rock by D8-ADVANCE type X-ray diffractometer. A typical XRD pattern is shown in Figure 1. Results of XRD test in Table 1 show that the gypsum rock is mainly composed of dihydrate gypsum, anhydrite, and quartz. The density and natural moisture content were tested according to the Chinese Soil Test Standard SL237. The measured density of gypsum rock ranged from  $2240 \text{ kg}\cdot\text{m}^{-3}$  to  $2370 \text{ kg}\cdot\text{m}^{-3}$ . The natural moisture content of gypsum rock was 0.12%.

**2.2. Test Procedure.** The samples of gypsum rock were dried under  $220^\circ\text{C}$  condition for 48 hours using a drying oven. The dried samples were put in a sealed bag for sealing. Lateral restraint swelling equipment SCY-2 shown in Figure 2 was used to conduct the swelling strain tests and swelling stress tests. The primary components of SCY-2 are a water container, a rigid snug-fitting restraint ring, dial gage, and a loading device.

The swelling strain is the change in height of the sample divided by the initial height of the sample immersed in water and expressed in percentage. The procedure of the swelling strain test is as follows:

- (1) Apply some Vaseline lotion around the inside of a rigid snug-fitting ring and place the rock sample in the ring. The ring containing the sample is placed in the water container.
- (2) Place the porous disks at the top and bottom of the sample.
- (3) Assemble the water container and dial gage. Check the dial gage and make sure it is precise. The top of the sample is not subjected to any axial load.
- (4) Add enough water into the water container so that swelling can start. The water level should be higher than the surface of upper porous disk.
- (5) Record the axial swelling movement of the sample as a function of time using the dial gage. The swelling test is finished when the axial swelling movement reaches an equilibrium value, that strain is the maximum swelling strain  $\epsilon_0$ .

Swelling stress is the ratio of the force which can inhibit the swelling strain caused by the water seeped into the sample to the sectional area of the sample. Swelling stress tests were performed to measure the swelling stress using balanced pressure method according to the Chinese Soil Test Standard SL237. Four sets of swelling stress tests were conducted to measure the swelling stress by controlling the axial strain equal to 0, 20, 40, and 60 percent of the maximum swelling strain measured in the swelling strain test. The procedure of the swelling stress tests is as follows:

- (1) Apply some Vaseline lotion around the inside of a rigid snug-fitting ring and place the rock sample in the ring. The ring containing the sample is placed in the water container.

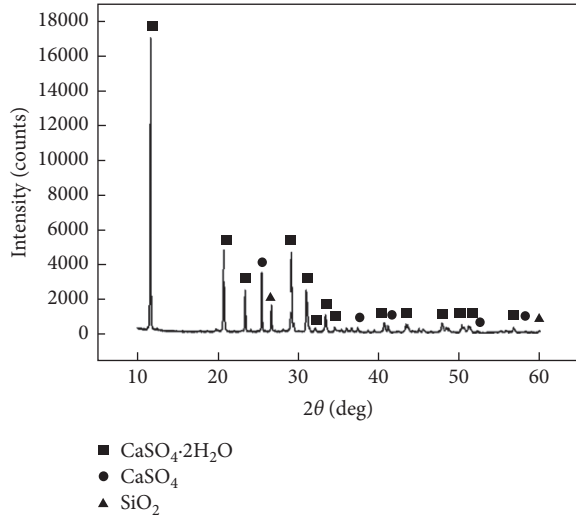


FIGURE 1: XRD pattern of gypsum rock.

TABLE 1: Mineralogical composition of gypsum rock.

Mineral	Composition of mineral (%)
Dihydrate gypsum ( $\text{CaSO}_4 \cdot 2\text{H}_2\text{O}$ )	75
Anhydrite ( $\text{CaSO}_4$ )	20
Quartz ( $\text{SiO}_2$ )	5

- (2) Place the porous disks at the top and bottom of the sample. The pressure sensor is placed at the top of the upper porous disk.
- (3) Assemble the water container, dial gage, and loading device. Check the dial gage and make sure it is precise.
- (4) Add enough water into the water container so that swelling can start. The water level should be higher than the surface of upper porous disk.
- (5) Record the swelling movement by the dial gage. Apply axial load to maintain the swelling movement constant when the swelling strain reaches the required value (0%, 20%, 40%, and 60% maximum swelling strain). The swelling test is finished when the axial swelling stress reaches an equilibrium value, that stress is the swelling stress under the induced swelling strain condition.

The swelling strain is maintained as 0% maximum swelling strain during the swelling stress tests; when the axial stress reaches an equilibrium value, that stress is the maximum swelling stress  $\sigma_0$ .

### 3. Results of the Swelling Test

**3.1. Swelling Strain.** Figure 3 presents a plot showing the variation of swelling strain with time. It can be seen from Figure 3(a) that the procedure of swelling for gypsum rock lasted for about 300 minutes. The maximum swelling strain was equal to 4.397%. Regression works were conducted based on maximizing the coefficient of determination  $R^2$ .

The regression result shows that there is a positive exponential relationship between swelling strain and time:

$$\varepsilon = 5.167 \exp\left(-\frac{36.2}{t}\right), \quad (1)$$

where  $\varepsilon$  is the swelling strain and  $t$  is the swelling time.

The slope of the dash curve (Figure 3(a)) is the derivative of equation (1), which increases first and then decreases with increasing the time as shown in Figure 4. A point of the dash curve represents the maximum derivative of equation (1), which corresponds to the swelling time of 18.1 minutes. The swelling strain of the point corresponding to the swelling time of 18.1 minutes was about 0.56%; this point on the swelling strain versus time curve was named as A. Once the swelling time exceeds 18.1 minutes, the slope of dash curve shows a decreasing trend as the time increases. The data point at which the swelling strain is 90% of the maximum swelling strain was selected as point B shown in Figure 3(a). The data point on the swelling strain versus time curve corresponding to the final time was named as point C. According to the three points, A, B, and C, the swelling strain versus time curve shown in Figure 3(a) can be divided into three parts: rapid swelling stage (path 0A), slow swelling stage (path AB), and stable stage (path BC).

The rapid swelling stage lasted for about 18 minutes. For rapid swelling stage, the swelling deformation was too small to be measured at the first three minutes. The voids in the gypsum rock were filled with the swelling deformations of rock that occurred at the first three minutes. As the filling of swelling deformations in the rock voids, the increment of swelling strain increases rapidly at the rapid swelling stage (Figure 3(b)). The slow swelling stage lasted for about 115 minutes, and the swelling strain ( $\varepsilon$ ) was 3.96%. The swelling strain generated in the slow swelling stage is 76% of the maximum swelling strain. The path BC in Figure 3(a) shows that the increment of swelling deformation gradually tends to zero with an increase in time, and the swelling strain ends up reaching an equilibrium value called the maximum swelling strain  $\varepsilon_0$ .

**3.2. Swelling Stress.** Results of swelling stress under conditions of controlling the swelling strain of 0%, 20%, 40%, and 60% maximum swelling strain are shown in Table 2. The measured maximum swelling stress was 3340 kPa for the gypsum rock tested in the present research.

## 4. Swelling Constitutive Model

**4.1. Development of the Swelling Constitutive Model.** For a certain type of swelling rock, the swelling characteristics are closely related to the intrinsic rock property without considering the environmental factors. The swelling behavior of rock is externally expressed in the form of swelling pressure and swelling deformation which are parameterized by swelling stress and swelling strain, respectively [32]. Different from the rock stress-strain relationship measured under external load, there is a negative correlation between



FIGURE 2: Swelling test apparatus.

swelling stress and swelling strain when considering the swelling behavior of rock. The swelling stress shows a decreasing trend with an increase in swelling strain. For the condition of maximum swelling stress, the swelling stress is the largest and the swelling strain is 0. For the condition of maximum swelling strain, the swelling stress is 0 and the swelling strain is the largest.

Assumptions were made to propose a swelling constitutive model considering the swelling behavior of rock as follows:

- (1) The swelling potential  $Q_s$  of a certain swelling rock only depends on its intrinsic property, which can be expressed by swelling stress or swelling strain.

- (2) Swelling pressure and swelling deformation are the external form of swelling behavior. The swelling potential can be decomposed into swelling potential expressed by swelling pressure  $Q_\sigma$  and swelling potential expressed by swelling deformation  $Q_\epsilon$ , which can be parameterized by swelling stress or swelling strain. The expression of swelling potential of rock is as follows:

$$Q_s = Q_\sigma + Q_\epsilon. \quad (2)$$

- (3) The virtual swelling moduli  $E_{p\epsilon}$  and  $E_{p\sigma}$  were introduced into the expressions of virtual swelling stress ( $\sigma_\epsilon$ , kPa) and virtual swelling strain ( $\epsilon_\sigma$ ), respectively:

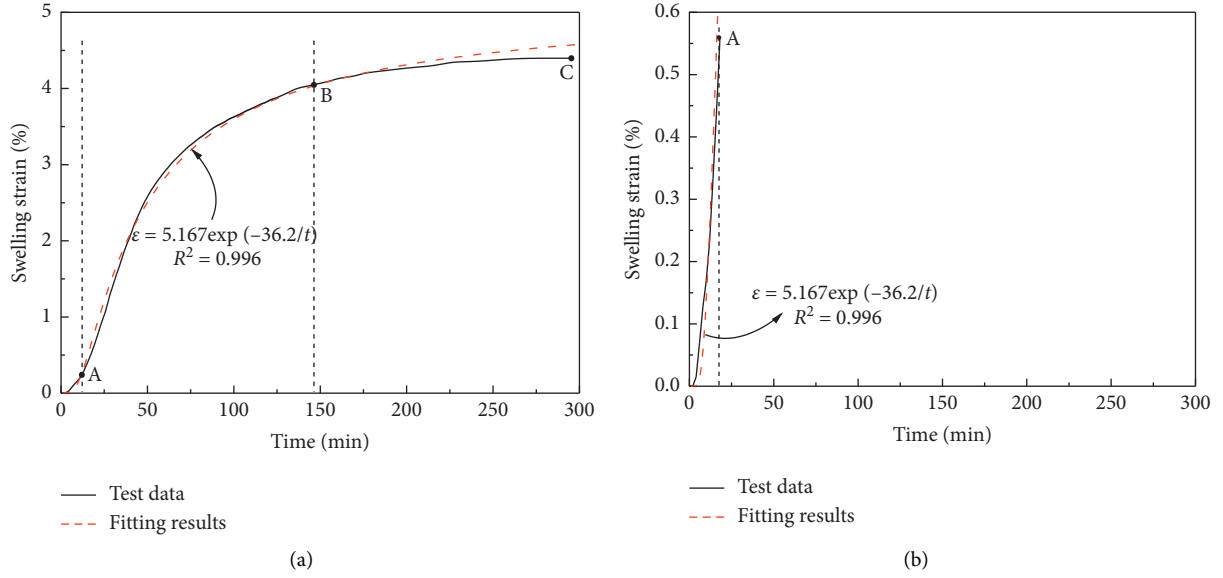


FIGURE 3: Variation of swelling strain with time.

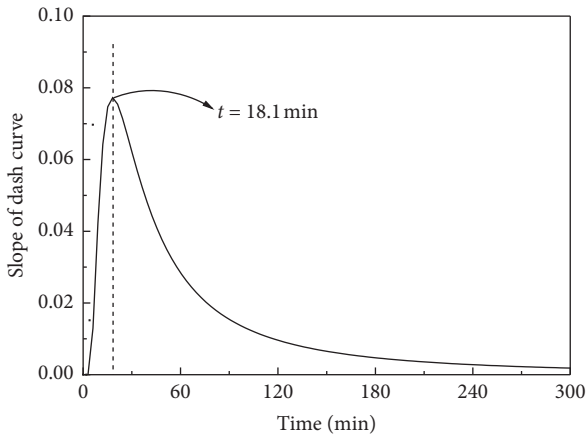


FIGURE 4: Variation of slope of dash curve with time.

TABLE 2: Results of swelling stress test.

$p_s$ (%)	$s$ (mm)	$\epsilon$ (%)	$\sigma$ (kPa)
0	0.000	0.000	3340
20	0.317	0.879	2720
40	0.633	1.759	1970
60	0.950	2.638	1120

$$\sigma_\epsilon = f(\epsilon, E_{p\epsilon}), \quad (3)$$

$$\epsilon_\sigma = f(\sigma, E_{p\sigma}), \quad (4)$$

where  $\epsilon$  is the actual swelling strain, and  $\sigma$  (kPa) is the actual swelling stress.

In this research, the swelling potential was parameterized by swelling stress. The swelling stress-strain relationship was analyzed using the experimental data from the swelling tests under lateral restraint condition. It is assumed that there are

linear relationships between swelling stress and swelling strain, so that equations (3) and (4) become

$$\begin{aligned} \sigma_\epsilon &= E_{p\epsilon}\epsilon, \\ \epsilon_\sigma &= \frac{\sigma}{E_{p\sigma}}. \end{aligned} \quad (5)$$

$Q_\sigma$  and  $Q_\epsilon$  are expressed using the actual swelling stress and virtual swelling stress, respectively, which can be written as follows:

$$Q_\sigma = \sigma, \quad (6)$$

$$Q_\epsilon = E_{p\epsilon}\epsilon. \quad (7)$$

Substituting equations (6) and (7) into (2) leads to

$$Q_s = \sigma + E_{p\epsilon}\epsilon. \quad (8)$$

Equation (8) is a general formula, which can represent the swelling behavior of a certain type of swelling rock under different conditions. The swelling rock under the condition of maximum swelling stress and maximum swelling strain are the two special conditions in equation (8).

The maximum swelling stress  $\sigma_0$  can be measured using the swelling stress test under lateral restraint condition. The axial swelling strain of a sample immersed in water is kept 0 by applying axial load; the maximum loading stress is the maximum swelling stress. For the condition of maximum swelling stress, equation (8) can be expressed as follows:

$$Q_s = \sigma_0. \quad (9)$$

The maximum swelling strain  $\epsilon_0$  is the final swelling strain measured from the swelling strain test under lateral restraint condition. The top of the rock sample is not subjected to any axial load. For the condition of maximum swelling strain, equation (8) can be written as

$$Q_s = E_{pe}\varepsilon_0. \quad (10)$$

For a certain swelling rock, the swelling potential  $Q_s$  is constant under different swelling conditions. Equations (9) and (10) can be rewritten as

$$E_{pe} = \frac{\sigma_0}{\varepsilon_0}. \quad (11)$$

Substituting equations (9) and (11) into (8), one can derive

$$\sigma_0 = \sigma + \frac{\sigma_0}{\varepsilon_0}\varepsilon. \quad (12)$$

Equation (12) can be rewritten as

$$\varepsilon = \varepsilon_0 \left( 1 - \frac{\sigma}{\sigma_0} \right). \quad (13)$$

Equation (13) is the swelling constitutive model developed in present research.

**4.2. Test of the Proposed Model.** The proposed constitutive model (equation (13)) was tested using the experimental data presented in this paper and the collected data from Chang et al. [14] and Liu et al. [11]. In the present research, the measured maximum swelling stress ( $\sigma_0$ ) and maximum swelling strain ( $\varepsilon_0$ ) were 3340 kPa and 4.397%, respectively. Figure 5 compares the measured swelling stress and those calculated using equation (13) for gypsum rock. Equation (13) has a  $R^2$  of 0.993 for the data in Table 2, which indicates that the proposed swelling constitutive model reproduces well the swelling stress-strain relationship for gypsum rock tested in the present research.

The experiments of Chang et al. [14] were conducted on red sandstone taken from Zhuzhou in China to measure the swelling strain by loading the specimen under one certain axial pressure in the condition of lateral restraint. The pressure acted on the rock sample can be considered as the swelling stress. The measured swelling strain is shown in Table 3. The maximum swelling stress ( $\sigma_0$ ) and maximum swelling strain ( $\varepsilon_0$ ) were not measured in the experiments of Chang et al. [14]. Linear interpolation method was used to determine  $\sigma_0$  and  $\varepsilon_0$  according to two sets of data points on line No. 1 and on another line shown in Table 3. For example, the  $\sigma_0$  on line No. 2 was calculated using the data of  $\sigma$  and  $\varepsilon$  on line No. 1 and on line 2, the same as  $\varepsilon_0$ . The average of the calculated  $\sigma_0$  was considered as the parameter of the proposed formula, the same as  $\varepsilon_0$ . The maximum swelling stress ( $\sigma_0$ ) and maximum swelling strain ( $\varepsilon_0$ ) of red sandstone were estimated as 163.10 kPa and 0.923%, respectively.

Figure 6 compares the predictions and measurements for the red sandstone tested by Chang et al. [14]. The  $R^2$  between the measured swelling stress and the calculated swelling stress is 0.975, which reveals that the proposed swelling model can be used to describe the swelling stress-strain relationship for red sandstone.

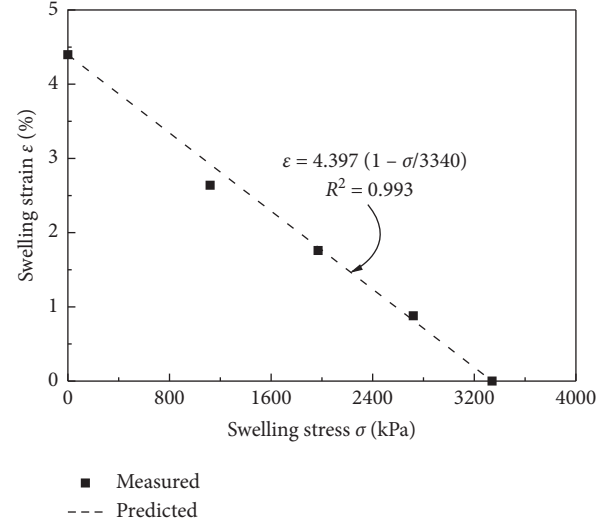


FIGURE 5: Comparison of measured and calculated swelling stress for gypsum rock.

TABLE 3: Experimental data of Chang et al. [14].

No.	$\sigma$ (kPa)	$\varepsilon$ (%)	$\sigma_0$ (kPa)	$\varepsilon_0$ (%)
1	38.86	0.7019	—	—
2	48.58	0.6462	161.34	0.924
3	68.09	0.5162	149.34	0.949
4	107.04	0.3086	160.54	0.926
5	146.05	0.1733	181.19	0.894

Liu et al. [11] studied the swelling properties of remolded rock in Middle Route Project of South-to-North Water Diversion using swelling strain tests and swelling stress tests. The swelling stress of rock was measured by remaining the swelling strain constant at 0%, 1%, 2%, and 3% for swelling rock with different initial water content  $w$ , 14%, 17%, and 20% (Table 4). The maximum swelling stress of rock with initial water content of 14%, 17%, and 20% was 1044, 1014, and 924 kPa, respectively. The maximum swelling strain was not measured by Liu et al. [11], which was calculated based on the experimental data shown in Table 4 using linear interpolation method mentioned in previous paragraph. The calculated maximum swelling strain for rock with initial water content of 14%, 17%, and 20% was 6.93%, 6.72%, and 6.67%, respectively. The variation of calculated maximum swelling strain with initial water content indicates that an increase in the initial water content leads to a decrease in swelling strain in the same external load state. This is consistent with the finding of Wang et al. [23].

Figure 7 shows the calculated and measured swelling strain for swelling rock tested by Liu et al. [11]. The  $R^2$  between the measured and calculated swelling strain for the three sets of tests is larger than 0.95, which reveals that the proposed swelling constitutive model performs well in describing the swelling stress-strain relationship for remolded swelling rock.

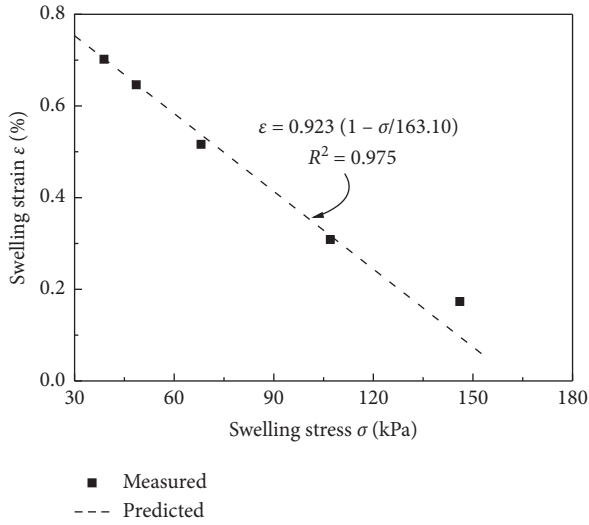


FIGURE 6: Comparison of measured and calculated swelling test data for red sandstone of Chang et al. [14].

TABLE 4: Experimental data of Liu et al. [11].

No.	ε (%)	σ (kPa)		
		w = 14%	w = 17%	w = 20%
1	0	1044	1014	924
2	1	886	846	758
3	2	740	711	654
4	3	616	604	560

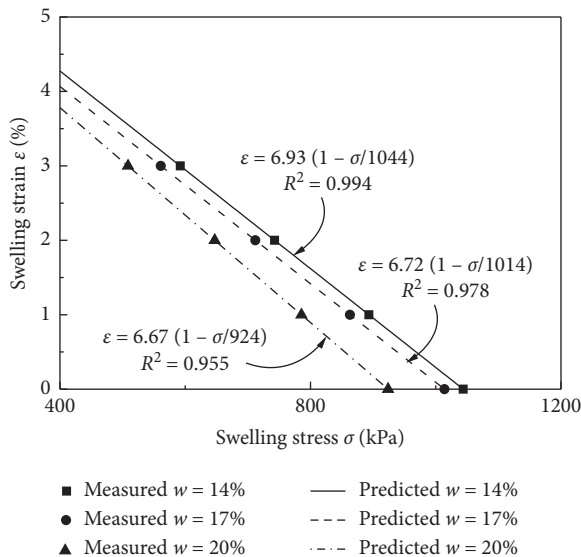


FIGURE 7: Comparison of measured and calculated swelling test data for swelling rock of Liu et al. [11].

### 5. Discussion

A constitutive model (equation (14)) proposed based on the experimental results of Huder and Amberg [25] was widely used in describing the swelling stress-strain relationship. The difference between the proposed model in present research

and the Huder–Amberg model was discussed. The Huder–Amberg model is written as follows:

$$\epsilon = K \left( 1 - \frac{\lg \sigma}{\lg \sigma_0} \right), \quad (14)$$

where  $K$  is the axial swelling strain when the swelling stress  $\sigma$  is 0.1 MPa.

The proposed constitutive model was compared with the Huder–Amberg model; it can be found that the expressions of the two models are similar. There is a linear relationship between swelling stress and swelling strain in equation (13), and the swelling strain shows a linear relationship with logarithm swelling stress in the Huder–Amberg model.

Some disadvantages of the Huder–Amberg model were found based on the analysis of equation (14). Variation of axial swelling strain varies with axial swelling stress when the maximum swelling stress  $\sigma_0$  is larger than 10 MPa. For example, when the axial swelling stress  $\sigma$  is larger than 1 MPa,  $\lg \sigma$  is larger than 0, the value of  $1 - \lg \sigma / \lg \sigma_0$  is less than 1. While, in the case of  $\sigma$  less than 1 MPa, the value of  $1 - \lg \sigma / \lg \sigma_0$  is larger than 1.

In the case of  $0 < \sigma < 0.1$  MPa and  $\sigma_0 > 1$  MPa, the calculated axial swelling strain is larger than the value of  $K$ , which is not in accordance with the definition of  $K$ . It is difficult to describe the stress-strain relationship in the case of  $\sigma \approx 0$ . The calculated swelling strain will be infinite if swelling stress is approximately 0 MPa, which is not consistent with the results of swelling test. The Huder–Amberg model is shown to be an inappropriate constitutive model to describe the swelling stress-strain relationship in the case of  $0 < \sigma < 0.1$  MPa. The analyzed disadvantages of the Huder–Amberg model did not exist in the proposed model (equation (13)).

The constitutive model (equation (13)) was proposed depending on the relationship between virtual swelling stress and swelling strain shown in equation (3) and the relationship between virtual swelling strain and swelling stress shown in equation (4). A linear assumption was introduced in equation (3) and equation (4), which leads to a linear relation between swelling strain and swelling stress. Different types of swelling rock show different swelling stress-strain relationships; a linear stress-strain relationship will not be suitable for all types of swelling rock. In order to optimize the proposed constitutive model, additional swelling tests and research need to be conducted.

### 6. Conclusions

Swelling strain and swelling stress are the main test results to evaluate the characteristics of swelling rock. In order to study the properties of swelling rock, the swelling strain test and swelling stress tests were performed on gypsum rock samples drilled from a tunnel jobsite in Shanxi province, China. The study on the swelling constitutive model is an important issue for swelling rock. Based on the experimental data of swelling stress tests, a constitutive law describing the relationship between swelling strain and swelling stress was proposed by introducing the virtual swelling strain and

virtual swelling stress. As a result of this study, the following conclusions were derived:

- (1) The measured maximum swelling strain of gypsum rock sample in the swelling strain test was 4.397%. Three stages of the swelling strain of gypsum rock were defined by the tests results, namely, rapid swelling stage, slow swelling stage, and steady stage. The slow swelling stage lasted for about 115 minutes in which the swelling strain accounted for 76% of the total swelling strain.
- (2) The measured maximum swelling stress of gypsum rock was 3340 kPa. There was a negative linear relationship between swelling stress and swelling strain for the gypsum rock tested in the present research.
- (3) The constitutive model was verified using the experimental data from the present research and the collected data from other literatures. The proposed constitutive model performs well in describing the variation of swelling strain with swelling stress for different types of swelling rock. The developed model has good agreements with test data in the condition of maximum swelling stress and maximum swelling strain.

In order to optimize the proposed constitutive model, additional swelling tests and research needs would be further conducted.

## Data Availability

The data used to support the findings of this study are available from the corresponding author upon request.

## Conflicts of Interest

The authors declare that they have no conflicts of interest regarding the publication of this paper.

## Acknowledgments

This work was financially supported by the Special Science and Technology Innovation fund of Research Institute of Highway Ministry of Transport (Grant no. 2019-C505), the Central Public-Interest Scientific Institution Basal Research Fund (Grant no. 2020-9032), and the Science and Technology Project of Department of Transportation of Shanxi Province (Grant no. 2017-1-6).

## References

- [1] M. Lei, L. Peng, C. Shi, and S. Wang, "Experimental study on the damage mechanism of tunnel structure suffering from sulfate attack," *Tunnelling and Underground Space Technology*, vol. 36, pp. 5–13, 2013.
- [2] D. Parsapour and A. Fahimifar, "Prediction of swelling rocks strain in tunneling," *Geotectonics*, vol. 50, no. 3, pp. 336–346, 2016.
- [3] C. Butscher, T. Mutschler, and P. Blum, "Swelling of clay-sulfate rocks: a review of processes and controls," *Rock Mechanics and Rock Engineering*, vol. 49, no. 4, pp. 1533–1549, 2016.
- [4] H. H. Einstein, "Tunnelling in difficult ground? swelling behaviour and identification of swelling rocks," *Rock Mechanics and Rock Engineering*, vol. 29, no. 3, pp. 113–124, 1996.
- [5] A. A. Jeschke, K. Vosbeck, and W. Dreybrodt, "Surface controlled dissolution rates of gypsum in aqueous solutions exhibit nonlinear dissolution kinetics," *Geochimica et Cosmochimica Acta*, vol. 65, no. 1, pp. 27–34, 2001.
- [6] X. Ou, Y. Tang, Z. Zhong, and J. Su, "Test research on expansive force under small deformation of remolded expansive rock and soil," *Chinese Journal of Rock Mechanics and Engineering*, vol. 32, no. 5, pp. 1067–1072, 2013.
- [7] M. R. Vergara and T. Triantafyllidis, "Influence of water content on the mechanical properties of an argillaceous swelling rock," *Rock Mechanics and Rock Engineering*, vol. 49, no. 7, pp. 2555–2568, 2016.
- [8] S. Zhang, X. Leng, Q. Sheng, B. Li, and Y. Zhou, "Swelling and shrinkage characteristics study of lushu expansive rock under dry and wet circulation," *Rock and Soil Mechanics*, vol. 40, no. 11, pp. 4279–4288, 2019.
- [9] Z. C. Tang, Q. Z. Zhang, and J. Peng, "Effect of thermal treatment on the basic friction angle of rock joint," *Rock Mechanics and Rock Engineering*, vol. 53, no. 4, pp. 1973–1990, 2020.
- [10] M. E. Bilir, D. Sari, Y. V. Muftuoglu, L. D. Suits, and T. C. Sheahan, "A computer-controlled triaxial test apparatus for measuring swelling characteristics of reconstituted clay-bearing rock," *Geotechnical Testing Journal*, vol. 31, no. 4, pp. 279–284, Article ID 100755, 2008.
- [11] J. D. Liu, Q.-Y. Li, and B.-W. Gong, "Swelling properties of expansive rock in middle route project of south-to-north water diversion," *Chinese Journal of Geotechnical Engineering*, vol. 33, no. 5, pp. 826–830, 2011.
- [12] K. Wang and X. Diao, "Secondary development study of swelling rock humidity stress field constitutive model," *Chinese Journal of Rock Mechanics and Engineering*, vol. 34, no. 2, pp. 3781–3792, 2015.
- [13] Z. C. Tang and Y. Y. Jiao, "Choosing appropriate appraisal to describe peak spatial features of rock joint profiles," *International Journal of Geomechanics*, vol. 20, no. 4, Article ID 04020021, 2020.
- [14] W. Chang, W. Gao, X. Tang, Z. Zhang, and Z. Zhang, "Experimental study of swelling constitutive model of red sandstone," *Journal of Hunan University of Arts and Science*, vol. 31, no. 3, pp. 71–76, 2019.
- [15] G. Anagnostou, "A model for swelling rock in tunnelling," *Rock Mechanics and Rock Engineering*, vol. 26, no. 4, pp. 307–331, 1993.
- [16] X.-L. Liu, S.-J. Wang, E.-Z. Wang, and Q. Xue, "Study on time-dependent swelling constitute relation of swelling rock," *Shuili Xuebao*, vol. 37, no. 2, pp. 195–199, 2006.
- [17] J. Zou, Y.-Y. Jiao, Z. Tang, Y. Ji, C. Yan, and J. Wang, "Effect of mechanical heterogeneity on hydraulic fracture propagation in unconventional gas reservoirs," *Computers and Geotechnics*, vol. 125, Article ID 103652, 2020.
- [18] M. E. Bilir, Y. D. Sari, A. Özarslan, M. Geniş, and İ. Sel, "Determination of the relationship between uniaxial and triaxial swelling equations for clay bearing rocks," *Bulletin of Engineering Geology and the Environment*, vol. 72, no. 3–4, pp. 565–577, 2013.
- [19] C. Butscher, P. Huggenberger, and E. Zechner, "Impact of tunneling on regional groundwater flow and implications for



- swelling of clay-sulfate rocks,” *Engineering Geology*, vol. 117, no. 3-4, pp. 198–206, 2011.
- [20] W. Steiner, P. K. Kaiser, and G. Spaun, “Role of brittle fracture on swelling behavior of weak rock tunnels: hypothesis and qualitative evidence,” *Geomechanics and Tunnelling*, vol. 3, no. 5, pp. 583–596, 2011.
- [21] Y.-M. Liu, H.-M. Yu, C. Wang, and C.-L. Wang, “Research on mechanism of damage of anhydrock in dolomite layer to tunnel structure,” *Rock and Soil Mechanics*, vol. 32, no. 9, pp. 2704–2708, 2011.
- [22] S. Ren, G.-L. Deng, J. Wu, and J. Chen, “Immersion tests on gypsum rocks using fresh water,” *Rock and Soil Mechanics*, vol. 38, no. 4, pp. 943–950, 2017.
- [23] J.-S. Wang, G. Wu, Z.-M. Zhao, L. Li, Q. Lian, and L. He, “Experimental study on factors influencing the expansive properties of disturbed swelling rock,” *Soil Mechanics and Foundation Engineering*, vol. 57, no. 1, pp. 84–91, 2020.
- [24] J. Liu and H. Zhang, “Water content influence on properties of red-layers in Guangzhou metro line, China,” *Advances in Materials Science and Engineering*, vol. 2017, Article ID 4808909, 12 pages, 2017.
- [25] J. Huder and G. Amberg, “Quellung in mergel, opalinuston und anhydrit (swelling in marl, opalinus clay and anhydrite),” *Schweizer Bauzeitung*, vol. 88, no. 43, pp. 975–980, 1970.
- [26] H. Grob, “Schwelldruck im belechtunnel,” in *Proceedings of the Berichte, Internationales Symposium für Untertagebau*, pp. 99–119, Luzern, Switzerland, September 1972.
- [27] P. Wittke-Gattermann and M. Wittke, “Computation of strains and pressures for tunnels in swelling rocks,” *Tunnelling and Underground Space Technology*, vol. 19, no. 4-5, pp. 422–423, 2004.
- [28] H. Einstein, “Comments and recommendations on design and analysis procedures for structures in argillaceous swelling rock,” *International Journal of Rock Mechanics and Mining Sciences & Geomechanics Abstracts*, vol. 31, no. 5, pp. 535–546, 1994.
- [29] X. Miao, A.-H. Lu, X. Mao, and D. Zhang, “Numerical simulation for roadways in swelling rock under coupling function of water and ground pressure,” *Journal of China University of Mining & Technology*, vol. 12, no. 2, pp. 120–125, 2002.
- [30] F. Chen, J. Wu, S. Ren, X. Ouyang, L. Wang, and J. Fan, “The swelling tests of anhydrite based on the humidity stress field theory,” *Rock and Soil Mechanics*, vol. 39, no. 8, pp. 2723–2731, 2018.
- [31] J. Yu, G. Liu, Y. Cai, J. Zhou, S. Liu, and B. Tu, “Time-dependent deformation mechanism for swelling soft-rock tunnels in coal mines and its mathematical deduction,” *International Journal of Geomechanics*, vol. 20, no. 3, Article ID 04019186, 2020.
- [32] T. Y. Elkady, M. F. Abbas, and M. A. Shamrani, “Behavior of compacted expansive soil under multi-directional stress and deformation boundary conditions,” *Bulletin of Engineering Geology and the Environment*, vol. 75, no. 4, pp. 1741–1759, 2016.